# Transactions of the ASME®

# Journal of Engineering for Gas Turbines and Power

Published Quarterly by The American Society of Mechanical Engineers
VOLUME 113 • NUMBER 1 • JANUARY 1991

Technical Editor,
**G. K. SEROVY**
Associate Technical Editors
Advanced Energy Systems
**M. J. MORAN**
Environmental Control
**H. E. HESKETH**
Fuels and Combustion Technologies
**D. W. PACER**
Gas Turbine
**S. A. MOSIER**
Internal Combustion Engine
**J. A. CATON**
Nuclear Engineering
**S. M. CHO**
Power
**R. W. PORTER**

**BOARD ON COMMUNICATIONS**
Chairman and Vice-President
**M. E. FRANKE**

Members-at-Large
**W. BEGELL**
**T. F. CONRY**
**T. DEAR**
**R. L. KASTOR**
**R. MATES**
**E. M. PATTON**
**R. E. REDER**
**R. D. ROCKE**
**A. VAN DER SLUYS**
**A. J. WENNERSTROM**
**W. O. WINER**
**B. ZIELS**

President, **A. E. BERGLES**
Executive Director,
**D. L. BELDEN**
Treasurer, **ROBERT A. BENNETT**

**PUBLISHING STAFF**
Mng. Dir., Publ.
**CHARLES W. BEARDSLEY**
Managing Editor,
**CORNELIA MONAHAN**
Sr. Production Editor,
**VALERIE WINTERS**
Production Assistant,
**MARISOL ANDINO**

**Transactions of the ASME, Journal of Engineering for Gas Turbines and Power** (ISSN 0022-0825) is published quarterly (Jan., Apr., July, Oct.) for $125.00 per year by The American Society of Mechanical Engineers, 345 East 47th Street, New York, NY 10017. Second class postage paid at New York, NY and additional mailing offices. POSTMASTER: Send address changes to Transactions of the ASME, Journal of Engineering for Gas Turbines and Power, c/o THE AMERICAN SOCIETY OF MECHANICAL ENGINEERS, 22 Law Drive, Box 2300, Fairfield, NJ 07007-2300.
**CHANGES OF ADDRESS** must be received at Society headquarters seven weeks before they are to be effective. Please send old label and new address.
**PRICES:** To members, $36.00, annually; to nonmembers, $125.00.
Add $15.00 for postage to countries outside the United States and Canada.

**STATEMENT from By-Laws.** The Society shall not be responsible for statements or opinions advanced in papers or . . . printed in its publications (B 7.1, para. 3).
**COPYRIGHT** © 1991 by The American Society of Mechanical Engineers. Reprints from this publication may be made on condition that full credit be given the TRANSACTIONS OF THE ASME—JOURNAL OF ENGINEERING FOR GAS TURBINES AND POWER, and the author, and date of publication be stated.

**INDEXED** by Applied Mechanics Reviews and Engineering Information, Inc.

## TECHNICAL PAPERS

**Contents Continued on p. 19**

Downloaded 03 Jun 2010 to 171.66.16.159. Redistribution subject to ASME license or copyright; see http://www.asme.org/terms/Terms_Use.cfm

(Contents Continued)

ANNOUNCEMENTS

**S. F. Powel IV**
Manager, F404 Advanced Programs,
GE Aircraft Engines,
Lynn, MA 01910

# On the Leading Edge: Combining Maturity and Advanced Technology on the F404 Turbofan Engine

*The overall design concept of the F404 afterburning turbofan engine is reviewed together with some of the lessons learned from over 2 million flight hours in service. GE Aircraft Engines' derivative and growth plans for the F404 family are then reviewed including the "Building Block" component development approach. Examples of advanced technologies under development for introduction into new F404 derivative engine models are presented in the areas of materials, digital and fiber optic controls systems, and vectoring exhaust nozzles. The design concept and details of the F404-GE-402, F412-GE-400, and other derivative engines under full-scale development are described. Studies for future growth variants and the benefits of the F404 derivative approach to development of afterburning engines in the 18,000-24,000 lb (80-107 kN) thrust class and non-afterburning engines in the 12,000-19,000 lb (53-85 kN) class are discussed.*

## Introduction

The medium thrust class of fighter aircraft engines, from 14,000 to 22,000 pounds (62-98 kN) thrust, has been the beneficiary of the most modern, innovative technology available over the last 35 years because engines in this thrust class have powered the majority of front line Western fighter/attack aircraft produced in this period. State-of-the-art second generation fighter engine designs, developed beginning in the mid-1950s, were characterized by pressure ratios in the 10-15 range, turbine inlet temperatures of 1700-1900°F (1200-1300 K) and thrust-to-weight ratios of 4-5. State-of-the-art-third-generation engines developed since the 1970s are characterized by pressure ratios in the 25-30 range, turbine inlet temperatures of 2400-2950°F (1600-1900 K), and thrust-to-weight ratios in the 7-10 range. This paper traces the F404 engine family evolution from its inception to models currently under development and into growth derivatives projected for development in the 1990s up to the 9-10 thrust-to-weight ratio class. The planned, continuous infusion into F404 model engines of advanced technology derived from other F404, military, or commercial engine programs at GE Aircraft Engines (GEAE) is designed to achieve growth in pressure ratio, turbine inlet temperature and thrust-to-weight ratio, while maintaining or improving the outstanding operability, reliability, maintainability and durability of the basic F404 engine, matured in over 2 million flight hours of experience.

The benefits offered by F404 derivatives in the 18,000-24,000 lb (80-107 kN) afterburning thrust class and the 12,000-19,000 lb (53-85 kN) non-afterburning thrust class, in contrast to development of completely new engines, are:

- economic, low-risk qualification programs
- an optimal balance of advanced technology and proven component design
- low engine unit cost due to high volume production
- mature engine reliability, maintainability, durability, and life cycle cost

## Review of F404 Technical Design Concept

Full-Scale Development (FSD) of the 16,000 lb (71 kN) thrust F404-GE-400 afterburning turbofan (Fig. 1) began in

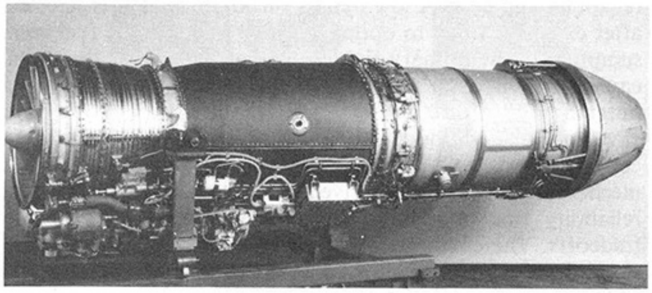

Fig. 1 F404-GE-400 augmented turbofan engine

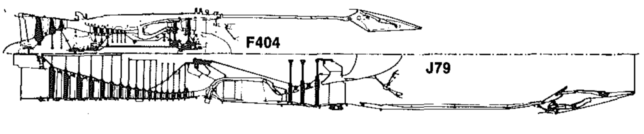

F404 Has

- Same Thrust
- One–Half The Weight
- Three–Quarters The Length
- One–Third Fewer Parts

Fig. 2 F404 technology payoff

---

Contributed by the International Gas Turbine Institute and presented at the 35th International Gas Turbine and Aeroengine Congress and Exposition, Brussels, Belgium, June 11-14, 1990. Manuscript received by the International Gas Turbine Institute February 14, 1990. Paper No. 90-GT-149.

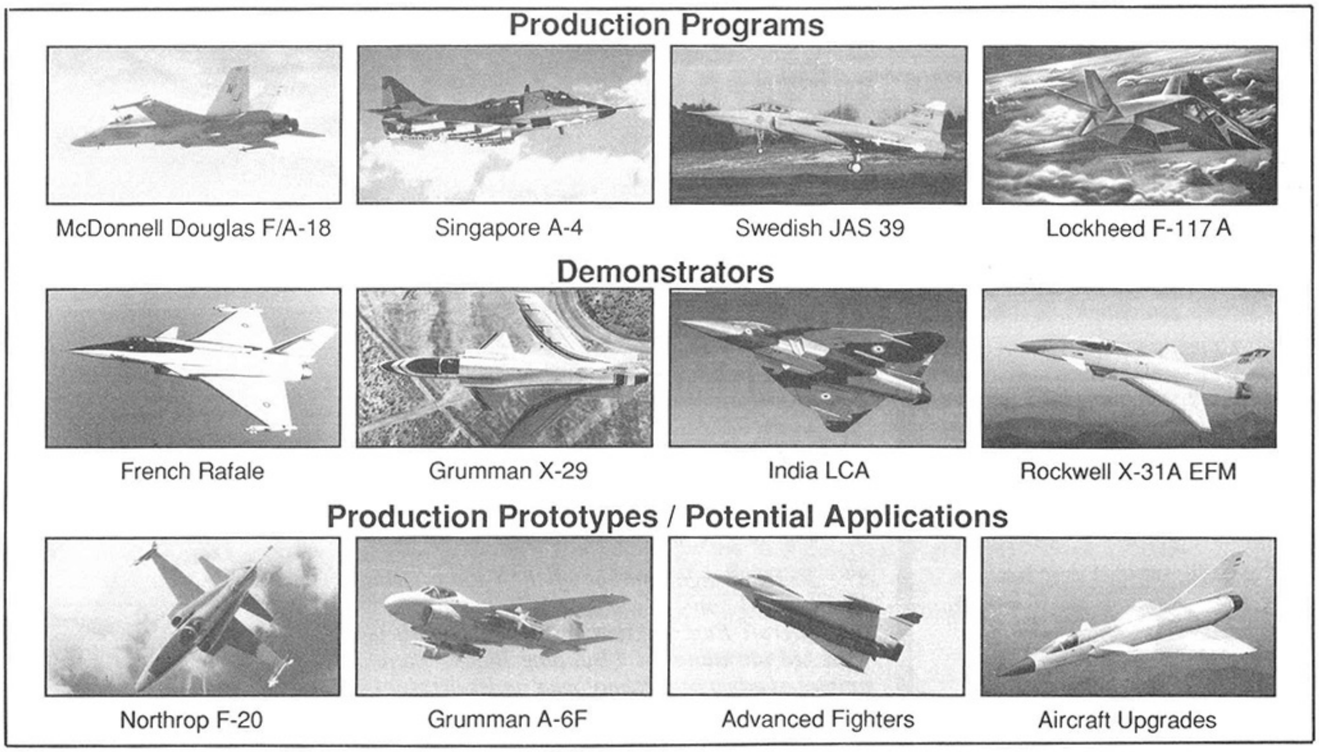

Fig. 3 F404 aircraft applications

1975 for the U.S. Navy/McDonnell Douglas F/A-18 Hornet, following a successful prototype development and flight test program as the YJ101 engine for the Northrop YF-17 aircraft. The highly simplified low-bypass, two-spool turbofan engine design layout includes three frames, three fan stages, seven compressor stages, and single-stage high and low-pressure turbines, made possible by advanced technology aerodynamics, materials, cooling design, and control systems. The F404 design concept was revolutionary at its inception due to a balanced approach that traded the ultimate in achieveable engine thrust-to-weight ratio to accomplish the higher priority objectives of operability, reliability, maintainability, durability, and low cost. A deliberate effort was made to reduce parts count dramatically over the previous generation of engines (1/3 fewer parts than the J79; see Fig. 2) because it was recognize that parts count was a direct driver of engine reliability and cost. A low bypass turbofan cycle was selected after extensive study to optimize thrust and specific fuel consumption in the primary fighter combat regimes of the flight envelope. This cycle also resulted in stall-free operation and outstanding afterburner performance throughout the envelope, in addition to the installation benefits of a self-cooled engine skin. The simplified engine aerodynamic and mechanical layout was arrived at following cost, weight, reliability and maintainability (R&M), and performance tradeoffs. The emphasis on low cost and R&M also drove a simplified control system. A complete description of the F404 FSD Program and design emphasis may be found from Rapp (1982). The basic design layout and development philosophy of the F404 are being emulated in other fighter aircraft engine designs projected to enter service in the 1990s.

## Program Status

Over 2000 engines have been shipped since the F404's first flight powering the F/A-18 in Nov. 1978. The F404 or its derivatives have been specified on five production aircraft programs: the F/A-18 (Engine Models: F404-GE-400; F404-GE-402), the Swedish JAS 39 Gripen (F404/RM12), the Singapore A-4S-1 Super Skyhawk (F404-GE-100D), the Lockheed F-117A (F404-GE-F1D2) and the McDonnell Douglas/General Dynamics A-12 (F412-GE-400). In addition, F404 derivatives have powered or are under development for demonstrator and production prototype programs including the French Rafale (F404-GE-400), Indian Light Combat Aircraft (F404/F2J3), Northrop F-20 Tigershark (F404-GE-100), Grumman A-6F Intruder (F404-GE-400D) and X-29 Forward Swept Wing Demonstrator (F404-GE-400), and Rockwell/MBB X-31 Enhanced Fighter Maneuverability Demonstrator (F404-GE-400); see Fig. 3.

In the more than 2 million engine hours flown in 10 years of operation, and in over 54,000 factory engine test hours logged on all models, the F404 has proven the success of the original design concept. Its excellent field reliability as measured by the key indices of Shop Visit Rate (SVR) and In-Flight Shut Down (IFSD) has been the standard of the industry, as shown in Fig. 4. The simple design, modular construction, and careful layout of controls and accessories has resulted in exceptional maintainability, both installed and in the shop. The stall-free performance without throttle restrictions has been consistently praised by pilots. And the ongoing initiatives to reduce engine manufacturing cost have resulted in a continuous decline in selling price to the customer, as shown in Fig. 5.

The F404 continues to be selected for new installations because of its outstanding operational performance, reliability and maintainability characteristics, its low development, acquisition, and operating cost, and its flexible adaptability to the varying mission requirements imposed by the various aircraft installations.

## Lessons Learned in Operational Experience

Several key lessons learned from operational use of the F404 relative to the initial design are described below and illustrated in Fig. 6.

The afterburner nozzle outer flaps and seals experienced early joint wear caused by a combination of the unique configuration of the F/A-18 boattail and the leading edge extension (LEX) vortices, which also excited the aircraft vertical tails. The impact of this type of installation effect is extremely difficult to predict, model, or factory engine test cost-effectively. Instead, operational experience was used to develop the shingled outer flap design, which combined the flap and seal into a single part while incorporating improved joints and wear strips. These improvements will be included in future F404 engine designs.

The afterburner liner design has been proven to have good aerothermodynamic performance and life characteristics. Unlike previous designs such as the original J85, which used axial rods for assembly of the liner sections and for buckling strength, the F404 liner is a brazed band assembly, which depends upon circumferential stiffening rings for buckling strength. As the F404 reached the 1 million engine flight hour plateau, several incidents occurred in the high Mach number/low altitude regime, in which a high pressure differential across the liner resulted in buckling of the liner. The problem was solved by retrofitting the liners with increased strength stiffening rings, which have flown without incident since 1988.

At virtually the same 1 million engine flight hour mark in 1987, compressor rotor blade failures caused by aeromechanical vibration, foreign object damage (FOD), or maintenance assembly errors resulted in enough debris to rub through the casing wear coating and cause friction-induced titanium fires, which burned/melted through the titanium compressor casing and fan outer duct. The problems were solved by the introduction of improved design stage 1 and 3 compressor blades and variable geometry vane lever arms. A unique viton rubber coating was also applied to the inside of the titanium outer duct. This coating was proven in bench testing to inhibit the melt-through of this duct, thereby reducing potential damage to the aircraft. The viton-coated titanium outer duct was a short-term solution to the molten titanium containment problem and was retrofitted on all field engines. It has now been replaced in production by a PMR-15 composite outer duct. This part, in development for several years under a U.S. Navy sponsored Manufacturing Technology program to reduce weight and cost relative to the chemically milled titanium version, has proven to have superior fire resistance properties. In addition, an M152 steel compressor casing has been qualified to replace the titanium casing, which will eliminate the possibility of titanium fires from jammed debris. The change to the steel casing and composite duct results in a net weight increase of only one pound.

The lesson learned from these two relatively high time failures is that subtle changes in aircraft usage and engine characteristics over time can result in problems that could not have been discovered under even the most exhaustive factory test program. The advantage of the mature F404 engine is that these subtleties have been discovered through operational experience and are being taken into account with relative confidence in designing subsequent derivative engines, such as the F404-GE-402 and F412-GE-400. As shown in Fig. 4, F404 reliability was back on track in 1989, proving the effectiveness of these design improvements.

The F404 control system has also contributed to the success of the engine by being easily adaptable to various afterburning and non-afterburning aircraft installations, by its "no-trim" capability and by its successful balance of performance, stall margin, and life requirements. The F404 control system was designed to schedule core and fan speed and limit turbine exhaust temperature (T5). As the engine ages, fan speed and the

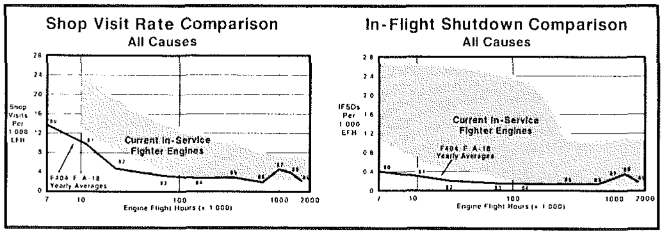

Fig. 4 F404 reliability

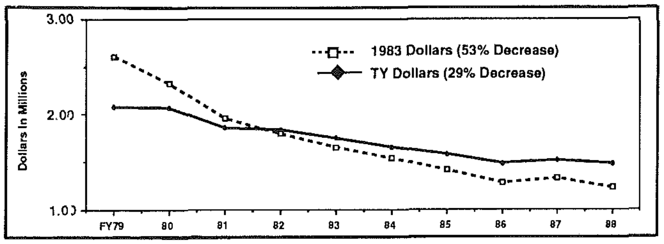

Fig. 5 F404 production engine cost

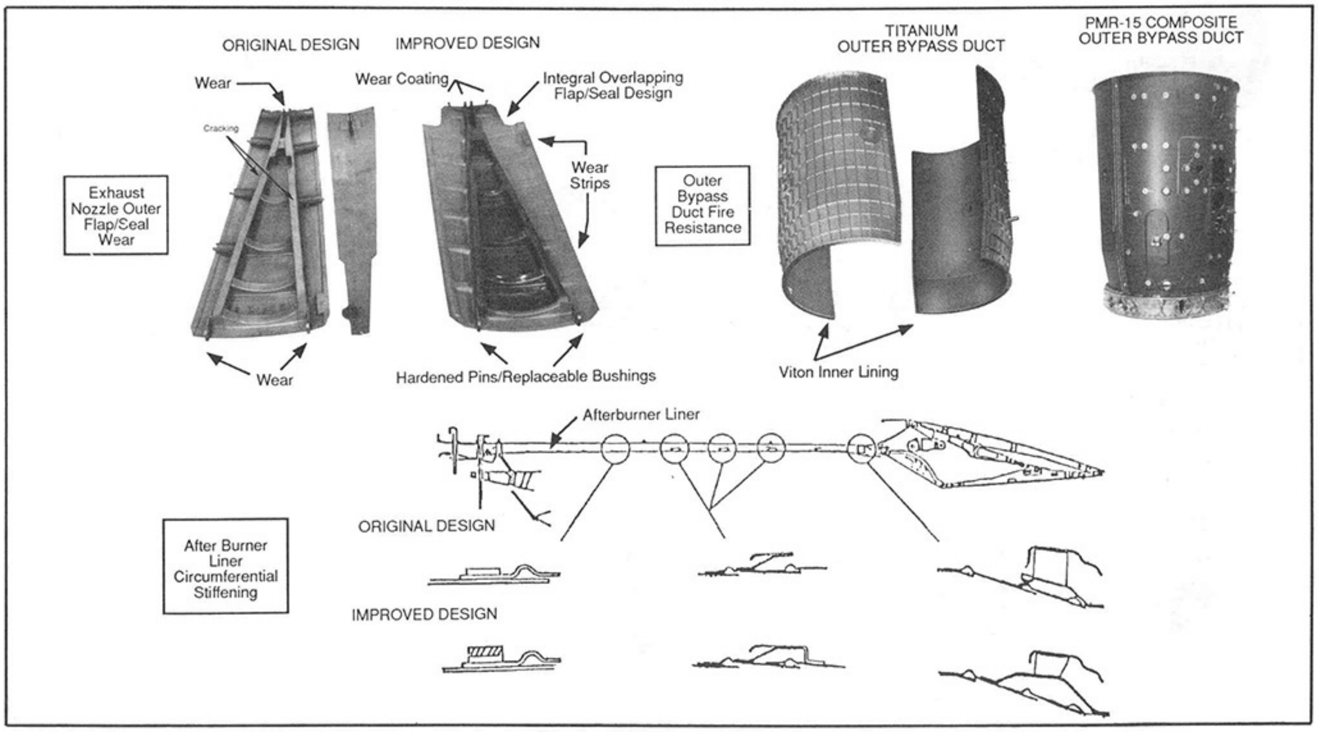

Fig. 6 F404 lessons learned

T5 limit are maintained by increasing the variable exhaust nozzle area, resulting in a lower fan operating line, which eventually results in reduced engine performance. With constant T5, engine operability and hot section life are maintained. In actual operation, the F404 control concept has been extremely successful. Although fleet average age is over 1000 flight hours, engine performance and stall-free operability remain outstanding and the full 2000 hour hot section life is expected to be achieved.

In summary, the F404 design has proven to be very flexible in adapting to its many aircraft installations without major changes to the basic design. The highly mature design of the engine, building on the experience over 2 million flight hours, has also proven to be a strong base from which to launch reliable, low-cost derivatives, as described in the following sections.

## F404 Advanced Technology Plan

A systematic, product-oriented component technology development plan has been in place since the early 1980s to integrate advanced technology into current models and growth derivatives of the F404 in order to keep the engine on the leading edge of technology in its thrust class. This technology plan includes initiatives in the following areas:

- *Growth Component/Engine Development and Test:* For example, advanced fans, core engines, combustors and afterburners.
- *Advanced System Technology Development:* For example, single engine reliability features, Full Authority Digital Electronic Controls (FADEC), fiber optic control systems technology, and Axisymmetric Vectoring Exhaust Nozzles (AVEN).
- *Advanced Manufacturing/Materials Technologies:* For example, thermal barrier coatings, complex structural and airfoil castings, composites, ceramics, monocrystal turbine blade and nozzle materials, and low aspect ratio integrally bladed disks (blisks).

These initiatives are combined with identified product requirements to create F404 engine derivatives of varying thrust levels. The F404/RM12, F404-GE-402 Enhanced Performance Engine (EPE), and the F412-GE-400 are examples of the first phase of this growth plan now under Full-Scale Development. The following sections of this paper describe these three components of the F404 advanced technology plan, and ways they have been combined to define afterburning and nonafterburning F404 derivatives for the mid-1990s.

**Growth Component/Engine Development and Test.** GE Aircraft Engines uses the proven "building block" approach to the development of growth engine derivatives of the F404. It should also be noted that the F404 draws on the technology base developed in other GEAE military engines such as the F101, F110, and F120 and from commercial engine experience on the CF6 and CFMF56. For example, the original F404 compressor design was derived from the F101 engine and the F110 fan was subsequently derived from the F404 fan design. Subcomponent designs also draw on this technology base. For example, the shingled outer flap nozzle design described in the F404-GE-400 lessons learned section of this paper was developed from the successful F110 nozzle design. Higher temperature capability turbine materials to be used on F404 derivatives have also been developed for and are in production on other GEAE military and commercial engine programs; see Fig. 7.

Since 1983, GEAE has conducted advanced fan, compressor, core engine, and full engine tests under the F404/RM12 and GEAE/U.S. Government-sponsored Advance Turbine Engine Gas Generator (ATEGG) and Joint Technology Demonstrator Engine (JTDE) programs as shown in Fig. 8. The status of current F404 component development is described below.

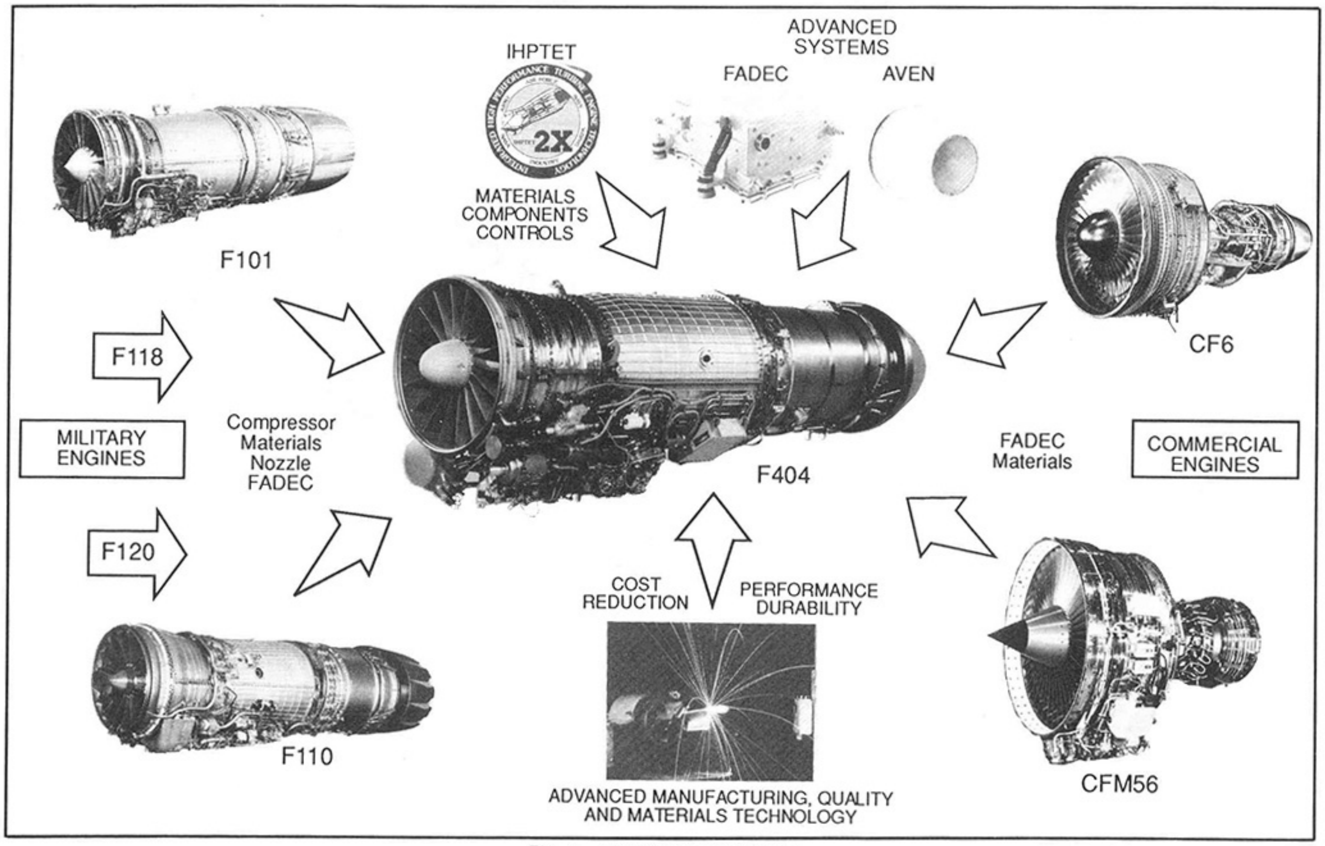

Fig. 7 F404 technology base

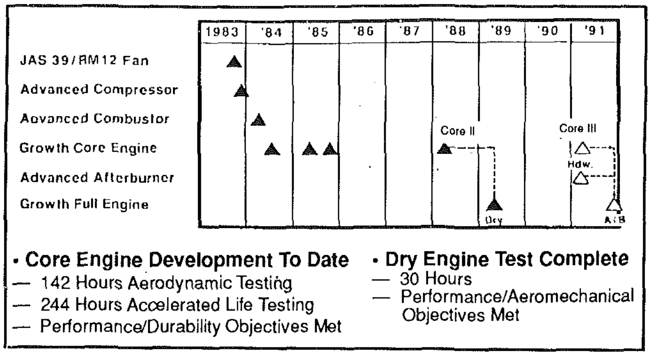

**Fig. 8 F404 technology demonstrator program**

*Fans.* Fan components defined for F404 afterburning derivatives include the original F404-GE-400 fan at 145 pounds per second (pps) airflow, the F404/RM12 fan at 160 pps airflow, and advanced fans at 170–180 pps airflow. Pressure ratios range from 4.2 to almost 5. These F404 derivative fans share the rugged, low aspect ratio, high pressure ratio, compact three-stage design characteristics of the -400 fan and will maintain the exceptional distortion tolerance and attentuation characteristics demonstrated by the -400 fan in service. The F404/RM12 fan completed all Production Verification Tests (PVT) for production qualification under the JAS 39 program in Aug. 1989 and has demonstrated distortion tolerance levels even better than the -400 fan, in addition to successfully demonstrating ingestion of a 1.1 lb bird. These qualification test results enhance confidence in GEAE design and performance prediction methodology for future F404 derivative fans.

In addition to the above, studies of non-afterburning F404 derivatives have included fans in the 200–550 pps airflow classes for engines with bypass ratios from 0.8 to 5.0.

*Compressors/Core Engines.* Core sizes defined for F404 derivatives include the original F404-GE-400 engine core and the advanced technology Core II and Core III. Core II technology, characterized by +200°F (+111 K) turbine inlet temperature, +5 percent airflow and +2 percent high-pressure turbine efficiency over the -400 model, was demonstrated under the ATEGG/JTDE programs in 1988 and 1989. Core III technology, characterized by +300°F (+167 K) turbine inlet temperature, +10 percent airflow, +2 percent compressor efficiency, and +2 percent high-pressure turbine efficiency compared to the -400, is to be demonstrated in core and full afterburning engine testing scheduled for 1991–92.

*Combustors.* Thermal barrier coatings on F404 combustor shells were demonstrated during component and engine testing under the F404-GE-100 engine program and were successfully flight tested in the F-20 Tigershark from 1983 to 1985. This technology has also been well proven on GEAE commercial engines and is being used on near-term derivatives such as the F404/RM12 and F404-GE-402 EPE. The multihole combustor design, shown in Fig. 9, was successfully demonstrated on the ATEGG/JTDE programs and promises substantial reductions in manufacturing cost, weight, and cooling requirements, with improved durability.

*Turbines.* Turbine technology research has focused on higher efficiency and turbine inlet temperature capability along with reduced cooling requirements. Among the technologies demonstrated on the ATEGG program are a 3 percent high-pressure turbine (HPT) efficiency improvement, a simplified higher work capability HPT design with 1/3 fewer vanes and 10 percent fewer buckets, reduced cooling requirements through improved internal design and thermal barrier coated airfoils, ceramic shrouds, and improved clearance control. Monocrystal alloy material vanes and buckets have been demonstrated on ATEGG/JTDE, F404-GE-400, F110, F120, and GE36 engines. A three-vane F404/ATEGG nozzle segment with thermal barrier coating is shown in Fig. 10.

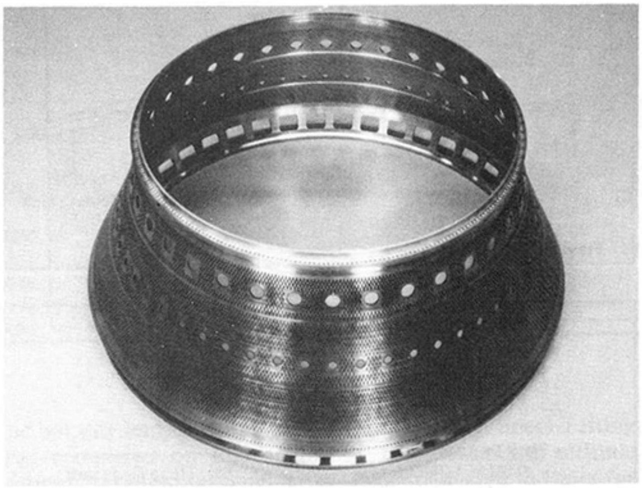

**Fig. 9 Multihole combustor inner shell**

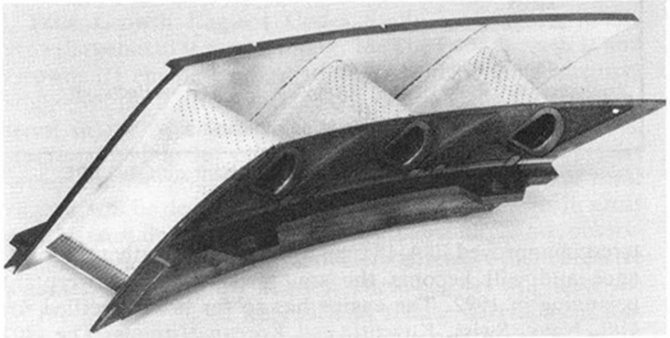

**Fig. 10 Three vane F404/ATEGG turbine nozzle**

*Afterburners.* Near-term growth afterburner development has been conducted principally under the F404/RM12 Full Scale Develpoment program. Efficiency improvements of 5–6 percent have been demonstrated in official sea level and altitude tests by means of reduced cooling and optimized fuel distribution and mixing, while liner, flameholder, and nozzle parts lives have been maintained by thermal barrier coatings and cooling pattern improvements. F404/RM12 afterburner configuration changes from the -400 are shown in Fig. 11. A higher temperature capability afterburner for higher thrust F404 derivatives is scheduled for demonstration on the JTDE program in 1991–92.

**F404 Growth Engine Derivatives in Development.** The F404/RM12, F404-GE-402 Enhanced Performance Engine, and F412-GE-400 are examples of GEAE's building block approach to F404 growth derivatives now undergoing Full Scale Development. In addition, the F404/F2J3 has completed flight qualification to power the prototype Indian Light Combat Aircraft (LCA).

*F404/RM12.* The F404/RM12 engine, rated at 18,100 lb (80 kN) thrust, makes use of the proven -400 engine core with minor modifications to hardware, materials, and cooling flows, primarily to handle the higher operating temperatures of the engine. This program is developing and qualifying the 160 pps airflow fan and improved efficiency afterburner as described previously. The F404/RM12 also makes use of a Digital Electronic Control and single engine reliability features as described in the Advanced Systems Technology section of this paper. A complete description of this engine and its associated development program may be found from Daub et al. (1988).

*F404-GE-402 Enhanced Performance Engine (EPE).* F404-GE-402 EPE was defined in response to customer in-

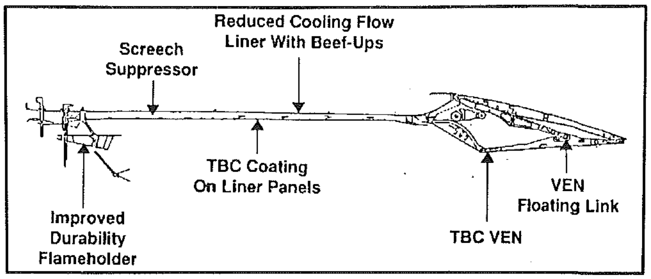

Fig. 11 RM12/-402 afterburner configuration

| | Improvement |
|---|---|
| • Specific Excess Power, $P_S$ | |
| — 0.9M/10k/1G/Max Power | 18% |
| • Sustained Gs | |
| — 0.65M/10k/Max Power | 2% |
| • Time To Accelerate | |
| — 0.8M to 1.2M/35k/Max Power | 5% (Time Reduced) |
| — 0.8M to 1.6M/35k/Max Power | 27% (Time Reduced) |
| • Mmax | |
| — 10k/Intermediate Power | 1% |
| • Time To Climb/Intercept | |
| — From Brake Release to 1.4M/50k | 31% (Time Reduced) |

No Change In Mission Radius

Fig. 12 F/A-18 performance improvement with -402 EPE

terest in improved F/A-18 time-to-climb and combat performance and will become the standard F/A-18 powerplant beginning in 1992. The engine has so far been specified for U.S. Navy, Swiss, Kuwaiti, and Korean Hornets. The -402 model will be rated at 17,700 lb (79 kN) thrust at sea level static conditions and will provide up to a 10–20 percent increase in installed thrust over the -400 model in key areas of the envelope, providing significant performance improvement for the F/A-18 at key combat conditions as shown in Fig. 12.

Full-Scale Development is being executed under a unique partnership arrangement between McDonnell Douglas, GEAE, and the U.S. Navy whereby development costs, hardware, and engine/aircraft testing are shared by the three parties. The U.S. Navy is the U.S. Government authority for specification requirements and production qualification.

The -402 engine configuration philosophy was driven by the following development criteria:

- Meet minimum time-to-climb performance—driven by the international competitive environment where the F/A-18 is frequently designated as the first-line interceptor
- Maintain existing F/A-18 inlet and engine bay configuration
- Maintain 2000 hour U.S. Navy mission hot section life
- Maximize engine parts commonality with existing -400 and F404/RM12 programs to reduce development cost and logistics impact.

The increased thrust of the -402 model will be achieved by increasing fan speed up to 2 percent, improving afterburner efficiency and raising turbine inlet temperature by +100°F (+56 K) at intermediate rated power, increasing to +175°F (+97 K) at maximum power. The dual level temperature schedule concept was developed to maintain the 2000 hour hot section life in the U.S. Navy mission.

Consistent with the building block approach, the -402 will use the -400 fan and F404/RM12 afterburner with hot section materials changes made to meet the hot section life requirement. Figure 13 shows the basic configuration changes made to the engine. Details of these changes are highlighted below:

- Fan: thickened stage 1 and 2 vanes for improved aeromechanical margin

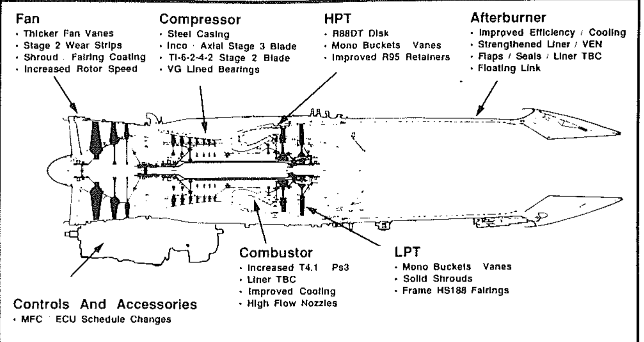

- 2,000 Hour USN Mission Hot Section Life
- Maintains F/A–18 Inlet/Engine Bay

Fig. 13 F404-GE-402 configuration

- Compressor: stage 2 and 3 blade material change to accommodate increased temperatures
- Combustor: thermal barrier coating, high flow fuel nozzles, modified casing for improved engine hot parts cooling
- HP Turbine: Monocrystal alloy material nozzles and buckets (both of which maintain the -400 aerodynamic/cooling design), improved process R95 material forward and aft blade retainers, improved power metal alloy material disk
- LP Turbine: Monocrystal alloy material nozzles/buckets
- Afterburner: F404/RM12 design (as described in previous section)

The decision to use the -400 fan instead of the F404/RM12 fan was consistent with the -402 configuration philosophy. Although the F404/RM12 fan would have provided greater thrust in the upper left corner of the envelope, the -400 fan provided sufficient flow in the low and central portions of the envelope where the engine was temperature, not airflow, limited. This better matched the optimum intercept time-to-climb profile of the aircraft. In addition, the need for significant inlet compatibility testing for the F404/RM12 fan in the F/A-18 was avoided, which would have increased the development flight test expense considerably.

Another significant feature of the selected configuration was the emphasis on fit and function interchangeability of improved -402 part designs in the -400 engine. This will provide the option for current users of the F404 engine to improve the life capability of their current engines by selective replacement of -400 parts with the -402 design if they do not wish to completely upgrade their engines to the -402 configuration. For example, the -402 HPT bucket maintains the mechanical and aerodynamic configuration of the -400 design, so use of the improved material -402 design will result in a significant improvement in bucket life if operated at the -400 cycle conditions. This also makes it possible to upgrade -400 engines to the full-402 configuration and performance level at the hot section replacement interval at only the incremental cost of the -402 unique parts versus the regular -400 parts replacement cost.

The engine Full-Scale Development program schedule is shown in Fig. 14. Five engines will accumulate over 3000 test hours covering stress, vibration, overtemperature (O/T), Accelerated Simulated Mission Endurance Testing (ASMET), Fighter Accelerated Mission Testing (FAMT), durability, Preliminary Flight Qualification (PFQ), Limited Production Qualification (LPQ), and Full Production Qualification (FPQ) requirements. These requirements are able to be met with this relatively small quantity of test hours because of the extensive component and material development testing performed under other initiatives and because of the minimum configuration changes incorporated on the -402.

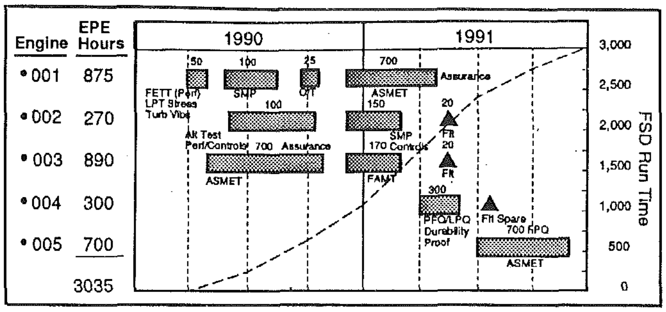

Fig. 14 F404-GE-402 development test plan

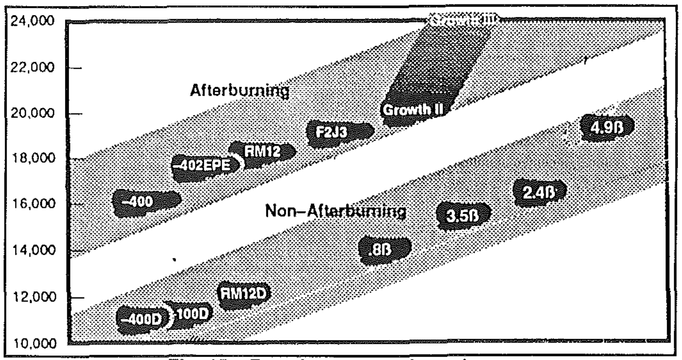

Fig. 15 F404 family growth roadmap

Only a limited flight test program will be required to qualify the -402 in the F/A-18. No aircraft structural or inlet ducting modifications are necessary and only minor changes will be required in the aircraft software for engine condition monitoring, and autothrottle limits. Since the software modification will allow the installation of either a -400 or -402 engine in an F/A-18, a discrete signal will also be provided to identify which model engine is installed and to provide a caution against the installation of a -402 and -400 engine in the same aircraft. The flight test program will consist of some 55 hours covering engine/airframe compatibility, engine operability, carrier suitability, single engine operation, and performance verification.

*F412-GE-400.* The F412 engine, a derivative F404 design optimized for the U.S. Navy's A-12 Advanced Tactical Aircraft, will incorporate many of the technologies demonstrated under the ATEGG/JTDE programs, including the advanced Core II compressor, multihole combustor, turbine aerodynamics, and monocrystal turbine materials. The engine also includes design improvements based on the lessons learned from F404 operating experience to enhance reliability, maintainability and safety, many of which could not be cost-effectively retrofitted into the operational F404-GE-400 engine.

The medium bypass engine will employ an advanced three-stage 200 pps airflow fan scaled from the -400 design with improved bird-strike, ice, and FOD resistance. The increased flow seven-stage high-pressure compressor section incorporates a steel compressor case and composite fan bypass duct for improved safety. The combustor's multihole design with "wavy wall" outer shell and a bolted dome produces a light, low-cost component with a more uniform temperature profile, which eliminates the need for thermal barrier coating. The two-stage low-pressure turbine design is derived from the high-efficiency F110 design.

The engine control system features an advanced Full Authority Digital Electronic Control (FADEC) with a fail-operational backup system. The FADEC incorporates extensive troubleshooting capability to improve maintainability and reduce life cycle costs. This capability includes control system fault isolation at the squadron maintenance level, as well as intermediate maintenance testability down to the subcomponent level.

F412 Full-Scale Development engine testing, which began in 1989, consists of over 9000 qualification test hours. This program will qualify many F404 growth components, such as the advanced compressor, combustor and turbine designs, which will then be available for other afterburning and non-afterburning F404 derivatives for the mid-1990s, thus reducing the cost and risk of these derivative engines.

*F404/F2J3.* This engine utilizes the F404/RM12 fan at the full 160 pps airflow rating, the -400 core with F404/RM12 modifications, and an F404/RM12 afterburner. The engine uses the -100/-100D gearbox and control system hardware with single engine features (described in the Advanced Systems section of this paper). The engine cycle has been optimized for the hot day temperatures of India. Flight Worthiness Testing was completed on this engine in 1989, including altitude testing, and flight test engines are being delivered to India for the Light Combat Aircraft (LCA) flight test program.

**F404 Growth Engines Under Study.** The F404 family growth roadmap is shown in Fig. 15. The F404 Growth II and Growth III engine configurations have undergone intensive study over the last two years in conjunction with increased interest in the McDonnell Douglas/U.S. Navy Hornet 2000 studies as well as for other aircraft applications. The precise cycles, configurations, and advanced system features of these engines will be determined by customer requirements in areas such as sustained supersonic cruise capability, low observables, high horsepower extraction for offensive and defensive avionics, and vectoring nozzles. These engines will make use of the building block approach to reduce development risk and cost. Users can have confidence in performance predictions due to the significant component development testing that has been completed, is underway or contemplated.

*F404 Growth II.* Growth II models currently defined are in the 8.5–9 thrust-to-weight ratio class. One design utilizes the F404/RM12 fan scheduled at 160 pps airflow and the Core II technology core coupled with an advanced low pressure turbine and afterburner to produce 20,000 pounds (89 kN) of thrust. A more powerful version of Growth II utilizes a 170 pps airflow fan and either Core II or Core III technology to produce an engine in the 21,500–23,000 lb (96–102 kN) thrust class. The control system will be commanded by a FADEC derived from the F412 FADEC.

*F404 Growth III.* The Growth III model utilizes a 180 pps airflow fan and the Core II technology core coupled with an advanced low-pressure turbine, afterburner, and FADEC to produce 22,500 lb (100 kN) thrust. A higher thrust version of Growth III, in the 9.5:1 thrust-to-weight ratio class, is also under study coupling the Core III technology core with the 180 pps fan to produce over 24,000 lb (107 kN) of thrust.

Advanced system options for Growth II and III model engines include conventional, two-dimensional convergent-divergent (2DCD) or AVEN exhaust nozzles and single engine features. Growth II and III technology engines are depicted in Fig. 16.

Figure 17 summarizes the unmatched test experience gained in F404 derivative qualification and component technology programs, which will serve to greatly reduce the cost and risk of a Full-Scale Development program of either the Growth II or Growth III model engines.

**Advanced System Technology.** A second area emphasized in the F404 technology development plan is integration of advanced system technology into current and future derivative engines. The following examples describe advanced system features that are either incorporated in existing F404 models, are under Full-Scale Development, or are under study for incorporation on future F404 models.

**+25–50% Takeoff Thrust**

**Utilizes Components From Other Development/ Demonstrator Programs**

- — RM12 (160 pps) or 170–180 pps Airflow Fans
- — Advanced Core II or III
- — Advanced LPT, Afterburner
- — FADEC

**Advanced System Options**

- — Conventional, 2DCD, AVEN Exhaust Nozzles
- — Single Engine Features

**Production Potential: 48-54 Months After Go**

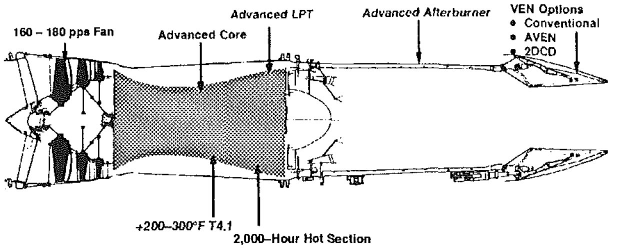

**20,000 — 24,000 Lbs Thrust**

Fig. 16 F404 growth II and III

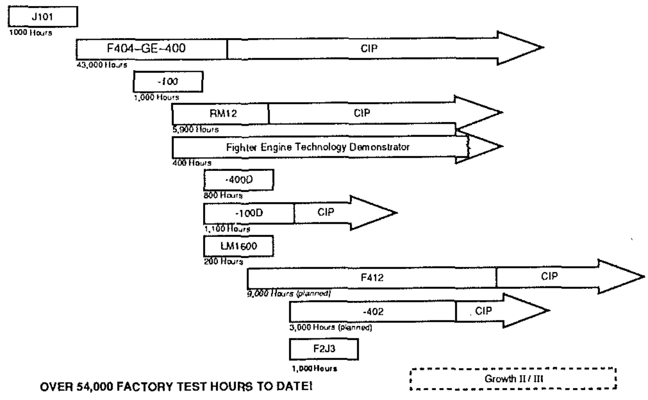

Fig. 17 F404 engine test experience

*Single Engine Features.* Single Engine Features (SEF) were developed to reduce or eliminate the consequences of control system component or sensor failures in a single engine aircraft application. The system architecture was developed under the F404-GE-100/F-20 and F404/RM12/JAS 39 programs and is also being used in the F404-GE-100D/A-4S-1 production program and the F404/F2J3/India LCA development program. The original -400 control system consists of two main control components: a hydromechanical Main Fuel Control (MFC) and the Electrical Control Unit (ECU). The SEF design includes an MFC Backup mode in a Digital Electronic Control (DEC), which provides full authority electrical control in the event of hydromechanical failures, and a DEC Disable mode, which provides hydromechanical backup in the event of electrical sensor or DEC failures. In addition, there are modes to limit failure-caused overspeed, overtemperature, and fan variable geometry system problems. The system also features dual exciters and main igniter plugs, and gearbox pads for backup aircraft hydraulic and generator components. Besides ensuring sufficient power to return the aircraft safely, these features provide nearly full mission capability of the engine in the event of control system failures.

*FADEC.* GEAE is using the lessons learned from nearly 10 years of development, test, flight test, and operational use of digital controls in both military (F404, T700, F110, F120, T407, LV100) and commercial (CF6-80, CFM56) applications to develop the F412 FADEC system architecture, hardware and software. In particular, the fail-operational architecture of the design was heavily influenced by software/hardware experience gained during development and operational use of the F404-GE-100/-100D/RM12 control systems and by the F110-GE-129 FADEC design now in production. The FADEC design incorporates fault isolation circuitry and a digital databus to allow monitoring and analysis of engine control system faults on the aircraft cockpit displays or through a ground station without opening engine access doors. The circuitry can distinguish between faults in the control system sensors/cabling and in the FADEC to avoid unnecessary and expensive removal and troubleshooting of the control when it is not at fault. In addition, the plug-in circuit card design eliminates potting and incorporates multiple test points to allow troubleshooting of individual circuit card subcomponents, providing exceptional troubleshooting and repair capability at the intermediate maintenance level.

The qualification of this FADEC design will significantly reduce cost and risk of developing a derivative control system for the F404 Growth II or Growth III engines. FADEC control systems are uniquely suited to the future demands of increasing integration of aircraft and engine control systems and to improved control system diagnostic capability.

*Fiber Optic Control System Development.* Fiber optic control system components and system architecture are promising areas for technology development for advanced engine designs due to their inherent immunity to Electro-Magnetic Interference (EMI), low weight, low cost, and improved response and bandwidth capability compared to components and cabling designed with metallic conductors. Optical technologies/materials also are uniquely suited to the aircraft engine environment because of their high temperature capability. GEAE has been involved in ongoing development and assessment of these technologies since the early 1980s and participated in the NASA sponsored Fiber Optic Control System Integration (FOCSI) contract study between 1985 and 1987, followed by a contract aimed at optimizing the architecture of an electro-optical control system. GEAE recently won a sole source three-year contract for the NASA FOCSI II initiative which will design and test a prototype passive optics and electro-optics control system which will be tested on an F404 engine in an F/A-18 test aircraft. GEAE was also selected to participate in the Phase I Opto-Electronic Control program sponsored by the U.S. Navy's Broad Agency Announcement. The goal of this program is to develop and build an active engine control system. A prototype optical T5 sensor, now on test in an F404, is shown in Fig. 18.

*Axisymmetric Vectoring Exhaust Nozzle (AVEN).* A final example of advanced system technology under development at GEAE is the AVEN. The GEAE concept design features pitch/yaw vectoring capability around a 360-deg arc and independent A8 and A9 variability. Studies including aircraft simulator work have demonstrated significant operational performance benefits of vectoring in addition to the added benefit of improved overall engine performance of independent A8/A9. The configuration of this nozzle design also lends itself to retrofit on current aircraft installations because of its similarity to the current F404 nozzle design; see Fig. 19.

**Advanced Manufacturing/Materials Technology.** The third element of the F404 technology development plan is the development and incorporation of advanced manufacturing methods and materials to reduce engine cost and weight and

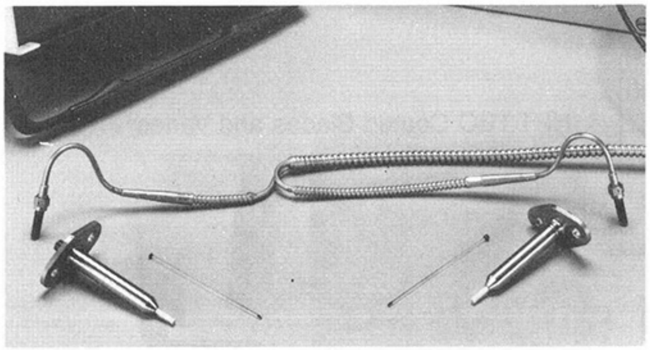

Fig. 18 Fiber optic F404 T5 sensor prototype

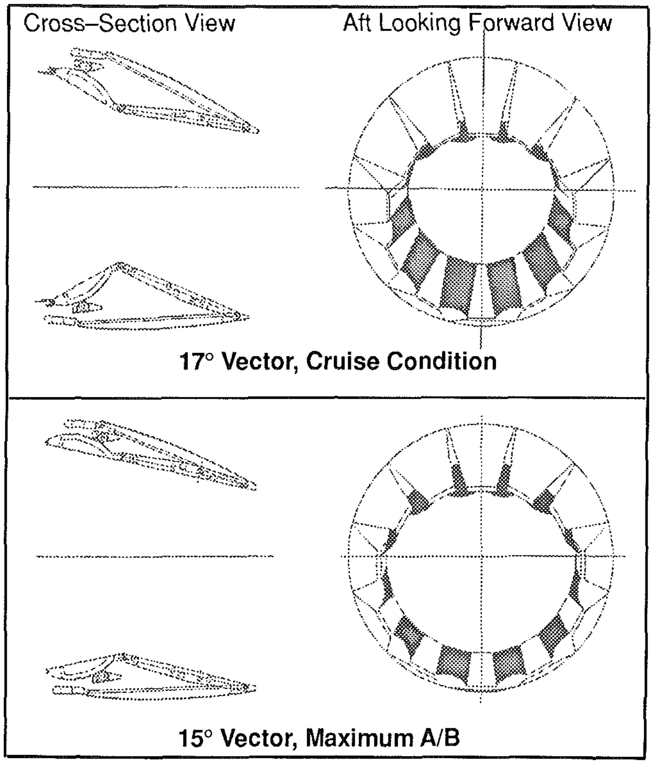

Fig. 19 Axisymmetric vectoring exhaust nozzle (AVEN)

improve engine performance. GEAE has been carrying out initiatives in these areas through three integrated paths: (1) the traditional materials laboratories and manufacturing engineering organizations, (2) the GEAE Manufacturing & Quality Technology Department, and (3) the Integrated High Performance Turbine Engine Technology initiative.

*Materials Laboratories/Advanced Manufacturing Engineering.* These organizations are tasked with developing advanced materials and manufacturing methods primarily for near-term engine production applications. Initiatives on the F404 have focused on the hot section to develop materials capable of withstanding the higher cycle temperatures of the growth engines; for example, the evolution of the high-pressure turbine bucket material from the original Rene 125 material, to directionally solidified DSR80H (for the -100, F404/RM12 and to improve life on the -400), to monocrystal alloy (for the -402 and F412). Other hot section materials developments include thermal barrier coated combustor, turbine, and afterburner components, and ceramic shrouds.

Casting technology development has been of particular interest, not only to develop the methods to cast the intricate turbine bucket cooling passages, but also to reduce the cost and weight of the engine. For example, a titanium version of the INCO 718 midframe, which is manufactured from a large casting and designed to save 30 pounds of weight, is in production for the -100D model and may be specified on other F404 models. A similar design is used on the F412 engine. All-cast versions of the Rene 41 engine nozzle flaps and seals are expected to reduce the shop cost of these parts versus the fabricated sheet metal versions by over 10 percent, as shown in Fig. 20.

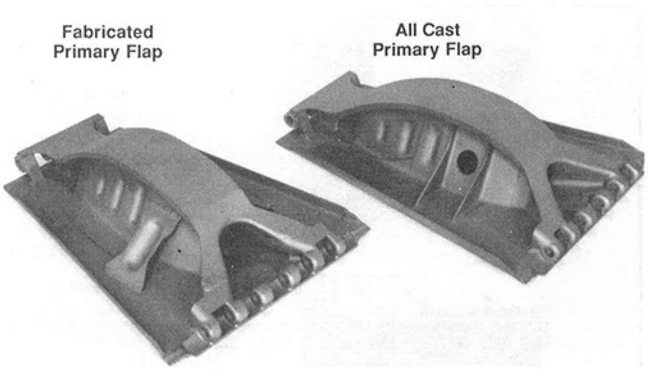

Fig. 20 F404 exhaust nozzle primary flap—subcomponent cost reduction

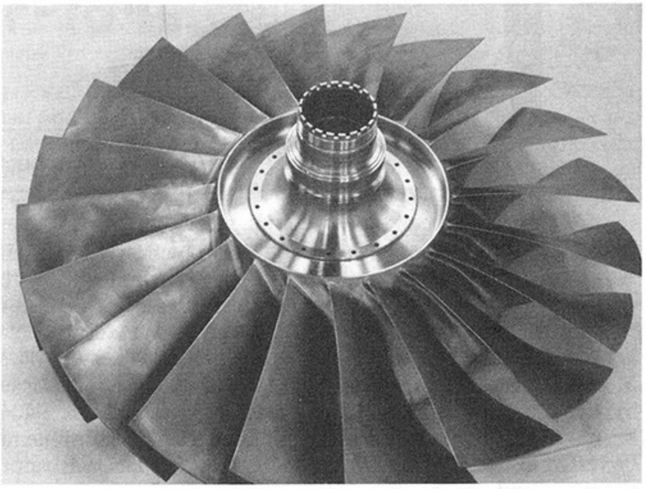

Fig. 21 Integrally bladed disk (blisk)

The previously mentioned composite fan outer bypass duct is another example of advanced materials development now in production -400 engines and specified for the -402 model and F412 derivative engines to reduce weight and improve safety.

*Manufacturing and Quality Technology Department.* The M&QTD is tasked with developing advanced manufacturing methods to ensure cost and quality superiority of GEAE products and to assure the producibility of new engine materials and designs. Once developed by the M&QTD, these technologies are integrated into the product design during the engineering phase or incorporated into product-specific manufacturing processes at the individual manufacturing/production facility. Examples of manufacturing/quality methods developed by the M&QTD in use on the F404 include laser drilling of cooling holes in combustors and turbine buckets/vanes, X-Ray Computed Tomography inspection of internal cooling cavities of turbine blades, and eddy current parts inspection. These methods significantly increase productivity and reduce costs of F404 parts manufacturing. For instance, the cooling holes on a turbine nozzle vane can be laser drilled four to five times faster than with Electro-Discharge Machining (EDM).

Another area of interest to growth F404 engines is the manufacture of integrally bladed disks (blisks). A blisk fan or compressor rotor provides significant benefits to engine per-

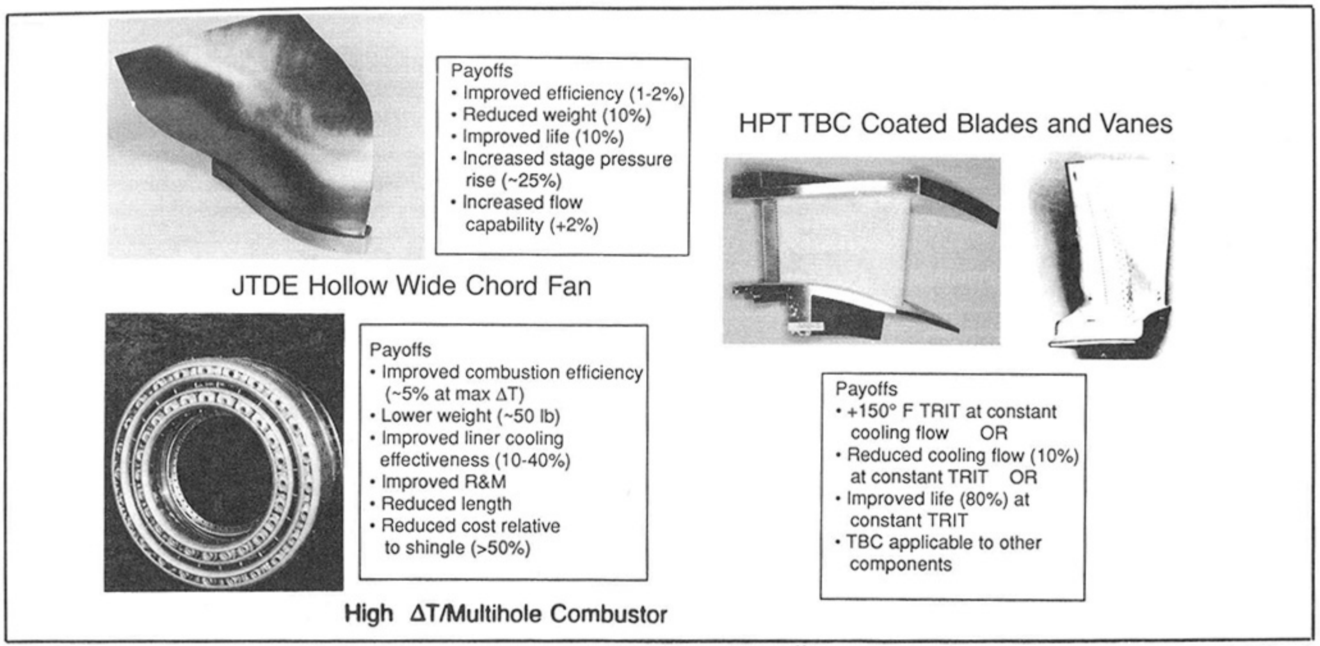

Fig. 22 IHPTET component payoffs

formance, cost, and weight through the reduction of dovetail mass, part complexity, and air leakage. GEAE has over 10 years' experience in the production of compressor rotor blisks for the T700 engine using both conventional five-axis machining centers and Electrochemical Machining (ECM). The M&QTD is further developing processes to manufacture blisks by ECM and pressure welding processes; see Fig. 21. F404 blisk fan and compressor rotors have been and will continue to be tested under the ongoing F404 Technology Demonstrator program, and are under development for the F120.

*Integrated High-Performance Turbine Engine Technology (IHPTET).* GEAE is participating in the IHPTET initiative of the U.S. Government, whose goal is to double turbine engine technology capability by the year 2003. In particular, these goals are to double engine thrust-to-weight ratio and core specific energy, and reduce fuel burn by 50 percent. A strong emphasis is being placed on developing the revolutionary material technologies required to reach these goals, followed by designs to use them. These materials include polymeric, metal matrix, and ceramic composites, intermetallics, high-temperature titanium, carbon-carbon material, refractory metal, coatings, and dry lubricants. It is estimated that these advanced materials will make up approximately 50 percent of engine volume by the turn of the century. As these new materials and manufacturing methods are proven and design applications are developed, they will be incorporated on advanced versions of the F404. Examples of IHPTET component payoffs, which are readily adaptable to nearer term F404 derivatives, are shown in Fig. 22.

## Summary and Conclusion

After over 2 million flight hours of operation, the basic F404 design has reached a full level of design maturity. This maturity is reflected in the excellent reliability, maintainability, and durability measures of its operators. The growth plan described in this paper is providing a systematic framework for introducing advanced technology into current and future derivatives of the engine. Careful attention is being paid to balance advanced technology with component designs proven and improved by factory testing—and by the lessons learned from extensive operational experience—so that the mature reliability, maintainability, and durability characteristics of the F404 will be maintained or improved.

The F404 family of engines in production, under development, or under study covers the 16,000–24,000 lb (71–107 kN) afterburning engine thrust range and the 11,000–19,000 lb (48–84 kN) non-afterburning engine thrust range. The simplified design made possible by advanced technology and the F404 family development philosophy has been very successful, based on operational experience, and has been emulated by other fighter engines projected to enter service in the late 1990s. The extension of the F404 engine design to the 20,000–24,000 lb (89–107 kN) thrust class, with thrust-to-weight ratio in the 9–10 class, is a low-risk proposition that will require substantially less funding for Full-Scale Development than a completely new engine design due to the extensive component and full engine testing that has been carried out under the F404 Technology Demonstrator program and under F404, F412, and other GE Aircraft Engines derivative engine programs already under development or in production. Advanced aircraft propulsion system requirements such as supersonic cruise capability, extremely high horsepower extraction for advanced electronic warfare avionics, FADEC, integrated aircraft/engine control systems, and single engine features can be readily incorporated in F404 growth derivatives due to advanced system development programs in process at GE Aircraft Engines.

The large production base of the F404, with over 2000 engines shipped to date, has resulted in low engine cost for the -400 and -402 model engines. New derivatives will benefit from the manufacturing lessons learned both in production engines and in the advanced manufacturing methods research being undertaken by GEAE as described in this paper. The low development, acquisition cost, and proven low operating costs that have resulted from the high reliability and maintainability of the F404 family of engines will contribute to a low life cycle cost for these future F404 engine derivatives.

## References

Daub, W. J., Larsson, L., and Veno, L. B., 1988, "Development of the F404/RM12 for the JAS 39 Gripen," ASME Paper No. 88-GT-305.

Rapp, G. C., 1982, "The F404 Development Program—A New Approach," AIAA Paper No. AIAA-82-1180.

**R. W. Cue**
Canadian Forces,
Ottawa, Canada

**D. E. Muir**
GasTOPS Ltd.,
Ottawa, Canada

# Engine Performance Monitoring and Troubleshooting Techniques for the CF-18 Aircraft

*The F404-GE-400 engines of the CF-18 aircraft are the first engines of the Canadian Forces to be maintained under a formal on-condition maintenance program. In support of this program, the Canadian Forces are developing advanced troubleshooting and performance monitoring procedures based on information recorded by the aircraft In-flight Engine Condition Monitoring System (IECMS). A suite of computer programs has been developed that enables maintenance personnel to access, display, and analyze in-flight event data recorded by the IECMS and to track the performance of individual engines based on "health indices" derived from the IECMS takeoff ground roll recordings. The new techniques have been under evaluation at each of the CF-18 main operating bases for a period of approximately 14 months. Results to date indicate that the IECMS recordings provide a considerable amount of information of benefit to engine technicians and maintenance planners.*

## Introduction

The air element of the Canadian Forces operates over 130 CF-18 fighter aircraft from main operating bases located in Cold Lake, Alberta; Bagotville, Quebec; and Baden-Soellingen, West Germany. Each CF-18 is powered by two General Electric F404-GE-400 engines, a twin-spool, afterburning turbofan with a maximum thrust rating of approximately 16,000 lb (71 kN). A layout of the engine defining the station numbers used for performance analysis is presented in Fig. 1.

The acquisition of the CF-18 by the Canadian Forces has resulted in a new approach to fighter engine maintenance. In particular, an on-condition maintenance philosophy has been adopted whereby maintenance actions are dictated primarily by observations and/or measurements of actual engine condition. This new approach is made possible by the design features of the engine (e.g., modular construction and borescope access) and by the aircraft's In-flight Engine Condition Monitoring System (IECMS).

The IECMS continuously monitors several engine performance parameters, evaluates component life consumption parameters, activates cockpit cautions, and sets maintenance codes whenever an engine operating limit is exceeded and automatically records engine condition data on a removable tape cartridge for postflight analysis. The original intent of the IECMS in-flight data recordings was to provide additional information to be used by maintenance technicians for fault isolation (Doane and Kinley, 1983). However, detailed procedures for the use of these recordings were not provided to the operators.

In 1985, the Canadian Forces contracted GasTOPS Ltd. to develop enhanced troubleshooting and performance monitoring techniques based on the data recordings provided by the IECMS. The initial development of these techniques was described by Muir et al. (1988). The new techniques, in the form of a suite of computer programs, are presently being evaluated by engineering personnel stationed at each of the CF-18 main operating bases.

This paper describes the advanced troubleshooting and performance monitoring techniques, the results of field evaluations to date, and the plans for future development work.

## In-Flight Engine Condition Monitoring System

Each CF-18 is equipped with a fully integrated In-flight Engine Condition Monitoring System (Doane and Kinley, 1983). The IECMS logic is implemented as software on the aircraft Mission Computer and includes the following major monitoring functions:

1 **Life Usage Evaluation.** Engine low cycle fatigue, thermal fatigue, and creep damage are evaluated by eight Life Usage Indices (LUIs). Running sums of each LUI are stored in the Mission Computer memory and are recorded twice per flight by the aircraft Maintenance Signal Data Recorder (MSDR).

2 **Operating Limit Surveillance.** The IECMS continuously monitors the status of the engine fan speed, compressor speed, exhaust gas temperature, oil pressure, and vibration signals with respect to predefined limits for safe operation. If a limit is exceeded, a cockpit caution is activated, a three-digit maintenance code is set at the Maintenance Monitor Panel

---

Contributed by the International Gas Turbine Institute and presented at the 35th International Gas Turbine and Aeroengine Congress and Exposition, Brussels, Belgium, June 11-14, 1990. Manuscript received by the International Gas Turbine Institute January 23, 1990. Paper No. 90-GT-357.

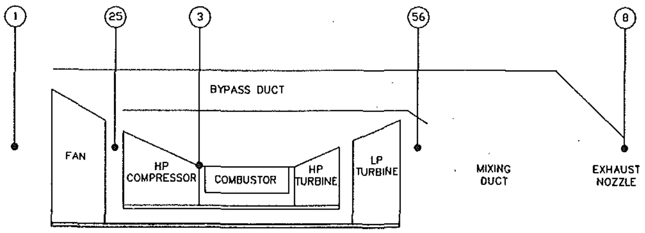

Fig. 1 F404-GE-400 engine layout

Table 1 IECMS event recording parameters

| Symbol | Description | Recording Rate (Hz) |
|---|---|---|
| $T_1$ | Inlet Temperature | 5/10* |
| $N_1$ | Fan Speed | 10 |
| $N_2$ | Compressor Speed | 10 |
| $W_{fm}$ | Main Fuel Flow | 10 |
| $T_{56}$ | Exhaust Gas Temperature | 10 |
| $P_{56}$ | Exhaust Gas Pressure | 5/10* |
| $P_{s3}$ | Compressor Discharge Pressure | 5/10* |
| EOP | Engine Oil Pressure | 1 |
| VF | Fan Vibration | 1 |
| VC | Compressor Vibration | 1 |
| VB | Broadband Vibration | 1 |
| PLA | Power Lever Angle | 10 |
| $A_8$ | Nozzle Position | 10 |
| BAD | Bleed Air Door Flag | 1 |
| APC | Approach Power Compensator Flag | 1 |
| VCS | Velocity Control System Flag | 1 |
| N2L | $N_2$ Lock-up Flag | 1 |
| BP | Boost Pressure Flag | 1 |
| DER | Derich Flag | 1 |
| REC | Pilot Record Flag | 1 |
| SEN | Sensor Failure Flag | 1 |
| AI | Anti-ice Flag | 1 |
| $F_c$ | Computed Thrust | 10 |
| M | Mach Number | 5/10* |
| AOA | Angle of Attack | 5/10* |
| $T_o$ | Total Temperature | 5/10* |
| $P_{alt}$ | Pressure Altitude | 5/10* |

* pre/post event recording rates

(MMP) located in the aircraft nose wheel-well, and approximately 40 seconds (5 seconds pre-event, 35 seconds post-event) of engine/aircraft performance data are recorded by the MSDR.

**3 Sensor Failure Detection.** The IECMS logic checks that the fan speed, compressor speed, compressor delivery pressure, exhaust gas pressure, engine inlet temperature, and engine oil pressure signal levels are within normal operating ranges. If a sensor failure is detected, an MMP code is set and a 40 second data recording is taken as described above.

**4 Flameout Detection.** The IECMS logic also includes a flameout detection algorithm based on the behavior of the compressor delivery pressure and rotor speed signals. If the IECMS criteria for flameout are satisfied, a cockpit caution is activated, an MMP code is set, and a 40 second event recording is initiated.

**5 Take-off Thrust Evaluation.** The IECMS automatically records engine and aircraft performance data during the ground roll of each take-off for the purpose of engine performance evaluation. A computed thrust value based on measured exhaust gas pressure and nozzle position is provided for cockpit display and is included as one of the recorded parameters.

**6 Pilot-Activated Recordings.** The IECMS logic enables the 40 second event recording feature of the system to be activated by a button located in the aircraft cockpit.

The IECMS data recordings are stored in the form of coded messages on a removable Maintenance Data Recorder Magazine (MDRM). Table 1 summarizes the major engine and aircraft parameters included in the IECMS event recordings and their frequency of recording.

## Ground Support Equipment

The gathering and processing of CF-18 maintenance data recordings, including the IECMS data, are accomplished by a network of ground-based processors, as illustrated in Fig. 2. Each squadron is equipped with a Ground Data Station, which stores a copy of the MDRM contents in an Aircraft Data File (ADF), erases the tape for return to service, and provides hardcopy reports of specific data records. The ADFs are automatically transferred from each squadron to a central Base Computing Facility and eventually archived onto nine-track tape. Prior to archiving, IECMS data are automatically extracted from each ADF for engine life usage tracking and performance monitoring applications.

## Troubleshooting Techniques

As previously described, in the event of an In-flight engine anomaly the IECMS sets a digital code at the aircraft nose wheel Maintenance Monitor Panel and initiates a recording of roughly 40 seconds of event data, including 5 seconds of buffered data collected prior to the event and 35 seconds of data collected after the event. The MMP codes, in turn, provide a direct entry point into the installed engine troubleshooting

## Nomenclature

$A_8$ = exhaust nozzle area
ADF = Aircraft Data File
CFB = Canadian Forces Base
CVG = compressor variable geometry
EOP = Engine Oil Pressure
EPR = Engine Pressure Ratio $= P_{56}/P_a$
ECU = Electronic Control Unit
IECMS = In-flight Engine Condition Monitoring System
IRP = Intermediate Rated Power
LUI = Life Usage Index
MDRM = Maintenance Data Recorder Magazine
MFC = Main Fuel Control
MMP = Maintenance Monitor Panel
MSDR = Maintenance Signal Data Recorder
$N_1$ = fan rotor speed
$N_2$ = compressor rotor speed
$P_a$ = ambient pressure
$P_{s3}$ = compressor delivery pressure
$P_{56}$ = exhaust gas pressure
$T_1$ = engine inlet temperature
$T_{25}$ = compressor inlet temperature
$T_{56}$ = exhaust gas temperature
VEN = variable exhaust nozzle
$W_1$ = engine inlet airflow
$W_{fm}$ = main fuel flow
$\delta_a$ = inlet pressure correction factor $= P_a/1$ bar
$\Theta_1$ = inlet temperature correction factor $= T_1/288$ K

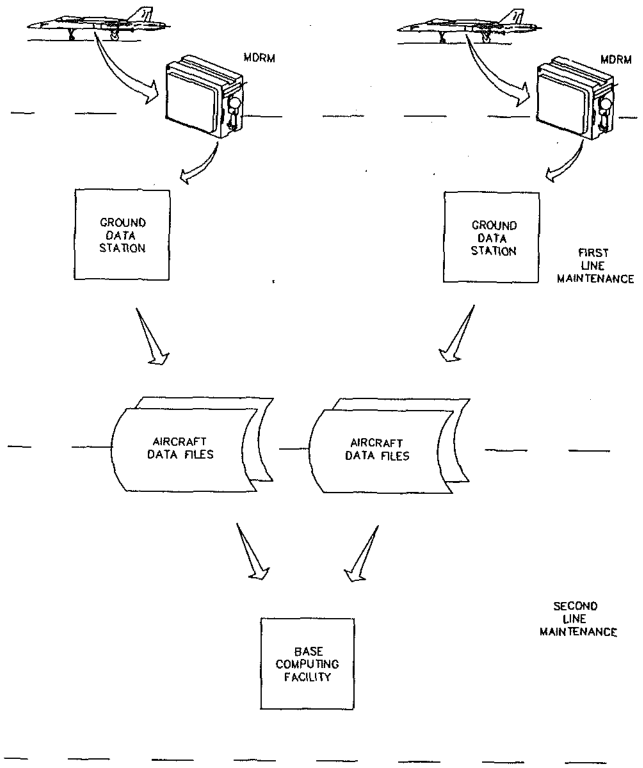

**Fig. 2 CF-18 ground support equipment**

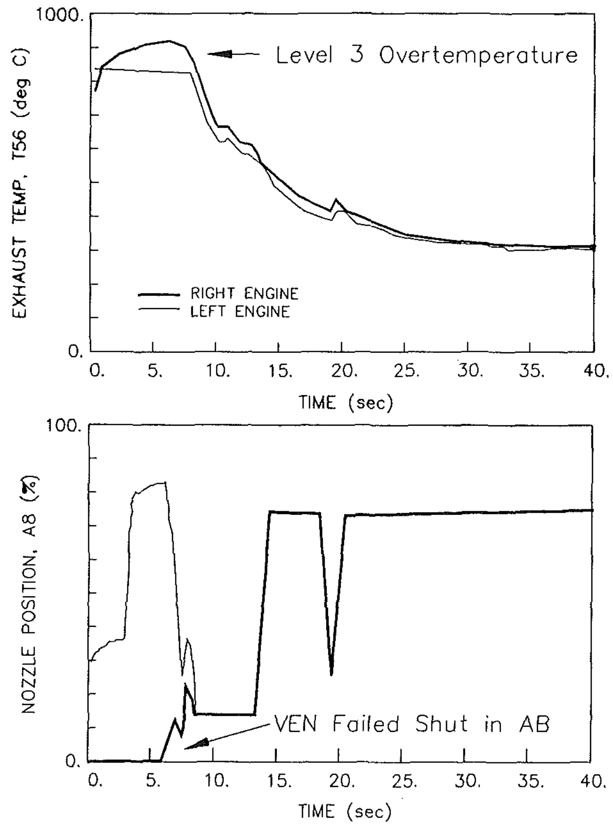

**Fig. 3 Graphic display of overtemperature event**

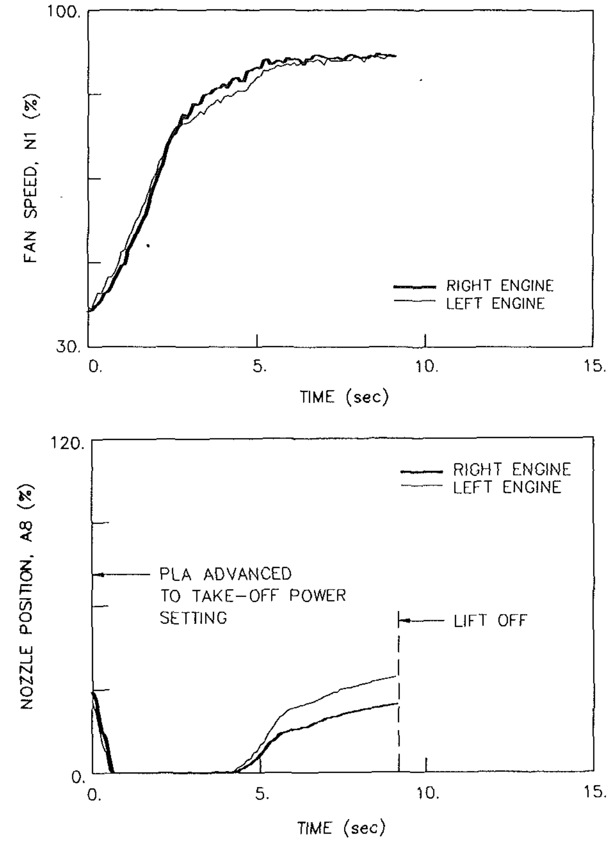

**Fig. 4 Representative take-off parameter traces**

manuals. In certain instances the troubleshooting manuals also call for use of the IECMS event data associated with specific codes (i.e., $T_I$ sensor failure, $N_I$ overspeed, and exhaust gas overtemperature codes). The Ground Data Station currently provides these data in a tabular format. This format has proven to be cumbersome for the technicians to use. Additionally, the aircraft Maintenance Signal Data Recorder does not always record the IECMS data in chronological order.

To overcome these difficulties IECMS event display software has been developed that accesses IECMS event data from an Aircraft Data File, identifies individual events, decodes and chronologically sorts the data, and provides the program user with a menu of parameters that may be graphically displayed, plotted, or printed. For example, Fig. 3 shows the left and right-hand engine nozzle position and exhaust gas temperature traces of an aircraft that experienced a right engine exhaust gas overtemperature. The general performance characteristics of each engine are readily apparent from these plots and the left to right comparison immediately exposes the problematic engine behavior. In this case the overtemperature is the result of a failure of the exhaust nozzle to open during afterburner operation.

## Performance Monitoring Techniques

The development of CF-18 engine performance monitoring procedures has centered on the take-off data recordings provided by the IECMS. These recordings are taken during the ground roll of each take-off and capture the dynamic response of the engines to a rapid throttle movement from ground idle to the take-off power setting (IRP). Representative traces of engine fan speed and nozzle area are presented in Fig. 4. The take-off recording begins when the pilot advances the throttle to IRP. Depending on how rapidly the throttle is advanced, the fan speed at the start of the recording can vary between ground idle (30 percent $N_1$) and 90 percent $N_1$. During the initial acceleration transient the engine control system maintains the exhaust nozzle at the fully closed position. When the fan speed reaches approximately 90 percent $N_1$, the nozzle is opened to maintain an acceptable exhaust gas temperature level. The recording terminates when the aircraft lifts off and this is usually well in advance of true steady-state operation.

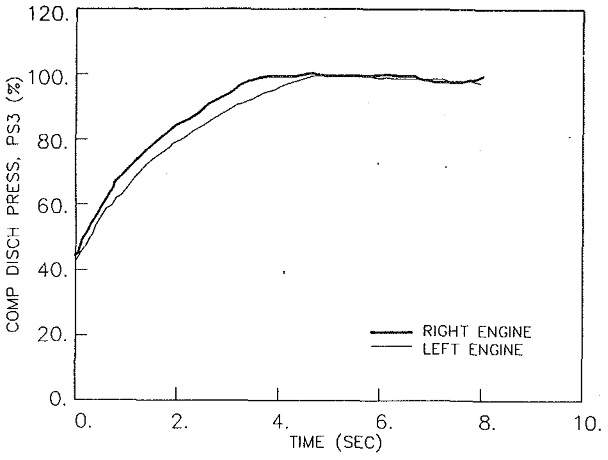

a) Before HP Compressor Damage

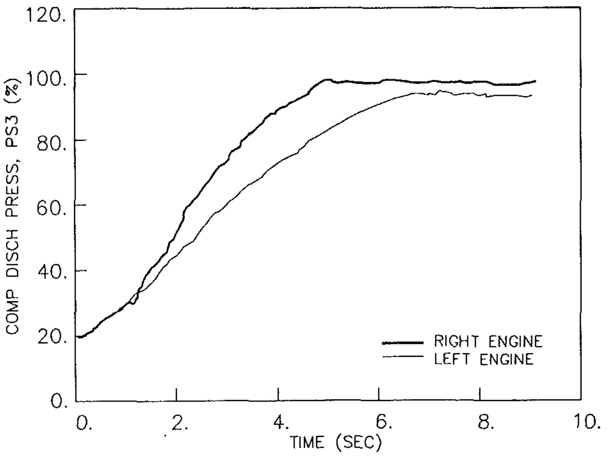

b) After HP Compressor Damage

**Fig. 5 F404 compressor discharge pressure traces**

The CF-18 engine performance monitoring procedures presently under evaluation are based on a number of relatively simple parameters or "health indices" derived from the IECMS take-off recordings. A brief description of these indices follows:

**(a) Compressor Delivery Pressure Rise Time.** The compressor delivery pressure ($P_{s3}$) rise time is defined as the time from ground roll initiation to a $P_{s3}$ value of 250 psi (17 bar). It is felt that this parameter may reveal cold end gas path damage and, possibly, control system problems. For example, Fig. 5 shows the $P_{s3}$ traces for the left and right-hand engines of an aircraft that experienced severe blade damage to the HP compressor of its left engine. The divergence of the left and right traces following the damage is clearly visible.

**(b) Fan Rotor Acceleration Time.** Immediately following a rapid throttle advance to IRP, the engine variable exhaust nozzle moves to a fully closed position and remains closed until the exhaust gas temperature limit of the engine is approached. It has been determined that the fan rotor speed acceleration times during an interval when the nozzle is closed (75-85 percent $N_1$) are remarkably consistent for healthy engines. Typical acceleration times are $0.75 \pm 0.10$ seconds. Field evaluations to date also indicate that these acceleration times are sensitive to control system performance and, to a lesser extent, gas path damage.

**(c) $N_1/N_2$ Speed Relationship.** Analysis of the IECMS take-off data indicates a consistent correlation between the two engine rotor speeds. In particular, at a corrected fan speed of 90 percent $N_1/\sqrt{\Theta_1}$ the value of $N_2/\sqrt{\Theta_1}$ for a large number of take-offs and different engines was found to be $88 \pm 1$ percent. The $N_2/N_1$ speed relationship of a twin spool engine is influenced by the effects of component flow and torque matching. It can be expected, therefore, that gas path problems may exhibit themselves as changes in the $N_1/N_2$ speed relationship.

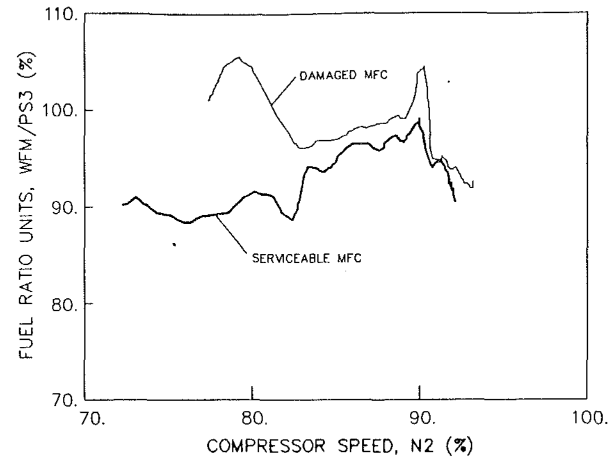

**Fig. 6 Fuel ratio unit traces taken before and after an MFC failure**

**(d) Fuel Ratio Units.** During a rapid acceleration from ground idle to take-off, the main fuel control (MFC) provides fuel to the engine according to a predefined schedule of fuel flow ($W_{fm}$) divided by compressor delivery pressure ($P_{s3}$), more commonly referred to as fuel ratio units. Analysis of a large number of take-offs has indicated that the recorded fuel ratio unit values are quite repeatable over a wide range of ambient temperatures and starting $N_1$ speed values if presented in the form $W_{fm}/P_{s3}\sqrt{\Theta_1}$ versus $N_2/\sqrt{\Theta_1}$. Furthermore, the fuel ratio unit parameter has been found to be useful in identifying problematic fuel controls. Figure 6, for example, presents the fuel ratio unit curves recorded before and after the removal of an MFC from an engine that experienced a flameout on startup. For field evaluation purposes, the fuel ratio unit values at 80 and 87 percent $N_2/\sqrt{\Theta_1}$, and the maximum $W_{fm}/P_{s3}\sqrt{\Theta_1}$ value are presently being monitored.

**(e) Maximum Thrust, Vibration, and Oil Pressure.** The maximum values of computed thrust, broadband vibration, and oil pressure recorded during each take-off have also been found to be reasonably repeatable for a given engine. These parameters are presently being monitored as general indicators of engine performance, vibration levels, and oil system performance, respectively.

**(f) Engine Airflow.** The IECMS take-off recordings provide measurements of nozzle area $A_8$, exhaust gas temperature $T_{56}$, and exhaust gas pressure $P_{56}$, from which an estimate of the engine airflow can be computed as follows:

$$\frac{W_1\sqrt{\Theta_1}}{\delta_a} = \frac{0.509\,P_{56}A_8\sqrt{\Theta_1}}{\sqrt{T_{56}}\,\delta_a}$$

The value of $W_1\sqrt{\Theta_1}/\delta_a$ at a corrected fan speed of 90 percent is presently being monitored as an indicator of potential fan, mixing duct, and exhaust nozzle problems. The multiplier of 0.509 has been determined from test cell measurements of engine inlet airflow.

The use of the engine health indices described above for performance monitoring is illustrated in Fig. 7. The take-off recordings, in the form of coded messages, are automatically extracted from each Aircraft Data File. The raw data points are then converted to engineering units and chronologically sorted prior to being stored in a second Take-off Data File. Each Take-off Data File is automatically processed by a data

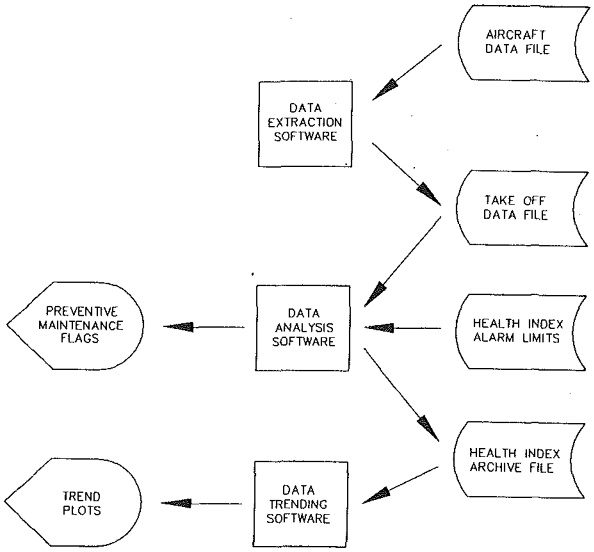

Fig. 7 CF-18 engine performance monitoring software

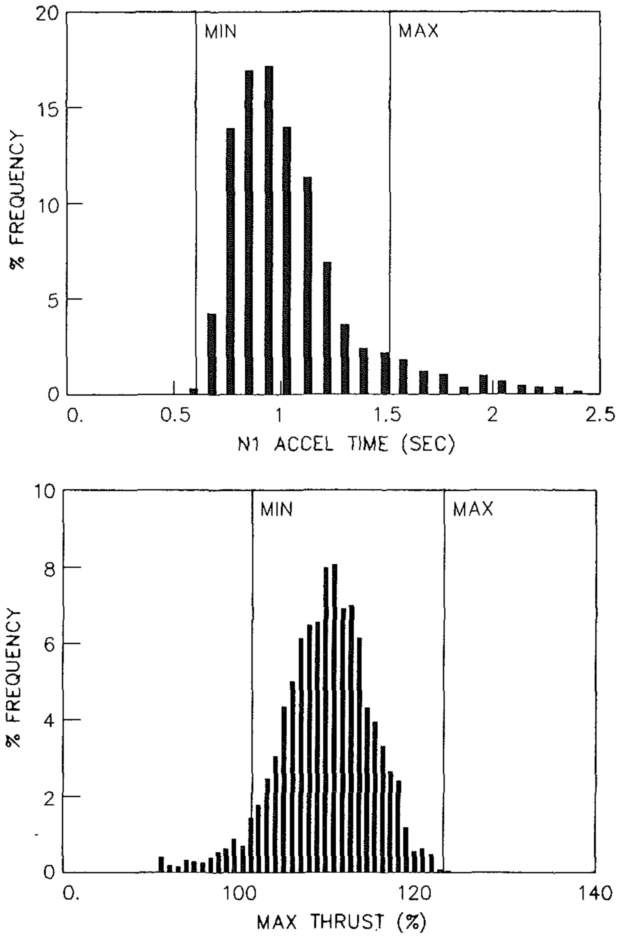

Fig. 8 Health index frequency distributions

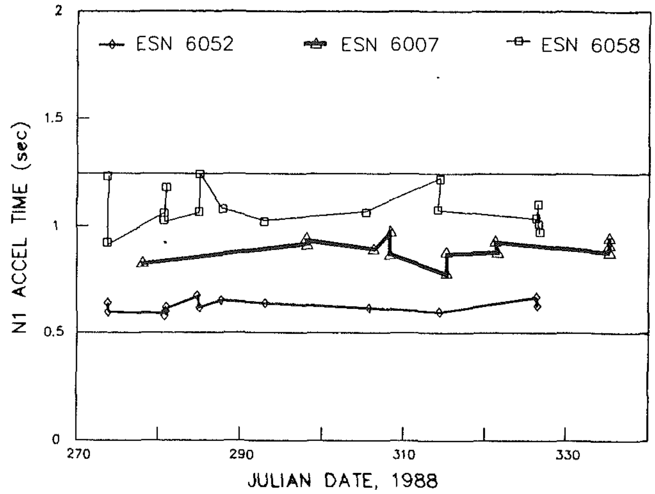

Fig. 9 Engine-to-engine variation in $N_1$ acceleration times

Table 2 CF-18 engine health index alarm limits

| Index | Alarm Limits | |
|---|---|---|
| | Min. | Max. |
| 1. $N_1$ Accel Time (sec) | 0.5 | 1.5 |
| 2. $N_2/\sqrt{\theta_1}$ at $N_1/\sqrt{\theta_1}$ = 90% (%) | 86.0 | 90.0 |
| 3. Fuel Ratio Units at $N_2/\sqrt{\theta_1}$ = 80% (pph/psia) | 26.0 | 31.5 |
| 4. Fuel Ratio Units at $N_2/\sqrt{\theta_1}$ = 87% (pph/psia) | 28.0 | 32.0 |
| 5. Maximum Fuel Ratio Units (pph/psia) | 29.0 | 34.0 |
| 6. Maximum Computed Thrust (%) | 100.0 | 125.0 |
| 7. Maximum Oil Pressure (psi) | 95.0 | 130.0 |
| 8. Maximum Broadband Vibration (ips) | - | 2.0 |
| 9. Engine Inlet Airflow (pps) | 105.0 | 120.0 |
| 10. Left - Right $P_{S3}$ Rise Time (sec) | -2.50 | 2.50 |
| 11. Left - Right $N_1$ Accel Time (sec) | -0.75 | 0.75 |

analysis program, which first smooths the as-recorded time traces and then computes the various health indices. The health index values are compared to predetermined alarm limits and, when a limit is exceeded, a preventive maintenance flag is displayed. Thus, in a manner analogous to the IECMS limit surveillance algorithms and MMP codes, a second level of engine monitoring is provided.

The alarm limits have been established by a statistical analysis of over 2000 take-offs and 200 different engines. As an example, Fig. 8 illustrates the frequency distributions obtained for the $N_1$ acceleration time and maximum thrust indices. It is apparent from these distributions that data scatter is reasonable (i.e., the indices are repeatable) and that meaningful alarm limits can be defined. In fact, the repeatability of the health index values for a given engine will be much better than that indicated in Fig. 8. To illustrate this point, the $N_1$ acceleration trend plots for three separate engines are presented in Fig. 9. From this figure it can be seen that the overall scatter in $N_1$ acceleration times arises primarily from engine to engine performance variations, rather than individual engine data scatter. Table 2 summarizes the alarm limits presently defined for each of the CF-18 engine health indices.

The health indices derived from each take-off are stored in a Health Index Archive File from which trend plots of these data may be obtained. Figure 10 shows a typical trend plot.

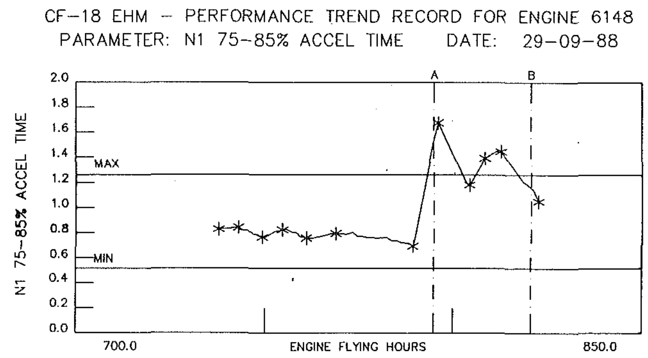

MAINTENANCE SUMMARY

A– ADP No. : KKK001 TIME : 795.0
SN 6148 (R) – LPT MODULE CHANGED

B– ADP No. : VM1234 TIME : 821.0
SN 6148 (R) – FOD CHECK – NO FAULT FOUND (SERV)

**Fig. 10 Typical trend plot**

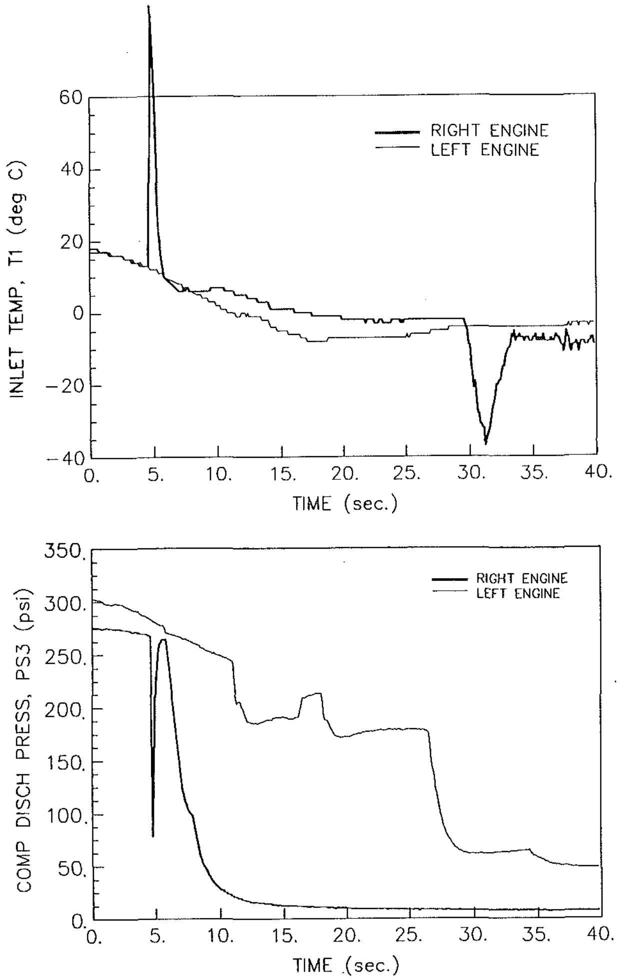

**Fig. 11 False $T_1$ sensor failure event recording**

Each health index can be trended on either an aircraft tail number or engine serial number basis. When trending by aircraft tail number, both left and right engine data or the difference (left – right) between the two engine index values can be displayed. The alarm limits are superimposed on the trend plots for reference purposes and significant maintenance actions can be annotated by a vertical dashed line. A printed summary of the maintenance actions can also be displayed as shown in the figure.

**Table 3 Summary of IECMS event recordings**

| Event Type | Valid | False | Unknown* | Total |
|---|---|---|---|---|
| Sensor Fail | 33 | 2 | 0 | 35 |
| Overspeed | 3 | 0 | 0 | 3 |
| Overtemp. | 16 | 39 | 3 | 58 |
| High Vibs. | 46 | 0 | 0 | 46 |
| Low EOP | 7 | 2 | 4 | 13 |
| Flameout | 0 | 352 | 0 | 352 |
| | 105 | 395 | 7 | 507 |

* MMP codes set without corresponding event recordings

## Field Evaluation

The flight line troubleshooting and performance monitoring techniques described above have been under evaluation by engineering personnel stationed at each of the CF-18 main operating bases since June of 1988. The results of these evaluations to date indicate that the IECMS event data recordings are very beneficial as a means of substantiating the occurrence of in-flight anomalies and determining their cause. To a lesser degree, the performance monitoring procedures have been successful in identifying problematic engines *before* an in-flight anomaly actually occurs.

A brief description of the field evaluation results follows.

**Substantiation of In-Flight Events.** The most obvious use of the in-flight event recordings is the substantiation of in-flight anomalies (i.e., did the event actually occur?). Automated engine monitoring systems have historically suffered from excessive false alarm rates resulting in a lack of confidence in these systems by the maintenance technicians. The IECMS event data recordings, however, provide a relatively quick and reliable means of determining whether or not an MMP code has been properly set. For example, Fig. 3 presented earlier in this paper clearly shows an exhaust gas overtemperature condition resulting from improper nozzle control. On the other hand, Fig. 11 illustrates a false $T_1$ sensor failure event. In this case the $T_1$ "spike" apparent in the figure is believed to have been caused by a compressor instability, as shown in the accompanying compressor delivery pressure trace.

Table 3 presents the results of an investigation into more than 500 IECMS event recordings. In general, the findings appear to confirm the maintenance technicians' suspicions that many MMP code occurrences are false alarms. However, the results are misleading in that most of the false alarms are flameout codes and are presently ignored unless confirmed by a pilot report. A large percentage of the false flameout codes are caused by operational practices (e.g., throttle advances with engines off and fuel valve shut-off tests), which are not properly accounted for in the IECMS flameout logic.

Most of the other false MMP codes are the result of sensor or signal conditioning problems. In this regard, it is noteworthy that the gradual deterioration of a measurement (e.g., sensor drift) is likely to result in a false limit overshoot prior to an IECMS sensor failure code. Thus, many of the false alarms themselves provide useful diagnostic information.

**Flight Line Troubleshooting.** Beyond the simple substantiation of an in-flight event, the IECMS data recordings have also proven to be useful in isolating specific component prob-

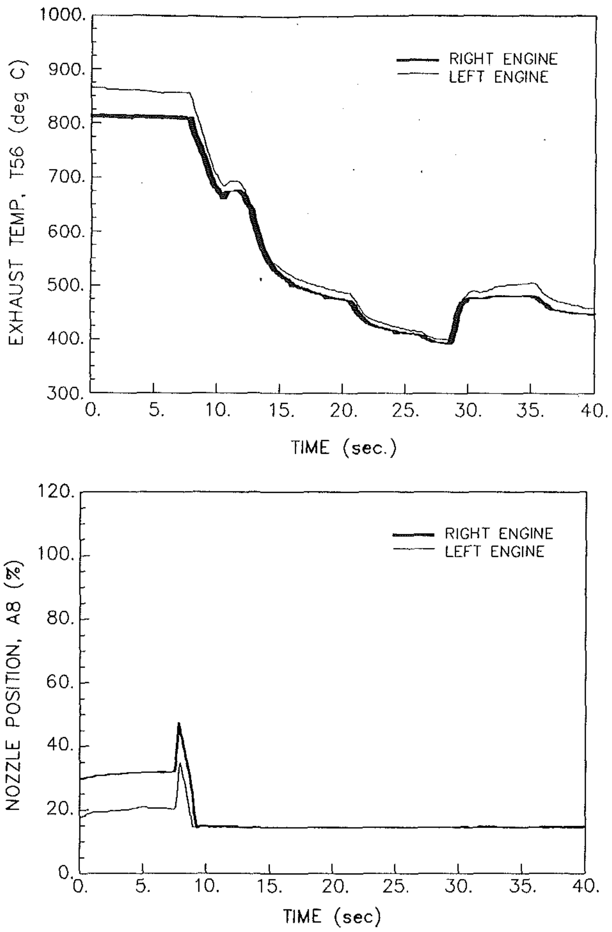

**Fig. 12 Exhaust gas overtemperature: improper VEN control at IRP**

lems. The best examples of this are the exhaust gas overtemperature recordings. Investigations to date indicate that most in-flight overtemperatures are the result of three common failure modes:

1 variable exhaust nozzle (VEN) closure in afterburning
2 improper VEN control at IRP
3 VEN transmitter failure

Furthermore, each failure mode results in a recognizable event recording, as shown in Figs. 3, 12, and 13. The overtemperatures due to improper VEN control at IRP or in afterburning are caused by Electronic Control Unit (ECU) malfunctions. The VEN transmitter failure (in this case an intermittent failure) results in a VEN position value of 140 percent, which corresponds to the transmitter open-loop voltage. When the ECU detects this open-loop signal it activates failsafe logic, which automatically closes the VEN. At high power settings, this usually causes an exhaust gas overtemperature.

Many of the valid overspeed events are also caused by improper VEN control. For example, Fig. 14 shows the nozzle position and fan speed traces from an engine that experienced an overspeed following a throttle chop from full afterburner to IRP due to a failure of the VEN to close.

**Performance Monitoring.** Evaluation of the performance monitoring procedures has been conducted largely on the basis of individual case studies. The results of these studies suggest that the IECMS take-off health indices provide a reliable means of tracking the general performance level of in-service engines and, in certain instances, can be used to identify specific problems. The following examples serve to substantiate these preliminary observations.

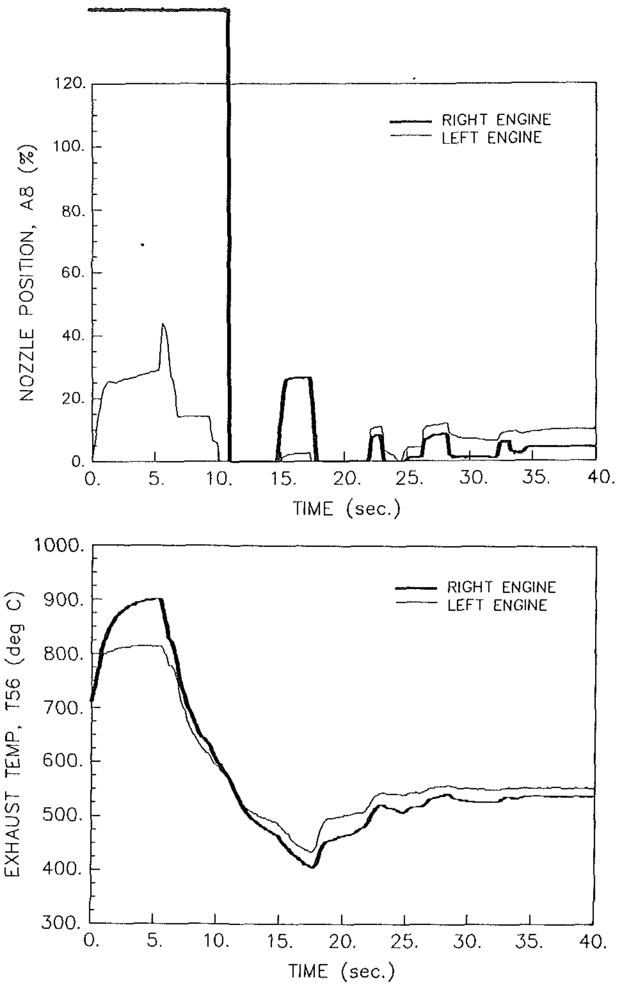

**Fig. 13 Exhaust gas overtemperature: VEN transmitter failure**

(*a*) *Case Study 1: Excessive Turbine Tip Clearance.* Over a period of approximately 6 months an engine located at CFB Baden experienced a number of performance-related problems (flameout on start-up, low thrust, wide nozzle area at IRP) and was eventually removed from service due to an out-of-limit nozzle area condition at IRP. During this period the engine was tested at the second line engine test facility on three separate occasions. On each occasion the engine exhibited large nozzle area ($A_8$) and low Engine Pressure Ratio (EPR) characteristics; however, both parameters were within acceptable limits. In an attempt to correct the performance problems a number of accessory components ($T_{56}$ harness, MFC, $P_{56}$ transducer, VEN power unit) were replaced, with little or no effect on the large $A_8$ and low EPR symptoms. Only after extensive disassembly and rebuild of the engine, including replacement of the HP turbine module, were the symptoms eliminated. Subsequent investigations revealed that the most likely cause of the poor engine performance was excessive HP turbine blade tip clearance.

Examination of the take-off health indices for this engine indicated extremely slow $N_1$ acceleration times, slow $P_{s3}$ rise times, and low thrust over the period of interest (for example, see Fig. 15). The fuel ratio unit parameter trends, however, indicated that the engine's MFC was at all times scheduling fuel in accordance with the proper acceleration schedule (see Fig. 16).

The performance trend plots of this case study clearly identify the engine as being problematic prior to its removal from service. Furthermore, the combination of slow acceleration, low thrust, and proper fuel scheduling are indicative of a gas

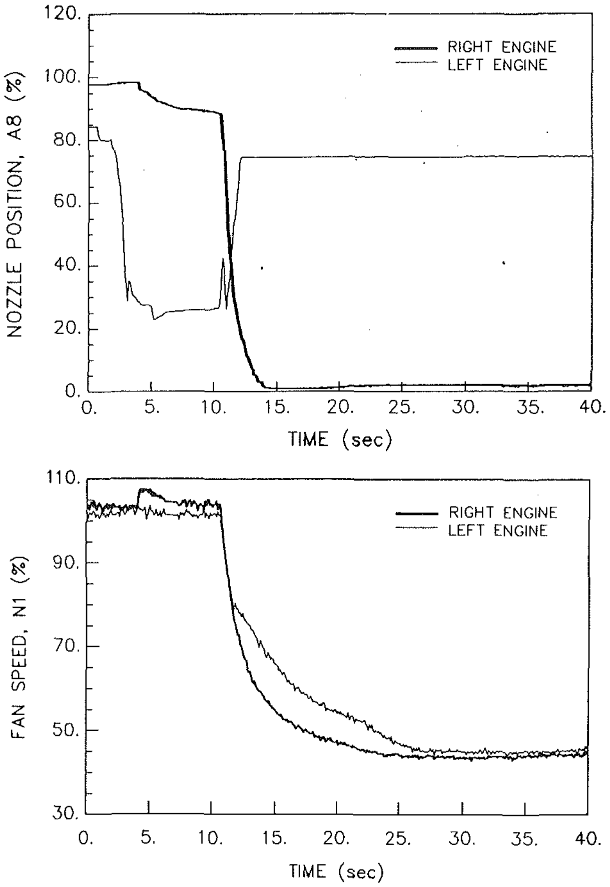

**Fig. 14** Fan overspeed due to failure of VEN to close

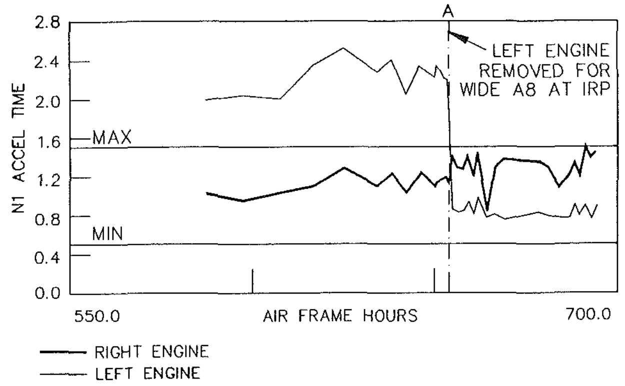

**Fig. 15** $N_1$ acceleration time trend plot: HP turbine tip clearance problem

path problem; hence, the replacement of numerous accessory components was unnecessary.

(*b*) *Case Study 2: Faulty $T_{25}$ Sensor.* In Feb. 1989 an aircraft located at CFB Cold Lake experienced an in-flight engine compressor stall. Analysis of the in-flight event data, in this case a $T_1$ sensor failure event caused by a momentary reversal of the engine core flow (see Fig. 11), confirmed that the compressor stall did in fact occur. The engine was removed from service and tested in the engine test facility, where the problem was eventually traced to improper compressor variable geometry (CVG) scheduling caused by a faulty $T_{25}$ sensor.

Analysis of the performance trends for the problematic engine showed all parameters within acceptable limits, with the exception of the $N_1$ versus $N_2$ speed relationship parameter. As illustrated in Fig. 17, this parameter was out of limits for all of the engine's monitored service. Upon review of the test cell records for this engine it was found that the engine had in fact failed a CVG schedule check at approximately 100 flight hours, but this had been attributed to CVG measurement difficulties.

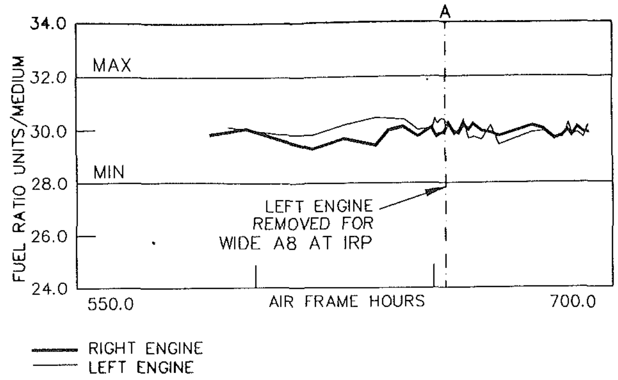

**Fig. 16** Fuel ratio unit trend plot: HP turbine tip clearance problem

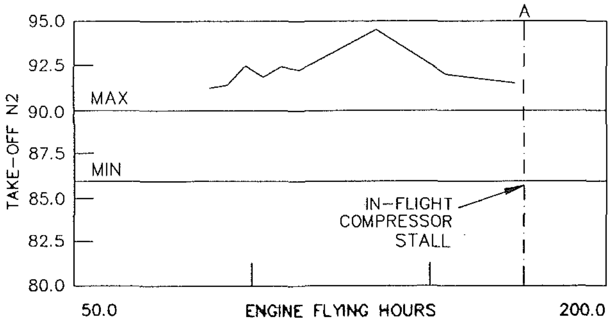

**Fig. 17** $N_1/N_2$ speed relationship trend plot: faulty $T_{25}$ sensor

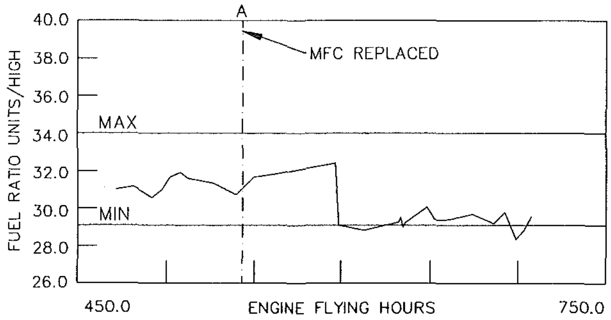

**Fig. 18** Fuel ratio unit trend plot: faulty MFC

As previously mentioned, the $N_1$ versus $N_2$ speed relationship parameter can be sensitive to gas path problems such as the CVG problem of this case study. It is also noteworthy that the installed instrumentation for the F404 engine does not include fan or compressor variable geometry position measurements. The $N_1$ versus $N_2$ parameter thus provides an indirect means of ensuring proper CVG scheduling without the need for an off-aircraft engine test.

(*c*) *Case Study 3: MFC Problem.* A mission was recently aborted at CFB Baden due to the failure of an engine to light in afterburning following take-off. Examination of the take-off event data provided by the IECMS revealed excessively slow acceleration times for the problematic engine. The cause of the slow engine response has been attributed to a faulty MFC, as indicated by the fuel ratio unit trend plot for the engine shown in Fig. 18. This plot clearly indicates a sharp drop in the fuel ratio unit parameter more than 100 flying hours before the incident occurred.

## Future Development Work

Development of the CF-18 engine performance monitoring and troubleshooting procedures is expected to continue until 1991, at which time the results of the development program are to be formally reviewed and those procedures that prove to be of definite benefit to the Canadian Forces will be incorporated into the F404 maintenance program. Prior to this time, the following development activities are planned.

**Troubleshooting Procedures.** Future development work on the use of IECMS event recordings for troubleshooting purposes will focus primarily on the definition of procedures for using the event plots in conjunction with existing installed engine troubleshooting manuals. The general objective in this regard is to establish a "library" of event traces, which the technicians can refer to when a specific MMP code is set. Additional software development is required to integrate the troubleshooting software with existing Ground Data Station capabilities and thus provide squadron maintenance personnel with rapid access to the enhanced troubleshooting information. Improvements to the software are also required to enable limited analysis of the event data traces such as the determination of peak parameter values and time spent in out-of-limit conditions and to compare the various parameter plots to a library of traces as previously mentioned.

**Performance Monitoring Procedures.** The objective of the development work in this area is to reduce the present complement of health indices to a smaller number of parameters that can be used by maintenance technicians to reliably monitor F404 engine performance. To this end, the analysis of field data on both a statistical and case study basis will continue. Additionally, the dynamic behavior of the engine during the take-off ground roll will be examined at a more fundamental level.

The general approach to be taken for investigating the dynamic performance of the F404 will be similar to previous steady-state gas path analysis work, described by Muir et al. (1988). In particular, a dynamic model of the engine, capable of simulating common engine faults at the component level, is currently under development. This simulation, when completed, will be used to refine the existing take-off data analysis techniques and, possibly, to develop complementary test cell troubleshooting procedures.

## Conclusion

Advanced engine troubleshooting and performance monitoring techniques have been developed using data provided by the CF-18 aircraft In-flight Engine Condition Monitoring System. The troubleshooting techniques are based on the graphic presentation of event data recorded at the time of an in-flight anomaly. The event data traces have proven to be extremely beneficial for verifying that an out-of-limit condition was in fact experienced and, in certain instances, for isolating specific component problems. The performance monitoring techniques are based on a number of relatively simple engine "health indices" derived from data recordings taken automatically during the ground roll of each take-off. The statistical analysis of a large number of take-offs indicates that these indices are repeatable measures of engine performance. Several case studies have shown that problematic engines can be identified by shifts or changes in the index values; thus the performance monitoring techniques are also useful in the troubleshooting process. Further field evaluation and refinement of the new troubleshooting and performance monitoring techniques are planned before they are reviewed and formally incorporated into the CF-18 engine maintenance program in 1991.

## References

Doane, P. M., and Kinley, W. R., 1983, "F/A-18A Inflight Engine Condition Monitoring System (IECMS)," Paper No. AIAA-83-1237.

Muir, D. E., Rudnitski, D. M., and Cue, R. W., 1988, "CF-18 Engine Performance Monitoring," *AGARD Conference Proceedings*, Paper No. AGARD-CP-448.

**J. C. Corde**
M88 Program Manager,
SNECMA,
Paris, France

# SNECMA M88 Engine Development Status

*After describing the historical origins of the SNECMA M88 engine development program, the paper presents the general development planning until the production engine flight qualification at the end of 1995. Then the technical aspects of the program are emphasized: The main new technologies involved in the engine, the general arrangement, and the performance are described and the engine development, status is fully presented (development philosophy, main component tests, and complete engine tests).*

## Program History

The SNECMA M88 engine main concepts and choices were settled at the end of the 1970s, when launching a complete demonstration for all main technologies involved in an advanced multipurpose engine to be competitive in the 1990s. The joint studies of both SNECMA and French Ministry of Defense at this early period concluded that a high overall pressure ratio and high turbine entry temperature (TET) were needed. The first component tests began in 1978, in order to realize a complete core engine able to reach a 1700 K TET level (TET being the temperature in front of the high-pressure turbine rotating blade), which was tested in a special bench from fall of 1983 to 1986. The program history is illustrated in Fig. 1.

Within the same period, due to good results of the component tests, the demonstration program was reoriented toward the much more ambitious goal of an 1850 K TET level. In fact, this temperature was actually reached within a new core engine in Feb. 1987, and since then more than five hours operation at this tempearture has been achieved. Meanwhile, the full level of technology, which had been demonstrated during the first core engine tests, was introduced within the first Demonstrator engine, which was a genuine engine, the so-called M88-1, fully designed the same way as future flight engine would be.

Then, taking into account the complete demonstration program results, SNECMA was able to accept a fixed price, cofinanced development contract with the French Ministry of Defense, valid until the very end of the full development program.

## Development Planning

The full development program (shown in Fig. 2) was launched at the beginning of 1986 for the core engine, and then at the beginning of year 1987 for the 75 kN-SNECMA M88-2 complete engine. The first run of the first development engine had been projected for the end of Feb. 1989, but it occurred on Feb. 27, 1989, and the max dry thrust was reached three days later.

Afterward, the nominal 75 kN thrust with max rehead was reached on Apr. 12, 1989, after less than 10 operation hours of the engine. These good results enabled SNECMA to achieve

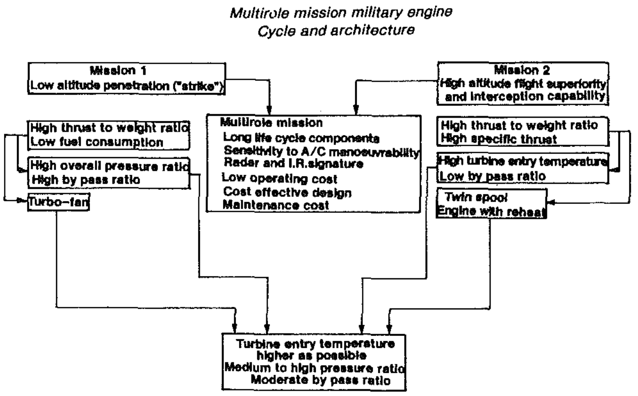

Fig. 1(*a*) History of program—mission requirements

The M88-2 engine is a 75kN (17 000lb) thrust class, two shaft augmented mixed flow turbofan, result of a complete research and demonstration program.

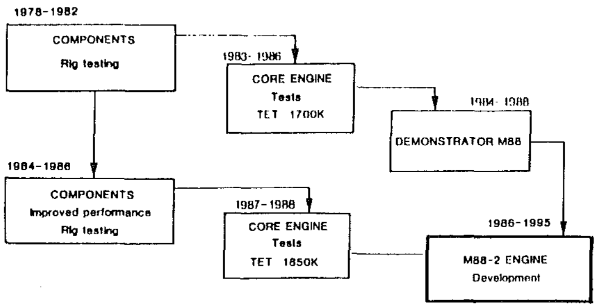

Fig. 1(*b*) History of program—test highlights

---

Contributed by the International Gas Turbine Institute and presented at the 35th International Gas Turbine and Aeroengine Congress and Exposition, Brussels, Belgium, June 11-14, 1990. Manuscript received by the International Gas Turbine Institute February 1, 1990. Paper No. 90-GT-118.

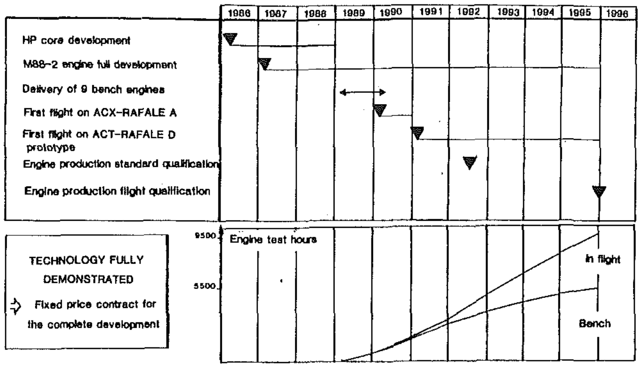

Fig. 2 Development planning

- ▶ METALLIC MATERIALS
  - ▶ Single crystal cooled turbine blades
    - AM1 alloy developed with ONERA, Paris "Ecole des Mines" Laboratory (located in SNECMA's Corbeil facility) and IMPHY s.a.
    - Sophisticated cooling system : the flow temperature is approximately 300 degrees higher than the melting point of material.
  - ▶ Powder metallurgy
    - Advantages : high temperature mechanical strength, low cracks progressing speed.
    - The first engines hot disks are made with well-known Astroloy : production engines hot disks will be made with french elaborated N18 alloy, also developed with ONERA, Paris "Ecole des Mines" Laboratory and IMPHY s.a.
    - A complete european N18 elaboration system is under construction.
- ▶ COMPOSITE MATERIALS
    - Hot and cold nozzle petals : SEP's silicium carbide matrix material.
    - By-pass duct : PMR 15 resine
- ▶ CALCULATION METHODS
    - Aerodynamic performances improvement .
    - 3D calculation for air flows and mechanical elements geometry.

Fig. 3 The main new high technologies

the first official performance test on Apr. 21, 1989, five months before the contractual milestone.

Meanwhile, the eight other bench engines of the program were delivered within the foreseen period, one of them being used for the first flight of the engine on the ACX-RAFALE demonstration aircraft.

During the second part of 1990, the second official test is required before the initial flight of the first ACT-RAFALE D prototype aircraft in the first quarter of 1991 with two SNECMA M88-2 engines.

Further, the engine production standard qualification is scheduled in the third quarter of 1992, and the engine production flight qualification is to be obtained at the end of 1995. This full development program includes 5500 bench test hours, both sea level and simulated altitude cell tests, and 4000 flight operating hours with 15 additional engines for five prototype aircraft, 600 flight hours of which to be made for specific engine tests.

## The Main New Technologies

Among the highly advanced technologies (Fig. 3) involved in the SNECMA M88-2 engine is the technique of cooled single crystal turbine blades, which opens the way to the extremely high TET. They are made with AM1 alloy, which has been developed in France by SNECMA, the research labs of ONERA and Paris "Ecole des Mines" located within the SNECMA's Cobeil facility, southeast of Paris, and the metallurgical company IMPHY. These blades need a most sophisticated cooling system, due to the fact that the airflow temperature around each of them is approximately 300 K higher than the melting point of the material.

In the material field, powder metallurgy must also be emphasized since this allows forging of high temperature resistance, low crack propagation rate alloys. The hot disks for the development engines are made of astroloy, but the production engine will use N-18 alloy, produced by the manufacturer that produces AM1 alloy.

Still in the material field, particularly important are the hot and cold nozzle flaps made with silicon-carbide matrix material developed by the Société Européenne de Propulsion, which is a SNECMA subsidiary. Also, another composite material (PMR 15) will be used on production engines to make the bypass duct of the engine, which is today made of chemically machined titanium. Other uses of composite materials are being studied for further mass reduction.

In the field of calculation methods, considerable progress has made possible very elaborate three-dimensional calculations, which perfectly represent the airflows, specifically unsteady and viscous phenomena, and give both compressors and turbines aerodynamic performance improvements.

A good idea of the whole technological progress made by SNECMA within the past 20 years is given by comparison of the ATAR 9K50 engine, which powers the Mirage F1 and the Mirage 50 aircraft, versus the M88-2 engine (Fig. 4). With both SNECMA engines of comparable thrust level, the M88-2 engine is 40 percent shorter and 45 percent lighter, and the thrust-to-weight ratio is improved by 88 percent!

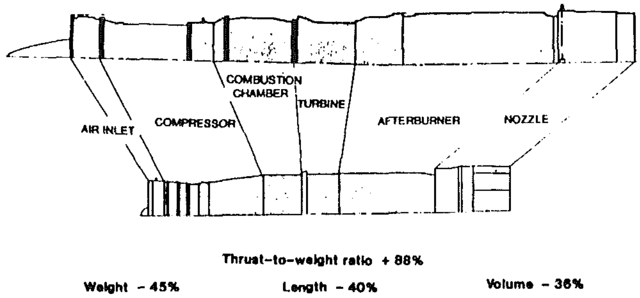

Fig. 4 SNECMA engineering—20 years of progress

Another highly advanced technology employed for the SNECMA M88-2 engine is redundant, full-authority digital electronic control, which allows the use of highly precise control rules, with utilization of all engine possibilities, without restriction of throttle movement throughout the flight envelope, regardless of the mission phase or the flight configuration of the aircraft (Fig. 5). This fully redundant system integrates two similar computers, which also do health monitoring and maintenance calculations, and also integrates a specific electric power source for more reliability.

## The Engine General Arrangement and Performance

As shown in Fig. 6, the SNECMA M88-2 engine is a two shaft augmented mixed flow turbofan; the main features of its architecture are the following:

- three-stage low-pressure (LP) compressor with variable inlet guide vane for better operation with very high angle of attack, due to unsteady distortion effects limitation, and with a front bearing inducing a very precise mechanical behavior;
- six-stage high-pressure (HP) compressor with three variable stator stages including a variable inlet guide vane, for better flow adaptation at any rotating speed. The number of stages are chosen for good surge margin and growth potential within the SNECMA M88 family, whose thrust range is 75 up to 105 kN with the same core engine;
- short combustor with aerodynamic injection;
- one-stage HP and one-stage LP turbine;
- converging nozzle for rear drag reduction during subsonic low altitude penetration mission, and mass limitation.

The max afterburner thrust of the SNECMA M88-2 engine is 75 kN (17,000 lb), while the specific fuel consumption is limited at 1.80 kg/daN/h (1.77 lb/lb/h), with an overall pressure ratio of 24.5.

## Engine Development Status

**Computational Methods and Tests.** Within the continual objective of reducing development costs for such a program, it must be taken into account that a very major part of these costs is due to component and complete engine testing. The major part is spent for bench engines and manufacture of rig components. This experimental part could be thought very excessive today, the main reason being that the engine manufacturer has no right to mistakes and must be completely sure to be right due to risks to human lives and economic risks which increase as time goes on.

These overall considerations show that it is important to limit the number of component and complete engine tests, and this has been made possible as a result of considerable recent improvements in computer technology and computational methods. Progressively, a new design philosophy has been developed and applied successfully, as indicated in Fig. 7.

This new approach is characterized by the following strong points:

- three dimensionality, viscosity, compressibility, and unsteadiness of airflows are altogether taken into account;
- analysis can be performed at design and off-design conditions;
- interesting test configurations and appropriately positioned instrumentation within the most interesting area can be defined prior to test;
- computer-aided test analyses use the same computational code as for the design phase, inducing easier and faster test/calculation comparison.

Then the first goal of the tests is to check validity of all kinds of calculation, mainly done during the demonstration program for the SNECMA M88-2 engine. However, some specific partial component tests have also been included as part of the full-scale development program for six major components (LP compressor, HP compressor, combustor, HP turbine, afterburner, and control system), together with one core engine machine.

## Main Component Tests

Figure 8 shows the main components tested.

**Low-Pressure Compressor.** The LP compressor was tested on component rigs from Aug. to Oct. 1989 to obtain complete knowledge of its aerodynamic and mechanical behavior. The expected results were excellent due to its very satisfactory operation during the first complete engine tests, which had been done earlier. In fact, the component test gave the most perfect example of the effectiveness of the previously described new design philosophy. The mechanical behavior of

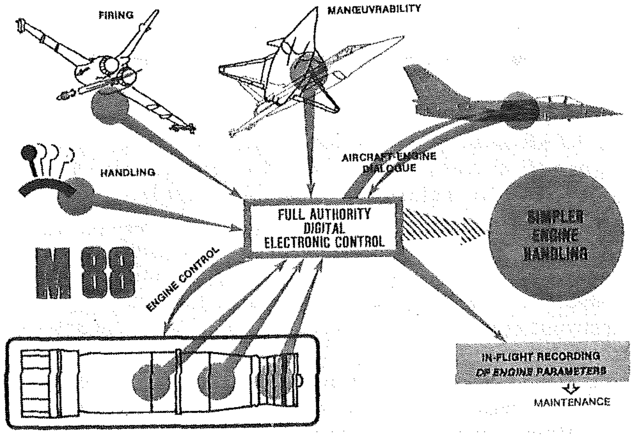

Fig. 5 Full authority digital control system benefits

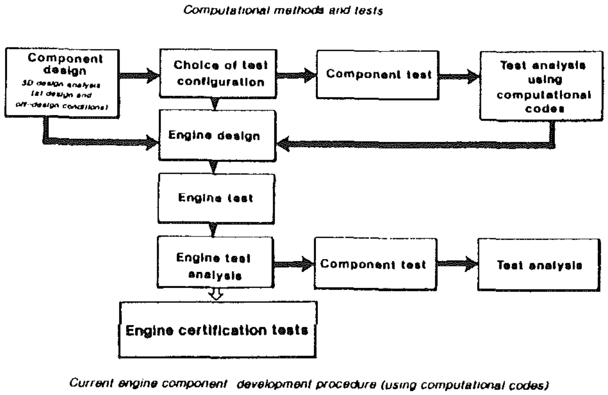
*Computational methods and tests*

*Current engine component development procedure (using computational codes)*

Fig. 7 Engine development process

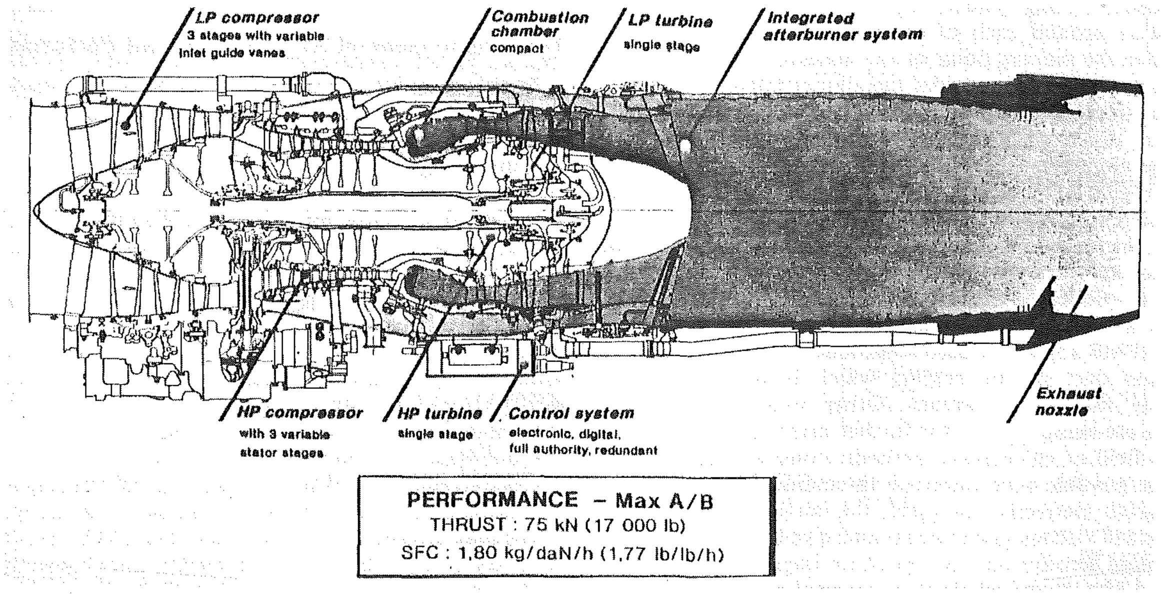

Fig. 6 Engine general arrangement

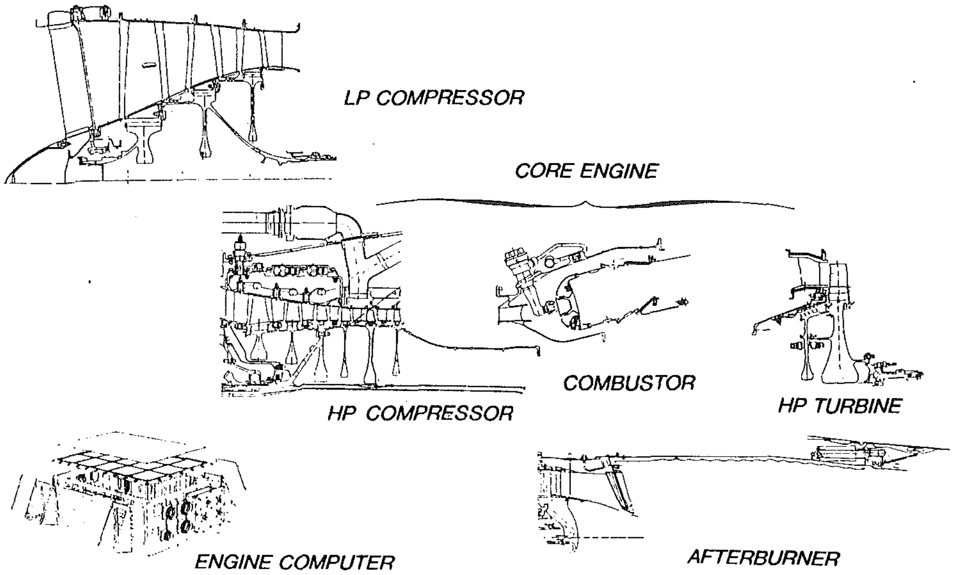

**Fig. 8 Main component tests**

the compressor has been perfect, and the aerodynamic performance was better than designed, slightly better for mass airflow and efficiency, and very much for stall margin.

**High-Pressure Compressor.** The HP compressor was the first tested component of the engine: five test series were done from Oct. 1988 to July 1989; the demonstrated behavior conformed to expectations on both the mechanical and aerodynamic fields. However, a few modifications have been tested in order to get closer to the working optimum of the rear stages, particularly around the inlet of the aircraft air bleed.

**Combustor.** The combustor was the second tested component; it took many test series to gather complete knowledge of pressure losses, circumferential and radial exhaust temperature uniformity, wall temperatures, combustion stability and relight fields, smoke, and pollution emission. All these tests showed that design objectives were realistic.

**High-Pressure Turbine.** The demonstration program enabled SNECMA to achieve a high TET level of 1850 K; as mentioned before, more than five operating hours were performed with a good efficiency level at this temperature, equivalent to more than 800 operational hours; this program also led to validation of the complete design techniques for such a turbine, among them the material choices and the cooling system. However, since this TET level had never been achieved within a production engine, SNECMA decided to invest in a complete turbine rig, with the special goal of optimizing the cooling air flow for maximum efficiency.

**Core Engine.** This rig machine integrates the three main hot components of the engine, which are the HP compressor, combustor, and HP turbine; the tests of this machine are made within a particular test cell in the Centre d'Ecole des Propulseurs (CEPr) in Saclay, near Paris, in which pressure and temperature air conditions in front of the HP compressor are simulated. The test campaign took place from June to Oct. 1989, and gave many very interesting results, among which were dynamic mechanical behavior of rotating parts, Reynolds number influence on aerodynamic working of the HP compressor, and operation for more than 30 minutes with maximum TET level. More than 150 operating hours were obtained with three core engine test machines, belonging first to the demonstration program and then to the full-scale development program.

**Afterburner.** The high exhaust temperature level within the LP turbine exit section led to the concept of an entirely new afterburner system, completely different from that in the SNECMA ATAR and M53 engines. The SNECMA M88-2 engine afterburner comprises an air-cooled radial flameholder system with front spray bars and both airflows are reheated. A complete component test campaign was included in the full-scale development program, in a simulated altitude test cell of the CEPr, for accurate knowledge and optimization of air cooling and fuel flow distribution. The first operation of this new afterburner on a complete engine was very successful, as will be indicated later in the section on complete engine testing.

**Control System.** The full-authority digital control system is made of many different hardware and software components, which all are separately tested in order to be sure of their own reliability and performance. These component tests are completed by block simulation tests in which the engine is represented by an on-line computer. These simulation tests enable the optimization of the control rules to be made safely, with no risk to the engine. Then the whole system was assembled for full engine tests.

## Full Engine Tests

As already mentioned, the full-scale development program comprises nine bench engines. Among them, six engines will be used for development tests, such as validations, calibrations, and comparisons with calculations; two engines are built for endurance tests; and one is the flight test engine on board the ACX/RAFALE A demonstrator aircraft.

Shortly after the first SNECMA M88-2 engine made successful runs at the beginning of 1989, the simulated altitude tests began in early July 1989, and quickly showed the good behavior of the engine throughout a large part of the flight envelope, from Mach 0.5 to Mach 1.2 at 20,000 ft and 30,000 ft. The engine behaved perfectly both in steady and unsteady operation, with and without afterburner, and demonstrated the required relighting envelope. The test setup is shown in Fig. 9.

During the same period, the first endurance tests with steady and unsteady operation were carried out, two engines reaching 55 hours and 70 hours. The second one, operating with preheated inlet airflow, simulated the Mach. 1.6 altitude flight temperature. The disassembly showed a very good

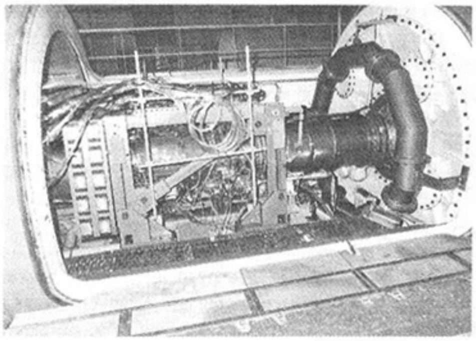
Full engine tests

The SNECMA M88-2 engine in altitude test cell

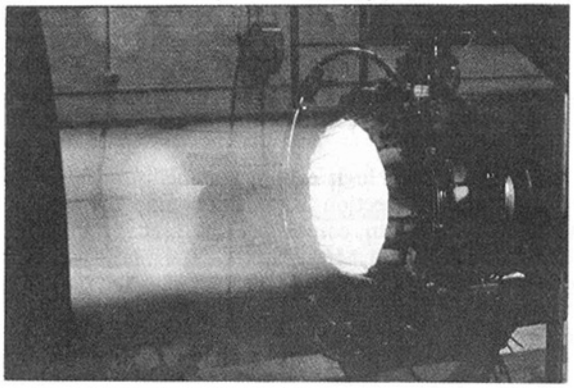
Full engine tests

12th April 1989 : First "max A/B rating" operation

Fig. 9 Complete engine test build

mechanical status of all parts of the engine, particularly the single crystal turbine blades and all the fixed and rotating pieces.

The pace of these first tests was very high: Within nine months, the total operating time was more than doubled, reaching 500 hours, taking into account the demonstration program. The following tests were to enable SNECMA to put the flight test engine on board the ACX/RAFALE A demonstration aircraft for the first flight to take place within the first quarter of 1990.

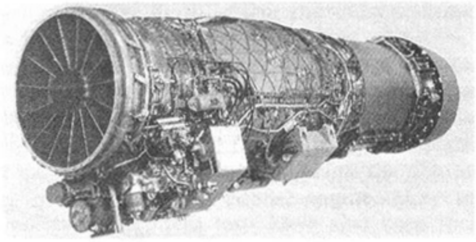
Fig. 10 The SNECMA M88-2 engine

At present, SNECMA lists the following satisfactory technical items:

- good general dynamic behavior;
- good quick transitory working, with perfect behavior of the compressors;
- maximum required performances quickly demonstrated;
- good vibration behavior for all blades;
- good thermal behavior for hot parts;
- required mass of the engine demonstrated for the first and all following engines;
- development cost at the scheduled level.

For SNECMA, the M88-2 engine represents the first priority, insofar as it gives complete mastership of all involved technologies, and it confirms capability and credibility for leading a complete and complex aircraft engine program.

## References

Choury, J. J., 1988, "Thermostructural Composite Materials in Aeronautics and Space Application," *COMDEF*, Washington, DC, Sept.

Geyer, P., and Galmiche, P., 1988, "The Control System of the SNECMA M88-2: A Modern Fighter Aircraft Engine," COMDEF, Washington, DC, Oct.

Mestre, M., 1900, "Utilisation des composites haute temperature dans les turboreacteurs," AGARD, pp. 449–450.

**R. J. Lane**
Chief Engineer.

**J. Behenna**
Chief Engineer.

Rolls-Royce plc,
Filton, Bristol BS12 7QE
United Kingdom

# EJ200—The Engine for the New European Fighter Aircraft

*This paper describes the concept and design of the EJ200 engine to meet the air staff targets for the European Fighter Aircraft. The international collaborative arrangements to support the program are shown and the lessons learned from previous collaboration illustrated. The excellent progress made in the program during the first year since the signing of the development contract is described to illustrate confidence in the ability to meet the design targets within the program time scales.*

## Introduction: The EJ200 Engine

The EJ200 combat engine is being designed and developed as a direct result of the new European Fighter Aircraft (EFA) requirement. The European Fighter Aircraft is to be built and operated by the United Kingdom, Germany, Italy, and Spain and will enter service in the second half of the 1990s.

The air staff target to which the EFA is being designed calls for a high-performance, high-agility aircraft, which is to be designed around a very low weight requirement with excellent reliability and ease of maintainability as a major design feature (summarized in Fig. 1). This paper describes the engine concept and engine solution that follows this requirement and describes the progress made in the program after the first year since the signing of the development contract.

The paper also illustrates the great improvement in European capability for a sophisticated and technologically advanced project such as EJ200, and compares early progress with that made on the RB199 engine, which is now a very successful engine in the Tornado project. Finally, the lessons learned on the Tornado program are shown to have been successfully applied with a consequent reduction in program risk and time scales and costs.

## Part I

**Aircraft and Engine Concept and Organization.** The EFA is a twin engine Canard Delta of compact size, very high performance, and high agility under both subsonic and supersonic flight conditions. It is powered by two EJ200 engines each of 90 Kn thrust class (20,000 lb), as shown in Figs. 2 and 3.

The main aircraft requirements are summarized in Fig. 4. This figure shows the emphasis on high performance and agility due to its fighter role, and also accentuates the need for aircraft and engine carefree handling throughout the flight envelope and, in addition, the need for excellent reliability and maintainability. As a condition of the specification the engine has to have at least 15 percent built-in thrust growth potential to cover future aircraft development. The total aircraft design is being monitored for the lowest possible total operating costs, and total life cycle costs.

**Overall Organization.** Under the four participating Nations an official organization called NEFMA has been set up

Europe has a European Staff Requirement (ESR) for a new fighter aircraft

Agreement by the armament directors of 4 countries at Turin August 1985:

- twin engined aircraft
- airframe mass 9.75 tonnes
- wing area 50 square metres
- engine reheated thrust 90kN class

Specified parameters

- performance
- cost
- operational targets

Fig. 1 Requirement

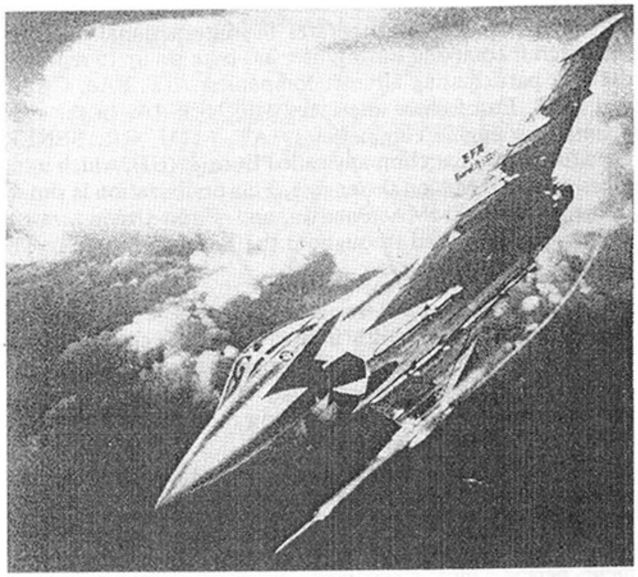

Fig. 2 EJ200 EFA

---

Contributed by the International Gas Turbine Institute and presented at the 35th International Gas Turbine and Aeroengine Congress and Exposition, Brussels, Belgium, June 11-14, 1990. Manuscript received by the International Gas Turbine Institute February 1, 1990. Paper No. 90-GT-119.

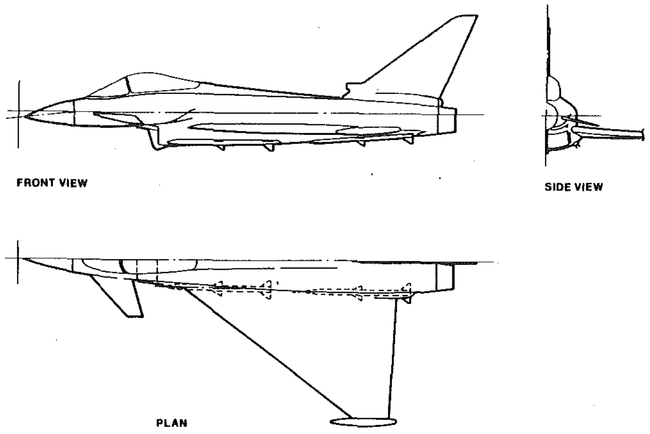

Fig. 3 EFA configuration

Detailed requirements specified in European Staff Requirement

- Emphasis on air-air role
- Point performance in both reheated and dry operation for high manoeuvrability and climb rate
- Critical mission requirements including minimum time intercept and long loiter air superiority
- *Carefree handling throughout extensive flight envelope*
- Excellent reliability, testability and maintainability
- At least 15% in built growth potential
- Design dictated by lowest possible life cycle costs

Fig. 4 Aircraft requirements

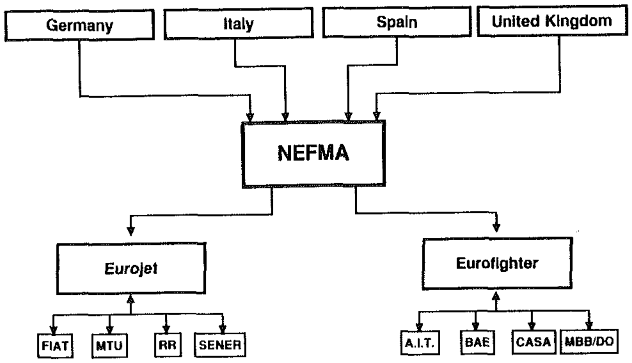

Fig. 5 Organization

in Munich. NEFMA is an organization comprising officials of all four nations, which operates the international contract. The aircraft company Eurofighter has been set up to represent the four participating aircraft companies, AIT, BAe, CASA, and MBB. Eurofighter interfaces with NEFMA. In the same manner the engine companies (FIAT, MTU, RR, SENER) have formed a joint company called Eurojet (EJ), which interfaces with NEFMA on the engine. This organization is similar to the proven NAMMA, Panavia, and Turbo-Union arrangement, which operated throughout the Tornado program. The layout is shown in Fig. 5.

**EJ Working Group Arrangements.** Figure 6 shows how Eurojet is organized, with a Board and Executive Control Committee and various working groups, which cover all aspects of the engine operation. At this time the largest organization is engineering, reflecting the design and development phase of the program.

The system is similar to that used for the RB199 in the Tornado program and, for instance, the engineering working group has comprehensive subgroups, which cover all aspects of the engine development program such as design, development, performance, mechanical technology, etc. Each working group has a formal representative from each of the partners who participate as necessary. The system works very well and this is due in no small part to the three Tornado program companies who know each other's ways and working practices and to a large extent operate in a similar manner. The ease with which the decisions are made and programs agreed and carried out shows how effective inter-European cooperation can be. The success will be illustrated later in the paper.

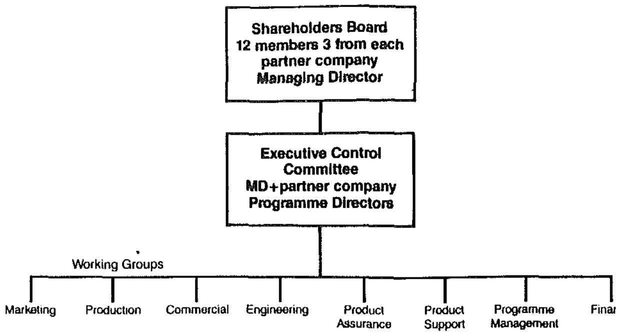

Working Group structure
*Chairman-Relevant full-time Eurojet staff member*
Members-Responsible full-time manager—Fiat, MTU, Rolls-Royce, SENER

Fig. 6 Eurojet working group concept

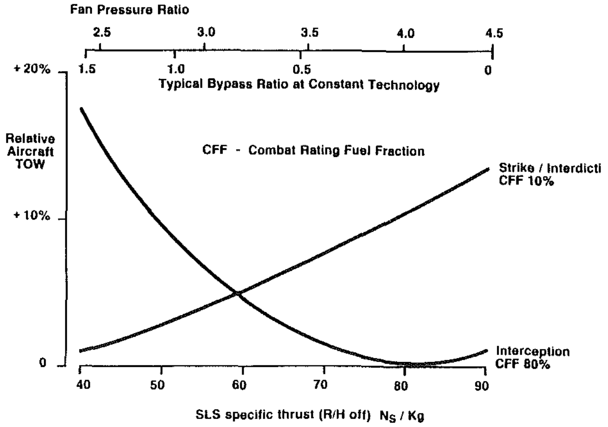

Fig. 7 Specific thrust—aircraft mission sensitivity

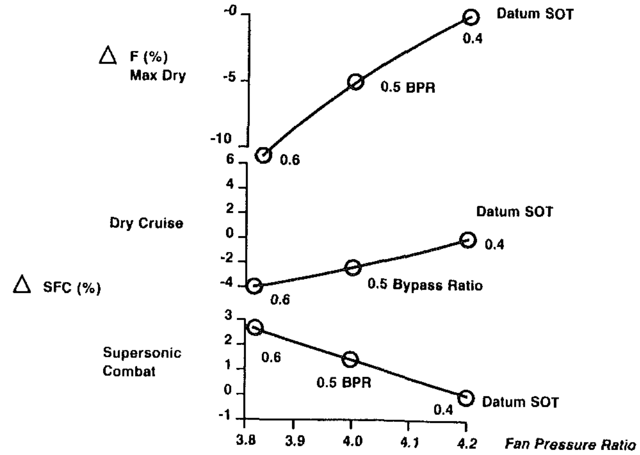

Fig. 8 Effect of fan pressure ratio on thrust and s.f.c.

## Part 2

**Engine Description.** The EJ200 engine concept requires a very compact lightweight configuration to fit within a closely cowled engine duct.

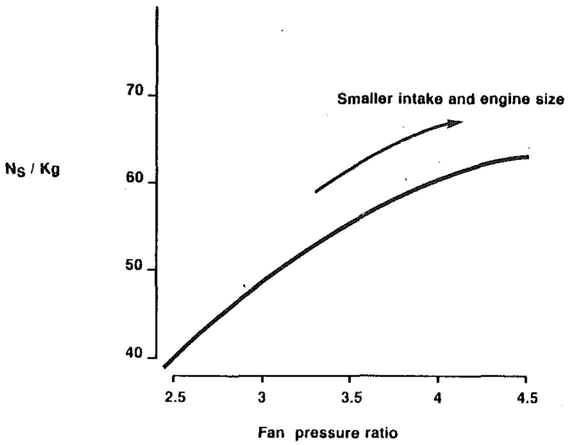

Fig. 9 Dry specific thrust (0.9 M, 20,000 ft)

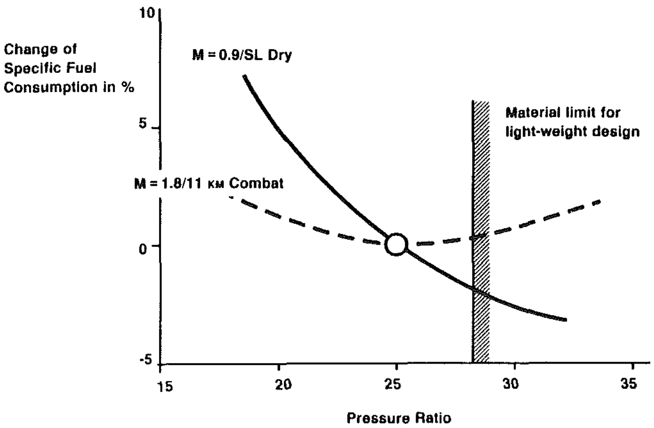

Fig. 10 Effect of overall pressure ratio on fuel consumption

| | |
|---|---|
| By Pass Ratio | 0.4 |
| Fan Pressure Ratio | 4.2 |
| Overall Pressure Ratio | 26 |
| Combat (Max Reheat) Thrust | 90 kN |
| Max Dry thrust | 60 kN |
| Turbine Temperatures | ~200°C Higher than current fighter engines |
| Thrust-weight Ratio Approx | 10 |

Fig. 11 EJ200 cycle parameters

| | |
|---|---|
| By Pass Ratio | - High growth potential<br>- High core power to cover offtakes |
| Fan Pressure Ratio | - High specific thrust (dry and reheat)<br>- Low reheated fuel consumption |
| Overall Pressure Ratio | - Low fuel consumption in dry cruise operation |
| Turbine Temperatures | - High Growth potential<br>- Long life turbines<br>- Small turbine sizes (low weight) |
| Convergent-Divergent | - High thrust and low specific fuel consumption at high mach no's (high nozzle pressure ratios)<br>- No penalty on long loiter missions |

Fig. 12 EJ200 cycle choice benefits

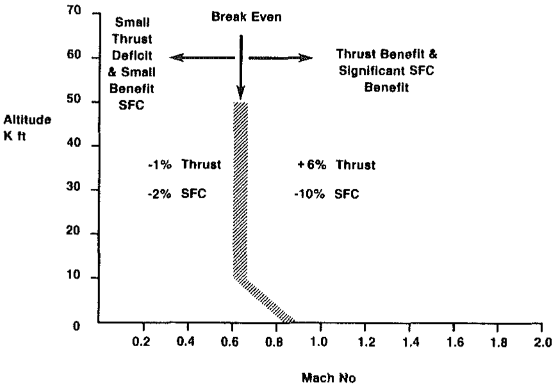

Fig. 13 Convergent-divergent versus convergent nozzle reheat operation

| | |
|---|---|
| Effects | - Significant improvements in aerodynamic performance particularly at high nozzle pressure ratios<br>- Increases in mass |
| Benefits | - Significant thrust increases and specific fuel consumption reductions during supersonic flight<br>- Considerable resultant increase in combat duration capability<br>- Virtually no loss in subsonic cruise/loiter performance<br>- No resultant penalty on long loiter missions |

Fig. 14 Convergent-divergent nozzle choice

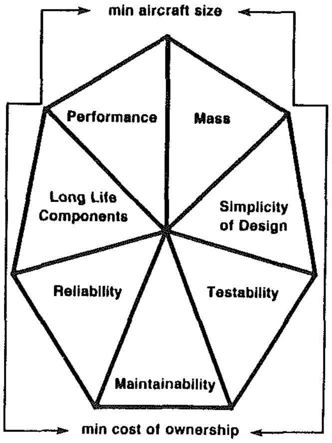

- Design has given equal priority to performance and life cycle costs

Fig. 15 Design requirements

The priority on the air-to-air role dictated by the European Staff Requirement leads to an emphasis on the requirement for low reheated s.f.c. levels. This is illustrated by Fig. 7, which shows that for supersonic interception mission some 80 percent of the fuel is used in combat as opposed to 10 percent in a strike/interdiction mission. In turn this leads to the requirement for a relatively high fan pressure ratio, and hence relatively low bypass ratio as shown in Fig. 8. By comparison the RB 199 was optimized for a low level strike role where the dry s.f.c. is relatively more important and this resulted in an intermediate bypass ratio engine.

**Cycle Choice.** A consequence of the move to high fan pressure ratios is a high level of specific thrust as illustrated by Fig. 9. For a given level of thrust requirement this has important implications on minimizing engine size and intake flow requirements.

The move to higher fan pressure ratios does have an adverse effect on dry cruise s.f.c. levels, as shown in Fig. 8. However, on the EJ200 engine the impact of this is minimized by setting the overall compression pressure ratio to the highest level possible within the constraints of engine and airframe materials, which dictate the maximum acceptable level of compression exit temperatures within the EFA flight envelope. The benefits of this on cruise s.f.c. are shown in Fig. 10.

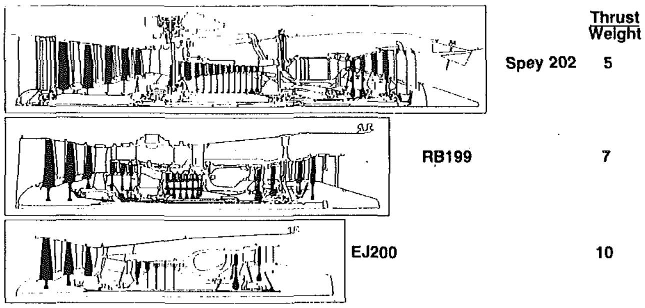

All scaled to same dry thrust at Mn 0.75, SL

**Fig. 16 Effect of technology on size**

## EJ200 details

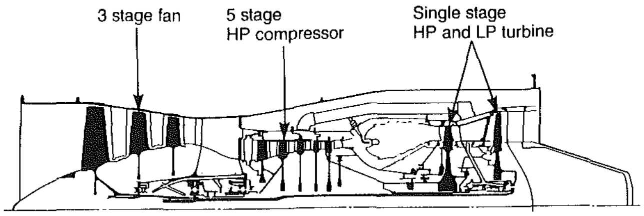

**Fig. 17 General arrangement—basic engine**

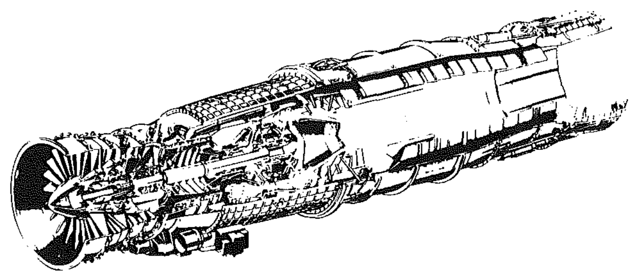

**Fig. 18 Whole engine**

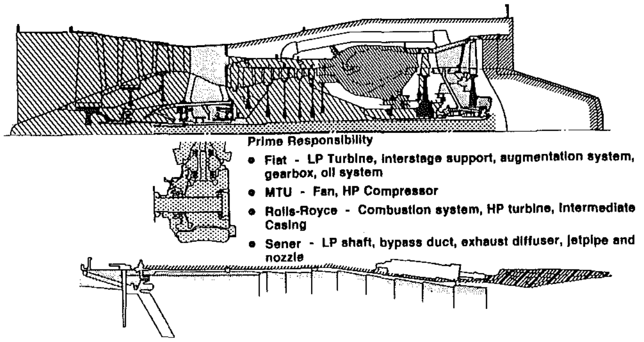

**Fig. 19 Work shares**

The resulting engine parameters are described in Fig. 11. The points of note are the fact that the engine is running at some 200°C higher turbine entry temperature than current fighter engines but despite this has a longer life and is to have a thrust weight ratio of 10 to 1 compared with 8 to 1 for the previous generation of engines. The reheat boost is lower than the RB 199 and earlier engines because the lower bypass ratio has been used and reheat has been limited for the best possible fuel consumption. The engine is fitted with a convergent/divergent nozzle for the first time on a European design.

Figure 12 summarizes the choice of various cycle parameters. The convergent/divergent nozzle was chosen because a higher reheated thrust at supersonic Mach numbers can be obtained due to the better nozzle expansion. Of more importance, this higher thrust at a given fuel flow improves the reheat s.f.c. even more and is a very important parameter for maintaining combat at supersonic speeds. The detailed study shows that the nozzle can be designed for negligible loss at subsonic missions and in particular for ferry and low-speed loiter missions. The performance of a convergent/divergent nozzle relative to the simpler convergent nozzle is compared in Figs. 13 and 14 to emphasize better thrust and even subsonic s.f.c. in reheat operation.

The relative importance of engine design parameters, how they affect the aircraft, and which affect cost of ownership is shown in Fig. 15. This separates out the performance and mass parameters for aircraft sizing and all the others such as lifting, simplicity, and reliability and maintainability in terms of the operating costs.

Improvements in design concept are made very clear in Fig.

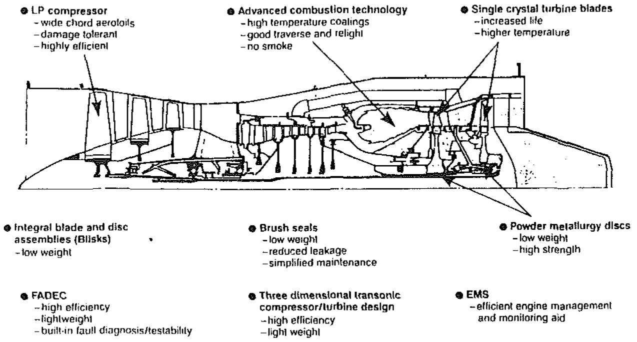

**Fig. 20 Technology features**

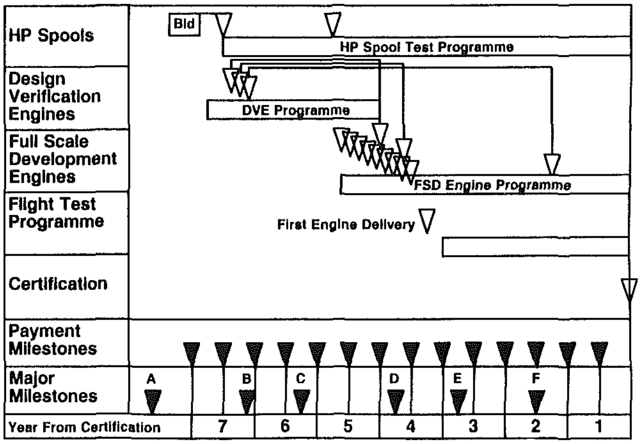

**Fig. 21 EJ200 initial development program outline**

| | |
|---|---|
| *RB199* | Component technology still being evolved after 1st engine run |
| *EJ200* | All components achieved performance on rigs at or close to production targets prior to 1st engine run |
| *Note:* | UK, German and Italian demonstration work had evolved necessary technology during EJ200 Project Definition Phase |

**Fig. 22 Comparison of component status on rigs before first engine run**

EJ200

no surge or other limiting problems

1st engine ran to full thrust within 1 week

Within 3% of guarantee SFC

Only two significant problems found

3rd Engine completed 155 hours and removed for strip experience only.
Did performance check, run through envelope in ATF and achieved 2700 cycles

Fig. 23 Engine experience in first year of program—1

EJ200

(a) Completed full steady state and transient X-rays successful
(b) Successful ATF running over flight envelope
(c) No engine handling problems or surge throughout testing
(d) Easy starting - no bleed and only one variable needed
(e) Heavy instrumentation over 1200 idents. All component performance, air and oil systems features understood
(f) All dynamic measurements taken on both spools

Fig. 24 Engine experience in first year of program—2

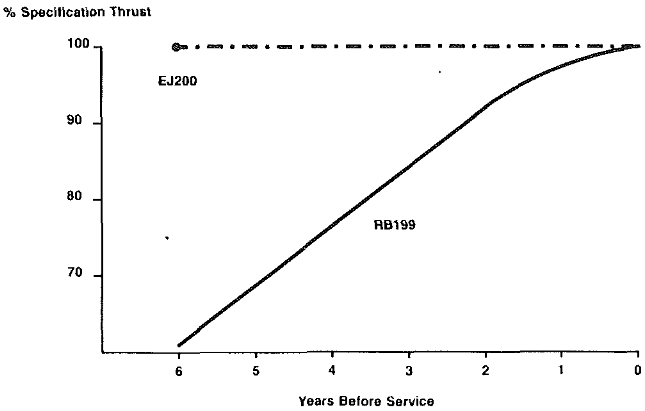

Fig. 25 EJ200 thrust achievement

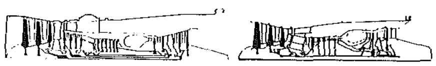

| | RB199 | EJ200 |
|---|---|---|
| Entry-into-service | 1979 | Mid - Late 1990's |
| Compression stages | 12 | 8 |
| Turbine Stages | 4 | 2 |
| Number of aerofoils | 2845 | 1800 |

Fig. 26 Technology will provide the cost benefits of design simplicity

16 where the relative size of the Spey, RB199, and EJ200 are compared when scaled to the same dry thrust at Mach point 0.75 and sea level operating conditions. The figure also shows the growth of engine thrust-to-weight ratio in the last 20 years. If the number of engine stages versus engine pressure ratio is compared this shows a remarkable improvement in aerodynamic capability in that time.

**EJ200 Details.** Coming now to the EJ200 details, Fig. 17 shows clearly the basic engine configuration: only eight compressor stages and two turbine stages for an engine with around 26 to 1 compression ratio. Three fan stages give over 4 to 1 pressure ratio and only 5 HP compressor stages over 6 to 1 pressure ratio. These are each driven by only one turbine stage. All the units are very efficient and the compressors have ample surge margin. Only one row of variable stators is used on the HP compressor and no variables are needed on the fan. Not only is this important in weight reduction and in terms of simplicity but it is also by far the best for minimizing bird strike damage on such an engine.

Figure 18 shows the whole engine in a sectioned form and here can also be seen a simple reheat arrangement and the convergent/divergent nozzle, which is very compact.

**The Workshare.** Workshare is illustrated in Fig. 19. In the simplest terms MTU is responsible for the two compressors, RR for the advanced technology titanium intercase, the combustion chamber, and the HP turbine, Fiat is responsible for the LP turbine and the reheat and the lightweight engine gear box, while the Spanish company Sener is responsible for the bypass duct, turbine exit casing, reheat pipe, and the convergent/divergent nozzle. Some joint responsibilities have been arranged so that the technology can be shared when necessary.

**Technology.** Technology features of the engine are outlined in Fig. 20. It can be seen that the engine not only uses advanced technology in aerodynamics, but also advanced materials are used in many parts of the engine. Particular attention should be drawn to the use of blisks on the third stages of the fan and the HP compressor. Brush seals are used instead of labyrinth seals on the air system almost throughout the engine and these have already been shown to be highly successful on engine running. The HP turbine uses advanced lightweight single crystal blades and both turbine disks are made from powder by a controlled process route.

Engine control is by an advanced lightweight Full Authority Digital Engine Control with full diagnostic and test capability. The hydromechanical element of the fuel system is of a new advanced type with minimum size and mass.

As materials improve and become available they will be incorporated into the design of the engine in order further to improve the in-service weight consistent with reliability. The use of carbon composites and ceramics on parts of the engine where they will improve mass or life is already planned. Advanced engineering programs are matched closely with the EJ200 project in order to ensure that they include standards that could be applicable to an engine such as EJ200 and its derivatives.

**The Engine Program.** The main layout of the engine development program is given in Fig. 21. Three design verification (prototype) engines, an HP spool, and a reheat rig have been built and tested. These have provided the proof of the design concept and have shown the problems that need to be solved for the production standard. These initial engines will be succeeded by the full-scale development engines. The latter engines are to a standard that will go forward to the flight development program and production.

Present planning is based upon the first flight of the EJ200 engine taking place 12 months after the EFA first prototype flies. The first two aircraft will be flown with RB199 engines. The engine bench program is planned to allow some 6000 hours before initial operational clearance. Although many details of the program are classified, Fig. 21 shows the general structure for an aircraft program that goes into service in the later part of the 1990s.

Figure 21 also shows the large number of milestones that have to be met during the development program. Each one of these is comprehensive in its own right and is being covered in another part of the paper. These milestones are linked to progress payments throughout the program. This is an important incentive on the Eurojet Partner Companies to maintain success throughout the development program.

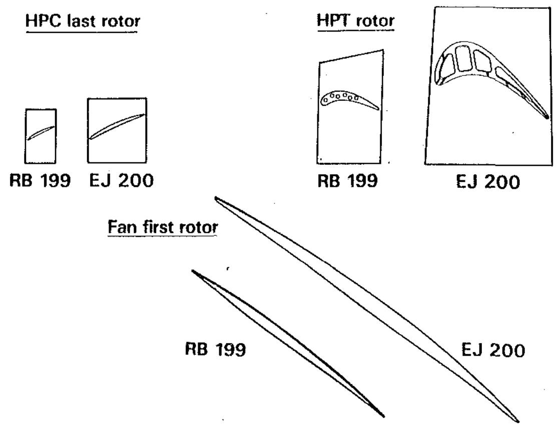

Fig. 27 Comparison of blade size

- **Contract Specification dictates equal priority to:**
  - *Flight Safety*
  - Performance (including mass)
  - Reliability
  - Maintainability
  - Timescales

Fig. 28 EJ200 specification requirements

- **Total Bench/Flight Development Programme subject to maximum price ceiling and divided into 15 price packages - for example:**
  - Engineering and testing between milestones
  - Full scale development engines initial build and associated hardware
  - Procurement, modification and repair of components and support of testing between milestones
  - Initial build of flight engines

Fig. 29 Typical examples of price packages

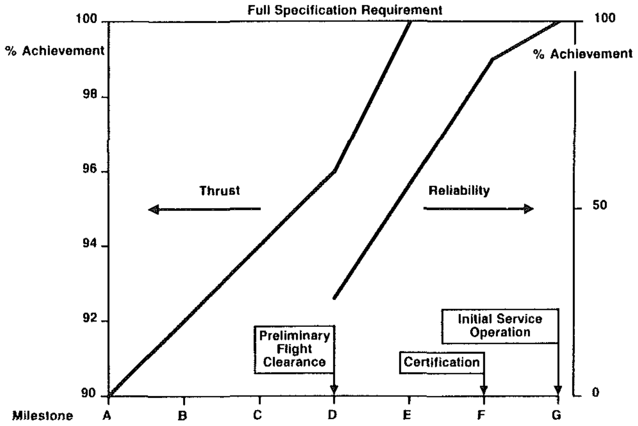

Fig. 30 Major milestone typical program

## Part 3

Figure 22 provides a comparison of the Rig Component Status before the first engine run of the RB199 and EJ200 engines. The table provides a comparison of the technology standard available on the EJ200 prior to the first engine run and the situation on the RB199 in 1972. It can be seen that the EJ200 was excellent in that all components achieved their full target efficiencies and other parameters on the rig before the engine ran. When the RB199 was started experience within Europe of such extensive collaboration was limited and the engine program was forced to begin with untried technology. The various rigs were either not available in time or when they were tested were well below target levels.

In the EJ200 case it is evident that the Europeans had achieved good coordination before the formal start of the program and most of the technology was obtained some two years before the engine ran. The advantages are obvious. In the United Kingdom there was the advantage of a successful XG 40 engine demonstrator program, which bears quite a close resemblance to the EJ200 concept, and in Germany and Italy their program had ensured that the necessary technology was available on compressors and turbines to support the EJ200 components.

The technology documentation has now been realized in engine run experience in the first year of the program, which is illustrated in Figs. 23 and 24. It can be seen that the very first EJ200 engine ran up to full dry thrust within one week of the engine going on the test bed. Performance is excellent and the high level of instrumentation is allowing correction of both the performance and mechanical deficiencies in a short time. Figure 25 compares the early RB199 thrust achievement against the EJ200.

It is worth noting that the third engine has completed 155 hours and was only removed from the test bed to permit more detailed examination of component parts of the engine. During the 155 hours the engine did extensive dry and reheat performance testing and was put into an altitude test facility and "flown" around the flight envelope before embarking on extensive endurance cycle testing simulating the expected EFA utilization.

The hot gas path parts have already satisfactorily achieved over 2500 engine cycles and were capable of many more. In addition to this the engine has been extensively X-rayed and engine handling has given no trouble at all. Engine starting both at sea level and at specification relight altitudes is very smooth and satisfactory and requires no bleed and only one row of HPC variable stators. This is a tremendous achievement in the first year of testing.

Some justification for the succes of EJ200 is its very simple construction, which was covered in an earlier part of the paper. The comparison with RB199 is made in Fig. 26, which shows the very greatly reduced number of compressor and turbine stages and of course the number of aerofoils involved. Obviously the simplicity of the design goes much further than this when the numbers of bearings and seals in the engine are considered.

As an example, EJ200 blades are much more robust than previous engines, and model tests show that high aerodynamic capability has been achieved without sacrificing the ability of the engine to withstand various damage and bird strike, a very important condition for a modern military aircraft. The cross section of typical compressor and turbine blades from both engines can be compared in Fig. 27 and is a clear demonstration that the early lessons of the RB199 in terms of preparation and availability of technology have been applied well.

## Part 4

**Specification of Requirements.** The detailed requirements on the engine emanating from the European Staff Requirement have been incorporated into the EJ200 Contract Specification, every detail of which was intensively negotiated with NEFMA. Additional requirements specifically relating to

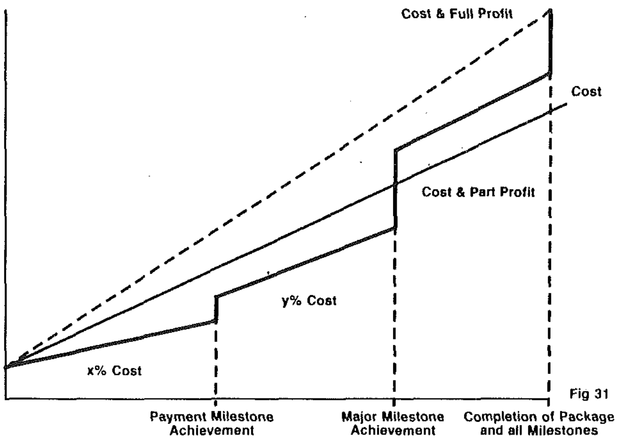

Fig. 31 Illustration of payment procedure for price packages

- All designs are approved by the Project to meet the following requirements
  - Performance
  - Mass
  - Life
  - Safety
  - Reliability
  - Maintainability
  - Life cycle costs

There is no priority in this list - all have to be satisfied.

Fig. 32 EJ200 design disciplines—1

- The design team consists of representatives of all these technical disciplines
- Should a satisfactory solution not be achieved, then the Chief Engineer must decide on a compromise to meet the requirement
- All the design parameters are covered by official requirements for specifications

Fig. 33 EJ200 design disciplines—2

- Designed for low life cycle costs through:
  - Competitive engine/module and component prices
  - High reliability
  - Optimum design for maintainability
  - Low component count
  - Long lifed components designed for arduous requirements
  - Low specific fuel consumption
  - Minimum application of variable geometry features

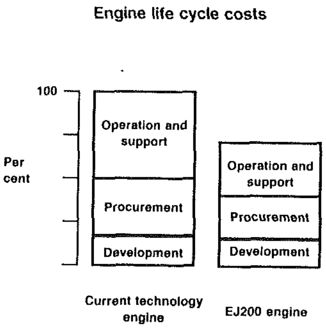

Fig. 34 Life cycle costs

| | |
|---|---|
| Mean time between defects | - Greater than 100 Engine Flying Hours (EFH) |
| In-flight shut down rate | - Less than 0.1/1000 EFH |
| Mission failure rate | - Less than 1.0/1000 EFH |
| Engine unscheduled removal rate (Engine related cause) | - Less than 1.0/1000 EFH |

Fig. 35 EJ200—requirements for reliability

| | |
|---|---|
| • Maintenance labour: | 0.5 direct maintenance man hours/engine flying hour (DMMH/EFH) at levels 1 and 2 (Fod & flight servicing excluded). |
| • Engine remove/replace: | Comparable with the fastest time achieved in the world |
| • Scheduled Maintenance: Interval | Except for health monitoring/oil replenishment - at least 400 flying hours |
| • Recovery times: | On-aircraft 50% of failures to be rectifiable within 45 mins<br>On-aircraft 95% of failures to be rectifiable within 3 hrs |

Fig. 36 The requirements for maintainbility—EJ200

the installation of the engine into the European Fighter Aircraft are defined in an Interface Control Document, which is jointly agreed by Eurojet, Eurofighter, and NEFMA.

Unlike many previous military specifications where prime emphasis was placed on performance, the requirements for EJ200 are specific that equal priority be given to cost of ownership through a range of parameters as shown in Fig. 28. This impacts upon the whole engine design process as is shown later.

**Program and Payment Structure.** The contract for EJ200 is subject to a maximum price with a commitment to progressive conversion to fixed price. The complete program, both bench and flight development, is subdivided into 15 price packages. These packages eventually become fixed price packages within the maximum price ceiling. Examples of price packages are shown in Fig. 29.

Payment against these packages beyond a basic level is dependent upon the satisfactory achievement of various milestones. Initial progress is made by the achievement of payment milestones, which relate to achievement of progress within a particular package. The second step is payable upon achievement of major milestones, which indicate progress on the program as a whole and hence relate to a number of price packages. These milestones demonstrate progress toward the achievement of full specification requirements on performance, mass, handling, reliability, testability, maintainability, and safety.

The final step is payable upon completion of the package including achievement of all relevant milestones. Typical examples of the progress toward full specification requirements set by the major milestones are illustrated in Fig. 30. The relationship between milestone achievement and payment for any given price package is illustrated in Fig. 31.

Additional monitoring of satisfactory program development is provided through progress indicators, which are not directly payment related. These are set at approximately six monthly intervals throughout the program and relate to the achievement of key technical items agreed with NEFMA. The progress indicators can be used by officials to check that the program is not running into major problems.

The maximum price type of contract does not involve officials in detailed decision making during the development program as it puts the responsibility and penalties squarely on the industrial partners themselves. However, a system of reporting has been arranged that keeps NEFMA and the Nations involved closely informed on progress, success, problems, and problem solving.

## Part 5

**Design Process.** The EJ200 designs were carefully approved by the main project team and very exacting requirements have been set against a wide range of parameters. These disciplines are every bit as exacting as those being applied on advanced US military engines. All requirements must be approved by the project team prior to release. The main parameters used in the design disciplines are shown in Figs. 32 and 33. In addition to the usual ones of performance, mass, and life, very high importance is put on the design for safety,

| | |
|---|---|
| ● Engine carcase | 24 years |
| ● Compressor Blade | > 12 years except for FOD or blades |
| ● Hot gas path parts | approx 5 years with repair of static parts |
| ● Hot nozzle parts | between 2 - 3 years with repair |

Fig. 37 EJ200 life requirement—typical military engine utilization

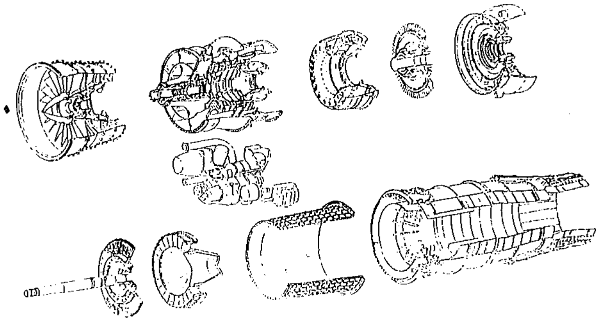

Fig. 38 Engine modular breakdown

reliability, and maintainability and the experts in these fields are a part of the integrated design team so that the designs are prepared in conjunction with them from the beginning.

Since the aircraft has to achieve the low levels of life cycle costs (LCC) shown in Fig. 34, a close monitor on the LCC of the engine is maintained and every design feature is subjected to a scrutiny of that parameter. A comprehensive model of the engine with all factors affecting the LCC has been established and can very readily determine whether a design/design change is putting the performance of that parameter at risk.

The engine companies are very aware of the need to keep down costs of operating advanced military aircraft for NATO or other countries to which such an engine or aircraft may be sold at a later stage. Design teams consist of representatives of all the technical disciplines mentioned, and, in Rolls-Royce, a totally integrated project arrangement operates where all disciplines can see each other at any time of the day and streamlining of the design processes is now possible.

**Reliability, Maintainability, and Life.** The requirements for R & M are being strictly applied in the design of the engine, its modular breakdown, and in the way in which the accessories are mounted on the engine. Some of the specification requirements for the engine are set out in Figs. 35, 36, and 37. These requirements have not yet been achieved on any military engine to date and the EJ200 will set new standards for military engines. Financial penalties are attached to failure to achieve the required values in service and during the development of the engine. Progress toward achievement of these parameters is being progressively monitored.

Engine Health Monitoring will be further developed during the forthcoming program before entry into service and when in service will be used by the Air Forces to detect impending problems using trend monitoring. The system used will be more sophisticated than anything used hitherto. Experience gained by the German and Royal Air Forces on Tornado, Harrier, and Hawk operations is being incorporated in the monitor design.

The EJ200 is naturally fully modular and past experience has shown that modularity enabled strip and rebuild of engines at the flight test centers with a very small team from the earliest days of flying. Apart from saving of resource, this procedure assists early evaluation of maintenance technique. EJ200 being even simpler will be that much easier to maintain in development and in service (see Fig. 38).

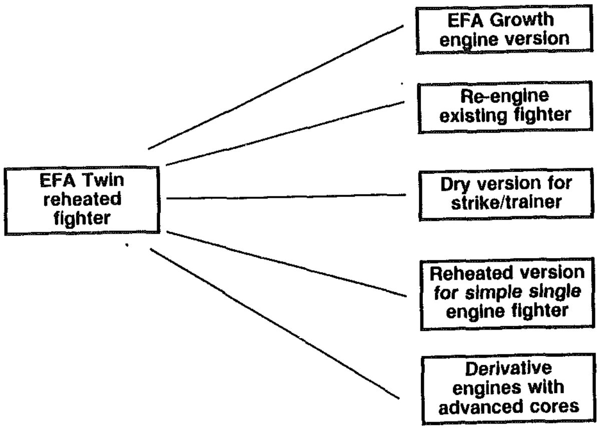

Fig. 39 EJ200 marketing application tree

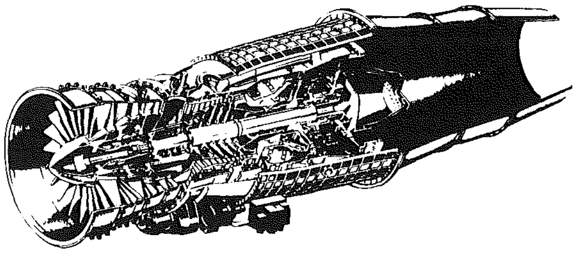

Fig. 40 Dry engine details

## Part 6

**EJ200 Future Potential.** As stated in the beginning of the paper the EJ200 engine was specified to have a growth potential of at least 15 percent in thrust. This was deemed necessary in order to be able to cope with normal aircraft equipment and capability increases during service.

The actual engine design has very deliberately been aimed at significantly larger growth than 15 percent so that the engine will remain a front line leader for at least 25 years in service on EFA and other applications.

The engine configuration allows the necessary growth in the following essential parameters:

(*a*) Fan pressure ratio
(*b*) Turbine entry temperature increase
(*c*) Core flow increases

within the existing engine scantlings.

Active programs are already running in the engine partner companies that will ensure that the technology will be available for application to growth versions when required. Additionally there are programs aimed at providing improved metal and composite materials for the hot and cold parts of the engine including structure, disks, and casings.

In addition to the EFA application the engine is suitable for re-engining existing aircraft and future generations of light fighter, strike and advanced trainer aircraft. A typical application tree is shown in Fig. 39. The engine can be offered in reheated or dry configuration. The dry configuration is illustrated in Fig. 40.

## Conclusion

This paper shows the excellent start made by the EJ200 engine in the first year of the development program following contract signature. It illustrates confidence in the ability of the engine companies to meet the design targets within the program time scales. It also demonstrates the ability of the partner companies to work together to prepare the technology data base prior to project launch and to meet the program requirements successfully.

# Advanced Technology Programs for Small Turboshaft Engines: Past, Present, Future

**E. T. Johnson**[1]
AATD, USAARTA (AVSCOM),
Fort Eustis, VA 23692

**H. Lindsay**
GE Aircraft Engines,
Lynn, MA 01982

*This paper addresses approximately 15 years of advanced technology programs sponsored by the United States Army Aviation Applied Technology Directorate and its predecessor organizations and conducted by GE Aircraft Engines (GEAE). Included in these programs is the accomplishment of (1) the 1500 shp demonstrator (GE12), which led to the 1700, and (2) the 5000 shp Modern Technology Demonstrator Engine (MTDE/GE27). Also included are several advanced technology component programs that have been completed or are ongoing through the early 1990s. The goals for the next generation of tri-service small advanced gas generator demonstration programs are shown. A prediction is thus made of the advancements required to fulfill the aircraft propulsion system established by the DoD/NASA Integrated High-Performance Turbine Engine Technology (IHPTET) initiative through the year 2000.*

## Introduction

Radar gave the British Royal Air Force a significant advantage during the Battle of Britain in 1940. Inventor Robert Watson-Watt called the concept Radio Direction-Finding (RDF) when he first discovered and demonstrated this significant advance in technology in 1935. Britain had a chain of 20 radar stations in 1939. In conjunction with the effective use of radar to detect oncoming Luftwaffe aircraft at distances of over 100 miles, the RAF fighter squadrons had available to them two advanced technology aircraft: the Hawker Hurricane (Fig. 1) and the Supermarine Spitfire (Fig. 2), both of which had the Rolls-Royce Merlin engine. The Spitfire is possibly the most famous combat aircraft in history. There is a story about a conversation between Goering and some Luftwaffe pilots: Goering: "What do you need to win the Battle of Britain?" Pilots: "Some Spitfires."

The above examples of advanced technologies illustrate the advantages of having technology available when the needs arise. It follows then that technology should always be advancing for national security. Research and development must never be short-changed to benefit producing more of yesterday's technology. Crash programs can produce if the technology is available. Crash programs cannot spawn nor demonstrate technology in time.

A large body of people in the United States Defense Department and the defense industries realize that some of the points made here are valid and, as a result, billions of dollars are invested annually in the United States on research and develop-

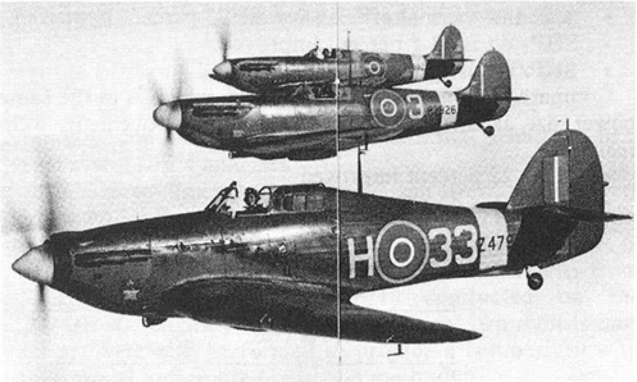

Fig. 1 Hawker Hurricane

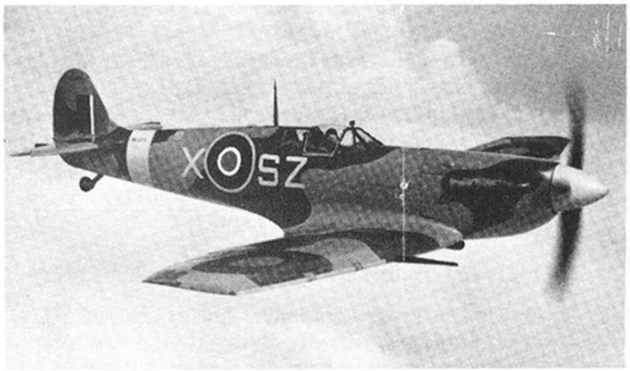

Fig. 2 Supermarine Spitfire

---

[1] Retired.

Contributed by the International Gas Turbine Institute and presented at the 35th International Gas Turbine and Aeroengine Congress and Exposition, Brussels, Belgium, June 11–14, 1990. Manuscript received by the International Gas Turbine Institute February 27, 1990. Paper No. 90-GT-267.

ment. This paper addresses a relatively small section of this large and complex endeavor, namely, aircraft gas turbine engines and, more specifically, small turboshaft engines.

## Small Turboshaft Advanced Technology Programs

One branch of the U.S. Department of Defense, whose charter is to sponsor and manage research and development, and advanced technology programs for Army aviation, is the Aviation Applied Technology Directorate (AATD) at Fort Eustis, VA.

The propulsion technical area of this directorate has been sponsoring meaningful engine demonstrator programs (6.3 funding) and component programs (6.2 funding) since 1964. This paper will discuss some of these programs, including those that were contracted to GEAE-Lynn, MA.

## Engine Demonstrator Programs

In the late 1960s, the successful AATD/GEAE GE12 1500 shp turboshaft engine demonstrator program was conducted. This program led to full-scale development and production of the T700-GE-700/-701/-701C and -401/-401C family of engines, which power eight helicopters in production, including the Sikorsky UH-60A (Black Hawk), the McDonnell Douglas AH-64 (Apache), the Bell Super Cobra, and the Kaman Super Seasprite.

The T700 engine is the "in production" baseline for small turboshaft engines against which improvements in future generations of engines in similar size classes will be measured (see Fig. 3).

Between 1983 and 1988, the 5000 shp-class Modern Technology Demonstrator Engine (MTDE) GE27 turboshaft engine demonstrator program was successfully conducted and completed with the following significant accomplishments. Relative to the T700-GE-701 engine:

- SFC and thermal efficiencies are 25 percent improved.
- SHP/Wt is 62.5 percent improved.
- SHP/W2 is 40 percent improved.

Compared to the T64-GE-416 engine, which is in the same power size as the GE27, the following improvements were realized:

- SFC is 25 percent improved.
- SHP/W2 is 43 percent improved.

The MTDE/GE27 led to the GE38 series of turboshaft and turboprop engines. The T407 engine, which derives from the GE38 family, is currently in full-scale development as the powerplant for the Lockheed P-7A for the U.S. Navy Long-Range Air ASW Capability Aircraft (LRAACA) program.

The next generation turboshaft demonstrator program in the 10–15 lb/s air flow class has just been initiated by AATD and has technology level goals for demonstration in the 1990s, which will ultimately lead to 40 percent improvements in thermal efficiency/SFC and 120 percent improvement in power/weight ratio on engines, which may be needed in the first decade of the 21st century.

## Component Technology Programs

For the engine programs to work efficiently and at the appropriate time, much effort is expended on component technology programs, which are funded and planned jointly

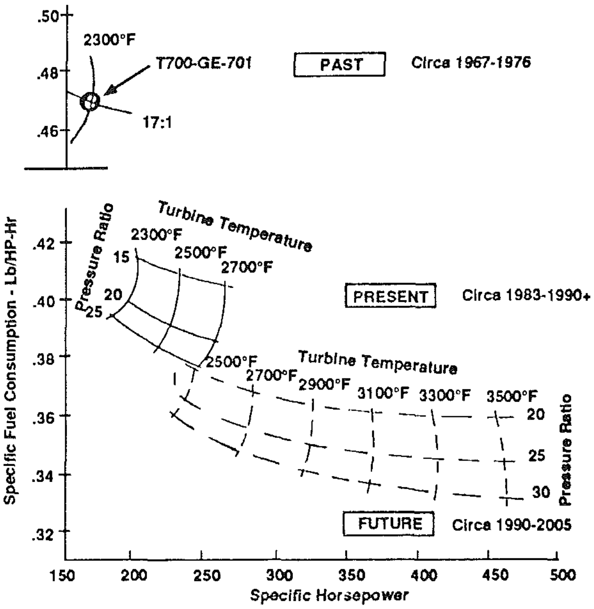

Fig. 3 Turboshaft technology trends

Table 1 Advanced engine technology base

| SIMPLE CYCLE | REGENERATIVE | VARIABLE CAPACITY |
|---|---|---|
| | DEDICATED TECHNOLOGY | |
| - Axi-Centrifugal Compressor Technology | - Advanced Inlet Particle Separator | - Variable Area Centrifugal Compressor |
| - Modern Technology Demonstrator Engine | - Recuperator Vulnerability Assessment | - Variable Area Gas Generator Turbine |
| - Booster Stage Demo | - Combustors for Regenerative Engines | - Advanced Tatical Fighter |
| - High Work Turbine | - Variable Area Power Turbine | - Variable Area Combustor |
| - Improved Turbine Casting | - Advanced Heat Exchanger | - Variable Area Power Turbine |
| - Improved Combustor Materials | - Small Engine Turbine | |
| - Advanced Combustor | - Elite Recuperator | |
| | GENERIC TECHNOLOGY | |
| | - Adaptive Control<br>- Nozzle Fatigue<br>- Bearing Technology<br>- High Stiffness Shaft<br>- 15:1 Centrifugal Compressor<br>- Cold Section Materials<br>- Inlet Particle Separator | |

Table 2 List of technology programs

| Contract Number | Title | Time Period |
|---|---|---|
| 84-C-0028 | Small Turbine Nozzle Fatigue Enhancement | Sept. 84 - Oct. 87 |
| 84-C-0032 | Advanced Airfoil Castings for Small Turbines | Oct. 84 - Dec. 86 |
| 85-C-0012 | Composite Gearbox Housing | Early 85 - April 90 |
| 85-C-0034 | Advanced Inlet Particle Separator | Aug. 85 - April 89 |
| 86-C-0019 | Optical Sensor Development for Helicopter Subsystems | Aug. 86 - Aug. 87 |
| 86-C-0020 | Advanced High Stiffness Power Turbine Shaft | Sept. 86 - Jan. 90 |
| 87-C-0002 | Evaluation of Emerging Cold Section Materials | Dec. 86 - Aug. 87 |
| 88-C-0001 | Preliminary Design of Advanced Turbine Engines (TAGG-M/Engine 21 PD) | March 88 - March 89 |
| 88-C-0007 | Electric Accessory Drive | July 88 - Jan. 91 |
| 89-C-0013 | Low Inertia Turbine Design | July 89 - Dec. 90 |
| 89-C-0030 | Application of Emerging Cold Section Materials | Nov. 89 - March 93 |

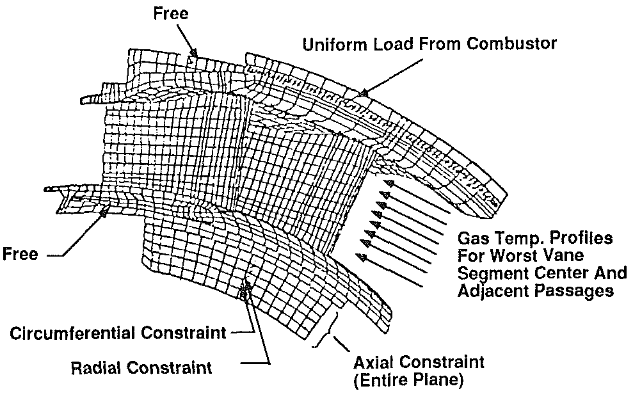

Fig. 4 Nozzle segment mechanical boundary conditions for stress analysis

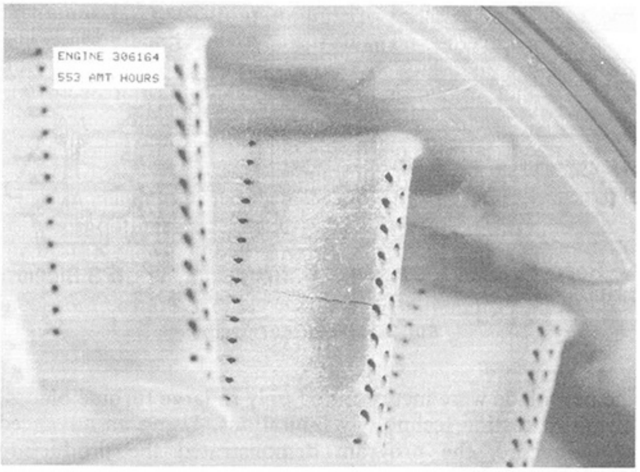

Fig. 5 T700-GE-700 nozzle crack after 553 AMT hours

by industry and the various agencies of the DoD. This paper addresses some examples of AATD's programs, which have been, or are being, conducted in the 1985–1990 time period.

The Department of Defense technology base through this time period was broad enough to cover a significant range of propulsion disciplines (see Table 1). The programs were planned and designed to stretch and demonstrate technologies at relatively low risk in readiness for future needs.

The list of technology programs identified in Table 2 is an example of programs contracted to GEAE by AATD between late 1984 and mid-1989. A summary of each program will be presented.

## Small Turbine Nozzle Fatigue Enhancement

An efficient advanced three-dimensional structural analysis design tool for a two-nozzle vane segment was provided as a result of this program. This tool reduces design analysis costs by 50 percent and reduces the need for extensive mechanical component testing.

Task I concentrated on the definition of the aero, thermal, and mechanical loading boundary conditions acting on the T700-GE-700 high-pressure turbine nozzle, including a three-dimensional finite difference heat transfer analysis of the two-vane segment (Fig. 4). A "worst-case" combustor exit temperature pattern was chosen to define the gas temperature conditions entering the nozzle. The nozzle aerodynamic boundary conditions were determined through a baseline quasi-three-dimensional flow field model, which was run to convergence for three radial temperature profiles in three adjacent nozzle flow passages. These results were used to initialize Euler three-dimensional models for solution of pressure, temperature, and velocity distributions on the surfaces of the nozzle vane and bands. These results provided boundary conditions for three-dimensional transient heat transfer and stress analyses.

Elastic three-dimensional finite element stress analyses were performed for the two-vane nozzle segment in Task II, and the results were used to predict low cycle fatigue life. The lives at the limiting locations were then compared with results from accelerated mission tests (AMT) conducted on the T700-GE-700 engine (Fig. 5). Conventional two-dimensional analyses were also performed to provide a comparison with conventional design life prediction methods.

An elastic/plastic transient stress analysis with zero hold time and with 3-min hold time was conducted for a single airfoil using boundary conditions at the ends of the airfoil determined from the analyses in Task II. A 100-hour steady-state creep analysis was also conducted for the airfoil in this task.

Results of the elastic/plastic analyses show total strain ranges at the leading edge and the trailing edge that are 20–30 percent higher than determined in the elastic analysis for the zero hold time case. The case with 3-min hold time showed little difference in total strain range compared to the zero hold time case. The results of the creep analysis showed that very little deformation occurs in the T700-GE-700 nozzle, which is consistent with test experience.

## Advanced Airfoil Castings for Small Turbines

The manufacturing technology to produce a small T700 serpentine-cooled, high-pressure turbine blade in a monocrystal alloy was achieved in this program (Fig. 6).

Heretofore, the heat transfer geometric features utilized in

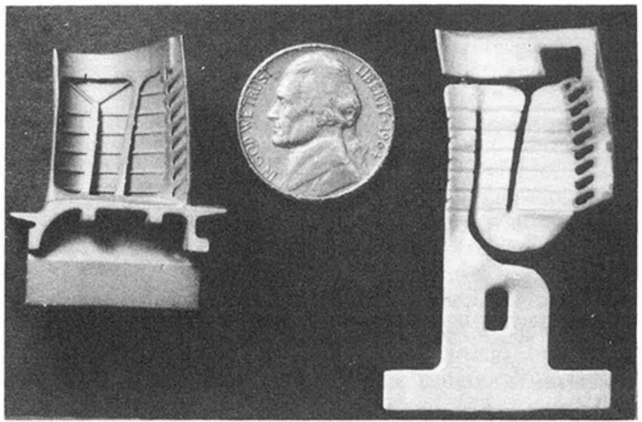

Fig. 6 Casting showing internal cooling scheme and core used

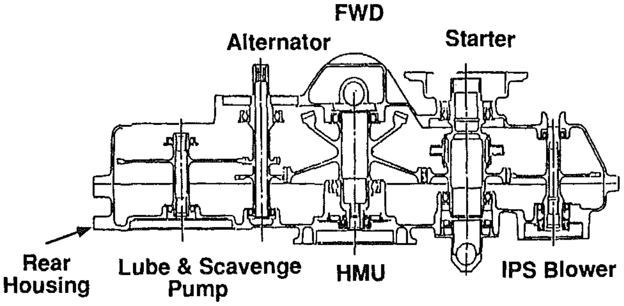

Fig. 7 MTDE/GE27 gearbox

the new blade were incorporated only in large turbine blades, owing to casting technology limitations. Using an advanced ceramic core, the program demonstrated the production capability of casting 0.014 in. by 0.038 in. trailing edge slots, an integral tip cavity, and detailed turbulators in the aggressive monocrystal solidification environment. The casting and machining processes and their associated tooling were evaluated and verified in a pilot production trial.

The casting tool was manufactured using a unique computer-aided design (CAD) interactive graphics (IAG) approach, which will now be standard for future toolmaking efforts.

The turbine blades produced in the pilot production run were excellent from a dimension, quality, and metallurgical standpoint; component testing deemed the blade sets suitable for endurance testing. A back-to-back T700 engine performance test demonstrated that this blade offered a 1 percent sfc reduction and a 4 percent shp increase over the current production blade.

## Composite Gearbox Housing

The accessory gearbox rear housing designed for the MTDE/GE27 engine was chosen as the basis to develop and demonstrate the manufacturing technology for polymeric matrix composite materials (Fig. 7). Housings have been manufactured using molded graphite fiber composites and action is underway to assemble and conduct component tests. Potential payoffs for this program include up to 20 percent weight reduction and 30 percent reduction in cost.

This project involves development of the techniques of molding and machining a complex composite gearbox housing. The material selected was one that has been used by GEAE in several production applications in aircraft engines.

Significant conclusions to date are:

1 The very complex shapes inherent in previously cast aluminum gearbox housings can be made from composite materials.

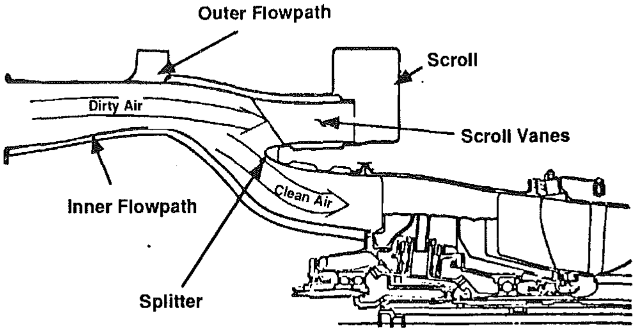

Fig. 8 GE27 IPS cross section

Table 3 Levels of separation

| Type of Sand | Capability by Weight (%) | Compared to MTDE/GE27 (% Improved) |
|---|---|---|
| AC Fine | 73.3 | 8.3 |
| AC Coarse | 87.5 | 2.5 |
| C-Spec. | 96.5 | 1.0 |

2 The molds involved and the technology involved require a complete redesign of the gearbox to accommodate the material.

3 Adequate stiffness and temperature capability of the composite housing has not yet been demonstrated.

4 An approach for making integral cored oil lines has not yet been fully developed. This is necessary for the approach to be competitive with aluminum castings.

## Advanced Inlet Particle Separator (IPS)

This program demonstrated high separation efficiency of an axial flow separator, in the 10 lb/s flow size, beyond the levels already established for the MTDE/GE27 engine IPS (Fig. 8).

The program was accomplished in four major tasks:

1 Analysis and design
2 Fabrication
3 Experimental evaluation
4 Data analysis and report

Table 3 shows the levels of separation capability achieved, both in terms of absolute levels and compared to the GE27 baseline.

These excellent results were obtained at acceptable pressure losses of 1.23 percent P/P. A design methodology (design guide) was prepared that will permit the design of axial flow separators that can outperform the swirl separators of the prior generation within the flow range of 5 pps to 30 pps.

## Optical Sensor Development for Helicopter Subsystems

An optical speed and torque sensor capable of application on current turbopowered aircraft engines was successfully designed, manufactured, and tested (see Fig. 9). Power turbine speed and torque system accuracy met or exceeded the program design objectives of ±1 percent. This system has the potential for greater reliability than the systems it will replace. It is smaller than the electromagnetic system and should be easier to maintain.

The Phase I program started with completion of the preliminary design and fabrication of a Breadboard design optical sensor for parametric testing. Testing consisted of performance in a typical engine oil and soot atmosphere at

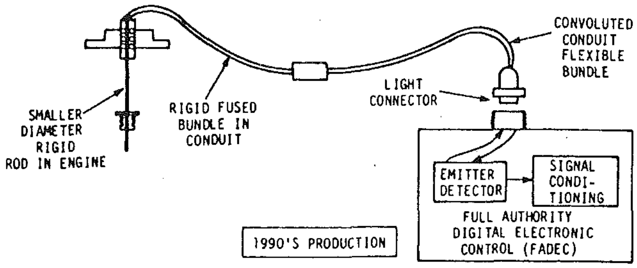

Fig. 9 Optical speed and torque sensor

various air gaps and speeds at a fixed torque setting. Vibration and sealing tests substantiated integrity of the design.

The Phase II program resulted in a Brassboard design, which incorporated design improvements to the Breadboard design. This Phase II Brassboard design (Fig. 9) successfully completed a simulated engine enivornmental test program. The testing involved torque and speed performance measurements at room temperature, maximum and minimum temperatures with oil contamination present, hermeticity, temperature shock, and vibration endurance.

The Brassboard design was trial-fitted on a T700 turboshaft engine installation to review maintainability and producibility factors.

The test programs for the Breadboard and Brassboard sensors subjected the designs to a simulated turboshaft engine environment, which produced the following conclusions:

1 The optical sensor demonstrated that engine power turbine speed and torque can be sensed as accurately as the T700 variable reluctance sensor.

2 The optical sensor with oil contamination of the sensing tip meets 1 percent torque accuracy using a running average of four torque readings, and speed accuracy obtained was better than 0.7 percent.

3 The optical sensor successfully passed environmental tests with no performance degradation.

4 The optical sensor was capable of −54°C to 204°C at the sensor tip, and 485°C in the engine exhaust strut area, which is the typical engine temperature environment. The sensor is also capable of severe engine vibration levels of 20 G over a 5–750 Hz engine excitation frequency range.

## Advanced High-Stiffness Power Turbine Shaft

A high-stiffness metal matrix power turbine shaft was designed, fabricated, and evaluated on this program. The shaft design comprised silicon carbide fibers in a titanium matrix with diffusion-bonded monolithic titanium end pieces. Significant bench testing has been accomplished and has demonstrated adequate ultimate torsional strength and fatigue torsional strength of the metal matrix tube itself, and the bond joints between the Metal Matrix Composite (MMC) and titanium splined end fittings. Shaft natural frequency and longitudinal stiffness results were obtained, which demonstrate the potential for meeting the objectives of higher critical speeds to permit subcritical operation of the power turbine shaft. Additional potential benefits from this technology include: simplified support structures, improved performance resulting from tighter clearances, decreased wear of splines, and reduced engine weight. A photograph of the completed shaft is shown in Fig. 10.

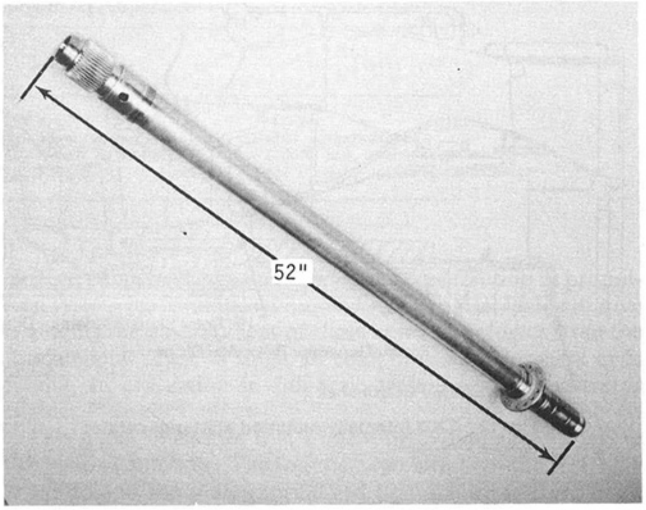

Fig. 10 Metal matrix composite shaft

## Evaluation of Emerging Materials for the Cold Section of Small Gas Turbine Engines

This program identified the advanced materials that will become available in the next 10 to 20 years, and can be used to benefit and be applicable to cold section components of aircraft gas turbine engines.

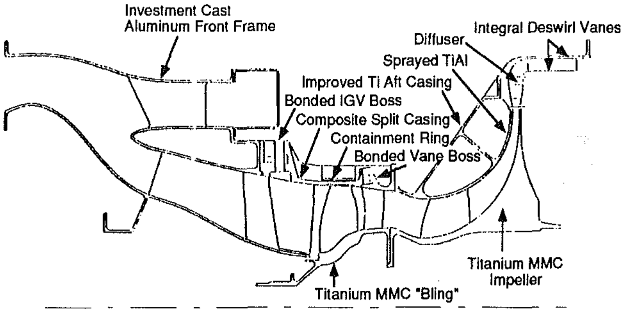

Fig. 11 Advanced concept cold section

The program consisted of three phases:

1 Material screening and selection
2 Material and component characterization
3 Benefit analysis

The most attractive emerging material applications recommended from this study are:

- Thin-wall cast aluminum front frame
- High-temperature titanium aft compressor casings
- Metal matrix composite impeller

It was concluded that 14 percent weight reduction and 35 percent reduction in acceleration times could be achieved using these technologies in the high-pressure-ratio, high-tip-speed compressor designs of the future. Figure 11 illustrates an advanced concept cold section.

## Electric Accessory Drive

The overall objective of this program is to investigate the applicability of advanced electric motors/generators and power electronics to drive aircraft engine and aircraft accessories, thus reducing weight and volume while improving reliability and reducing cost. The baseline engine to be used for comparison throughout this program is the T700 turboshaft.

This contract is divided into three tasks:

- **Task 1—Concept Formulation.** In Task 1, the concept of using an appropriately sized starter/generator together with electrically driven accessories was evaluated. This was done in terms of total aircraft benefits, such as weight, cost, reliability, and performance.

- **Task 2—Preliminary Design.** Under this task, preliminary designs of an engine electric accessory drive system are performed based on the concept evaluation con-

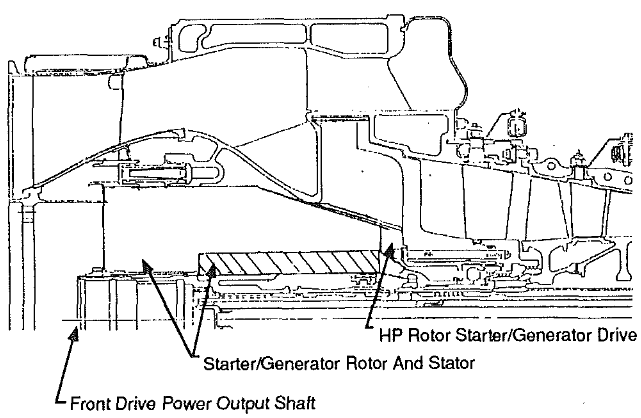

Fig. 12 T700 internally mounted starter/generator

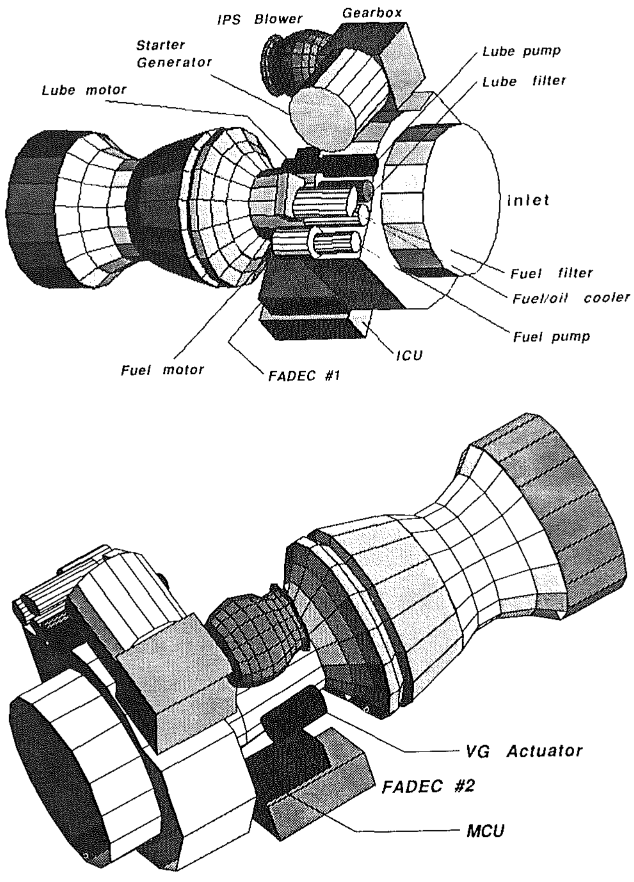

Fig. 13 External starter/generator accessory arrangement

ducted in Task 1. Comparison will be made between this approach and the conventional mechanically driven accessory system.

Also in this task, critical technologies will be defined that need further development.

- **Task 3—Component Development.** System integration tests of a 270 VDC switched reluctance starter/generator, an inverter/converter unit, an electrically driven aircraft engine fuel pump, and associated electronics will be conducted to demonstrate aspects of an electric accessory drive system.

At the time of writing, effort is continuing on this program. Some of the results indicate to date that the concept investigated in Task 1 is promising in terms of overall system benefits and should be considered in future aircraft designs.

A priori, intuitively, it was felt that internal mounting of the starter/generator on an extension of the gas generator main shaft was the proper approach (see Fig. 12). It now appears that, for a front-drive turboshaft engine, external mounting is more appropriate.

Some of the detractions with internal mounting are: increased engine length and weight, PT shaft dynamics, and maintenance aspects. Engine accessory packaging with the externally driven starter/generator looks attractive (see Fig. 13).

## Low Inertia Turbine Design

At the time of writing, good progress has been made on the Preliminary Design phase. Single- and two-stage designs have been considered. A cycle is defined, and parametric studies and design iterations are being conducted.

The technical objectives for the program are:

*Improvements Relative to T700-GE-701*

| | |
|---|---|
| • Power/weight | 80 percent |
| • SFC | 30 percent |
| • Turbine rotor inertia | −20 percent |

*Mechanical Design Goals*

| | |
|---|---|
| • Blade and vane | 7500 cycles |
| • Disk | 15,000 cycles |
| • Turbine life | 6000 hours |

The goals for performance improvement are consistent with the DoD IHPTET initiatives of doubling proplusion capability by the turn of the century. A significant reduction in weight and inertia of the rotating components promotes improved rotor dynamics and rapid acceleration rates.

## Preliminary Design of Advanced Turbine Engines

Goals for this program were to identify cycles and technologies that would provide improved performance in terms of specific fuel consumption (SFC) (18–22 percent), specific power (SHP/W2) (30–40 percent), and HP/weight (40–50 percent) relative to the T700-GE-701/-401 engine family. The four tasks completed included a technology survey; a cycle parametric analysis of simple, variable capacity (VCC), and regenerative cycles; a preliminary design of each cycle type; and a development plan outline. In addition, an Integrated High Performance Turbine Engine Technology (IHPTET) plan was defined.

All three cycle types (simple, variable capacity, and regenerative) have the potential for meeting all of the program goals, with the exception of the VCC, which cannot meet the SFC goal.

Benefit analyses indicate that the regenerative cycle is competitive with the simple-cycle engine and may offer a life cycle cost (LCC) savings for applications with relatively high fuel usage, such as an advanced ASW helicopter.

However, the higher acquisition and development costs associated with the regenerative engine, as well as its inherently greater vulnerability, remain as barriers to its serious consideration for military aircraft.

Emerging technologies in materials, component aerodynamics, manufacturing processes, and controls and accessories have the potential for providing future turboshaft gas turbines that meet or exceed the performance goals. Benefit analyses indicate potential LCC savings of $1 to $3 billion for engines incorporating these technologies.

## Application of Emerging Cold Section Materials

This new program was started in Nov. 1989. The purpose of this effort is to design, fabricate, and test a centrifugal compressor diffuser made of an advanced high-strength, lowweight material capable of operating at the temperature levels required by figure engine applications. This component will be

**Table 4 Milestones: air-breathing propulsion**

| | 1991<br>(Phase I) | 1997<br>(Phase II) | 2003<br>(Phase III) |
|---|---|---|---|
| Tech. Demo<br>(Turboshaft/Prop) | -20% sfc<br>+40% power/weight<br>+300°F max. temperature<br>1000°F comb. inlet temp. | -30% sfc<br>+80% power/weight<br>+600°F max. temperature<br>1200°F comb. inlet temp. | -40% sfc<br>+120% power/weight<br>+1100°F max. temperature<br>1400°F comb. inlet temp. |

sized in the 15 lb/s flow class and, after satisfactory conduct of component testing, should have the potential for engine testing within the Joint Turbine Advanced Gas Generator (JTAGG) program.

## Summary

Some comments about the programs that have just been discussed are as follows:

1 They are diversified in scope and discipline.

2 The study programs are relatively short and almost always are executed within the original plan.

3 Hardware and test programs are relatively long and sometimes have to be extended because the "unexpected" happens. This is something of a "norm" for R&D work.

4 The eleven programs listed represent a relatively small part of the total activity in which AATD gets involved. We know from the contract numbers that there were at least 30+ contracts in 1984 and 1985.

5 (A) Some of the programs are paying off now:

- Small Turbine Nozzle Fatigue Enhancement
- Advanced Airfoil Castings for Small Turbines
- Preliminary Design of Advanced Turbine Engines

(B) Some have established clear direction for the future:

- Advanced Inlet Particle Separator
- Advanced High Stiffness Power Turbine Shaft
- Optical Sensor Development for Helicopter Subsystems
- Evaluation of Emerging Cold Section Materials

(C) The remaining four need more work:

- Composite Gearbox Housing
- Electric Accessory Drive
- Low Inertia Turbine Design
- Application of Emerging Cold Section Materials

## Future Plans

This concluding section will express a summary of future expectations for small turboshaft engines. The Department of Defense has launched an Integrated High Performance Turbine Engine Technology (IHPTET) program. The integration is between all contributing departments, i.e., U.S. Army, Navy, Air Force, DARPA, NASA, etc. The aim of the program is to double aircraft gas turbine propulsion system capability by the turn of the century. A direct quote from the DoD follows:

"A dramatic leap in aircraft propulsion capability occurred in the early 1940s with the introduction of the gas turbine engine, and substantial improvements have been made since then. Today, technological barriers in aerodynamics, materials, structural design, and operating temperatures are close to being broken again, and another revolution in propulsion system performance is impending. The IHPTET initiative is guiding the development of these new technologies from the fundamental research stage, to component development and, finally, to evaluation in full-scale technology demonstrator engines."

This paper illustrates that something is happening to make this vision come true. The founders/architects of the IHPTET program and the planners realized that achieving the overall goal of doubling performance should be tackled in three phases with interim goals established for each phase.

In the context of this paper and of particular interest are the goals for turboshaft/turboprop engines; these are shown in Table 4.

As mentioned earlier, the next generation Joint Turbine Advanced Gas Generator (JTAGG) demonstration programs have been initiated with two contracts awarded in Oct. 1989, jointly by U.S. Army, Navy, and Air Force: (1) to Textron-Lycoming, and (2) to a team of GEAE and Allied Signal Garrett Engine Division. The technology demonstrator core gas generators planned for these programs will attempt to take the first significant step in the IHPTET program by demonstrating, through a culmination of the earlier, well-planned component technology programs, the Phase I goals shown in Table 4 in the 1991 time period.

The authors support and applaud the IHPTET sponsors and planners, and are proud to be part of the team involved in trying to make it happen.

## Conclusions

Over the past decade, significant progress has been achieved in the design, demonstration, and application of advanced technology for small aircraft gas turbine engines. Current engines are smaller, lighter, tougher, and more efficient than their predecessors.

The solid continuing wise investment of Research, Development, Test and Evaluation (RDT&E) funding by DoD, AATD, and industry (in component programs like the examples given in this paper) has permitted significant improvements in engine capability to occur. These RDT&E efforts must continue if the IHPTET vision of another revolution in propulsion system performance is to be achieved.

In conclusion, we would like, again, to return to World War II and pose a "What if" technology question for us all to ponder:

If there had been the equivalent of an IHPTET plan in Britain prior to World War II, with all the cooperation, sponsorship, and appropriate R&D funding, would Sir Frank Whittle's engine have been developed years earlier (in the 1930s), and would the advent of aircraft jet propulsion have shortened the war?

# Computational Fluid Dynamic Applications for Jet Propulsion System Integration

**R. H. Tindell**
Grumman Corporation,
Bethpage, NY 11714

*The impact of computational fluid dynamics (CFD) methods on the development of advanced aerospace vehicles is growing stronger year by year. Design engineers are now becoming familiar with CFD tools and are developing productive methods and techniques for their applications. This paper presents and discusses applications of CFD methods used at Grumman to design and predict the performance of propulsion system elements such as inlets and nozzles. The paper demonstrates techniques for applying various CFD codes and shows several interesting and unique results. A novel application of a supersonic Euler analysis of an inlet approach flow field, to clarify a wind tunnel-to-flight data conflict, is presented. In another example, calculations and measurements of low-speed inlet performance at angle of attack are compared. This is highlighted by employing a simplistic and low-cost computational model. More complex inlet flow phenomena at high angles of attack, calculated using an approach that combines a panel method with a Navier-Stokes (N-S) code, is also reviewed. The inlet fluid mechanics picture is rounded out by describing an N-S calculation and a comparison with test data of an offset diffuser having massively separated flow on one wall. Finally, the propulsion integration picture is completed by a discussion of the results of nozzle-afterbody calculations, using both a complete aircraft simulation in a N-S code, and a more economical calculation using an equivalent body of revolution technique.*

## Introduction

Propulsion systems for advanced military aircraft tend to be more intimately integrated with the vehicle's architecture and control system than ever before. This is the direct result of very ambitious and broadly varying mission requirements, driven in part by economics and by ever-improving threat technology. The impact to the propulsion system designer is that the complex flow fields resulting from the interactions of the closely coupled engine and aircraft must be understood early in the preliminary design process, so that the designs may be efficiently tailored before structure and air passage lines are firmed up. Subsequent wind-tunnel testing will still be necessary to optimize the design, but failure to accommodate the preliminary design requirements dictated by complex propulsion-aircraft flow fields could lead to excessive risk and costs.

For example, highly compact propulsion systems make extensive use of offset inlet ducts and engine tailpipes. Efficient design and performance assessment of these systems require reliable knowledge of the secondary flow fields inherent in them, and the ability to predict flow separations, hot spots on tailpipe surfaces, and plume temperature fields.

Experience teaches that not only futuristic, highly integrated propulsion-aircraft concepts, but also relatively mundane aircraft may need to be more thoroughly evaluated during preliminary design to preclude major development problems. Past airplane projects have suffered from major propulsion-system development problems that could have been avoided by the use of a sufficiently powerful preliminary design analysis. For example, forebody flowfield upwash has been shown to be the cause of severely limited inlet-engine compatibility that was subsequently cured by a redesigned plow-diverter system. At the other end of the propulsion system, low afterbody drag was developed for modern aircraft, only after many expensive wind-tunnel entries. Reliable and user-friendly analyses were not available to reduce the expense and risk of these 1960–1975 propulsion system integrations.

During the 1980s, powerful and relatively friendly computational fluid dynamics (CFD) methods have been, and continue to be, developed. They have given propulsion system designers greater ability to design and tailor propulsion system elements, e.g., inlets, engines, nozzles, and their integration into aircraft. These computational tools, when properly applied, can reduce the cost and risks of developing new propulsion systems, including more efficient use of wind tunnel and other experimental facilities. They also can allow the relatively rapid evaluation of new and innovative concepts that otherwise might not get their day in court. It is fair to say that CFD

---

Contributed by the International Gas Turbine Institute and presented at the 35th International Gas Turbine and Aeroengine Congress and Exposition, Brussels, Belgium, June 11-14, 1990. Manuscript received by the International Gas Turbine Institute January 22, 1990. Paper No. 90-GT-343.

methods, when appropriately integrated into the preliminary design development format, can provide significant improvements in productivity.

The primary use for computational methods in aircraft development is as a preliminary design tool when, in conjunction with wind tunnel testing, the aircraft designer attempts to simulate full-scale flight conditions. Both the computational and experimental methods need to be sufficiently integrated to allow the potentially large cost-effective benefits to be realized. Another important use for CFD is to help resolve anomalies that first come to light during flight test operations, when model testing is frequently impractical.

There is still much ongoing development and improvement in CFD methods, from both the code developers' and the users' points of view. This paper, concentrating on the latter, presents five examples of applications of CFD codes to the development of modern propulsion system integrations.

## Background

In order to select the most appropriate computational method for a particular design or analysis application, the engineer must understand the physical flow to be simulated and the capabilities and shortcomings of the candidate methods. Frequently a combination of several methods is the best approach, after consideration of technical applicability of the codes and computing resources. The following is a brief overview of the primary computational methods used at Grumman for propulsion integration technology.

The solution of Navier-Stokes (N-S) equations is necessary for the designer to predict total pressure losses and to calculate separated flows. These equations, which represent near-complete simulation of the physical flow, including viscosity and turbulence, are solved in the Propulsion Section at Grumman through application of any of three different codes: ARC, PARC, and FLUENT. ARC (Pulliam and Steger, 1980), a thin-layer Navier-Stokes Code (TLNS), was developed by NASA/Ames Research Center, CA, and was primarily intended for external aerodynamics applications. The Baldwin-Lomax algebraic turbulence model is employed. PARC (Cooper, 1987) is a tailored version of ARC, which is made to be more conveniently applicable to the internal flow problems generally associated with propulsion technology, i.e., inlets, ducts, nozzles, etc. It allows the options of multidirectional viscous calculations. PARC was developed by the Arnold Engineering Development Center, TN. Both of these codes run on the CRAY-XMP computer and are applicable from subsonic through hypersonic speeds. The N-S code FLUENT, which is applicable subsonically in its present formulation, was developed by CREARE, Inc., of Dover, Maine. It employs a two-equation ($K$-$E$) turbulence model. Its primary attribute is that it is very easy to use, by virtue of its interactive sessions and friendly menus. The version that we used requires the use of a Cartesian coordinate system, thus necessitating that curved contours be modeled by a series of steps. An updated version having a body-fitted grid capability is presently being evaluated.

Grumman engineering uses several formulations of Euler equations, some of which were developed in-house and others by NASA. The formulation used in the example of this paper was developed by Frank Marconi et al. (1975). The computational time for Euler equations, which does not reflect any effects of viscosity, is, of course, much faster than for the N-S equations. Euler solutions may be useful for internal flows that are not boundary-layer dominated, and for defining the supersonic external flow environment of the propulsion system, particularly the inlet.

Finally, the panel method formulation, VSAERO, developed by Analytical Methods Inc., Bellview, WA, is the simplest mathematical approach, and the fastest runner on the computer. It solves linearized potential flow equations at subsonic and transonic speeds. Since it is automatically coupled to a boundary-layer calculation, it is useful for calculating internal and external-internal flows up the point of separation. The following applications of these computational methods reflect their utility as efficient preliminary design and post-test analysis tools.

## Supersonic Inlet-Airframe Effects on Performance: A Novel Use of CFD Results

It is well known that aircraft forebody/canopy effects can significantly affect the supersonic flow field approaching a side-inlet installation. The inlet incidence must be compatible with the resultant downwash and/or sidewash to assure adequate performance over the required angle of attack/angle of yaw range. Accordingly an inlet design was based upon a database that reflected isolated and forebody/inlet integrated wind-tunnel models to assure a successful inlet-airframe integration. Flight-test measurements subsequently documented the fact that a compatible inlet-engine configuration had indeed been achieved. An annoying disparity between wind-tunnel and flight-test, high-speed, pressure-recovery levels, however, remained. To solve the problem, we developed an analysis that uses an Euler code to calculate the complex supersonic flow field governing the inlet's environment (Tindell, 1982).

Figure 1 shows the fuselage geometry model employed along with a schematic illustrating shock wave patterns. Also shown are wind-tunnel and flight-test measurements of inlet total pressure recoveries. Superimposed on these data are results of employing the Euler analysis. Inlet pressure recovery levels presented here were computed in the following manner. Theoretical shock recovery curves are generated by computing pressure losses through the inlet's three oblique and single normal shock waves. Duct-friction losses account for the gap between this prediction and the isolated-inlet test results. The shaded area represents pressure degradation, computed using the Euler analysis, caused by the fuselage forebody. The top shaded area is derived by determining the mean flow angularity over the inlet face. This angle increment is then added to the free-stream incidence to recompute pressure losses through the inlet shock system. The bottom shaded area, computed directly by the Euler method, represents the pressure losses through

## Nomenclature

$A$ = area
$C_D$ = drag coefficient
$C_P$ = static pressure coefficient
$H$ = height of duct normal to duct centerline
$L$ = length of duct, lip to engine face

M = Mach number
NPR = nozzle pressure ratio $= P_T/P_{\text{amb}}$
$P_{T_2}/P_{T_0}$ = total pressure recovery
$R_e$ = radius at nozzle exit
$\alpha$ = angle of attack

**Subscripts**

$TH$ = throat
1 = duct upstream station
2 = duct downstream station, engine face station

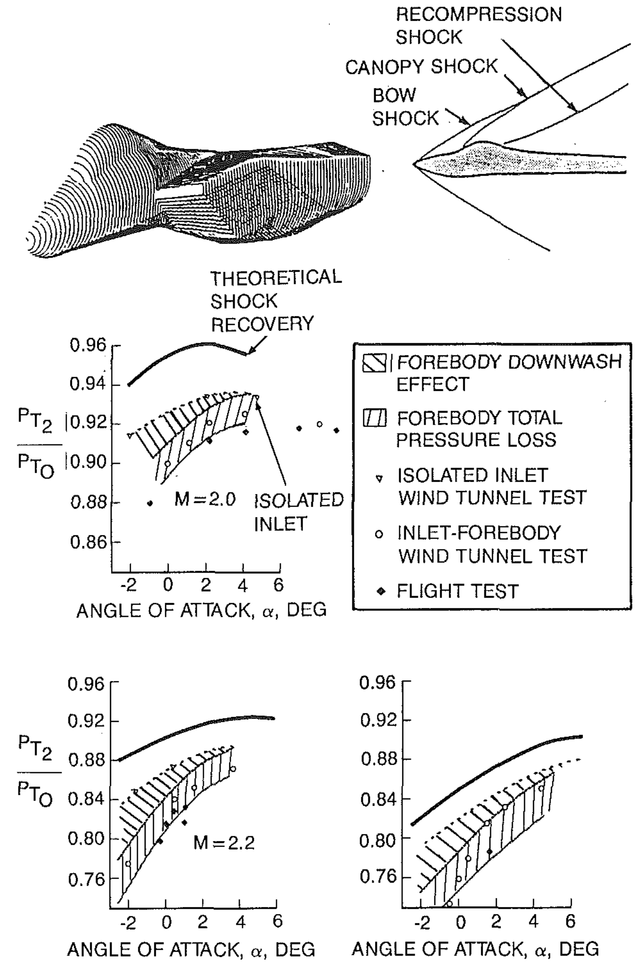

**Fig. 1 Prediction of inlet recovery levels using Euler calculation results**

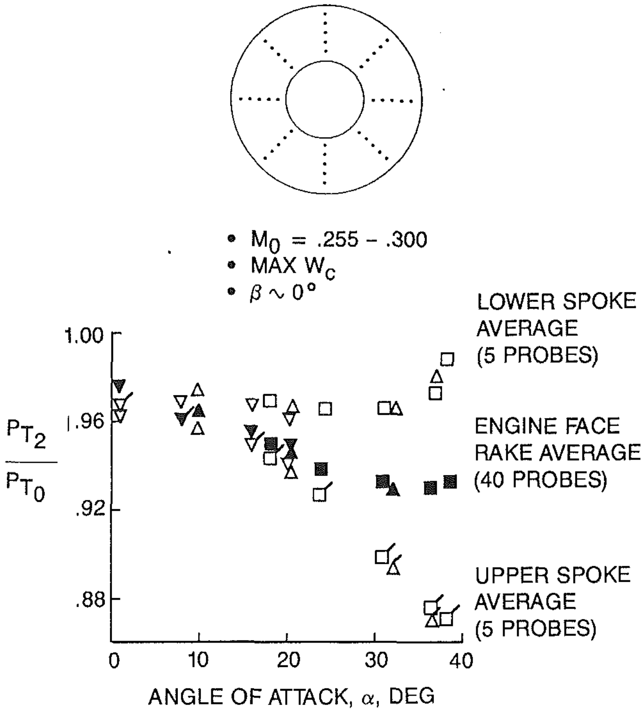

**Fig. 2 Inlet performance at angle of attack; flight test data**

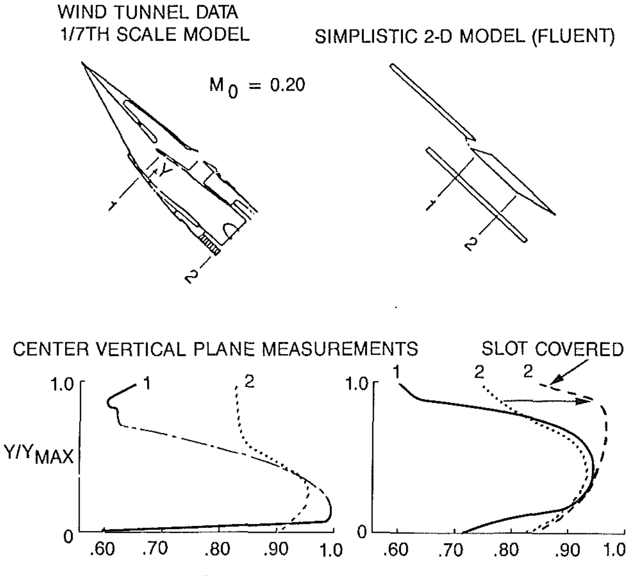

**Fig. 3 Inlet local $P_T$ characteristics at $\alpha=40$ deg**

the forebody shock systems. It can be seen that the computational results reproduce the flight test results at all Mach numbers. The wind-tunnel results systematically show higher recovery levels. It is suspected that the wind-tunnel results were contaminated by erroneous crossflow, especially at the higher angles of attack.

The conclusion to be drawn here is that the computational flow simulations can be used as referees on certain occasions to resolve differences between wind tunnel and flight tests. An aircraft might be undergoing flight testing and a decision must be made whether or not to pursue the performance discrepancy that results from the pressure losses identified. The analysis predicting the proper trends with a high confidence level can be used to define physical limits for which flight modifications will provide no improvements. Considerable time and resources can be saved.

## High Angle-of-Attack Inlet Performance Predictions With Simplified Modeling

Inlets having horizontally oriented compression surfaces can maintain high total pressure recoveries over broad ranges of angles of attack, even with relatively thin lips, because the lip stagnation points tend to remain on the internal cowl surfaces as angle of attack is increased. Separation due to flowing around the lip contour then occurs externally. Substantiation of this is shown on Fig. 2, which presents flight-test measurements of engine-face total pressure characteristics over a 40-deg range of angle of attack. The average of the lower spoke pressures (open symbols without ticks) remains high and even rises slightly at $\alpha=40$ deg. The average of the upper spoke (ticked symbols) closely matches the engine face average (filled in symbols) up to $\alpha=18$ deg, above which it is much lower. While these results support the anticipated lower-lip performance trend, they define a total pressure loss that seems to be incurred on the upper surface. To shed light on this problem, we conducted a wind-tunnel test of a 1/7th-scale inlet/forebody model. Total pressure measurements were made at the diffuser entrance station as well as at the simulated engine face. The results at an angle of attack of $\alpha=40$ deg, plotted on the left side of Fig. 3, show a 40 percent total pressure loss directly aft of the bleed slot, apparently due to a reverse flow through the slot. Downstream mixing effects ameliorate this loss, but leave the upper engine-face total

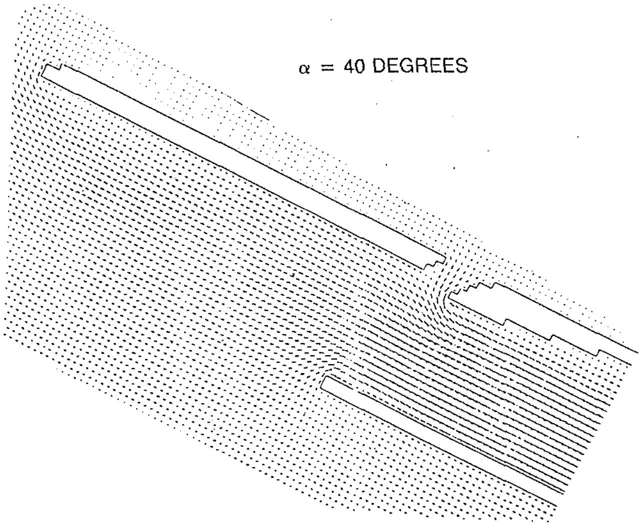

Fig. 4 Velocity field for simplistic inlet model

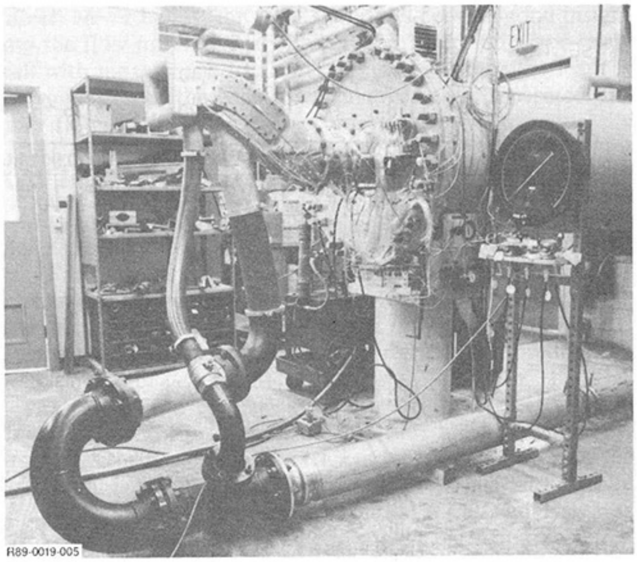

Fig. 5 Highly offset diffuser test rig

pressure with an 18 percent loss. Notice that the lower surface pressure profile at station 1 is a healthy one, which also has its level significantly improved at the engine-face station.

Subsequent to this test we acquired the Navier–Stokes code FLUENT, and used it to see if a simplistic model, necessarily a Cartesian coordinate-system version that requires square edges and straight lines, could model the flow system. A two-dimensional analytical model comprised of 4000 grid points (Fig. 4) was constructed in only a few hours, the rapid setup time being a major attribute of FLUENT. The results for an angle of attack of $\alpha = 40$ deg are shown on the right side of Fig. 3. They include total pressure predictions for both stations corresponding to the wind-tunnel data, as well as results for the effect of eliminating or covering over the bleed slot on the engine-face pressures. The FLUENT model had, nominally, 20 grid points across the duct, thus precluding accurate boundary-layer analysis. Nevertheless, the calculated results compare quite well with the test measurements. This indicates that the fluid mechanical model, simulating basic bleed-slot and cowl-lip orientation, and not exact-contour simulation, is sufficient to define the flow-field effects to a first-order estimate.

The forward-station upper-surface calculated pressures are very close to the measured 60 percent levels; however, the lower-surface minimum pressure is higher than the test counterpart. The downstream mixing effects are modeled reasonably well, but the calculated engine-face pressure levels are generally 2–8 percent too low. The calculated effect of covering the bleed slot is 10–15 percent improvement in the upper total pressure field. It should be noted that excellent engine-inlet compatibility and maneuvering performance are achieved with present production aircraft. Nevertheless, the FLUENT analysis suggests that potential exists for a further improvement in both maneuvering performance and engine stability margin. The crude model has produced important and useful information.

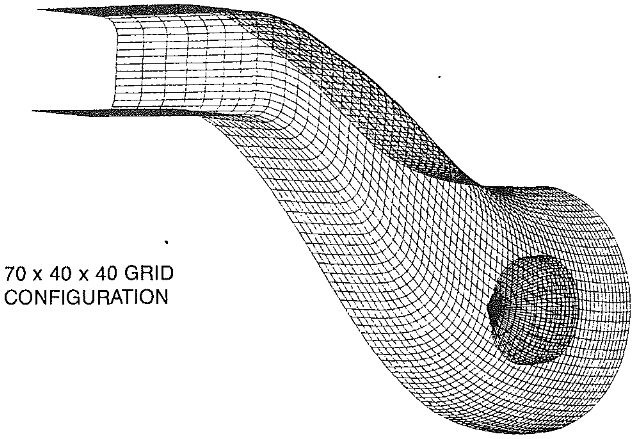

Fig. 6 Highly offset diffuser surface grid model

## Offset Diffuser

A highly offset diffuser, designed to investigate separated flow field phenomena and boundary layer control methods, was tested and analyzed using the Navier–Stokes code ARC3D (Tindell, 1988). Figures 5 and 6 show the test rig and the computational surface grid. The rig had a 25.4-cm exit diameter diffuser with an offset of 1.05 diameter, a length of 2.20 diameter, an area ratio of 1.89, and a throat aspect ratio of 2:1. Approximately 112,000 grid points were used to model half of the diffuser. Six hours of CPU time were expended on the Grumman CRAY-XMP to calculate the flow field, corresponding to a four-order-of-magnitude reduction of the maximum residuals. The results discussed below are for a throat Mach number of $M_T = 0.70$.

Figures 7, 8, and 9 show the calculated velocity development throughout the diffuser and compare several total pressure profiles with test data. The expanded views of Fig. 7 show that the verge-of-separation station on the lower surface is $X/L = 0.40$. It is seen that there is no separation on the upper surface, but that the boundary layer is quite thick near the downstream stations.

The computed velocity field within the symmetry plane (Fig. 7) illustrates the mechanism for the measured improvement in total pressure recovery of the lower section flow. High-quality core flow in the vicinity of stations $X/L = 0.80$–$0.90$ is entrained into the lower-flow strata at approximately station $X/L = 1.00$, through the action of the reverse-flow vortex created by the lower separated flow. This should result in a total pressure increase at the simulated engine face station, 1.09. The velocity field shown at the top of Fig. 7 is in the plan view of contour *a–a*, which illustrates the three-dimensional influence of the lower-flow separation. Notice that the outward flow near the symmetry plane begins at $X/L = 0.40$, consistent with the verge-of-separation results shown in the side view. Also note that the velocity vectors in *a–a* near the symmetry plane at $X/L = 1.09$ are reverse flowing, and are therefore most responsible for the total pressure loss measured at the simulated engine face, which will be discussed below.

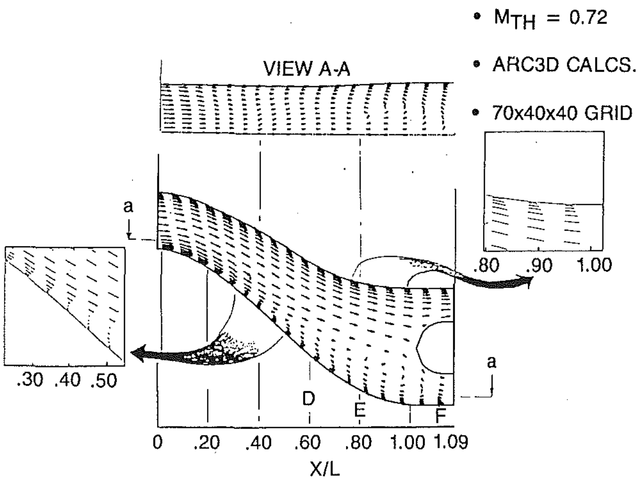

Fig. 7 Velocity field

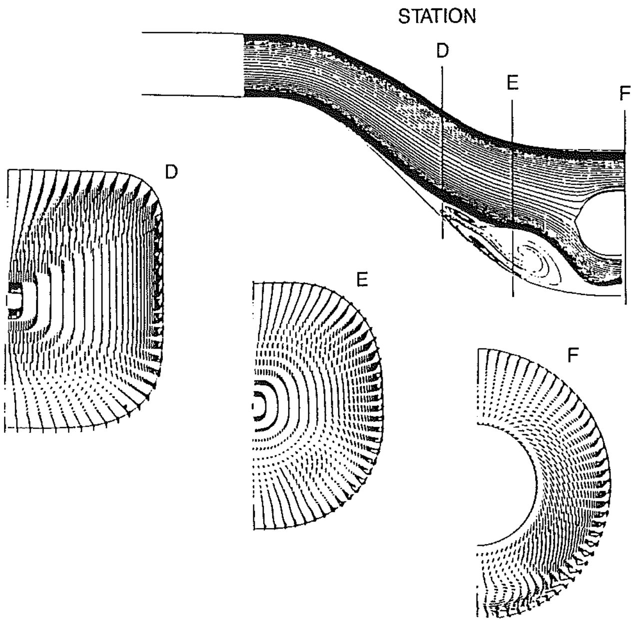

Fig. 8 Crossflow velocities

Crossflow velocities, shown in Fig. 8, indicate that the secondary flow is predominantly downward. At station D, the formation of upward and outward components of a vortex in a lower quadrant is seen. The vortex continues to occupy the lower quadrant of downstream stations.

Comparison of the calculated longitudinal development of lower-surface total-pressure profiles with test data (Fig. 9) is fair at the three stations shown. The data are for rakes situated normal to the lower surface at each station, as indicated. The comparison is poorest near the wall. The calculation overpredicts the separated-wall total pressures at the forward station, D, and then underpredicts them at the two downstream stations. It does show the significant improvement between the last two stations, although not near the wall. More grid points may be required in this vicinity. It is also possible that the Baldwin-Lomax turbulence model is not well suited for this flow. Profile shapes and pressure levels calculated for $Y/H > 0.25$ agree with the test measurements. Upper total pressure calculations at the final station agree with the measured total pressure loss in the boundary layer, but show a small loss near the bullet surface that was not measured.

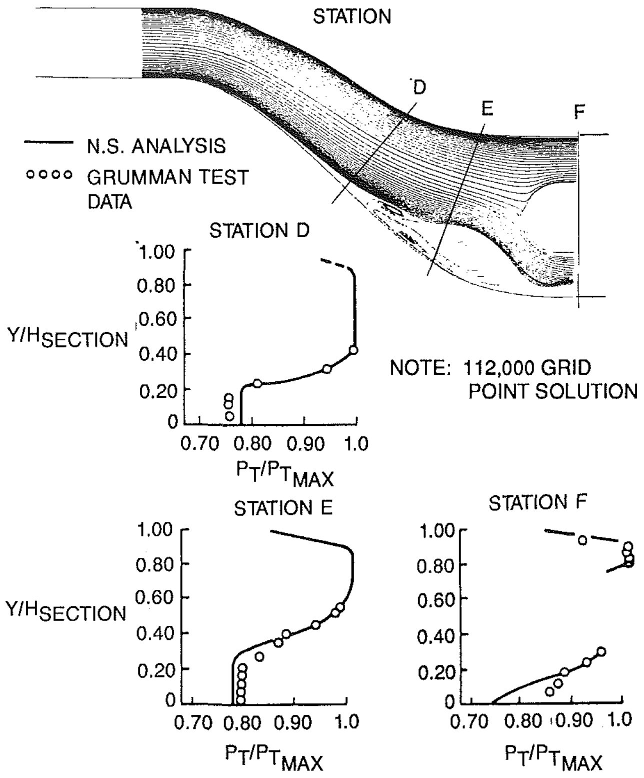

Fig. 9 Diffuser total pressure profiles

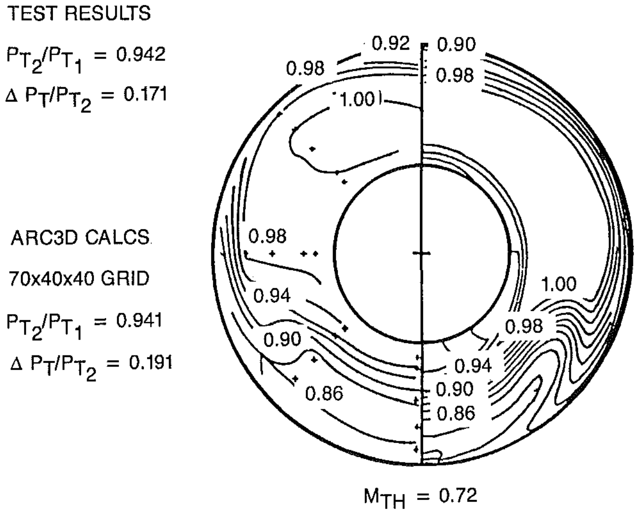

Fig. 10 Diffuser exit total pressure contours

Figure 10 compares the total pressure profiles, measured and calculated, across the simulated engine face. The vortex "signatures" in the lower quadrants are similar. The calculations overpredict the losses near the outer wall and underpredict them near the inner wall. Upper-section total pressures are in very good agreement, particularly within the thick boundary layer at the top. Calculated total pressures were integrated according to the total pressure probe weightings used for the experimental results. The resulting integrated total pressure recoveries are very close, and the distortions are within 2 percent. This close agreement is not indicative of the intrinsic modeling capability of ARC3D for severely separated diffuser flows, since the integration process averaged out pressure levels that were higher and lower than measured

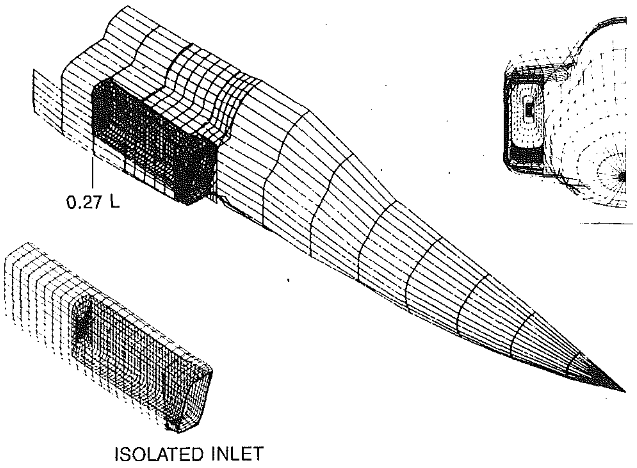

**Fig. 11 VSAERO computational models**

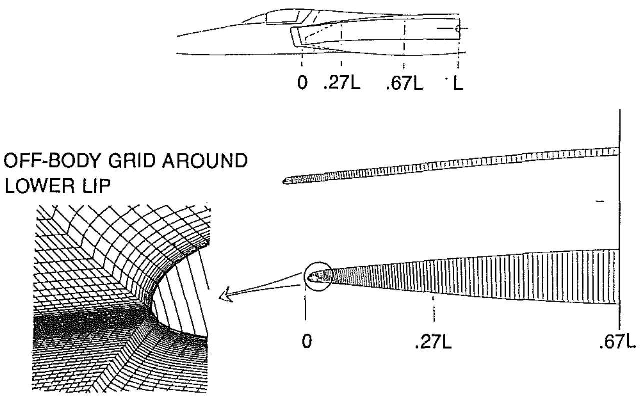

**Fig. 12 Two-dimensional grid model for Navier-Stokes analysis**

valves. Nevertheless, the ARC3D results provide good insight into the flow mechanisms within the diffuser and agree fairly well with most of the total pressure data. Most significant is the validation of the code to calculate severely separated diffuser flows with reasonable accuracy.

## X-29 Inlet Performance at Very High Angles of Attack

Most wind tunnels cannot accommodate inlet/aircraft models to very high angles of attack, say in excess of $\alpha = 50$ deg. For those aircraft that require inlet performance and/or inlet-engine compatibility to be evaluated in this range, a CFD analysis can be useful. It may be the only reliable means for estimating high inlet performance during the preliminary design phase of development.

The inlets of a technology demonstrator aircraft feed a single engine through a bifurcated side-inlet system. This design has the capability for efficient maneuverability into the very high angle-of-attack range, which it has successfully demonstrated over the past few months. A CFD analysis was employed to evaluate the angle-of-attack performance in excess of $\alpha = 50$ deg, which was the limiting wind-tunnel capability for a 1/8th-scale inlet/forebody model.

In the ideal, the goal was to evaluate an accurate three-dimensional model of the inlet-aircraft configuration, including viscous and separated flow effects. This would allow the calculation of duct exit total pressure characteristics over the range of required angles of attack and yaw. However, we anticipated that limitations of the computational tools and resources would constrain the scope and depth of the study. The following brief overview of the CFD analysis that was performed shows the balance that was struck between reduced sophistication of the analytical model to meet reasonable cost levels, and the calculation of useful information.

Because the primary goal of this work was the prediction of inlet flow-separation phenomena and total pressure losses, a Navier-Stokes (N-S) computer code was required. An accurate three-dimensional N-S code model of the inlet-aircraft would require upward of 1.5 million grid points, which would require a prohibitively long CPU time on the CRAY-XMP for each angle-of-attack case. However, since it is anticipated that only the internal flow will incur separation and total-pressure losses, the external fuselage-induced inlet-approach flow field was calculated using a faster running, simpler code. The external flow must be evaluated to determine the severity of local upwash/outwash at the inlet station. VSAERO, a subsonic panel method that calculates three-dimensional potential flow, was selected to model the external flow fields. This code was used to evaluate the flow approaching the inlet, across the required angle-of-attack range. Figure 11 shows the VSAERO model. The entire maximum allowable number of panels (3000) were required to define a sufficiently accurate single side of the forward part of the aircraft. The constraint of modeling only one side of the aircraft precluded evaluating angle-of-yaw effects.

The plan was to evaluate the three-dimensional flow fields at the inlet entrance station. Also, by running an isolated inlet model (Fig. 11) at the same angle of attack as the fuselage-inlet model, we would determine the effects of the fuselage on the local inlet cowl-lip environment. Notice that the inlet duct is considerably foreshortened, only 27 percent of the actual aircraft duct, but sufficient to allow proper simulation of the inlet mass-flow effects.

Since the primary loss mechanisms we were looking for in this analysis are cowl-lip separation effects, a N-S calculation of the external-internal flow is also necessary. A foreshortened and two-dimensional, rather than three-dimensional, inlet-duct model was adapted in the interest of minimizing the grid size. The two-dimensionality precluded the ability to simulate duct offset and secondary flow effects. A 51,000 grid-point model of the inlet was formulated using the N-S code PARC (Fig. 12). The inlet vertical centerline profile, from the leading edge of the cowl lips to the exit plane, 67 percent of the total duct length, was the basis for the model. The subsequent analysis would show that the foreshortened duct is too great a restriction for this study, because it precluded visibility of the complete lower-surface separated zone at very high angles of attack. Nevertheless, the results will show that this relatively economical modeling approach strikes a good balance between resources, expenses, and significant results.

Inlet test data from a 1/8th-scale wind-tunnel test describe duct exit total pressure characteristics to an angle of attack of 49 deg. These data were used to validate the computational results. The wind-tunnel data were acquired at $M_o = 0.15$. All calculations in the present sutdy were also done at $M_o = 0.15$. The inlet airflow rate for this study corresponds to a throat Mach number of $M_o = 0.70$.

The effect of the fuselage on the inlet flow field can be quantified by evaluating and comparing the local angle-of-attack profiles just upstream of the inlet station, for both the complete model and the isolated inlet. Figure 13 shows the results of such a comparison for angles of attack of $\alpha = 10$ deg, 49 deg, and 80 deg. The comparisons are made at a station that is approximately 0.30 m upstream of the bottom-lip projection. The results show that the fuselage imposes an upwash and also a small yaw-plane asymmetry.

At a 10-deg angle of attack there is a 4-deg fuselage-induced upwash at the lower lip. The 49-deg angle-of-attack case shows a fuselage-induced upwash of approximately 7 deg

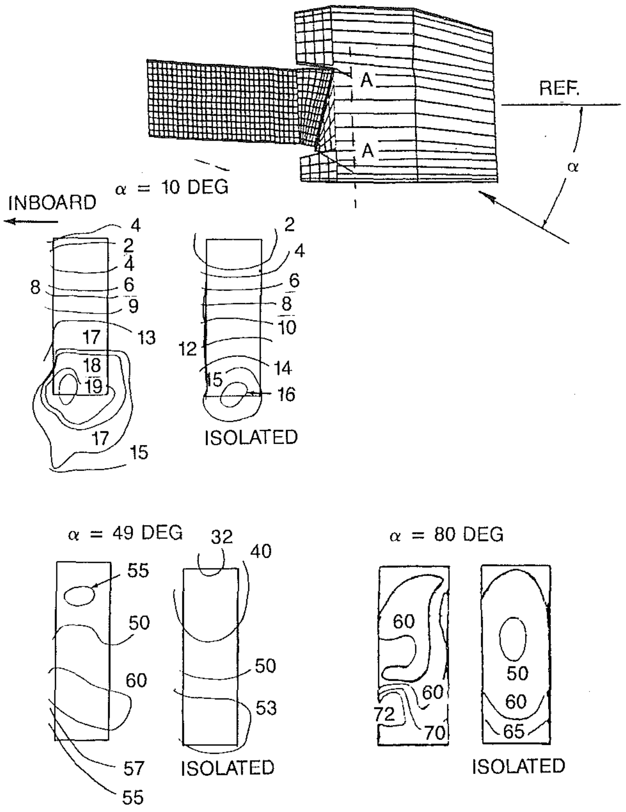

Fig. 13 Local angle-of-attack contours ahead of inlet

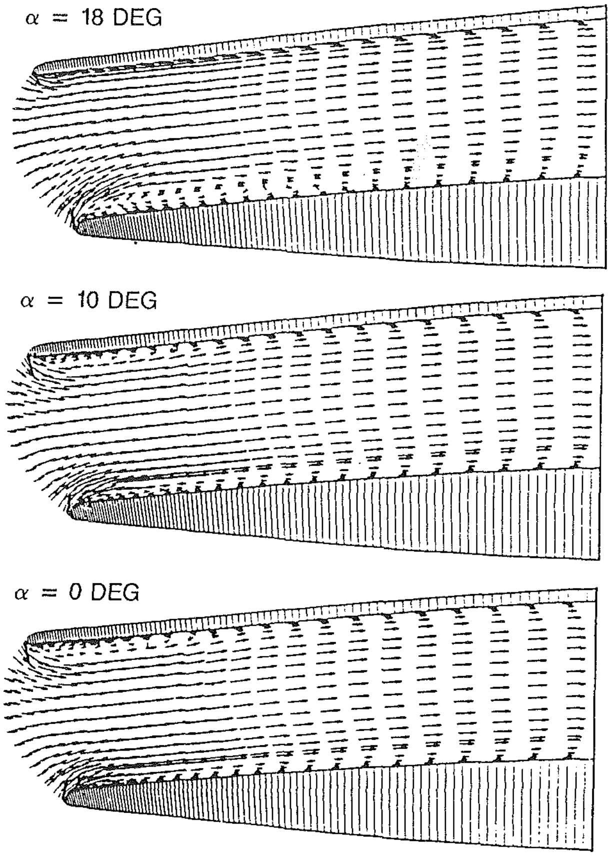

Fig. 14 Velocity fields

across the lower lip. At $\alpha = 80$ deg, we see the strong effect of the engines' suction in reducing the local angles of both cases by 5–10 deg. There still appears to be a fuselage-induced upwash across the lower lip of 5 deg. The fuselage-induced upwash may be used to bias the angle-of-attack versus internal performance results of the N–S analysis, which will be done for an isolated inlet. Because this effect is small, and in the interest of clarity, the N–S analysis will not use this approach. The angle of attack will be the actual angle of the inlet relative to free-stream direction.

Before reviewing the N–S results, we will give a brief overview of the inlet-lip geometry. Inlet total-pressure losses will occur as the result of separation on the internal surface of the cowl lip in direct proportion to the internal-area contraction. The upper cowl lip of the inlet has the smallest contraction, i.e., it is the sharpest lip, having an area contraction ratio of 1.06. The lower cowl lip has the thickest contour, represented by a contraction ratio of 1.16. These contours reflect the design strategy of striking an efficient balance between low drag for supersonic operation, requiring thin lips, and a relatively generous lower-lip contour for good angle-of-attack performance. The lower lip is expected to separate at approximately $\alpha = 13$ deg, but the long duct ($L/D = 7.5$) will allow sufficient mixing so that adequate duct exit flow quality will be developed over the required angle-of-attack range.

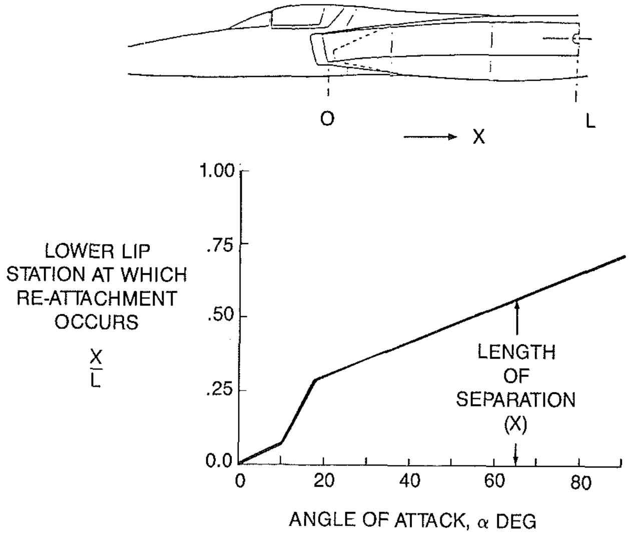

Fig. 15 Length of lower lip separation

A graphic picture of the lip- and duct-flow characteristics with angle of attack is provided by employing the N–S code PARC. Figure 14 shows velocity fields within the inlet. Separation and reverse flow are seen at $\alpha = 0$ deg on the upper-lip internal surface. At $\alpha = 10$ deg the lower-lip reverse flow is clearly seen, and the upper-lip reverse flow area is somewhat smaller. At $\alpha = 18$ deg the upper-surface separation is gone, and lower-surface reattachment is achieved at approximately $0.30L$. Figure 15 plots the longitudinal station at which the calculation shows reattachment on the lower surface, thereby defining the length of the separation bubble as a function of angle of attack. The length of reverse flow increases markedly above $\alpha = 10$ deg and continues to increase, although at a lower rate, at $\alpha > 18$ deg. At 90 deg, angle-of-attack reattachment is predicted at approximately $0.75L$, leaving $0.25L$ of duct length within which to promote development of a uniform flow. These calculated two-dimensional results may be modified by three-dimensional effects such as secondary flows, which may accelerate mixing, in the actual inlet.

Total pressure recoveries at the exit plane of the calculation were determined by integrating the flow-field results across the

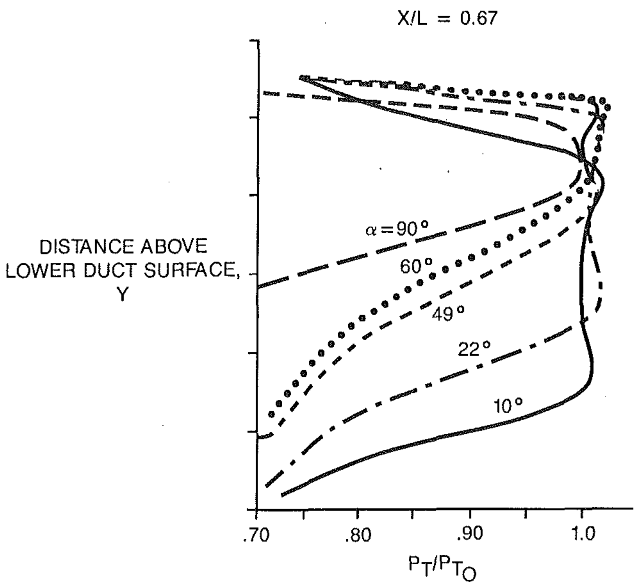

Fig. 16 Effects of angle of attack on total pessure profiles

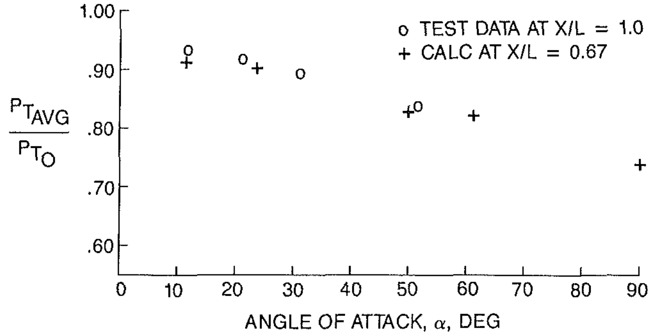

Fig. 17 Effects of angle of attack on average pressure recovery

duct, for various angles of attack. Figure 16 shows the total pressure profiles from $\alpha = 10$ deg to 90 deg. Notice that the lower half of the duct has almost all of the low-quality flow, and that the maximum level is very close to 100 percent even at $\alpha = 90$ deg. The area-weighted averages of the profile are plotted on Fig. 17, where they are compared with test data from a 1/8th-scale model. Good agreement is achieved to $\alpha = 49$ deg, the maximum angle-of-attack capable in the wind tunnel. The calculation shows no anomalous effects to $\alpha = 90$ deg.

## Nozzle/Afterbody Integration

The effects of the airframe forebody on nozzle integration can be much more significant than an inlet system integration. The local approach field upstream of the nozzle boattail reflects boundary-layer thicknesses developed over long, and possibly complex, three-dimensional surfaces. The energy and momentum content reflects "memory" of previous gradients and mixing interactions. This means that computational modeling of nozzle/afterbody configurations must include the ability to simulate forebody effects. Modeling of complete forebody geometry can result in very large grid fields. One half of an aircraft, for example, was modeled by the Grumman Aerodynamics Section with 330,000 grid points (Fig. 18). This includes a sting, which modeled a nozzle exit area that simulates a dry-cruise condition. Because of the relatively large size of the problem, the expense of computing an N-S calculation to investigate nozzle phenomena, especially during preliminary design, could be prohibitive.

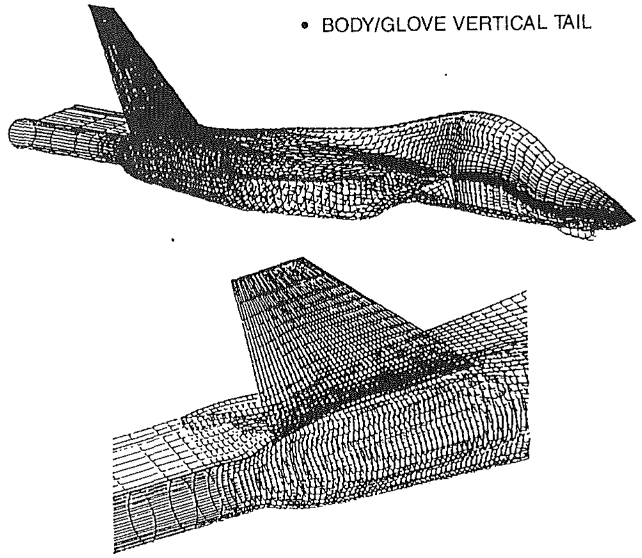

Fig. 18 Three-dimensional grid model for Navier-Stokes analysis

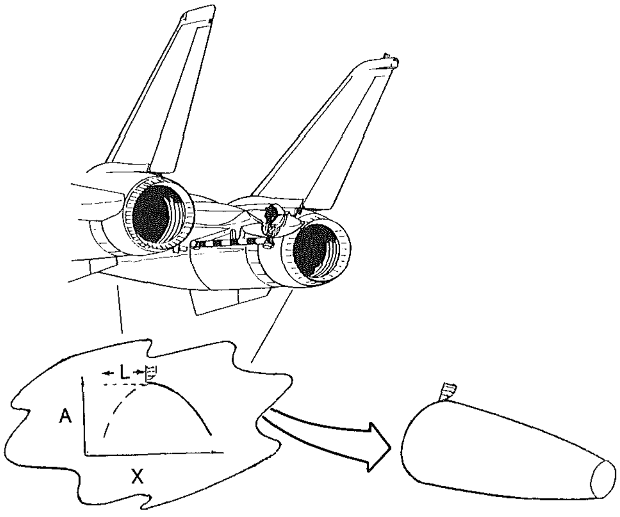

Fig. 19 Equivalent body of revolution (EBR) concept

We have developed a more economical approach to nozzle/afterbody computational analysis that allows simulation of jet-afterbody interactions, but requires empirically derived factors to account for most three-dimensional effects. It is the Grumman Level II Nozzle/Afterbody Installed Performance Prediction Program (Miller and Delaney, 1988). The basic approach is to translate the aircraft longitudinal area distribution into an equivalent body of revolution (EBR). That is, the actual cross-sectional area of the afterbody, minus empennage, is converted into equivalent area circles, and the radius-versus-station data become the radius-versus-length function for an EBR of the afterbody (Fig. 19). This geometric distribution, together with external flow field properties such as Mach number, Reynolds number, friction coefficient, and boundary-layer thickness, comprise the input for the analysis. In addition, exhaust-nozzle exit properties such as exit angle, static and total pressures, and Mach number are also necessary inputs.

The computational method, denoted the Grumman Boattail Code, iteratively solves for the five flowfield regions illustrated on Fig. 20. The transonic calculation is used below $M_o = 1.20$, and the supersonic calculation is used above $M_o = 1.50$. An interpolation process is used for the intermediate Mach number range. Results of this analysis include the friction and pressure drag on the EBR in the presence of the exhaust plume.

The next step is to apply a correction factor to the drag data to account for three-dimensional flow-field effects on the afterbody. The final step, applying vernierlike corrections to the flow-field calculated drag data, adjusts the drag data for aircraft configuration and component effects, such as empennage location and geometry, nozzle spacing, booms, interfairings, base area, and proximity of lifting surfaces.

The Grumman Level II method was applied to an aircraft and compared to 1/12th-scale, powered model wind-tunnel results. The model drag data are for the complete metric afterbody, including empennage, as shown on Fig. 21. The nozzle surfaces were not metric but were extensively surveyed with static pressure taps. Figure 21 compares the calculated and "measured" afterbody drag-versus-Mach number characteristics.

The "measured" afterbody drag includes the corrected balance measurement plus the integrated nozzle drag, plus a calculation of nozzle friction drag. Reasonably good agreement between measured and calculated Level II afterbody drag is achieved. The calculation of the EBR drag, also plotted on Fig. 21, is seen to range between 30 and 60 percent of the total drag. The difference between the two calculated curves is attributable to the drag of the empennage plus the interactive effects of forebody, wing, and empennage on the EBR, plus the three-dimensional effects that differentiate the EBR from the actual afterbody shape.

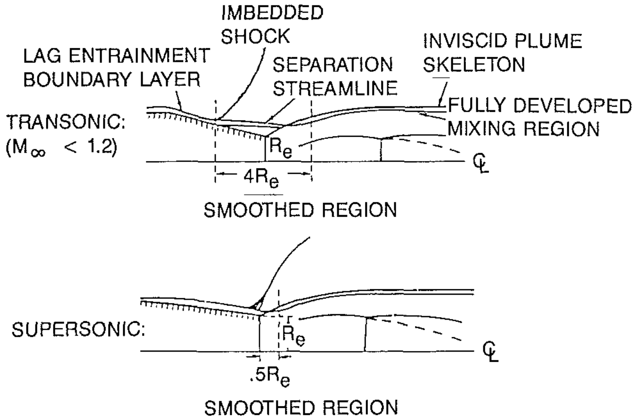

- EXTERNAL INVISCID FLOW - MAPPED REGION, CONVENTIONAL SLOR WITH ROTATED DIFFERENCE SCHEME
- BOUNDARY LAYER - GREEN'S INTEGRAL METHOD FOR $\delta$
- RECIRCULATING FLOW REGION - CONTROL VOLUME ANALYSIS FOR SEP. & REATT. POINTS
- SUPERSONIC EXHAUST PLUME - SALAS' FINITE DIFFERENCE MARCHING SCHEME
- PLUME ENTRAINMENT - MIXING PROFILE TO YIELD EQUIVALENT DISPLACEMENT THICKNESS

**Fig. 20 Boattail-plume models for the Grumman Boattail code**

Employing the EBR as the focal point for calculating the afterbody flow field provides a significant simplification, which, when combined with the Level II Nozzle/Afterbody correction factors, offers a reasonably accurate preliminary design tool. A more insightful use of the Boattail Code is provided by generating EBRs by rotating the local surface contour of interest. This approach allows the Boattail Code to calculate the local external-nozzle surface aerodynamics more accurately. Although it would require additional complications for inclusion in the Level II Nozzle/Afterbody method, it is a good stand-alone approach for evaluating asymmetric nozzle geometry effects more accurately than the single EBR method.

An example of the accuracy of this approach is shown on Fig. 22, which compares measured and calculated pressure distributions along a top-surface buttline just inboard of the vertical fin. Two Boattail code calculations are shown, one for the complete body EBR and another for an EBR generated using the top buttline profile shown on the sketch. In addition to the Boattail Code calculations, results of an N-S calculation using PARC and the three-dimensional grid method of Fig. 18 are also shown. The PARC results agree very well with the wind-tunnel measurements, although the minimum pressure is lower than the minimum test data. This is a good estimate of the actual minimum pressure that the sparcity of pressure taps on the model precluded resolving. The Boattail code results for the complete body EBR overpredict the minimum pressure relative to the PARC results by 40 percent. The Boattail code results for the buttline profile EBR also overpredict the minimum pressure, but by only 9 percent. Both boattail calculations show a more forward location of the peak. Upstream pressures of the Boattail Code results are considerably lower than the N-S and test results, which is probably due to the inability of the Boattail Code to model the three-dimensional effects of the vertical fin/nacelle intersection. The overall comparison of Fig. 22 shows surprisingly good agreement of the Boattail Code results for the buttline profile EBR with those of the test measurements and the PARC N-S Code.

A comparison of jet-induced drag effects, shown on Fig. 23, also shows good agreement between test data and the Boattail Code when the approach of rotating local contours to generate EBRs was used. In this case a top and a bottom EBR was generated, and the average of the two resulting drag calcula-

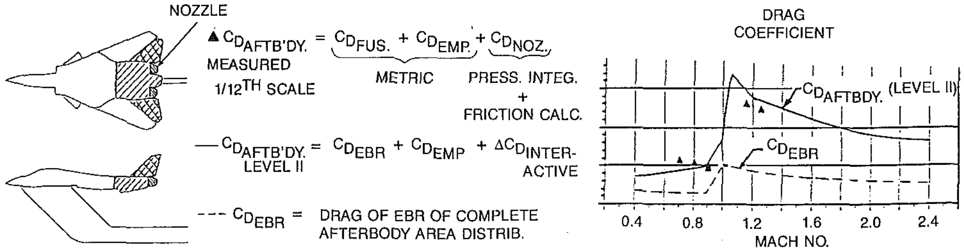

**Fig. 21 Afterbody drag with maximum *A/B* nozzle**

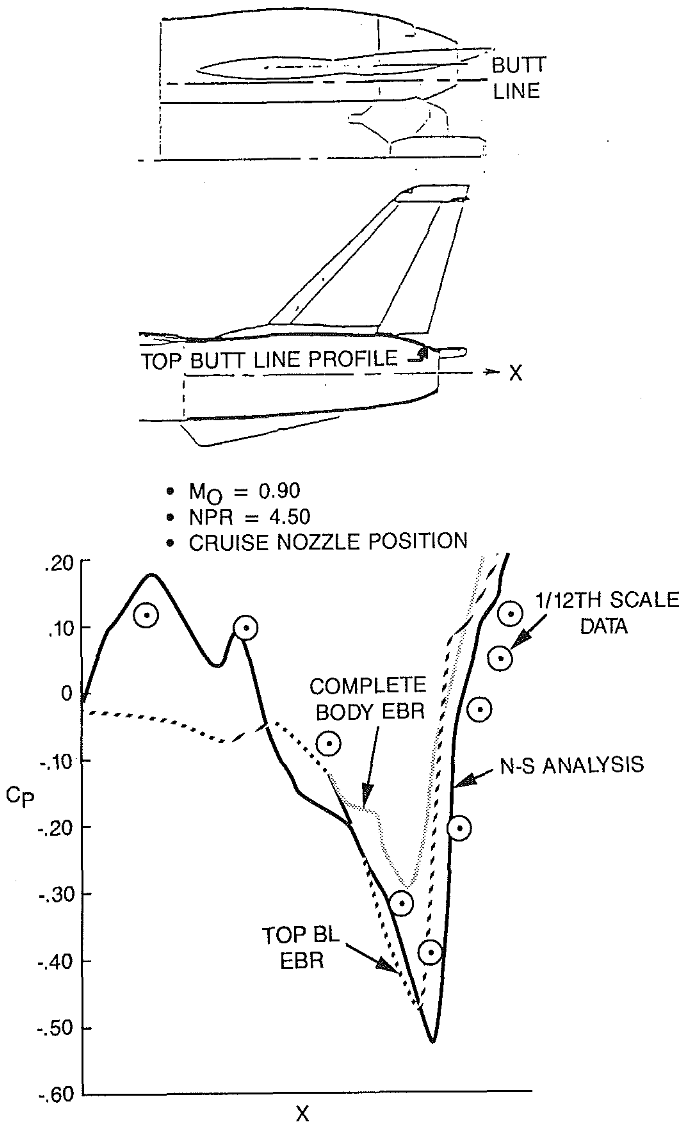

**Fig. 22 Static pressure coefficients along top surface**

tions was plotted. These results show the drag increase as nozzle pressure ratio is reduced below a reference value, which is due to the lower jet-induced static pressures being imposed over the afterbody.

## Conclusions

The applications of CFD for propulsion system integration shown here have demonstrated a strong capability to improve the design/development process. The design engineer has the job of selecting the best methodology for a particular design, which can be quite a complex task. Although the introduction of many new CFD codes allows the designer more potential preliminary design flexibility, he must develop a proper sense of "the right code for the right job." This requires lots of experience. Additionally, he must develop new techniques for applying CFD results to solve design problems. The indirect use of an Euler code's results, which cast doubt on the supersonic wind-tunnel data of the inlet-airframe problem described herein, is an example of such a technique.

Although good inlet design practice should preclude separated flows throughout most of the required operating envelope, the design engineer still needs to be able to estimate effects of flow separation. The offset diffuser problem that was described showed that the N-S code ARC can calculate the flow field in a severely separated diffuser, with sufficient accuracy for preliminary design purposes.

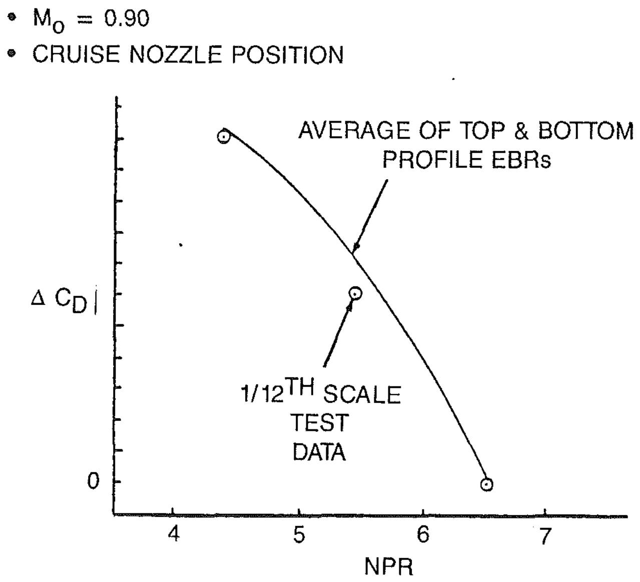

**Fig. 23 Effects of jet total pressure on afterbody drag**

Our experience with the simplistic modeling of an inlet at a high angle of attack demonstrated that a very unsophisticated model coupled with a user-friendly N-S calculation can provide useful and important information at a relatively low cost. This example demonstrates that a high premium is placed on using the simplest method that can provide the required engineering information. Knowledge of the driving fluid mechanical forces is required to select the best method.

We have shown that the extraordinarily expensive calculation of a full three-dimensional fuselage forebody/inlet simulation, necessarily an N-S calculation since separated flows and total pressure losses are required, can be replaced by a simpler and less expensive approach. The inlet performance was calculated over a broad angle-of-attack range using a rapid-running inviscid panel method for the external flow field, coupled with a two-dimensional N-S calculation of the internal flow field that sustained the losses. Good agreement was shown with wind-tunnel measurements of total pressure recovery, up to the maximum angle of attack that the wind tunnel was capable of: $\alpha = 49$ deg. The calculation showed no precipitous falloff in performance at higher angles up to $\alpha = 90$ deg.

The Grumman Level II Nozzle/Afterbody/Installed Performance Prediction Program, which combines an equivalent body of revolution (EBR) technique with empirically derived factors that adjust for three-dimensional effects, was shown to provide good simulation of 1/12th-scale-model drag measurements at transonic speeds. The Boattail Code, an economical computational method for nozzle/afterbody analysis, is the program that calculates the EBR aerodynamics. It was shown to provide good simulation of jet-boattail interactions resulting from nozzle pressure ratio variations. While an N-S simulation of a complete aircraft provided static pressure distributions that compared very well to test results, the large expense of creating and running such a model, especially for preliminary design purposes, is prohibitive. More CFD development work is needed to provide low-cost and more convenient methods for accurate nozzle/afterbody analysis.

## Acknowledgments

The author gratefully acknowledges the contributions of Dr. Thomas Alston, Dr. Warren Davis, Frank Delaney, James Doonan, and Dr. William Hill to the work described in this paper.

## References

Cooper, G. K., 1987, "The PARC Code: Theory and Usage," AEDC-TR-87-24, Oct.

Creare Inc., 1987, "FLUENT User's Manual, Version 2.9," Creare Inc. Technical Note TN-369 Rev. 3, June.

Marconi, F., et al., 1975, "Development of a Computer Code for Calculating the Steady Supersonic/Hypersonic Inviscid Flow Around Real Configurations," NASA CR-2675.

Miller, E. H., and Delaney, F. J., 1988, "Level II Nozzle/Afterbody Installed Performance Prediction Program," Vol. 1-4, AFWAL-TR-88-3004, Dec.

Pulliam, T. H., and Steger, J. L., 1980, "Implicit Finite-Difference Simulations of Three-Dimensional Compressible Flow," *AIAA Journal*, Vol. 18, pp. 159-167.

Tindell, R. H., Hoelzer, C. A., and Alexander, D., 1982, "F-14 Inlet Development Experience," ASME JOURNAL OF ENGINEERING FOR POWER, Vol. 104, pp. 751-759.

Tindell, R. H., 1988, "Highly Compact Inlet Diffuser Technology," *AIAA Journal of Propulsion and Power*, Vol. 4, No. 6, pp. 557-563.

# Airframe/Propulsion Integration at Transonic Speeds

**W. P. Henderson**
Applied Aerodynamics Division,
NASA Langley Research Center,
Hampton, VA 23665

*A significant level of research is ongoing at NASA's Langley Research center on integrating the propulsion system with the aircraft. This program has included nacelle/pylon/wing integration for turbofan transports, propeller/nacelle/wing integration for turboprop transports, and nozzle/afterbody/empennage integration for high-performance aircraft. The studies included in this paper focus more specifically on pylon shaping and nacelle bypass ratio studies for turbofan transports, nacelle and wing contouring, and propeller location effects for turboprop transports, empennage effects, and thrust vectoring for high-performance aircraft. The studies were primarily conducted in NASA Langley's 16-Foot Transonic Tunnel at Mach numbers up to 1.20.*

## Introduction

The interactions between the propulsion system and the airframe can have a significant impact on the performance of an advanced airplane design. These interactions are inherent in most designs, particularly in those concepts where the inlet and nozzle are closely coupled or when the propulsion system is located close to a wing or to other aircraft components. It is not only very difficult to predict these complex flow interactions accurately, but it is also extremely difficult to develop the necessary experimental apparatus/models that can be utilized to develop a full understanding of the complex flow interactions, and to determine the impact of these interactions on the performance of advanced aircraft.

Over the last decade NASA Langley Research Center (LaRC) has been actively involved in developing the needed technology base for the effective integration of the propulsion system into a wide variety of aircraft concepts. The primary focus of attention has included the development and verification of innovative analytical methods for predicting airframe-propulsion interaction effects; the integration of inlet and nozzle concepts into advanced high-performance aircraft designs; and the integration of high bypass ratio turbofans or advanced high-speed turboprops into the advanced transport aircraft.

This paper will present the results of several of these studies conducted by LaRC's Applied Aerodynamics Division, which have contributed to the development of the needed technology base. This paper will concentrate on the integration of various aircraft components such as the engine nacelle/pylons and propeller/nacelles for turbofan and turboprop transports, respectively; and the integration of aircraft components such as the nozzle and empennage into high-performance aircraft.

A vital part of any airframe/propulsion integration activity is the development and verification of computational methods that can be efficiently utilized in defining key experiments, which will aid in the design process and in developing an understanding of the basic flow interactions. The results of several studies will be included in an attempt to define the benefit derived from the use of these advanced computational methods.

## Discussion

The mission requirements for the next generation fighter aircraft may dictate a highly versatile vehicle capable of operating over a wide range of flight conditions. This aircraft will most likely be designed for high maneuverability and agility, operate in a highly hostile environment, and possess STOL landing characteristics to operate from bomb-damaged airfields [1]. Many design guidelines tend to be contradictory for the subsonic and supersonic speed regimes and aircraft performance can be compromised by small changes in these design considerations.

The attainment of high performance is highly dependent upon the minimization of interference resulting from the integration of the propulsion exhaust system into the airframe, one of the most critical design features of an aircraft [2]. An indication of the relative importance of this area is illustrated in Fig. 1 where the percent of total aircraft drag attributed to the aircraft afterbody is presented for four twin-engine fighter aircraft. Representative aircraft from an "ideal" research configuration tested in 1961 to the F-18 aircraft tested in 1978 are shown. The afterbodies of these models comprised from 20 to 25 percent of the total model length, but produced 38 to 50 percent of the total aircraft drag. Up to half of this afterbody drag results from adverse interference in the afterbody region and pressure drag on the afterbody [3-9].

At the same time the designer is striving for a low drag configuration, he is also required to improve the maneuvering capability of the aircraft. This usually requires high thrust to weight and lift drag ratio, high usable lift coefficient, and adequate stability and control characteristics over a very wide operating envelope.

In responding to the need to reduce nozzle/afterbody drag and enhance vehicle manueverability, the Propulsion

---

Contributed by the International Gas Turbine Institute and presented at the 35th International Gas Turbine and Aeroengine Congress and Exposition, Brussels, Belgium, June 11-14, 1990. Manuscript received by the International Gas Turbine Institute January 22, 1990. Paper No. 90-GT-338.

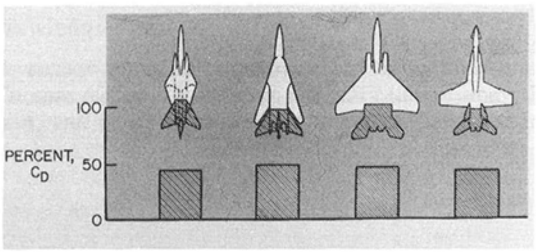

Fig. 1 Propulsion integration characteristics for high-performance aircraft

Axisymmetric dry power nozzle, aft horizontal tails, α = 0°

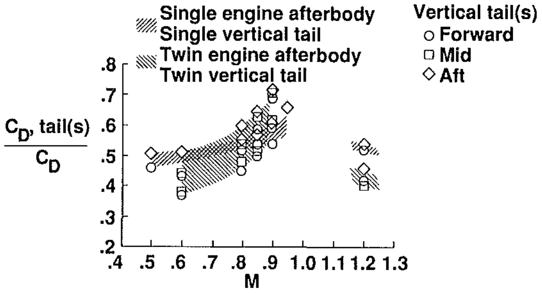

Fig. 2 Effect of empennage on afterbody drag

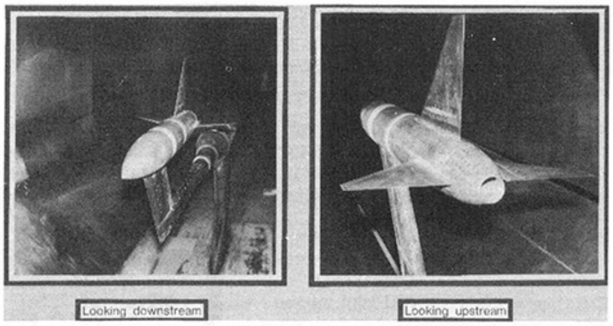

Fig. 3 Single-engine configuration in the Langley 16-foot transonic tunnel

Table 1

| Part | $x$, in. | $x/l$ |
|---|---|---|
| Forebody | 0–40.89 | 0–0.57 |
| Afterbody | 40.89–64.89 | 0.57–0.91 |
| Nozzle | 64.89–71.70 | 0.91–1.00 |
| Tail Surfaces | Variable | Variable |

Aerodynamics Branch at the Langley Research Center has conducted a number of responsive experimental and theoretical research programs.

In these studies it was found that one of the prime contributors to the high nozzle/afterbody drag is the empennage arrangement. A summary of the empennage effects on the single and twin engine models is presented in Fig. 2 and discussed in [7]. Empennage drag increments ratioed to total aft-end drag $C_D$ are presented as a function of Mach number. The two data bands represent the range of data with varying vertical tail location when the horizontal tails are in the aft location. It is obvious from these data that empennage interference effects comprise a significant portion of the total aft-end drag, particularly in the high subsonic and transonic speed regime. It is also obvious that vertical tail location has a large impact on the magnitude of empennage interference. In the transonic speed regime empennage effects account for over half of the total aft-end drag depending upon vertical tail location and afterbody type. Based on the data of these figures coupled with more detailed analysis, it is indicated that up to half of the total afterbody drag (afterbody, nozzle plus empennage) results from adverse interference on the nozzle/afterbody empennage configuration.

In an effort to address this critical area, NASA's Langley Research Center has undertaken a number of studies aimed at reducing the adverse interference drag on nozzle/afterbodies. The first research effort has been aimed at determining the effects of various empennage parameters on the aft-end drag and tail interference drag characteristics for twin engine [8] and for single-engine configurations [9]. These studies were conducted in NASA Langley's 16-Foot Transonic Tunnel. Photographs of the single-engine tail interference afterbody model used in one of these studies are shown in Fig. 3.

The overall model arrangement, representing a typical single-engine fighter aft end, is composed of four major parts located as shown in Table 1.

The forebody consists of an ogive nose 24 in. in length with an initial angle of 14 deg and a constant-radius cylinder thereafter. The afterbody was designed to simulate closure ahead of the nozzle typical of a single-engine fighter configuration. The afterbody had provisions for mounting the vertical and horizontal tails at two different axial location (forward and aft). The tail surfaces were tested in three empennage arrangements: aft, staggered, and forward. Figure 4 illustrates the relative position to the tails for the three

## Nomenclature

$b$ = tail span
$c$ = local chord
$C_D$ = drag coefficient
$C_L$ = lift coefficient
$C_n$ = yawing moment coefficient
$C_P$ = static pressure coefficient
$C_T$ = thrust coefficient
$D_n$ = nozzle drag
$F$ = thrust
$F_i$ = ideal thrust
$H_T$ = horizontal tails
M = Mach number
NPR = nozzle pressure ratio
$q$ = free-stream dynamic pressure
$V_T$ = vertical tail
$x$ = distance from model nose along model centerline
$y$ = distance spanwise from model centerline
$z$ = model length
$\Delta C_{D,it}$ = increment in drag coefficient due to interference effects
$\Delta C_{D_{N/P}}$ = increment in drag coefficient due to nacelle/pylons
$\Delta C_{D_{\mathrm{Tail}}}$ = increment in drag due to horizontal and vertical tails
$\delta_{v,p}$ = thrust deflection in pitch direction
$\delta_{v,y}$ = thrust deflection in yaw direction

### Abbreviations

AFT = aft locations
Fwd = forward location
Stag = staggard location
L.E. = leading edge

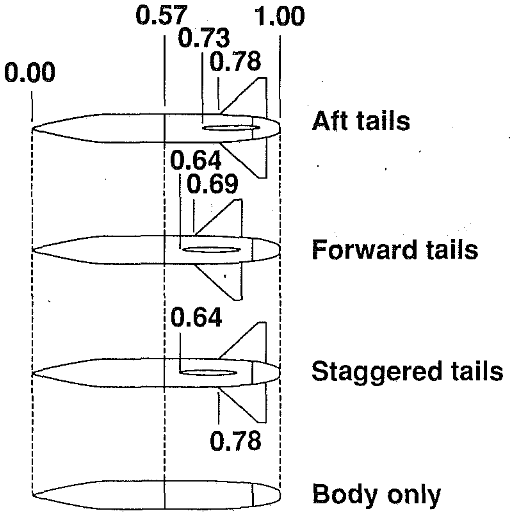

Fig. 4 Empennage arrangements studied

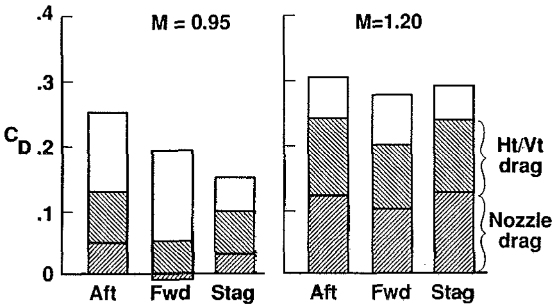

Fig. 5 Effect of empennage arrangement on nozzle/afterbody drag; NPR = scheduled

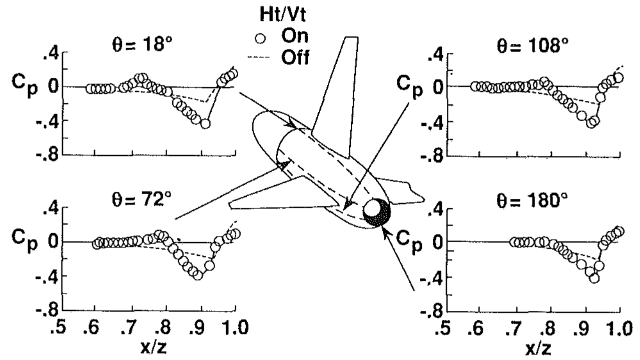

Fig. 6 Effect of empennage on afterbody pressures; M = 0.95, NPR = 3.02

empennage arrangements. In addition, the model was tested with all tails removed. The nozzle used for this investigation simulated a variable geometry (fixed in dry power mode for this test), convergent-divergent, axisymmetric nozzle typical of those currently in use on modern fighter aircraft.

The effect of empennage arrangement on the total aft-end drag coefficient is presented in Fig. 5. The drag increments attributed to the nozzles, obtained by integrating surface pressures, and the horizontal and vertical tails, obtained by appropriate drag estimation procedures, are also presented in this figure. At a Mach number of 0.95 the total drag decreases as the empennage is moved away from the nozzle. Moving the empennage appears to eliminate or reduce an adverse interference of the tails on the nozzle drag. However, moving the tails forward transfers some of this adverse interference to the afterbody. Note the magnitude of its open bar for the forward tail location as compared to the magnitude for its aft-tail configuration. Staggering the tail surfaces further reduces the drag of the aft end of the configuration. This effect appears to result from a reduction in adverse interference on the afterbody, which is larger than the increase in nozzle drag obtained as the horizontal tails are moved closer to the nozzle.

At a Mach number of 1.20 the lowest total aft-end drag is provided by the forward empennage arrangement. According to the data, the primary benefits results from a reduction in the nozzle drag as the tails are moved away from the nozzles.

The effect of empennage on the nozzle/afterbody pressure distribution (data taken from [11]) is shown in Fig. 6. The circular symbols are the experimentally determined pressure distributions for the configuration with the empennage in the aft location. The dashed line is the experimental pressure distribution for the nozzle/afterbody with empennage off.

At a Mach number of 0.95, the empennage caused a large increase in velocities over the aft portion of the afterbody and forward portion of the nozzle ($x/l = 0.82$ to 0.92), which results in the formation of a shock wave at about $x/l = 0.92$ and flow separation over much of the nozzle (pressures on the nozzle are less positive than on the body alone). (See data for $\phi = 72$ deg, for example.) These high negative pressure coefficients acting on the rearward-facing projected area of the nozzle/afterbody along with the absence of pressure recovery on the nozzle (flow separation) cause the high level of interference drag.

It is of interest to note that the effects of the empennage are not limited to the regions close to the tail surface but extend completely around the nozzle/afterbody.

Eliminating these adverse interference effects will require the development of focused experimental and theoretical programs. NASA has spent considerable effort in this area and some of the results are shown in the next several figures. Several prediction methods for afterbody flow problems have been under study. One of the methods is a full-potential finite-volume transonic code called FLO-30V [12], which is used to calculate the pressure distributions over the nozzle/afterbody including the effects of the empennage. In this code an integral boundary-layer calculation is performed in strip fashion. The resulting effective body and tails are used as input to the code. This developmental code utilizes the method of Caughey and Jameson, which is based upon the full potential equation, and a mesh generation technique, which wraps a C-type grid around the body and tails.

The calculated results from the FLO-30V for the staggered empennage arrangement at subsonic speeds are compared with the experimental data in Fig. 7. The staggered tails arrangement was chosen because the results presented herein show that the empenange interference effects were less for this configuration than for the other configurations studied, and it is believed that a better agreement could be obtained. The calculated results show reasonably good agreement with the experimental data at the lowest test Mach number (M = 0.60). At the higher subsonic test Mach numbers, M = 0.90, the discrepancy between the experiment and theory becomes significant. The major reason for the discrepancy could probably be attributed to the approximations made to model the vertical tails and the lack of a model of the wake of the vertical tail. The FLO-30V calculations do account for viscous effects, but the boundary layers on the body and tail were computed separately as two-dimensional elements so that the influence of the empennage is not included in the afterbody boundary-layer calculations. As a result, the FLO-30V calculation shows some influence of the empennage on nozzle/afterbody

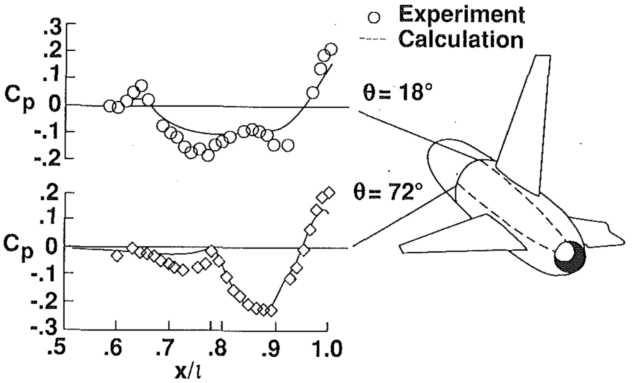

Fig. 7 Comparison of experimental and theoretical pressure coefficients; M = 0.90, NPR = 5.0

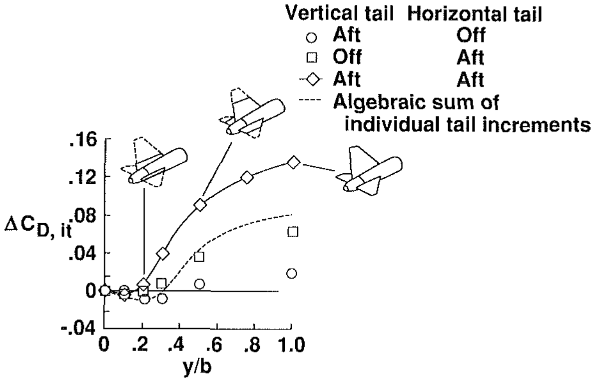

Fig. 8 Effect of tailspan on interference drag; M = 0.95, NPR = 3.97

pressures but fails to predict the severity of the interference effects at the higher Mach numbers.

One of the methods of reducing the nozzle/afterbody interference drag would be to reduce the size of the empennage. The effect of empennage size on the interference drag (measured drag increments removed from data) is presented in Fig. 8. In this figure the interference drag $\Delta C_{D,it}$ is presented as a function of horizontal and vertical tail spans. The circular symbols are the data for the configuration with only the vertical tails, the square symbols are for the configuration with only the horizontal tails, and the diamond symbols are for the configuration with both the horizontal and vertical tails. Contrary to the expected result, the data of this figure indicate that most of the adverse tail interference ($\Delta C_{D,it}$) on the aft end is not caused by the portion of the tails closest to the afterbody but by the outer portion. For example, at $M = 0.95$, tail interference effects on the aft end were favorable (negative $\Delta C_{D,it}$) for $y/b$ less than 0.16. For $M \leq 0.85$, however, tail interference effects were small or favorable for all tail arrangements when $y/b < 0.50$. These results indicate that it may be possible to integrate a short-span surface such as a ventral fin with an increase in aft-end drag equal to or less than the drag on the surface itself.

If the horizontal and vertical tails are reduced in size or eliminated alternate methods of providing the necessary control power must be included. One method of providing the required control forces is through the utilization of thrust vectoring.

Methods of providing pitch vectoring have been under study for some time [14]. These studies have shown that many nozzles can be designed to provide high levels of pitch vectoring without a significant adverse impact on aircraft thrust performance. The challenge now becomes one of providing, in addition to the pitch vectoring, a high level of yaw vectoring.

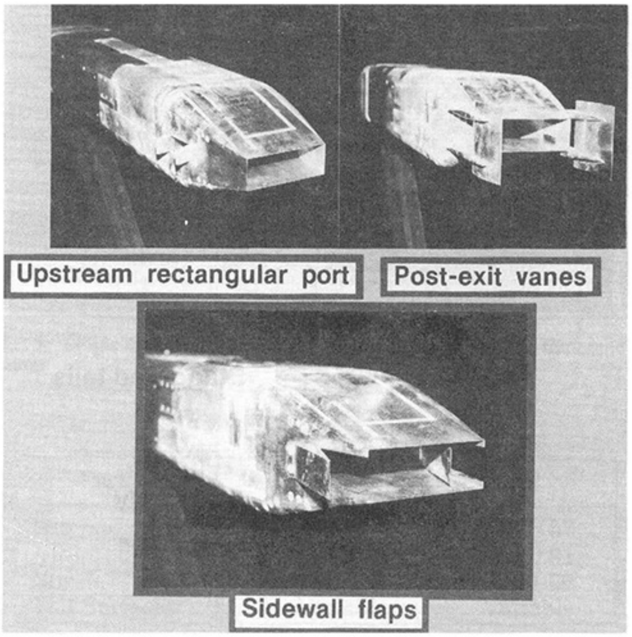

Fig. 9 Yaw vector concepts

A number of configurational concepts have been studied and are shown in Fig. 9.

The upstream yaw vectoring concept was achieved by modifying one of the nozzle sidewalls with a rectangular port located upstream of the nozzle throat. The port was sized to have an area equal to 30 percent of the unvectored dry power nozzle throat area. The port operates by deflecting two flaps. The forward flap was a simple flap hinged at the nozzle sidewall and extended into the external flow. The aft flap was also hinged at the nozzle sidewall, but it deflected both into the external flow and into the internal flow (about 45 percent of the internal nozzle width). The flaps were deflected at an angle of about 70 deg to the axial thrust direction.

The downstream (of throat) yaw vectoring concept (sidewall flaps) is based on modifying either the left or right sidewall or both sidewalls with a hinged flap extending downstream of the nozzle throat. The sidewall flaps hinged directly at the nozzle throat. Consequently, for a positive yaw vector angle (produces positive side force), the left sidewall flap extends out from the internal nozzle flow (expansion turn), while the right sidewall flap extends into the flow (compression turn). This type of concept does have some limitations in that there would be some interference between surfaces when simultaneous pitch and yaw vectoring are required.

The third concept consisted of externally mounted vanes, one on each side of the nozzle. The vanes, which are hinged at the nozzle exit, are deflected such that one vane extends into the jet exhaust flow whereas the outer extends away from the jet exhaust flow. The height of the vanes was determined by the location of the nozzle when pitch vectoring is included. For a ±15 deg nozzle pitch vectoring angle, the lower (or upper) trailing edge of the nozzle coincides with the lower (or upper) edge of the vane.

The external flow effects on the yaw vectoring produced by these three concepts are shown in Figs. 10–12. In these figures, the yawing moment multiplied by free-stream dynamic pressure is presented as a function of Mach number. It should be noted that for presentation purposes, the sign on yawing moment was changed from negative values (which would result from the positive flap deflections shown in Fig. 9) to positive values (which would result from negative flap deflections). On each of these figures, three pieces of data are presented. The circular symbols are the yawing moment based

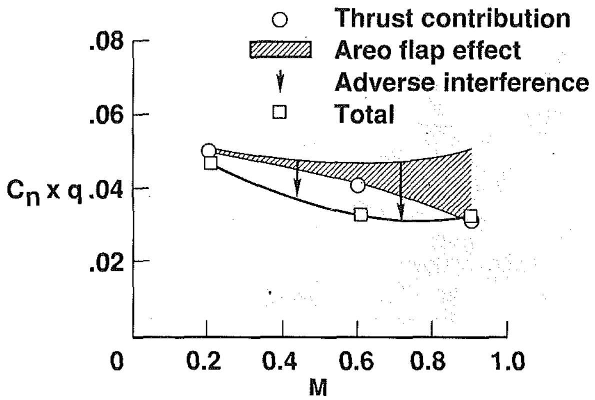

Fig. 10 External flow effects on yawing moment; upstream rectangular port concept; $\alpha = 0$ deg, $\delta_{v,y} = 19.6$ deg, $\delta_{v,p} = 0$ deg, NPR = 3.0

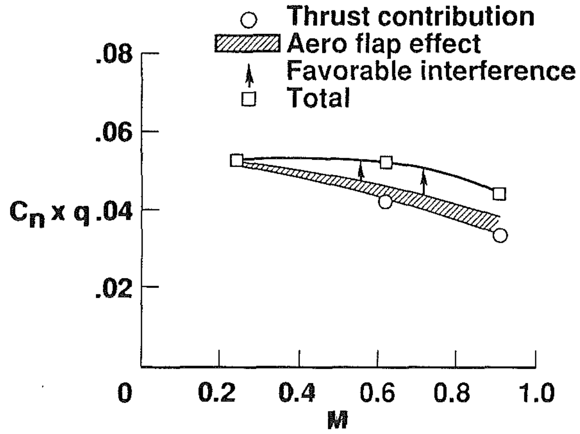

Fig. 11 Internal flow effect on yawing moment; sidewall flap concept; $\alpha = 0$ deg, $\delta_{v,y} = 20$ deg, $\delta_{v,p} = 0$ deg, NPR = 3.0

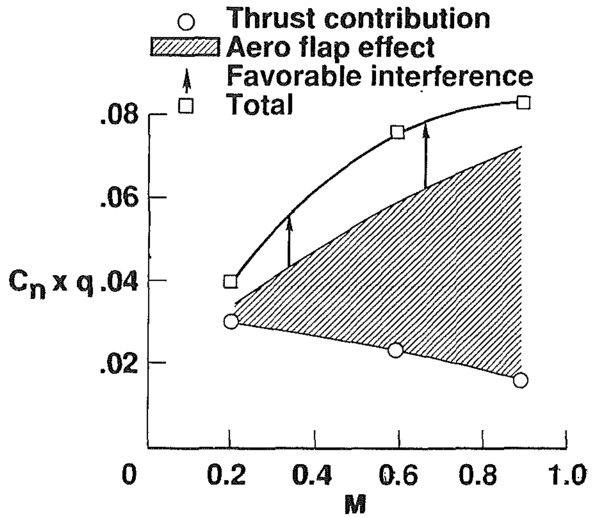

Fig. 12 External flow effects on yawing moment; postexit vane concept; $\alpha = 0$ deg, $\delta_{v,y} = 20$ deg, $\delta_{v,p} = 0$ deg, NPR = 3.0

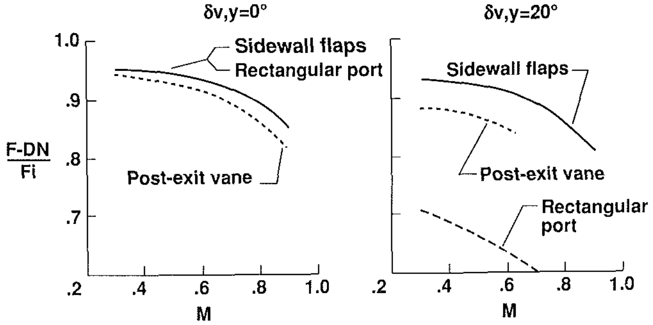

Fig. 13 Effect of yaw vectoring concepts on thrust performance

on the direct thrust contribution. These data were obtained from the yawing moment measured at static (wind-off) conditions multiplied by the ratio of the free-stream static to the free-stream dynamic pressure. The shaded area is the aerodynamic contribution of the vectoring device to the yawing moment measured by conducting the experimental test at jet-off conditions with external flow. The square symbols are the measured yawing moment at jet on conditions with external flow. The arrows shown in Figs. 10–12 indicate an induced external flow contribution to yawing moment caused by any interaction of the external flow with the jet-on vectored exhaust plume and any surrounding model surfaces. For the three cases presented in Figs. 10–12, the jet nozzle pressure ratio is 3.0. The yawing moment as a function of Mach number is presented for the upstream port in Fig. 10, for the sidewall flaps in Fig. 11, and for the post exit vanes in Fig. 12. For the upstream rectangular port configuration, the small flaps protruding from the side of the nozzles results in a small positive increment (aero flap effect) in yawing moment, which increases as the Mach number increases. The induced external flow contribution at jet-on conditions, illustrated by the arrows, indicates that the external flow has an adverse contribution to the yawing moment. It is thought that this adverse effect could either be caused by the external flow altering the angle of the jet plume as it emanates from the side of the nozzle or by creating large negative pressures on the sidewall behind the jet plume. For the sidewall flap configuration (see Fig. 11), both the flaps themselves and the induced external flow contributions produced a positive increment in yawing moment. The increments are relatively small, which is expected since the flaps are small, and the deflection angle is only 20 deg. The largest external flow effects show up on the postexit vane configuration (see Fig. 12). As shown, increasing Mach number causes large increases in the yawing moment obtained. The major portion of this increase is the result of a jet-off aerodynamic effect on the vanes themselves. This is to be expected since the vanes are fairly large and protrude into the airflow, acting essentially like a vertical tail. A summary of the thrust characteristics of these three nozzle concepts is presented in Fig. 13. In this figure the thrust minus nozzle drag divided by the ideal thrust is presented as a function of Mach number for the three nozzles at a yaw vector angle of 0 and 20 deg. For thrust vectored configurations reductions in this ratio from 1.0 are caused by the four following mechanisms: (1) skin friction, internal flow separation, and exhaust flow divergence losses, (2) under- and over-expansion losses, (3) turning of the gross thrust vector away from the axial direction, and (4) additional skin friction and pressure losses caused by the deployed thrust vectoring hardware and the actual turning process itself. The unvectored baseline configuration is affected by the first two mechanisms only. At a vector angle of 0 deg, the nozzle with the sidewall flaps and the upstream port exhibit the same performance, which should be expected, since neither has any additional exposed yaw vectoring hardware. However, adding the postexit flaps causes a loss in performance due to the added skin friction and pressure drag of the external undeflected flaps. For the vectored case (right side of Fig. 13), the configuration with the sidewall flaps exhibits a thrust ratio very close to those for the unvectored nozzle. This result indicated that only a small loss occurs due to turning the exhaust flow for this yaw vector concept. The post-exit vane configuration exhibited a 5 percent lower thrust ratio than the unvectored nozzle concept and about 6 percent lower thrust ratio than the configuration with the sidewall flaps. The lower performance for this configuration probably results from supersonic exhaust flow separation (on the vane deflected away from the exhaust flow). The results for the upstream rectangular port configuration show extremely large thrust ratio losses. This loss is not surprising since about 30 percent of the flow does not pass through the main nozzle throat and thus is not efficiently expanded by the nozzle divergent flaps. In addition, this concept probably also has additional separation losses from the backside of the aft flap, which extends into the internal exhaust stream.

Future civil transport aircraft must offer substantially improved performance at a lower operating cost if the viability of the commercial airlines is to be maintained. Accomplishing this task will require the development and application of many innovative and advanced technologies. With respect to airframe/propulsion integration, the objective of this research is to eliminate any adverse interference penalties associated with the installation of the engines and even possibly developing methods of creating and taking advantage of any favorable interference effects. Key technology elements will have a significant impact on the propulsion system integration characteristics for future aircraft and subsequently the performance and cost will be coupling of very high bypass ratio turbofan engines and/or counterrotating turboprop engines with advanced high aspect ratio supercritical wings. It is believed that with the proper integration of these propulsion technologies a 15 to 30 percent reduction in fuel consumption is possible. Incorporation of these technologies in conjunction with others such as laminar flow control, composite structures, and advanced control concepts indicate the potential for even larger fuel savings.

A number of airframe/propulsion integration studies related to turbofan engine integration have been conducted at the Langley Research Center [15]. From these studies the primary problem associated with integrating a nacelle/pylon/wing can be established. For example, in [16] the results of a study on a high wing transport model representative of a STOL aircraft concept are presented. A photograph of this model is presented in Fig. 14. The wing of this model has an aspect ratio of 7.52 and a quarter-chord sweep angle of 30 deg. An axisymmetric long-duct flow through nacelle was mounted in a conventional location at a semispan station of 0.328. As illustrated in Fig. 15, the nacelle/pylon significantly changes the wing pressure distribution at M = 0.80, particularly around the wing leading edge. The velocity increases on the wing lower surface, reducing the lift on the wing and altering the wing span load distribution, thereby increasing the wing drag due to lift, which shows up as an unfavorable interference effect. Reducing this unfavorable effect therefore can be accomplished by reducing these local velocity increases. The rest of this section on turbofan aircraft will concentrate on reducing or eliminating these unfavorable velocity perturbations. According to the data presented in Fig. 16, the major part of the unfavorable effects is caused by the pylon and not by the nacelle/pylon combination. As shown in this figure, essentially all of the lift loss is due to adding the pylon as well as the larger portion of the drag. The drag increase at cruise lift for the nacelle/pylon combination is probably attributed to the skin friction drag of the long duct nacelles. In view of these results, NASA undertook a study using the model in Fig. 14 to investigate various pylon shapes (no engine nacelle required) on the wing pressure distributions.

In this study (described in [17]) several pylon shapes were studied including pylon contoured to the shape of the streamlines of the local flow on the undersurface of the wing and a second series called compression pylons. These pylons increased linearly in thickness along the chord with the maximum thickness occurring at the wing trailing edge station. That means that all of the pylon closure was achieved behind the wing trailing edge. A photograph of the high wing transport model with 12 percent thick compression type pylon is presented in Fig. 17. This pylon was located at a semispan station of 0.39 with its leading edge located at the wing leading edge and its maximum thickness station at the wing trailing edge. The pressure coefficient data measured inboard of the pylon for several pylons are presented in Fig. 18. As indicated previously, the flow accelerates around the pylon/wing juncture for the conventional pylon causing the loss in lift on wing lower surface. The compression pylon eliminates this velocity increase (solid symbols) such that the pressure coefficient distribution for the wing with the compression pylon is very

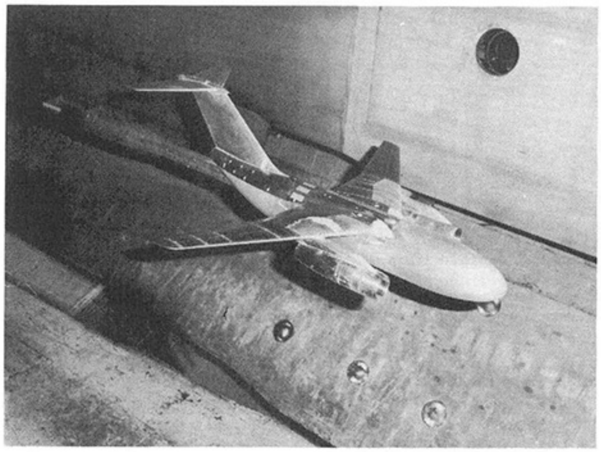

Fig. 14 High wing transport in the 16-foot transonic tunnel

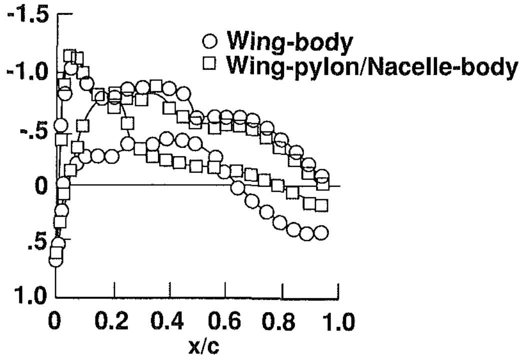

Fig. 15 Effect of engine nacelle/pylon on wing pressure distributions; M = 0.80, $\alpha = 1.24$ deg, $y/b/2 = 0.328$

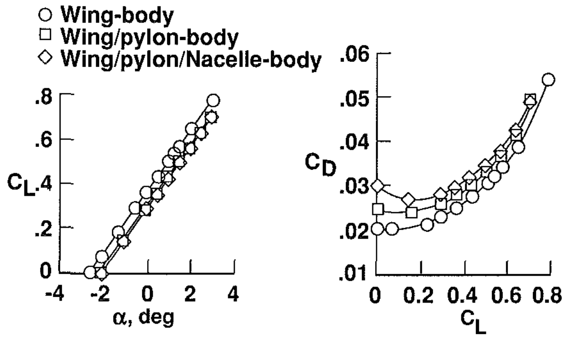

Fig. 16 Effect of engine nacelle/pylon on lift and drag characteristics; M = 0.80

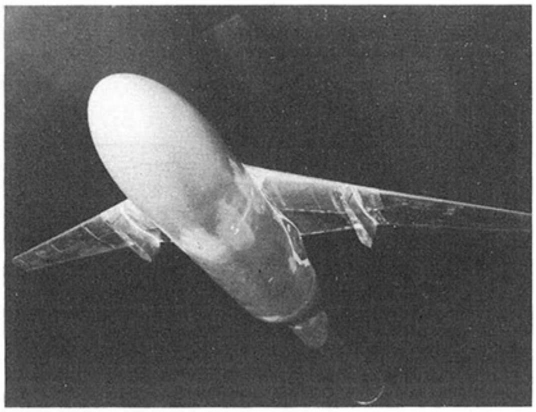

Fig. 17 Photograph of model with compression pylons

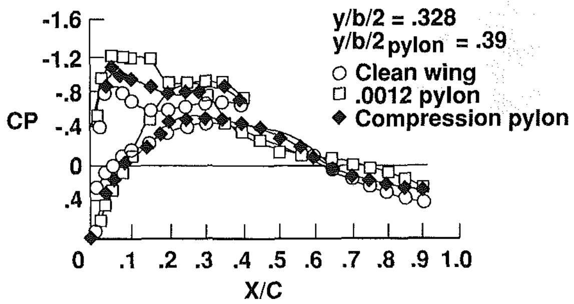

Fig. 18 Effect of pylon shapes on wing pressure distributions; M = 0.80, $C_L \approx 0.50$

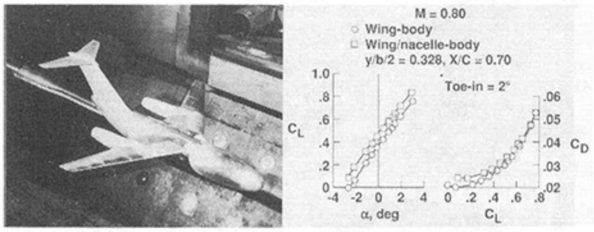

Fig. 19 Effects of wing aft-mounted nacelles on the lift and drag characteristics

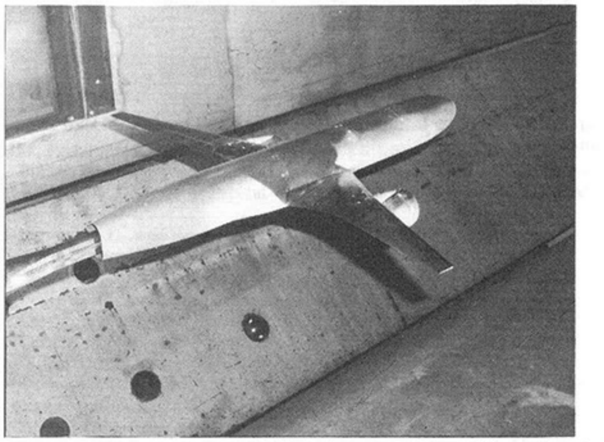

Fig. 20 Low wing transport with high bypass ratio nacelles in Langley 16-foot transonic tunnel

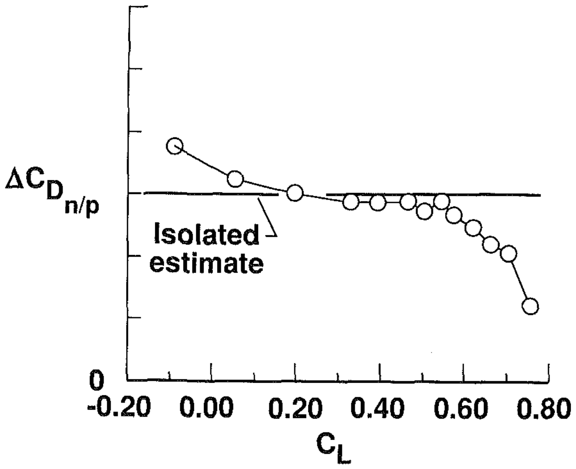

Fig. 21 Drag increment due to nacelle/pylon; M = 0.77

similar to the pressure coefficient distribution for the wing alone.

An alternate nacelle integration arrangement, which tends to exhibit much the same effect as the compression pylon, is shown in Fig. 19. This nacelle is mounted to the undersurface of the wing such that the inlet is located at a 70 percent wing chord station (see [15]). The aerodynamic characteristics also presented in this figure show that adding the nacelle results in an increase in lift coefficient instead of the decrease noted for the conventional engine nacelle arrangement. This lift increase results in a reduction in the drag due to lift. In fact, for this engine installation favorable interference is achieved. That is, the nacelles were added such that the resulting additional drag was less than the skin friction drag attributed to the nacelles.

Several new models have been considered during the past few years to match the evolving aircraft proposals from the various companies more closely. One of these models, designed in 1983–85 and constructed in 1986–88, was tested in the Langley 16-Foot Transonic Tunnel in Jan. and Mar. of 1989. Figure 20 is a photograph of the 1/17-scale, supercritical airfoil, low-wing transport model taken from [18]. It represents a 150 passenger, twin-engine transport with design cruise Mach number of 0.77, a wing quarter chord sweep angle of 21 deg, and a wing aspect ratio of about 10.8. Since only the interference effects of the nacelles on the wing and vice versa were being studied, no attempt was made to add tail surfaces to the model. Instead, a simple afterbody was used to fair into the base surrounding the model support string. A six-component strain gage balance located on the fuselage centerline near the quarter chord of the wing mean aerodynamic chord was used to measure aerodynamic forces and moments on the model.

In this study several advanced nacelle designs were studied. One of them shown in the photograph was a flow-through nacelle representing a very high bypass ratio (BPR ≈ 20) or superfan nacelle. It was expected that because of the large size of this nacelle the adverse interference drag would be significant. However, in the design process the local areas around the pylon wing juncture was carefully tailored in order to avoid the large velocity increases. As can be seen from the data presented in Fig. 21, where the increment in drag due to the nacelle is shown as a function of lift coefficient, the increment associated with the nacelle is slightly less than the skin friction drag of the nacelles. This means that with careful design the adverse interference drag can eliminated.

The recent world-wide fuel crisis caused a significant level of interest in developing new technologies for decreasing fuel consumption. One of the most significant new technologies under study is related to the integration of advanced high-speed turboprop engines. NASA's Langley Research Center is conducting studies aimed at developing an understanding of the flow interactions associated with turboprop integration; obtaining detailed pressure for use in code validation; and the

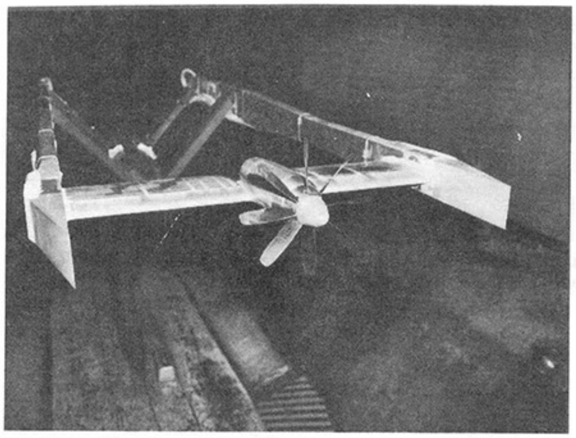

Fig. 22 Turboprop integration model in the Langley 16-foot transonic tunnel

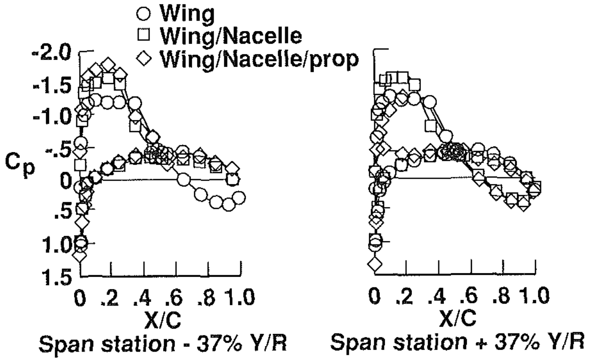

Fig. 23 Effect of propeller rotation on wing pressure distributions; $M = 0.77$, $\alpha = 3$ deg, $C_T = 0.392$, $J = 3.24$

aerodynamic integration characteristics for conventional and unconventional aircraft concepts.

Since the goals of this study were to develop an understanding of the basic flow characteristics, the study was comprised of a straight wing and a swept wing both having the same chord length and the same isolated wing pressure distribution. A photograph of the straight wing model with a single rotation turboprop installation is presented in Fig. 22. The basic flow interaction for this straight wing/turboprop model is presented in Fig. 23. The wing pressure coefficient data for two stations are shown, one for the upwash side of the propeller (left side of figure) and the other for the downwash side. From these data it is easy to determine the integration problems that will be encountered in designing a transport aircraft. For example, these data show that adding the nacelle (without the propeller) causes a flow acceleration over the surface of the wing. However, adding the propeller with its thrust effects and swirling flow causes an increase in lift on the upwash side of the propeller and a significant decrease in lift on the downwash side. This means that to integrate the nacelles properly with the wing may require a wing design that is different for the right and left sides of the aircraft (assuming a twin engine aircraft with single rotation propellers).

The result of a study aimed at integrating a counterrotating propeller onto a swept wing configuration is presented in Fig. 24. This study will illustrate some of the configuration modifications that have to be considered to integrate a turboprop engine properly. This study used a model of an advanced 150-passenger transport and was conduced with the aid of a computational method developed for NASA Langley Research Center by the Boeing Company. A sketch of the basic wing with a symmetric nacelle is presented on the right side of this figure as the solid line. The Euler code was used to predict the pressure distributions over the wing at a station just inboard of the nacelle and the results are presented in this figure. The straight nacelle/wing combination caused a significant increase in velocities on the wing upper surface, which probably resulted in a fairly strong shock wave and its accompanying high wave drag and the potential for flow separation. Several modifications were studied with this code. These included, as illustrated by the configuration represented by the dashed lines, a leading-edge strake on the inboard portion of the wing and some local contouring of the nacelle. This contouring was accomplished by calculating a local flow streamline over the wing and wrapping the nacelle evenly around the streamline. The pressure distribution for the model with these modifications is presented also in Fig. 24 and shows that the high velocities over the wing have been significantly reduced. Similar modifications made on a model with an underwing nacelle were very effective in reducing the installation drag.

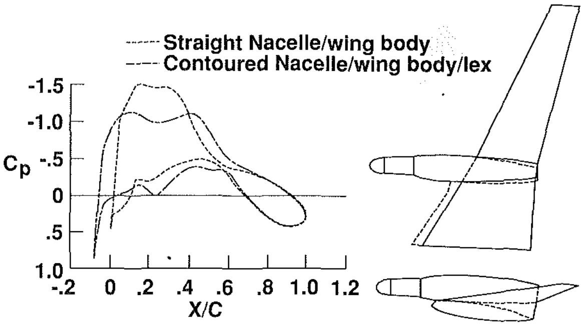

Fig. 24 Effect of nacelle shape on wing pressure distributions; $M = 0.77$, $C_L = 0.55$, $y/b/2 = 0.35$

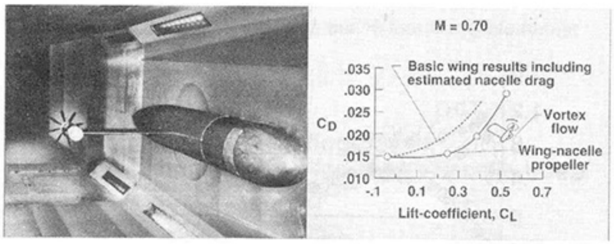

Fig. 25 Effect of wing-tip mounted turboprop on the drag characteristics

In addition to the relatively conventional turboprop installations that have been under study, a fairly sizable effort has been devoted to unconventional concepts, which may offer the potential for significant performance increases. One such configuration shown in Fig. 25 is the wing tip turboprop model (see [19]). In undertaking this program, it was felt that a propeller located behind the wing trailing edge at the wing tip in the crossflow of the wing tip vortex could possibly recover part of the vortex energy as an increase in propeller thrust. Additionally, using the propeller wake to disrupt the wing vortex system could result in a reduction in the lift-induced drag as well. The results of this study conducted in NASA Langley's 7- by 10-Foot High-Speed Tunnel at a Mach number of 0.70 are also represented in Fig. 25.

The effect of the wing-tip mounted pusher turboprop on drag is shown on this figure where drag coefficient is presented against lift coefficient. At zero lift coefficient, where no vortex exists, the measured drag coefficient for the configuration, with a propeller pitch angle of 57.1 deg, is equal, approximately, to the wing along drag plus the skin friction drag of the turboprop nacelle (calculated flat plate skin friction drag of the nacelle based on $C_f = 0.0035$). The reduction in induced drag obtained by the pusher turboprop/vortex interaction is approximately 30 percent of the induced drag of the wing alone adjusted drag at $C_L = 0.35$.

## Conclusions

A significant research program is ongoing at NASA's Langley Research Center on integrating the propulsion system with the aircraft. This program has included nacelle/pylon/wing integration for turbofan transports, propeller/nacelle/wing integration for turboprop transports, and nacelle/afterbody empennage for high performance aircraft. The results indicate the following:

1 A significant portion of the afterbody drag is due to the horizontal and vertical tails.

2 Thrust vectoring concepts are effective in providing combined pitching and yawing moments.

3 Careful contouring of the pylon/wing and nacelle/wing for transport aircraft is required if the adverse interference effects are to be eliminated.

4 Advanced configurational concepts have shown the potential for significant performance increases.

## References

1 Flecther, J., and Burns, B. R. A., "Supersonic Combat Aircraft Design," AIAA Paper No. 79-0699, Mar. 1979.

2 Nichols, M. R., "Aerodynamics of Airframe-Engine Integration of Supersonic Aircraft," NASA TND-3390, 1966.

3 Corson, B. W., Jr., and Runckel, J. F., "Exploratory Studies of Aircraft Afterbody and Exhaust-Nozzle Interaction," NASA TN X-1925, 1969.

4 Runckel, J. F., "Interference Between Exhaust System and Afterbody of Twin-Engine Fuselage Configurations," NASA TN D-7525, 1974.

5 Glasgow, E. R., and Santman, D. M., "Aft-End Design Criteria and Performance Prediction Methods Applicable to Air Superiority Fighters Having Twin Buried Engines and Dual Nozzles," AIAA Paper No. 72-1111, Nov.-Dec. 1972.

6 Glasgow, E. R., "Integrated Airframe Nozzle Performance for Designing Twin-Engine Fighters," AIAA Paper No. 73-1303, Nov. 1973.

7 Berrier, B. L., "Empennage/Afterbody Integration for Single and Twin Engine Fighter Aircraft," AIAA Paper No. 83-1126, 1983.

8 Leavitt, L. D., "Effect of Various Empennage Parameters on the Aerodynamic Characteristics of a Twin-Engine Afterbody Model," AIAA Paper No. 83-0085, 1983.

9 Berrier, B. L., "Effect of Empennage Interference on Single-Engine Afterbody/Nozzle Drag," AIAA Paper No. 75-1296, 1975.

10 Burley, J. R., and Berrier, B. L., "Investigation of Installation Effects on Single-Engine Convergent-Divergent Nozzles," NASA TP-2078, Nov. 1982.

11 Henderson, W. P., and Burley, J. R., II, "Effect of Empennage Arrangement on Single-Engine Nozzle/Afterbody Static Pressures at Transonic Speeds," NASA TP-2753, Nov. 1987.

12 Putnam, L. E., and Bissinger, N. C., "Results of AGARD Assessment of Prediction Capabilities for Nozzle Afterbody Flows," AIAA Paper No. 85-1464, July 1985.

13 Burley, J. R., and Berrier, B. L., "Effect of Tail Span and Empennage Arrangement on Drag of a Typical Single-Engine Fighter Aft End," NASA TP-2352, Sept. 1984.

14 Berrier, B. L., and Re, R. J., "A Review of Thrust-Vectoring Schemes for Fighter Applications," AIAA Paper No. 78-1023, July 1978.

15 Henderson, W. P., and Patterson, J. C., Jr., "Propulsion Installation Characteristics for Turbofan Transports," AIAA Paper No. 83-0087, 1983.

16 Lee, E. F., Jr., and Pendergraft, O. D., Jr., "Installation Effects of Long-Duct Pylon-Mounted Nacelles on a Twin-Jet Transport Model With Swept Supercritical Wing," NASA TP-2457, 1985.

17 Carlson, J. R., and Lamb, M., "Integration Effects on Pylon Geometry and Rearward Mounted Nacelles for a High-Wing Transport," AIAA Paper No. 87-1920, 1987.

18 Pendergraft, O. C., Jr., Ingraldi, A. M., Re, R. J., and Kariya, T. T., "Nacelle/Pylon Interference Study on a 1/17th-Scale, Twin-Engine, Low-Wing Transport Model," AIAA Paper No. 89-2480, 1989.

19 Patterson, J. C., Jr., and Bartlett, G. R., "Effect of a Wing-Tip Mounted Pusher Turboprop on the Aerodynamic Characteristics of a Semi-Span Wing," AIAA Paper No. 85-1347, 1985.

# Integrated Propulsion System Requirements for Control of STOVL Aircraft

**G. W. Gallops**

**C. F. Weiss**

**R. A. Carlton**

Pratt and Whitney,
United Technologies Corporation,
West Palm Beach, FL 33410-9600

*This paper describes an evaluation of propulsion system requirements and capability for a Short Take-Off/Vertical Landing (STOVL) aircraft employing modulation of the propulsive lift distribution for pitch and roll control in hover. The effects of propulsive lift nozzle configuration and propulsion system dynamic response were evaluated using a combined system simulation consisting of a six degree of freedom aircraft model, engine model, and integrated flight/propulsion control. The response and stability of propulsive lift control are compared with control by reaction jets supplied by engine bleed. Aircraft performance is demonstrated in simulated STOVL maneuvers using a dynamic pilot model. The conclusion of this study is that propulsive lift control of aircraft pitch and roll is feasible and can provide as much as a 10 percent increase in engine lift rating over systems that employ reaction control alone. The dynamic response of practical propulsive lift configurations, however, is less than that of reaction control configurations, which must be offset through integration of the propulsion system and its control.*

## Introduction

Recently, the use of propulsive forces to provide aircraft attitude control is being considered for a number of applications where vectoring and reversing nozzles are being used to improve maneuverability, to avoid and recover from departure, and to reduce approach speeds. While the most significant activity is in the area of military applications, benefits are available to commercial applications as well where lower approach speeds result in reduced runway length requirements and lower structural weight and where redundant attitude controls improve flight safety. The subject of this paper is a new generation of Short Take-Off/Vertical Landing (STOVL) aircraft that is being studied, which employ propulsive lift for attitude control as well as for lift augmentation below wingborne speeds (Roth et al., 1981; Kerr et al., 1981; Wilson et al., 1982; Ward and Lewis, 1987; Berg et al., 1988).

Current VTOL systems employ reaction control jets supplied by engine bleed to provide aircraft attitude control in hover. While bleed provides effective control with a minimum of integration between the aircraft and propulsion control systems, sustained bleed causes an increase in engine hot section temperature that results in a reduction of the engine lift thrust capability and/or hot section life. In future STOVL aircraft configurations the distribution and vector of propulsive lift provide forces for aircraft attitude control supplementing or eliminating reaction control bleed.

Roth et al. (1981) and Kerr et al. (1981) describe a NASA funded study, which was one of the first to consider propulsion system integration as a means of improving VTOL aircraft performance by obtaining aircraft attitude control forces from the propulsive lift nozzles. That study established propulsion requirements for supersonic VTOL aircraft and identified candidate integrated control concepts. The study described in this paper continues the theme of that prior NASA study and specifically explores the possibility that reaction control bleed can be eliminated in a notional STOVL aircraft, thereby increasing engine lift thrust rating and aircraft performance.

In addition to providing the aircraft requirements and initial concepts for the current study, Roth et al. (1981) also describe a conceptual design and evaluation methodology based on exercising combined simulations of the aircraft and engine and their control systems. This approach allows consideration of nonlinear and discontinuous system effects such as communication delays, actuator rate and travel limits, and control mode changes, which are difficult to evaluate using classical control analysis. Since the current study focuses on the flight regime below wingborne speeds, relatively simple models of the aircraft (Etkin, 1972) and engine are employed. Additionally, Ward and Lewis (1987) and Fozard (1978) provide guidance in establishing STOVL aircraft maneuvers and operating procedures that are used in exercising the combined simulation. Fozard (1978) and Taylor (1986, 1988, and 1989) provide aircraft characteristics and dimensional data.

## Study Configuration

Considering studies published in the open literature (Wilson et al., 1982; Ward and Lewis, 1987; Berg, 1988), the only significant commonality among the numerous STOVL aircraft

---

Contributed by the International Gas Turbine Institute and presented at the 35th International Gas Turbine and Aeroengine Congress and Exposition, Brussels, Belgium, June 11-14, 1990. Manuscript received by the International Gas Turbine Institute February 21, 1990. Paper No. 90-GT-364.

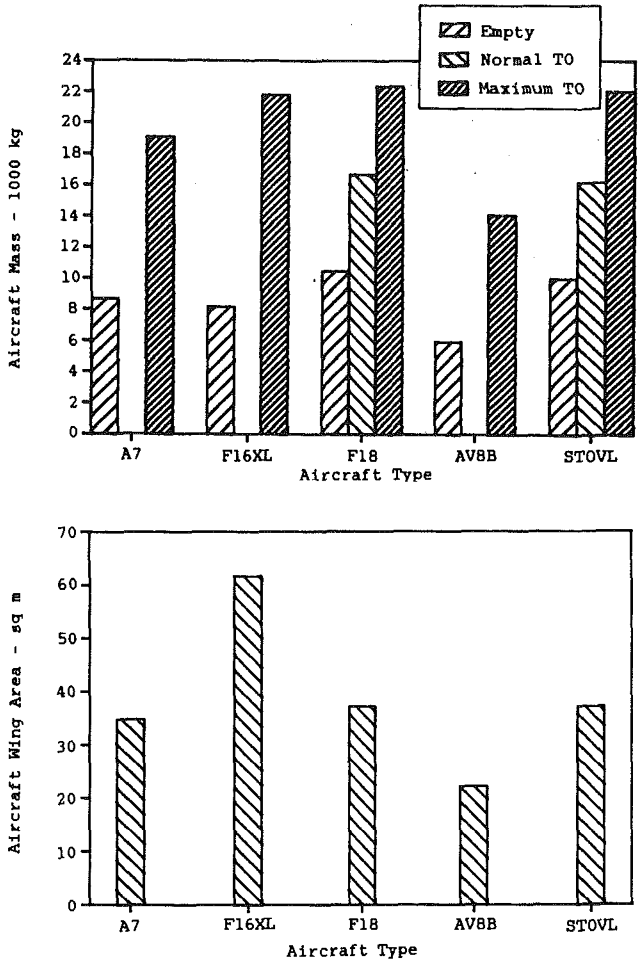

Fig. 1 Comparison of multirole aircraft mass and wing area

configurations is that it is a single engine multirole aircraft. To avoid the controversy attendant with choosing one or more of these configurations as candidates for this study, a notional STOVL aircraft configuration was devised based on current examples of aircraft of this mission type. When the mass and wing area of some examples for this type (Taylor, 1986, 1988, 1989) are compared as in Fig. 1, several conclusions may be drawn concerning a possible STOVL configuration: (1) The ratio of maximum take-off mass to empty mass is two; (2) the maximum wing loading is on the order of 6 kN/sq m; (3) the size will be on the order of 1.5 times that of the AV8B. For the study described here a conservative approach is taken and the mass and wing area are selected at the upper range of the examples.

The STOVL propulsion system must satisfy conflicting bypass ratio requirements for high net thrust in both hover and supersonic flight. Several alternatives to the subsonic vectored thrust configuration of the AV8B are considered by Ward and Lewis (1987) and Berg (1988), each offering some aspect of improvement but none with a clear overall advantage at this time. For this study an evolutionary engine concept is selected that maintains the proven four post list nozzle configuration of the AV8B, but which transitions to a more conventional, single nozzle configuration for wingborne flight.

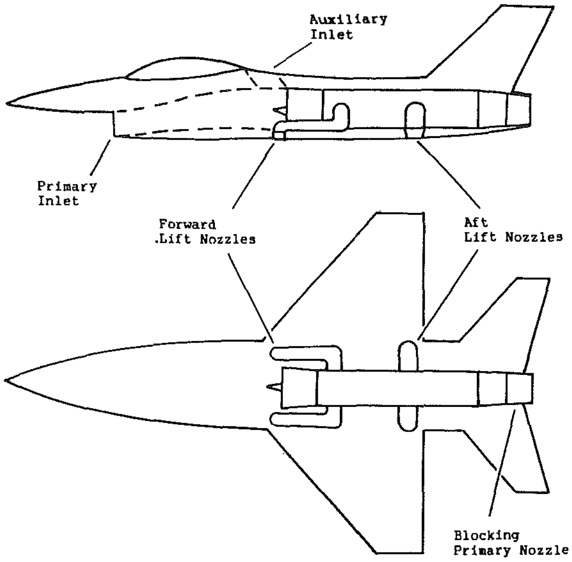

Fig. 2 Notional STOVL aircraft features

Figure 2 and Table 1 illustrate the pertinent features and physical characteristics of the notional STOVL aircraft configuration. The aircraft has both a conventional primary nozzle and a four post lift nozzle configuration like the AV8B. Like its conventional counterparts, the notional STOVL aircraft has an aft-mounted engine with a relatively long supersonic inlet. The engine location requires that the forward lift nozzles be supplied by ducts to obtain static longitudinal balance in hover. An auxiliary inlet or blowin door provides low loss for hovering flight and allows the primary inlet to be optimized for conventional flight. Location of the auxiliary inlet near the aircraft center of gravity reduces yawing moments created by gusts. Dimensions of the notional aircraft are consistent with the previously cited types. The moments of inertia are scaled from Roth et al. (1981) proportional to mass and square root of wing area.

The weight penalty associated with adding the hardware necessary to allow modulation of the propulsive lift distribution is not quantified in this paper since it is strongly dependent on the STOVL configuration and the specific aircraft design. Although adding the capability for propulsive lift control may significantly increase aircraft weight, one can observe that many of the STOVL concepts now under consideration already employ variable area on some or all of their exhaust nozzles. These have utility for increased hover performance, supersonic operation, engine cycle changes, or other mission specific functions. While overall system simplicity is a desirable attribute, little additional hardware is required to provide the capability to modulate the propulsive lift distribution of most STOVL concepts.

## Nomenclature

*A*8 = primary nozzle area
*A*16 = fan bypass mixing area
*A*18 = aft lift nozzle area
*A*28 = forward lift nozzle area
*CG* = center of gravity
*Ixx* = roll axis moment of inertia
*Iyy* = pitch axis moment of inertia
*Izz* = yaw axis moment of inertia
MAX = maximum
MIN = minimum
PLC = propulsive lift control
*RC* = reaction control
STOVL = short take-off/vertical landing
*TO* = take-off
*VL* = vertical landing
VTOL = vertical take off/landing

Table 1 Notional STOVL aircraft physical characteristics

| | |
|---|---|
| Mass | |
| Empty | 10000 kg |
| Normal TO | 16200 kg |
| Maximum TO | 22000 kg |
| Maximum VL | 12200 kg |
| Wing Area | 37.2 sq m |
| Moments of Inertia | |
| Ixx | 20000 kg m |
| Iyy | 70000 kg m |
| Izz | 85000 kg m |
| Control Moment Arms | |
| Reaction Jets: | |
| Pitch | 7.0 m |
| Roll | 5.0 m |
| Yaw | 7.0 m |
| Forward Lift Nozzles: | |
| Pitch | 2.1 m |
| Roll | 1.0 m |
| Aft Lift Nozzles: | |
| Pitch | 1.9 m |
| Roll | 1.0 m |

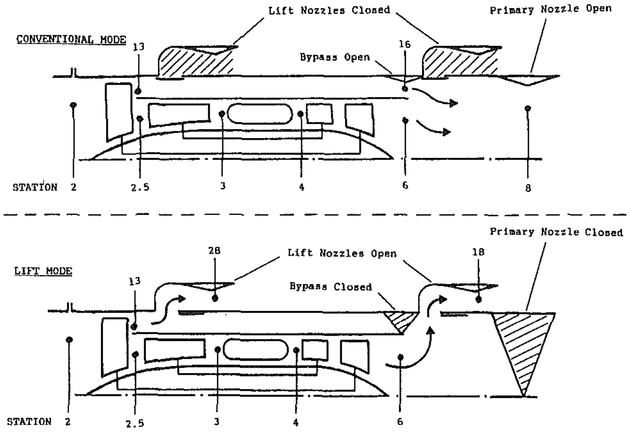

Fig. 3 Notional variable cycle STOVL engine

Thrust size for the notional engine is set by the vertical landing mass of 12,200 kg. Using the AV8B as a guide, minimum thrust-to-weight ratio should be on the order of 1.15, which dictates a lift mode unaugmented thrust rating of 138 kN. With an augmentation ratio of 1.4 in conventional mode, this engine can provide an aircraft thrust-to-weight ratio of 0.90 at the maximum take-off weight.

The notional STOVL engine is a variable cycle configuration, as illustrated in Fig. 3. In conventional mode the engine functions as a mixed flow turbofan with the lift nozzles closed. In lift mode the engine functions as an unmixed flow turbofan with the lift nozzles open and the bypass and primary nozzle closed. Transition between modes is achieved by coordinating the lift nozzles with the bypass and primary nozzle in a manner similar to thrust reverse transition in commercial transport engines. In lift mode roll moments are provided by reciprocal nozzle area variation, whereas pitch moments are provided by

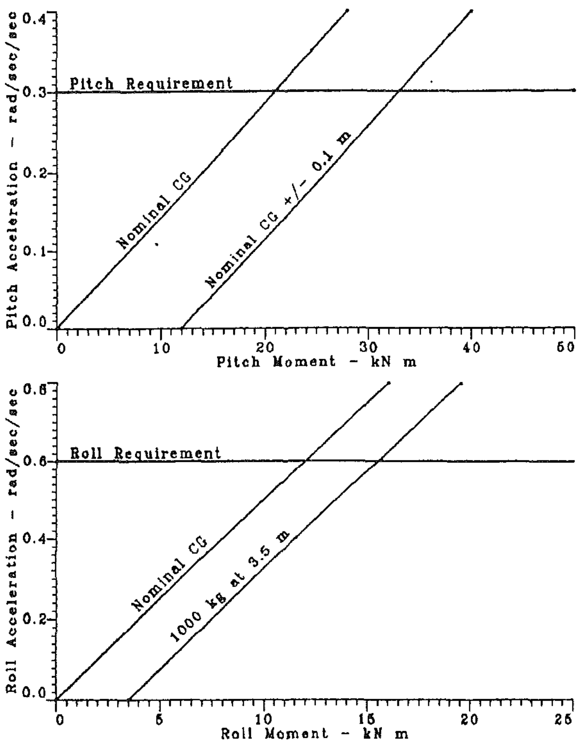

Fig. 4 Requirements for propulsive lift control

altering the forward to aft thrust balance with the aft nozzle area. Yaw control is provided by reaction control jets as in the AV8B.

Although a specific engine concept is selected for this study, the requirements that follow in this section and the control approach described in later sections are basically applicable to other concepts as well, including those that employ mixed flow cycles and/or auxiliary lift engines.

Of the aircraft attitude control requirements listed by Roth et al. (1981), pitch and roll acceleration requirements drive the propulsive lift control design. These requirements are illustrated in Fig. 4 for both balanced and unbalanced aircraft. Using the notional aircraft nozzle locations, the requirements for an unbalanced aircraft can be met with 7 percent differential thrust variation individually or 14 percent combined. Equivalent requirements for reaction control bleed are shown in Fig. 5 including yaw. Figure 6 illustrates the effect of reaction control bleed on engine lift thrust rating. Fortunately, maximum bleed is required for only short time intervals and does not establish the engine rating (Fozard, 1978). Engine rating is determined by the sustained bleed requirement, which is a function of environmental, aircraft system, and human factors. Assuming that the nominal bleed requirement is one half of the maximum, the engine lift rating for an aircraft employing propulsive lift for pitch and roll control is on the order of 10 percent greater than an equivalent configuration employing reaction control.

## Integrated Control Laws

Even in a highly integrated aircraft such as this it is desirable to partition the engine control laws into a separate subsystem of the overall aircraft system. This allows the engine and its control laws to be developed and validated independently before integrating as a complete system. Partitioning does not require that the engine and aircraft control laws execute in separate processing systems; however, factors such as limited processor capacity, the large number of high rate analog engine sensors, and lower cabling weight make a separate engine control processor attractive. Communication delay is not a factor in these systems because of the availability of high-speed digital data buses.

The integrated control law architecture illustrated in Fig. 7 is partitioned into an aircraft control, which is concerned with achieving a desired attitude through the command of aerodynamic and propulsive forces, and an engine control, which is concerned with interpreting the aircraft control commands in terms of engine process commands and then using the engine control effectors to achieve them. Inputs to the engine control include the conventional total thrust command plus differential thrust commands for aircraft attitude control. Also included are cycle and nozzle mode selectors for engine transition. Command of reaction control bleed and lift nozzle vector angle are not included as engine control functions since these do not significantly influence the engine in any way that cannot be compensated either internally or through the engine control inputs. Engine status concerning limit proximity, thrust capability, faults, etc. is provided to the aircraft control to aid in defining maneuver trajectories. Loop closure for the aircraft attitude control laws, however, is solely through the aircraft rate sensors.

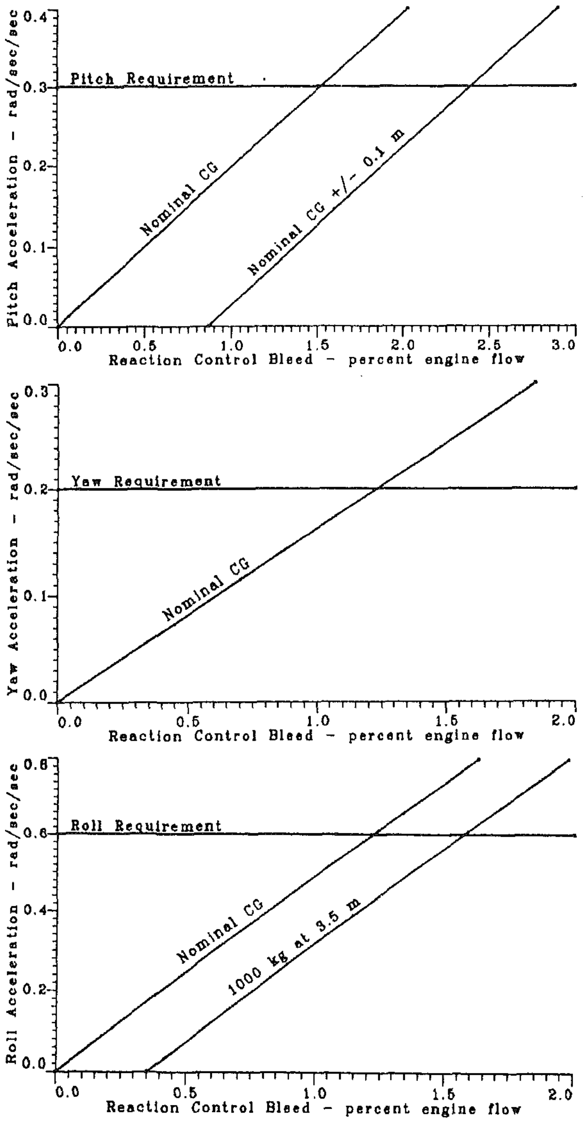

Fig. 5 Requirements for reaction control

**Engine Control Laws.** Figure 8 is an overview of the four major functional modules of the engine control laws. Except for the added functions to provide pitch and roll differential thrust, they are organized similarly to a conventional engine control. The mode transition and nozzle control modules perform standard area scheduling functions for the cycle and nozzle transition and are not discussed further in this paper. The thrust scheduling and process control modules perform the primary functions of converting the aircraft thrust commands to corresponding engine process commands and providing the closed-loop process control and thermal and structural limiting.

The engine process control module that provides the closed-loop control to the process demands and engine internal limits is an obvious application for modern multivariable control design methodology. However, adequate performance is

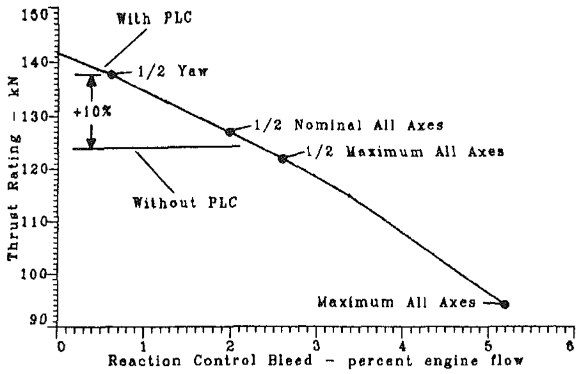

Fig. 6 Effect of reaction control bleed on engine lift thrust rating

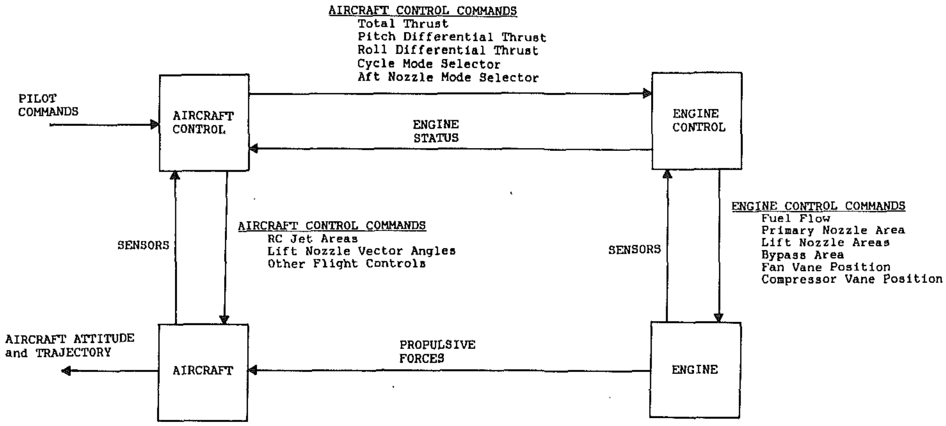

Fig. 7 Integrated control law architecture

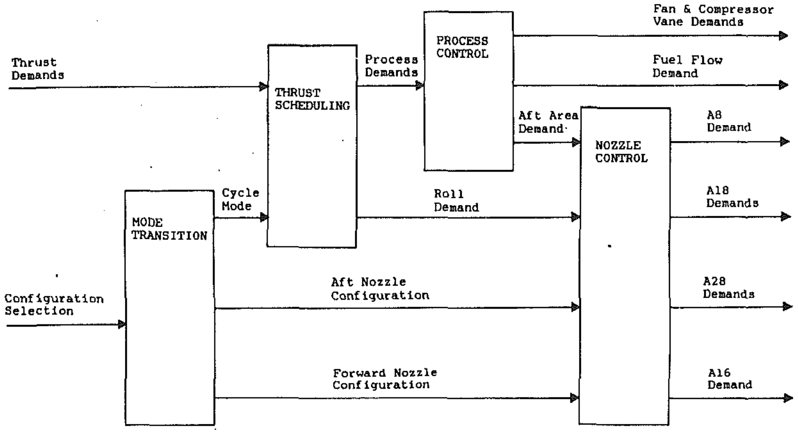

Fig. 8 Engine control law architecture

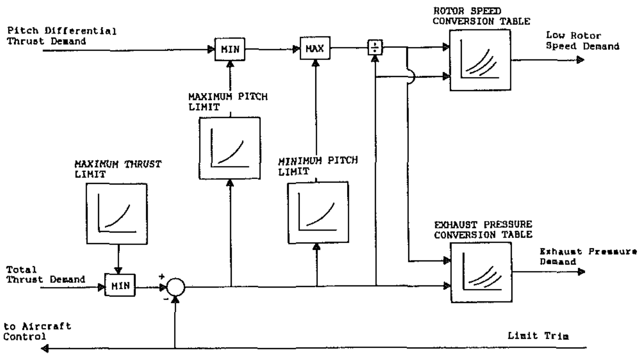

Fig. 9 Thrust scheduling module

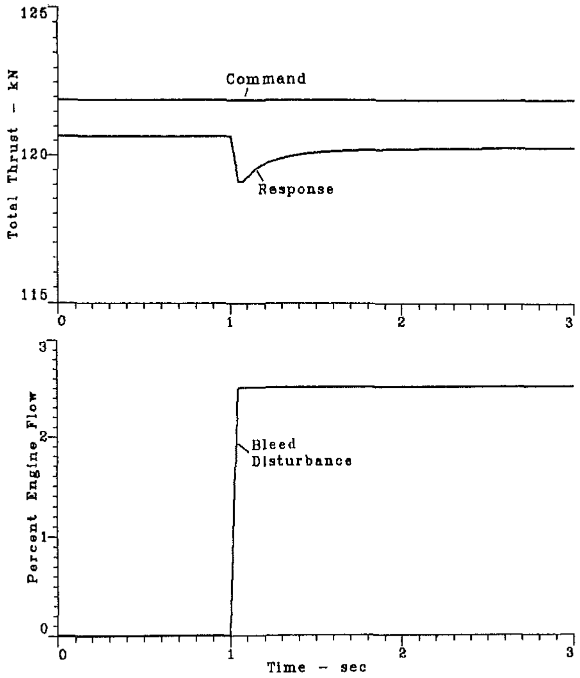

Fig. 10 Propulsion system response to reaction control bleed

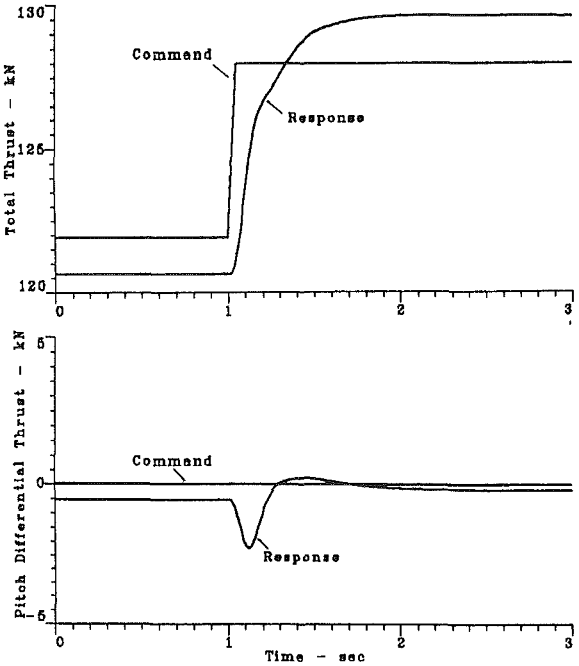

Fig. 11 Propulsion system response to total thrust demand

achieved for this study using parallel proportional plus integral controllers for low rotor speed and aft nozzle pressure as described by Kerr (1981). Engine variable geometry is scheduled conventionally as functions of corrected rotor speeds. The digital control is simulated with a frame time of 0.01 s and an internal computation delay of 0.01 s. Actuators are simulated as first-order lags with time constants of 0.03 s.

Figure 9 illustrates how the thrust scheduling module converts the aircraft total and pitch differential thrust demands to corresponding low rotor speed and aft nozzle pressure demands based on a corresponding pair of bivariant thrust conversion tables. The thrust conversion tables are preceded by thrust demand limiting tables that keep demands within the capabilities of the engine and control. In effect these tables represent specifications of engine capability that can be mutually agreed upon by the aircraft and engine designers and demonstrated in engine ground tests. A similar approach (not shown in the figure) provides roll differential thrust scheduling for the left and right lift nozzle areas. In the event that engine internal limits are encountered, a limit trim provided by the engine process control module adjusts total thrust demand and informs the aircraft control of the reduced engine capability.

Examples of the engine control response to step commands in reaction control bleed, total thrust, and pitch differential thrust are illustrated in Figs. 10, 11, and 12. These examples demonstrate reasonable dynamic behavior and good steady-

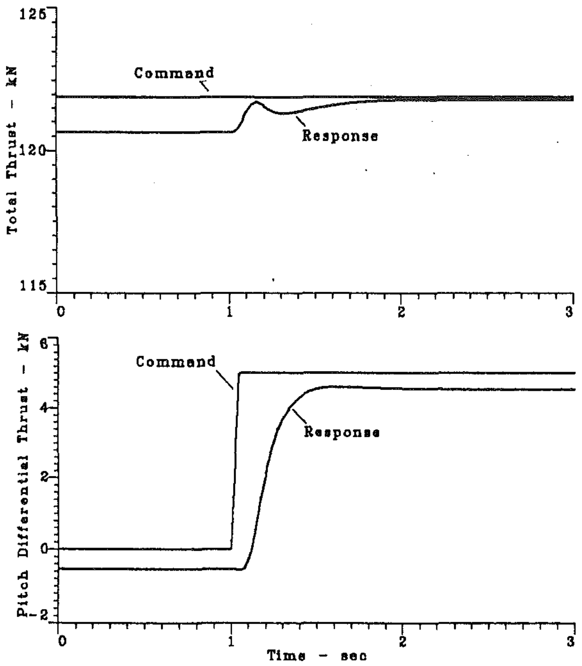

Fig. 12 Propulsion system response to pitch differential thrust demand

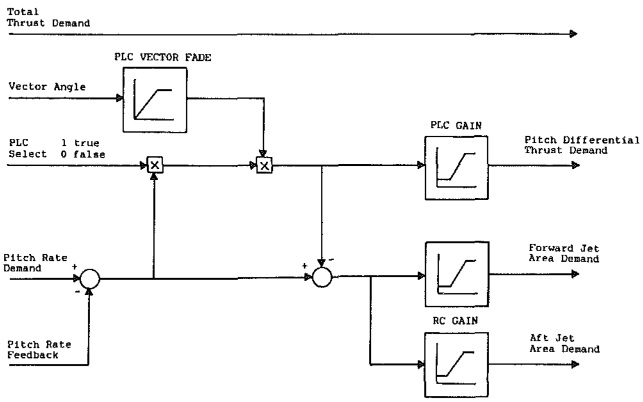

Fig. 13 Aircraft control laws

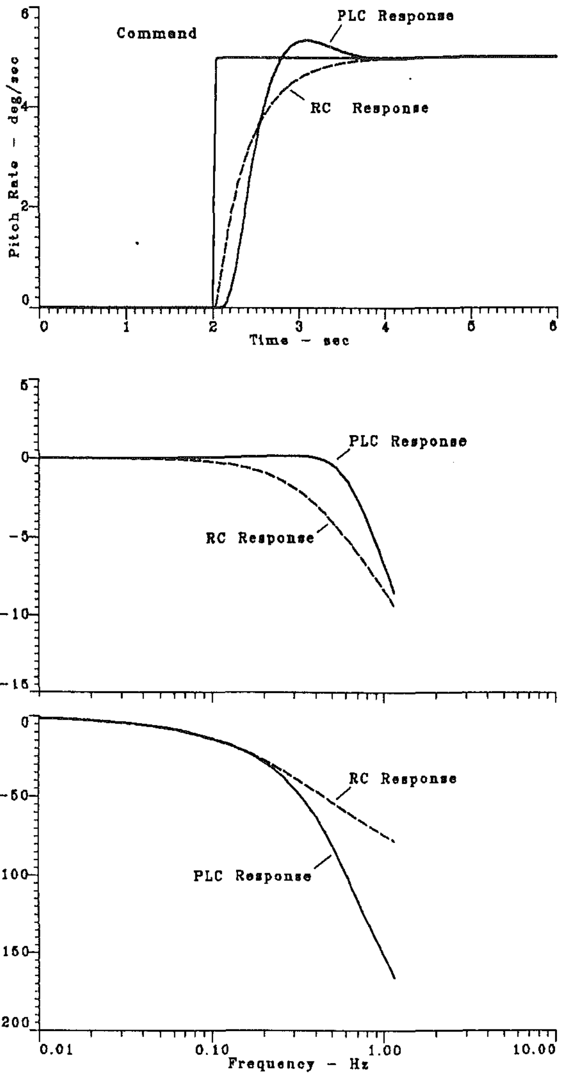

Fig. 14 Aircraft system response to pitch rate demand

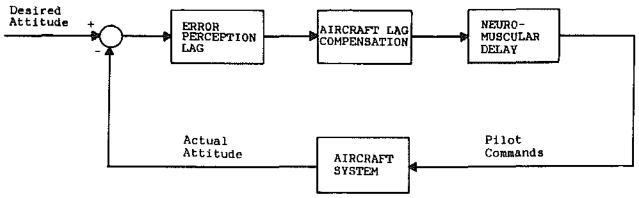

Fig. 15 Pilot maneuvering model

state decoupling of the propulsion system responses. The steady-state errors between the actual and commanded thrusts are caused by a coarse representation of the engine in the thrust conversion tables. Examples in the next section will demonstrate that these errors are not significant since the aircraft control loops are closed with the aircraft rate sensors. Bandwidth of the complete engine control and engine is on the order of 5 rad/s.

**Aircraft Control Laws.** The aircraft control laws illustrated in Fig. 13 are derived from a concept described by Roth et al. (1981). The original concept provided proportional control of aircraft pitch, roll, and yaw rate errors by commanding reaction control forces in parallel with aerodynamic surface deflections. In this study a third command path is added with a switch to select between reaction control and propulsive lift forces. Roll control (not shown in the figure) is identical to the pitch control. The gains are sized to achieve the same aircraft response as in the referenced work with either propulsive lift or reaction control. Note that propulsive lift control is faded out as the nozzles are vectored full aft. The digital control is simulated with a frame time of 0.01 s and a delay of 0.01 s as in the engine control. A 0.02 s communication bus delay is simulated between the aircraft and engine controls.

Figure 14 illustrates the response of the combined aircraft system to a step command in pitch rate. The response using propulsive lift control is somewhat slower than reaction control because of the engine match changes required. Piloted simulation examples in the next section demonstrate that the response is adequate, however. As expected, the roll rate response of propulsive lift and reaction control are equivalent (not shown) since no engine match changes are required. Bandwidth of the pitch and roll controls is on the order of 2.0 and 1.5 rad/s, respectively.

## Piloted System Performance

To demonstrate the capabilities of a piloted system, ex-

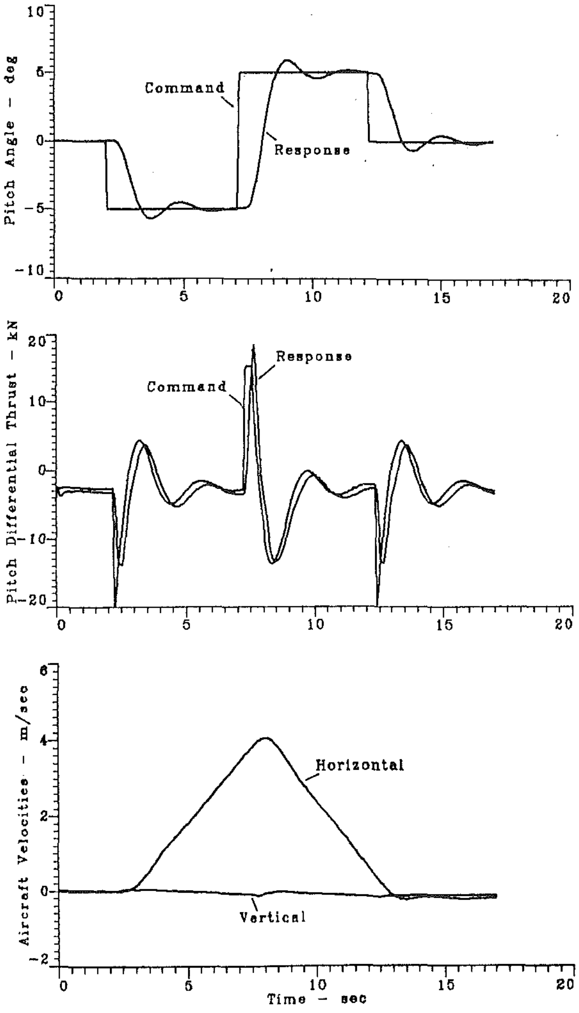

Fig. 16 Piloted pitch maneuver in hover

amples of a short take-off and vertical landing are discussed below. These are performed by predefining required thrust, attitude, and nozzle vector commands for a dynamic pilot maneuvering model to achieve the desired aircraft trajectories. The examples are selected to illustrate the basic system capabilities and do not necessarily represent optimum system performance.

**Pilot Maneuvering Model.** To evaluate the overall aircraft system performance properly requires a pilot in the loop. Short of developing a real time simulation for piloted evaluation, a pilot model may be employed to evaluate some of the effects of the pilot as part of the dynamic system. The pilot model employed here is based on a relatively simple approach described by Etkin (1972), which is consistent with more elaborate models recently developed (Zacharias and Brun, 1988; Thompson and McRuer, 1988). Figure 15 shows that in maneuvers the pilot model performs the reflexive task of maintaining a desired aircraft attitude. Represented in the model are error perception lag, compensation for the aircraft dynamics, and neuromuscular delay. The pilot model omits the thought processes that lead to the desired attitude; therefore, these must be input as predetermined functions of time to perform the desired maneuvers.

Figure 16 illustrates how the aircraft is maneuvered in hovering flight. In this example the nozzles are vectored full down and total thrust request is held constant. Starting from a static initial condition, the aircraft is first pitched nose down to accelerate forward and then nose up to arrest the forward motion. The responses to commands at the pilot and propulsion system levels are stable and the aircraft motions are stable and uncoupled.

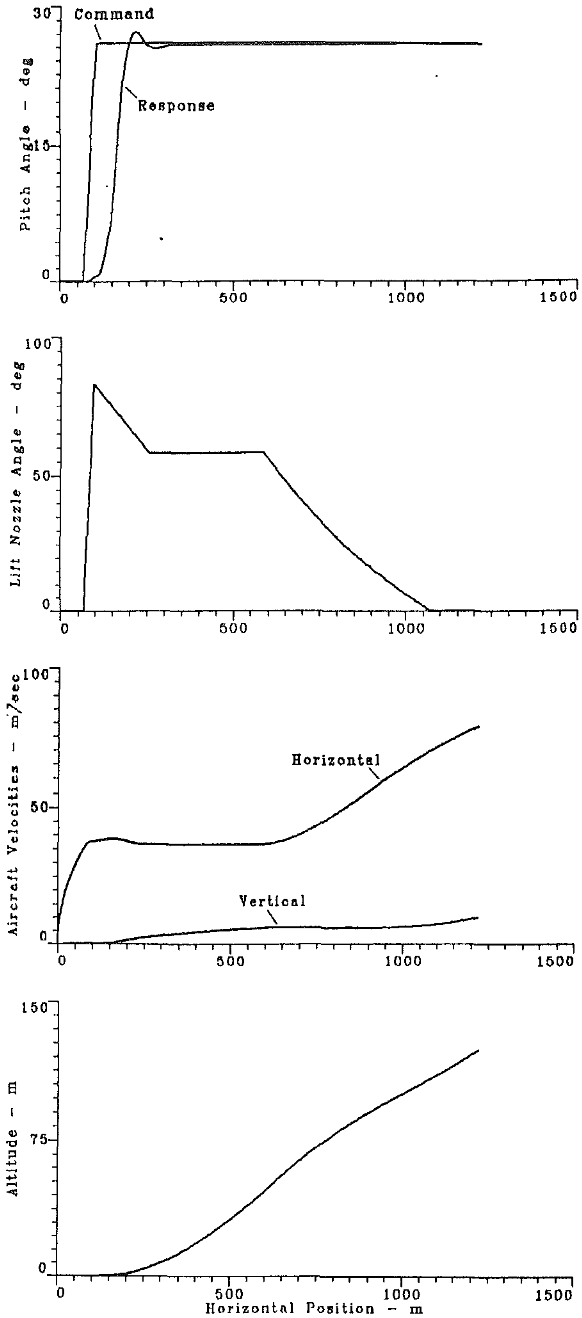

Fig. 17 Short take-off at 16,000 kg mass

## Short Take-Off

Figure 17 illustrates a short take-off at the normal take-off mass of 16,200 kg using a procedure described by Ward and Lewis (1987). Take-off roll begins with lift nozzles vectored full aft (0 deg). At rotation velocity the nozzles are vectored down 85 deg and the aircraft pitched to the take-off attitude with propulsive lift control. Maximum lift coefficient is 1.2 at lift off, amounting to less than 1/5 of the aircraft weight. After lifting off, the nozzles vector to 60 deg during the initial climb. Pitch attitude is maintained at a constant angle by propulsive lift control alone. As the aircraft approaches wing-borne velocity the lift nozzles vector fully aft.

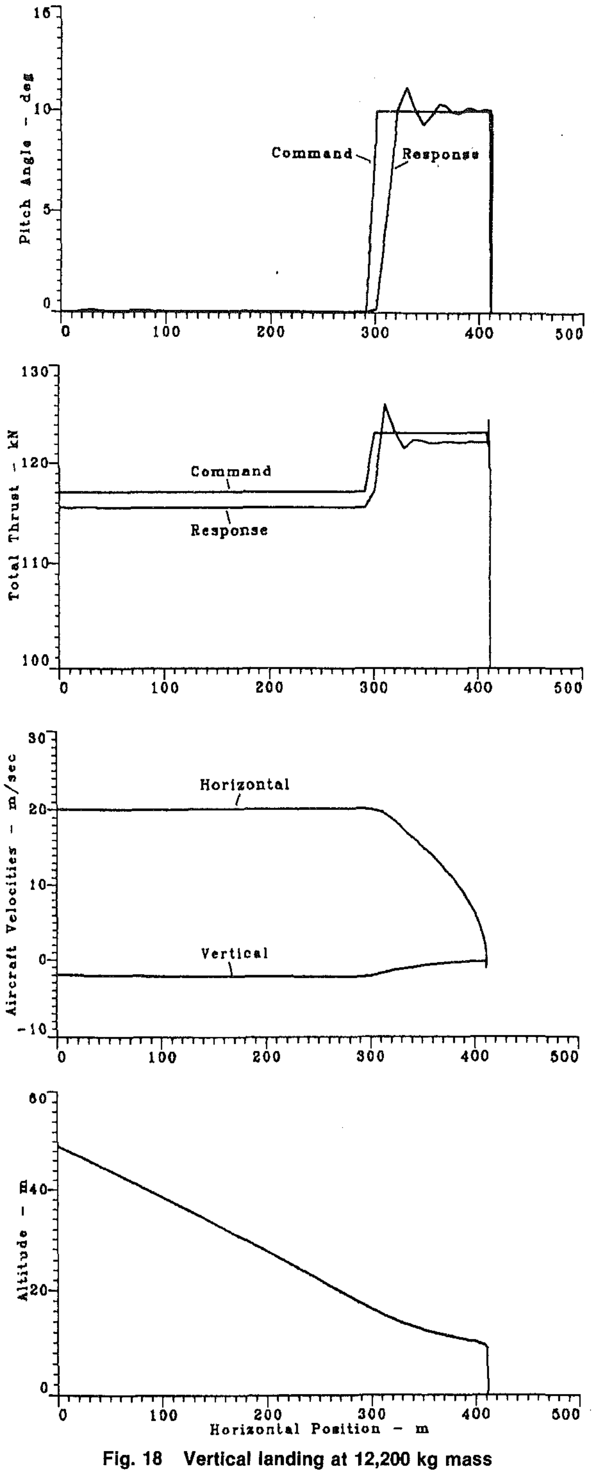

Fig. 18 Vertical landing at 12,200 kg mass

Total ground distance required to clear a 15-m obstacle is 350 m. Initial rate of climb at this distance is 5 m/s. During rotation, lift off, and initial climb under propulsive lift control, the pitch attitude is stable.

## Vertical Landing

The vertical landing illustrated in Fig. 18 employs attitude commands similar to those of the previous hover example to decelerate the aircraft from a stabilized approach to a soft, vertical touchdown. Overall the landing is not exciting, which is as it should be. The maneuver begins after the aircraft has transitioned from wingborne flight to a stabilized propulsive lift configuration with lift nozzles vectored down. As the aircraft descends past 15 m it is pitched nose up and thrust increased to arrest the forward velocity and rate of descent. When the forward movement has stopped, the pitch attitude is leveled and thrust reduced immediately before touchdown. Vertical velocity at touchdown is 0.3 m/s.

## Conclusion

This study has shown that providing STOVL aircraft attitude control with moments supplied from the propulsive lift nozzles instead of by reaction bleed jets can result in as much as a 10 percent increase in engine lift thrust rating or a corresponding increase in engine hot section life. It has also shown, using conventional control strategies and conservative system specifications, that propulsive lift control can provide adequate dynamic response and control power for these aircraft.

## References

Berg, D. F., Elliot, D. W., and Simmons, J. R., 1988, "Comparison Study of Supersonic STOVL Propulsion Systems," AIAA Paper No. AIAA-88-2808.

Etkin, B., 1972, *Dynamics of Atmospheric Flight*, Wiley, New York.

Fozard, J. W., 1978, *The Jet V/STOL Harrier*, AIAA Professional Study Series, British Aerospace Aircraft Group, Surrey, United Kingdom.

Kerr, W. B., Roth, S. P., Miller, R. J., and Creekmore, R. E., 1981, "V/STOL Propulsion Control Analysis—Phase II Final Report," NASA Contractor Report, NASA CR-165522.

Roth, S. P., Creekmore, R. E., and Walter, W. A., 1981, "V/STOL Propulsion Control Analysis—Phase I Final Report," NASA Contractor Report, NASA CR-165208.

Taylor, J. W., 1986, 1988, and 1989, *Jane's All the World's Aircraft*, Jane's Information Group Limited, United Kingdom.

Thompson, P. M., and McRuer, D. T., 1988, "Comparison of the Human Optimal Control and Crossover Models," AIAA Paper No. AIAA-88-4183-CP.

Ward, B. D., and Lewis, W. J., 1987, "Advantages of Thrust Vectoring for STOVL," AIAA Paper No. AIAA-87-1708.

Wilson, S. B., Kidwell, G. H., Turney, G. E., and Rogers, A., 1982, "Supersonic STOVL Research Aircraft," SAE Paper No. 821375.

Zacharias, G. L., and Brun, H. M., 1988, "OCM Based Parametric Learning Model," AIAA Paper No. AIAA-88-4184-CP.

**K. C. Amuedo**

**B. R. Williams**

**J. D. Flood**

McDonnell Aircraft Company,
McDonnell Douglas Corporation,
St. Louis, MO 63161

**A. L. Johns**

NASA Lewis Research Center,
Cleveland, OH 44135

# STOVL Hot Gas Ingestion Control Technology

*A comprehensive wind tunnel test program was conducted to evaluate control of Hot Gas Ingestion (HGI) on a 9.2 percent scale model of the McDonnell Aircraft Company model 279-3C advanced Short Takeoff and Vertical Landing (STOVL) configuration. The test was conducted in the NASA-Lewis Research Center 9 ft by 15 ft Low Speed Wind Tunnel during the summer of 1987. Initial tests defined baseline HGI levels as determined by engine face temperature rise and temperature distortion. Subsequent testing was conducted to evaluate HGI control parametrically using Lift Improvement Devices (LIDs), forward nozzle splay angle, a combination of LIDs and forward nozzle splay angle, and main inlet blocking. The results from this test program demonstrate that HGI can be effectively controlled and that HGI is not a barrier to STOVL aircraft development.*

## Introduction

Advanced supersonic STOVL aircraft are being designed for an Initial Operational Capability near the turn of the century. Supersonic STOVL aircraft development is driven by an increasing need for a versatile multirole fighter/attack aircraft, which can operate from damaged runways, austere remote sites, and small air-capable ships. Successful design of such an aircraft requires development of STOVL specific technologies. One of these key technologies is HGI. Hot gas ingestion occurs when hot engine exhaust gas recirculates to the engine inlet and is ingested. Reingestion increases engine airflow temperature, which can result in thrust loss, and engine face temperature distortion, which could produce engine stall.

Successful testing, analysis, and development of HGI control techniques requires a fundamental understanding of the HGI phenomena. This HGI phenomenon consists of two components:

- Near-field HGI—primary source
- Far-field HGI—secondary source

The near-field hot gas originates from exhaust jets, which impinge on the ground, are deflected outward and upward, and recirculate to the engine inlets. For multiple nozzle aircraft such as the McDonnell Aircraft Company Model 279-3C (Fig. 1) the individual exhaust jets spread radially along the ground and meet to form an upward-flowing fountain of highly turbulent hot gases (Fig. 2). This fountain is the primary source of HGI. Near-field HGI is characterized by a strong dependence on the aircraft height and exists only within ground effect. The near-field HGI flow field establishes itself nearly instantaneously.

The far-field HGI phenomenon occurs when the ground jet flow separates from the ground forward of the aircraft and recirculates back to the inlets, also shown in Fig. 2. Ground jet separation is caused by opposing headwind flow and thermal buoyancy. This recirculation is a secondary source of HGI. Far-field HGI is characterized by a strong dependence on headwind velocity and, to a lesser extent, aircraft height. Above a certain height, separated hot gases will pass under the inlet and far-field HGI will not occur. The far-field flow pattern requires time to become established. The length of time depends on headwind velocity and ground flow dynamic pressure decay. Therefore, the magnitude of far-field HGI depends on aircraft vertical landing dynamics and headwind strength.

With this understanding of HGI phenomena, and the critical need to develop HGI control techniques for STOVL aircraft, the following test program objectives were established:

- Define the baseline Model 279-3C HGI characteristics: inlet temperature rise and inlet temperature distortion.
- Investigate configuration variables and LIDs to control and reduce HGI.
- Validate the NASA-Lewis Hot Gas Ingestion Test Facility and test procedures.
- Develop temperature scaling laws to predict full-scale inlet temperature rise and distortion from subscale HGI test results.

This paper addresses the first three objectives. The test approach, model design, test facilities, and instrumentation used to meet these objectives are presented, followed by a discussion of the test results. A more detailed review of the test program and results obtained is presented by Strock et al. (1988).

## Test Approach

Hot gas ingestion is of primary concern during aircraft transition to hover and vertical landing as the aircraft descends into ground effects. The test approach developed to investigate HGI control techniques during these modes of operation was to:

---

Contributed by the International Gas Turbine Institute and presented at the 34th International Gas Turbine and Aeroengine Congress and Exhibition, Toronto, Ontario, Canada, June 4–8, 1989. Manuscript received at ASME Headquarters February 23, 1989. Paper No. 89-GT-323.

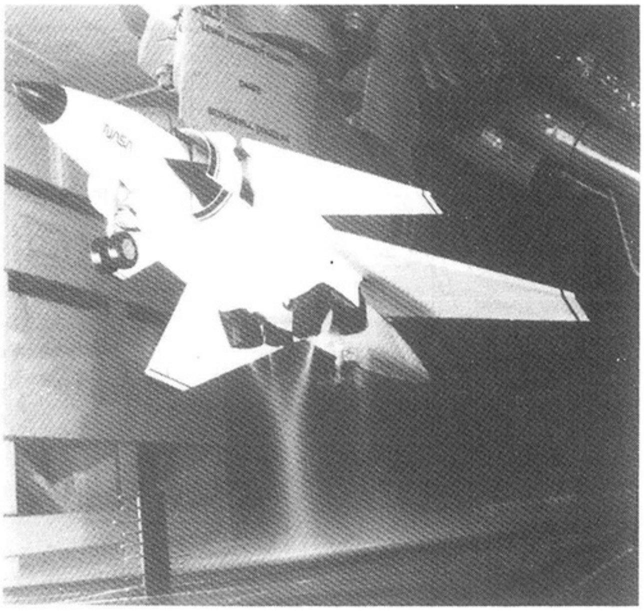

Fig. 1 MCAIR 279-3C advanced STOVL hot gas ingestion model

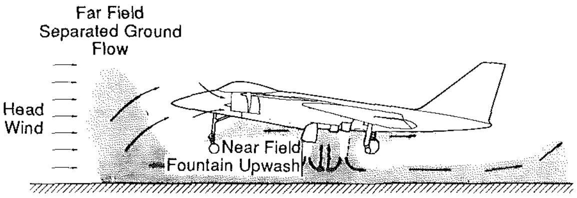

Fig. 2 Hot gas ingestion sources

- Establish baseline HGI levels for the clean (no LIDS) aircraft configuration.
- Conduct comparative LIDs testing to determine the preferred LIDs configuration.
- Conduct parametric tests with the preferred LIDs to optimize its configuration for minimum HGI.

The determination of HGI levels during transition to hover and vertical landing required the control of several configuration, environmental, and operational variables during testing. Fourteen such variables were controlled during the test program. This paper limits discussions to the four variables that had the most influence on HGI levels:

- Height above the ground
- Headwind velocity
- Forward nozzle splay angle
- Main inlet blockage

A matrix of the aircraft configurations and variables tested is provided in Fig. 3.

STOVL aircraft landing procedures consist of transition from conventional flight to a hover over the landing site. Hover occurs at approximately 100 feet, well out of ground effects, and is free of any HGI. As the aircraft descends to a vertical landing, the exhaust jets will interact with the landing surface. This interaction results in the formation of a fountain and ground flow field, which interact with the aircraft flowfield. The strengths of these interactions, and consequently the magnitude of HGI, are strongly dependent on the aircraft height above the ground. The model height was controlled during the test and is defined as shown in Fig. 4. Measurements were made at the model heights shown in the test matrix of Fig. 3 to determine HGI levels in simulated vertical landings and vertical takeoffs.

| | Aircraft Configuration | | |
|---|---|---|---|
| Variable | Clean | LIDs Comparison | Preferred LIDs |
| • Main Landing Gear Height Model Scale (in.) | -0.2, 0.1, 0.2, 0.4, 0.6, 0.8, 1.2, 1.3, 2.2, 2.3, 4.7, 7.9, 10.8 | 0.4 | -0.2, 0.1, 0.2, 0.4, 1.2, 1.3,2.2, 2.3, 4.7 |
| • Headwind (kts) | 5, 10, 16, 24, 30, 40, 50, 60, 70, 80, 90 | 5, 10, 16, 24 | 5, 10, 16, 24, 30, 40, 50, 60, 70, 80, 85, 90 |
| • Forward Nozzle Splay Angle (deg) | -12, -6, 0, 6, 12, 18 | -6 | -6, 0, 6, 12, 18 |
| • Inlet | Main + Auxiliary<br>Main Inlet Blocked | Main + Auxiliary | Main + Auxiliary |

Fig. 3 Test matrix

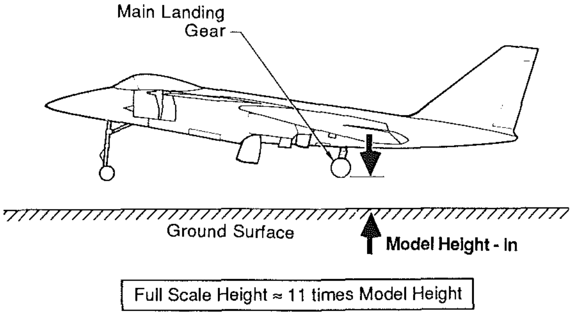

Fig. 4 Model height definition

Headwind velocity, in combination with aircraft height, determines the magnitude and influence of far-field HGI. Although headwind velocity is not controllable in actual operation, its effect on HGI was evaluated to identify potential problems. A range of headwind velocities based on facility control capabilities were tested, as shown in Fig. 3, to assess HGI from simulated transition velocities through hover.

Nozzle splay angle is the relative inboard or outboard orientation angle between the jet exhaust exit plane and the aircraft vertical centerline (butt line 0.0), as illustrated in Fig. 5. The splay angle of the forward nozzles (i.e., forward nozzle splay angle) has a significant influence on the aircraft height at which the fountain forms and the strength of the fountain. The forward nozzle splay angles tested are shown in Fig. 3.

Main inlet blocking was tested to determine if the near-field HGI could be reduced by supplying engine air through auxiliary inlets positioned away from the central fountain flow. On the Model 279-3C, the main inlets are located low and close to the fuselage center, which is a strong fountain flow region. The auxiliary inlets, incorporated for high inlet recovery at low speeds, are located on the inlet nacelles well outboard and above the main inlet away from the fountain.

## Model Design

Accurate HGI test results require that the model accurately simulate the aircraft configurations, jet exhaust, inlet flow field, and aircraft contours. To ensure accurate flow field simulations, the model was equipped with flowing nozzles for jet exhaust simulations and an inlet system that used suction to simulate an operating engine. The nozzles could operate at the design full-scale nozzle pressure ratio (~3.0) and up to nozzle pressure ratios of 5.0 for investigation of alternate engine concepts. Nozzle and model materials were selected for a planned operating gas temperature of 1000°F. Nozzle and inlet internal surfaces, as well as the entire forward fuselage and model undersurface, were fully contoured. The tested model design is shown in Fig. 6.

The nozzles were calibrated for thrust, thrust angle, and mass flow rate. During the HGI test, the nozzle thrusts were

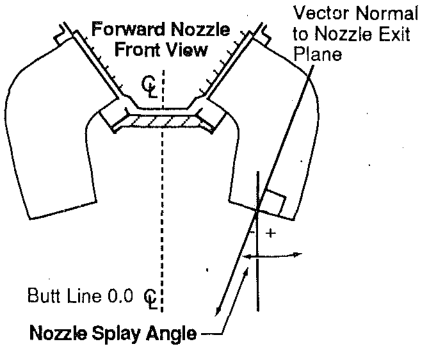

Fig. 5 Nozzle splay angle

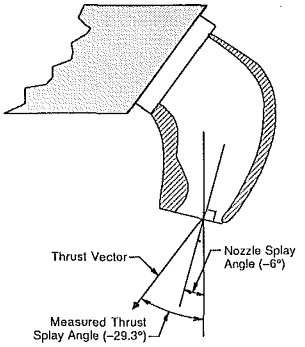

| | Nozzle Splay Angle (deg) | Measured Thrust Splay Angle (deg) | Nozzle Exit Spacing (in.) |
|---|---|---|---|
| | Forward Nozzles | | |
| | −12 | −35.3 | 3.66 |
| Baseline | −6 | −29.3 | 4.45 |
| | 0 | −23.3 | 5.23 |
| | 6 | −17.2 | 7.64 |
| | 12 | −11.0 | 8.39 |
| | 18 | −4.7 | 9.11 |
| | Aft Nozzles | | |
| Baseline | +5.4 | −6.9 | 6.72 |

Fig. 7 Nozzle calibration results

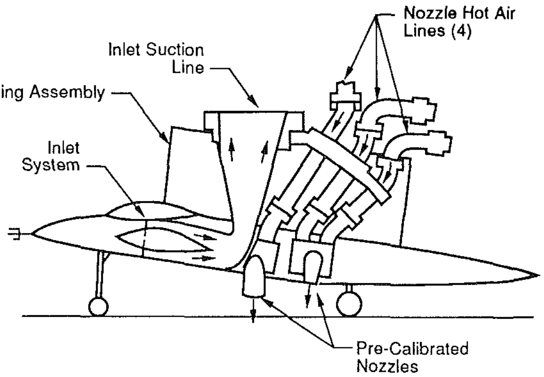

Fig. 6 Hot gas ingestion model

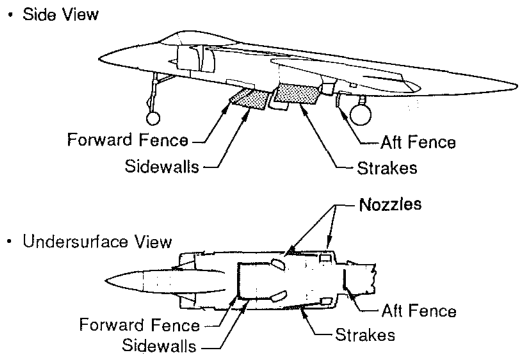

Fig. 8 Lift improvement devices

set using the thrust calibration data to obtain an accurately simulated jet exhaust flow field. The calibration tests on the forward nozzles found that the thrust vector was not normal to the nozzle exit plane, as expected, but was splayed an additional 23 deg inboard (Fig. 7). This angularity was caused by the nozzle internal geometry and would have also occurred on the full-scale nozzle since the model incorporated full-scale nozzle internal geometries. This additional splay significantly affects the strength of the fountain and consequently the near-field HGI. A significant error in the data base for future HGI predictions would have occurred if this additional splay had not been discovered during nozzle calibration. It is therefore essential for accurate HGI results that pretest calibrations be conducted on all lift nozzles.

The forward nozzle splay angle was manually adjustable from −12 deg to +18 deg in 6 deg increments by inserting wedge plates between the nozzles and their supply plenums. This also changed the forward nozzle exit plane spacing. A complete tabulation of nozzle splay angle, nozzle exit plane spacing, and nozzle thrust splay angle is given in Fig. 7.

Lift improvement devices could be installed on the model for evaluation of their effectiveness in reducing HGI. The LID system is composed of six doors (i.e., a forward fence, two sidewalls, two strakes, and an aft fence), which form a rectangular box on the aircraft undersurface (Fig. 8). On an operational aircraft, the LIDs are extended during vertical landing and retracted during conventional flight.

The LIDs perform two main functions: (1) vertical lift improvement, and (2) HGI reduction, as demonstrated on the currently operational AV-8B Harrier VSTOL aircraft. These benefits result from the LIDS capturing the fountain upwash and redirecting it away from the aircraft. Improved lift performance is obtained from the upward force, which is created by reversing the fountain upwash momentum. Hot gas ingestion is reduced because the LIDs prevent the fountain upwash from flowing along the undersurface to the inlet.

Eight LID configurations were tested on the model (Fig. 9).

| Configuration Number | Depth | Configuration | | | |
|---|---|---|---|---|---|
| | | Forward Fence | Sidewalls | Strakes | Aft Fence |
| 1 | Short (12 in.)* | X | | | |
| 2 | ↓ | X | X | | |
| 3 | ↓ | X | X | X | |
| 4 | ↓ | X | X | X | X |
| 5 | Normal (18 in.)* | X | X | | |
| 6 | ↓ | X | X | X | |
| 7 | ↓ | X | X | X | X |
| 8 | Extended (34 in.)* | X | X | X | X |

*Full scale

Fig. 9 Comparative LID configurations

The LIDs were designed so that components (i.e., forward fence, sidewalls, strakes, aft fence) could be added to build up the LIDs and allow a comparative evaluation of different configurations. Additionally, each component was available in three different depths: 12, 18, and 34 inches full scale. Previous tests have shown that increased LID depth improves vertical lift as the result of higher fountain capture levels. It was expected that these higher fountain capture levels would also reduce HGI.

## Facility Description

Testing was conducted in the NASA-Lewis 9 ft by 15 ft Low Speed Wind Tunnel. The HGI test facility is located in the return leg of the 8 ft by 6 ft Supersonic Wind Tunnel. The HGI test model is shown installed in the tunnel in Fig. 10. A detailed description of the tunnel modifications necessary for HGI testing is documented by Johns et al. (1988).

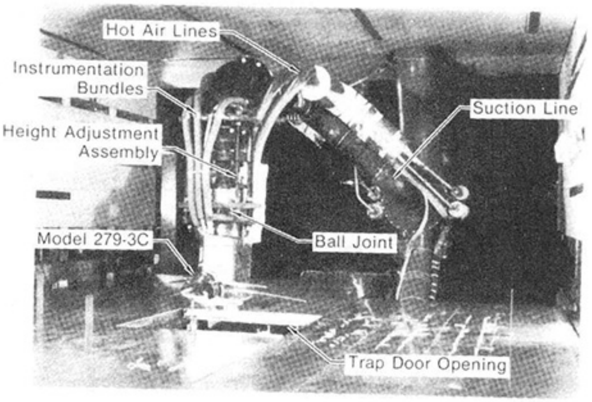

Fig. 10 Hot gas ingestion model and support system in NASA Lewis 9×15 ft. Low Speed Wind Tunnel

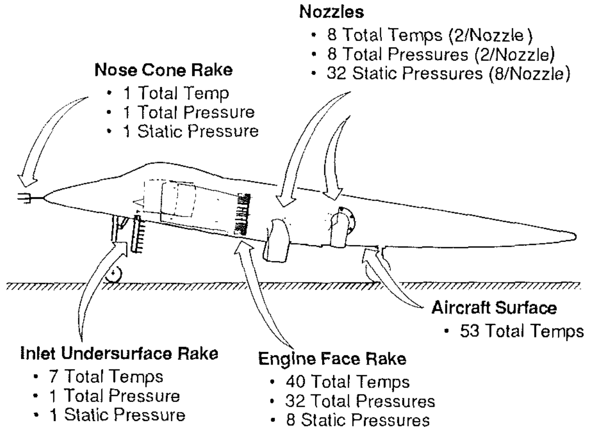

Fig. 11 Model instrumentation

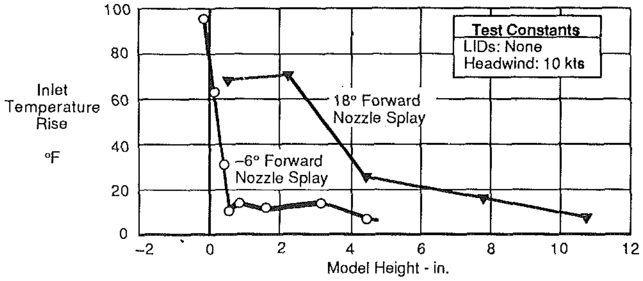

Fig. 12 Height effect on inlet temperature rise

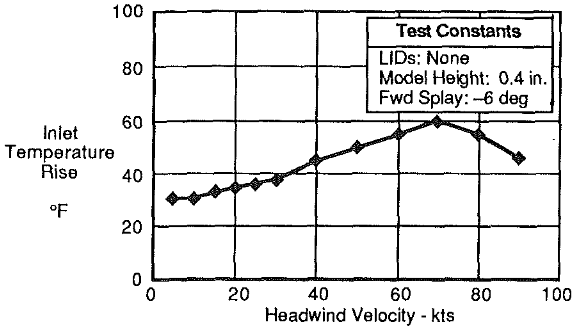

Fig. 13 Headwind effect on inlet temperature rise

The HGI test facility contains a model support system, which was manually adjustable to provide variation in model height and attitude. A hot air supply system provided the nozzles with air at temperatures between ambient and 500°F. The majority of the test was conducted at the maximum of 500°F compared to a full-scale nozzle temperature of 1755°F. Temperature scaling laws were used to project the measured HGI levels to full-scale temperature levels as detailed by Strock et al. (1988). A suction line was attached to the model for simulating engine airflow.

An instrumented, elevated ground plane was installed in the test section to measure the ground flow temperatures and pressures. A trap door scavenging system was installed in the ground plane below the model to capture nozzle exhaust. The door was open while setting and stabilizing test conditions. The door was rapidly closed to establish the flowfield for test point recording. A sidewall scavenging system was also incorporated to prevent hot ground flow from recirculating and spuriously heating the test section.

The data acquisition and monitoring system was automated using the facility computer system. All testing was monitored and controlled from the central wind tunnel control room.

## Instrumentation

Both the model and facility were heavily instrumented to define accurate test conditions. The model contained 193 measurands for defining pressures and temperatures as shown in Fig. 11. Measurements included an engine face rake containing 40 total temperature probes, 32 total pressure probes, and 8 static pressure taps. These measurements provided the primary data for assessing HGI. The remaining instrumentation was used to set individual nozzle temperatures and flow conditions for accurate flow field simulation and for monitoring model surface air temperatures to determine the potential for aircraft structural heating.

The facility instrumentation consisted of temperature and pressure probes for monitoring test section heating and flow characteristics. A propeller anemometer measured test section headwind velocity over the full range tested (5-90 knots).

Tunnel reference temperature, against which all temperature rises were computed, was measured immediately upstream of the tunnel test section. Two thermocouples, one on each side of the tunnel, were averaged to provide a reference free-stream temperature. A detailed discussion of the model and tunnel instrumentation is provided by Strock et al. (1988).

## Test Results

The test results are presented in a sequence that parallels the overall test approach:

- Clean model results
- LID comparison results
- Preferred LID results

The clean model (no LIDs) was tested first to determine the baseline HGI levels. Next, LID comparison tests were conducted on eight different LID configurations and a preferred configuration was selected on the basis of reduction in HGI, vertical lift improvement, and integration with the aircraft. Finally, parametric tests were conducted on the preferred LID configuration to further define and optimize the configuration for minimum HGI.

**Clean Model Test Results.** The clean model was tested to obtain baseline data for comparison against the LID configurations. The key test variables for this baseline testing were aircraft height, headwind, and forward nozzle splay angle. In addition to the baseline testing, the effect of blocking the main inlets with engine airflow supplied by only the auxiliary inlets was investigated.

*Height Effect.* The inlet temperature rise as a function of model height above the ground for two forward nozzle splay

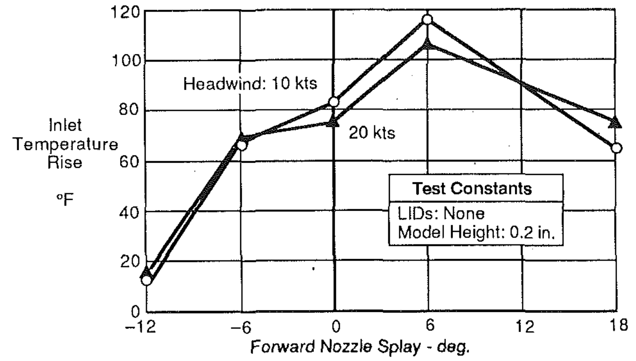

**Fig. 14 Forward nozzle splay effect on inlet temperature rise**

| Model Configuration | Inlet Temperature Rise (°F) | |
|---|---|---|
| | 10 kts | 20 kts |
| Clean | 30 | 34 |
| Short Lift Improvement Devices (12in) | | |
| Forward Fence | 15 | 15 |
| Above + Sidewalls | 13 | 12 |
| Above + Longitudinal Stakes | 11 | 13 |
| Above + Aft Fence | 12 | 13 |
| Normal Lift Improvement Devices (18in) | | |
| Forward Fence + Sidewalls | 11 | 12 |
| Above + Longitudinal Strakes | 10 | 12 |
| Above + Aft Fence | 11 | 12 |
| Extended Lift Improvement Devices (34 in) | | |
| Full Set | 9 | 12 |

- -6 Deg Forward Nozzle Splay Configuration
- 0.4 in. Model Main Gear Height

**Fig. 15 Comparative lift improvement device configuration test result summary**

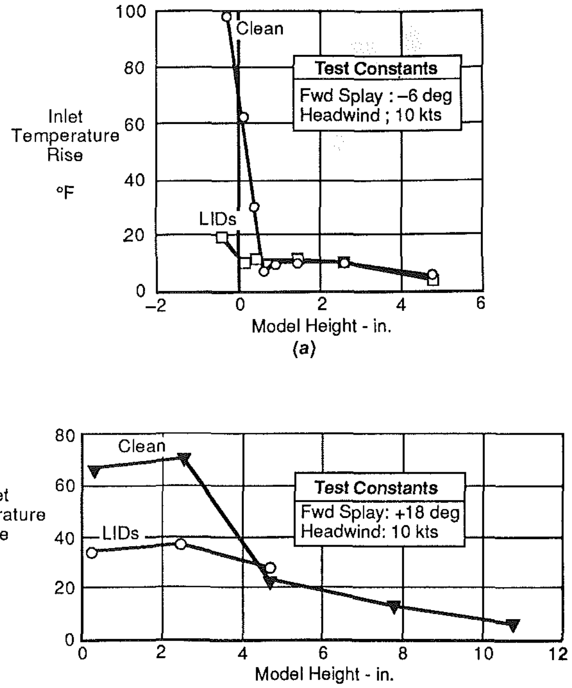

**Fig. 16 Effect of LID as function of height**

angles, − 6 deg (baseline) and 18 deg, is shown in Fig. 12. As model height decreases into ground effect the initial change of inlet temperature rise is small due to changes only in far-field HGI. With further descent, the model eventually reaches the height at which the fountain forms and near-field HGI begins. The inlet temperature rise increases rapidly below this height because the fountain upwash is a strong source of HGI. The fountain formation point (transition to "in ground effect") is indicated as a distinct change in slope of the inlet temperature rise curve. This slope change is seen in the −6 deg forward nozzle splay data at 0.6 in. model height, and in the 18 deg splay data at 4.7 in. model height. The formation height and magnitude of the near-field HGI can therefore be altered through changes in forward nozzle splay angle. Knowledge of such HGI changes with height are essential for accurate prediction of STOVL aircraft vertical landing performance.

*Headwind Effect.* The effect of headwind on the baseline HGI levels at low model height is shown in Fig. 13. From 5 to 70 knots headwind, the inlet temperature rise increases because the headwind moves the ground flow separation point closer to the model and the far-field HGI mixes less with ambient air. At 70 knots, the inlet temperature rise reaches a maximum because the ground flow separation point is coincident with the inlet and minimal mixing occurs prior to ingestion. Further increases in headwind decrease the inlet temperature rise because the separation point moves behind the inlet. Headwind velocity therefore affects HGI levels by changing the ground flow separation point, and the far-field cloud mixing characteristics and height. The results show that headwind effects increase the inlet temperature rise at low aircraft heights for the baseline range of headwinds (5-25 knots) and therefore, should be included in all STOVL aircaft HGI assessments.

*Forward Nozzle Splay Effect.* The effect of forward nozzle splay is shown in Fig. 14. At −12 deg forward nozzle splay, the inlet temperature rise is low because the jets converge before hitting the ground and no fountain forms; hence, far-field HGI is the dominant factor. At the baseline −6 deg forward nozzle splay, the fountain forms, resulting in a strong influence of near-field HGI as indicated by a significant inlet temperature rise. As the forward nozzle splay was increased to 0 deg and then to 6 deg, additional inlet temperature rise occurred. This was the result of a combination of increased fountain upwash strength and the increased spacing between the forward nozzle exits. Increased forward nozzle exit spacing allows proportionally larger amounts of the total fountain upwash to travel forward along the fuselage undersurface to the inlet. This trend of increasing inlet temperature rise reversed when the forward nozzle splay angle was further increased to 18 deg and was caused by a decrease in the fountain upwash strength.

Forward nozzle splay angle is a powerful tool for controlling HGI. It establishes the formation height and strength characteristics of the fountain upwash that have a direct influence on near field HGI. Optimization of the forward nozzle splay angle can provide significant performance improvements for a STOVL aircraft operating in ground effect.

*Main Inlet Blocking.* The effect of blocking the main inlet in hover with only the auxiliary inlets open was investigated. The effect was significant: inlet temperature rise dropped approximately 50 percent, from 63°F to 31°F, at the conditions tested (0.2 in. model height, $-6°$ forward nozzle splay, 10 knots headwind). This resulted from the auxiliary inlets being better positioned than the main inlets for near-field HGI avoidance. The fountain upwash is concentrated along the centerline of fuselage undersurface, and since the main inlets are mounted low and close to the centerline, they ingested the upwash easily. The auxiliary inlets were located on the inlet nacelles outboard and above the main inlets, which provided better isolation from the fountain upwash. It is expected that even larger HGI reductions could be realized by positioning the auxiliary inlets further from the fountain upwash, for example, on top of the aircraft.

Main inlet blocking is a promising HGI control technique that should be considered for advanced STOVL aircraft. The demonstrated effectiveness of an inlet blocking system may very well offset the blocking system weight and complexity. An inlet blocking system would provide the additional benefit of a reduction in engine foreign object damage due to the ingestion of debris generated by plume interaction with the ground.

**Comprative Lift Improvement Device Test Results.** Comparative LID testing was conducted to select a "preferred" configuration. The testing was conducted with the baseline −6 deg forward nozzle splay angle and at a model main gear height of 0.4 in. for headwinds of 10 and 20 knots. Three sizes of LIDs were tested: short, normal, and extended. The normal size LIDSs, 18 in. full scale, represent the baseline aircraft design configuration. The short and extended sizes are simply a contraction and extension of this baseline. Slight reductions in inlet temperature rise were observed as the LIDs size increased as summarized in Fig. 15. Additional testing for the short and normal sizes was accomplished at progressive stages of buildup to evaluate the relative reduction in inlet temperature rise due to the different LID components. The results (Fig. 15) indicate the forward fence alone provides a very significant inlet temperature rise reduction. It does so by redirecting the fountain flow along the undersurface into the ground flow field. The addition of forward fence sidewalls prevents heated air spillage around the forward fence and provides a further, although less substantial, reduction in inlet temperature rise. Further addition of longitudinal strakes also reduces the inlet temperature rise slightly, whereas the addition of an aft fence increases inlet temperature rise.

The selection of a preferred LIDs configuration must take into consideration not only HGI, but jet-induced lift, and airframe integration. Since jet-induced lift testing was not conducted for the LID configurations, a preliminary selection was made based on MCAIR V/STOL experience. This experience indicated that incorporation of a forward fence and longitudinal strakes would provide acceptable jet-induced lift and that the addition of an aft fence would provide little benefit. Also increased LID depth would increase jet-induced lift. With respect to airframe integration, the largest feasible LIDs were the normal sized configuration. Finally, considering the HGI data (Fig. 15) together with the jet-induced lift and airframe integration, the normal sized LIDs with a forward fence, sidewalls, and longitudinal strakes were selected as the preferred configuration.

**Preferred Lift Improvement Device Test Results.** With selection of a preferred LIDs configuration, full parametric testing was conducted to determine the effect of height, headwind, and forward nozzle splay angle. Testing was also conducted to determine combined effects of the preferred LIDs and nozzle splay angle on inlet temperature distortion as compared to the clean configuration. Main inlet blocking tests were not conducted because of test time constraints.

*Height Effect.* Inlet temperature rise as a function of height for both the clean and preferred LIDs configuration is shown in Fig. 16(*a*) for a forward nozzle splay angle of −6 deg. The LIDs capture the fountain upwash and redirect it downward away from the inlets. This results in substantial decreases in HGI for heights where a fountain has formed (below 0.6 in. for −6 deg splay). LIDs also have a positive effect when the foward nozzle splay is 18 deg (Fig. 16*b*). As before, there is a significant reduction in HGI over the heights where there is a fountain upwash (below 4.7 in). The LIDs are less effective for reducing HGI with this nozzle splay because the impact area of the fountain on the fuselage undersurface extends beyond the perimeter of the LIDs and the fountain is not captured as well as with −6 deg nozzle splay.

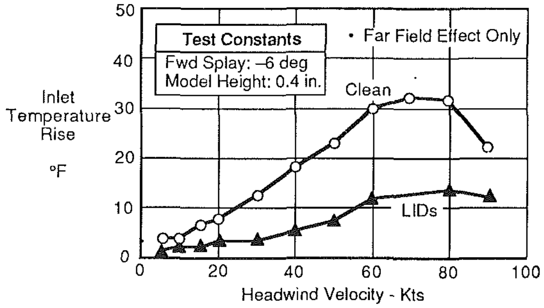

**Fig. 17 Effect of LIDs as function of headwind velocity**

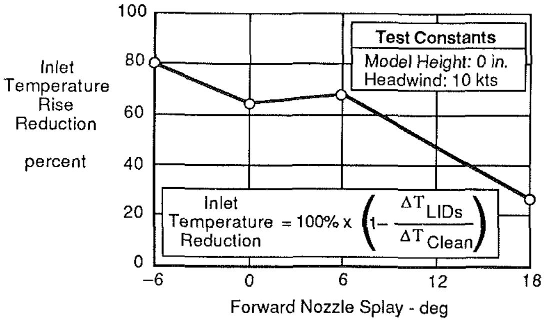

**Fig. 18 LID inlet temperature rise effectiveness as function of forward nozzle splay angle**

*Headwind Effect.* The effect of LIDs on inlet temperature rise with variations in headwind is shown in Fig. 17. Only the far-field HGI component of inlet temperature rise is shown. The far-field component is calculated from the total inlet temperature rise by subtracting the rise associated with the near-field HGI. The near-field inlet temperature rise is generally constant with headwind for fixed height and can be determined by extrapolating the total inlet temperature rise to the zero headwind condition where there is no far-field HGI. Inlet temperature rises obtained with LIDs as a function of headwind have a lower maximum far-field inlet temperature rise, which occurs at a higher headwind velocity, compared to the clean configuration. This results from the downwash flow off the LID forward fence, merging with and strengthening the ground jet flow in front of the aircraft. This pushes the far-field separation point away from the aircraft so the far field inlet temperature rise decreases. This is a significant result since the LIDs were previously believed to control only the near-field HGI.

*Forward Nozzle Splay Effect.* The LID effectiveness in reducing inlet temperature rise is strongly dependent on forward nozzle splay (Fig. 18). The LID inlet temperature rise effectiveness is defined as the percent reduction of the clean configuration inlet temperature rise that occurs when LIDs are installed. The maximum inlet temperature rise effectiveness obtained was a significant 80 percent at a forward nozzle splay of −6 deg. The inlet temperature rise effectiveness of the LIDs generally decreases with increased forward nozzle splay. This is caused by changes in the fountain upwash that occur with increased nozzle splay and spacing. As splay and spacing increase, the fountain impact area on the fuselage becomes larger and the fountain is not captured as well by the LIDs.

*Inlet Temperature Distortion.* The main source of inlet temperature distortion in ground effect is the near-field HGI. In the clean configuration, ingestion of near-field HGI causes

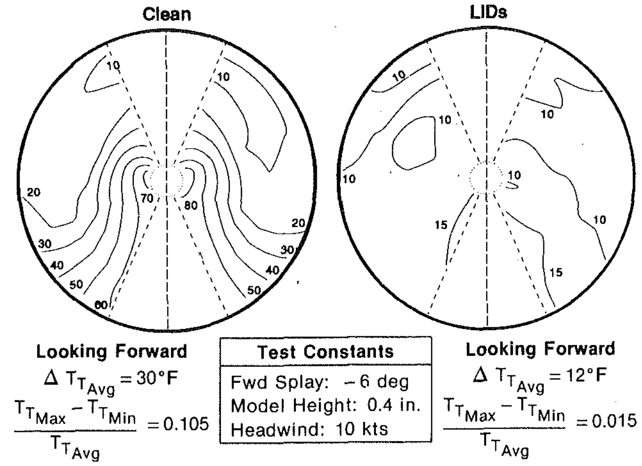

**Fig. 19 Engine face temperature rise contour plots**

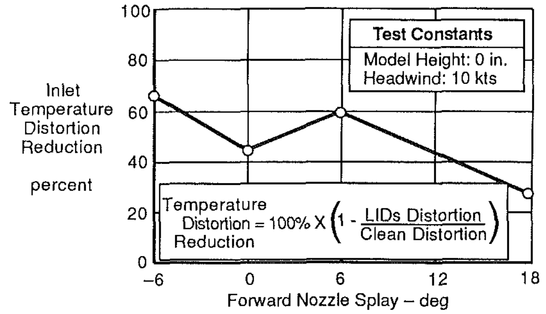

**Fig. 20 LIDs inlet temperature distortion effectiveness as function of forward nozzle splay angle**

inlet temperature distortion in the form of a localized high temperature region at the bottom of the engine face (left side of Fig. 19).

LIDs were found to be very effective in reducing inlet temperature distortion. They minimize near-field HGI by inhibiting the forward movement of the upwash along the fuselage. When LIDs were added, the temperature distortion at the engine face was significantly reduced (right side of Fig. 19), due to elimination of near-field HGI. This causes the far-field HGI to dominate and since it is better mixed with the ambient air, engine face temperature distortion is essentially eliminated.

The effectiveness of the LIDs in reducing inlet temperature distortion also depends on the forward nozzle splay (Fig. 20). The LID inlet temperature distortion effectiveness is defined as the percent reduction from the clean configuration inlet temperature distortion that occurs when LIDs are installed. A significant LIDs temperature distortion effectiveness of 66 percent was obtained at a forward nozzle splay of −6 deg. As forward nozzle splay and spacing increase, the LID temperature distortion effectiveness generally decreases. The mechanism reducing the effectiveness is an enlargement of the area on the undersurface where the fountain upwash impinges and the progressive inability of the LID to capture the total upwash. The fountain upwash is the primary source of temperature distortion, and as the LIDs capture less upwash, they become less effective at reducing this distortion. This parallels the previously discussed decrease of LID inlet temperature rise effectiveness with increased forward nozzle splay.

## Conclusions

The basic objectives of this program, to develop and demonstrate STOVL HGI control techniques, were successfully met. Significant reductions in HGI were obtained through the combined use of LIDs and forward nozzle splay angle. The documented improvements over the clean baseline configuration were:

- 80 percent reduction in inlet temperature rise
- 66 percent reduction in inlet temperature distortion

The test program also produced an extensive data base for increased understanding of HGI phenomena. The data will be used to improve HGI empirical prediction techniques for screening future STOVL aircraft concepts during preliminary design.

The NASA Lewis HGI test facility was validated as an excellent facility for accurately testing STOVL HGI. This validation established NASA Lewis as a national facility for STOVL HGI testing. Model design criteria and HGI test techniques were also derived from this program for application to future HGI programs.

In summary, we believe that this test program demonstrated that with proper design, HGI can be eliminated as a barrier to development of an operational STOVL aircraft.

## References

Johns, A. L., Flood, J. D., Strock, T. W., and Amuedo, K. C., 1988, "Hot Gas Ingestion Testing of an Advanced STOVL Concept in the NASA Lewis 9 by 15 foot Low Speed Wind Tunnel With Flow Visualization," Paper No. AIAA-88-3025.

Strock, T. W., Amuedo, K. C., and Flood, J. D., 1988, "Hot Gas Ingestion Test Results of a Four-Poster Vectored Thrust STOVL Concept," NASA CR-182115 (Limited Distribution).

# Introduction to the Basic Technology of Stealth Aircraft: Part I—Basic Considerations and Aircraft Self-Emitted Signals (Passive Considerations)

**D. Howe**
Professor of Aircraft Design and
Head of College of Aeronautics,
Cranfield Institute of Technology,
Bedford, United Kingdom

*This paper reviews information that may be used by a potential enemy to detect and track an aircraft. In particular it is concerned with a passive approach by the enemy, namely the interception of acoustic, infrared, visual, and miscellaneous self-emissions. The origins of these emissions are described and means of eliminating them or reducing their intensity are discussed. Emphasis is placed on the impact of these so-called stealth techniques on the design of the aircraft as a whole.*

## 1 Introduction

From time immemorial it has been an accepted military tactic for an attacker to do his utmost to conceal his presence from his enemy. The native hunter who approaches his victim from the noiseless and odorless upwind shadow zone is but one example of this. The application of so-called "stealth" technology to modern aerospace design is simply an up-to-date application of the age old principle. The aim of stealth is essentially to reduce the probability of the aircraft being detected by the enemy, and thereby have a greater potential for the successful completion of its mission without loss. Of course the stealth concept is but one facet of the total approach to ensure the success and survivability of an aircraft. Other aspects include such matters as passive warning devices and design for reduced vulnerability.

Although some aspects of stealth technology have always been employed on military aircraft, they have been traditionally regarded as being secondary issues to be adopted providing there was no undue impact upon the basic design. In comparison with this the interest in stealth techniques of the past two or so decades has been directed toward the tailoring of the whole aircraft to minimize the probability of its detection. Since many stealth considerations are clearly associated with the external shape of the aircraft, this more recent approach has a profound effect upon the overall configuration as well as internal layout.

While not specifically part of stealth design, the survivability of an aircraft can be increased by equipping it with devices that give the crew warning of detection by the various means used by the enemy, such as radar, thermal, laser, or visual illumination.

A selected bibliography is included at the end of the text.

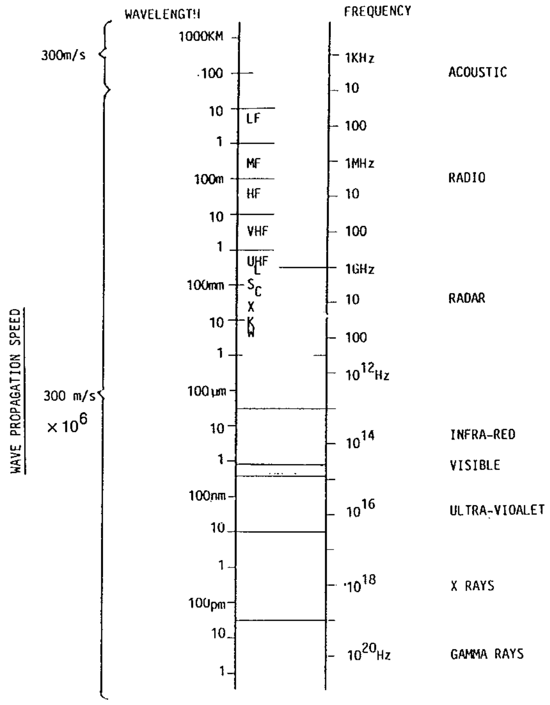

Fig. 1 Electromagnetic spectrum

## 2 The Radiation Spectrum – Aircraft Signals

The nature of the electromagnetic radiation spectrum is shown in Fig. 1. For completeness the audible range is included, although acoustic emissions are not electromagnetic. In terms of frequency it starts with the low-frequency audible signals, through the radio wave spectrum, and on through the very high frequency band around visual wavelengths to the

---

Contributed by the International Gas Turbine Institute and presented at the 35th International Gas Turbine and Aeroengine Congress and Exposition, Brussels, Belgium, June 11-14, 1990. Manuscript received by the International Gas Turbine Institute February 1, 1990. Paper No. 90-GT-116.

ultrahigh frequency X and Gamma rays. All but the very highest frequency signals may be used by a potential enemy to detect and track an attacking aircraft. The means by which this may be achieved can be broadly placed into two categories:

1 The use of passive signals, that is the interception of signals emitted by the aircraft itself. In practice the frequency of such signals may be of any value in the large range between acoustic and visible wavelengths.

2 Active systems where the defender illuminates the target in some way and uses the characteristic of the reflected signal to provide the required information. In this case the freqencies used are normally above one GHz, that is in the radar, infrared, and optical bands. Lower frequencies do not, in general, provide sufficiently accurate reflected data.

From the point of view of stealth technology it is clearly desirable to eliminate, or failing this, suppress the emissions that enable the enemy to use passive methods of interception. Because of the wide frequency band the effects of this are varied. In the case of active interception the use of stealth concepts is largely concerned with the reduction to a minimum of the reflected signal for which the major consideration is the effective external shape of the attacking aircraft.

## 3 Passive Signals

As an inevitable consequence of its existence and mission, the aircraft will radiate signals over most of the frequency range, at least up to visual wavelengths. The method of handling them to reduce their potential as an aid to detection by the enemy demands particular consideration.

**3.1 Acoustic Emissions.** Audible signals from the aircraft are of lowest frequency. Although it is likely that the emissions will have directional characteristics, the reduction of intensity with distance from the source follows an inverse square law. When allowance is made for atmospheric effects, the typical attenuation is 6.3 dB for each doubling of the distance from the source. Thus the distance over which the aircraft can be heard is very limited but is still important, especially in tactical situations. Another consideration is the low velocity of propagation of sound waves, which is of the same order as the velocity of the aircraft. Indeed a supersonic aircraft will arrive before its acoustic signature. This may be a tactical advantage but it does not, in general, remove the need to minimize the effect. Slower flying aircraft, especially rotorcraft, will give advanced notice of their arrival and it is very important to reduce the effect as much as possible.

*3.1.1. Sources of Acoustic Emissions* (*see Fig. 2*)

(*a*) *Powerplant.* The powerplant is always a significant source of audible signals. Because of the noise nuisance of powerplants, experience with civil transport aircraft has led to a good understanding of the causes of gas turbine engine noise. Essentially there are three components, namely, that due to the fan/compressor assembly, the combustion/turbine, and the exhaust. The relative importance of each of these is dependent upon the engine cycle, especially bypass ratio. With piston engines the major noise sources are the exhaust and reciprocating machinery, especially valves.

(*b*) *Unducted fans/propellers and rotors.* Propeller and rotor systems are also a major noise source, especially when the disk loading is high. The noise generating mechanism is quite complex due to the interaction of the differing flow and vortex shedding among the multiple blades.

In the case of rotorcraft there may also be a large contribution from the interaction of the main and tail rotors.

(*c*) *Airframe.* There can be a noise contribution from the airframe as a whole, especially for a large aircraft, which has a high wing loading. In detail the main causes are local flow interactions rather than overall boundary layer noise, and these are most severe in high lift configurations with landing gear extended. This noise source is unlikely to be of real significance. An exception to this general rule is shock wave propagation.

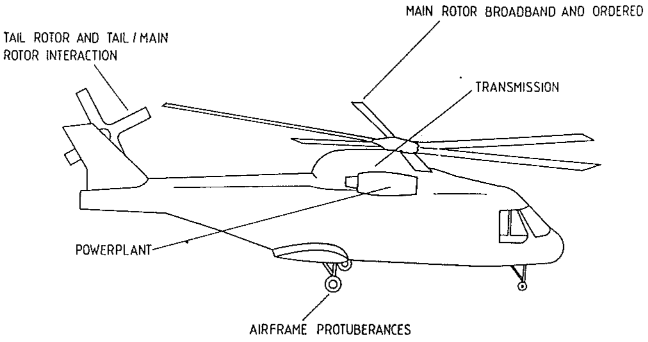

**Fig. 2 Sources of aircraft noise**

*3.1.2. Reduction of Audible Emissions.* There are three ways of approaching the problem of reducing acoustic emissions:

(*i*) By reduction of the intensity of noise sources
(*ii*) By adapting the shape of the noise spectrum to make it less noticable, e.g., by suppressing discrete tones.
(*iii*) By the use of local attenuation and absorption media and shielding techniques.

The actual application is dependent upon the noise source.

(*a*) *Powerplant noise.* The biggest single reduction in noise results from increase of bypass ratio, at least up to values of the order of 5 or so. The main effect of this is the reduction of exhaust velocity and the more efficient mixing with the ambient air. Unfortunately the use of such high bypass ratio is limited to subsonic flight, although in any application some bypass effect is beneficial in reducing the intensity of the exhaust noise source. Increase of bypass ratio tends to cause an increase in engine front end noise but the impact of this can be reduced by such means as the elimination of inlet guide vanes. In addition to those techniques that reduce the noise intensity, further improvement may be made by the addition of acoustic insulation lining in the ducts of the powerplant, and by introducing some degree of front-end noise shielding in the form of a long, curved inlet duct.

The noise emitted by piston engines may be reduced by appropriate provision of an exhaust muffler system. This is likely to result in some loss of performance as the price to pay for quietening. Liquid-cooled powerplants are generally less noisy than air-cooled ones because of the insulating/blanketing effect of the coolant system.

(*b*) *Propellers and rotors.* The most effective way of lessening the noise of rotors is to reduce the tip speed and the blade loading. Thus stealth considerations suggest the use of large-diameter, multiple blade units, which are operated at low rotational speed. Appropriate detail aerodynamic design of the blade tips may also provide further gains, especially in reducing the impact of discrete tones in the total noise spectrum. On the whole the use of sound-absorbing material is not applicable and shielding leads to the concept of ducted rotors.

**3.2 Thermal Signals.** Thermal signals from the aircraft may result from either self-emissions or incident reflections. The wavelengths are typically in the infrared range of about 1 to 100 $\mu$m. This short wavelength means that the infrared signature is much more suited to target detection, identification, and tracking than are long audible waves. The actual wavelength is related to the absolute temperature of an emitter. The wavelength associated with the spectral radiant emission of a black body is given by Wien's displacement law as

$$\lambda = 2893/T \ \mu\text{m}$$

where $T$ is the absolute temperature (K). Thus the wavelength of the peak emissions from an aircraft flying at Mach 2 in the stratosphere will be around 7 $\mu$m, while that from the exhaust plume will be about 4 $\mu$m.

A further important property is the emissivity of the radiating surface. This is effectively a measure of the efficiency with which a surface radiates energy at a given temperature. The emissivity is unity for a "black body" but less than this for all other surface conditions. The energy radiated is also directly proportional to the fourth power of absolute temperature.

The attenuation of infrared radiation in the atmosphere is highly frequency and temperature dependent. Although the amount of radiation scattering is usually small, both the absorption and transmission effects are relatively large and these depend upon two critical parameters. In the practical range of infrared radiation frequencies there exist a number of so-called "windows" where the transmittance is high. Between these windows are absorption bands, mainly due to the presence of water vapor and/or carbon dioxide in the atmosphere. Thus at low altitude, especially in cloud or fog conditions, the transmission is low. Water vapor content decreases significantly with increase of altitude and so, to a lesser extent, does the carbon dioxide content. Hence infrared radiation is transmitted over much greater distances at higher altitudes.

*3.2.1 Sources of Infrared Emissions* (*see Fig. 3*)

(*a*) *Powerplant.* The heat generated in the powerplant will radiate outward from the cowlings and nacelle, the exhaust nozzle, and also possibly from the air intake system. For many aircraft this source is a significant one and since there will inevitably be a wide range of associated surface temperatures there will be a correspondingly wide range of wavelengths in the signal. Almost certainly some of these will correspond with the transmission windows. A further difficulty is that improved powerplant performance is achieved by increasing the cycle temperatures, with a consequent large effect upon transmitted energy.

(*b*) *Exhaust.* The exhaust plume from a jet engine is also an intense source of thermal energy. However, since the exhaust gases contain large quantities of water vapor and carbon dioxide, the wavelength is such that substantial atmospheric absorption is likely to occur and the transmitted energy will be much reduced. This is less true of the heat energy emitted from the hot rear end of the engine through the exhaust plume.

(*c*) *Airframe.* There are two aspects of airframe emission, namely the reflected energy from sunlight, etc., and the self-generated energy due to the general temperature of the airframe itself. In overall terms the latter is primarily a function of speed and altitude. At subsonic speeds the basic airframe temperature is relatively low, say around 300 K at sea level and 220 K at high altitude. These correspond to relatively long wavelengths of the order of 10 $\mu$m or more. The highest temperatures occur in regions where the airflow is stagnated and this is usually very local.

(*d*) *Local heat sources.* There are many internal items in an aircraft that generate local sources of heat. These include avionics equipment, environmental control, and crew. Particular problems may occur at cooling air outlets.

*3.2.2. Reduction of Thermal Emissions.* There are a number of generally applicable ways of reducing the intensity of thermal emissions:

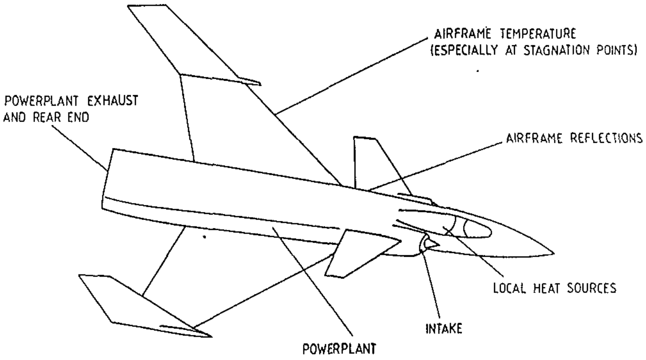

**Fig. 3 Sources of thermal emissions**

(*i*) Reduction of temperature which has the effect of increasing the wavelength of the emission and more importantly the radiated energy, since this latter is directly porportional to the fourth power of temperature.

(*ii*) Reduction of the radiating surface area, either absolutely or by masking.

(*iii*) Reduction of surface emissivity by appropriate treatment of the surface.

(*iv*) Reduction of surface reflectivity.

The ways of applying these techniques are dependent upon the infrared source.

(*a*) *Powerplant.* Cooling of the outside shell of the nacelle, or the use of local heat insulation may be used to reduce temperature. Radiation from the surface can be reduced by using an infrared absorbent coating. Increase of bypass ratio will naturally work in the beneficial sense. Heat energy emitted from the front of the engine may be masked to some degree by having a curved intake layout.

(*b*) *Exhaust.* The exhaust plume presents something of a problem, but again high bypass ratio is of significant help. An alternative is to induce rapid mixing with cold air using special ejector pumps. Curved exhaust pipes may be used to mask the radiation from hot internal engine parts, such as turbine blades, as well as to reduce the signal from the plume itself. The use of two-dimensional rather than circular exhaust nozzles also helps by increasing the perimeter over which gas flow mixing occurs.

(*c*) *Airframe.* For the external emission from the airframe as a whole, there are two considerations. First there is the need to reduce the reflected signals, especially those due to sun glint on transparencies, etc. Appropriate surface treatment can help, but a better solution is to mask these areas as much as possible and to use flat surfaces to minimize the angles over which radiation may be detected. The second requirement is to reduce the effect of kinetic heating as much as possible. The potential here is limited but some improvement can be made by avoiding sharp edges, corners, etc., likely to result in stagnation temperatures. Alternatively a slower flight speed may have to be accepted.

(*d*) *Local heat sources.* These are best dealt with either by using cooling and insulation, or by locating them so that the associated thermal emissions are radiated away from critical directions.

*3.2.3 "Active" Stealth Techniques for Avoiding Thermal Detection.* An alternative approach to the one that tackles the problem of infrared stealth by adapting the design of the aircraft, is the use of a jammer, deceiver, or decoy. The former functions by emitting a large thermal energy in the

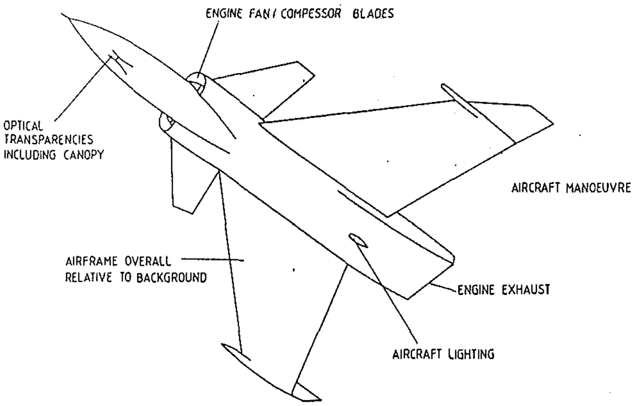

**Fig. 4 Sources of visual signals**

bandwidth of the enemy sensor with the purpose of saturating or even damaging it. The second device is based on the use of a modulated infrared signal from a special emitter, which will have the effect of causing the enemy seeker to predict an incorrect target location. In some cases the seeker can be confused by producing a source of thermal radiation, such as a flare, which ignites at a distance from the aircraft or a towed decoy.

**3.3 Visual Considerations.** The visual signature from an aircraft is determined by the contrast with the background and any reflected light. The range over which an aircraft may be observed by the naked eye is not great, but augmentation by the use of automatic, sophisticated, optical tracking systems can greatly increase this. The observed signal may be that of the aircraft itself, or an effect that reveals its presence, such as vapor trails or smoke emitted from engine exhausts.

The physical characteristics of the signature that affect the probability of the aircraft being detected are:

(*i*) The overall intensity, or luminescence
(*ii*) The wavelengths in the visual range—colors
(*iii*) The nature of the background, especially whether it is uniform or cluttered
(*iv*) The speed and maneuverability of the aircraft

*3.3.1 Main Sources of Visual Signals* (*see Fig. 4*)

(*a*) *Airframe.* The airframe as a whole will have a visibility that is primarily dependent upon its contrast to the background and the overall reflectivity of the surface. There are specific areas that justify special consideration and the most significant of these are the canopy and other optical transparencies. Because of the need for these to be transparent treatment of the surface is limited. Incident light is likely to be reflected from such surfaces and as the aircraft moves can result in a flashing or glint effect.

Contrails due to wing tip vortices can arise when the atmospheric humidity is high. This is most likely at low altitudes.

(*b*) *Rotor and propeller blades.* The rotation of any visible blade system may also result in a glint effect, which draws attention to the aircraft. The problem is most severe at lower blade passing frequencies, especially as far as observation by the naked eye is concerned. In this case the glint problem is greatly reduced when the blade frequency is more than 16 Hz to 20 Hz, so the effect is not as significant on propellers as it is with helicopter rotors.

(*c*) *Engine exhaust.* As previously mentioned an opaque exhaust plume can betray the presence of an aircraft. There is also the possibility of detection from an aft aspect because of the glow from the hot parts of the engine.

(*d*) *Aircraft lighting.* External aircraft lighting is intended to indicate the presence of the aircraft and should therefore be removed as far as possible in stealth conditions. However there still remains the matter of internal lighting, which is necessary to enable the crew to perform their function.

*3.3.2 Methods of Reducing the Visual Signature*

(*a*) *Airframe.* Apart from making the aircraft as small as possible the main aims are to minimize contrast effects on the airframe itself and relative to its background and to bring transparency glint effects to a similar visual level.

Minimization of contrast may be achieved by appropriate surface treatment. By using paints of different reflectivity it is possible to reduce the contrast across the whole surface of the airframe or against the background. The treatment varies according to aircraft role, for example whether the aircraft normally operates at high altitude against a more or less uniform background, or at very low altitude against a terrain or foliage background. Classical camouflage techniques have been primarily, but not exclusively directed toward the latter including the rendering of the aircraft less observable while it is on the ground.

Another technique that is particularly applicable to aircraft operating against a uniform background is to use local lighting on the airframe to disguise dark areas such as air intakes and other cavities or shadowed regions. Such optical camouflage techniques require automatic adaptation of lighting intensity to balance the contrast.

The glint problem may be considerably helped by the use of flat rather than curved transparencies. Since flat reflectors cause a signal over only a small incident angle the glint effect as perceived by an observer is brief and likely to be inadequate for tracking.

(*b*) *Rotor blades.* Apart from the use of multiple blades to give a higher blade frequency for a given rotational speed, the use of surface treatment is appropriate. This should allow for reflective effects. The elimination of markings intended for safety or other purposes needs to be given consideration.

(*c*) *Engine exhaust.* Correct design of the engine combustion system should result in a smoke-free exhaust plume. The rear end glow from the engine itself may be masked by using a curved exhaust system as mentioned in the section on thermal radiation.

Contrails due to the water vapor in the exhaust plume may be suppressed by the use of additives in the fuel or direct injection into the exhaust. These techniques have associated practical difficulties.

(*d*) *Aircraft lighting.* Where it is essential to retain exterior lights for operational reasons, it is essential that these are masked in those directions where observance by the enemy may occur. This masking must also consider the possibility of the lamp reflecting rays from sun or moonlight. Internal lighting must also be kept at an absolulte minimum. In some cases it is possible to use illumination of instruments by using lighting outside the visible spectrum, for example ultraviolet.

*3.4 Other Emissions From the Aircraft.* As an integral part of its mission, the aircraft may need to radiate signals over a wide range of wavelengths for such purposes as navigation, target location, weapon aiming, etc. The stealth aspects of this topic present a considerable challenge to the system designer since it is essential that these functions be covered in the achievement of a successful mission. One approach is to accept the use of less efficient, more expensive, or more complex systems as a consequence of stealth requirements. For example:

(*i*) The use of laser radars, rather than conventional ones. The shorter wavelengths may result in significant atmospheric attenuation and relatively short range.

(*ii*) Forward-looking infrared (FLIR) for low-level navigation and weapon aiming. Again this system is susceptible to atmospheric effects.

(*iii*) Radar systems using low energy and intermittent emissions to give a low probability of detection, and tracking.

(*iv*) Navigation relying upon inertial systems, updated possibly by intermittent terrain matching, satellite data, or even celestial navigation.

## 4 Conclusions

The minimization of the probability of detection by the enemy using passive techniques presents many severe problems to the designer. In the case of visual detection the consequences are likely to have an impact upon the overall layout. The same may be true for other means of detection although more detailed considerations are then likely to be dominant.

## Selected Bibliography

Ball, R. E., 1985, *The Fundamentals of Aircraft Combat Survivability Analysis and Design*, AIAA, New York.

Barton, D. K., and Ward, H. F., 1969, *Handbook of Radar Measurement*, Prentice-Hall, Englewood Cliffs, NJ.

Engelhardt, M., 1988, *Infrared Radiation Analysis*, Advanced Technology International.

Fuhs, A. E., 1984, "Radar Cross Section Lectures," AIAA, New York.

Hudson, R. D., 1969, *Infrared System Engineering*, Wiley-Interscience, New York.

Jones, J., 1989, *Stealth Technology—Art or Black Magic?*, Tabb Books, Blue Ridge Summit.

Knott, E. F., Shaeffer, J. E., and Tuley, M. T., 1985, *Radar Cross Section (Its Prediction and Measurement)*, Artech House Inc.

Richardson, D., 1989, *Stealth Warplanes*, Salamander Books.

Ridenour, L. N., 1947, *Radar System Engineering*, McGraw-Hill, New York.

Skolnik, M. I., 1980, *Introduction to Radar Systems*, McGraw-Hill, New York.

Sweetman, R., 1986, *Stealth Aircraft*, Airlife Publications.

Sweetman, R., 1989, *Stealth Bomber*, Motorbooks International.

**D. Howe**
Professor of Aircraft Design and
Head of College of Aeronautics,
Cranfield Institute of Technology,
Bedford, United Kingdom

# Introduction to the Basic Technology of Stealth Aircraft: Part 2—Illumination by the Enemy (Active Considerations)

*On of the most significant considerations of stealth technology is the technique used to reduce the probability of detection of an aircraft by radar. This paper is concerned with the nature of the various contributions to the radar cross section, and the means by which their effect may be reduced. A survey of the impact of stealth technology on some specific designs is included, from which the conclusion is drawn that the achievement of good stealth characteristics demands attention to both the overall configuration and detail design.*

## 1 Introduction—Active Interception

Although the design of an aircraft to reduce the likelihood of betraying its presence is of considerable importance, as discussed in Part 1, it is also essential to minimize the probability of its detection under circumstances when the enemy employs active search and tracking techniques. In general the means that have to be used to meet this threat have a profound effect upon the concept of the aircraft as a whole, as well as upon the detailed aspects of its design. The majority of the issues involved are concerned with signals in the ratio portion of the total radiation spectrum, and the bibliography attached to Part 1 is relevant here also.

**1.1 Visible Signals.** Conventional searchlight systems were the earliest devices used actively to locate and track an attacking aircraft. It was necessary to sweep the sky, often using aural signals as a guide, with the intention of illuminating the aircraft. Several individual, relatively narrow beam, lights were normally used to criss-cross the target and provide the aim point for anti-aircraft guns or comparable weapons. Thus the contrasting signal of the aircraft relative to the background was received at both the searchlight and gunnery ground locations.

Laser illumination of a target aircraft is an adaptation of the earlier searchlight concept. The general area of the target may be automaticcally scanned by a very narrow beam until it is located and the reflected signal received by the search system. Doppler effects may be used to assist in the identification and tracking of the target.

The detection of a target by systems intended to illuminate it generally may be made more difficult by appropriate surface treatment aimed at reducing contrast and reflectively or by using a surface shape to minimize glint effects, as discussed in Part 1, paragraph 3.3.2.

**1.2 Radar Wavelength.** The use of radar (Radio Detection and Ranging) systems is without doubt the most common technique used to locate a potential enemy aircraft. The principle of operation is similar to that of the visual technique referred to above, in that the target is illuminated by a radio beam and the returned echo is used to identify and track it. The wide range of frequencies available in the 1 to 100 GHz spectrum gives scope for an appropriate choice of characteristics to match the range and discrimination requirements, with due allowance for atmospheric attenuation, etc. The design of an aircraft that has stealth characteristics from the radar aspect is complex but in some cases it is the most important consideration. The main criterion for judging this stealth characteristic is the degree by which its "Radar Cross Section" (RCS) can be reduced. The definition and assessment of RCS is thus worthy of special discussion.

## 2 Radar Cross Section

**2.1 Basic Radar Considerations.** Theoretically a radio signal may be emitted uniformly over a spherically shaped volume, but in practice this is not desirable and variously shaped antennas are used to give appropriate directional characteristics. Thus a search radar will be designed to give a deep, narrow beam, while a weapon guidance radar is more likely to use a generally narrow or "pencil" beam. The signal emissions may be pulses or continuous, according to the application.

The basic radar range equation may be written in various forms; one that neglects possible signal multipath effects is

$$R^4 = \frac{PA^2\sigma}{4\pi\lambda^2\, L\cdot\eta\cdot\xi}$$

---

Contributed by the International Gas Turbine Institue and presented at the 35th International Gas Turbine and Aeroengine Congress and Exposition, Brussels, Belgium, June 11–14, 1990. Manuscript received by the International Gas Turbine Institute February 1, 1990. Paper No. 90-GT-117.

where $P$ is the peak transmitted power; $A$ is the effective area of the transmitting/receiving antenna, and is typically about 60 percent of the antenna frontal area; $\lambda$ is the wavelength of the transmitted signal; $L$ is a loss factor, which is effectively a measure of the weakening in power of the received target echo due to such matters as atmospheric attenuation, signal processing and polarization. As written $L$ is greater than unity and the actual received echo power is obtained by dividing the theoretical value by $L$; $\eta$ is the power of the noise within the bandwidth of the receiver. This may arise from many sources both from outside and within the radar system, although a large part of it usually arises from the front end of the receiver; $R$ is the maximum range to a given probability, at which the radar can detect a target for a given value of the signal-to-noise ratio; $\xi$ is the ratio of the received echo power to the noise power, $\eta$; $\sigma$ is the Radar Cross Section of the target, that is, the effective echoing area of the target for the particular wavelength, $\lambda$, and the aspect it presents to the receiving antenna.

It is clear from the above that the RCS, $\sigma$, is the parameter to which the designer of a stealth aircraft must pay close attention since it is the only one within his control. It should be noted that a reduction in $\sigma$ by an order of magnitude only reduces the detection range by 44 percent, although it does have a bigger effect on search area and search volume. A very large reduction in $\sigma$ is therefore essential to have a significant effect.

**2.2 Electromagnetic Wave Scattering.** The electromagnetic signal that impinges upon a target is scattered by a variety of mechanisms, which taken together make up the Radar Cross Section.

(*a*) *Specular.* Specular wave scattering is essentially a reflection of the signal. The main contribution arises when the signal vector is perpendicular to the local surface. There may well be side lobes to the reflected signal due to local diffraction.

(*b*) *Diffraction.* Diffraction scattering occurs when there is a discontinuity in the target geometry, for example at the tip of a conical nose. The scattered wave satisfies the boundary conditions.

(*c*) *Traveling Wave.* A traveling wave may result when the radiation is more or less aligned along the length of a long, thin body. The scattering arises when the wave encounters surface discontinuities, the end of the body, or changes in the electromagnetic properties of the surface of the body, for example different materials.

(*d*) *Creeping Wave.* Some regions of a body may well be in the shadow of the radiated signal, but even so there may be creeping waves in these regions, which result in scattering. These are associated with body currents and can result in unfavorable interference with specular waves.

(*e*) *Electromagnetic Boundary Condition Changes.* Scattering will occur wherever an incident wave, which is propagating along the surface of a body, reaches a discontinuity such as a sharp change in slope, different material, a gap, or an edge. The cause, as in diffraction scattering, is the need to satisfy boundary conditions.

In some circumstances these different effects combine to give greater scattering. For example back-scattered creeping waves may combine with spectral radiation.

### 2.3 Radar Cross Section

(*a*) *Definition.* The Radar Cross Section may be considered as the projected area of an equivalent reflector, which has uniform properties in all directions. This equivalent reflector is a sphere, which will return the same power per unit solid angle (steradian) as the aircraft. By comparison with its surface area there are $4\pi$ steradians in a sphere. For any solid shape other than a sphere the value of the RCS will be dependent upon its aspect relative to the receiver.

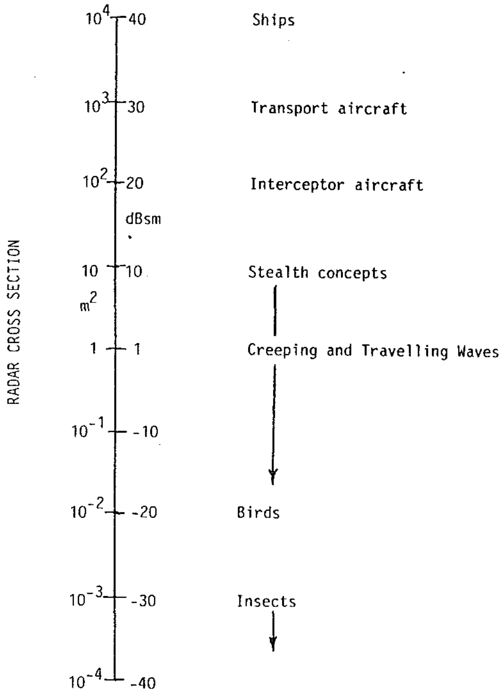

**Fig. 1 Magnitudes of Radar Cross Sections (Part 1: Fuhs, 1984)**

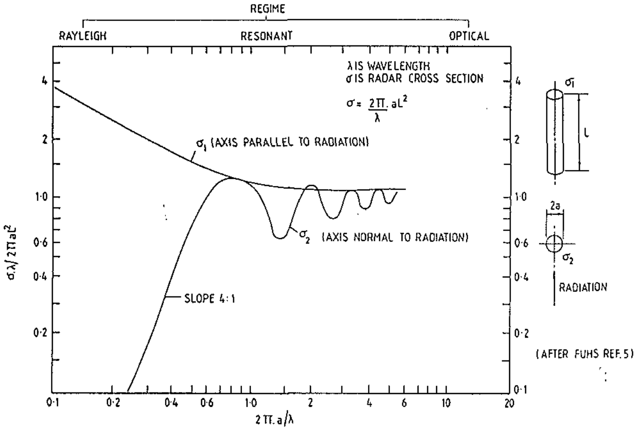

**Fig. 2 Radar Cross Section of cylinder**

The datum reference for an RCS is often taken as a sphere of 1 m$^2$ echoing area, that is, a sphere of 1.12 m diameter. Thus the RCS of a given aircraft at a given aspect may be stated in terms of area relative to the datum sphere on a logarithmic scale:

$$\text{Rel. magnitude of RCS} = 10 \log \sigma \text{ dB } (\text{m}^2)$$

where $\sigma$ is the RCS in m$^2$; dB (m$^2$) is the decibel level (based on RCS). The usefulness of using the logarithmic scale is shown by reference to Fig. 1, which shows the wide range of typical RCS values that may be encountered in practice.

(*b*) *Variation of RCS With Wavelength.* The RCS is not, in general, independent of the wavelength of the illuminating signal although the case of the sphere is an exception providing its diameter is significantly greater than the wavelength.

An important aspect of this is the polarization of the scattered or reflected signal relative to the incident signal at the target. The polarization is specified in terms of the orientation of the vector of the radiation field relative to the direction of a major dimension of the target, $\alpha$. Cross polarization, that is,

| Shape | Radiation Direction | RCS - $\sigma$ $m^2$ |
|---|---|---|
| Sphere of dia. a. | Any | $\Pi a^2$ |
| Flat plate of area A | Normal to surface | $\frac{4\Pi A^2}{\lambda}$ |
| Cone of semi-angle $\delta$ | Parallel to axis | $\frac{\lambda^2 \tan^4\delta}{16\Pi}$ |
| Ellipsoid of revolution major and minor axes 2a and 2b resp. | Parallel to axis 2a | $\frac{\Pi b^4}{a^2}$ |
| Paraboloid with apex radius of curvature $\rho$ | Parallel to axis | $4\Pi \rho^2$ |
| Circular ogive nose semi-angel, $\delta$ | Parallel to axis | $\frac{\lambda^2}{4\Pi} \tan^4\delta$ |
| Circular cylinder length L and radius a | Perpendicular to axis | $\frac{2\Pi}{\lambda} a L^2$ |

Fig. 3 Radar Cross Sections of various shapes

the change of polarization due to the target, does not significantly affect the magnitude of the RCS when the wavelength, $\lambda$, is less than the dimension $\alpha$. It is possible to identify three regimes that determine the dependence of RCS upon wavelength:

(*i*) The so-called "Rayleigh" regime where $\lambda \geq 2\pi\alpha$. In this regime $\sigma$ varies smoothly with variation of $\lambda$. It is proportional to the reciprocal of the wavelength to the power of four, and to the square of the volume of the body.

(*ii*) A "Resonant" or "MIE" regime where rapid changes of $\sigma$ are likely to occur, possibly due to interactions between various scattering mechanisms.

(*iii*) The "Optical" regime where $\lambda \leq 2\pi\alpha$. Here $\sigma$ varies smoothly with wavelength and may tend to a definite value for $\lambda$ very much less than $2\pi\alpha$.

These regimes are illustrated in Fig. 2, which shows the basic case of a circular cylinder of length $L$ and radius $a$. The RCS is defined as $\sigma_1$ when the axis of the cylinder is parallel to the incident radiation vector and $\sigma_2$ when the axis is perpendicular to it. The variation of $\sigma_1$ and $\sigma_2$ in the three regimes is shown. Especially of note is the variation of $\sigma_2$ in the Resonant regime where the cylinder diameter is of similar magnitude to the wavelength.

(*c*) *Variation of RCS With Geometry.* For simplicity the discussion of the effect of RCS variation with geometry will be limited to the optical regime.

(*i*) It can be shown that for a curved surface

$$\sigma = \pi \rho_1 \rho_2$$

where $\rho_1$ and $\rho_2$ are the radii of curvature of the surface in the two orthogonal directions.

In the case of a sphere $\rho_1 = \rho_2 = a$, so that $\sigma = \pi a^2$, as has already been noted.

(*ii*) The RCS of some other solid shapes are given in Fig. 3.

(*d*) *Comparison of RCS of Sphere and Flat Plate.* It is instructive to compare the values of the RCS at a given radiation frequency, for example 3 GHz, which corresponds to a wavelength of 0.1 m, for a sphere and flat plate of the same incident area of 1 $m^2$. For the flat plate of area $\bar{A}$ normal to the incident radiation

$$\sigma = \frac{4\pi \bar{A}^2}{\lambda^2}$$

Thus in this case, $\sigma = 4\pi/(0.1)^2 = 1260$ $m^2$. This shows clearly the significance of flat areas normal to the incident radiation vector.

| Surface Curvature | | Surface/Body | n |
|---|---|---|---|
| $\rho_1$ | $\rho_2$ | | |
| Infinity | Infinity | Flat plate | -2 |
| Infinity | Finite* | Cylinder | -1 |
| Infinity | Zero | Wedge | 0 |
| Finite* | Finite* | Ellipsoid | 0 |
| Finite* | Zero | Curved Edge | 1 |
| Zero | Zero | Tip of cone, etc | 2 |

* Finite, but not zero

$\sigma = \Pi \rho_1 \rho_2$ and $\sigma$ proportional to $\lambda^n$

Fig. 4 Wavelength dependence of specular reflection

(*e*) *Wavelength Dependence of Specular Reflection Effects.* In the optical regime the variation of RCS with wavelength is due to the specular reflection effects. The effect may be interpreted by considering the form, $\sigma = \pi\rho_1\rho_2$ and defining $\sigma$ as proportional to $\lambda^n$. The values of $n$ that apply are then as shown in Fig. 4.

The RCS of a cylinder and ellipsoid, as well as of a flat plate, may be interpreted in terms of

$$\sigma = \frac{4\pi A_p^2}{\lambda^2}$$

where $A_p$ is the area of an equivalent flat plate. In the case of a sphere, for example, it can be shown that

$$A_p = \frac{\lambda a}{2}$$

as would be expected.

Likewise for the circular cylinder

$$A_p = \frac{L(a\lambda)^{1/2}}{2}$$

(*f*) *Other RCS Considerations.* Two specific contributions to RCS require special mention.

(*i*) *Cavities.* Radar cavities may arise from such items as powerplant intakes and exhausts, cockpit canopy and radomes, which are transparent to a given wavelength of radiation. The RCS of a cavity is determined by the properties of the contents of the airframe within the cavity. In some cases a simple flat plate representation may give a reasonable indication of the associated RCS but there may well be special features that amplify this. Examples of such are scattering due to the radar antenna and spectral reflection from internal equipment. Another form of cavity could occur when an aircraft structure uses a radar-transparent composite skin construction with flat internal metallic components.

(*ii*) *Retroreflectors.* Retroreflectors occur where two or more surface planes intersect so that radiation is reflected by all the surfaces, over a wide range of incident angles. Two surfaces intersecting in a right angle form a corner reflector and can be common in aircraft layouts. When present, retroreflectors make a major contribution to RCS.

**2.4 Contributions to the Radar Cross Section.** The RCS of an aircraft is determined by the magnitudes of two distinctly different contributions:

(*i*) The size and shape, both overall and in detail.

(*ii*) The electromagnetic properties of the airframe materials.

As has been noted, the RCS will be both radar frequency and aspect dependent. Often the direction of radiation will result in the illumination of the target aircraft primarily in the front elevation and hence the RCS values are sometimes quoted for the frontal aspect. However it is obvious that consideration must also be given to other aspects, including those

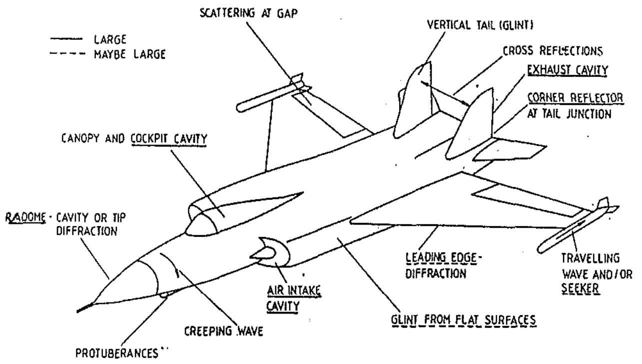

Fig. 5 Contributions to Radar Cross Section

from below or to one side when ground-based radar is the threat.

In detail the RCS will be made up of a complex series of effects due to the various forms of wave scattering discussed in paragraph 2.2. Depending upon the wavelength of the incident radiation and the critical dimensions of the local geometry the scattering may be in any or all of the three regimes defined in paragraph 2.3. In the case of an aircraft where no special techniques have been used to reduce RCS, it is likely that the consequent large value of RCS will be the result of scattering in the optical region. This is not necessarily true in cases where the design aim is to achieve low RCS, since otherwise secondary effects in the Rayleigh and resonant regions may now become of significance.

The main sources of wave scattering for a conventional aircraft are illustrated in Fig. 5. They are:

(*a*) Flat surfaces, which result in spectral reflection and glint.

(*b*) Cavities, as discussed in paragraph 2.3 (*f*). These scatter signals over a wide angular region.

(*c*) Surface intersections that form corner reflectors.

(*d*) Rounded surfaces such as leading edges or noses, where scattering is caused by diffraction.

(*e*) Discontinuities such as sharp trailing edges, changes in airframe materials, and gaps where scattering may result from diffraction to satisfy boundary conditions, or traveling waves.

(*f*) Local surface protuberances and larger protuberances such as weapons, fixed landing gear, and aerials.

(*g*) Propeller and rotor blades where spectral reflection glint effects are likely, and may be large.

(*h*) Exposed mechanisms, etc., such as rotor hubs.

**2.5 Typical Values of Aircraft RCS.** While Fig. 1 gives some indication of the order of magnitude of RCS values for aircraft, it is instructive to consider the matter in somewhat more detail. Comparison of quoted values for RCS can be misleading since the magnitude is so critically dependent upon the aspect presented by the aircraft to the radar receiver. Thus, for example, a broadside aspect may give a value two or three times the frontal aspect and there may be very much more variation when the aspect is inclined in all directions. As previously noted, for many applications the frontal aspect is the most significant. Figure 6 is according to Richardson (1989; Part 1). The values of RCS are likely to be those appropriate to the true head-on view illustrated and for the nonstealth designs at least would be significantly higher for small departures from this aspect. However the figure does clearly indicate the potential gains to be made by adopting stealth techniques.

## 3 Reduction in Radar Cross Section

The RCS may be reduced in several basically different ways:

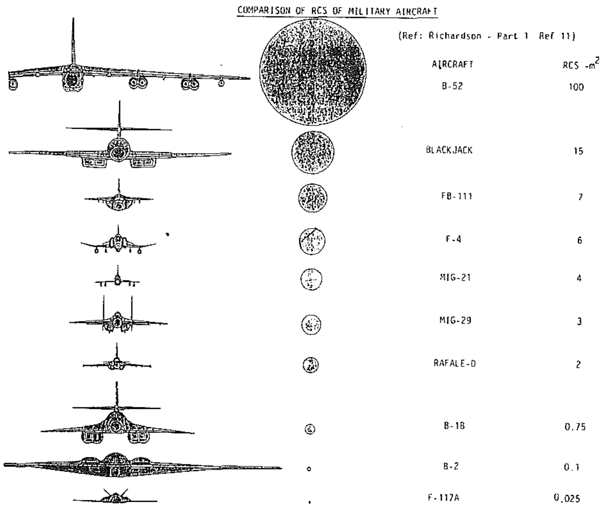

Fig. 6 Comparison of RCS of military aircraft (Part 1: Richardson, 1989)

(*a*) Reduction of the scattering of the incident waves in the general direction of the receiver.

(*b*) By treating the surface of the aircraft with Radar Absorbent Material (RAM). This is particularly appropriate when the radar wavelength is short in comparison with target dimensions.

(*c*) By using local impedances on the surface to altar the pattern of the surface currents. This technique is complementary to RAM in that it is most useful when the radar wavelengths are similar to or greater than the dimensions of the surface effects.

**3.1 Relative Contributions to RCS for a Conventional Design.** It is useful to note the relative contributions to RCS of the various effects in the case of a conventional aircraft, since this indicates the areas where most improvement is possible.

Large contributions may be expected from:

Air inlets for engines
Engine front faces, if intakes are straight
External stores, including missiles with nose mounted seekers
Wing leading edge, especially if unswept
Corner reflectors at intersections of horizontal and vertical tails
Wing from directly below
Radome, if transparent to illiminating radar
Cockpit, including cavity effect
Powerplant exhausts, when viewed from rear
Flat, slab sided fuselage from normal to its side

Smaller, but nevertheless significant contributions arise due to

Fuselage, in head-on view
Wing trailing edge and control surface gaps
Local air intakes, i.e., for cooling or conditioning
Local surface protuberances
Vertical and horizontal tails in isolation
Long, thin fairings or missiles

**3.2 Reduction of Reflections Toward Receiver.** A number of techniques may be employed to reduce the intensity of the reflections from the target toward the receiver. In this context it should be noted that a different approach is likely to be necessary when the detection system uses a bi-static, as opposed to a mono-static radar. The latter is the more usual case of a coincident transmitter-receiver system while the former occurs when the receiver is located at a significant distance from the transmitter, as would be the case, for example, of a semi-active missile guidance system.

There are two distinctly different approaches to establishing the overall shape of the aircraft:

(*i*) By adopting a compact, smooth blended external geometry. This technique is emplified by the Northrop B-2 and Lockheed SR-71. One aim is to use shapes of a continuously varying curvature.

(*ii*) By employing a "faceted" configuration, using flat surfaces arranged to minimize normal reflections back toward the illuminating radar and, it is hoped, eliminate glint. The Lockheed F-117A would seem to have been based on this concept.

Which of these techniques is the most appropriate must depend upon a number of considerations. Among these may be the ease of manufacture, the use of RAM referred to in paragraphs 3 and 3.4, and the aspect likely to be presented to the radar.

Within this overall approach there are a number of more detailed objectives:

(*a*) Minimize the overall size of the aircraft.

(*b*) Eliminate the cockpit transparency cavity by employing an unmanned vehicle, or alternatively reduce cavity effects by treating them with a thin conducting layer.

(*c*) Develop a clean external geometry with no protuberances. Thus all stores should be carried internally.

(*d*) Use swept leading edges with rounded tips to the wings

(*e*) Cant vertical surfaces to avoid right angle corner reflectors.

(*f*) Avoid flat and re-entrant surfaces likely to be normal to the incident radiation.

(*g*) Design and manufacture any internal structure within radar transparent skins to reduce reflections in given directions, for example by using multifaceted shapes.

**3.3 Special Problem of Engine Installations.** The engine air intake cavities present a particular design difficulty. It is necessary to achieve an acceptable compromise between the conflicting requirements of stealth and performance. Among the devices that may be used are:

(*a*) Buried powerplants with air intakes and exhausts located over the upper surface of the airframe. The idea is to mask the cavity from the illuminating radar as far as is reasonably possible.

(*b*) Extended length inlet guide vanes, arranged to cause internal reflections and mask the cavity itself.

(*c*) A screen placed over the intake effectively to close the radar cavity. To be effective the mesh size must be less than the wavelength of the illuminating radar.

(*d*) Curved S-shaped inlet ducts.

(*e*) Location of internal baffles in the intake ducts, as on Rockwell B-1B.

(*f*) Shaping of intake lips, as on the Northrop B-2.

(*g*) Adding shields along sides of intake and exhausts as on the Lockheed F117A.

**3.4 Use of Radar Absorbent Material.** Radar Absorbent Material (RAM) is, as its name indicates, intended to reduce the scattered signal by absorbing some part of the incident radiation. RAM may function in one of two distinctly different ways:

(*i*) By admitting the signal and then attenuating its intensity. This type is particularly suited for use against a wide range of radar frequencies, and is sometimes referred to as broadband RAM.

(*ii*) By generating internal reflections of the received signal, which interfere with the signal reflected from the outer surface. In this case the application is to the situation when a particular frequency is being dealt with. It is sometimes known as resonant RAM.

Apart from these different operating mechanisms, there are also several means of achieving the objective. They may be selected according to the overall design requirements for the aircraft.

When a radar signal travels through air and then impinges upon the surface of the aircraft, the reflected portion of the signal is given by

$$|\gamma_M - \gamma_A| / (\gamma_M + \gamma_A)$$

where $\gamma_M$ and $\gamma_A$ are the electromagnetic characteristic impedances of the surface material and air, respectively. Thus, ideally, the impedance of the surface material should be the same as that of air, which is 377 Ω. However the impedance of most aircraft metals is near zero, since they are good conductors, and hence when a signal strikes a metal surface, most of it is reflected.

Apart from the requirement to possess an impedance close to that of air, RAM should also be capable of rapidly absorbing the energy of the signal as it passes through it. This latter effect may be achieved by using a surface covering consisting of energy absorbing ("lossy") dielectric, magnetic, or ferritic material. The energy absorbed depends upon the angle of incidence of the wave, the thickness, and the particular material properties. The RAM itself may consist of a thin layer or mesh of a nonmetallic material in which are embedded particles of carbon or ferrite. Broadband RAM uses seveal layers of different materials to give a dialectric gradient. Lossy dielectrics tend to be relatively thick, but light, while the opposite is true of lossy magnetics.

Examples of resonant RAM are the Dallenbach layer technique and the Salisbury screen. The former consists of a lossy layer of particular thickness placed in front of the skin of the aircraft. The thickness is selected to meet the threat from a specific radar wavelength. The Salisbury screen is a thin layer of lossy material, which is separated from the skin of the aircraft by a lossless dielectric. In practice there may be several screens, each of which results in internal reflections to interfere with the outer surface reflection, and give a wider frequency coverage. While this type of RAM may well be the most effective, it is usually thick and expensive.

In general RAM techniques are likely to be most useful when the wavelength of the illuminating radar is less than the characteristic dimensions of the aircraft.

**3.5 Alteration of Surface Currents.** Unlike RAM, this approach is applicable to the case when the radar wavelength is at least similar to that of the characteristic length of the scattering surface. Impedences are located at various positions on the surface and may be used to modify the RCS.

**3.6 Gains Resulting From Reduction of RCS—Jamming.** As was stated in paragraph 2.1, the effective radar detection range for a given signal-to-noise ratio is proportional to the fourth root of the RCS. While this is not, apparently, a very strong dependence it should be noted that the search area is proportional to the square root of RCS and the search volume is proportional to RCS to the 3/4 power. Both of these considerations assist in reducing the probability of detection by a given search radar.

However, a more significant consideration is the effect of RCS reduction on the capability of a device carried on the aircraft to jam the search radar. Both the echo from the target aircraft and the jamming signal are effectively emitted from the aircraft in the direction of the search radar.

The echo signal strength, $S$, at the aircraft is

$$S = \frac{P A \sigma}{\lambda^2 R^2}$$

The power of the jammer, $J$, in the direction of the radar may be written as

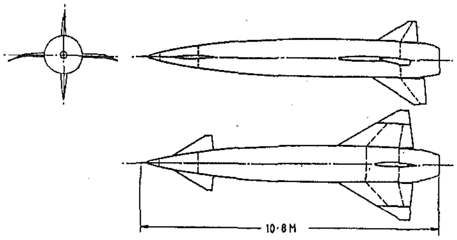

Fig. 7 Layout of Blue Steel

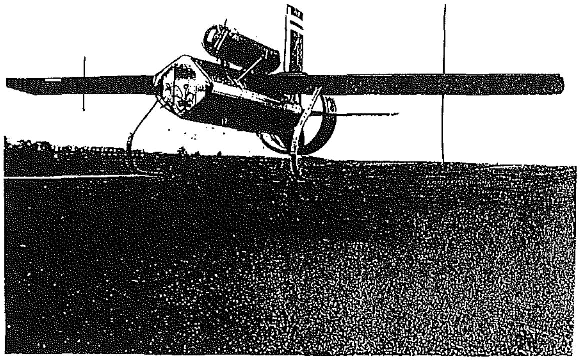

Fig. 8 Marconi-Avionics Machan RPV

$$J = P_j\, B\, G_j$$

where $P_j$ is the jammer power density emitted over the bandwidth of the receiving radar $B$, and $G_j$ is the gain of the jammer antenna in the direction of the radar. Both the echo and jamming signals have to travel the same distance to the receiver and thus the ratio of $J$ to $S$ is established at the target and remains constant throughout the return path to the receiver

$$\frac{J}{S} = \frac{P_j B G_j \bullet \lambda^2 \bullet R^2}{P A \sigma}$$

As the aircraft approaches the receiving radar the echo strength increases, since $R$ is decreasing, but the jammer signal strength is constant. Eventually a point will be reached when the ratio of $J/S$ has decreased so that the echo signal may be identified, even in the presence of the jammer. The range at which this occurs is known as the "burnthrough" range $R_B$ and is given by

$$R_B = \left(\frac{P A \sigma C}{P_j B G_j^2 \lambda}\right)^{1/2}$$

where $C$ is the minimum value of $J/S$ that can conceal the target echo.

While burnthrough range is actually dependent upon variation in target aspect and RCS, it can be seen that the required jammer power for a given value of $C$ is inversely proportional to RCS.

**3.7 Radar Deceivers and Decoys.** One of the main types of radar deceiver is chaff. This consists of a large quantity of small dipole relectors, which are ejected by the aircraft to confuse the search radar. The idea is that the echo produced by the chaff will mask that due to the aircraft itself. The effectiveness of this technique is variable since soon after ejection the behavior of the chaff becomes different to that of the aircraft and it may well be possible to distinguish between the two echos.

An alternative is to use a decoy. A reflecting device that mimics the echo of the aircraft would be positioned away from the aircraft by some means and hence provide a false target.

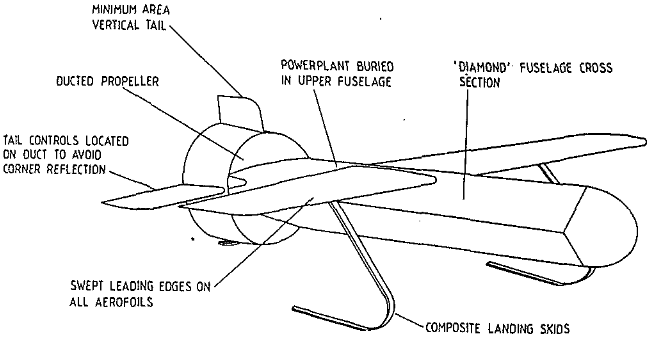

Fig. 9 Machan RPV—reconnaissance version

Neither of the above devices is true stealth since the aim is to confuse the search radar rather than to avoid detection.

## 4.0 Examples of Stealth Concepts

In conclusion it is interesting to consider some examples of design where stealth was a major design consideration.

**4.1 Blue Steel.** Blue Steel (Fig. 7; Frances, 1964) was a stand-off weapon designed to be launched from the RAF 'V' bombers. The vehicle was some 11 m in length and designed to penetrate a substantial distance into enemy territory after being launched from outside the defensive area. The success of the operation was based on high-speed, high-altitude flight with a low probability of detection. This last requirement dictated a low value of RCS, especially in the frontal aspect. The elimination of an intake cavity was one of the primary considerations in the choice of a rocket engine. Care was taken to maintain a smooth curved shape, broken only by the essential but thin, highly swept, aerofoil surfaces. Interestingly it has been recently reported that during radiation properties testing a traveling wave phenomenon was discovered, probably when the wave from the nose encountered the leading edge of a lifting surface. This suggests that the RCS had a very low value. The airframe used steel construction and the inertial guidance system was self-contained.

**4.2 Marconi—Avionics Machan RPV.** The Machan (Hamill, 1981) was an unmanned aircraft used to test and develop systems and components for unmanned aircraft. In this role its configuration is shown in Fig. 8. However the original concept was for its use for battlefield reconnaissance. The configuration for this role is shown in Fig. 9. The significant differences are wings of reduced span, elimination of the range safety parachute pod, and the consequent reduction in size of the vertical yaw damping surface. Stealth was a major consideration in the layout, the aim being to present low RCS to search radar located primarily below the vehicle.

The techniques employed to reduce the probability of detection included:

(*a*) The somewhat unusual diamond-shaped fuselage cross section. Apart from simplifying manufacture and powerplant installation, this had the prime advantage of minimizing glint due to illumination by ground-based radar. In an operational role the radar transparent nose would have been treated appropriately to the type of sensor being used.

(*b*) Swept-back leading edges to all lifting surfaces.

(*c*) Powerplant installation masked as far as possible from the ground by burying it in the upper fuselage behind the wing. The two cylinders of the two-stroke piston engine were within the cross section and cooled by air ducted in from upper surface intakes. Provision was made for an exhaust muffler system to reduce the distinctive noise emission of this type of powerplant.

(*d*) Propulsion was by means of a rear-mounted ducted propeller driven through a shaft from the engine. The use of the circular duct was an inevitable compromise. However the

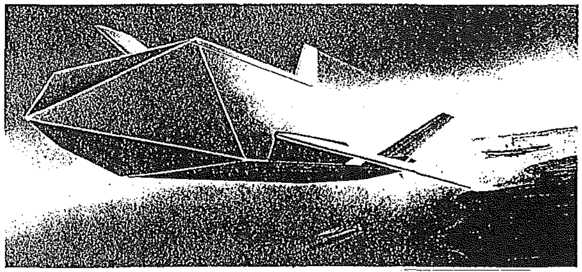

REF. AVIATION WEEK 30/10/89

Fig. 10 Texas Instruments standoff weapon

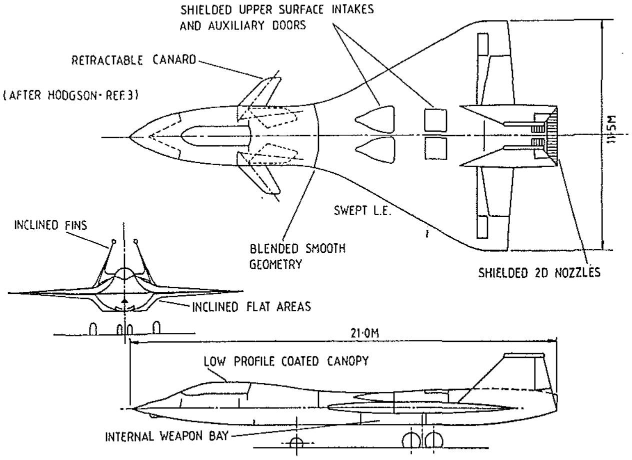
(AFTER HODGSON· REF.3)

Fig. 11 Supersonic stealth bomber

length was kept as small as possible to minimize the reflecting area. The duct supports used swept leading edges, and the three rear control surfaces were mounted off the duct to minimize corner reflection effects.

(*e*) All moving control surfaces were used to avoid the adverse effect of gaps and hinges. The vertical yaw damper surface was made as small as feasible to take full advantage of masking by the duct and horizontal surfaces.

(*f*) Much of the lower surface of the mainplane was flat, again to minimize glint. Wing-fuselage intersection created a sharp acute angle on the lower wing surface.

All lifting surfaces were primarily of reinforced plastic construction. An alternative glass fiber fuselage was developed to replace the normal metallic construction.

Interestingly a somewhat similar configuration has recently been proposed by Texas Instruments for a new US Navy standoff weapon (Fig. 10). The layout is stated as employing low observable technology.

**4.3 Supersonic Stealth Bomber Study.** As part fulfillment for the requirements of an MSc S. W. Hodgson (1987) undertook a study of a supersonic bomber (Fig. 11). The high-altitude cruise requirement was $M = 1.6$, with a $M = 0.9$ low-altitude case. Low observability was the primary consideration and the configuration proposed incorporates many of the previously discussed features that lead to low RCS.

The logic behind the derivation of the layout was based on a smooth, blended configuration.

(*a*) *Wing.* A highly swept basically delta wing with rounded tips was chosen. This combines good supersonic wave drag and favorable stealth behavior. The wing is mounted as low on the body as allowed by other considerations to minimize the wing-body blending needed to avoid introducing corner reflectors. Stealth considerations dictated that leading edge devices should not be employed, but the inner leading edge is swept forward to form a chine along the sides of the forward fuselage. This has the consequence of eliminating vertical fuselage surfaces and providing a shielding to the cockpit canopy and engine air intakes, as well as enhancing wing-body lift.

(*b*) *Body.* All stores are carried in a bay located beneath the wing structure. The somewhat large canopy was chosen to give good visibility to the crew. This led to the need to shield it as much as possible, although it was proposed to give the transparencies a nonreflective metallic coating.

(*c*) *Powerplant Installation.* The two powerplants are buried in the fuselage behind the wing carry-through structure to minimize frontal RCS. The air intakes are located on the upper surface of the blended wing-body and are thus largely shielded from in front and below. Although shaped in plan similarly to flush intakes they do, in fact, face forward and slightly upward. Some reliance is placed on the leading edge vortex to feed air into the intake region. Auxiliary doors are provided for low speed, the main intakes being of fixed geometry optimized at $M = 0.9$. The intake ducts are long, curved and lined with RAM. Two-dimensional exhaust nozzles are located on the upper side of the extreme end of the fuselage.

(*d*) *Vertical Fins.* The vertical stabilizing area is split into two to minimize side area and the pair of surfaces canted inward from the aft end of the wide fuselage. In this configuration the fins provide a side shield for the exhausts and the adverse effect of corner reflection at the wing junction is minimized.

(*e*) *Canards.* Low-speed takeoff and landing performance dictated the need for a small canard lifting surface. Although this could be used to provide gust alleviation during low level penetration, it is not required for performance or control at high subsonic and supersonic speed. Since the canard is a severe disadvantage from stealth considerations it is proposed that it be retracted into the fuselage sides for normal cruising flight.

(*f*) *Overall Considerations.* Much of the construction employs composite materials. Care has been taken to avoid cutouts and discontinuities on all upper surfaces. Lower access doors would have to be sealed and bonded. The main landing gear retracts into the wing-body blend fillet alongside the weapon bay and does not present a frontal discontinuity, although traveling waves could be a problem. Nose wheel retraction is conventional. Powerplant access is difficult and the high engine thrust line introduces a trim drag penalty, but these matters are part of the price that must be paid for low observability.

## 5 Conclusions

The demand for stealth characteristics, especially in relation to the achievement of low radar cross section, has a profound effect upon the design of an aircraft. In many respects the techniques needed to achieve an aircraft with a very low probability of detection are in direct conflict with the requirements for good performance. This is especially true in the case of air-breathing propulsion systems. The reduction of the RCS contribution of air intake and other airframe cavities demands a careful compromise in the stealth/performance balance. While the overall layout of a configuration is also of great importance, very significant improvements may be made by attention to detail.

Reference may be made to the bibliography located at the end of Part 1 for further reading.

## References

Frances, R. H., 1964, "The Development of Blue Steel," *Journal Royal Aeronautical Society*, May.

Hamill, T. G., 1981, "Machan—An Unmanned Aircraft Flight Research Facility," presented at the Second International RPV Conference, Bristol.

Hodgson, S. W., 1987, "Preliminary Design Study of a Stealth Configured Tactical Bomber," MSc Thesis, Cranfield Institute of Technology.

**R. H. Smith**

**J. D. Chisholm**

McDonnell Aircraft Company,
McDonnell Douglas Corporation
St. Louis, MO 63043

**J. F. Stewart**

NASA-AMES/DRYDEN,
Edwards Air Force Base, CA 93523

# Optimizing Aircraft Performance With Adaptive, Integrated Flight/Propulsion Control

*An adaptive, integrated flight/propulsion control algorithm called Performance Seeking Control (PSC) has been developed to optimize total aircraft performance during steady-state engine operation. The multimode algorithm will minimize fuel consumption at cruise conditions; maximize excess thrust (thrust minus drag) during aircraft accelerations, climbs, and dashes; and extend engine life by reducing Fan Turbine Inlet Temperature (FTIT) when the extended life mode is engaged. On-board models of the inlet, engine, and nozzle are optimized to compute a set of control trims, which are then applied as increments to the nominal engine and inlet control schedules. The on-board engine model is continually updated to match the operating characteristics of the actual engine cycle through the use of a Kalman filter, which accounts for anomalous engine operation. The PSC algorithm will be flight demonstrated on an F-15 test aircraft under the direction of the NASA Ames/Dryden Flight Research Facility. This paper discusses the PSC design strategy, describes the control algorithm, and presents results from high-fidelity, nonlinear aircraft/engine simulations. Simulation results indicate that thrust increases as high as 15 percent and specific fuel consumption reductions up to 3 percent are realizable by the PSC system.*

## I Introduction

Traditionally, aircraft flight and inlet control systems are designed to operate independently of the engine control system. This design philosophy often produces a system where performance is compromised to ensure operability. For example, engine operating point and variable vane positions are scheduled to produce high engine performance, while maintaining adequate fan stall margin to accommodate the most severe aircraft maneuvers. Therefore, when an aircraft is at moderate angles of attack, there is excess engine stability margin, which can usually be traded for increased thrust or extended engine life.

Another problem with conventional aircraft and engine control is the difficulty in designing trim schedules to account for the wide range of operating conditions experienced by modern tactical aircraft. Trim settings are typically generated by optimizing the best available system model for a number of steady-state points spanning the design operating envelope and then storing the results in tabular form in aircraft and engine control computers. Control system parameters that might be stored as trim values include canard and wing flap deflections for flight control, ramp and bypass door positions for inlet control, and internal pressures and rotor speeds for engine control. Sensed variables, such as Mach number, temperatures, and pressures, are used to schedule these stored trim values in flight. These schedules must often be modified after initial flight tests, when better data become available. Even then, aircraft-to-aircraft aerodynamic variations, variable aircraft store loadings, engine-to-engine component variations, engine deterioration, changing levels of engine bleed and horsepower extraction requirements, and nonstandard atmospheric conditions are seldom explicitly taken into account. Such system variations will limit the performance of schedules that do not adapt to off-nominal operating characteristics.

The emergence of digital flight, inlet, and engine controllers, as well as multiplex data buses for communicating between them, has provided the means for mechanizing integrated control solutions to the above problems. Further, advances in control technology, estimation techniques, and system modeling have provided better analytical tools with which to design multivariable control laws. Because of this opportunity, a number of studies have been conducted to design integrated flight/propulsion control algorithms, which improve overall aircraft performance.

Under the Air Force's Design Methods for Integrated Control Systems (DMICS) program, two multidisciplinary teams developed methodologies for designing integrated control laws for advanced tactical fighters (Joshi et al., 1983; Clifton et al., 1983). The targeted aircraft had a high degree of airframe/engine coupling, brought about by such features as thrust vectoring and propulsive lift. The emphasis of the DMICS program was improving aircraft dynamic response with inner-loop integration, and both design teams

---

Contributed by the International Gas Turbine Institute and presented at the 35th International Gas Turbine and Aeroengine Congress and Exposition, Brussels, Belgium, June 11–14, 1990. Manuscript received by the International Gas Turbine Institute February 21, 1990. Paper No. 90-GT-252.

demonstrated multivariable control laws through high-fidelity simulations. Another Air Force program, Performance Seeking Control (PSC), produced an adaptive trim control algorithm that minimizes fuel consumption during cruise, even when the aircraft and engine are operating in an off-nominal fashion (Tich et al., 1987). The work done under these Air Force programs, combined with the pioneering work under the NASA HIDEC program, led to the initiation of the NASA Performance Seeking Control program, which is the subject of this paper.

Under the NASA Highly Integrated Digital Electronic Control (HIDEC) program, four integrated flight/propulsion control modes were developed and flight demonstrated on an F-15. One, Trajectory Guidance, generates flight trajectories for minimizing mission fuel usage or time to reach a specified end point. The other three modes improve aircraft operation through sophisticated scheduling techniques, which integrate information from the engine and airframe. HIDEC test results proved that substantial gains in excess thrust (thrust minus drag), for increased performance, or reductions in Fan Turbine Inlet Temperature (FTIT), for extended engine life, can be realized through integrated trim schedules (Yonke et al., 1987). It is anticipated that additional benefits can be realized by replacing the HIDEC schedules, which are based on a nominal engine, with a model-based trim control algorithm that adapts to engine variations.

The goal of the Performance Seeking Control program, sponsored by the NASA Ames/Dryden Flight Research Facility, is to develop such an adaptive, integrated flight/propulsion control algorithm and to flight demonstrate the concept on a NASA F-15 aircraft in 1990. McDonnell Aircraft Company (MCAIR) is the prime contractor for the PSC program, with Pratt & Whitney (P&W) as principal subcontractor.

The multimode PSC algorithm, which is currently in the final stage of development, minimizes fuel consumption during aircraft cruise; maximizes excess thrust (thrust minus drag) during accelerations, climbs, and dashes; and extends engine life by reducing FTIT when the extended life mode is engaged. On-board models of the inlet, engine, and nozzle are optimized to compute a set of control trims, which are then applied as increments to the nominal engine and inlet control schedules. The adaptive feature of PSC is provided through a Kalman filter, which estimates engine component deviations to account for off-nominal engine performance. The component deviation estimates are used to match the on-board engine model to the operating characteristics of the actual engine cycle. This process provides the on-line trim optimization with an accurate representation of that particular propulsion system over the entire life of the engine.

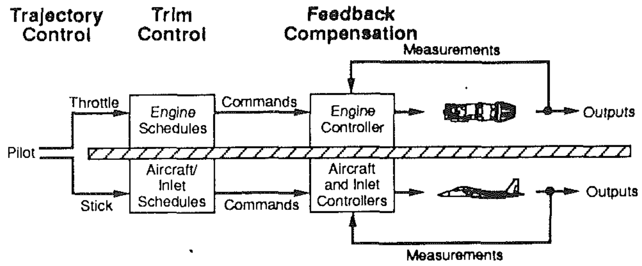

Fig. 1 Original F-15/PW1128 control structure

## II Control Integration Strategy

Before describing the PSC algorithm, it is useful to put it in proper perspective by discussing its relationship to other problems, which can be addressed within the context of integrated flight/propulsion control. A good place to begin is with an examination of a conventionally designed, minimally integrated aircraft/engine control structure. Figure 1 depicts an example of such a system, the original (pre-HIDEC) NASA F-15 aircraft, equipped with PW1128 engines.

The figure shows the aircraft/engine control structure divided into three areas: (1) trajectory control, (2) trim control, and (3) feedback compensation. This division of control structure by tasks is described by Clifton et al. (1983), and is borrowed here for its usefulness in characterizing integrated control problems.

As shown in Fig. 1, the only integration of aircraft/engine controls in the original F-15/PW1128 was carried out by the pilot as he tried to optimize throttle and stick commands for a given mission. Trim control and feedback compensation were carried out by separate flight, inlet, and engine controllers without the benefit of shared information. Of course, the designers of the inlet control laws were aware of the nominal airflow demands of the PW1128, and designed the F-15 variable inlet geometry schedules accordingly. Likewise, designers of the DEEC control for the PW1128 had knowledge of the pressure distortion levels likely to be encountered behind the F-15 inlet and produced engine control laws with sufficient stability margin to accommodate these

## Nomenclature

AJ = Nozzle Throat Area
CEM = Compact Engine Model
CIVV = Compressor Inlet Variable Vanes
DEEC = Digital Electronic Engine Control
DEFCS = Digital Electronic Flight Control System
DFCC = Digital Flight Control Computer
EAIC = Electronic Air Inlet Controller
EPR = Engine Pressure Ratio (PT6/PT2)
FNP = Net Propulsive Force
FTIT = Fan Turbine Inlet Temperature
HIDEC = Highly Integrated Digital Electronic Control
LP = Linear Programming
MCAIR = McDonnell Aircraft Company
NASA = National Aeronautics and Space Administration
N1C2 = Corrected Fan Speed
PASCOT = Programmable Asynchronous Serial Communication Translator
PLA = Power Lever Angle
PSC = Performance Seeking Control
PB = Burner Pressure
PPH = Pounds Mass per Hour
PT# = Total Pressure at Engine Station #
P&W = Pratt & Whitney
RCVV = Rear Compressor Variable Vanes
SDF = Six Degree-of-Freedom
SFC = Specific Fuel Consumption
SSVM = Steady-State Variable Model
TT# = Total Temperature at Engine Station #
$\mathbf{u}$ = Control Vector
WF = Combustor Fuel Flow
WFAB = Augmentor Fuel Flow
W2C = Corrected Fan Airflow
$\mathbf{x}$ = State Vector
$\mathbf{y}$ = Output Vector
$\alpha$ = Angle of Attack
$\beta$ = Angle of Sideslip

levels and still yield high performance. Because these subsystems were not designed to communicate in flight, however, performance compromises were unavoidable.

Clifton et al. (1983) point out that improved aircraft performance can be achieved by integrating flight/propulsion controls in either or all of the aforementioned areas: trajectory control, trim control, or inner-loop feedback/feedforward compensation. Because both the goals and control design techniques are different for each of the three, a brief discussion of these areas is useful.

Trajectory control is the generation of flight profiles that achieve a desired design goal. The benefits are improved mission performance and reduced pilot workload. Typical design goals are: minimizing mission fuel usage, minimizing the time to reach a specified end point, and minimizing the fuel expenditure to reach a specified endpoint at a specific time. By nature, trajectory optimization is open loop and relies on ground-based or on-board model predictions. If the Mach numbers, altitudes, and power settings commanded by the pilot or trajectory-generating algorithm do not produce the desired results, there is no way (short of reflying the mission) to correct the problem. For this reason, accurate system models are essential for the success of trajectory control.

The second area suitable for control integration, trim control, is the determination of the best set point about which to regulate the system. Once the pilot or trajectory control algorithm has determined a flight condition and power setting, the steady-state trim control sets the engine operating point and nominal aircraft/inlet control surface deflections. Typical design goals are: minimizing fuel flow for a given cruise condition, minimizing engine turbine temperature at constant thrust, or maximizing excess thrust (thrust minus drag) during an aircraft acceleration.

The final area where controls can be integrated is within the inner-loop feedback/feedforward compensation. Inner-loop compensation is the modification of system dynamics to improve response characteristics. Both the goals and design techniques used in this area of work are those most commonly associated with controls engineering. Typical goals include: minimizing response time while maintaining adequate damping, minimizing tracking error with minimum control effort, and providing disturbance rejection and insensitivity to plant variations. The Air Force DMICS program emphasized inner-loop integration, and Clifton et al. (1983) and Joshi et al. (1983) describe design approaches for carrying out this task.

Of the three areas where aircraft and engine controls can be integrated, trim optimization offers the greatest payoff potential. The reason is that the propulsion system operates the great majority of time at trimmed conditions. For a typical air superiority mission, nearly 85 percent of flight time and 45 percent of fuel is spent during cruise segments (Clifton et al., 1983). Adding the time spent during climbs, accelerations, and dashes (where the power setting is usually constant), it is found that over 95 percent of the air superiority mission is carried out with the propulsion system operating near steady state. To demonstrate the benefits of integrated aircraft/engine trim optimization, NASA initiated the HIDEC program.

Under the NASA HIDEC program, the contracting team of MCAIR and P&W developed and flight demonstrated three integrated flight/propulsion trim control modes for the F-15/PW1128. The modes are: (1) Adaptive Engine Control System (ADECS), (2) Extended Engine Life (EEL), and (3) Inlet Integration. In the ADECS mode, excess fan stall margin is traded for additional engine thrust. Yonke et al. (1987) report that FNP increases from 2 to 12 percent are achieved through this technique at subsonic flight conditions. In the EEL mode, instead of increasing thrust, turbine operating temperatures are decreased while maintaining constant thrust, thereby reducing wear on the engine. Recent flight evaluations of this mode have demonstrated FTIT reductions as high as 100°F. The inlet integration mode (Chisholm et al., 1990) realizes increased aircraft performance by controlling inlet ramp positions based on a DEEC calculation of engine airflow. Increases in excess thrust (thrust minus drag) as high as 12 percent over the nominal F-15/PW1128 have been achieved in flight.

The NASA F-15/PW1128 control structure modifications made under the HIDEC program are depicted in Fig. 2. The three trim control modes described above use the same basic approach, predefined schedules that integrate information between subsystems. The schedules are implemented as increments to the nominal control trim settings so that the aircraft can be flown with or without HIDEC engaged. The trim settings are calculated off-line using the best aircraft/engine simulations and databases available to the control law designer. Although these schedules are optimum for a nominal aircraft/engine, they do not adapt to off-nominal operating characteristics such as engine deterioration and nonstandard atmospheric conditions.

Two approaches are available for designing trim control laws that do adapt to off-nominal conditions: (1) direct plant perturbation search and (2) adaptive model-based optimization. In the first of these, the control effectors are perturbed, and their impact on the objective function (fuel flow for instance) is measured. The controls are then moved in the direction of improved performance, and the process is repeated. Unfortunately, performance is usually lost during the perturbation process; actuator life is shortened; system stability may be decreased; the objective function gradient is difficult to measure accurately, and the perturbation process may disturb the pilot. Because the second technique, indirect model-based optimization, does not have these disadvantages, it is preferred over direct plant perturbation.

NASA initiated the PSC program in 1988 to demonstrate the benefits of adaptive, model-based, aircraft/engine trim optimization. In addition to accounting for off-nominal conditions, model-based optimization is also more versatile than trim schedules. Multiple modes, such as minimum fuel consumption, maximum excess thrust, or extended engine life, can be implemented by simply changing the objective function in the on-board optimization routine. With trim scheduling, each mode requires that a new set of schedules be generated and stored on-board.

Under PSC, the HIDEC trim schedules, depicted in Fig. 2, are replaced with adaptive models, constraint calculation, and on-line optimization. Because the PSC on-board models must run within the limitations of flight-worthy computers, they are much simpler than the off-line simulations used to generate the HIDEC trim schedules. The PSC approach has the advantage, however, of being able to tune these models in flight, to match the actual system operating condition.

The challenge of the PSC design problem is to create on-board models that provide a better representation of system

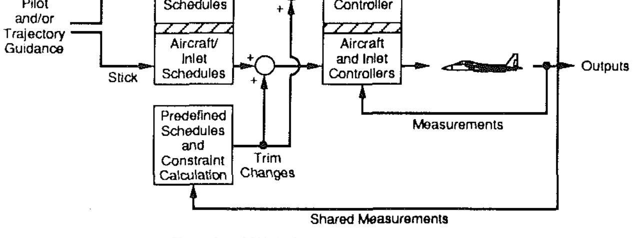

Fig. 2 HIDEC control structure

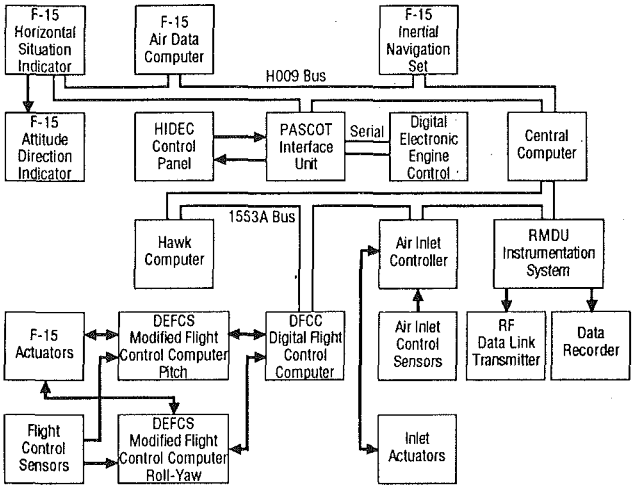

Fig. 3 Performance seeking control architecture

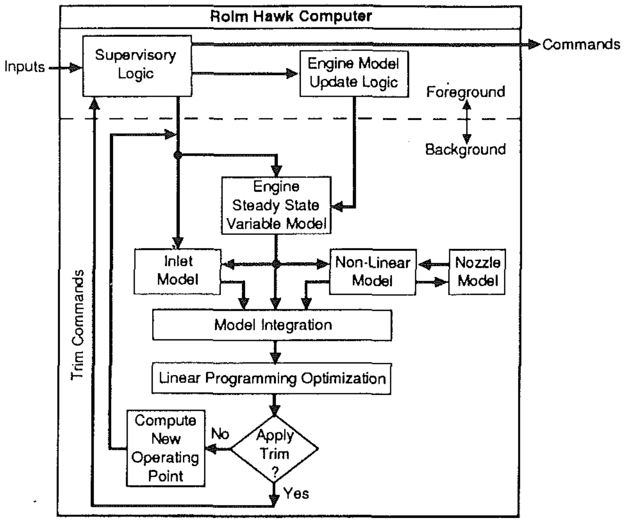

Fig. 4 PSC control logic

performance over the life of a particular engine than the best ground-based nominal models. With this accomplished, performance improvements beyond those available through the HIDEC approach will be realized.

## III Algorithm Description

Under the direction of NASA, the MCAIR/P&W team has developed a PSC system for optimizing aircraft steady-state performance under four different modes: (1) minimum SFC at constant thrust, (2) maximum excess thrust, (3) minimum FTIT at constant thrust (extended life), and (4) maximum excess thrust at constant FTIT. This section contains an overview of the PSC system design and provides descriptions of the system models, the integration of these models, and the optimization procedure.

**Overview.** A diagram of the PSC system architecture is shown in Fig. 3. The primary components in the system architecture are the Digital Electronic Engine Controls (DEECs), Electronic Air Inlet Controllers (EAICs), Digital Flight Control Computer (DFCC), and Rolm Hawk computer. In addition, the Inertial Naviation System, Air Data Computer, and flight control sensors supply information used by the PSC algorithm. These components are linked together by data buses, which allow information exchange between the various subsystems. Communication with the DEECs is via serial data link. The PASCOT interface unit translates DEEC inputs and outputs between the serial link and the H009 bus. The H009 and 1553 data buses exchange information through the Central Computer.

The majority of the PSC logic resides in the Hawk computer. The compact propulsion system models, engine model update logic, optimization routine, and supervisory logic modules comprising the PSC control law are all contained in the Hawk. The PSC logic uses information from the other flight/propulsion control subsystems to calculate optimum trim commands, which are then applied to the EAIC and DEEC. The PSC trim commands sent to the DEEC adjust the engine operating point, the variable stator vane positions, and the afterburner operation. The trim commands sent to the EAIC adjust the cowl and third ramp positions on the variable geometry F-15 inlet.

An important part of the PSC logic that is not contained in the Hawk is the alpha/beta predictor. This logic, which resides in the DFCC, sends predicted angle-of-attack, $\hat{\alpha}$, and sideslip angle, $\hat{\beta}$, to the Hawk computer, where it is used in the maneuver accommodation logic to maintain engine stability during aircraft maneuvers. The DFCC predicts $\alpha$ and $\beta$ 0.5 seconds in the future, based on air data measurements and inertial angular body rates. As the F-15 maneuvers, the pressure distortion at the engine fan face increases, resulting in decreased stall margin. Although the PSC optimization logic constrains stall margin in the trimmed state, aircraft transient maneuvers can be executed significantly faster than the PSC trim optimization time. To prevent engine stall from occurring during rapid aircraft maneuvers, the PSC maneuver accommodation logic monitors $\hat{\alpha}$, $\hat{\beta}$, and the engine operating point. If a fan stall situation is predicted, this logic rapidly reduces Engine Pressure Ratio (EPR) to regain adequate stall margin. This same approach was successfully demonstrated in the HIDEC program.

A flow diagram of the PSC logic within the Hawk computer is shown in Fig. 4. The split between the foreground and background tasks is indicated. The foreground tasks are carried out every 50 ms, while the background tasks are computed as time permits. Initial timing estimates predict that the Hawk background will compute optimum propulsion system trims every 6 seconds. Simulation results show that this trim rate is adequate to optimize aircraft performance during cruise segments, accelerations, and climbs.

The supervisory logic, which runs in the Hawk foreground, performs three main tasks: maneuver accommodation, velocity hold, and engine transient detection. The Maneuver accommodation logic, which is described above, protects against engine stalls during aircraft maneuvers generating significant inlet distortion. The velocity hold logic is a flight test option, which can be selected during the minimum SFC or minimum FTIT (extended life) modes of operation. During these modes, the PSC trims are calculated to hold thrust constant. If, however, model inaccuracies result in minor thrust changes, the velocity hold logic will issue autothrottle commands to compensate. The purpose of the transient detection logic is momentarily to suspend the operation of the PSC algorithm if a significant engine transient is detected. The PSC trims are computed to optimize performance when the engine is near steady state; they are not valid during engine power transients.

The Hawk background contains compact models of the engine, nozzle, and inlet, as well as the optimization logic. The models compute propulsion system parameters, such as inlet drag and fan stall margin, which are not measurable in flight. The compact engine model receives information from the engine model update logic, which runs in the Hawk foreground, to match it to the operating characteristics of the actual engine. In addition to calculating propulsion system

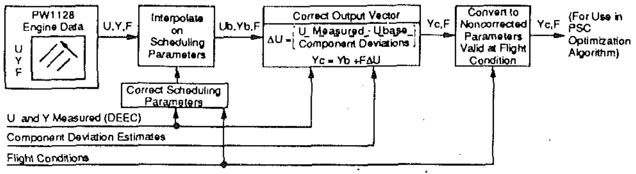

Fig. 5 PSC steady-state variable model (SSVM)

outputs, the compact models also compute sensitivities of these parameters to changes in control variables.

The model outputs and sensitivities are mathematically combined to form an overall propulsion system model. This propulsion system model is then optimized using a Linear Programming (LP) optimization scheme. The goal of the optimization is determined from the selected PSC mode of operation. The resulting trims can either be applied directly to the DEEC and EAIC or used to compute a new operating point, about which the optimization process is repeated. The latter method is used to calculate an overall (global) optimum before applying the trims to the controllers.

**Compact Engine Model.** The compact engine model (CEM) calculates engine output parameters and the sensitivity of these output parameters to changes in control variables. The CEM outputs include temperatures, pressures, rotor speeds, airflows, thrust, and stall margins. The control variables are primary and augmentor fuel flows (WF, WFAB), augmentor entrance total pressure (PT6), and variable fan and compressor stator vane positions (CIVV, RCVV).

The compact engine model consists of two parts: (1) a piecewise-linear steady-state variable model (SSVM), which represents engine gas generator operation and (2) a nonlinear model, which represents those engine effects for which linear relationships are generated on-board. The SSVM represents engine operation on and off the nominal operating line throughout the entire F-15 flight envelope. Characterizing engine operation off the nominal operating line is essential, since the PSC commands will generally move the engine operating point off the baseline schedules. An overview diagram of the SSVM is provided in Fig. 5.

The foundation of the SSVM is a set of linear point models located on and off the operating line for a reference flight condition. Full envelope capability is achieved by modeling the engine in terms of corrected parameters.[1] Each point model consists of a basepoint control vector ($\mathbf{u}_b$), a basepoint output vector ($\mathbf{y}_b$), and a sensitivity coefficient matrix (**F**), which relates changes in control positions to changes in outputs. The point models are scheduled with sensed engine parameters. By interpolating between the models with the scheduling parameters, a single point model ($\mathbf{u}_b$, $\mathbf{y}_b$, and **F**) to be used for optimization is formed. The output vector is adjusted for control deviations (the difference between the actual control positions and the model basepoint values) and engine component deviations, as identified by the Kalman filter in the update logic. The output vector and **F** matrix are then uncorrected, shifting them to the current flight condition for the optimization procedure.

The nonlinear model contains those engine effects that cannot be accurately approximated with linear relationships (i.e., augmentor operation). This model calculates both the nonlinear parameters and the linear sensitivities of these parameters to changes in controls. The nonlinear parameters are calculated using the measured control settings, $\mathbf{u}_m$, and the SSVM output vector, $\mathbf{y}_c$. The sensitivities are determined by mathematically perturbing the elements of the control vector and calculating the resulting changes in the nonlinear parameters.

**Engine Model Update Logic.** The goal of the engine model update logic is to match the compact engine model to the operating characteristics of the actual engine. To accomplish this task, a Kalman filter has been designed to account for anomalous engine performance. The filter, similar to that described by Luppold et al. (1989), estimates five component deviations that fully characterize off-nominal engine performance. The five parameters are low spool efficiency adder, high spool efficiency adder, fan airflow adder, compressor airflow adder, and high turbine area adder. Due to the limited number of sensed engine parameters, isolation of efficiency changes to a specific component is not possible. However, off-nominal performance can be isolated to a particular spool. Changes to the fan and low turbine efficiencies are combined into a low spool adder, while those of the compressor and high turbine are lumped into the high spool adder. This technique has been found to work well within the PSC system and can also be adapted for use in engine monitoring and fault detection.

The component deviation estimates are augmented to the SSVM control vector to improve the accuracy of the compact engine model (CEM) output calculations. Extensive evaluations of the Kalman filter/CEM tandem have been conducted with nonlinear simulations. Hundreds of flight conditions spanning the F-15 subsonic flight envelope have been analyzed, with several levels of engine deterioration simulated. Results show that, with the engine model update logic, the CEM accuracy in computing steady-state outputs satisfies the ±2 percent design goal at nearly all conditions, when compared to a nonlinear aero/thermodynamic engine model (truth model).

**Compact Nozzle Model.** The PSC nozzle model computes the incremental F-15 aft end drag due to the engine exhaust plume and the external nozzle aeroydnamics. The compact nozzle model was designed by curve-fitting wind tunnel jet effects data. The model consists of multivariable equations, each corresponding to a specific free-stream Mach number. Each equation expresses nozzle drag as a function of external nozzle exit area and the ratio of exit static pressure to ambient pressure.

The F-15 does not have an actuator to control the nozzle exit area independently. Instead, the exit area is mechanically linked to the nozzle throat area and floats within the bounds provided by the linkage, based on internal and external pressures. Therefore, at a given flight condition, nozzle drag is a function of only the engine control variables, which determine both the exit area and exit static pressure. To optimize overall aircraft performance, it is important to know how nozzle drag changes as the engine controls are varied. The compact nozzle model supplies the PSC optimization with these sensitivities through an on-line linearization procedure similar to that carried out in the nonlinear portion of the compact engine model.

**Compact Inlet Model.** The compact inlet model calculates inlet performance and sensitivities for the variable three-ramp F-15 inlet, illustrated in Fig. 6. The model will be designed for the full F-15 envelope, although only the subsonic portion has been developed to date. In subsonic operation, inlet performance is calculated in terms of total pressure recovery and inlet drag. In supersonic operation, inlet performance will also be calculated in terms of shock displacement ratio and percent

---

[1] It is standard engineering practice to correct engine rotor speeds, temperatures, pressures, and mass flows as a function of engine face pressure and temperature. The resulting corrected parameters provide a basis for the comparison of engine operation at different atmospheric and flight conditions.

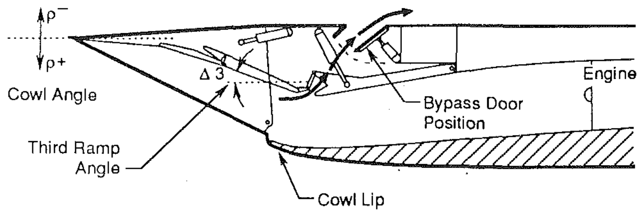

Fig. 6 F-15 air induction system

critical mass flow. In addition to performance levels, the inlet model also calculates the sensitivity of the performance parameters to changes in the inlet input variables. For PSC, the inlet input variables are cowl angle, third ramp angle, and engine corrected airflow. The PSC system will not adjust the bypass door position since it is positioned closed for best performance, as is already done. The inlet controller only opens the bypass door at the onset of inlet flow instabilities.

Subsonically, PSC will not alter the inlet ramp positions either. Analysis has shown that the best subsonic inlet performance is obtained with the inlet scheduled wide open, as is currently done. However, the influence of engine-corrected airflow on inlet performance must be computed to account for the coupling between the inlet and engine. Therefore, the subsonic portion of the compact inlet model consists of curve-fit equations to calculate total pressure recovery and inlet drag as a function of engine corrected airflow. The curve-fits were generated from MCAIR's best analytical/empirical representation of the F-15 inlet. The inlet sensitivities are calculated by mathematically perturbing the input variables, using a technique similar to that described for the nonlinear engine model.

**Model Integration.** The compact models produce outputs and the sensitivity of those outputs to control changes. The sensitivities from the compact models are then combined to form an overall propulsion system model. The primary goal in this step is to account for the coupling between engine corrected airflow (W2C) and total pressure at the engine face (PT2). When an inlet is used to supply the engine airflow, total pressure losses occur in the inlet duct due to diffuser geometry and surface friction. The amount of total pressure loss increases with increasing W2C. In the compact engine model, PT2 is modeled as an independent input, which does not vary with engine outputs, such as W2C. To account for this coupling, the engine and inlet sensitivities are mathematically combined to form an overall propulsion system matrix. This matrix relates changes in engine and inlet controls to changes in the propulsion system outputs. Included are relationships, such as the sensitivity of inlet drag to changes in CIVV position, that can only be determined from an integrated model.

***Linear Programming Optimization.*** Determination of the global optimum for each mode of operation requires solving a constrained nonlinear programming problem. The PSC approach to solving this problem is to perform a series of linear programming (LP) optimizations. For each optimization, a linear representation of the propulsion system about the specific operating point is provided by the propulsion system matrix. Maximum allowable control input changes are computed to prevent violation of model linearization assumptions. Constraints for each system model output are also computed to prevent violation of physical operating limits.

An LP problem is set up and solved, using the Simplex method, to obtain the local optimum under these constraints. The resulting control changes are then used to compute a new system operating point, about which the models are again linearized. The above procedure is again performed, and a new local optimum is obtained. By repeated linearization of the on-board models at each intermediate solution, a sequence of control variable changes is generated, which converges to the global optimum solution.

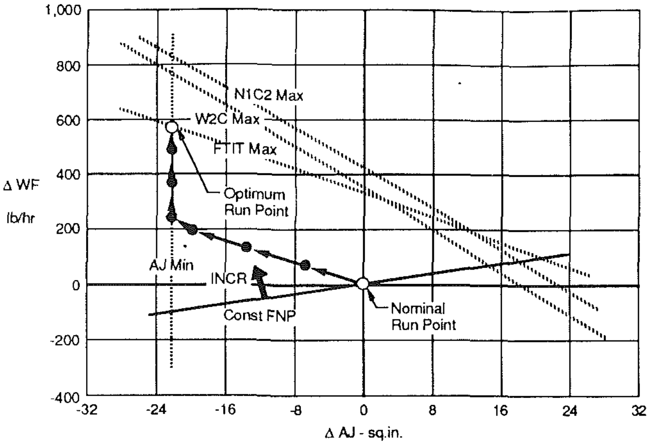

Fig. 7 Determination of the global optimum

This process is illustrated in Fig. 7 for a maximum thrust mode optimization. To simplify the illustration, the PSC optimization is reduced to a two-dimensional problem (two control variables). The global optimum for this case is located at the intersection of the minimum nozzle throat area constraint and the maximum FTIT constraint. A series of local optimums is computed to reach the global optimum.

## IV Performance Evaluations

Three simulations have been developed to evaluate the PSC system: (1) a steady-state simulation, (2) a dynamic propulsion system simulation, and (3) a six-degree-of-freedom (SDF) simulation. In all these simulations, the PW1128 engine is represented by an aerodynamic/thermodynamic model, which is P&W's most complete analytical representation of engine performance. To complete the propulsion system model, the F-15 installation program is added. This program contains MCAIR's highest fidelity analytical/empirical representation of the F-15 inlet, nozzle, and engine parasitics (e.g., compressor bleed and horsepower extraction). Through these simulations, the operation of the PSC system is verified, and the PSC performance benefits are quantified.

The simulation results shown here are for the minimum SFC and maximum thrust modes, which are the two modes that have been analyzed most extensively to date. Results are shown for the subsonic portion of the F-15 flight envelope, which is where the first PSC flight test evaluations will be flown. The original, pre-HIDEC F-15/PW1128 is the baseline for all the performance improvements presented.

The steady-state simulation is used to evaluate the steady-state interaction between the PSC logic and the propulsion system. The aero/thermodynamic engine model is operated in a steady-state mode. When the PSC trims are applied to the engine simulation, they have immediate effect, eliminating engine dynamics. In addition, the simulation is operated at a fixed flight condition since no airframe interaction is modeled.

The steady-state simulation has been used to evaluate PSC operation in all four modes, throughout the subsonic flight envelope. The performance benefits in the maximum thrust mode are quantified in Fig. 8. The percent increase in net propulsive force (FNP) achieved by PSC at Military power (maximum nonafterburning power setting) is plotted for the subsonic flight envelope. The FNP increase is seen to range from 5 percent up to 15 percent. The largest performance improvements are achieved in the upper left portion of the flight envelope. In this operating region, improved thrust is achieved primarily through increased engine pressure ratio (EPR). EPR is raised by increasing fan speed while decreasing nozzle throat

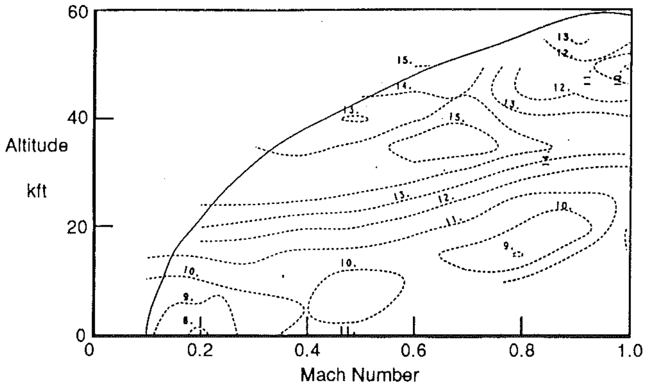

**Fig. 8 PSC maximum thrust mode performance; percent increase in FNP, military power**

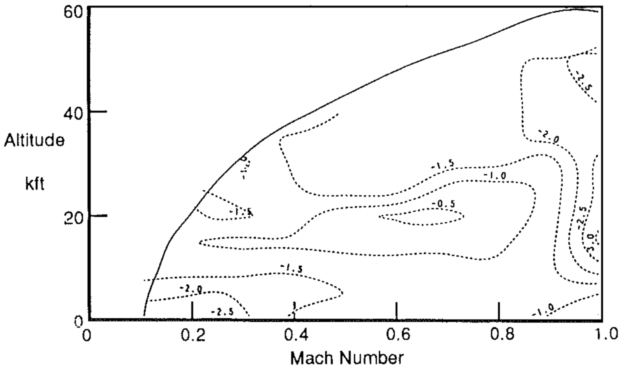

**Fig. 9 PSC minimum SFC mode performance; percent change in SFC, cruise power**

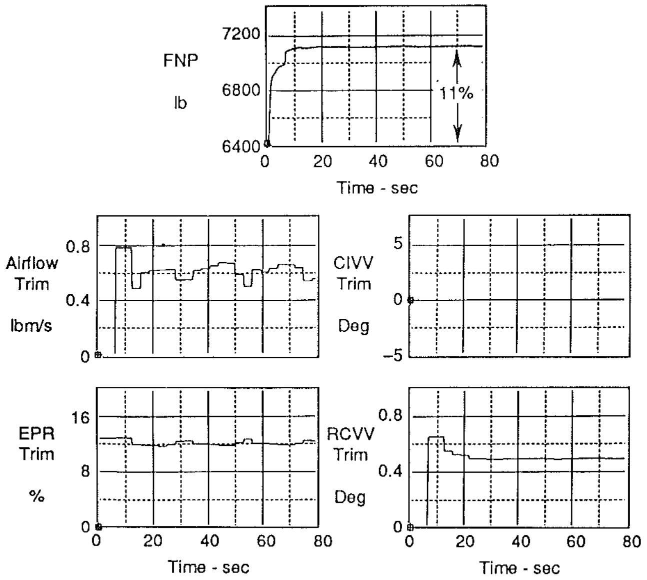

**Fig. 10 PSC dynamic response—max thrust mode; maneuvering flight condition, mil power**

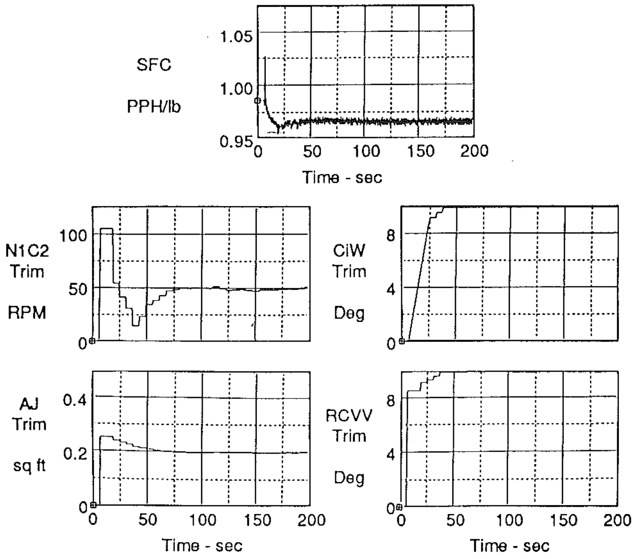

**Fig. 11 PSC dynamic response—min SFC mode; typical cruise condition**

area. The EPR increase is limited by fan stall margin requirements and the maximum allowable fan speed and turbine temperature.

The performance benefits in the minimum SFC mode are quantified in Fig. 9. The percent change in specific fuel consumption achieved by PSC at a cruise power setting is plotted across the subsonic flight envelope. PSC decreases SFC by up to 3 percent. To minimize SFC in the lower left-hand portion of the flight envelope, PSC decreases W2C by cambering the CIVVs and lowering N1C2. Thrust is maintained by increasing EPR. In the upper right-hand portion of the flight envelope, PSC increases W2C by moving CIVVs axially and increasing N1C2. Thrust is held constant decreasing EPR. Throughout the flight envelope PSC moves the RCVVs axially. The more efficient propulsion system operation results in the SFC reductions.

To verify that the PSC system captures all the performance improvements available, PSC results have been compared to truth model optimization results. In the truth model optimization, the nonlinear propulsion system simulation is directly optimized using linear programming in a repeated linearization scheme.[2] This procedure eliminates any modeling errors associated with the PSC compact models. Results from this analysis show that the PSC system captures the great majority of the available benefit for all modes of operation.

The dynamic propulsion simulation is used to evaluate the time-dependent PSC operating characteristics. The aero/thermodynamic engine model is run in a dynamic mode to simulate the actual engine response. The PSC logic is split into foreground and background tasks to accommodate the timing issues associated with dynamic operation. The foreground contains the Kalman filter and a small portion of the supervisory logic associated with trim application. The background contains the compact propulsion system models and optimization logic. This simulation is also operated at a fixed flight condition.

The dynamic response of the PSC system in the maximum thrust mode is shown in Fig. 10 for a subsonic maneuvering condition at Military power. The propulsion system responds rapidly to the PSC trims, achieving 90 percent of the thrust improvement in under 10 seconds. The PSC trim commands to the DEEC are seen to settle to their steady-state values within 15 seconds. The dynamic response in the minimum SFC mode is shown in Fig. 11 for a typical cruise condition. The engine SFC is seen to reach a minimum within 20 seconds. The PSC trim commands have a settling time of up to 75 seconds. Between 20 and 75 seconds, PSC trims are attempting to equalize the FNP. This response is more than adequate for a

---

[2] An earlier analysis (Landy, 1987) showed that equivalent results are obtained using a nonlinear programming technique.

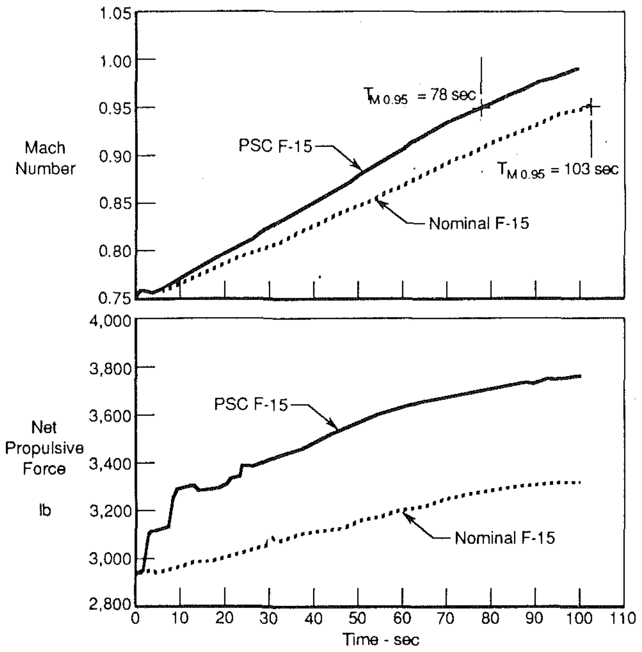

**Fig. 12 SDF results: max thrust mode, 45,000 ft, mil power**

cruise condition where the aircraft will spend long periods of time.

The SDF simulation, our highest fidelity simulation, is used to evaluate PSC's interaction with the airframe and propulsion system. A nonlinear six-degree-of-freedom F-15 aircraft model is used in the simulation, and the PSC trims are applied to both engines. The actual PSC flight test code is used in this simulation. This code contains major portions of the supervisory logic not included in the dynamic propulsion simulation.

The SDF simulation has been used to evaluate PSC performance for aircraft cruise segments, accelerations, and climbs. The aircraft response to the PSC maximum thrust mode is shown in Fig. 12 for a 45,000 ft, Military power acceleration from Mach 0.75. In this figure, the Mach number and FNP are plotted for both a nominal F-15 and one equipped with PSC. The PSC system reduces the time to reach Mach 0.95 by 24 percent.

## V Summary and Conclusions

An adaptive, model-based, Performance Seeking Control algorithm has been developed to optimize steady-state aircraft/engine performance. On-board models of the inlet, engine, and nozzle are optimized to compute a set of control trims, which are then applied as increments to the nominal engine and inlet control schedules. Extensive simulation evaluations have shown that significant increases in thrust (up to 15 percent), and reductions in specific fuel consumption (up to 3 percent) are realizable by the PSC system. The PSC system will be flight demonstrated on the NASA Ames/Dryden Research Facility F-15 in 1990.

The most difficult challenge in the development of the PSC system has been the creation of on-board models accurate enough for the on-line optimization. If the models do not provide a good representation of the actual propulsion system operation, the potential benefits of adaptive control will not be realized. The models in the current system are the results of several years of development effort. This effort has required close coordination among NASA, MCAIR, and P&W.

Although the PSC system is currently targeted toward a specific aircraft and engine type, the modeling and optimization procedures that have been developed are applicable to a wide variety of aircraft. In fact, the anticipated PSC payoffs are greater for aircraft with thrust vectoring, where flight/propulsion control integration becomes essential, or for transatmospheric vehicles such as the National Aersopace Plane (NASP), where the extremely large operating envelope and limited data base make conventional control trim scheduling extremely difficult. Another potential application is using the PSC system to minimize engine exhaust temperature for heat signature reduction in tactical aircraft.

## References

Chisholm, J. D., Nobbs, S. G., and Stewart, J. F., "Development of the HIDEC Inlet Integration Mode," ASME JOURNAL OF ENGINEERING FOR GAS TURBINES AND POWER, Vol. 112, pp. 565–572.

Clifton, J. V., Smith, K. L., Lehtomaki, N. A., and Langton, R., 1983, "Design Methods for Integrated Control Systems," Paper No. AIAA-83-2562.

Joshi, D. S., Shaw, P. D., Hodgkinson, J., Rock, S. M., Vincent, J. H., and Fisk, W. S., 1983, "A Design Approach to Integrated Flight and Propulsion Control," SAE Paper No. 831482.

Landy, R. J., 1987, "Multivariable Control System Optimization," MDC Q0885-7 (PD 112).

Luppold, R. H., Roman, J. R., Gallops, G. W., and Kerr, L. J., 1989, "Estimating In-Flight Engine Performance Variations Using Kalman Filter Concepts," Paper No. AIAA-89-2584.

Tich, E. J., Shaw, P. D., Berg, D. F., Shrider, A., Swan, J. A., and Skira, C. A., 1987, "Performance Seeking Control for Cruise Optimization in Fighter Aircraft," Paper No. AIAA-87-1929.

Yonke, W. A., Landy, R. J., and Stewart, J. F., 1907, "HIDEC Adaptive Engine Control System Flight Evaluation Results," ASME Paper No. 87-GT-257.

**I. H. Ismail**
Research Scholar.

**F. S. Bhinder**
Professor.

Hatfield Polytechnic,
Hatfield, Hertfordshire AL10 9AB,
United Kingdom

# Simulation of Aircraft Gas Turbine Engines

*The paper describes a computer program to simulate aircraft gas turbine engines. The program has been written for IBM-compatible microcomputers and is modular in its appraoch. Either analytical equations or detailed performance characteristics of individual components are used to model the steady-state operation of the complete engine.*

## Introduction

An aircraft gas turbine engine represents a complex system comprising a number of rotating and stationary components, each with its own performance characteristics. The performance of the complete engine depends on the performance characteristics of the individual components or subsystems and matching. Moreover, in service an engine operates over a wide range of flight conditions. Hence, testing a complete engine to explore its full performance envelope can be both very costly and extremely laborious. Therefore, simulating the operation of the aero gas turbine engine on a computer has obvious advantages. Consequently, a number of papers have been published on this subject in the open literature.

Broadly speaking, gas turbine simulation models that have been produced may be divided into three categories, namely:

(*i*) analog simulation models;
(*ii*) hybrid simulation models;
(*iii*) digital simulation models.

These models may be used to represent either the steady state or the dynamic operation of the engine.

A review of the available simulation models, both analog and nonlinear digital (the so-called Dynasar) was given by Durand Harlan [1]. Evans [2] described a method that graphically illustrated the fundamentals of matching the compressor, turbine, and primary nozzle components of a single-spool turbojet engine. Saravanamuttoo and Fawke [3, 4, 5] used the compressor and turbine characteristics and applied the analyses to a range of engines, including a twin spool engine, which was then under development. Their approach essentially consisted of synthesizing the thermo-dynamic relationships that described each engine component. Sufficient dynamic equations were introduced to describe transient behavior between components. They claimed good agreement between test results and simulation. The method advanced by Saravanamuttoo was adopted by Cottington [6] who produced a computer code using DIGISIM, a standard simulation language at that time. The investigations of Schobeiri [7], Mats and Tunakov [8], and Prokof'ev [9] also cover various aspects of simulation.

From the brief review of the published work cited here, it would appear that there is still a need for a general simulation model that may be used to represent different engine configurations and to study, particularly at the conceptual design stage, the effect of component performances on the overall performance of the engine. Hence, it is important to ensure that the package is suitable for use by the design office staff.

The aim of this paper is to describe a microcomputer-based program that has been developed for digital simulation of the steady-state performance of gas turbine engines.

## Design Aims for Simulation Programs

A modern gas turbine engine for aircraft propulsion may be either a simple turbojet, a turboprop, a ducted turbofan, or an unducted turbofan. It may have a single, twin, or triple spool construction. A computer simulation program should permit the user to assemble the components in any desired configuration.

Each component has its own distinct performance characteristics, which may be modeled either analytically or by experimentally obtained performance data. The program should allow the user to model the components in a preferred manner.

The program should be modular so that, if desired, individual modules may be used to study the performance of the components or subsystems comprising a particular engine configuration.

## Description of the Program

The program can be divided into three main sections as follows:

(*i*) program control section;
(*ii*) component description and modeling section, e.g., compressor, combustion chamber, turbine, etc.
(*iii*) processes section, e.g., diffusion, compression, combustion, etc.

The link between the three sections is shown in Table 1. The control section provides the interface between the user and the program. Once all the subsystems that make up the engine have been defined, the control section then proceeds sequentially, taking the necessary geometric data and/or perform-

---

Contributed by the International Gas Turbine Institute and presented at the 35th International Gas Turbine and Aeroengine Congress and Exposition, Brussels, Belgium, June 11-14, 1990. Manuscript received by the International Gas Turbine Institute January 22, 1990. Paper No. 90-GT-342.

Table 1 Program sections

| Components | Program Control | Processes |
|---|---|---|
| Intake | System description, data entry and modelling | Diffusion |
| Compressor | | Compression |
| Combustion Chamber | Execution | Combustion |
| Turbine, etc. | Output | Expansion, etc. |

ance data from the components section and the relevant analytical expressions or experimental data from the processes section. Finally, the results are presented to the user by the program control section.

The program is modular in its approach and has been written in Fortran 77 for the IBM and compatible microcomputers. A flow diagram showing the program logic is given in Fig. 1.

## Theoretical Background

The main components of a turbojet engine and the corresponding thermodynamic cycle are shown in Figs. 2(*a*) and 2(*b*), respectively.

The modeling of each component is described below.

**Air Intake.** Air entering the engine intake at approximately the flight Mach number must be decelerated to satisfy the compressor entry velocity triangle. The intake process, which produces pressure rise due to the ram effect, is shown in Fig. 3. The governing equations are

$$T_{01}=T_\infty+\frac{(V_f-V_1)^2}{2C_p} \tag{1}$$

$$P'_{01}=P_\infty\left(\frac{T_{01}}{T_\infty}\right)^{\frac{\gamma}{\gamma-1}} \tag{2}$$

$$P_{01}=P'_{01}-\Delta P_{0-\text{intake}} \tag{3}$$

$$\Delta P_{0-\text{intake}}=\sum_{1}^{n}\delta P_0 \tag{3a}$$

$$T'_{01}=T_\infty\left(\frac{P_{01}}{P_\infty}\right)^{\frac{\gamma}{\gamma-1}} \tag{4}$$

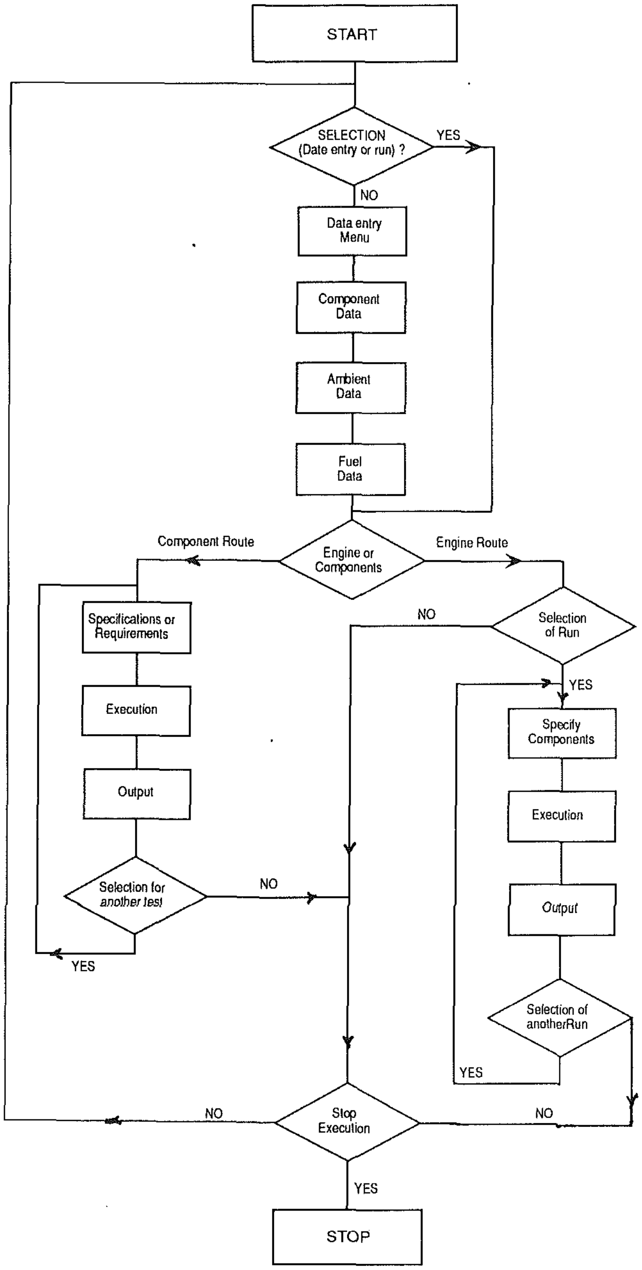

Fig. 1 Flow diagram (gas turbine simulation)

$$\eta_{\text{intake}}=\left\{\frac{T'_{01}-T_\infty}{T_{01}-T_\infty}\right\} \tag{5}$$

## Nomenclature

$C_s$ = velocity equivalent of isentropic enthalpy drop, m/s
$C_p$ = specific heat at constant pressure, kJ/kg°C
$d$ = rotor tip or rms diameter, m
$f$ = fuel/air ratio
LCV = lower calorific value, kJ/kg
$\dot{m}$ = mass flow rate, kg/s
M = Mach number
$N$ = rotational speed, rev/s
$P$ = pressure, bar or N/m$^2$
$Q$ = heat release or transfer, kJ/kg
$S$ = entropy, kJ/kg•K
$T$ = temperature, K
$U$ = rotor tangential velocity, m/s
$\gamma$ = ratio of specific heats
$\delta$ = ratio $= P/P_{\text{standard}}$
$\Delta$ = small increment
$\eta$ = isentropic efficiency
$\eta_{\text{comb}}$ = combustion efficiency
$\theta$ = ratio $= T/T_{\text{standard}}$
$\tau$ = torque, N/m

### Subscripts and Superscripts

$a$ = actual
$i$ = isentropic
0 = total
$\infty$ = ambient conditions
1 = compressor entry
2 = compressor delivery/combustion chamber inlet
3 = combustion chamber outlet/turbine entry
4 = turbine outlet/propelling nozzle entry
5 = propelling nozzle outlet

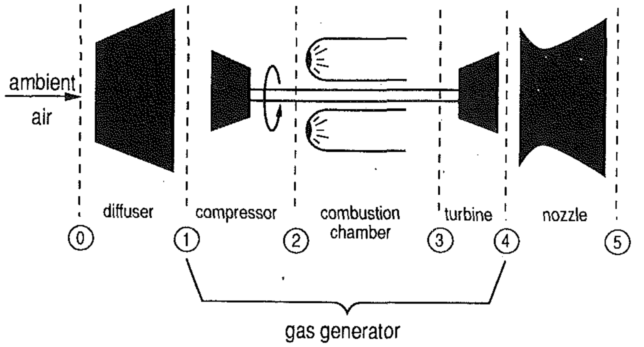

**Fig. 2(*a*) Schematic diagram for turbojet engine**

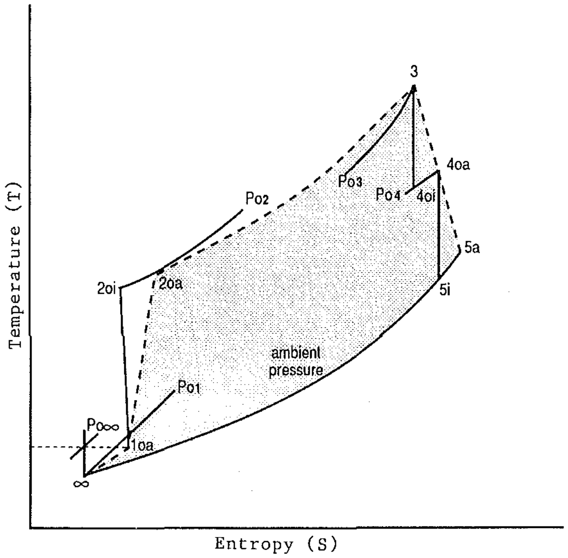

**Fig. 2(*b*) Temperature-entropy diagram for turbojet engine**

where

$\delta P_0$ = the loss of stagnation pressure in an elemental length (1); $n$ = number of elemental steps in the intake.

The overall loss of stagnation pressure can be calculated in a step-by-step manner by using the Darcy formula for friction and at the same time satisfying the well-established diffuser performance criteria.

**Compressor.** The performance of a compressor is fully described by a number of either dimensionless or normalized parameters as given below:

$$\frac{\tau}{d_2^3 P_{01}} = \frac{1}{2\pi}\cdot\frac{1}{\eta_c}\left(\frac{d_2 N}{\sqrt{C_p T_{01}}}\right)^{-1} \cdot\frac{\dot m\sqrt{C_p T_{01}}}{d_2^2 P_{01}}\cdot\left\{\left(\frac{P_{02}}{P_{01}}\right)^{\frac{\gamma-1}{\gamma}} - 1\right\} \tag{6}$$

$$\frac{\tau}{\delta} = f\left(\eta_c, \frac{N}{\sqrt{\theta}} -, \frac{\dot m\sqrt{\theta}}{\delta}, \frac{P_{02}}{P_{01}}\right) \tag{7}$$

where $\delta = (P_{01}/P_{0\,\mathrm{ref}})$; $\theta = (T_{01}/T_{0\mathrm{ref}})$.

The performance characteristics are usually plotted as shown in Fig. 4. In order to use the performance characteristics in a simulation program it is necessary to consider one of the following two options:

(*i*) determine the coefficients for equation (7) and then use the equation to calculate the parameters for an arbitrarily selected point on the performance map;

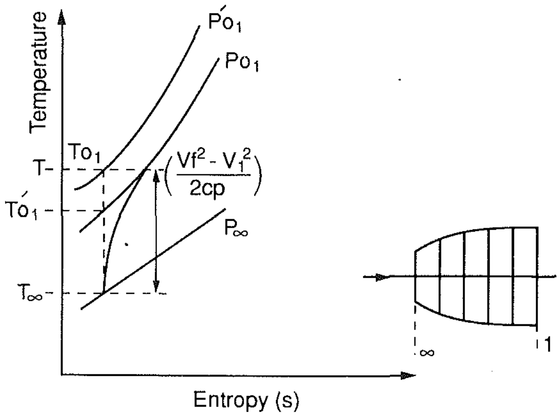

**Fig. 3 Intake process**

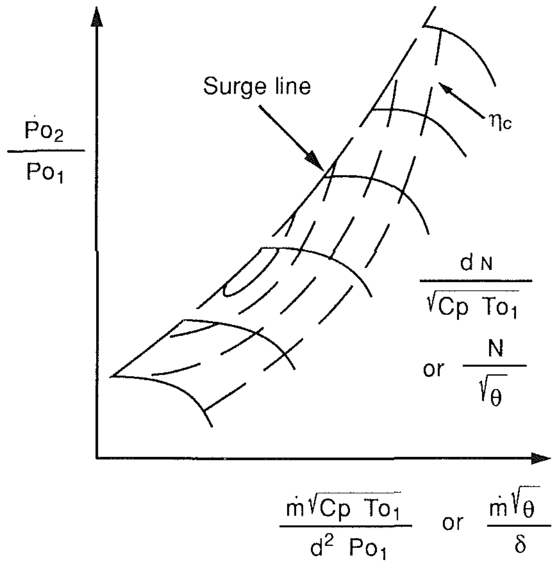

**Fig. 4 Compressor performance characteristics**

(*ii*) store the characteristics in look-up tables and then use an interpolation technique to determine the values of the performance parameters for any arbitrarily selected point on the performance maps.

In the present program the second option was chosen because it produced a more reliable estimate of the performance parameters at any point on the performance map. The format of the look-up tables used in the program is shown in the Tables 2(*a*) and 2(*b*).

If the values of two parameters are specified, the program searches for the other two from these look-up tables. Lagrangian interpolation is used to estimate the values lying at intermediate points.

**Combustion Chamber.** The combustion chamber entry conditions are assumed to be those given by the compressor discharge. The routine handling of the combustion chamber calculates the following:

(*i*) the loss of stagnation pressure during combustion;

(*ii*) the temperature of gas at the outlet of the combustion chamber.

The loss of stagnation pressure is, quite often, assumed to be a constant percentage of the compressor delivery pressure. In this program the loss of pressure is calculated. The governing equations are

$$Q_{\mathrm{gas}} = Q_{\mathrm{theoretical}} - Q_{\mathrm{lost}} \tag{8}$$

$$m_a(1+f)C_{pg}(T'_{03} - T_{02}) = f m_a \mathrm{LCV} - Q_{\mathrm{lost}} \tag{9}$$

Table 2(*a*) **Mass flow versus pressure ratio characteristics**

| N<br>Pr | ⟶ |
|---|---|
| ↓ | mass flow. rate |

Table 2(*b*) **Compressor efficiency versus pressure ratio**

| N<br>Pr | ⟶ |
|---|---|
| ↓ | compressor efficiency |

$$\eta_{\text{comb}} = \frac{Q_{\text{gas}}}{Q_{\text{theoretical}}} \tag{10}$$

$$\Delta P_{0-\text{total}} = \Delta P_{0-\text{momentum}} + \Delta P_{0-\text{friction}} \tag{11}$$

$$\Delta P_{0-\text{momentum}} = P_{02} - P_{03} \tag{11a}$$

$$\frac{P_{03}}{P_{02}} = \frac{\gamma_{av}}{\gamma_{av}+1}\left[1 - \frac{\gamma_2}{\gamma_{av}} M_2^2\right]$$

$$\left\{\left[\frac{\gamma_{av}}{\gamma_a+1}\left(1 - \frac{\gamma_2}{\gamma_{av}} M_3^2\right)\right]^2 - 2\frac{\gamma_2^2}{\gamma_2-1}\,\frac{\gamma_{av}-1}{\gamma_{av}+1} M_3^2\right.$$

$$\left.\left(1 + \frac{\gamma_2-1}{2} M_2^2\right)\frac{Q_{\text{gas}}}{C_{p2} T_{02}}\right\}^{1/2} \tag{12}$$

$$\Delta P_{0-\text{friction}} = \int \frac{dP_0}{P_0}$$

$$= \left(\frac{\gamma M_2^2/2}{1 + \frac{\gamma-1}{2} M_2^2} - \frac{1 + \frac{\gamma-1}{2} M_2^2}{2\left(1 + \frac{\gamma-1}{2} M_2^2\right)}\right)$$

$$= \int \frac{dM^2}{M} \tag{13}$$

**Turbine.** The performance of a turbine, like that of a compressor, is also fully described by a number of either fully dimensionless or normalized parameters as given below:

$$\frac{\tau}{d_2^2 P_{03}} = \frac{1}{2\,\pi} \cdot \eta_t \left(\frac{d_2 N}{\sqrt{C_p T_{03}}}\right)^{-1}$$

$$\cdot \frac{\dot{m}\sqrt{C_p T_{03}}}{d_2^2 P_{03}} \cdot \left\{1 - \left(\frac{P_{04}}{P_{03}}\right)^{\frac{\gamma-1}{\gamma}}\right\} \tag{14}$$

$$\frac{\tau}{\delta} = f\left(\eta_t, \frac{N}{\sqrt{\theta}} -, \frac{\dot{m}\sqrt{\theta}}{\delta}, \frac{P_{04}}{P_{03}}\right) \tag{15}$$

where $\delta = (P_{03}/P_{0\,\text{ref}})$; $\theta = (T_{03}/T_{0\,\text{ref}})$.

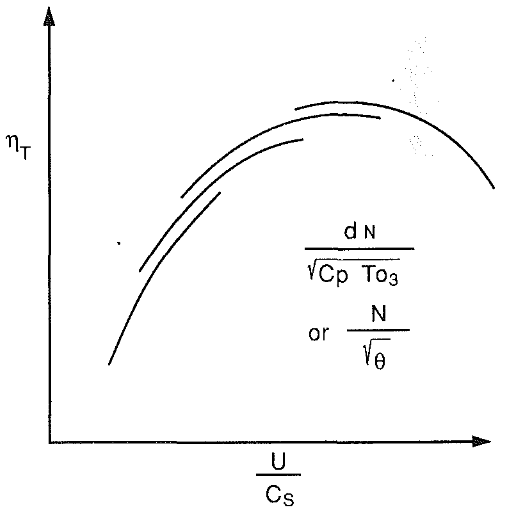

Fig. 5(*a*) **Turbine flow characteristics**

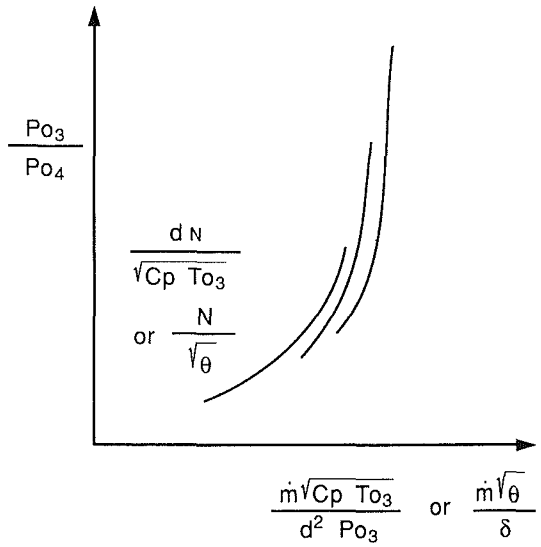

Fig. 5(*b*) **Turbine efficiency versus velocity ratio**

The performance characteristics are usually plotted as shown in Fig. 5. It can be seen from Fig. 5(*b*) that turbine efficiency is a function of the velocity ratio ($U_2/C_s$) and the speed parameter. The relationship between velocity ratio, pressure ratio, and speed parameter is of the form

$$\frac{U_2}{C_s} = \frac{\pi}{\sqrt{2}}\left(\frac{d_2 N}{\sqrt{C_p T_{03}}}\right)\left\{1 - \left(\frac{P_{04}}{P_{03}}\right)^{\frac{\gamma-1}{\gamma}}\right\}^{-1} \tag{16}$$

As in the case of the compressor, the performance characteristics of the turbine also are stored in two-dimensional look-up tables.

**Propelling Nozzle.** The propelling nozzle is intended to accelerate the exhaust gas leaving the turbine exit to the velocity of the jet. The expansion process is shown in Fig. 6. The pressure at the nozzle outlet may be greater than, equal to, or less than the prevailing free-stream pressure. The equations governing the nozzle flow are

$$T_5 = T_{04} - \frac{V_j^2}{2C_p} \tag{17}$$

$$P_{05} = P_{04} - \Delta P_0 \tag{18}$$

where $\Delta P_0 = \sum_1^n \delta P_0$; $\delta P_0$ = the loss of stagnation pressure in elemental length (1); $n$ = number of elemental steps in the nozzle.

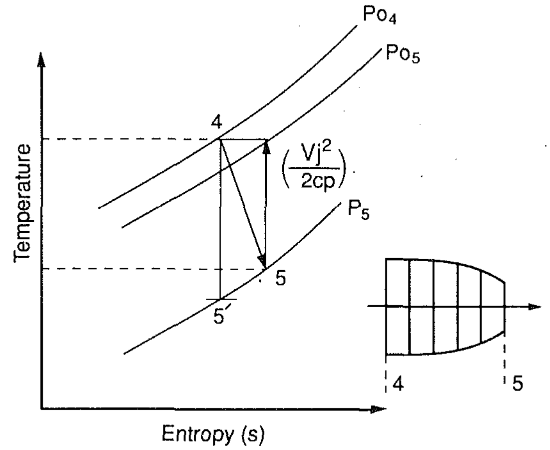

Fig. 6 Propelling nozzle process

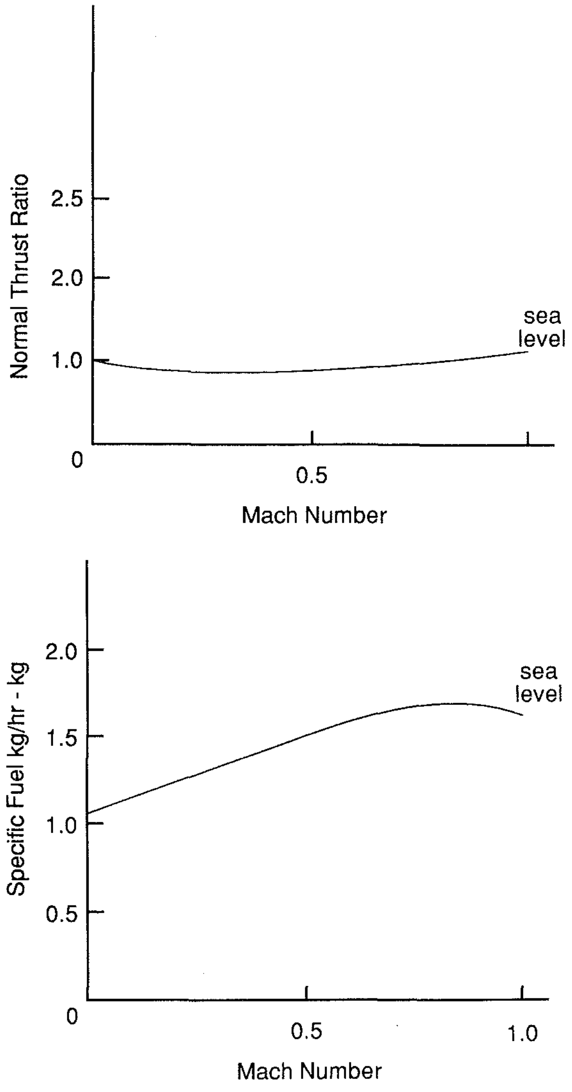

Fig. 7 Calculated performance

$$P_5 = P_{05}\left(\frac{T_5}{T_{04}}\right)^{\frac{\gamma}{\gamma-1}} \tag{19}$$

$$T_5' = T_{04}\left(\frac{P_5}{P_{04}}\right)^{\frac{\gamma}{\gamma-1}} \tag{20}$$

$$\eta_{\text{nozzle}} = \left\{\frac{T_{04} - T_5}{T_{04} - T_5'}\right\} \tag{21}$$

## Hardware and Software Requirements

The program has been written for the IBM-AT or compatible microcomputers with at least 1 Megabyte RAM, 40 Megabyte hard disk and Maths coprocessor. It should also run on PS/2-50 or higher systems.

The code uses Fortran 77 language. The output is saved in ASCII files; therefore the results as well as the input data can be plotted in the graphic form by using a suitable graphics package such as Microsoft CHART or any other advanced graphics package.

## Results

The program was used to calculate specific thrust and fuel consumption for a set of data from a proprietary engine. The results are shown in Fig. 7. The calculations were performed by increasing the flight Mach number in small increments. It has not been possible to compare the results with measured data for a variety of reasons; however, the trends shown in the diagrams appear to be acceptable.

## Conclusions

1 The paper describes a procedure that has been used to develop a program for simulating gas turbine engines. The program has been written in Fortran 77 for IBM AT or compatible microcomputers.

2 The main feature of the procedure is that components can be assembled to represent different engine configurations; therefore it should prove to be useful for exploratory studies at the design stage.

3 Although it has not been possible to compare the results obtained by calculations with test data, the trends shown appear to be acceptable.

## References

1 Durand Harlan, P., "Simulation of Jet Engine Transient Performance," ASME Paper No. 65-WA/MD-16, Nov. 1965.

2 Evans, D. G., "Method for Determining Component Matching and Operating Characteristics for Turbojet Engines," NASA-TM-X-1945, 1970.

3 Saravanamuttoo, H. I. H., and Fawke, A. J., "Simulation of Gas Turbine Dynamic Performance," ASME Paper No. 70-GT-23, May 1970.

4 Fawke, A. J., and Saravanamuttoo, H. I. H., "Digital Computer Method for Prediction of Gas Turbine Dynamic Response," SAE Paper No. 710550, June 1971.

5 Fawke, A. J., and Saravanamuttoo, H. I. H., "Digital Computer Simulation of the Dynamic Response of a Twin Spool Turbofan With Mixed Exhausts," *Aeronautical Journal*, Vol. XX, Sept. 1973, p. 471.

6 Cottington, R. V., "Total Power Plant Simulation," NASA Star Conf., Paper issue 15, ref. 75N23594, 1975.

7 Schobeiri, T., "A General Computational Method for Simulation and Prediction of Transient Behaviour of Gas Turbines," ASME Paper No. 86-GT-180, June 1986.

8 Mats, E. B., and Tunakov, A. P., "Requirements on Modern Mathematical Models of Gas Turbine Engines II," *Izvestiya vuz. Aviatsionnaya Tekhnika*, Vol. 25, No. 1, 1982, pp. 99-102.

9 Prokof'ev, A. N., "Mathematical Modelling of Regenerative Gas Turbine Engines," Allerton Press, Inc., United Kingdom, 1983.

**Y. Tsujikawa**

**M. Nagaoka**

Department of Aeronautical Engineering,
University of Osaka Prefecture,
Mozu-umemachi,
Sakai 591 Japan

# Determination of Cycle Configuration of Gas Turbines and Aircraft Engines by an Optimization Procedure

*This paper is devoted to the analyses and optimization of simple and sophisticated cycles, particularly for various gas turbine engines and aero-engines (including the scramjet engine) to achieve maximum performance. The optimization of such criteria as thermal efficiency, specific output, and total performance for gas turbine engines, and overall efficiency, nondimensional thrust, and specific impulse for aero-engines has been performed by the optimization procedure with the multiplier method. Comparison of results with analytical solutions establishes the validity of the optimization procedure.*

## Introduction

As the area of application of a gas turbine engine is extended, the thermodynamic cycle of the gas turbine becomes more sophisticated. The gas turbine engine basically consists of a compressor, a combustor, and a turbine. By the inclusion of heat exchangers such as a regenerator, an intercooler, and a precooler, the thermal efficiency and/or specific output can be improved. The increase of the number of components, however, requires more elaborate calculations to determine an optimum working cycle. In the case of the aero-engine, the basic system configuration is rather simple compared to that of a stationary gas turbine engine. However, the ambient conditions such as temperature, pressure, and flight Mach number are variable, and optimization of the cycle would be also necessary. Although there have been a few papers published (Giannuzzi et al., 1981; Sato et al., 1963) on the optimization of gas turbines and aero-engines, the optimization is not sufficient.

In the present study, the gas turbine is regarded as a system consisting of a number of subsystems (components). The operating state is expressed by the parameters that govern such subsystems. The optimization of criteria such as thermal efficiency, specific output, and total performance can be treated as a nonlinear programming problem. Using the multiplier method, even for complicated cycles, the optimum values of parameters can be calculated in a short time.

## Application of Optimization Procedure to Stationary Gas Turbine

A gas turbine consists of such components as a compressor, combustor, turbine, regenerator, and intercooler. A number of combinations are theoretically possible if, in addition to the positioning of the compressor and turbines, a distinction is drawn between the inclusion and omission of a regenerator and intercooler. A conventional three-group notation is adopted here (Mallinson et al., 1948). The first group gives the number of turbocompressor rotors. In this study, a single rotor is used and the symbol is, therefore, 1/ or 1/*C*. The second group indicates the position of the power turbine in the series of turbines, using the symbol *LP* for low-pressure turbine. The third group uses the symbols *I* and *E* to indicate the use of intercooler and regenerator, respectively. The calculation is carried out for the following schemes: 1/*C*, 1/*C*/*E*, 1/*C*/*I*, 1/*LP*, and 1/*LP*/*E*.

If the inlet condition of the working fluid is given, the outlet condition of each component can be determined using some parameters. Pressure ratio, temperature ratio, and component efficiency are generally used as parameters. In the present analysis, efficiencies and pressure losses of each component are assumed to be known in advance. Considering a relationship between temperature and pressure ratios of the components, the latter is transformed to temperature ratio by the following equation:

$$\theta_C = \frac{T_{\rm out}}{T_{\rm in}} = \left\{\left(\frac{P_{\rm out}}{P_{\rm in}}\right)^m - 1\right\}/\eta_C + 1 \tag{1}$$

where $m = R/C_p$ and $\eta_C$ is the adiabatic efficiency. A block diagram of the compressor is shown in Fig. 1. Since the temperature ratio for the combustor is calculated from compressor outlet temperature and turbine inlet temperature, the maximum temperature ratio of the cycle is introduced. It is defined as a ratio of turbine inlet temperature to ambient temperature. In the optimization procedure of the stationary gas turbine, the following assumptions are made:

1 The working fluid is a perfect gas with constant specific heat.

2 The temperature ratio of the cycle is constant.

---

Contributed by the International Gas Turbine Institute and presented at the 35th International Gas Turbine and Aeroengine Congress and Exposition, Brussels, Belgium, June 11-14, 1990. Manuscript received by the International Gas Turbine Institute February 5, 1990. Paper No. 90-GT-115.

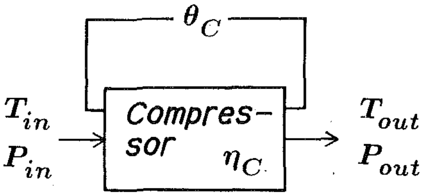

**Fig. 1 Block diagram of compressor**

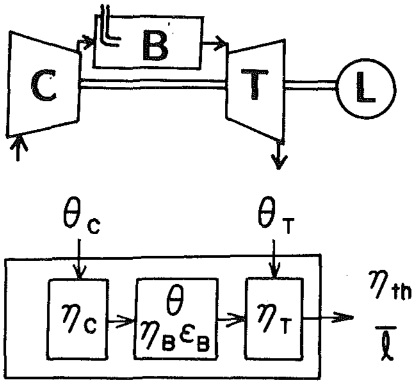

**Fig. 2 Arrangement and block diagram of stationary gas turbine scheme 1/C**

3 The increase of mass flow rate due to fuel addition and the mechanical loss are neglected.

First, a scheme $1/C$ is exemplified. The arrangement of cycle and the block diagram are depicted in Fig. 2. Using the temperature ratios of various components, nondimensional specific output and thermal efficiency are given by

$$\bar{l}=l/(C_pT_0)=\theta(1-\theta_T)-(\theta_C-1) \tag{2}$$

$$\eta_{th}=\eta_B\{1-(\theta\theta_T-1)/(\theta-\theta_C)\} \tag{3}$$

These parameters must satisfy the pressure equilibrium between inlet and outlet of the gas turbine, expressed by

$$h(\Theta)=\{1+(\theta_C-1)\eta_C\}\{1-(1-\theta_T)/\eta_T\}\times(1-\epsilon_B)^m-1=0 \tag{4}$$

The temperature ratios of compressor and turbine are constrained by the following inequalities:

$$\begin{aligned} g_1(\Theta)&=1-\theta_C\leq 0\\ g_2(\Theta)&=1-\theta\theta_T\leq 0\\ g_3(\Theta)&=-\eta_{th}\leq 0\end{aligned} \tag{5}$$

Therefore, a problem determining the design point of scheme $1/C$ is reduced to the constrained optimization problem by equations (4) and (5). It aims to obtain the parameter vector $\Theta=(\theta_C,\ \theta_T)$, which maximizes the criteria for evaluation, equations (2) and (3). However, as the temperature ratio that gives the maximum thermal efficiency, $\eta_{th_{\max}}$, generally differs from that for the maximum specific output, $l_{\max}$, the following objective function is newly introduced to determine the design point in accordance with demand:

$$Z_\alpha=\alpha\frac{\eta_{th}}{\eta_{th_{\max}}}+(1-\alpha)\frac{\bar{l}}{\bar{l}_{\max}} \qquad 0\leq\alpha\leq 1 \tag{6}$$

where $\alpha$ is a weighting factor. From this objective function, the optimum working condition can be obtained uniquely for any value of $\alpha$. The problem is arranged as follows:

Objective function $f(\Theta)=\eta_{th}$ or $\bar{l}$ or $Z_\alpha \Rightarrow$ maximize
Equality constraint $h_i(\Theta)=0$
Inequality constraint $g_j(\Theta)\leq 0$

The problems for any other schemes are reduced to the constrained optimization problem in the same manner.

## Search for Optimum Condition Using Multiplier Method

In order to solve the problem mentioned above, the multiplier method is used and the following augmented Lagrangian is introduced (Powel, 1969; Tapia, 1977):

$$\begin{aligned}\mathbf{L}_{t,r}(\Theta,\ \mu,\ \lambda)=&f(\Theta)+\sum_{i=1}^{m}\mu_ih_i(\Theta)+\frac{1}{2}r\{h_i(\Theta)\}^2\\ &+\frac{1}{2}\sum_{j=1}^{n}\{[\max\{0,\ \lambda_j+tg_j(\Theta)\}]^2-\lambda_j^2\}\end{aligned} \tag{7}$$

where $t$, $r$, $\mu_j$, and $\lambda_j$ are the constants. The algorithm of solution is shown below:

## Nomenclature

$A$ = cross-sectional area, $m^2$
$B$ = bypass ratio
$C_p$ = specific heat, kJ/kgK
$F$, $\bar{F}$ = specific thrust, N/(kg/s); nondimensional thrust
$f(\Theta)$ = objective function
$g(\Theta)$ = inequality constraint
$h(\Theta)$ = equality constraint
$H_u$ = lower heating value, kJ/kg
$I_{sp}$ = specific impulse, s
$l$, $\bar{l}$ = specific output, kW/(kg/s); nondimensional specific output
$L_{t,r}(x,\ \mu,\ \lambda)$ = augmented Lagrangian
$M_0$ = flight Mach number
$\dot{m}$ = mass flow rate kg/s
$r$ = variable used in multiplier method
$Z$ = evaluating function

$\alpha$ = weighting factor
$\beta$ = variable used in multiplier method
$\gamma$ = pressure ratio
$\epsilon$ = pressure loss coefficient
$\eta_B$ = combustion efficiency
$\eta_C$ = adiabatic efficiency of compressor
$\eta_{EX}$ = effectiveness of regenerator
$\eta_{HT}$ = adiabatic efficiency of high-pressure turbine
$\eta_{LT}$ = adiabatic efficiency of low-pressure turbine
$\eta_N$ = nozzle efficiency
$\eta_0$ = total efficiency
$\eta_{PR}$ = pressure recovery factor of inlet or diffuser
$\eta_{th}$ = thermal efficiency
$\Theta$ = parameter vector

$\theta$ = temperature ratio or cycle maximum temperature ratio
$\kappa$ = ratio of specific heat
$\lambda$ = constant used in multiplier method
$\mu$ = constant used in multiplier method
$\phi$ = equivalence ratio
$\omega$ = multiplying factor

### Subscripts

$B$ = combustor
$C$ = compressor
$CN$ = core nozzle
$D$ = diffuser
$EX$ = regenerator
$F$ = fan
$FN$ = fan nozzle
$HT$ = high-pressure turbine
$IC$ = intercooler
$LT$ = low-pressure turbine
$N$ = nozzle
$T$ = turbine

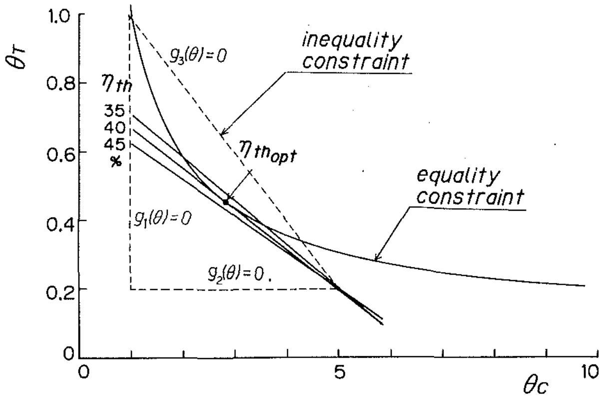

**Fig. 3 Optimum thermal efficiency of 1/C type under equality and inequality constraints**

[Step 0] $k=0$ and initial values of $t$, $r$, $\mu_j$, and $\lambda_j$ are given.
[Step 1] Initial components of parameter vector $\Theta$ are given.
[Step 2] The unconstrained optimization problem for $L_{t^k, r^k}(\Theta, \mu^k, \lambda^k)$ is solved by the conjugate gradient method. A solution is expressed as $\Theta^k$.
[Step 3] For sufficiently small value of $\epsilon$ (for example less than $10^{-6}$ or $10^{-7}$), if $h_i(\Theta^k)<\epsilon$ and $\max\{g_j(\Theta^k), (-\lambda_j^k/t^k)\}<\epsilon$ then [STOP], $\Theta^*=\Theta^k$ or else go to [Step 4]
[Step 4] For a multiplying factor $\omega>1$, $r^{k+1}=\omega r^k$, $\mu_i^{k+1}=\mu_i^k+r^k h_i(\Theta^k)$ in regard to $h(\Theta)$ and $t^{k+1}=\omega t^k$, $\lambda_j^{k+1}=\max\{0, \lambda_j^k+t^k g_j(\Theta^k)\}$ in regard to $g(\Theta)$.
[Step 5] $k=k+1$. Go to [Step 2].

$f(\Theta)$ is maximized for $\Theta^*$ obtained in the above procedure. For Scheme $1/C$, Fig. 3 shows an objective function, $f(\Theta)=\eta_{th}$, equality constraint, $h(\Theta)=0$, and inequality constraint $g_j(\Theta)\le 0$ in the $\theta_T-\theta_C$ plane. From this figure, the optimum condition is obtained as a point of contact between a curve of $h(\Theta)=0$ and line of $\eta_{th}=\text{const}$ within the region under the inequality constraint.

## Optimum Conditions for Stationary Gas Turbine Schemes

For other stationary gas turbine schemes, the equations in regard to the optimization problem are given as follows:

**Scheme 1/*C*/*E*:** $\Theta=(\theta_C, \theta_E, \theta_T)$

$$\begin{aligned}
&\bar{l}=\theta(1-\theta_T)-(\theta_C-1)\\
&\eta_{th}=\eta_B\{\theta(1-\theta_T)-(\theta_C-1)\}/(\theta-\theta_C\theta_E)\\
&h_1(\Theta)=\{1+(\theta_C-1)\eta_C\}\{1-(1-\theta_T)/\eta_T\}\\
&\quad\times\{(1-\epsilon_B)(1-\epsilon_{EX})^2\}^m-1=0\\
&h_2(\Theta)=\theta_C(\theta_E-1)-\eta_{EX}(\theta\theta_T-\theta_C)=0\\
&1\le\theta_C,\quad 1\le\theta_E,\quad \theta_C\theta_E\le\theta,\quad 0\le\theta_T\le 1
\end{aligned}\tag{8}$$

where $\eta_{EX}$ and $\epsilon_{EX}$ are the temperature efficiency of the regenerator and the pressure loss coefficient.

**Scheme 1/*C*/*I*:** $\Theta=(\theta_{C_1}, \theta_{C_2}, \theta_{IC}, \theta_T)$

$$\begin{aligned}
&\bar{l}=\theta(1-\theta_T)-(\theta_{C_1}-1)-(\theta_{C_2}-1)\\
&\eta_{th}=\eta_B\{\theta(1-\theta_T)-(\theta_{C_2}-1)-(\theta_{C_1}-1)\}/(\theta-\theta_{IC}\theta_{C_1}\theta_{C_2})\\
&h_1(\Theta)=\{1+(\theta_{C_1}-1)\eta_C\}\{1+(\theta_{C_2}-1)\eta_C\}\\
&\quad\times\{1-(1-\theta_{HT})/\eta_T\}\times\{(1-\epsilon_B)(1-\epsilon_{IC})\}^m-1=0\\
&h_2(\Theta)=\theta_{C_1}(1-\theta_{IC})-\eta_{IC}(\theta_{C_1}-T_W/T_0)=0\\
&1\le\theta_{C_1},\quad 1\le\theta_{C_2},\quad \theta_{IC}\le 1,\quad \theta_{C_1}\theta_{C_2}\le\theta,\quad 0\le\theta_T\le 1
\end{aligned}\tag{9}$$

where $\eta_{IC}$, $T_0$, and $T_W$ are temperature efficiency of intercooler, ambient temperature, and water temperature, respectively.

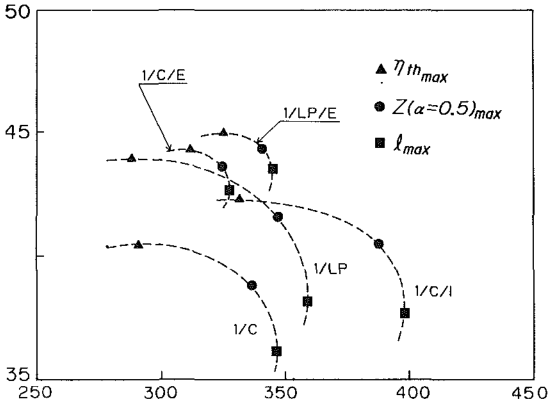

**Fig. 4 Performance of various gas turbine schemes**

**Scheme 1/*LP*:** $\Theta=(\theta_C, \theta_{HT}, \theta_{LT})$

$$\begin{aligned}
&\bar{l}=\theta\theta_{HT}(1-\theta_{LT})\\
&\eta_{th}=\eta_B\{\theta\theta_{HT}(1-\theta_{LT})\}/(\theta-\theta_C)\\
&h_1(\Theta)=\{1+(\theta_C-1)\eta_C\}\{1-(1-\theta_{HT})/\eta_{HT}\}\\
&\quad\times\{1-(1-\theta_{LT})/\eta_{LT}\}(1-\epsilon_B)^m-1=0\\
&h_2(\Theta)=\theta_{C_1}(1-\theta_{HT})-(\theta_C-1)=0\\
&1\le\theta_C\le\theta,\quad 0\le\theta_{HT}\le 1,\quad 0\le\theta_{LT}\le 1
\end{aligned}\tag{10}$$

**Scheme 1/*LP*/*E*:** $\Theta=(\theta_C, \theta_E, \theta_{HT}, \theta_{LT})$

$$\begin{aligned}
&\bar{l}=\theta\theta_{HT}(1-\theta_{LT})\\
&\eta_{th}=\eta_B\{\theta\theta_{HT}(1-\theta_{LT})\}/(\theta-\theta_C\theta_E)\\
&h_1(\Theta)=\{1+(\theta_C-1)\eta_C\}\{1-(1-\theta_{HT})/\eta_{HT}\}\\
&\quad\times\{1-(1-\theta_{LT})/\eta_{LT}\}\{(1-\epsilon_B)(1-\epsilon_{EX})^2\}^m-1=0\\
&h_2(\Theta)=\theta_{C_1}(1-\theta_{HT})-(\theta_C-1)=0\\
&1\le\theta_C,\quad 1\le\theta_E,\quad \theta_E\le\theta,\quad 0\le\theta_{HT}\le 1,\quad 0\le\theta_{LT}\le 1
\end{aligned}\tag{11}$$

**Optimum Performances for Various Gas Turbine Schemes.** The results of calculation for various gas turbine schemes are tabulated in Table 1, and shown in Fig. 4. As shown in this figure, by changing the weighting factor $\alpha$ from zero to unity, the total performance $Z(\alpha)$ draws the arcs depicted by the dotted lines between $\eta_{th_{\max}}$ and $\bar{l}_{\max}$. These curves also show those obtained by varying the pressure ratio of the compressor. The results for various gas turbine schemes are compared with the analytical solutions (Sato et al., 1963; Matsumoto, 1978) as listed in Table 2, which shows better agreement with an accuracy of more than four figures.

## Optimum Conditions for Aircraft Engines

For aircraft engines, the overall efficiency $\eta_0$ and nondimensional specific thrust $\bar{F}$ are used as the objective functions in place of the thermal efficiency and nondimensional specific output. The specific fuel consumption, $\text{sfc}_{\min}$, however, is equivalent to $\eta_{0_{\max}}$. When the temperature ratio of the cycle is given and the flight Mach number is introduced as a parameter, the maximum overall efficiencies, $\eta_{0_{\max}}$, for turbojet and turbofan engines coincide to those of ramjet engine. If ram temperature ratio $\theta_D$ is given in addition to $\theta$, the optimum conditions can be determined corresponding to the flight Mach number. For some aircraft engines, the equation in relation to the optimization problem is given as follows:

**Table 1 Optimum values of various stationary gas turbine schemes**

| Type | Objective Function | Value of parameters | | | | $\eta_{th}$ | $\ell$ |
|---|---|---|---|---|---|---|---|
| | | $\theta_C/\phi_C$ | $\theta_E$ | | $\theta_T$ | (%) | (kW/kg s) |
| $1/C$ | $\eta_{th}$ | 2.837/38.53 | | | 0.4541 | 40.43 | 291.3 |
| | $\bar{\ell}$ | 2.133/13.72 | | | 0.5620 | 36.12 | 346.8 |
| | $Z_{0.5}$ | 2.400/20.98 | | | 0.5141 | 38.79 | 337.1 |
| $1/C/E$ | $\eta_{th}$ | 1.833/8.00 | 1.558 | | 0.6393 | 44.33 | 311.4 |
| | $\bar{\ell}$ | 2.152/14.14 | 1.236 | | 0.5656 | 42.71 | 327.6 |
| | $Z_{0.5}$ | 2.001/11.05 | 1.363 | | 0.5962 | 43.79 | 324.6 |
| | | $\theta_{C1}/\phi_{C1}$ | $\theta_{C2}/\phi_{C2}$ | | $\theta_T$ | $\eta_{th}$ | $\ell$ |
| $1/C/I$ | $\eta_{th}$ | 1.317/2.53 | 2.492/24.01 | | 0.4175 | 42.35 | 331.5 |
| | $\bar{\ell}$ | 1.619/5.16 | 1.619/5.16 | | 0.4925 | 37.67 | 398.8 |
| | $Z_{0.5}$ | 1.490/3.86 | 1.933/9.64 | | 0.4600 | 40.49 | 388.1 |
| | | $\theta_C/\phi_C$ | $\theta_E$ | $\theta_{HT}$ | $\theta_{LT}$ | $\eta_{th}$ | $\ell$ |
| $1/LP$ | $\eta_{th}$ | 3.028/48.90 | | 0.6006 | 0.7054 | 43.97 | 288.4 |
| | $\bar{\ell}$ | 2.187/15.00 | | 0.7678 | 0.7150 | 38.12 | 359.0 |
| | $Z_{0.5}$ | 2.497/24.18 | | 0.7065 | 0.6992 | 41.59 | 347.8 |
| $1/LP/E$ | $\eta_{th}$ | 1.866/8.52 | 1.517 | 0.8297 | 0.7600 | 44.98 | 325.1 |
| | $\bar{\ell}$ | 2.199/15.31 | 1.194 | 0.7645 | 0.7242 | 43.53 | 344.8 |
| | $Z_{0.5}$ | 2.073/12.39 | 1.300 | 0.7892 | 0.7353 | 44.40 | 341.5 |

$\theta = 5,\ \eta_C = 0.85,\ \eta_B = 0.98,\ \eta_T = \eta_{HT} = 0.90,\ \eta_{LT} = 0.88,$
$\eta_{EX} = 0.75,\ \eta_{IC} = 0.85,\ \varepsilon_B = \varepsilon_{EX} = \varepsilon_{IC} = 0.03,$
$C_p = 1.114\ (\mathrm{kJ/kgK}), T_0 = T_w = 288.15\ \mathrm{K}$

**Table 2 Comparison of the results obtained with those of analytical solutions**

(*a*)

| Type | Objective Function | Analytical Solution | Numerical (This study) |
|---|---|---|---|
| $1/C$ | $\eta_{th}$ | 2.8374 | 2.8373 |
| | $\bar{l}$ | 2.1335 | 2.1335 |
| $1/C/E$ | $\eta_{th}$ | 1.8331 | 1.8331 |
| | $\bar{l}$ | 2.1517 | 2.1516 |

(values of $\theta_C$)

(*b*)

| Type | Objective Function | Analytical Solution | Numerical (This study) |
|---|---|---|---|
| $1/C/I$ | $\eta_{th}$ | 42.37 | 42.35 |

(values of $\eta_{th}$)

**Turbojet Engine:** $\Theta = (\theta_C, \theta_T, \theta_N)$

$$
\begin{aligned}
&\bar{F} = F/\sqrt{C_p T_0} = \sqrt{2\theta\theta_T(1-\theta_N)} - \sqrt{2(\theta_D - 1)}\\
&\eta_0 = 2\eta_B\{\sqrt{\theta\theta_T(1-\theta_N)(\theta_D-1)} - (\theta_D - 1)\}/(\theta - \theta_D\theta_C)\\
&\mathrm{sfc} = 3600\sqrt{2C_pT_0(\theta_D-1)}/Hu/\eta_o\\
&h_1(\Theta) = \theta_D\{1 + (\theta_C - 1)\eta_C\}\{1 - (1-\theta_T)/\eta_T\}\\
&\quad \times\{1-(1-\theta_N)\eta_N\}\{(1-\epsilon_B)(1-\epsilon_D)\}^m - 1 = 0\\
&h_2(\Theta) = \theta(1-\theta_T) - \theta_D(\theta_C - 1) = 0\\
&1 \le \theta_C,\quad \theta_D\theta_C \le \theta,\quad 0 \le \theta_T \le 1,\quad 0 \le \theta_N \le 1
\end{aligned}
\tag{12}
$$

As shown in the above equation, if $\theta_D$ is kept constant, sfc is inversely proportional to $\eta_0$. In regard to ramjet engine, the calculation of $\Theta = (\theta_D, \theta_N)$ can be performed when $\theta_C = \theta_T = 1$ and $\theta_D$ is used as variable. The pressure loss coefficient of the diffuser $\epsilon_D$ is assumed to be zero for a subsonic transport. On the other hand, a supersonic diffuser uses external compression and is followed by internal compression, which involves three oblique shocks and a normal shock (Künkler, 1973). The minimum pressure loss coefficient is obtained for various flight Mach numbers using the multiplier method.

**Ramjet Engine:** $\Theta = (\theta_D, \theta_N)$

For a ramjet engine, in equation (12) $\theta_C = \theta_T = 1$. $\theta_D$ and $\theta_N$ are used as parameters

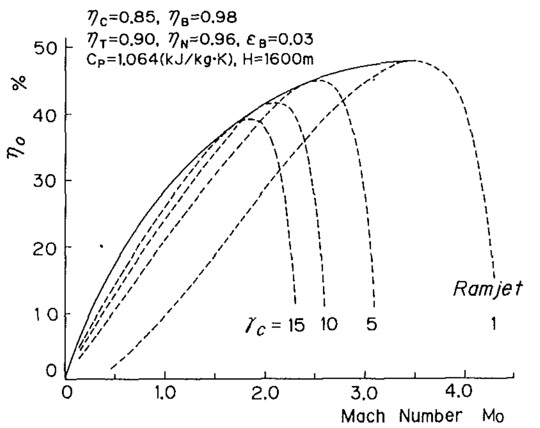

**Fig. 5 Optimum overall efficiency of turbojet engine with various compressor pressure ratio**

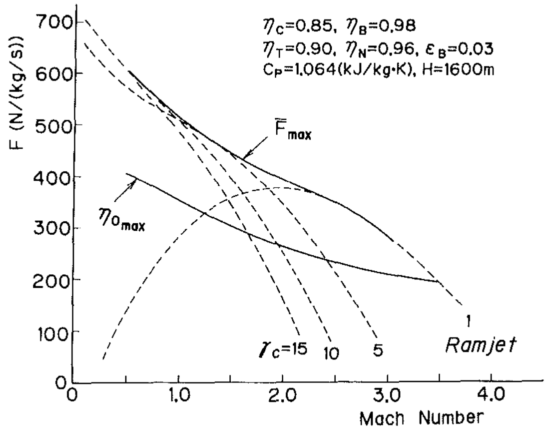

**Fig. 6 Optimum specific thrust of turbojet engine versus flight Mach number ($\theta = 5$)**

$$
\begin{aligned}
&\bar{F} = \sqrt{2\theta(1-\theta_N)} - \sqrt{2(\theta_D - 1)}\\
&\eta_0 = 2\eta_B\{\sqrt{\theta(1-\theta_N)(\theta_D-1)} - (\theta_D-1)\}/(\theta - \theta_D)\\
&h_1(\Theta) = \theta_D\{1-(1-\theta_N)/\eta_N\}\{\eta_{PR}(1-\epsilon_B)\}^m - 1 = 0\\
&1 \le \theta_D,\quad \theta_D \le \theta,\quad 1 \le \theta\theta_N,\quad \theta_N \le 1
\end{aligned}
\tag{13}
$$

**Turbofan Engine:** $\Theta = (B, \theta_F, \theta_C, \theta_T, \theta_{CN}, \theta_{FN})$

In order to compare the results with those obtained by Sato (1963), the same equations and assumptions are adopted. The polytropic efficiencies of fan, compressor, and turbine are used

$$
\begin{aligned}
&\bar{F} = \sqrt{2\eta_{CN}\theta\theta_T(1-\theta_{CN})} + B\sqrt{2\eta_{FN}\theta_D\theta_F(1-\theta_{FN})}\\
&\quad -(1+B)\sqrt{2(\theta_D - 1)}\\
&\eta_0 = 2\eta_B\{\sqrt{\eta_{CN}\theta\theta_T(1-\theta_{CN})(\theta_D-1)} + B\sqrt{\eta_{FN}\theta_D\theta_F}\\
&\quad \times\sqrt{(1-\theta_{FN})(\theta_D-1)} - (1+B)(\theta_D-1)\}/(\theta-\theta_D\theta_C)\\
&h_1(\Theta) = \theta_D\theta_C^{\eta_{PC}}\theta_T^{1/\eta_{PT}}\theta_{CN} - 1 = 0\\
&h_2(\Theta) = \theta_D\theta_F^{\eta_{PF}}\theta_{FN} - 1 = 0\\
&h_3(\Theta) = \theta(1-\theta_T) - \theta_D(\theta_C - 1) - B\theta_D(\theta_F - 1) = 0\\
&0 \le B,\quad 1 \le \theta_F,\quad 1 \le \theta_C \le \theta,\quad 0 \le \theta_T \le 1,\quad 0 \le \theta_{CN} \le 1,\\
&\quad 0 \le \theta_F \le 1
\end{aligned}
\tag{14}
$$

where $\theta_{CN}$, $\theta_{FN}$ denote temperature ratios by isentropic expansion of core nozzle and fan nozzle, respectively.

**Optimum Performances for Various Aircraft Engines.** The optimum overall efficiency obtained for a turbojet engine and those for a ramjet engine are shown in Fig. 5. Increasing flight Mach number for turbojet engine, temperature ratios of

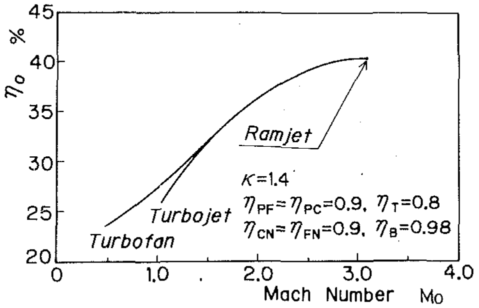

**Fig. 7 Optimum overall efficiency of various aircraft engines versus flight Mach number**

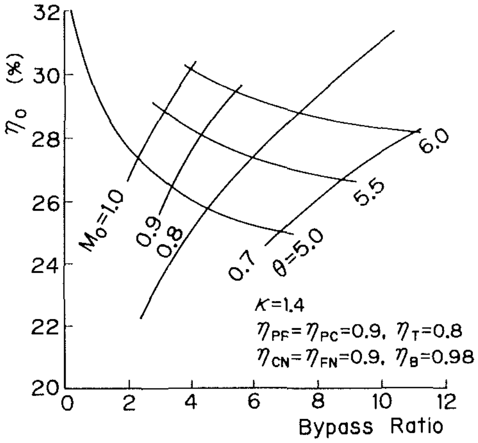

**Fig. 8 Relation between optimum overall efficiency and bypass ratio**

compressor and turbine, $\theta_C$ and $\theta_T$, asymptote unity correspond to the values of the ramjet engine. Dotted lines show the results for constant pressure ratio. The envelope (solid line) of those curves forms the optimum overall efficiency. For turbojet engines, the values of various parameters that maximize the overall efficiency differ from those for maximum nondimensional specific thrust. Hence, it is recommended to introduce a new criterion for total performance. Figure 6 shows the maximum (optimum) specific thrust of the turbojet engine, which is optimized for overall efficiency or nondimensional specific thrust as an objective function.

The optimum conditions of the turbofan engine are depicted in Fig. 7. As shown in this figure, for $\theta = 5$ the turbofan engine is superior to turbojet in overall efficiency for $M_0 < 1.5$. However, as Mach number increases, the corresponding bypass ratio of turbofan engine decreases to zero for approximately $M_0 = 1.5$. The turbojet engine is superior for $M_0 > 1.5$. As shown in Fig. 8, for higher maximum temperature, the large bypass ratio and large compressor pressure ratio are required, which suggests the advent of ultrahigh bypass ratio engines and unducted fan engines.

## Application of Optimization Procedure to Scramjet Engine

The schematic presentation of the scramjet engine used in this study is shown in Fig. 9, and is a generic derivation of some recent scramjet powered vehicle concepts. For simplicity, and to be consistent with some of the engine configurations that have been proposed, it is assumed that the scramjet inlet is located beneath the main body and sufficiently far aft that the effects of forebody compression are negligible.

### Analysis

*Inlet.* Schematics of external compression inlet are shown in Fig. 10. The air capture ratio $A_0/A_I$ is a function of flight

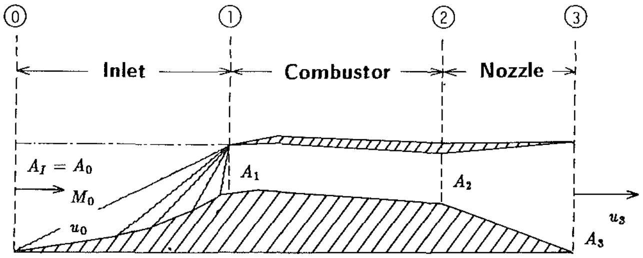

**Fig. 9 Schematics of scramjet engine**

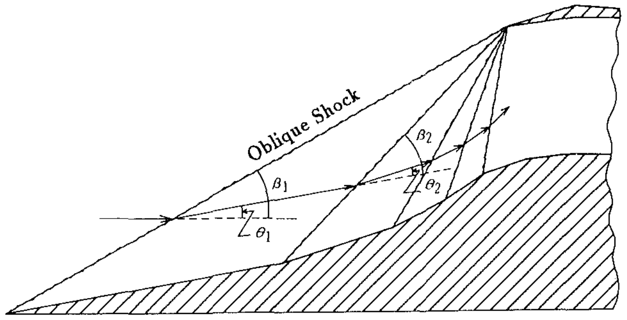

**Fig. 10 Schematics of external compression inlet**

Mach number, where $A_I$ denotes the cross-sectional area of the inlet. For simplicity, it is assumed to be unity in the present analysis. Multi-oblique shock external compression inlet is adopted. The pressure recovery factor through one oblique-shock stage, therefore, is expressed by

$$\left(\frac{p_{t_2}}{p_{t_1}}\right)_i = \left(\frac{2\kappa}{\kappa+1} M_1^2 \sin^2 \beta - \frac{\kappa-1}{\kappa+1}\right)^{-1/(\kappa-1)} \times \left[\frac{\{(\kappa-1)/2\} M_1^2 \sin^2\beta + 1}{\{(\kappa-1)/2\} M_1^2 \sin^2\beta}\right]^{-\kappa/(\kappa-1)} \tag{15}$$

*Combustor.* In the combustor, the pressure-area relationship suggested by Crocco (1958) is used as

$$pA^{\epsilon/(\epsilon-1)} = \text{const} \tag{16}$$

For simplicity, specific heat is constant; the wall shear and heat conduction through the wall are assumed to be neglected. The relationship between the ratio of total temperature and Mach number is written as

$$\frac{T_{t2}}{T_{t1}} = \left[\frac{N(M_2)}{N(M_1)}\right]^2 \tag{17}$$

where

$$N(M) = M\sqrt{1 + \frac{\kappa-1}{2} M^2/(\epsilon + \kappa M^2)}$$

The total pressure loss is a key parameter and is expressed by

$$\frac{p_{t2}}{p_{t1}} = \frac{p_2}{p_1}\left[\left(1 + \frac{\kappa-1}{2} M_2^2\right)\Big/\left(1 + \frac{\kappa-1}{2} M_1^2\right)\right]^{\kappa/(\kappa-1)} = \left[\frac{\epsilon + \kappa M_1^2}{\epsilon + \kappa M_2^2}\right]^{\epsilon} \left[\frac{2 + (\kappa-1) M_2^2}{2 + (\kappa-1) M_1^2}\right]^{\kappa/(\kappa-1)} \tag{18}$$

*Engine Performance.* In the nozzle, the calculations were made for frozen-nozzle expansions, i.e., the composition in the expansion process is fixed at that corresponding to equilibrium at the combustor exit. Engine thrust is expressed by

$$F = \lambda(\dot{m}_a + \dot{m}_f) u_3 - \dot{m}_a u_0 \tag{19}$$

where $\lambda = (1 + \cos \alpha_N)/2$. The specific impulse is shown as

$$I_{sp} = F/(\dot{m}_f g) \tag{20}$$

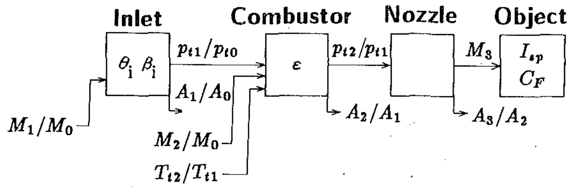

Fig. 11 Block diagram of scramjet engine

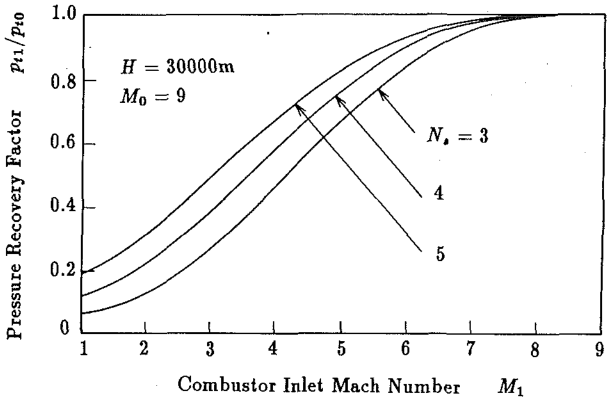

Fig. 12 Optimum pressure recovery factor of inlet ($M_0 = 9$)

**Development of Optimization.** Figure 11 shows the block diagram of scramjet engine. The specific impulse is regarded as an objective function. The parameter vector is shown as $\Theta = (M_1/M_0, M_2/M_0, T_{t2}/T_{t1}, \epsilon)$. In the same manner as that for gas turbine schemes, the equality and inequality constraints are written by

$$I_{sp} \Rightarrow \text{maximize}$$
$$h_1(\Theta) = \frac{T_{t2}}{T_{t1}} - \left[\frac{N(M_2)}{N(M_1)}\right]^2 = 0$$
$$h_2(\Theta) = M^2_{\text{crit}} - \{\kappa/\epsilon - (\kappa-1)\}^{-1} = 0$$
$$1 \leq \epsilon \leq (\kappa-1)/\kappa, \quad 1 \leq T_{t2}/T_{t1} \leq (T_{t2}/T_{t1})_{\phi=1} \qquad (21)$$

**Results of Optimization.** In the present study, since only the external compression is adopted, much better pressure recovery can be obtained by taking advantage of a characteristic of shock waves: For a given Mach number, a series of weak shocks produces much less stagnation pressure loss than one strong shock. The pressure recovery factor versus combustor-inlet Mach number with the number of oblique shocks as parameter is shown in Fig. 12. The further gains are obtained by introducing more oblique shocks. The penalty in weight due to more complicated mechanics, however, is inevitable.

The total pressure loss distribution is shown in Fig. 13. The total pressure is divided into three parts. Region ① shows the total pressure loss generated in the inlet, and ② shows that in the combustor. Therefore, region ③ means the total pressure remained at nozzle inlet. Finally, the optimization of the scramjet engine is a trade-off between ① and ②. The total pressure at nozzle inlet decreases with the increase of the equivalence ratio.

The optimum specific impulse is shown in Fig. 14 for $\phi = 1$. A high specific impulse of more than 3000 s is realized. It decreases with the increase of flight Mach number and flight altitude.

## Concluding Remarks

The optimum working conditions for various stationary gas turbine schemes and aircraft engines have been determined by the method of optimization. The conclusions of this research can be summarized as follows.

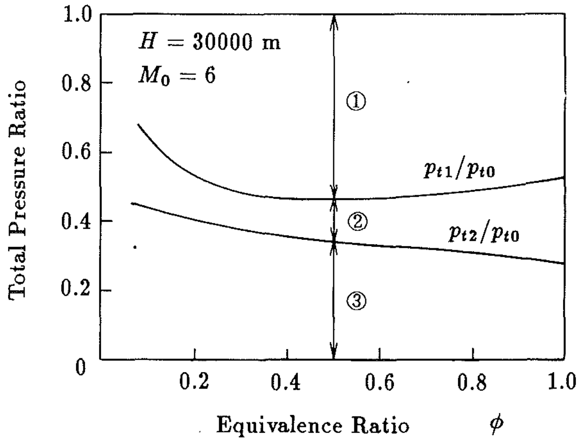

Fig. 13 Total pressure loss distribution at components

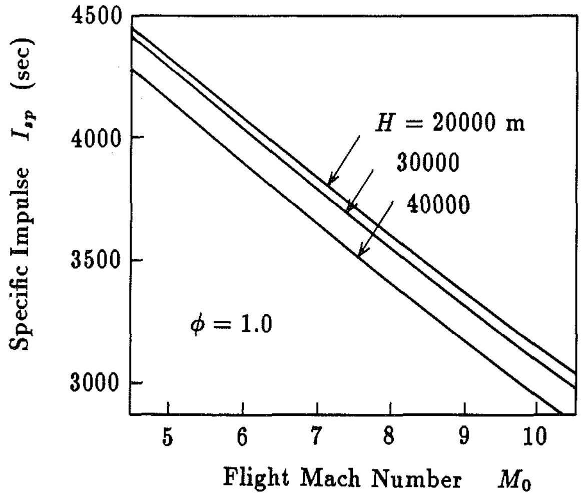

Fig. 14 Optimum specific impulse

In the design procedure of various gas turbine schemes, an optimum working cycle can be determined by the multiplier method in a short calculation time. This method of optimization can be applied to other complicated gas turbine schemes and aircraft engines (including scramjet engines). The optimum working conditions obtained agree very well with those obtained from analytical solutions and conventional trial and error methods with changing pressure ratio.

Consequently, if a new engine concept is to be considered, the working cycle can be optimized preliminarily by using this method before the details of design are completed.

## References

Crocco, L., 1958, *Fundamentals of Gas Dynamics*, Princeton University Press, Princeton, NJ.

Giannuzzi, L. F., et al., 1981, ASME Paper No. 81-JPGG-GT-6.

Künkler, H., 1973, "Der Einfluss der Luftvorkühlung vor der Verdichtung bei Luftatmenden Antrieben eines Raumfahrzeugträgers," Ph.D. Thesis, Technische Hochschüle Aachen, Germany.

Mallinson, D. H., et al., 1948, "The Part-Load Performance of Various Gas-Turbine Engine Schemes," *Proc. IMechE*, Vol. 159, pp. 198–219.

Matsumoto, N., 1978, "Study on Static and Dynamic Characteristics of Gas Turbine by Applying the Optimization Procedure," Ph.D. Thesis, Sophia University.

Powel, M. J. D., 1969, "A Method for Nonlinear Constraints in Minimization Problems," in: *Optimization*, R. Fletcher, ed., Academic Press, New York.

Sato, T., et al., 1963, "The Calculation of the Optimum Conditions of Bypass Engine," *Trans. JSME*, Vol. 29, pp. 979–987.

Tapia, R. A., 1977, "Diagonalized Multiplier Methods and Quasi-Newton Methods for Constrained Optimization," *J. Optimization Theory and Appl.*, Vol. 22, pp. 135–194.

# A New Method of Predicting the Performance of Gas Turbine Engines

**Wang Yonghong**
Department of Power Machinery Engineering,
Shanghai Jiao Tong University,
Shanghai, The People's Republic of China

*This paper points out that the turbine performance computation method used widely at present in solving the performance of gas turbine engines is a numerically unstable algorithm. Therefore a new method, namely an inverse algorithm, is proposed. This paper then further proposes a new mathematical model for solving the stable performance of gas turbine engines. It has the features of not only being suitable for an inverse algorithm for turbine performance, but also having fewer dimensions than existing models. It has the advantages of high accuracy, rapid convergence, good stability, fewer computations, and so forth. It has been fully proven that the accuracy of the new model is much greater than that of the common model for gas turbine engines. Additionally, the time consumed for solving the new model is approximately 1/4 ~ 1/10 of that for the common model. Therefore, it is valuable in practice.*

## Introduction

In the calculation of gas turbine engine performance, it is necessary to solve the following set of nonlinear equations:

$$\mathbb{E}(X) = 0, \qquad X \in D \subset R^n, \qquad \mathbb{E} \in R^n \tag{1}$$

Although the methods of solving equations (1) have been published previously in the literature, calculation practice shows that one of the most effective methods is the iterative calculation of the Newton–Raphson formula

$$X^{k+1} = X^k - J(\mathbb{E}, X)^{-1}_{x=x^k} \mathbb{E}^k \tag{2}$$

where $J(\mathbb{E}, X)$ is the Jacobian matrix of the residual values $\mathbb{E}$, of order $(n \times n)$, i.e.,

$$J(\mathbb{E}, X) = \begin{bmatrix} \dfrac{\partial E_1}{\partial x_1} & \dfrac{\partial E_1}{\partial x_2} & \cdots & \dfrac{\partial E_1}{\partial x_n} \\ \dfrac{\partial E_2}{\partial x_1} & \dfrac{\partial E_2}{\partial x_2} & \cdots & \dfrac{\partial E_2}{\partial x_n} \\ \dfrac{\partial E_n}{\partial x_1} & \dfrac{\partial E_n}{\partial x_2} & \cdots & \dfrac{\partial E_n}{\partial x_n} \end{bmatrix} \tag{3}$$

When the performance of gas turbine engines is solved with the help of the *N-R* method, the following problems exist and have not been solved satisfactorily to date:

1 When a gas turbine engine works at part load, the surge of compressor and the over-temperature of turbine have great influences upon the work of the gas turbine engine. It can greatly decrease the work range of the engine and make the local convergence region narrower. It follows that the initial approximate solution has to be chosen close to the correct solution, but that is hard to do. Thus, the iteration in the computational process sometimes fails to converge.

2 Experience from computation tells us that when the dimensions of the Jacobian Matrix in Newton–Raphson iteration formula (2) are greater than or equal to 3, its inverted matrix is liable to become ill conditioned.

3 The mathematical model (1) cannot be expressed by an analytic formula. Therefore, the Jacobian matrix in formula (2) can be determined only by finite difference method. If $X$ is a vector of the order $(n \times 1)$, then using the forward or backward difference, the time required for calculating $J(\mathbb{E}, X)$ is $n$ times that for calculating $\mathbb{E}(x)$. Thus, the amount of work for computation is large.

4 In a variety of current algorithms, computation of the performance of a turbine in the gas turbine engine is conducted in the sequence of high-pressure, intermediate pressure, and low-pressure turbines. The $\pi_T^*$ value of every turbine is obtained from the given $\bar{G}_{HT}$, according to the characteristic curves of every turbine. This algorithm will be called "sequential algorithm" in this paper. It has been found through research that the sequential algorithm is a numerically unstable algorithm. It will result in significant errors on turbine performance and overall performance under certain conditions (see the next section).

This paper will discuss why the sequential algorithm resulted in error, and a new method, that is, the inverse algorithm, will be proposed. Then, a new model for solving the performance of gas turbine engines will be recommended to obtain a more rapidly converging and more accurate solution.

## Analysis and Study of Turbine Performance

While solving the set of equations (1), the computation of

---

Contributed by the International Gas Turbine Institute and presented at the 35th International Gas Turbine and Aeroengine Congress and Exposition, Brussels, Belgium, June 11–14, 1990. Manuscript received by the International Gas Turbine Institute January 22, 1990. Paper No. 90-GT-337.

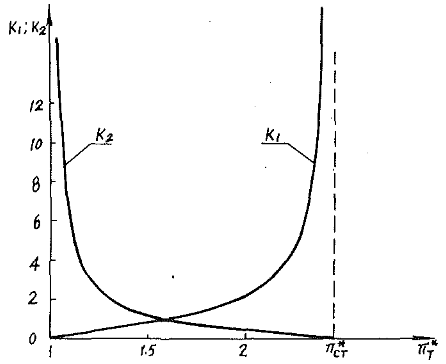

**Fig. 1** Variations of $K_1$ and $K_2$ with $\pi^*_T$ in a certain turbine

turbine performance will be involved. The reason leading to error in the sequence algorithm, which is used widely at present, may be analyzed as follows.

With respect to the flow characteristic curve at a certain value of $\lambda_u$ in a conventional turbine characteristic diagram, we have the following differential equation:

$$\frac{d\bar{G}}{d\pi^*_T} = f^2 \frac{(\pi^*_{cr} - \pi^*_T)}{\bar{G}} \tag{4}$$

where $f$ is the correction factor when the flow characteristic curve at a certain value of $\lambda u$ does not coincide with the ellipse rule completely. By rearranging equation (4) we have

$$\delta\pi^*_T = k_1 \delta\bar{G} \tag{5}$$

where the operator $\delta$ is the relative error, for example, $\delta\bar{G} = d\bar{G}/\bar{G}$, $\delta\pi^*_T = d\pi^*_T/\pi^*_T$ and so on. $K_1$ is the propagation factor of error and it is given by

$$K_1 = \frac{\bar{G}^2}{f^2 \pi^*_T (\pi^*_{cr} - \pi^*_T)} \tag{6}$$

It is seen in equation (5) that when $\pi^*_T$ is obtained from $\bar{G}$ by the sequential algorithm and the $\bar{G}$ at the inlet of a turbine has a deviation of $\delta\bar{G}$ because of round-off error and interpolation error, the value of $\delta\pi^*_T$ is surely $K_1$ times $\delta\bar{G}$. The relationship between $K_1$ and $\pi^*_T$ for a conventional turbine, by the use of equation (6), is shown in Fig. 1. It is shown in the figure that $K_1$ increases with the increase of $\pi^*_T$. When $\pi^*_T$ approaches its critical value $\pi^*_{cr}$, $K_1 \to \infty$, theoretically. Therefore, when the turbine works at high load, a significant error may result.

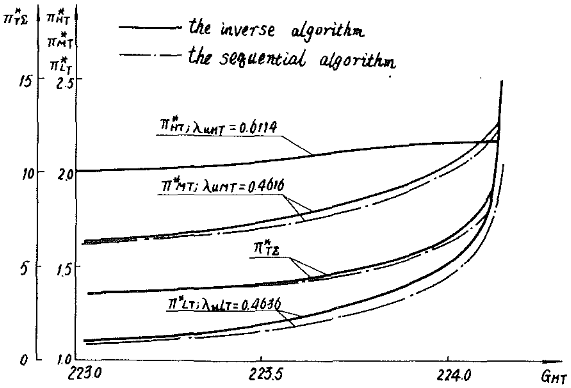

**Fig. 2** Variations of $\pi^*_{HT}$, $\pi^*_{MT}$, $\pi^*_{LT}$, and $\pi^*_{T\Sigma}$, with $G_{HT}$

To reduce errors, a new computation method for predicting turbine performance, which is called the inverse algorithm, is proposed here. By inverse algorithm it is meant that by the use of the $\pi^*_T$ of the last turbine, the $\bar{G}$ of every preceding turbine can be found according to the turbine characteristic curves. Rearranging equation (5), we have

$$\delta\bar{G} = k_2 \delta\pi^*_T \tag{7}$$

where $k_2$ is the propagation factor of error and is given by

$$K_2 = \frac{1}{K_1} = \frac{f^2 \pi^*_T (\pi^*_{cr} - \pi^*_T)}{\bar{G}^2} \tag{8}$$

It is shown in equation (7) that when $\bar{G}$ is obtained from $\pi^*_T$ by inverse algorithm, the $\delta\bar{G}$ is surely $K_2$ times $\delta\pi^*_T$. Figure 1 also shows the relationship between $K_2$ and $\pi^*_T$ for a conventional turbine by the use of equation (8). It is shown in the figure that $K_2$ decreases with the increase of $\pi^*_T$, when $\pi^*_T$ approaches its critical value $\pi^*_{cr}$, $K_2 \to 0$, theoretically. Thus, a high load on the turbine will result in a smaller propagated error. The combination of $\pi^*_T = 1$ and $K_2 \to \infty$ is impossible in a gas turbine. This is because the expansion ratio of all turbines is always larger than 1 even if it is idling.

In order to analyze the differences between the two algorithms further, we cite an example for explanation. The high-pressure, intermediate pressure, and low-pressure turbines of a certain marine gas turbine engine operate in series connection. The $\pi^*_T$ and $\bar{G}$ of every turbine and the total expansion ratio $\pi^*_{T\Sigma}$ are calculated by the sequential algorithm

## Nomenclature

$be$ = fuel rate
$Cp$ = constant pressure specific heat
$D$ = mean diameter at inlet of first stage rotor blade of turbine
$\mathbb{E}$ = residual values, vector of order $(n \times 1)$
$E$ = residual value
$f$ = fuel–air ratio, or correction factor
$G$ = mass flow quantity
$\bar{G}$ = reduced flow quantity
$k$ = adiabatic exponent
$N$ = rotational speed
$P$ = power output, or pressure
$R$ = gas constant
$T$ = initial temperature
$X$ = independent variables, vector of order $(n \times 1)$
$x$ = independent variable
$\eta$ = adiabatic efficiency
$\eta_m$ = mechanical efficiency
$\eta_{m1}$ = mechanical efficiency of low-pressure rotor
$\eta_{m2}$ = mechanical efficiency of high-pressure rotor
$\lambda_u$ = corrected rotational speed in dimensionless form
$\pi$ = expansion ratio of turbine, or compression ratio of compressor
$\sigma$ = recovery factor of total pressure
$\tau(\lambda)$ = temperature ratio; $\tau(\lambda) < 1$
$\omega$ = relaxation factor

**Subscripts**

$B$ = combustion chamber
$C$ = compressor
$cr$ = critical value
$e$ = effective
$ex$ = exit
$g$ = gas
$H$ = high pressure
$in$ = inlet
$L$ = low pressure, or load
$M$ = intermediate pressure
$T$ = turbine, or intermediate transition sector
$o$ = design condition
1 = inlet of low-pressure compressor
2 = inlet of high-pressure compressor
3 = inlet of combustion chamber
4 = inlet of high-pressure turbine
5 = inlet of intermediate pressure turbine
6 = inlet of low-pressure turbine
7 = exit of low-pressure turbine

**Superscripts**

$*$ = stagnation
$k$ = $(k)$th iteration
$k+1$ = $(k+1)$th iteration

and inverse algorithm, respectively, assuming the $\lambda_{\mathrm{UHT}}$ values, the $\lambda_{\mathrm{UMT}}$ values, the $\lambda_{\mathrm{ULT}}$ values, and the $\bar{G}_{HT}$ values are the same. The relative error is also calculated to be

$$\delta\pi_T^* = \frac{(\pi_T^*)_{\text{sequential}} - (\pi_T^*)_{\text{inverse}}}{(\pi_T^*)_{\text{sequential}}}$$

$$\delta\bar{G} = \frac{(\bar{G})_{\text{sequential}} - (\bar{G})_{\text{inverse}}}{(\bar{G})_{\text{sequential}}}$$

The calculated results are shown in Fig. 2. It is known from the figure that:

1 When $\bar{G}_{HT}$ increases, the difference between two $\pi_T^*$ obtained respectively from two algorithms increases gradually, while the difference between two $\pi_{T\Sigma}^*$ increases more rapidly. On the other hand, the difference between two $\pi_T^*$ decreases gradually with the decrease of load and so does the difference between two $\pi_{T\Sigma}^*$. The differences almost vanish at low load. This shows that the calculated results of these two algorithms are almost the same when the turbine works at low load.

2 The high-pressure turbine has the smallest $\delta\pi_{HT}^*$, but the low-pressure turbine has the largest $\delta\pi_{LT}^*$ under the same $\bar{G}_{HT}$.

3 Increase of the number of turbines will result in a larger cumulative error. The turbines downstream on the expansion line have more notable calculating errors than those upstream. Taking the design point as an example, $\delta\pi_{HT}^* = -0.02$ percent; $\delta\pi_{MT}^* = 1.57$ percent; $\delta\pi_{LT}^* = 14.79$ percent; $\delta\pi_{T\Sigma}^* = 16.11$ percent.

4 $\bar{G}_{HT}$ is assumed to have no error in our example. In common computation for gas turbines, the $\bar{G}_{HT}$ is obtained through interpolation of compressor characteristics and other calculations; thus, it surely has an error $\delta\bar{G}_{HT}$. It is obvious that calculating the turbine performance on the $\delta\bar{G}_{HT}$ basis via sequential algorithm will result in more significant errors.

As has been said before, the round-off errors and the interpolation errors have a great influence upon the computational results of the sequential algorithm under some conditions. It is called a numerically unstable algorithm in mathematics. When the sequential algorithm is used to compute turbine performance, it will result in errors in turbine performance and overall performance.

To sum up, it is necessary to apply the inverse algorithm in solving the performance of gas turbine engines in order to raise the accuracy of the computation.

## A New Mathematical Model for Steady-State Performance of Gas Turbine Engines

Following is the derivation of a new mathematical model for a typical form of marine gas turbine engine, which has three turbines and two compressors (HT drives HC, MT drives LC, and LT drives load).

Listed below are the flow continuity equations and power balance equations of the high-pressure rotor and the low-pressure rotor, and the coupling equations of the two rotors.

$$\frac{G_{HC}\sqrt{T_2^*}}{P_2^*} = \frac{G_{HT}\sqrt{T_4^*}}{P_4^*}\sqrt{\frac{T_2^*}{T_4^*}}\,\frac{\sigma_B\pi_{HC}^*}{(1+f)\zeta_2} \tag{9}$$

$$\frac{T_2^*}{T_1^*} = \left[(\pi_{LC}^*)^{\frac{\kappa_{LC}-1}{\kappa_{LC}}} - 1\right]\frac{1}{\eta_{LC}^*} + 1 \tag{10}$$

$$\left[(\pi_{HC}^*)^{\frac{\kappa_{HC}-1}{\kappa_{HC}}} - 1\right]\frac{1}{\eta_{HC}^*} = (1+f)\zeta_2\,\frac{T_4^*}{T_2^*}\,\frac{C_{\mathrm{PHT}}}{C_{\mathrm{PHC}}}\,[1-\tau^*(\lambda)_{HT}]\eta_{m2} \tag{11}$$

$$\left[(\pi_{LC}^*)^{\frac{\kappa_{LC}-1}{\kappa_{LC}}} - 1\right]\frac{1}{\eta_{LC}^*} = \zeta_1\zeta_2\zeta_3(1+f)\,\frac{C_{\mathrm{PMT}}}{C_{\mathrm{PLC}}}\,\tau^*(\lambda)_{HT}\,\frac{T_4^*}{T_2^*}\,\frac{T_2^*}{T_1^*}\,[1-\tau^*(\lambda)_{MT}]\eta_{m1} \tag{12}$$

$$\frac{G_{LC}\sqrt{T_1^*}}{P_1^*} = \frac{G_{HC}\sqrt{T_2^*}}{P_2^*}\sqrt{\frac{T_1^*}{T_2^*}}\,\pi_{LC}^*\zeta_1 \tag{13}$$

$$\pi_{HT}^*\bullet\pi_{MT}^*\bullet\pi_{LT}^* = \pi_{HC}^*\bullet\pi_{LC}^*\bullet\sigma_{in}\bullet\sigma_{ex}\bullet\sigma_B\bullet\sigma_T \tag{14}$$

where $\zeta_1 = \dfrac{G_{HC}}{G_{LC}}$, $\zeta_2 = \dfrac{G_B}{G_{HC}}$, $\zeta_3 = \dfrac{G_{MT}}{G_{HT}}$, and $\zeta_4 = \dfrac{G_{LT}}{G_{MT}}$. In order to simplify the solving of the equations, the aerodynamic parameters of the compressors can be expressed as a function of the gas parameters in turbines obtained by the inverse algorithm. Substitution of equation (9) into equation (11) gives

$$\left(\frac{G_{HC}\sqrt{T_2^*}}{P_2^*}\right)^2\left[(\pi_{HC}^*)^{\frac{\kappa_{HC}-1}{\kappa_{HC}}} - 1\right]\frac{1}{\eta_{HC}^*}\,\frac{1}{(\pi_{HC}^*)^2} = \frac{\sigma_B^2}{(1+f)\zeta_2}\,\frac{C_{\mathrm{PHT}}}{C_{\mathrm{PHC}}}\,[1-\tau^*(\lambda)_{HT}]\left(\frac{G_{HT}\sqrt{T_4^*}}{P_4^*}\right)^2\eta_{m2} \tag{15}$$

Similarly, from equations (10), (12), (13), and (14)

$$\left[(\pi_{LC}^*)^{\frac{\kappa_{LC}-1}{\kappa_{LC}}} - 1\right]\frac{1}{\eta_{LC}^*}\left(\frac{G_{LC}\sqrt{T_1^*}}{P_1^*}\right)^2 = \frac{\zeta_3}{(1+f)\zeta_1\zeta_2}\,\frac{C_{\mathrm{PMT}}}{C_{\mathrm{PLC}}}\,\tau^*(\tau)_{HT}\bullet[1-\tau^*(\lambda)_{MT}]\eta_{m1}\left(\frac{G_{HT}\sqrt{T_4^*}}{P_4^*}\right)^2\left(\frac{\pi_{HT}^*\pi_{MT}^*\pi_{LT}^*}{\sigma_{in}\sigma_{ex}\sigma_T}\right)^2 \tag{16}$$

Equations (16) and (15) can be written as

$$E_1 = \left[(\pi_{LC}^*)^{\frac{\kappa_{LC}-1}{\kappa_{LC}}} - 1\right]\frac{1}{\eta_{LC}^*}\left(\frac{G_{LC}\sqrt{T_1^*}}{P_1^*}\right)^2 - C_1 = 0 \tag{17}$$

$$E_2 = \left[(\pi_{HC}^*)^{\frac{\kappa_{HC}-1}{\kappa_{HC}}} - 1\right]\frac{1}{\eta_{HC}^*}\left(\frac{G_{HC}\sqrt{T_2^*}}{P_2^*}\right)^2\frac{1}{(\pi_{HC}^*)^2} - C_2 = 0 \tag{18}$$

where

$$C_1 = \frac{\zeta_3}{(1+f)\zeta_1\zeta_2}\,\frac{C_{\mathrm{PMT}}}{C_{\mathrm{PLC}}}\,\tau^*(\lambda)_{HT}[1-\tau^*(\lambda)_{MT}]\bullet\eta_{m1}\left(\frac{G_{HT}\sqrt{T_4^*}}{P_4^*}\right)^2\left(\frac{\pi_{HT}^*\pi_{MT}^*\pi_{LT}^*}{\sigma_{in}\sigma_{ex}\sigma_T}\right)^2$$

$$C_2 = \frac{\sigma_B^2}{(1+f)\zeta_2}\,\frac{C_{\mathrm{PHT}}}{C_{\mathrm{PHC}}}\,[1-\tau^*(\lambda)_{HT}]\left(\frac{G_{HT}\sqrt{T_4^*}}{P_4^*}\right)^2\eta_{m2}$$

$C_1$ and $C_2$ include only the aerodynamic parameters of turbines. They can be obtained when the performance computation of turbines in series is done by inverse algorithm, assuming a certain $\pi_{LT}^*$. In fact, the $\pi_{LT}^*$ here is the parameter representing a certain part load of gas turbine engine. Some coefficients in the expressions can be assumed to be the same as design values when lacking data. $C_{\mathrm{PHT}}$, $C_{\mathrm{PMT}}$, $C_{\mathrm{PLT}}$, $C_{\mathrm{PHC}}$, $C_{\mathrm{PLC}}$, and $f$ can also be corrected in successive iterations.

Equations (17) and (18) may be expressed in vector form (1), wherein $\mathbb{E} = (E_1, E_2)^T$. The $\mathbb{E}$ here is a hybrid residual expressing power, flow rate, pressure ratio, and so forth. Therefore, equations (17) and (18) can also be called hybrid residual equations. The hybrid residual equations involve six unknown quantities: $\pi_{LC}^*$, $\eta_{LC}^*$, $G_{LC}\sqrt{T_1^*}/P_1^*$, $\pi_{HC}^*$, $\eta_{HC}^*$, and $G_{HC}\sqrt{T_2^*}/P_2^*$. Therefore, we still need four supplementary equations to solve equations (17) and (18), two of which are coupling equations of high and low-pressure rotors. Incorporating and rearranging equations (17), (10), and (13), we have

$$\left(\frac{G_{LC}\sqrt{T_1^*}}{P_1^*}\right)^2 = \zeta_1^2\left(\frac{G_{HC}\sqrt{T_2^*}}{P_2^*}\right)^2 (\pi_{LC}^*)^2 - C_1 \tag{19}$$

Equation (14) can be rewritten as

$$\pi_{HC}^* \cdot \pi_{LC}^* = C_3 \tag{20}$$

where $C_3 = \pi_{HC}^*\pi_{MT}^*\pi_{LT}^*/(\sigma_{in}\sigma_{ex}\sigma_B\sigma_T)$.

The other two equations are the characteristic equations of high and low-pressure compressors

$$\eta_{LC}^* = f\left(\frac{G_{LC}\sqrt{T_1^*}}{P_1^*},\quad \pi_{LC}^*\right) \tag{21}$$

$$\eta_{HC}^* = f\left(\frac{G_{HC}\sqrt{T_2^*}}{P_2^*},\quad \pi_{HC}^*\right) \tag{22}$$

By simultaneously solving the six equations, that is equations (17), (18), (19), (20), (21), and (22), we can determine the values of the six unknowns and obtain a set of unique solutions. Of the six unknowns, $\eta_{HC}^*$, $\eta_{LC}^*$, $\pi_{HC}^*$, and $G_{HC}\sqrt{T_2^*}/P_2^*$ are all functions of $\pi_{LC}^*$ and $G_{LC}\sqrt{T_1^*}/P_1^*$. If we put $x_1 = \pi_{LC}^*$ and $x_2 = G_{LC}\sqrt{T_1^*}/P_1^*$, equations (17) and (18) can be written as

$$\begin{aligned} E_1 &= f_1(x_1, X_2) = 0 \\ E_2 &= f_2(x_1, X_2) = 0 \end{aligned} \tag{23}$$

By Newton-Raphson's iteration method, we obtain the solution of equations (23) to be

$$X^{k+1} = X^k - \omega_k J^{-1}(\mathbb{E}, X)_{x=x^k}\mathbb{E}^k \qquad k=0, 1, \ldots \tag{24}$$

where $\omega_k$ represents the relaxing factor of $(k)$th iteration, and $J(\mathbb{E}, X)$ represents Jacobian matrix ($2\times 2$ dimensions) with respect to residuals. The hybrid residual equations (23) do not satisfy the rotational speed equality equation. Therefore, it is necessary to use a rotational speed iterative equation to do the correction of rotational speed. The general expression of rotational speed iterative equation can be expressed as follows:

$$x^{k+1} = \psi(x^k) \qquad (k=0, 1, 2, \ldots) \tag{25}$$

where $x$ corresponds to $N_{HT}$, or $N_{MT}$, or $N_{LT}$; $\psi(x)$ represents the process which is used to calculate rotational speeds of compressors or a propeller from the given rotational speed of the turbine. $\psi(x)$ may be called an iterative function, while $\{x^k\}$ is called an iterative sequence or iterative format. In the first iteration, $x$ may be selected as the design value of $N_{HT}^{(0)}$, or $N_{MT}^{(0)}$, or $N_{LT}^{(0)}$. Then the rotational speed is corrected in terms of two different situations.

**Determination of Corrected Rotational Speed of the High and Intermediate Pressure Turbines.** $N_{HC}^1$ and $N_{LC}^1$ can be determined from characteristic curves of high or low-pressure compressors, respectively, after solving equations (23). If $N_{HC}^{(1)} \neq N_{HT}^{(0)}$ or $N_{LC}^{(1)} \neq N_{MT}^{(0)}$, we put $N_{HC}^{(1)} = N_{HT}^{(1)}$ or $N_{LC}^{(1)} = N_{MT}^{(1)}$. The correction formulas of reduced rotational speeds of high or low-pressure turbines can be expressed as follows:

$$\lambda_{\mathrm{UHT}}^{(1)} = \frac{\pi D_{HT} N_{HT}^{(1)}}{60\sqrt{\frac{2k}{k+1} R T_4^*}} \tag{26}$$

or

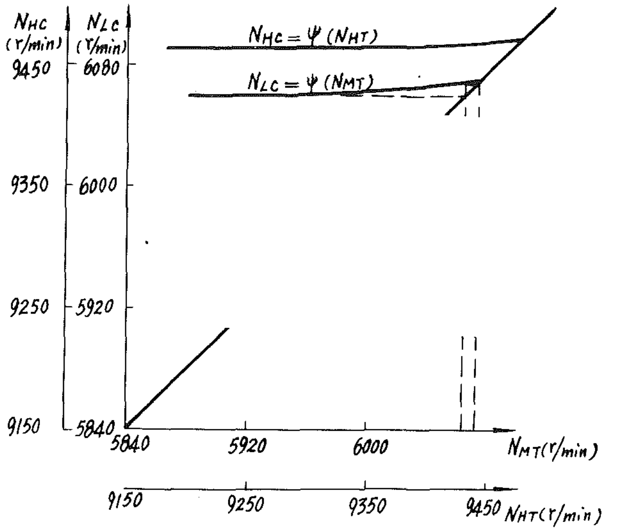

Fig. 3 Relation between $n_{HC}$ (or $n_{LC}$) and $n_{HT}$ (or $n_{MT}$) under the condition of the inverse algorithm, with $Ne/Ne_0 = 0.64$ and $|n_{HC}^{k+1} - n_{HT}^k| < 1$ rpm; or $|n_{LC}^{k+1} - n_{MT}^k| < 1$ rpm

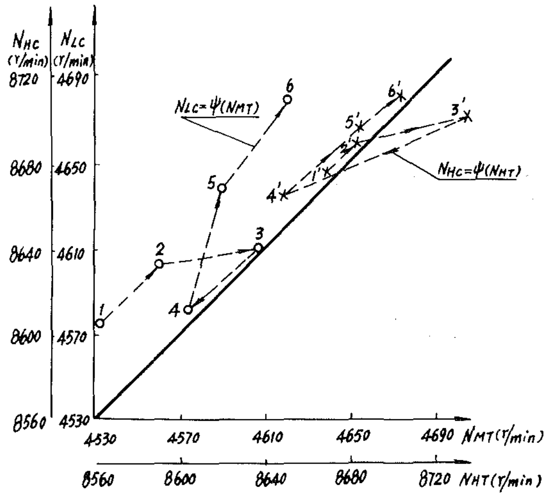

Fig. 4 Relation between $n_{LC}$ (or $n_{HC}$) and $n_{HT}$ (or $n_{MT}$) under the condition of the sequential algorithm, with $Ne/Ne_0 = 0.23$ and $|n_{HC}^{k+1} - n_{HT}^k| < 50$ rpm; or $|n_{LC}^{k+1} - n_{MT}^k| < 50$ rpm

$$\lambda_{\mathrm{UMT}}^{(1)} = \frac{\pi D_{MT} N_{MT}^{(1)}}{60\sqrt{\frac{2k}{k+1} R T_5^*}} \tag{27}$$

**Determination of Corrected Rotational Speed of the Low Pressure Turbine (or Power Turbine).** The power output of a gas turbine engine $P_e^{(1)}$ can be obtained after solving equations (23). Assume the design power output of a gas turbine engine is $P_e^{(0)}$ and design rotational speed of the load is $N_L^{(0)}$. Since the propeller is driven by the low-pressure turbine, we take approximately

$$\frac{P_e^{(1)}}{P_e^{(0)}} = \left(\frac{N_L^{(1)}}{N_L^{(0)}}\right)^3$$

i.e., $N_L^{(1)} = N_L^{(0)}\sqrt[3]{\frac{P_e^{(1)}}{P_e^{(0)}}}$.

If $N_L^{(1)} \neq N_{LT}^{(0)}$, we put $N_L^{(1)} = N_{LT}^{(1)}$. Then, the reduced rotational speed of the low-pressure turbine may be corrected with following equation:

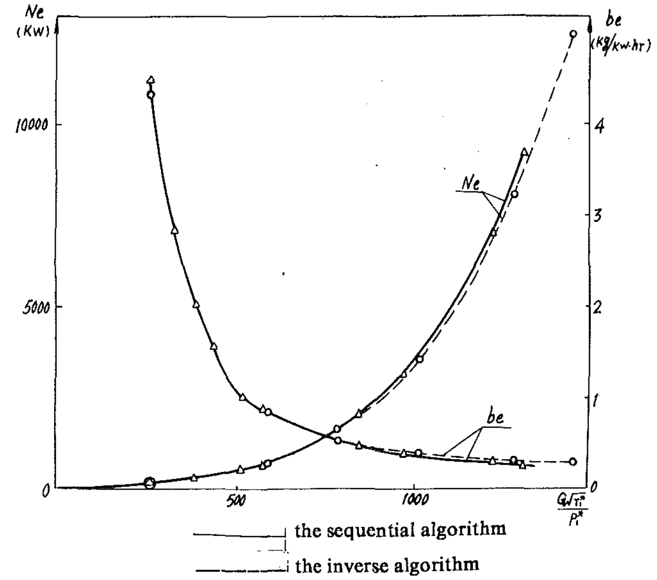

Fig. 5 Variatons of Pe and *be* with $G\sqrt{T_1^*}/P_1^*$ in a certain gas turbine engine under two different algorithms

$$\lambda_{\mathrm{ULT}}^{(1)} = \frac{\pi D_{LT} N_{LT}^{(1)}}{60\sqrt{\frac{2k}{k+1} R T_6^*}} \tag{28}$$

To sum up, by successively iterating equations (26), (27), and (28) we can obtain three sequences of approximate solutions: $\lambda_{\mathrm{UHT}}^{(0)}, \ldots, \lambda_{\mathrm{UHT}}^{(k)}, \ldots; \lambda_{\mathrm{UMT}}^{(0)}, \ldots, \lambda_{\mathrm{UMT}}^{(k)}, \ldots; \lambda_{\mathrm{ULT}}^{(0)}, \ldots, \lambda_{\mathrm{ULT}}^{(k)}, \ldots$, until $|N_{HC}^{(k+1)} - N_{HT}^{(k)}| < \epsilon_1$; $|N_{LC}^{(k+1)} - N_{MT}^{(k)}| < \epsilon_2$; $|N_{L}^{(k+1)} - N_{LT}^{(k)}| < \epsilon_3$. In the next section we will explain roughly that this iterative equation has a good convergence.

## Discussion

**Features of the New Mathematical Model.** In the last section we proposed a new mathematical model in which the problem of solving three-dimensional residual equations is reduced to a mixed problem of solving two-dimensional residual equations together with extracting a root of a one-dimensional nonlinear equation. This compound model has the following features:

1 This model is suitable for the use of these algorithms. It has good accuracy and numerical stability to obtain the performance of turbines and compressors.

2 The dimensions of hybrid residual equation (23) are less than those of the model used widely at present. Therefore, it is easy to converge in iteration and needs less computation.

3 When the inverse algorithm is used in the computation of turbine performance, it is very effective to correct rotational speed with the iterative method. Besides, it also has rapid convergence and good stability.

As to the last feature mentioned above, whether the iteration of rotational speed will surely converge is a problem of common interest. Here we explain it briefly as follows:

In higher mathematics, the following convergence principle about iteration is given: If the equation $x = \psi(x)$ satisfies the conditions: $\psi(x)$ remains continuous on $[a, b]$ and if to any $x$ $[a, b]$, there exists $|\psi'(x)| \leq L < 1$, then the iteration process $x^{k+1} = \psi(x^k)$ $(k = 0, 1, \ldots)$ will converge with any initial approximate $x_0$ $[a, b]$, and $\lim_{k\to\infty} x^k = x^*$.

The $\psi(x)$ in this paper is only an algorithm and therefore has no concrete analytical expression in the course of solving of gas turbine engine performance. Thus, it is difficult to derive $\psi'(x)$. But it is shown in the example calculation that the iterations of rotational speed will converge rapidly when the inverse algorithm is used to calculate turbine performance. This is mainly because the inverse algorithm is numerically more stable and the round-off error only slightly affects the calculated accuracy. Thus, $\psi(x)$ is a continuous function (see Fig. 3). It is also shown in the example calculation that when the load of the gas turbine engine is high, $\psi'(x)$ is much less than 1. Thus, the iterative sequence $x^{k+1} = \psi(x^k)$ $(k = 0, 1, \ldots)$ will rapidly converge to the solution of the original equation according to the principle of convergence. But since the sequential algorithm is numerically unstable, it results in the accumulation and enlargement of the error. Besides, it also leads to a fluctuation and jump of the $\psi(x)$, so it cannot guarantee $|\psi'(x)| < 1$ everywhere. Thus, the iteration of rotational speed is not only slow but also frequently cannot converge (see Fig. 4).

**Table 1 Values of $\epsilon$ under two different algorithms**

| $\frac{G\sqrt{T_1^*}}{P_1^*}$ | | 442.71 | 583.60 | 980.79 | 1319.8 |
|---|---|---|---|---|---|
| $\epsilon$, rpm | Sequential algorithm | 1 | 5 | 50 | 175 |
| | Inverse algorithm | 1 | 1 | 1 | 1 |

**Table 2 CPU times consumed for the computation under different part loads**

| $Ne/Ne_0$ | 0.057 | 0.130 | 0.284 | 0.642 | 1.0 |
|---|---|---|---|---|---|
| CPU time | 1 min 19 s | 1 min 18 s | 46 s | 40 s | 36 s |

**Accuracy and Computation Time of the New Type of Mathematical Model.** Because this model is on the basis of simultaneously solving continuity equations, power balance equations, pressure ratio equality equation, and rotational speed equality equation, there is no doubt that it is theoretically correct. In practice this method has been used for the computation of the performance of a marine gas turbine engine and has obtained satisfactory results.

In order to explain clearly the advantages of this method, the sequential algorithm and the inverse algorithm are respectively used to compute turbine performance under the conditions of the same type of gas turbine engine and the same form of mathematical model (23). The computational results are shown in Fig. 5. It can be seen from Fig. 5 that the computational results of the two algorithms almost coincide at low load, but the calculating error from these two algorithms increases gradually with the increase of load. When the inverse algorithm is used in the new model (23), the difference of absolute rotation betwen turbine and compressor, that is, the accuracy $\epsilon$ of iterated rotational speed, can be taken as 1 rpm at different part load. When the sequential algorithm is used in the new model (23), the value of $\epsilon$ has to increase with the increase of load, otherwise the computation fails to converge. This is because the numerical instability of the sequential algorithm will be larger with the increase of load. For the example above, the values of $\epsilon$ under two different algorithms are shown in Table 1.

It may be seen from this table that, with the increase of the values of $\epsilon$, the sequential algorithm will doubtlessly result in remarkable errors under the conditions of the higher load of the gas turbine engine.

The new model (23) involved in the inverse algorithm will rapidly converge with high accuracy under the condition of any part load of gas turbine engine, because the values of accuracy $\epsilon$ may be taken to be a small and constant quantity with the variation of load. Besides, it also involves less computation. Listed in Table 2 are the CPU times consumed for the computation under the conditions of different part loads with DPS 8 computer.

It can be seen in the table that larger loads result in less time consumed for the same accuracy. The time consumed for this method is approximately 1/4 ~ 1/10 less than that for common methods.

## Conclusions

1 It is proposed in this paper to use the compound model composed of two-dimensional hybrid residual equations and a one-dimensional nonlinear equation as the new model for calculation of steady-state performance of marine gas turbine engines. It has the advantages of high accuracy, rapid convergence, good stability, and less computation. The model is also appropriate for land gas turbine engines and aero-gas turbine engines.

2 The inverse algorithm, a new method proposed in this paper for the computation of the performance of turbines in series connection, has good numerical stability. It also has a good effect on reducing the accumulation and propagation of round-off errors and interpolation errors. Using this algorithm to solve the performance of gas turbine engines, the accuracy and stability of computation can be greatly improved.

3 The use of two-dimensional hybrid residual equations proposed in this paper will prevent the equations from becoming ill-conditioned. It has a rapid convergence due to the application of the inverse algorithm. It has not been found that the inversion of the Jacobian Matrix has ever failed.

4 This paper proposes to use one-dimensional nonlinear equation for solving the rotational speed by use of iteration method. Because, in this method, the performance of series turbines is obtained by an inverse algorithm, it can well satisfy the convergence principle of iteration. The example computation shows that it is not difficult to limit the difference between rotational speeds of turbines and that of compressors in less than 1 rpm.

## References

Wang Yonghong, 1989, "The Mathematical Model of Predicting Turbine Performance and the Accuracy Analysis," presented at the Annual Meeting of Turbomachinery—Boiler Society, Shanghai [in Chinese].

Weng Shile, Wang Yonghong, and Su Ming, 1986, "A Fitting of Variable Geometry Turbine Performance," presented at the International Marine Engineering Conference, Shanghai.

# An Algorithm and Criteria for Compressor Characteristics Real Time Modeling and Approximation

**A. M. El-Gammal**
Ph.D. Candidate,
Jet Propulsion Laboratory,
Faculty of Mechanical Engineering,
Belgrade, Yugoslavia

*Numerous problems are encountered in realizing an adequate real time model for an aircraft engine. The purpose of this article is to propose a systematic approach for modeling and approximating the characteristics of an engine or engine component parts, and to apply this approach to the Viper compressor (VC) characteristics. The proposed approach introduces a set of quantitative model-performance measures. Monitoring these measures makes it possible to take care of the multiple objectives of the model simultaneously and individually, and to attach a guarantee level to the model behavior. A set of (66) models are considered, from which the adequate VC model for real time (RT) simulation purposes is determined.*

## Introduction

Advanced propulsion control systems design concepts are developed for performance and operability improvements of aircraft engines. In this context real time engine simulation acquires new responsibilities as a complete partner in the electronic control system hardware. The required reliability levels are guaranteed using mathematical redundancy (Astrom and Wittenmark, 1984). In this way, control system reliability may be realized within systems of reasonable size and weight, in contrast to the large size and weight if physical redundancy (e.g., multilanes) is adopted.

The majority of problems in developing an adequate RT model for an aircraft engine are related to inaccuracies in modeling components, assumptions imposed by the available modeling approaches, and interactions between components. This may be due to the lack of a systematic modeling approach and quantitative measures for model performance evaluation.

In this paper a different perspective to the problem of modeling and characteristics approximation is considered, and problems of model specification and quantitative model performance measures are tackled. By monitoring a set of inferred quantitatively rated performance indices, a systematic way of finding the approximate model is accomplished.

## Compressor Models

Modeling a compressor requires formulation of the functional relations that exist between compressor variables. There are basically two methods that can be used to model multistage fans or compressors. The first uses individual stage models, while the second involves the use of overall component performance (Szuch, 1982). As a result, the aerothermodynamic performance of a fan or compressor can be given in several ways, including: (1) relations between pressure ratio, efficiency, mass flow, and operational speed (Horlock, 1982); (2) relations between flow coefficient, work coefficient, loss, and a pseudoflow Mach number in terms of "backbone" and "off-backbone" curves (Converse and Giffin, 1984).

Engine transients are of the utmost importance if an engine RT simulation is to be considered. Realizing as much as possible of the potential performance of an engine depends, to a great extent, on the accuracy and reliability attached to the estimates of engine transient (paths). Determination of these (paths) followed by the engine operating point requires knowledge of the compressor characteristics, and particularly of the momentary compressor angular velocity (Oates, 1988). Thus, the accuracy and reliability of the estimates of compressor characteristics significantly affects the attainment of the potential performance of an engine.

A system model has to present knowledge of that system in a usable form (Eykhoff, 1974). If an RT simulation is to be considered, a detailed approach or a complete mathematical description of compressor behavior is not proper. Sometimes, equivalent model (model fitting approach) is considered nonrigorous and does not have a theoretical basis. Such an attitude ignores the important fact that sophisticated detailed models require many assumptions and approximations, and we usually cannot fully justify our decisions (Garland, 1989). Thus, a model form is usually assumed, and a suitable technique is used to extract information from available compressor maps.

## Compressor Modeling Problems

**Fitting Problems.** Since we are concerned with fitting the compressor characteristics, a global examination of the considered VC map (Figs. 1 and 2) focuses attention on five potential sources of trouble. These are:

1 The uneasily identifiable shape.

2 The nonuniqueness problem, especially at the area of high speed curves.

---

Contributed by the International Gas Turbine Institute and presented at the 34th International Gas Turbine and Aeroengine Congress and Exposition, Brussels, Belgium, June 11-14, 1990. Manuscript received by the International Gas Turbine Institute January 22, 1990. Paper No. 90-GT-336.

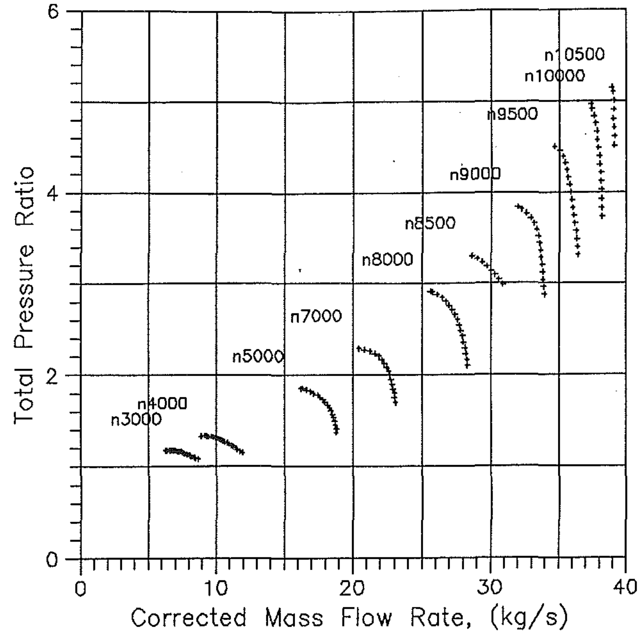

**Fig. 1 Viper compressor compression**

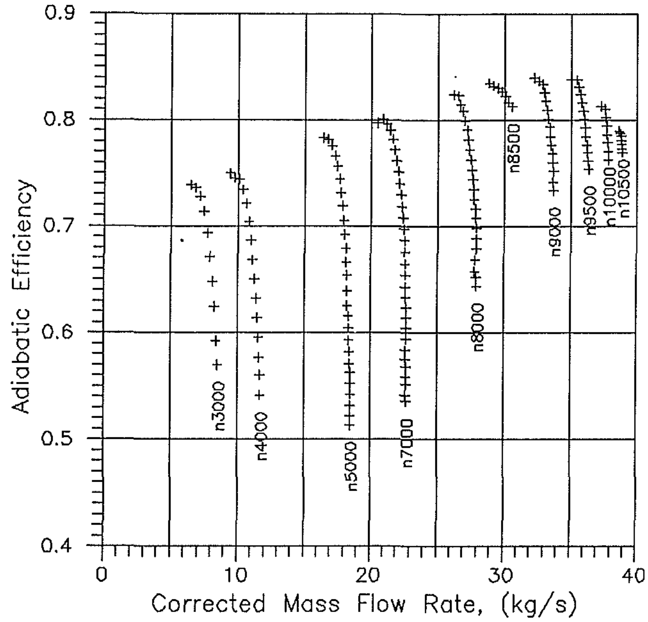

**Fig. 2 Viper compressor efficiency**

3 The ill-conditioning problem, where small changes in the variable of one coordinate produce large changes in the other coordinate variable.

4 The large variation encountered in the variables if a full envelope of compressor (engine) operation is desired.

5 The differences in the order of magnitude of variables.

Strongly related to these problems is the need for different functions to fit the low and high-speed portions of the characteristics, along with a methodology for switching from one function to the other.

**Utilization Problems.** After identifying parameters in a compressor map, an interpolation algorithm is used to calculate values of parameters at intermediate points, where the corresponding engine variables are evaluated. For an adequate estimate of characteristics, the interpolation algorithm may require a quite narrow calculation step, in order to follow the variation of parameters. Therefore, the RT simulation problem becomes one of reducing the calculation time, taking measures to permit the step size to be increased, or both (Szuch, 1982). Reducing the calculation time can be realized in several ways, including model simplification and reduction, parallel processing, or integer calculation. Permitting the step size to be increased includes the use of more suitable numerical techniques or more suitable model representation (with which we will be more concerned).

Error limits for the model outputs are guaranteed at the originally given data points, while errors at intermediate points do not have a guarantee. The reproduced engine characteristics at these intermediate points usually suffer unreal fluctuations. These fluctuations may be related to the unreasonable values of the predicted model parameters at these points, due to the inconsistency of the interpolation algorithm and/or the adopted (unsmooth) variation of the estimated parameters as a consequence of its predecessor faculty representation. To obtain better model outputs, model parameters possessing easily predictable (smooth) variation are required; these are to be used in conjunction with a consistent interpolation algorithm, or

## Nomenclature

$a_i$ = $i$th parameter in a model
CMI = curve-monotonic behavior indicator (normalized)
cri1, 2,.. = model performance index 1, 2,..
$er$ = relative error
erm = mean absolute relative error
germ = grand mean absolute relative error for the map
gerx = grand maximum absolute relative error for the map
MARE = mean absolute relative error
mgerm = modeling grand MARE for the map
$n$ = model order (number of parameters), or rotational speed
$\bar{n}$ = relative speed (curve parameter)
nai = number of terms for fitting the parameter $a_i$
$nc$ = number of points on a parameter curve
$no$ = number of turning or inflection points
$np$ = number of used data points of a curve
pgerm = prediction grand MARE for the map
$Q$ = corrected mass flow rate kg/s
$r$ = $(x^2 + y^2)^{0.5}$
sdp = map monotonic behavior indicator
$sl_{i,i+1}$ = slope values in the intervals ($i$, $i+1$)
sld$_i$ = difference of the slope values at point (i)
slo = slope-attitude-variation indicator of a parameter
$X$ = new bundle of variables on horizontal axis
$x$ = scaled value of independent variable = $Q/Q_{su}$
$Y$ = new bundle of variables on the vertical axis
$y$ = scaled value for dependent variable = $\pi/\pi_{su}$ or $\eta/\eta_{su}$
$\pi$ = total pressure ratio
$\sigma$ = standard deviation of errors along a curve
$g\sigma$ = grand standard deviation of errors across the map

### Subscripts

$su$ = for values at the surge line

for finding the appropriate closed-form analytical expressions for the model parameters. Thus, something more than an error criterion is needed. This is what we call the monotonic behavior of the parameters.

**Need for a Multi-Objective Algorithm.** Modeling techniques usually focus only on one type of model performance measure. This often narrows, too much, the designer's overall view of system-model performance. On the contrary, modeling has to be considered as a multi-objective process. Besides the well-known error limitations usually considered, a model and modeling algorithm has to guarantee the following: (1) highly accurate predictability of engine behavior, and RT execution capability, in order to cope with the new role attached to engine simulations; (2) monotonic variation of the model parameters, in order to relax the strenuous requirements imposed for adequate RT estimates of the needed characteristics (e.g., small step size and therefore large calculation capacities and fast computers).

**Model Qualities.** An exact quantitative specification of model objectives is rarely available in practice. In order for the modeling process to proceed in a systematic fashion, it is necessary that each of the model qualities be rated quantitatively, by means of a suitable performance index. In that way, it may be possible to take care of modeling objectives. Besides, the model performance indices should clearly reveal the ability of the model to predict engine behavior, as well as the qualities of that prediction, at all engine operating points.

## Characterization of Model Qualities

In the following, the adequate quantitative rating and mathematical formulation of model qualities are considered. The investigated ratings are:

1 Error rating
2 Rating of parameters' monotonic behavior
3 Predictability rating
4 Calculation load and execution time rating
5 Global model-performance rating

**Characterization of a Monotonic-Behavior Indicator.** Here it is intended: (1) to find an analytical tool for checking the monotonic behavior of a given data set along a specified interval, and (2) to establish a proper scale for evaluating the discrepancy of the data set from the monotone. Thus if

$$\mathrm{sld}_i = \mathrm{sli}_{i,i+1} - sl_{i-1,i} \tag{1}$$

and

$$\mathrm{slo} = \sum_{1}^{no} |\mathrm{sld}_i| \tag{2}$$

then the slo value is a representative of the total slope oscillations, which may be used as an indicator for discrepancies, or deviations, of parameter values from the monotone. If

$$\mathrm{CMI} = \frac{\mathrm{slo}}{(nc-2)(|\mathrm{aix}-\mathrm{ain}|)} \tag{3}$$

where aix and ain are the maximum and minimum values, respectively, of the model parameter $a_i$, then CMI gives an unbiased normalized indicator in the sense that it does not depend on the number of data points, or on the order of magnitude of the parameter considered. If

$$\mathrm{sdp} = \sum_{1}^{\mathrm{nai}} \mathrm{CMI} \tag{4}$$

then sdp will reflect the monotonic behavior of the complete set of model parameters. It also correlates with the deficiency of increase in the number of parameters. In that way, it is possible to evaluate the behavior of any parameter set analytically, and thus to evaluate and compare the monotonic behavior associated with various models, even if different data sets or different numbers of parameters are used.

**Characterization of Error Indicator.** Usually, an error measure is used to assess a good fit. However, the least-squares error has two serious deficiencies as an indicator of a good fit. It can be large, because the number of data points is large, even if the fit is fairly good. More important, it depends on the scale used for the data values (Maron, 1987). Since we are concerned with a general scale that can be used both for evaluating model performance and for comparing different models (even if different data sets are used), the intended measure of error has to compensate for the changeable number of data points, and for the scale variation, if any. Thus, it is necessary that a considered error estimate be (1) unbiased (i.e., the expected mean/data point); and (2) evaluated in the same original and traditional plane of reference.

In order to analyze the discrepancy between the predicted data values and their original values, we may use: (1) the relative error; (2) the mean absolute relative error; and (3) the standard deviation. These values are evaluated for each curve in the characteristic, as well as for the considered map as a whole. Thus

$$\mathrm{germ} = \left[\sum_{1}^{nc}\sum_{1}^{np} |er|\right] \Bigg/ \left[\sum_{1}^{nc} np\right] \tag{5}$$

$$g\sigma = \left[\sum_{1}^{nc}\sum_{1}^{np} |er|^2 \Big/ \sum_{1}^{nc} (np-1)\right]^{0.5} \tag{6}$$

Evaluation of the standard deviation gives a picture of the error dispersion about the considered data mean. However, it is useful if we know about the encountered maximum error values.

**Characterization of the Predictability Indicator.** To obtain a possible definition for a model predictability, we consider that the available data are divided into two distinct sets, with the first set used for model deduction, and the second set used for measuring the deduced model predictability. If the error measure evaluated for the first set is (mgerm), and for the second set is pgerm, the form

$$\mathrm{cri6} = 1 - 2\cdot\mathrm{pgerm}/(1 + \mathrm{mgerm} + \mathrm{pgerm})$$

meets the proper logic requirements: (1) It has a constant value (one) at the zero prediction error, whatever the value of modeling error is: (2) it weighs the effect of modeling error mgerm even when its value is equal to pgerm; (3) the departure of its value from the ideal value of one increases as the predicted error increases; and (4) its value is bounded even at the zero value of the prediction error pgerm. Besides, this form is also adequate as a measure for the model validity.

**Characterization of the Execution Time Indicator.** If cat denotes the time needed to get a required data point, then the value of this time may be utilized to weigh the model execution qualities. However, this time has to be properly scaled, according to its range of variation.

## Harmonization of Performance Indicators

As a result of the model performance characterization, various factors have to be included. These factors usually represent competing objectives, and the intended model has to tradeoff between them. Thus it is useful if the previously mentioned factors are cast into an adequate mathematical formulation. But how can this be easily achieved?

Having indicators $x$ and $y$ that have to be included together in a suitable combined measure, it is appropriate if the form $(1 + x)\cdot(1 + y)$ is adopted for that purpose. Beside other advantages, this form keeps the information content related to nonzero factor(s) even at a possible zero for the other factors ($x$, $y$, etc).

## Model Performance Measures

Accentuating the model qualities of interest, previously introduced, and the proposed harmonization procedure, the following performance measures are defined:

$$\text{cri1} = (1+\text{germ})(1+g\sigma) \tag{7}$$

$$\text{cri2} = (1+\text{germ})(1+\text{sdp}) \tag{8}$$

$$\text{cri4} = (1+\text{germ})(1+g\sigma)(1+\text{sdp})(1+\text{gerx}) \tag{9}$$

$$\text{cri6} = 1-2\bullet\text{pgerm}/(1+\text{mgerm}+\text{pgerm}) \tag{10}$$

## Inference of the Global Criterion for Modeling

Using the (cri4) measure enables grasping the resultant interaction of the mean error, maximum error, standard deviation, and monotonic behavior of parameters. If we combine this measure together with the predictability indicator in the form

$$\text{cri7} = \text{cri4}/\text{cri6}$$

we get a global modeling criterion that measures the overall model behavior. In the ideal case the predictability cri6 = 1 and cri4 = 1; therefore the departure of cri7 from the value of one will reflect the deviation of the model from the ideal.

We are now in a position to evaluate and compare various models, even if they possess small differences in different performance indices (error, monotonic behavior, etc.). This is realized in a well-defined and mathematically precise way.

## Evolution of the Intended Modeling Algorithm

**Data Smoothing.** Experiments entail many approximations (Garland, 1989), but we have to acknowledge that, normally, the real characteristics of the compressor as a physical system have to be smooth. In other words, it is necessary (immediately before beginning the step of extracting model parameters) to be sure that the characteristics are not depraved, due to any previous handling or acquisition (e.g., measuring, transforming, A/D converting, or even tabulating a given map).

**Data Rescaling.** The largest error in the design chain is likely to arise because the original process data is not sufficiently representative (Leigh, 1985). For modeling, as a design process, it is of utmost importance to keep the data to be modeled from contamination until they are introduced to the model. Of the same importance, the information content in these data also has to be kept from being corrupted due to any handling. Mathematical operations may cause distortion to the information content of the original data. This is especially true if the variables used have different orders of magnitudes, or if these variables are exposed to large variations (e.g., as the compressor covers its operating envelope).

It is necessary to keep the same order of magnitude, for all the variables to be manipulated, even as these variables change their values throughout the full range of compressor operation. This may call for the rescaling of the original data before they are mathematically manipulated. From possible rescaling strategies, it is clear that using the curve parameter (i.e., compressor speed) in its relative form, while rescaling the abscissa and ordinate variables with respect to the corresponding surge line values is the most convenient strategy. This what we refer to as the dynamic rescaling. If the exact surge line is not available, it has to be estimated. In reality we are searching for an appropriate moving origin, for handling each of the speed curves. A second-order estimate of the surge line for VC is found to be adequate. For modeling in this case, the surge line pressure $\pi_{su}$, efficiency $\eta_{su}$, and corrected mass flow rate $Q_{su}$ as functions of the rotational speed $n$ are

$$\pi_{su} = 1.4400-2.4770\ 10^{-4}\bullet n+5.8320\ 10^{-8}\bullet n^2 \tag{11}$$

$$\eta_{su} = 0.5718+0.6272\ 10^{-4}\bullet n-0.3828\ 10^{-8}\bullet n^2 \tag{12}$$

$$Q_{su} = -4.395+33.22\ 10^{-4}\bullet n+7.822\ 10^{-8}\bullet n^2 \tag{13}$$

**Table 1 Final matrix for bundle up of parameters on $x$ and $y$ axes.**

| | $j$ | 1 | 2 | 3 |
|---|---|---|---|---|
| | New $Y$ coordinate | $r$ | $y$ | $(y/y_{su})^{0.5}$ |
| $i$ | New $X$ coordinate | | | |
| 1 | $x/y$ | | | |
| 2 | $x/(y\bullet\bar{n})$ | | | |
| 3 | $x/(y\bullet\bar{n}^2)$ | | | |
| 4 | $\bar{n}+x/(y\bullet\bar{n})$ | | | |
| 5 | $\bar{n}+x/(y\bullet\bar{n}^2)$ | | | |
| 6 | $\bar{n}^2+x/(y\bullet\bar{n}^2)$ | | | |
| 7 | $\bar{n}^2+x/(y\bullet\bar{n})$ | | | |
| 8 | $1/\bar{n}+x/y$ | | | |
| 9 | $1/\bar{n}+x/(y\bullet\bar{n})$ | | | |
| 10 | $\bar{n}+x/y$ | | | |
| 11 | $\bar{n}^2+x/y$ | | | |
| 12 | $x\bullet y$ | | | |
| 13 | $x\bullet y\bullet\bar{n}$ | | | |
| 14 | $x$ | | | |
| 15 | $x+y$ | | | |
| 16 | $(x+y)\bullet\bar{n}$ | | | |
| 17 | $x+y+1/x$ | | | |
| 18 | $(x+y+1/x)\bullet\bar{n}$ | | | |
| 19 | $(x+y+1/x)\bullet y$ | | | |
| 20 | $(x+y)\bullet x$ | | | |
| 21 | $(x+y)^2$ | | | |
| 22 | $(x+y+1/x)(x+y)$ | | | |

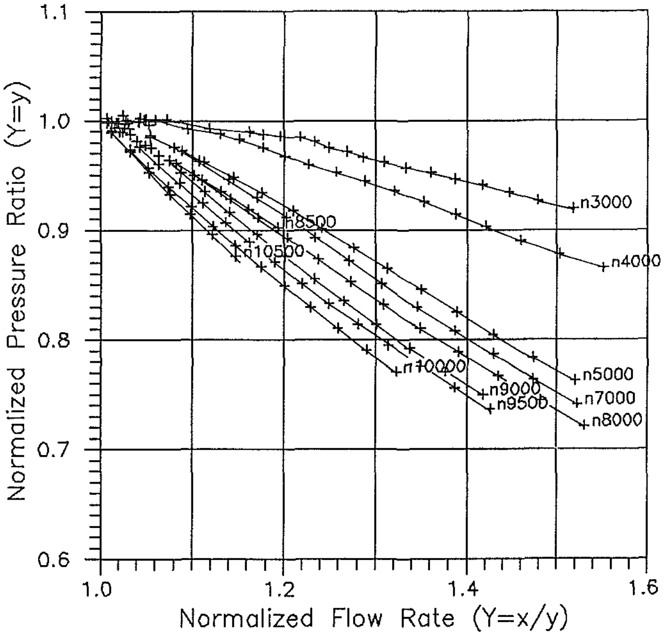

**Fig. 3 New (rescaled and transformed) map for the Viper compressor compression**

**Transformation of Axes.** For a good model we have to preserve a degree of the compressor internal behavior and cross couplings. This is accomplished through a superficial or external transformation, by regrouping the compressor variables into new lumps. These lumps maintain various shapes for connecting variables and preserving interactions in compressor, according to their individual forms.

In order to realize the intended, monotonic behavior of parameters, the previously explained concept of bundling up

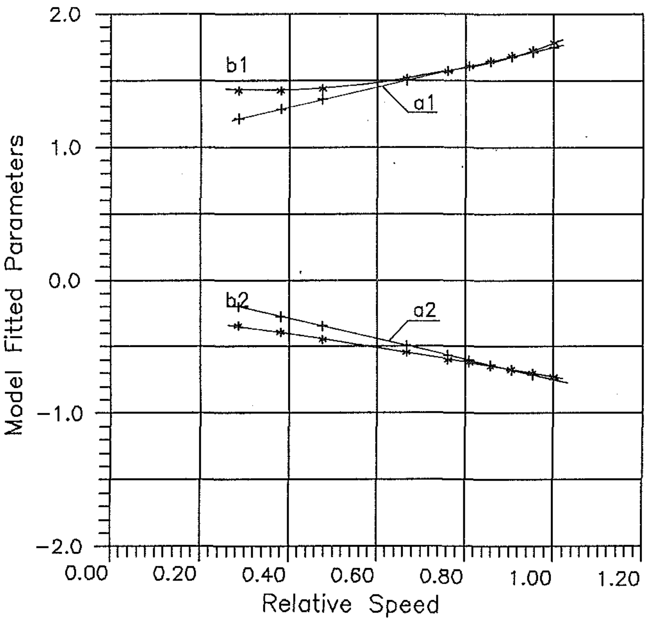

**Fig. 4 Analytically fitted model parameters: + pressure ratio model; * *adiabatic efficiency model***

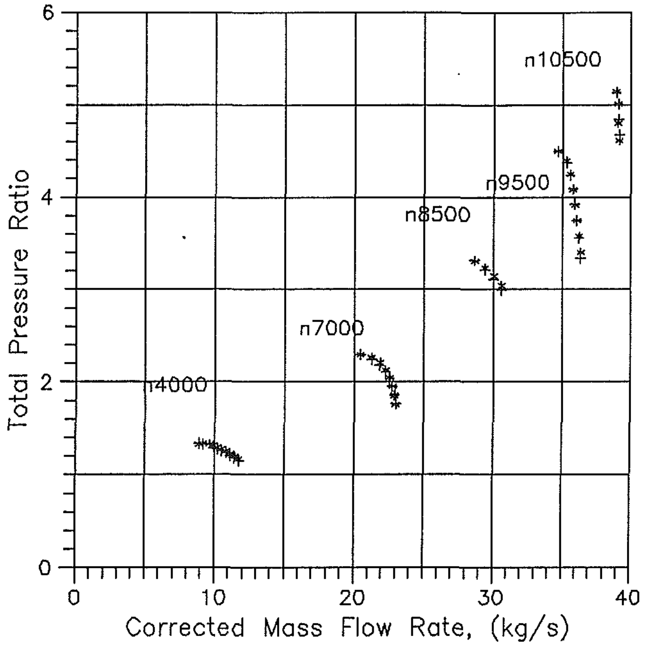

**Fig. 5 Original (*) and corresponding predicted (+) compressor map points**

variables is exercised with various transformations. Table 1 presents the final transformation matrix (of dimension 22 × 3). Thus it is possible to combine 66 different transformations. For each case, the guess function is exercised, with increasing numbers of terms to determine the optimum lumping with its compatible parameters.

**Fitting of New Map of Compressor.** For a new rescaled map as shown in Fig. 3, it is possible to realize that we have a data set that can fit well by a guess function whose graph is monotonic over the entire interval. Two parameters are generally sufficient to achieve a good fit in this special case (Maron, 1987). Yet, for exercising changeable powers and numbers of parameters, a more general form for the guess function is considered as

$$Y(X)=\sum_{1}^{n} a_i \bullet X^{i-1} \tag{14}$$

## Estimation of Parameters

However models with lower sdp are obtained, it is not easy—through a trial-and-error process—to attain the model that guarantees the intended monotonic behavior of parameters. Besides, the major drawback when implementing RT engine simulation on digital computers is that the time it takes to evaluate all the required calculations is longer than the time step necessary to provide good resolution (Szuch, 1982). The following should be noted:

1 Measurements are made with real, and thus imperfect instruments (Maine and Biff, 1985). Thus there is no justification for requiring that the model parameters have to be exactly the identified ones.

2 The model structure and model parameters form a compatible set; for another model structure, the system information content may be redistributed between the new model constitutents and its related parameters (DeHoff et al., 1981; DeHoff and Hall, 1978).

3 Simulation is an objective oriented process. Therefore, *the information content of the engine characteristics has to be fitted to an adequately usable form.*

Therefore, especially for the RT simulation uses, it may be valuable if closed analytical forms are tuned for the model parameters.

## Viper Compressor Approximation

**If Accuracy Is of Utmost Importance.** For utmost accuracy, the VC pressure ratio optimum model $y = f(x, \bar{n})$, is

$$y=a_1+a_2 \bullet [x+(1/x)+y] \bullet y \tag{15}$$

where

$$a_1 = (-0.07575 + 0.3324 \bullet \bar{n}) \tag{16}$$

$$a_2 = (0.3581 - 0.1096 \bullet \bar{n}) \tag{17}$$

this form guarantees modeling MARE$\leq$0.56 percent, where $x$, $y$ are the corrected mass flow rate and pressure ratio values, each rescaled with respect to its corresponding surge line value at the considered speed.

The VC efficiency optimum model $y=f(x, \bar{n})$, is

$$y=b_1+b_2 \bullet [x+(1/x)+y] \bullet y \tag{18}$$

where

$$b_1=(0.1359 + 0.05538 \bullet \bar{n} + 0.05414 \bullet \bar{n}^2) \tag{19}$$

$$b_2=(02949 - 0.04200 \bullet \bar{n}) \tag{20}$$

This form guarantees a modeling MARE$\leq$0.1 percent; in this case, $x$, $y$ are the corrected mass flow rate and efficiency values, each rescaled with respect to its corresponding surge line value at the considered speed.

**If Real Time Execution Is of Utmost Importance.** The previous model guarantees a high level of accuracy. However, it may not be the most appropriate for the RT purposes as a solver will also be needed. Thus an explicit model will be preferable. The resulting pressure ratio model, with a modeling MARE$\leq$1.08 percent, is obtained as

$$y=a_1+a_2 \bullet (x/y) \tag{21}$$

or

$$x=(y-a_1)(y/a_2) \tag{22}$$

where

$$a_1 = (1.001 + 0.7461 \bullet \bar{n}) \tag{23}$$

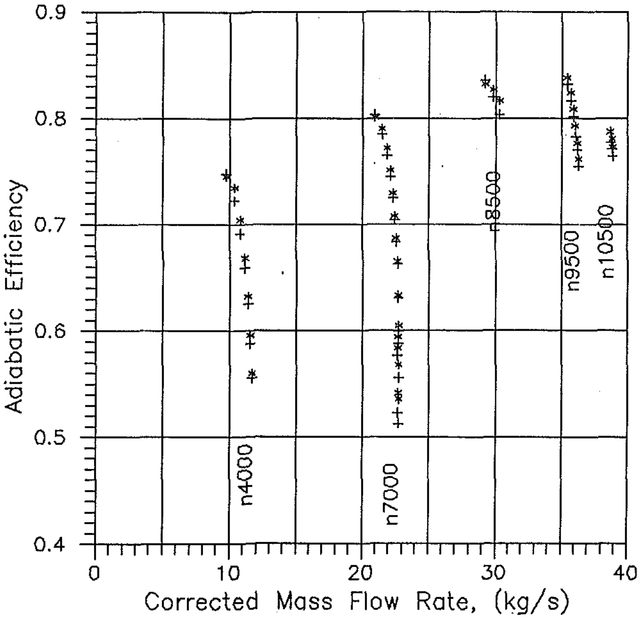

**Fig. 6 Original (*) and corresponding predicted (+) compressor efficiency points**

$$a_2 = (0.01897 - 0.7680 \cdot \bar{n}) \tag{24}$$

An efficiency model with attached modeling MARE ≤ 3.33 percent is

$$x = (y - b_1)(y/b_2) \tag{25}$$

where

$$b_1 = (1.499 - 0.5044 \cdot \bar{n} + 0.7836 \cdot \bar{n}^2) \tag{26}$$

$$b_2 = (-0.1941 - 0.5291 \cdot \bar{n}) \tag{27}$$

Parameters $a_1$, $a_2$ for this pressure ratio model, and parameters $b_1$, $b_2$ for the efficiency model are given in Fig. 4.

## Validation of Algorithm and Model Predictability

In order to validate the algorithm, the available data are divided into two distinct groups, as previously introduced, with the first group used to determine model parameters, and the second group to evaluate the model predictability. Comparing the predicted data points with the corresponding original points allows one to assess the model as a predictor. Figure 5 illustrates the original and predicted pressure ratio values, while Fig. 6 shows the original and predicted efficiency values.

Exercising the proposed algorithm with various compressors, it is possible to say that the algorithm has general validity for the compressors considered.

## Summary of the Methodology

The proposed modeling technique can be summarized as follows:

1 Be sure that the input data to be modeled are free from all possible input errors, or data smoothing may be needed.

2 Carry out the needed dynamic rescaling of the given characteristics with respect to the surge line values at each speed.

3 According to the shape of the new map a suitable fitting function type is chosen (e.g., polynomial, exponential, etc.).

4 The proposed list for axes transformations is exercised in order to determine the adequate form (e.g., $X = x/y$, $Y = y$), in connection to model order, and number and order of parameters (e.g., linear model with two parameters; each is of linear form in curve parameter, i.e., relative speed).

5 Divide the available data into two distinct data sets.

6 With the first data set (modeling set): The optimum model is determined by keeping track of various performance measures (individually and simultaneously) until a satisfactory performance level is attained or no further improvement is possible. This is achieved through a two-directional search where the model order and the order of each model parameter are changed, one at a time, in order to fix the model form, with its compatible parameters forms and their coefficient values. However, in each step, it is necessary to decide which performance index shall be improved and what is the possible expense in degrading other performance indices.

7 In the previous step, it is necessary to notice that map-fit and parameter-fit are compatible processes. Mutual interaction and cross coupling exist between both actions. Thus the optimum solution is only possible through a systems approach strategy.

8 With the second data set (validation set): Evaluate the predictability of each candidate configuration. This unveils the model validity. The value evaluated for the predictability (validity) measure is also included as one of the model performances that are tracked during the modeling processes. This enables the choice of an adequate model with a guaranteed predictability measure.

9 Renewing of axes transformation matrix and/or guess function type is also possible, in order to attain the required model behavior and performance level.

## Discussion and Concluding Remarks

This paper presents systematic approach for modeling compressor characteristics. This is realized through keeping track of the developed, quantitatively rated, model performance measures. In this way it is possible to evaluate and keep track of each intended character of the candidate model, as well as its global behavior, in comparison to any other model. Thus, it is objectively possible to choose the most adequate model structure according to the intended application.

This approach, contrary to the method of synthesizing detailed thermodynamic and mechanical relations, provides simple models for RT simulations, even for complex engines. Besides, it is well suited to deal with practical simulation and controller realization considerations, as the modeler is free to specify the model structure, and to combine simulation, control, and technical considerations. Also, the introduced predictability measure makes it possible to guarantee the model operation as a predictor. This is well suited for redundancy considerations in digital electronic controls.

Dynamic rescaling makes it possible to preserve the deduced-model validity along the whole operating envelope. The algorithm has general validity. The results of applying the algorithm to the VC characteristics show that it is possible, with only four operating points, to predict the complete characteristics, with MARE value ≤ 0.56 percent for the compressor pressure ratio, and ≤ 0.31 percent for the compressor efficiency, if accuracy has the first priority, and with MARE value ≤ 1.08 percent for the compressor pressure ratio, and ≤ 3.33 percent for the compressor efficiency, if RT execution is intended.

## Acknowledgments

This work is sponsored by the Egyptian Air Force. Many helpful discussions with Professor B. Jojic, of the Jet Propulsion Laboratory, Faculty of Mechanical Engineering, Belgrade are gratefully acknowledged. Also, thanks are due to the cooperating staff of the Air Force Technical Academy for their assistance.

## References

Astrom, K. J., and Wittenmark, B., 1984, *Computer Controlled Systems Theory and Design*, Prentice-Hall, Inc., Englewood Cliffs, NJ.

Converse, G. I., and Griffin, R. G., 1984, "Extended Parametric Representation of Compressor Fans and Turbines," NASA CR-174645.

DeHoff, R. I., and Hall, W. E., Jr., 1978, "Jet Engine Systems Models. Part II. State Space Techniques and Modeling for Control," *Control and Dynamic Systems—Advances in Theory and Applications*, C. T. Leondes, ed., Academic Press, New York, Vol. 14, pp. 260-298.

DeHoff, R. I., Rock, S. H., and Akhter, M. M., 1981, "Development of Multivariable Controllers for Aircraft Turbine Engines," *Theory and Applications of Optimal Control in Aerospace Systems*, AGARD-AG-215.

Eykhoff, P., 1974, *System Identification*, Wiley, London.

Garland, W. J., 1989, "Fundamental Concepts of Modeling: The Science of Simulation," *Proceedings of the International Forum on Mathematical Modeling of Processes in Energy Systems*, Sarajevo, Yugoslavia, Mar. 20-24.

Horlock, J. H., 1982, *Axial Flow Compressor*, Robert E. Krieger Publishing, Malabar, FL.

Leigh, J. R., 1989, "Digital Control Algorithms," *Applied Digital Control*, Prentice-Hall International, UK, Ltd.

Maine, R. E., and Biff, K. W., 1985, *Identification of Dynamic Systems*, R. K. Bogue, eds., AGARD Flight Test Techniques Series, AGARD-AG-300, Vol. 2.

Maron, M. J., 1987, "Curve Fitting and Function Approximation," *Numerical Analysis: a Practical Approach*, 2nd ed., Macmillan Publishing Company, New York, pp. 201-258.

Oates, G. C., 1988, "Engine Off-Design Performance," *Aerothermodynamics of Gas Turbine and Rocket Propulsion Revised and Enlarged*, J. S. Przemieniecki, ed., AIAA Education Series, Washington, DC.

Szuch, J. R., 1982, "Advancements in Real-Time Engine Simulation Technology," *Proceedings of the AIAA/SAE/ASME 18th Joint Propulsion Conference*, June 21-23.

Zeller, J., Lehtinen, B., and Merrill, W., 1982, "The Roll of Modern Control Theory in the Design of Controls for Aircraft Turbine Engines," NASA TM-82815.

**G. L. Morrison**
Professor.

**M. C. Johnson**
Graduate Student.

**G. B. Tatterson**
Associate Professor.

Mechanical Engineering Department,
Texas A&M University,
College Station, TX 77843

# 3-D Laser Anemometer Measurements in a Labyrinth Seal

*The flow field inside a seven-cavity labyrinth seal with a 0.00127-m clearance was measured using a 3-D laser-Doppler anemometer system. Through the use of this system, the mean velocity vector and the entire Reynolds stress tensor distributions were measured for the first, third, fifth, and seventh cavities of the seal. There was one large recirculation region present in the cavity for the flow condition tested, $Re = 28{,}000$ and $Ta = 7000$. The axial and radial mean velocities as well as all of the Reynolds stress terms became cavity independent by the third cavity. The azimuthal mean velocity varied from cavity to cavity with its magnitude increasing as the flow progressed downstream.*

## I Introduction

Labyrinth seals are used extensively in high-speed turbomachinery to reduce leakage from high-pressure areas to low-pressure areas. Applications include pumps, compressors, and turbines. In all of these machines, if the leakage can be reduced, there will be an accompanying increase in the efficiency of the device. Ludwig and Bill [1] have documented the effect of increasing the sealing upon overall efficiencies of gas turbines.

The majority of studies [2–5] concerning labyrinth seal leakage have been empirical studies of leakage rate as a function of shaft speed, clearance, pitch, tooth height, step height, etc. These have resulted in empirical leakage prediction techniques. A few studies (e.g., Stoff [6], Rhode et al. [7], Demko [8–10], and Wittig et al. [11]) have included numerical computations of the turbulent flow field present inside labyrinth seals. These studies were based upon solutions of the time-averaged turbulent Navier–Stokes equations using a finite difference solution technique with a $\kappa$–$\epsilon$ turbulence model. The numerical solutions predicted the flow field but there are almost no data that can be used for verification. Stoff [6] presented some azimuthal velocity distributions along the centerline of the seal cavity for a large-scale (clearance = 0.005 m) labyrinth seal using water as the working fluid and a one-dimensional laser-Doppler anemometer to make the measurements. The Reynolds and Taylor numbers were 30,000 and 12,000. Demko et al. [10] performed crossed hot-wire measurements in a large-scale seal (0.00635 m clearance) as well. These measurements resulted in axial and azimuthal velocity distributions over the teeth and at three axial locations inside the seal cavity. Wittig [11] compared his computational results to pressure distributions measured along a planar two-dimensional stepped labyrinth seal. Hauck [12] performed some pressure probe measurements, which produced average azimuthal and axial velocity distributions in the seal. No turbulence data were recorded.

The measurements available in general are not adequate to perform a detailed comparison between computational predictions and experimental data. Experimental studies must have extensive information about initial conditions, including mean velocity profiles, turbulence intensities, and Reynolds stresses. Only with these data can a direct comparison between the subsequent downstream experimental data be made with the numerical predictions.

## II Objectives

The objective of this study is to perform detailed flow measurements inside a straight-through labyrinth seal operating at Taylor and Reynolds numbers similar to production turbomachinery. These detailed flow measurements include mean velocity (axial, radial, and azimuthal velocity components) distributions as well as entire Reynolds stress tensor distributions. These measurements are important to gaining an understanding of the flow inside labyrinth seals.

The information is also valuable to researchers modeling flow through labyrinth seals. Researchers using methods based upon the time-averaged turbulent flow Navier–Stokes equations require both the mean velocity distributions for comparison with their results and the Reynolds stress tensor information for refinement and development of turbulence models. These studies also require the detailed inlet flow conditions that were measured in this study in order to perform direct comparisons between theory and measurements.

## III Facilities and Instrumentation

**3-D Laser Anemometer System.** The 3-D laser anemometer system of the Turbomachinery Laboratories at Texas A&M University was capable of measuring three independent velocity components simultaneously, resolving from those the three orthogonal velocity components, as well as the mean velocity vector, their turbulence intensities, the time-averaged

---

Contributed by the International Gas Turbine Institute and presented at the 33rd International Gas Turbine and Aeroengine Conference and Exhibition, Amsterdam, The Netherlands, June 5–9, 1988. Manuscript received at ASME Headquarters August 1990. Paper No. 88-GT-63.

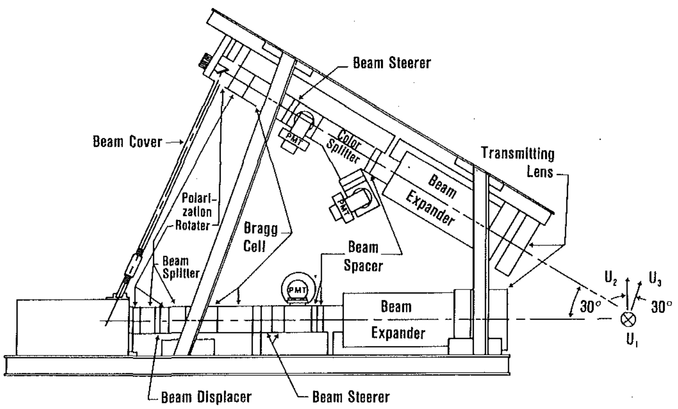

Fig. 1 3-D laser-Doppler anemometer system

Reynolds stress tensor, the mean and turbulent kinetic energy, and other statistical quantities such as eddy viscosities.

The optical portion of the laser anemometer system (see Fig. 1) consists of an argon-ion laser from which three different colors are utilized (green, blue, and violet). Each different color was used to measure an independent velocity component using the dual-beam LDA method. The optical train for each color was equipped with light polarization units, Bragg cells, and 8.5× beam expanders. The light, reflected from the seed particles, was collected in an off-axis back scatter mode at an angle 30 deg from the axis of the optical train transmitting the light. In the current configuration, there were two optical trains, one mounted above the other, whose axes intersected at a 30 degree angle. The lower optical train transmitted the blue and green light and collected light scattered from the violet light. The top optical train transmitted the violet light and collected light scattered from the green and blue light. The photomultiplier tubes, used to mesure the scattered light, were equipped with a color filter so that only the specific color (blue, green, or violet) was sensed by the respective photomultiplier tube.

This optical arrangement produced a composite measurement volume that was $0.025 \times 0.025 \times 0.102$ mm in size. This size was substantially smaller than is present in a standard 2-D back scatter system ($0.076 \times 0.076 \times 0.508$ mm). This allowed greater spatial resolution, which was of prime importance in the small clearance (1.32 mm) of the labyrinth seal studied. A standard system would not have been able to perform the mesurements. In order to place this small measurement volume accurately in space, the entire optical system (laser and optics) was mounted on a three-degree-of-freedom traversing system, which located the measurement volume in space with a resolution of 0.0025 mm and a repeatable accuracy of 0.0102 mm.

The entire laser anemometer system was interfaced to a PDP 11/23+computer system, which was programmed to control the traverse system and record data supplied by the frequency counter systems. There were three counters (one for each velocity component), which were interfaced together so that only data acquired at the same instant in time (within 10 $\mu$s) for all three velocity components was transferred to the computer. This assured that all three counters were simultaneously analyzing data generated by the same seed particle in the flow. The photomultiplier tubes and the counter systems had frequency responses of 200 MHz.

The computer system was programmed to record the instantaneous data supplied by the frequency counters and convert it into instantaneous velocities. The time histories of the instantaneous velocities acquired at the various spatial locations were used statistically to determine the mean velocity, turbulence intensities, Reynolds stresses, and various other statistical quantities of interest.

**Error Analysis.** The errors introduced in LDA systems come from several sources including velocity biasing, fringe biasing, statistical biasing, low-frequency noise, high-frequency noise, and counter resolution. Each of these sources has been considered and dealt with.

The velocity bias was estimated by evaluating several bias correction schemes. The raw LDA data (individual particle velocities) were reduced employing a straight statistical method, McLaughlin–Tiederman [13] velocity bias correction method, and TBD (time between data points) method. It was found that all three methods yielded virtually identical results in both mean velocities and Reynolds stresses.

Fringe bias was eliminated by insuring that each color component was getting enough fringes (16 fringes were used). This was done by using a 40 MHz frequency shifter. The statistical bias was eliminated by taking a large sample group for each physical location (2048 individual realizations were used).

The error due to counter resolution can be calculated based on the 1-ns clock resolution. This leads to a ±0.025 m/s error on each velocity measurement. Since these errors are averaged over 2048 samples, the mean velocity error due to clock resolution was negligible. The effect of these small errors on calculated Reynolds stress components was complicated but can be estimated. The result (which will be outlined in a later publication) was an estimated increase in variance (square of standard deviation) of 0.00021 $m^2/s^2$.

The last source of measurement error was noise. Low and high-frequency noises on the Doppler signal affect the loca-

## Nomenclature

$A$ = leakage area $= \pi Dc$, $m^2$
$c$ = clearance between the rotor tooth and stator, m
$D$ = rotor diameter, m
$D_p$ = seed particle diameter, m
$f$ = frequency response of the seed particles, Hz
$Q$ = leakage rate, $m^3/s$
$r$ = radial distance from the shaft centerline, m
Re = Reynolds number $= 2\rho Uc/\mu$
Ta = Taylor number $= [\rho W_{sh} c/\mu]\,[2c/D]^{1/2}$
$U$ = average leakage velocity $= Q/A$, m/s
$u_x$ = axial mean velocity, m/s
$u_r$ = radial mean velocity, m/s
$u_\theta$ = azimuthal mean velocity, m/s
$u_x'u_r'$ = time-averaged Reynolds stress, $m^2/s^2$
$u_x'u_\theta'$ = time-averaged Reynolds stress, $m^2/s^2$
$u_r'u_\theta'$ = time-averaged Reynolds stress, $m^2/s^2$
$u_x'u_x'$ = time-averaged Reynolds stress, $m^2/s^2$
$u_r'u_r'$ = time-averaged Reynolds stress, $m^2/s^2$
$u_\theta'u_\theta'$ = time-averaged Reynolds stress, $m^2/s^2$
$W_{sh}$ = azimuthal velocity of the rotor surface, m/s
$x$ = axial direction, m
$\kappa$ = turbulence kinetic energy $= 1/2(u_x'u_x' + u_r'u_r' + u_\theta'u_\theta')/U^2$
$\psi$ = axial downstream distance from the center of the inlet tooth, m
$\lambda$ = radial distance above the tooth top, m
$\eta$ = radial distance above the cavity bottom, m
$\theta$ = azimuthal angle
$\tau$ = time constant, s
$\mu$ = absolute viscosity of the fluid (water), $Ns/m^2$

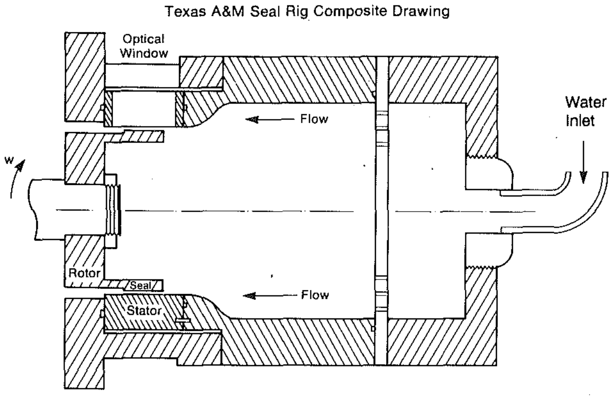

**Fig. 2 Labyrinth seal test section**

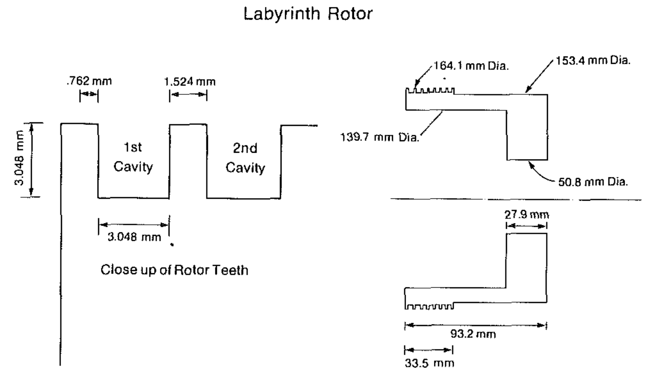

**Fig. 3 Labyrinth seal rotor**

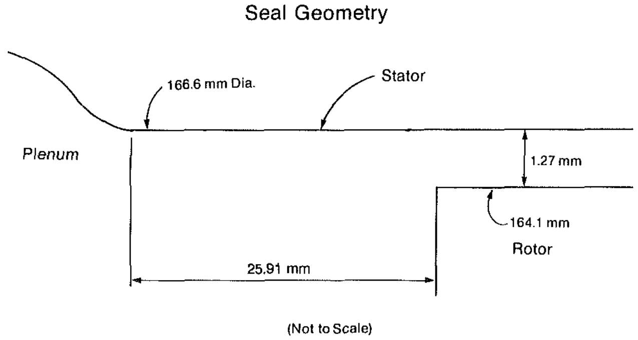

**Fig. 4 Labyrinth seal inlet geometry**

tion of the zero crossing, which was used by the counter to time the Doppler burst. Experience has shown that this results in an average error of approximately 2/10 of the period of one cycle in the Doppler burst. This leads to as much as a 20 percent increase in the value of a given color turbulence intensity but little error in the mean velocity.

The errors discussed above were the errors experienced in each individual color. To understand how these errors propagate into the actual values calculated for the three orthogonal components it is necessary to understand the transformation matrix from the color coordinates to $x$-$r$-$\theta$ coordinates. In the present work, it was found that in the $x$ and $\theta$ directions the resulting error was again 20 percent on the turbulence intensities and 1 percent on the mean values. However, in the on-axis direction ($r$) this error was magnified to 100 percent on the radial turbulence intensities and 2 percent on the mean velocity. This was due to the very small angle between color trains. This angle began at 30 degrees but due to geometry and refraction effects in the water this angle was reduced to 14 degrees.

The value of the coincidence window (the maximum time allowed for all three counters to validate a Doppler burst) was found to be critical in the accuracy of the on-axis (radial direction) turbulence quantities. If this window was opened up beyond 20 $\mu$s, different counters may validate signals from separate seed particles. This caused substantial (order of magnitude) broadening of the standard deviation of the measured quantities. The coincidence window used in this study was significantly smaller than the average time between particles producing usable Doppler signals as indicated by the individual counter validation rates. This helped to insure that only one particle in the flow produced the signals validated by all three counters within one coincident window time.

The accuracy of the mean velocities was verified by applying the differential continuity equation to each measurement point of the flow field. It was found that continuity was satisfied within 3 percent at all points of the flow.

**Test Facility.** Water was used as the working fluid. A 3.75 m$^3$ storage tank supplied water to a centrifugal pump. The pump output was metered by a turbine meter. The flow rate was set by a throttling valve and held constant at 0.00486 m$^3$/s during the experiments. After metering, the water was introduced into the seal rig. The water leaving the seal rig was returned to the storage tank. The storage tank was sufficiently large that the temperature of the water did not vary significantly during the time the measurements were made. The temperature rise through the labyrinth seal was less than 0.5 K.

In order for the LDA system to function properly, seeds were added to the water. For the current case, Expansel 462 WU was used. This plastic particle had a mean diameter of 6 $\mu$m and a specific gravity of 1.23. Calculations based upon the equations: $f = 1/(2\pi\tau)$ where $\tau = \rho_p D_p^2/(18\mu)$ show that in water these particles would follow flow fluctuations that possessed frequencies up to 44,000 Hz. This was deemed acceptable for the present study. It was visually observed that the storage tank was sufficiently agitated by the returning fluid to maintain the seed particles in suspension.

A seal test facility designed for use in air or water is shown in Fig. 2. The basic design was a 50.4-mm-dia overhung shaft directly coupled to a 37-kW electric induction motor. The electric motor was driven by a variable frequency power supply. The variable frequency drive allowed the motor to be operated at speeds from 0 to 5300 rpm.

The seal itself was composed of an acrylic rotor (Fig. 3) with an outside diameter of 0.1641 m and a stainless steel stator. The rotor was optically coated by a vacuum-deposition technique to reduce reflected light intensity. The seal stator was constructed of stainless steel with a smooth finish. A flat optical window was installed in a narrow slit along the axis of the seal. This window allowed access for the LDA system. A flat window was used since there would not be a lens effect. The deviation from roundness resulting from the addition of this small flat surface was only 1.5 percent of the clearance or 0.027 percent of the rotor radius. The window was also optically coated. The clearance between the stator and rotor was 1.27 mm. The labyrinth seal was a straight-through design with a tooth width of 1.52 mm, a tooth pitch of 4.57 mm, and a tooth height of 3.05 mm.

Upstream of the seal was a plenum, which had a fine screen stretched in front of a thick (12.7 mm) stainless steel plate. This plate had been perforated with 3.2-mm-dia holes. These holes effectively acted as flow straighteners. The combination of the two-distributed the flow evenly around the plenum and straightened the flow. There was sufficient distance between the perforated plate and the seal so that there was no evidence of residual wakes due to the holes. The outer wall of the plenum contracted toward the centerline along a smooth contour as the flow approached the seal. The surface was

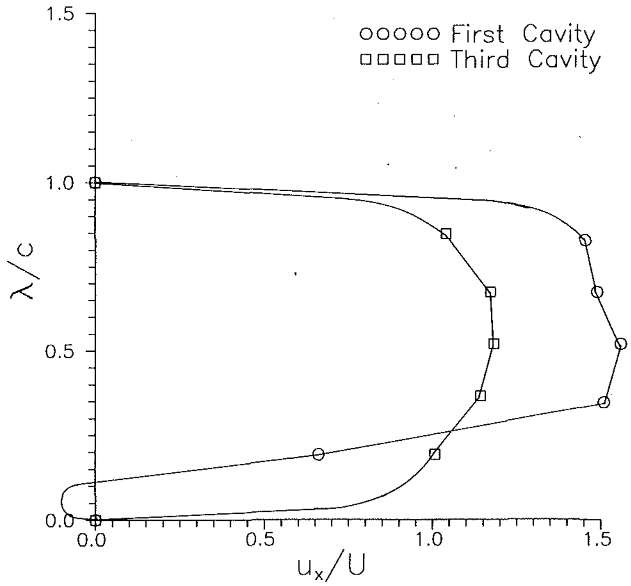

Fig. 5 Inlet axial velocity

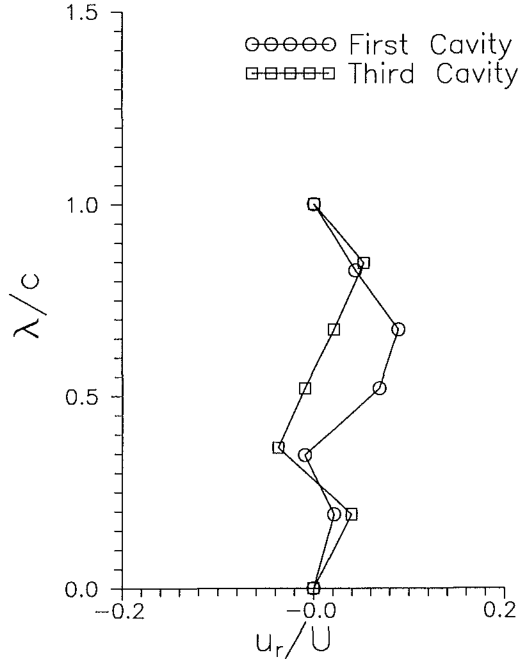

Fig. 6 Inlet radial velocity

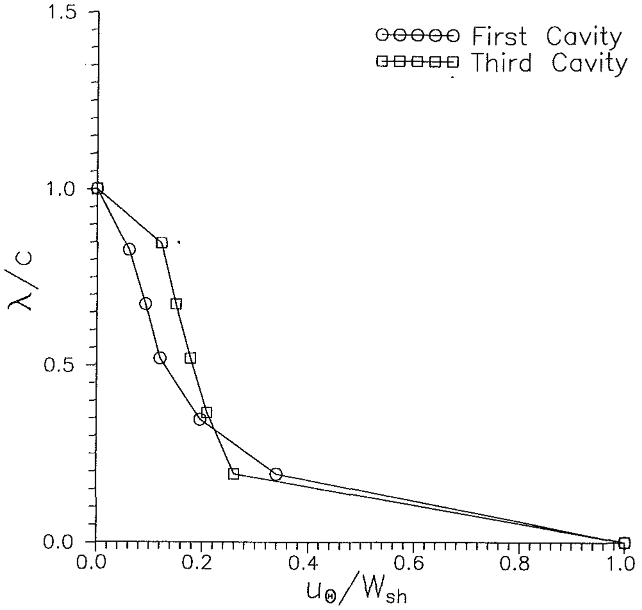

Fig. 7 Inlet azimuthal (swirl) velocity

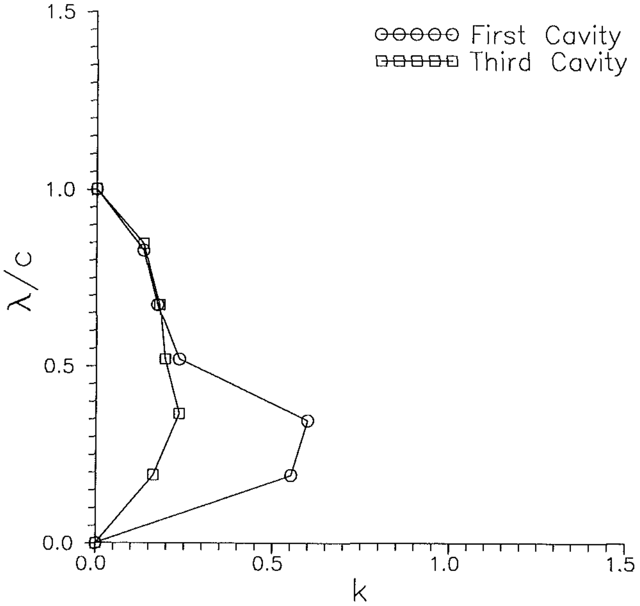

Fig. 8 Inlet turbulence kinetic energy

described by a third-order polynomial. A the end of the contraction, the outer wall mated smoothly with the stator (Fig. 4).

For this particular application, the rotor was rotated at 3600 rpm, which resulted in a Taylor number of 7000 and an azimuthal velocity for the rotor teeth of 28.7 m/s. For the leakage rate of 0.00486 $m^3/s$, the leakage Reynolds number was 28,000, with an average axial mean velocity of 7.04 m/s above the rotor teeth. Both the Reynolds and Taylor numbers were well within normal operating values obtained in production turbomachinery. The ratio of rotor speed to average leakage velocity was 4.08.

## IV Results

**Inlet Conditions.** Figure 5 illustrates the axial inlet velocity distribution for the first and third cavities of the labyrinth seal studied. All the inlet measurements were made along the center of the upstream tooth. The axial velocity profile indicates that there was a flow separation over the first tooth while there was no separation observable at the inlet to the third cavity. This separation in the initial cavity was due to a vena contracta effect caused by the fluid rushing in from the plenum into the labyrinth seal. Detailed measurements in the flow reversal region or near the wall were not possible with the laser anemometer. However, it should be noted that these measurements were made within 0.175$c$ (0.267 mm) of the wall.

The mean radial velocity profiles (Fig. 6) show outward velocity present over the entire inlet region for the first cavity. For the third cavity, the flow is tending away from the center of the clearance with outward velocity in the top half of the clearance and inward velocity in the bottom half.

The swirl velocity $u_\theta$ (Fig. 7) shows that the rotor caused the fluid in the plenum to prerotate at about 10 percent of the rotor's speed. This prerotation increased to 20 percent by the third cavity.

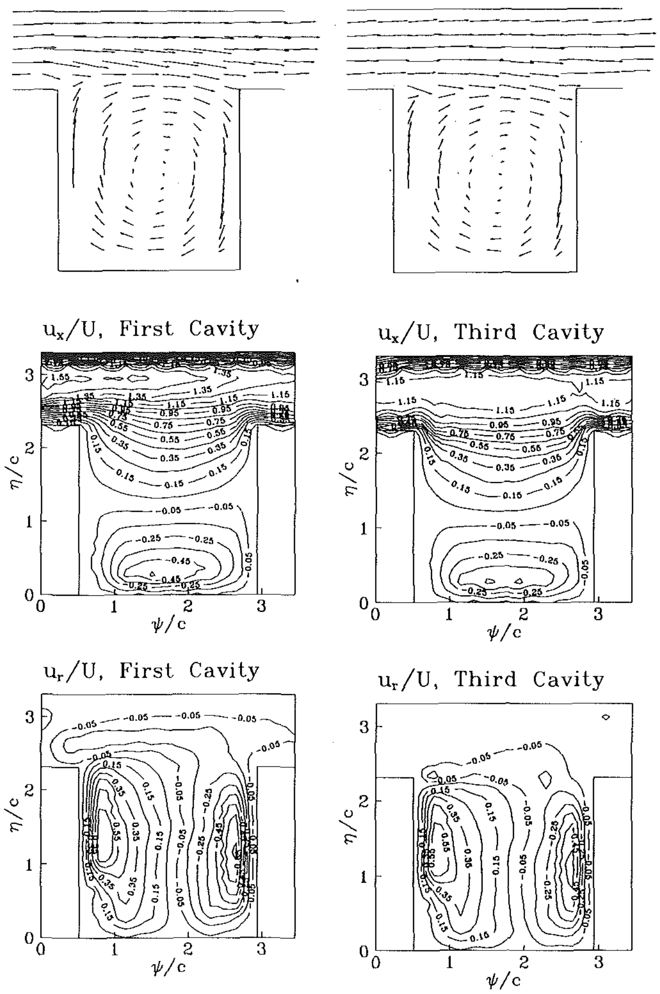

Fig. 9 Axial-radial velocity vector and amplitude contour plots

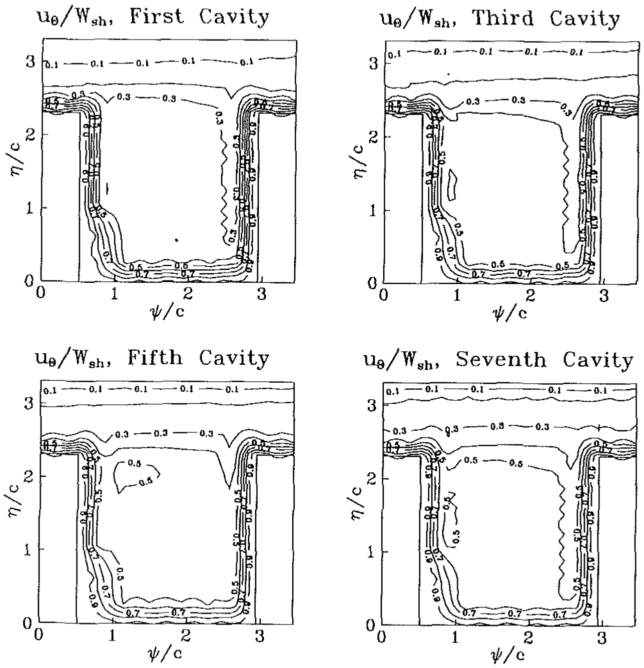

Fig. 10 Azimuthal mean velocity amplitude contours

The flow for both cavity inlets was turbulent, as indicated by the turbulence kinetic energy ($\kappa$) plot shown in Fig. 8. Over the top half of the clearance, $\kappa$ was about 0.15 (which corresponds to an 18 percent turbulence intensity) for both cavities. The third cavity maintained the same value in the lower half. The flow in the lower half of the first cavity was considerably more turbulent, reaching values of 0.58 for $\kappa$. This represents a highly turbulent flow and was caused by the vena contracta effect over the tooth.

**Mean Velocity Vector Fields.** Figure 9 shows the mean velocity vector field for an $r$-$x$ ($\theta = \text{const}$) plane for the first and third seal cavities. The data recorded for the fifth and seventh seal cavities were essentially identical to those of the third cavity for the distributions of the mean axial and radial velocity components. The first cavity showed a vena contracta effect as the fluid accelerated from the large plenum into the small clearance. Since the outer wall (the stator) mated smoothly with the outer wall of the plenum, the flow remained parallel to and attached to the stator wall. The rotor face was fully exposed to the plenum and hence there was a significant vena contracta effect on the lower regions. This resulted in a downward flow of the high-speed fluid above the large recirculation zone on the downstream side of the vena contracta.

For the third cavity, the leakage flow above the teeth was essentially straight through with only small amounts of radial velocity, in contrast to the first cavity. In both cases, there was a single large recirculation zone inside the labyrinth cavity. The strength of the recirculation was larger for the first cavity.

**Mean Velocity Contours.** Mean axial and radial velocity contour plots for the first and third seal cavities are presented in Fig. 9. For both of these mean velocity components, the fifth and seventh cavities had the same contour lines as in the third cavity. The inlet vena contracta effect was observable with axial velocities exceeding the average leakage velocity by 50 percent in the region above the seal tooth. By the time the flow exited the first cavity, the effects of the vena contracta had dissipated and the average axial velocity was near the average leakage velocity. In the regions between the top of the teeth and the stator, there was a rapid decrease in the axial velocity near the tooth surface. This shear layer spread in width as the flow progressed over the labyrinth cavity until the center was reached. The radial gradient of the axial velocity then increased as the flow began to adjust for its entrance into the region over the downstream tooth.

Inside the cavity, the axial velocity was very small near the vertical walls of the teeth and reached a maximum along the cavity centerline. The axial velocity was near zero along a horizontal line near the center of the cavity. Above the line, the flow was downstream and below the line it was upstream (negative values) reaching a maximum value of 50 percent of the average leakage velocity ($0.5U$).

The third, fifth, and seventh cavities had essentially the same flow pattern. They differed from the first cavity by the absence of the vena contracta effect and a reduction in the magnitude of the maximum negative axial velocity ($0.4U$). This corresponded to the reduction of the maximum positive axial velocity ($1.2U$), which was directly caused by the absence of the vena contracta effect.

The vena contracta effect was evident for the radial velocity contours with a significant radial velocity component ($0.1U$) present over the tooth at both the inlet and exit of the first cavity. In the subsequent cavities, the radial velocity in these regions was significantly smaller.

Inside the cavity, the recirculation zone had positive radial velocities along the back side of the inlet tooth and negative velocities along the front side of the downstream tooth. The magnitude of the recirculation was higher in the first cavity ($0.7U$ maximum) than in the subsequent cavities ($0.5U$ maximum) as shown by the larger (40 percent) maximum value of the radial velocities in the first cavity. This corresponded with

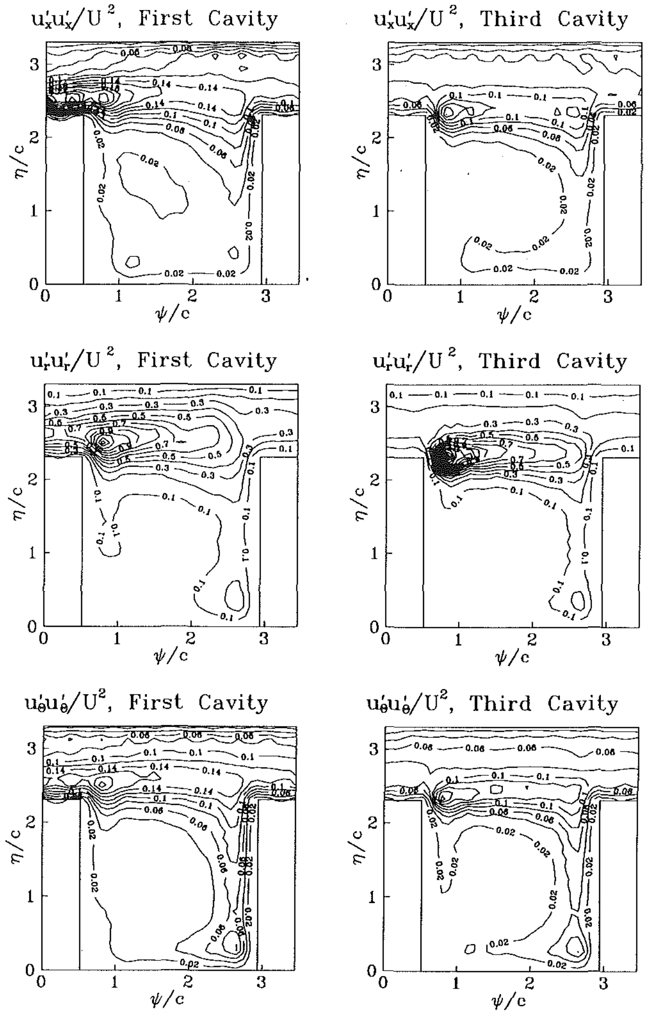

Fig. 11 Normal Reynolds stress amplitude contours

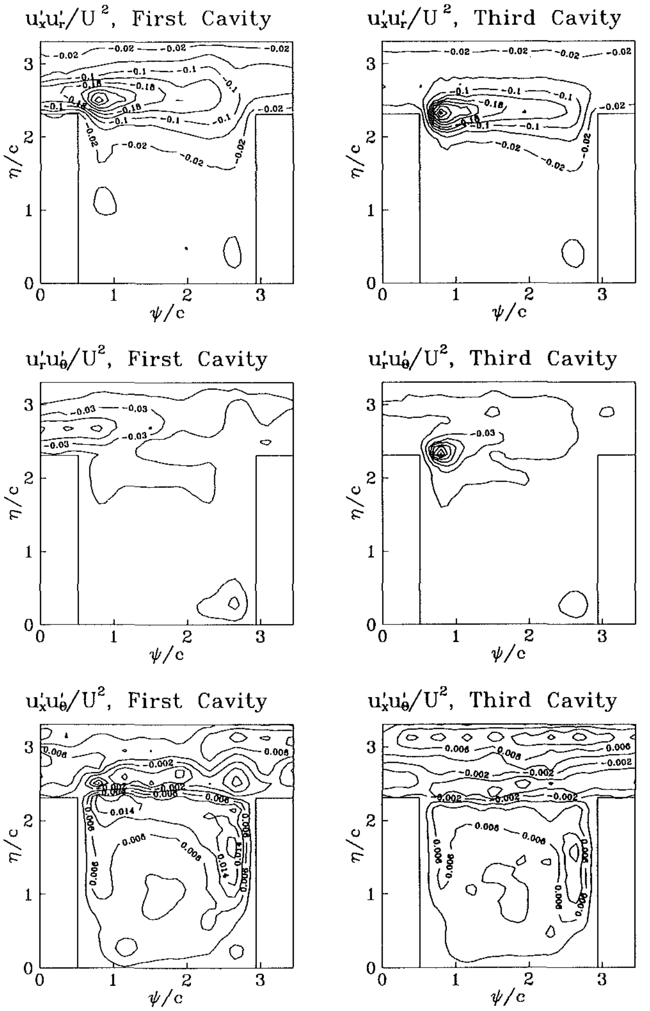

Fig. 12 Reynolds stress amplitude contours

the 25 percent larger values seen in the axial velocity contours for the first cavity compared to the others. The third, fifth, and seventh cavities all exhibited the same radial velocity contour distributions.

Azimuthal mean velocity contours are shown in Fig. 10. Along the surface of the tooth there was a significant gradient in the azimuthal velocity with the central 2/3 of the cavity having a constant azimuthal velocity. The magnitude of the azimuthal velocity in the central region increased from $0.35W_{sh}$ to $0.43W_{sh}$ to $0.50W_{sh}$ to $0.55W_{sh}$ as the flow progressed from the first to the third to the fifth and to the seventh cavity. Hence, after the fifth cavity, the azimuthal velocity field inside the cavity was close to becoming fully developed. The rate of increase in the azimuthal velocity in the central regions decreased as the flow progressed downstream.

In the regions above the teeth, the amount of swirl was continually increasing as the flow progresses from cavity to cavity. For this region, the azimuthal velocity distributions never became cavity independent. Hence, the azimuthal velocity field required considerably more seal cavities (at least seven) to become fully developed (cavity independent) while the axial and radial mean velocities became fully developed by the third cavity.

**Reynolds Stress Contours.** Figure 11 presents the contour plots for the nondimensionalized normal Reynolds stresses ($u_x'u_x'/U^2$, $u_r'u_r'/U^2$, and $u_\theta'\mu/U^2$) for the first and third cavities. Areas of high rates of strain produce large Reynolds stresses. This happened in the shear layer along the top of the seal cavity. The figure shows maximum values of the nondimensionalized normal axial Reynolds stress along this region with the largest values just downstream of the inlet tooth. The nondimensionalized normal axial Reynolds stress was larger in the first cavity than in the subsequnet cavities by 65 percent. After the first cavity, there was negligible difference in the contour lines from the third cavity to the seventh cavity. The first cavity again reflected the effects of the vena contracta with the larger mean axial velocity and the associated gradients, which produced more turbulence in the region above the teeth.

The nondimensionalized radial normal Reynolds stress ($u_r'u_r'/U^2$) had similar dependence upon the vena contracta with significantly larger fluctuation levels in the above-tooth region in the first cavity compared to the other cavities. The third, fifth, and seventh are essentially identical. The overall turbulence level for the nondimensionalized radial normal Reynolds stress was about four times higher than for the axial component. It should be noted that the radial velocity component was the "on-axis" component and had the maximum error of any velocity component. This error tended to maximize itself in the turbulence terms, which contained the radial velocity component. Past measurements in free jets showed this error to cause $u_r'u_r'$ to be at most 50 percent larger than the other two normal Reynolds stress terms. Therefore, the 400 percent increase in this term over the other terms in this case was definitely caused by the flow field. This was reasonable since the mean radial velocity had significantly higher gradients in the radial direction than the mean axial velocity did in the axial direction.

The nondimensionalized azimuthal normal Reynolds stress ($u_\theta' u_\theta'/U^2$), shown in the last row of Fig. 11, exhibits behavior similar to the nondimensionalized axial normal stresses. The magnitudes and their distributions were very similar. The larger nondimensionalized azimuthal normal Reynolds stress level in the first cavity compared to subsequent cavities was due to the larger difference in azimuthal velocity in the core region of the cavity with the rotor speed, hence larger velocity gradients.

Figure 12 presents the rest of the Reynolds stress tensor for this flow field ($u_x' u_r'/U^2$, $u_x' u_\theta'/U^2$, $u_r' u_\theta'/U^2$). Only the first and third cavities are shown since there was no variance from the third to the seventh cavity. The top row consisted of the $u_x' u_r'/U^2$ correlation contour plots. The magnitude of this nondimensionalized shear stress term was comparable to the normal stresses $u_x' u_x'/U^2$ and $u_r' u_r'/U^2$ in the clearance region of the seal and in the top protion of the cavity. This indicates a high level of coherence in the turbulence due to the eddies being generated by the $\partial u_x/\partial r$ mean velocity gradient in this region. However, inside the cavity, the correlation was very small. The maximum value occurred just downstream of the inlet tooth in the shear layer produced by the throughflow interacting with the recirculating fluid. This was also the location where the nondimensionalized normal shear stresses maximized. These values were all negative.

The third row of Fig. 12 shows the $u_\theta' u_x'/U^2$ nondimensionalized shear stress component. In this case, the nondimensionalized shear stress became negative in the shear layer at approximately the tooth height in the region between the teeth. The value was relatively small compared to the magnitudes that occurred for the $u_x' u_r'/U^2$ shear stress (10 percent). Overall $u_x' u_\theta'/U^2$ was substantially smaller than the $u_x' u_r'/U^2$ terms. As the flow progressed to downstream cavities, the magnitude of the $u_x' u_\theta'/U^2$ nondimensionalized stress steadily decreased in the recirculation zone of the cavity and there was an island of maximum strength just in front of the downstream tooth. The magnitude of the negative nondimensionalized stresses also decreased as the flow progressed downsteam. However, the $u_x' u_\theta'/U^2$ nondimensionalized stress in the throughflow area above the teeth remained essentially the same from cavity to cavity.

The $u_\theta' u_r'/U^2$ stress contour lines are shown in the second row of Fig. 12. The magnitudes of these stresses were comparable to those observed for the $u_x' u_\theta'/U^2$ stresses. However, for the $u_\theta' u_r'/U^2$ stresses the positive region occurred in the lower downstream corner of the cavity. The remainder of the flow field was characterized by negative values of $u_\theta' u_r'/U^2$. Again as had been the case for all of the nondimensionalized stresses (shear and normal), the maximum absolute value occurred just downstream of the inlet tooth in the highly sheared region where the throughflow met the recirculation zone. In the first cavity, there was considerable stress in the region above the inlet tooth. This was due to the development of the flow jetting into the first cavity and beginning rapidly to gain azimuthal velocity. In subsequent cavities, this region had relatively low values of $u_\theta' u_r'/U^2$ with minimal change from cavity to cavity.

## V Conclusions

Three-dimensional laser-Doppler measurements have been performed inside a seven-cavity labyrinth seal with a clearance of 0.00127 m (0.050 in.). These measurements included the mean velocity vector ($u_x$, $u_r$, and $u_\theta$) and the entire Reynolds stress tensor. The mean velocity data showed there was a vena contracta effect on the inlet to the first cavity. This caused significant differences in both the mean flow and Reynolds stresses between the first cavity and the third cavity. All cavities had a large single recirculation zone centered in the cavity. The axial and radial mean velocities became fully developed (independent of how many cavities upstream) by the third cavity. However, the azimuthal mean velocity was still developing by the seventh and last cavity.

The nondimensionalized normal Reynolds stresses became fully developed by the third cavity. The $u_r' u_r'/U^2$ stress component was substantially larger (four times) than the other two nondimensionalized normal stresses, yet all of the spatial distributions were essential the same for all three nondimensionalized normal stresses.

The nondimensionalized shear stresses ($u_x' u_r'/U^2$, $u_x' u_\theta'/U^2$, and $u_r' u_\theta'/U^2$) were dominated by the $u_x' u_r'/U^2$ term, which was several times larger than the other two terms. This term was always negative and maximized in the shear layer just downsteam of the inlet tooth. The $u_x' u_\theta'/U^2$ stress was negative in this same region and attained a positive maximum just in front of the downstream tooth half way down into the cavity. Of comparable value was the $u_\theta' u_r'/U^2$ stress, but it reached a negative maximum in the shear layer just downstream of the inlet tooth and a positive maximum in the lower downstream corner of the cavity. All the nondimensionalized Reynolds stresses were fully developed by the third cavity.

## Acknowledgments

This work was supported by the Air Force Office of Scientific Research through the purchase of equipment and the support of Mr. Johnson by the AFRAPT graduate student program. NASA Lewis (NAG3-181) supported the work through continued financial support for the operation of the facility and the support of staff under the supervision of Bob Hendricks.

## References

1 Ludwig, L. P., and Bill, R. C., "Gas Path Sealing in Turbine Engines," NASA Technical Memorandum 73890, 1978.

2 Sneck, H. J., "Labyrinth Seal Literature Survey," ASME *Journal of Lubrication Technology*, Vol. 102, Oct. 1980.

3 Buchter, H. H., *Industrial Sealing Technology*, Wiley, New York, 1980.

4 Falseh, J. I., "Review and Summary of Labyrinth Seal Theory and Design," Rocketdyne Report No. TMR 2115-3351, 1972.

5 Morrison, G. L., Rhode, D. L., Cogan, K. C., Chi, D., and Demko, J. A., "Labyrinth Seals for Incompressible Flow," Final Report for NASA Contract NAS8-34536, Nov. 1983.

6 Stoff, H., "Incompressible Flow in a Labyrinth Seal," *Journal of Fluid Mechanics*, Vol. 100, 1980.

7 Rhode, D. L., Demko, J. A., Traigner, U. K., Morrison, G. L., and Sobolik, S. R., "The Prediction of Incompressible Flow in Labyrinth Seals," ASME *Journal of Fluids Engineering*, Vol. 108, Mar. 1986, pp. 19-25.

8 Demko, J. A., Morrison, G. L., and Rhode, D. L., "Effect of Shaft Rotation on the Incompressible Flow in a Labyrinth Seal," *Proceedings of the 5th International Conference on Numerical Methods in Laminar and Turbulent Flow*, Montreal, Canada, July 1987.

9 Demko, J. A., "The Prediction and Measurement of Incompressible Flow in a Labyrinth Seal," Ph.D. Dissertation, Texas A&M University, College Station, TX, May 1986.

10 Demko, J. A., Morrison, G. L., and Rhode, D. L., "The Prediction and Measurement of Incompressible Flow in a Labyrinth Seal," AIAA Paper No. 88-0190, 1988.

11 Wittig, S., Schelling, U., Kim, S., and Jacobsen, K., "Numerical Predictions and Measurements of Discharge Coefficients in Labyrinth Seals," ASME Paper No. 87-GT-188, 1987.

12 Hauck, L., "Measurement and Evaluation of Swirl-Type Flow in Labyrinth Seals of Conventional Turbine Stages," presented at the Rotordynamic Instability Problems in High-Performance Turbomachinery—1982, NASA Conference Publication 2250, May 1982.

13 McLaughlin, D. K., and Tiederman, W. G., "Biasing Correction for Individual Realization of Laser Anemometer Measurements in Turbulent Flows," *Physics of Fluids*, Vol. 16, 1973, p. 2082.

# The Influence of the Recirculation Region: A Comparison of the Convective Heat Transfer Downstream of a Backward-Facing Step and Behind a Jet in a Crossflow

**V. Scherer**
Dr. -Ing.,
ABB Corporate Research,
6900 Heidelberg,
Federal Republic of Germany

**S. Wittig**
o. Prof. Dr.-Ing.,
Lehrstuhl and Institut für Thermische
Strömungsmaschinen,
Universität Karlsruhe (T.H.),
7500 Karlsruhe 1,
Federal Republic of Germany
Mem. ASME

*Convective heat transfer is examined in two typical examples of separated flows, namely, the flow over a backward-facing step and a two-dimensional jet entering a crossflow. Local Nusselt numbers were determined in and behind the recirculation region. The main parameters influencing the heat transfer, the Reynolds number, and the momentum flux ratio of the jet and the crossflow have been varied over a wide range. In addition to heat transfer measurements, the flow field has been documented using an LDA system and oil film technique. The static pressure distribution at the wall within the separated flow is also given. The measurements are compared with the results of a numerical code, based on a finite volume method, where the well known k-$\epsilon$ model is employed. The differences in Nusselt numbers predicted with one- and two-layer models are shown to demonstrate the influence of wall functions on heat transfer. The numerical and experimental results are compared with available data, and the differences and similarities in the heat transfer behavior of separated flows are discussed.*

## Introduction

Flow separation occurs on many thermally highly loaded gas turbine components. Typical examples are the flow fields in diffusers, on the suction side of a turbine blade, or in a combustion chamber. The existence of a separation bubble can lead to a considerable increase in the local as well as the overall heat transfer coefficients. A recirculation region on a solid body can be caused by a strong positive pressure gradient, a sharp edge, or the injection of a jet entering a crossflow. In spite of the different natures of these separation processes, similarities in the heat transfer pattern can be observed.

The majority of heat transfer work in two-dimensional separated flows has been concentrated on configurations involving an abrupt change in flow geometry (Fletcher et al., 1974; Kottke, 1983). The backward-facing step is the most extensively treated case of two-dimensional flow separation; here the conditions of a fixed separation point and parallel streamlines up to separation are nominally fulfilled. The magnitude of the heat transfer downstream of a step is characterized by the following: relatively low values in the separation bubble itself, a maximum near the flow reattachment point, and values typical for attached boundary layers downstream of reattachment. The experimental studies can be divided into three groups: laminar (Aung, 1983; Sparrow et al., 1987), transitional (Aung and Goldstein, 1970; Kottke, 1983) and turbulent (Seban, 1964; Vogel and Eaton, 1985) boundary-layer conditions upstream of the step. Here we consider only the case of turbulent boundary layers upstream of separation. Under these conditions the Reynolds number based on the step height, $\mathrm{Re}_S$, is the primary quantity influencing the flow field and heat transfer. Therefore, the Nusselt number in the separation bubble can be correlated with the step Reynolds number, i.e., $\mathrm{Nu} \sim \mathrm{Re}_S^n$. The values given in the literature for the exponential factor $n$ vary between 0.64 (Vogel and Eaton, 1985) and 0.87 (Seban, 1964). The cited literature involving flow past a backward-facing step was believed to be of sufficient quality and detail that this geometry was chosen to test the validity of the experimental setup and the utility of the numerical code.

When a two-dimensional jet is injected into a crossflow, the recirculation region is not induced by a solid body but by a hydrodynamic obstacle, the jet itself. Therefore, in addition to the Reynolds number of the crossflow, $\mathrm{Re}_H$, the momentum flux ratio of the jet to the crossflow, $J$, occurs as a second

---

Contributed by the International Gas Turbine Institute and presented at the 34th International Gas Turbine and Aeroengine Congress and Exhibition, Toronto, Ontario, Canada, June 4-8, 1989. Manuscript received at ASME Headquarters January 13, 1989. Paper No. 89-GT-59.

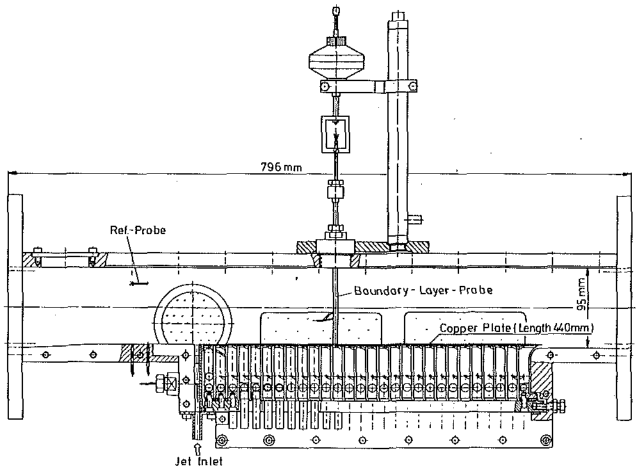

**Fig. 1 Layout of the test section**

scale factor, which determines the length and height of the separation bubble. The velocity and temperature distributions in such flow fields have been examined by our group (Wittig et al., 1984) and by several other authors (Kamotani and Greber, 1974; Mikhail et al., 1975), although very little documentation exists concerning the heat transfer distribution downstream of injection. Publications involving film cooling configurations are limited predominantly to low values of the momentum flux ratio ($J<1$) to prevent flow separation. The only results concerning high momentum flux ratios are given by Goldstein and Taylor (1982) for circular jets and by Wittig and Scherer (1987) for a two-dimensional jet, both injected in a crossflow. Wittig and Scherer (1987) detected the same heat transfer behavior in the separation bubble downstream of a jet and downstream of a backward-facing step. The magnitude of the heat transfer was low in the separation bubble; a maximum occurred near the reattachment point and was followed downstream of reattachment by a fast recovery to turbulent boundary-layer values. The maximum Nusselt number was determined to be a function of the crossflow Reynolds number and the momentum flux ratio. Further, it was shown that the heat transfer is dominated by the Reynolds number, whereas the momentum flux ratio determines the flow field, e.g., the location of flow reattachment.

The present study considers the similarities in the heat transfer behavior of recirculating flows. It is our intent to compare detailed measurements with numerical results obtained by using a modified computer code, which approximates turbulent elliptic flows. The code, employing finite difference schemes, has been successfully applied by our group to combustor flows (Noll et al., 1987) and to flows through labyrinth seals (Wittig et al., 1987). It has been extended using a two-layer near-wall model to demonstrate the influence of the wall functions on heat transfer.

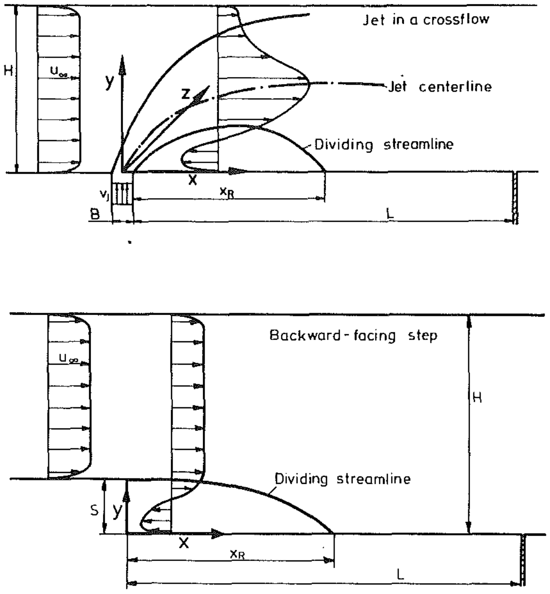

**Fig. 2 Test section and notation**

## Experimental Apparatus and Measurement Techniques

The major components of the experimental setup have been previously described by Wittig and Scherer (1987). The setup consists of a compressor, an electrical heater, and the test section itself. After heating, the air is divided into the main flow and the jet. Mass flow rates of both streams are measured by orifice meters and are individually controlled. The mixing jet enters the test section through a slot of 125 × 6 mm (see Fig. 1). The slot spans the distance between the side walls of the rig. The tunnel floor in front of the jet inlet can be replaced by a

## Nomenclature

$B$ = slot width
$c_p$ = pressure coefficient = $(p_s - p_\infty)/(\rho\,\bar{u}^2)$
$ex$ = expansion ratio = $H/(H-S)$
$H$ = channel height
$H_{12}$ = boundary-layer shape factor = $\delta_1/\delta_2$
$J$ = momentum flux ratio = $\rho_j \bar{v}_j^2/\rho\,\bar{u}^2$
$k$ = turbulent kinetic energy
$L$ = copper plate length
$\mathrm{Nu}_H$ = Nusselt number = $\dot{q}\,H/(T_\infty - T_w)\lambda$
$\mathrm{Nu}_S$ = Nusselt number = $\dot{q}\,S/(T_\infty - T_w)\lambda$
$\mathrm{Nu}_{xsh}$ = averaged shear layer Nusselt number = $1/L \int \dot{q}\,x_{sh}/(T_\infty - T_w)\lambda\,dx$
$p$ = pressure
$\dot{q}$ = heat flux
$\mathrm{Re}_H$ = Reynolds number = $u_\infty H/\nu$
$\mathrm{Re}_S$ = Reynolds number = $u_\infty S/\nu$
$\mathrm{Re}_{xsh}$ = shear layer Reynolds number = $u_\infty x_{sh}/\nu$
$\mathrm{Re}_{\delta_2}$ = Reynolds number = $u_\infty \delta_2/\nu$
$S$ = step height
$T$ = temperature
$\bar{u}$ = mean value of velocity detected by orifice meter
$\bar{v}_j$ = mean value of jet velocity detected by orifice meter
$u$, $v$, $w$ = time-averaged local velocity in $x$, $y$, $z$ directions
$x$ = streamwise coordinate
$x_R$ = reattachment distance
$x_{sh}$ = shear layer length
$y$ = distance from the wall
$y_v$ = laminar sublayer thickness
$z$ = distance in the spanwise direction
$\delta$ = boundary-layer thickness upstream of flow separation
$\epsilon$ = dissipation rate of turbulent kinetic energy
$\lambda$ = thermal conductivity of air
$\rho$ = density

**Subscripts**

$\infty$ = free stream
$j$ = denote jet values
$s$ = static
$t$ = total
$w$ = wall

**Table 1 Differential equations of turbulent flows**

2 D - Time-Averaged Navier-Stokes

$$\frac{\partial}{\partial x_i}(\rho u_i \Phi) = \frac{\partial}{\partial x_i}\left(\Gamma_\Phi \frac{\partial \Phi}{\partial x_i}\right) + S_\Phi$$

Convection = Diffusion + Source term

| Equation | $\Phi$ | $\Gamma_\Phi$ | $S_\Phi$ |
|---|---|---|---|
| Momentum | $u_i$ | $\mu_{eff}$ | $\frac{\partial}{\partial x_i}\left[\mu_{eff}\left(\frac{\partial u_i}{\partial x_j} - \frac{2\partial u_k}{3\partial x_k}\cdot\delta_{ij}\right)\right] - \frac{\partial}{\partial x_i}\delta_{ij}\left(p + \frac{2}{3}\rho\cdot k\right)$ |
| Energy | $h$ | $\mu_{eff}/Pr_{eff}$ | 0 |
| Turbulence | $k$ | $\mu_{eff}/C_k$ | $G_k - \rho\cdot\varepsilon$ |
|  | $\varepsilon$ | $\mu_{eff}/C_\varepsilon$ | $\frac{\varepsilon}{k}(C_1 G_k - C_2 \rho\cdot\varepsilon)$ |
| Continuity | 1 | 0 | 0 |

| $C_1$ | $C_2$ | $C_\mu$ | $C_\varepsilon$ | $C_k$ |
|---|---|---|---|---|
| 1.44 | 1.92 | 0.09 | 1.30 | 1.00 |

**Table 2 Near-wall models**

<table>
<tr><th>1-layer model</th><th colspan="4">2-layer model</th></tr>
<tr><td>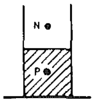 </td><td>Near-wall cell</td><td>Turb.kin. energy</td><td>Dissipation rate</td><td>Turb. wall shear stress</td></tr>
<tr><td></td><td colspan="4">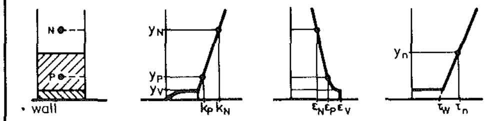 </td></tr>
<tr><td>$\epsilon_P = \frac{C_\mu^{\frac{3}{4}} k_P^{\frac{3}{2}}}{\kappa y_P}$<br>$\tau_W = const$</td><td colspan="4">Viscous sublayer $(0 < y^+ < 11)$: ▧<br>$k = k_v\left(\frac{y}{y_v}\right)^2$ $\quad\epsilon = 2\nu\left(\frac{\partial k^{\frac{1}{2}}}{\partial y}\right)^2$ $\quad\tau = 0$<br>Fully turbulent region $(11 < y^+ < 400)$: ▨<br>$k = \frac{k_n - k_v}{y_n - y_v}y + \left(k_P - \frac{k_P - k_N}{y_P - y_N}y_P\right) = by + a$ $\quad\epsilon = \frac{k^{\frac{3}{2}}}{C_l y}$ $\quad\tau = \tau_W + (\tau_n - \tau_W)\frac{y}{y_n}$<br>with $a = k_P - \frac{k_P - k_N}{y_P - y_N}y_P$ $\quad b = \frac{k_n - k_v}{y_n - y_v}$</td></tr>
<tr><td>Spalding</td><td colspan="4">Chieng and Launder</td></tr>
<tr><td colspan="5">$\frac{(T_p - T_w)c_p\rho\sqrt{k}c_\mu^{\frac{1}{4}}}{\dot{q}_w} = \frac{Pr_t}{\kappa}ln\left[\frac{Ey_p(c_\mu^{\frac{1}{2}}k_p)^{\frac{1}{2}}}{\nu}\right] + P$ $\quad P = 9.0\left[\left(\frac{Pr_l}{Pr_t}\right) - 1\right]\left[\frac{Pr_l}{Pr_t}\right]^{-\frac{1}{4}}$</td></tr>
</table>

backward-facing step element. The channel height and length were fixed at 95 and 800 mm, respectively.

The test section is equipped with a 440×125 mm copper plate with an integral surface. The copper plate is divided into 28 insulated segments, each of which is cooled separately. Water is used as the cooling fluid, and is held at a constant temperature by means of a thermostat. The mass flow rates in each segment are individually controlled by valves. This cooling process ensures a constant wall temperature boundary condition. On the other hand, the segmentation of the plate guarantees the local resolution of the heat transfer rates. The heat flux within the cooled segments is derived from one-dimensional heat conduction analysis, i.e., from the temperature difference determined by thermocouple measurements in the segments. The Nusselt numbers are obtained from the local heat flux. The assumption of one-dimensional heat conduction is supported by finite element heat conduction analysis. The static pressure distribution was obtained using static pressure taps drilled into the copper segments. Velocity and temperature profiles could be taken across the channel height at ten different streamwise locations along the spanwise center of the channel.

For the flow analysis, a two-color, four-beam, frequency-shifted LDA was used. The LDA was operated in forward scattering mode to obtain a better signal-to-noise ratio. Counter-based signal processing units were utilized together with a PDP-11/23 computer for data acquisition and reduction. To achieve a sufficient data rate, solid seeding particles were injected into the crossflow and the mixing jet.

The oil film technique (Maltby and Keating, 1962) has been applied to visualize the surface flow within and downstream of the separation bubble. The oil paint was mixed using engine oil, $TiO_2$ particles, linseed oil, and kerosine. The viscosity of the oil paint was adapted to the wall shear stress in the recirculation zone to assure that the oil film moved with the surface flow of the air. Therefore, kerosine was added to reduce the viscosity of the mixture depending on the Reynolds number of the flow. The installation of a removable plexiglass channel roof allowed observation of the oil film motion throughout the experiment. A repetition of the experiments under the same flow conditions yielded excellent reproducibility of the results, especially regarding the flow reattachment line. Test runs were carried out using different temperature levels of the free stream to assure that the oil film technique yielded identical results for the reattachment length under the same experimental conditions ($Re_H$, $J$=const).

## Experimental Conditions

The typical characteristics of the backward-facing step and the jet mixing flow are illustrated in Fig. 2. In determining the boundary-layer characteristics in front of the separation zone, detailed measurements using a pitot probe were performed. For both flow configurations the boundary layer was fully turbulent, with a typical value of the shape factor $H_{12}$ of 1.4.

The boundary-layer thickness for flow past a backward-facing step varied between 6.5 and 10 mm, depending on the step Reynolds number, $Re_s$. The step Reynolds number itself was held between $0.9\times10^4$ and $8.4\times10^4$ ($250<Re_{\delta_2}<2000$), and the heat transfer measurements were carried out with a free-stream temperature level of about 160°C. The expansion ratio is defined as the ratio of the channel height downstream and upstream of the step ($ex$ = 1.36).

For the perpendicular injection of the jet into the crossflow, the Reynolds number of the crossflow, $Re_H$, was altered between $6\times10^4$ and $20\times10^4$ ($800<Re_{\delta_2}<2500$) and the momentum flux ratio between 1.8 and 12. Typically, boundary-layer thicknesses between 8 and 10 mm could be observed, depending on crossflow Reynolds number and momentum flux ratio. The freestream temperature, $T_\infty$, was constant for each of the experimental runs, but varied between runs in the range from 104° to 184°C. The temperature of the mixing jet was slightly below the free-stream temperature due to heat losses. Two series of heat transfer measurements with different free-stream temperature levels (Series 1: $T_\infty = 109$°C, Series 2: $T_\infty = 170$°C) were carried out (see Wittig and Scherer, 1987, for further details). For both flow configurations, the wall temperature was kept nearly constant ($T_w = 30$°C).

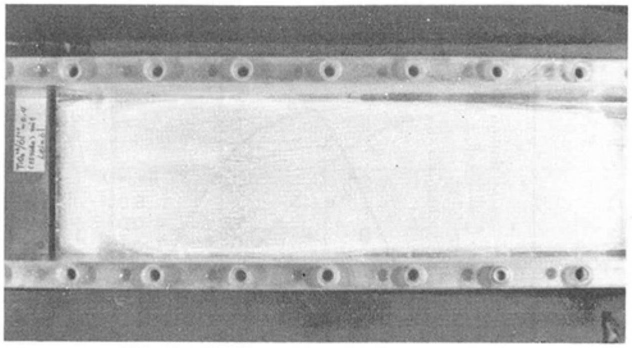

Fig. 3 Oil film pattern (jet in a crossflow)

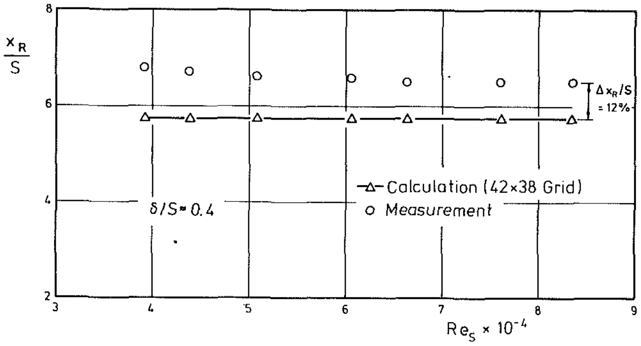

Fig. 4 Reattachment distance of backward-facing step flow

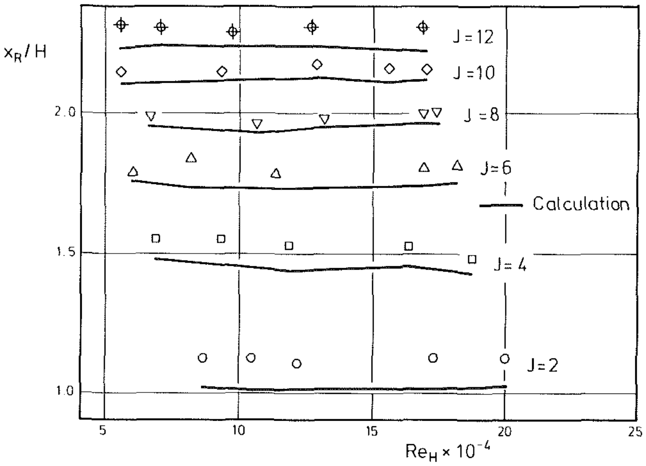

Fig. 5 Reattachment distance of a jet in a crossflow

## Numerical Procedure

For the calculation of a two-dimensional turbulent flow field, the time-averaged Navier-Stokes and the energy equations have to be solved. The behavior of turbulence in the present case is described by the well-known $k$-$\epsilon$ model. Table 1 summarizes the system of differential equations and the set of empirical constants used in the present study. A Cartesian grid has been applied to discretize the equations in the conventional manner, using the QUICK[1] scheme (Leonard, 1979) for the convective fluxes of thermal energy and momentum. The resulting system of nonlinear algebraic equations is solved by means of the SIMPLE[2] algorithm of Patankar and Spalding (1972). Typically, 40 × 40 grid nodes were used to simulate the flow field. The total calculation time strongly depended on the geometry—backward-facing step or jet in a crossflow—and the flow conditions, i.e., Re and $J$. However, CPU time was about 10 min (1000 iterations) on a Siemens 7881 computer (6 MIPS).

Usually, wall functions are utilized to avoid an extremely fine grid near the wall and to assure the convergence of the iterative solution procedure. Different assumptions have been proposed for the relations of the wall shear stress, the kinetic energy $k$, and the dissipation rate $\epsilon$ in the near-wall cell. The so-called one-layer model and the two-layer model of Chieng and Launder (1980), both installed in the present program, are compared in Table 2. The two-layer model divides the near-wall cell into a viscous sublayer and a fully turbulent region. Accordingly, the mean generation and dissipation rate of the $k$ equation is evaluated using the proposed variations of the turbulence quantities. The sublayer thickness $y_v$ is assumed to be a universal constant. More details of the solution procedure in the near-wall region are described by Chieng and Launder (1980). It should be noted that the two-layer near-wall model was developed for the calculation of backward-facing step and pipe expansion flows. The utility of the model for jet mixing flows is tested in the present paper.

## Results and Discussion

**Flow Field.** To obtain a comprehensive understanding of the heat transfer in separated flows a detailed account of the mean velocity, temperature, and turbulence fields is essential. The most important integral length scale of a separated shear layer is the reattachment length. As mentioned before, the reattachment length $x_R$ was determined using the oil film technique.

Taking as an example an oil film pattern of the jet mixing flow (see Fig. 3), the principle behavior of the surface streamlines in the region of separated flow can be discussed. This picture was taken through the plexiglass top wall onto the copper plate of the test section. The injection slot is visible on the left side of the photograph. Two important flow phenomena can be observed. First, two counterrotating corner vortices exist just downstream of the injection slot. They originate from channel side wall shear stress effects and disturb the two-dimensionality of the flow immediately downstream of separation. Second, the reattachment line approximately in the center of the test section is shown. It spans the distance between the channel side walls. The reattachment line, being only slightly curved, implies a satisfactory two-dimensionality of the flow in the neighborhood of reattachment. An oil film pattern for the flow past a backward-facing step looks very similar; especially, two counterrotating vortices immediately downstream of separation could be detected.

In Fig. 4 the measured dimensionless reattachment length for the backward-facing step is plotted versus the step Reynolds number. The reattachment distance shows almost no dependence on step Reynolds number. This is in agreement with the data given by Schmitt (1987). He found that for turbulent boundary-layer conditions upstream of the step, the reattachment length is independent of the Reynolds number. The reattachment length is underpredicted by the numerical calculations by about 12 percent. Although the QUICK scheme underpredicts the experimental data—a typical trend of the $k$-$\epsilon$ model—it provides an improved numerical solution when compared against simpler discretization schemes. Finally, it should be mentioned that the near-wall one- and two-layer models have negligible influence on the flow field.

In Fig. 5 the results for the jet mixing flow are presented.

---

[1] QUICK scheme (Quadratic Upstream Interpolation of Convective Kinematics): parabolic interpolation of the variables to be solved at the faces of the control volumes.

[2] SIMPLE algorithm (Semi-Implicit Method for Pressure Linked Equations): solution procedure, which treats the pressure velocity interaction by a pressure correction technique.

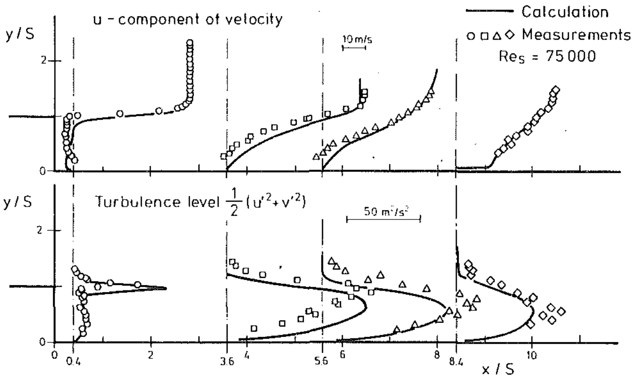

**Fig. 6 LDA measurements and calculations (backward-facing step)**

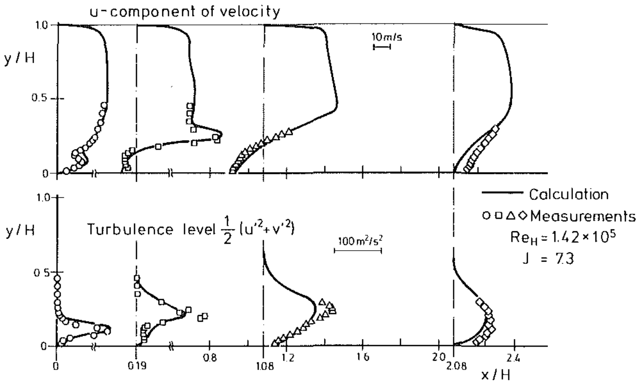

**Fig. 7 LDA measurements and calculations (jet in a crossflow)**

Note that the channel height serves as the length scale to nondimensionalize the reattachment length and to evaluate the Reynolds number. It is evident that this kind of presentation is only valid for this specific test geometry and cannot be transferred to other configurations, e.g., other channel heights. However, it is interesting to note that for the jet mixing flow too, the reattachment length is independent of the Reynolds number for turbulent boundary conditions upstream of the injection slot. The reattachment distance increases when the momentum flux ratio is increased, as indicated in Fig. 5. The same discrepancy as has been detected for the step flow, the underprediction of the reattachment length, occurs between the experimental and numerical results. Nevertheless, the oil film experiments have demonstrated that the $k$–$\epsilon$ model is able qualitatively to predict the physical behavior of the reattachment length of turbulent separated flows. Both flow configurations, backward-facing step and a jet in a crossflow, indicate little or no dependence of the reattachment length on Reynolds number as long as turbulent flow conditions exist upstream of separation.

Documentation of the flow field was accomplished by measuring mean velocity and turbulence intensity profiles.

To verify the oil film experiments, the location of flow reattachment was checked by means of the LDA system. For flow past a backward-facing step ($\mathrm{Re}_S = 4.8 \times 10^4$) the reattachment point was detected measuring the line of zero velocity. The LDA measurements indicated the location of flow reattachment at $x/S = 6.8$, whereas the oil film pattern yielded $x/S = 6.7$. This is an excellent agreement between the measurement methods taking into account the limited accuracy of the oil film technique.

Measurements of the $u$ component of the mean velocity and the turbulence level, obtained at different streamwise positions, are shown in Fig. 6 for flow past the backward-facing step; the results of the numerical study are included for comparison. The velocity is well predicted, except in the immediate neighborhood of the step, where inaccuracies occur presumably due to three-dimensional effects. Additionally, the predicted length of the separation bubble is too short, as mentioned earlier. However, downstream of reattachment (at $x/S = 8.4$), excellent agreement between measurements and calculations was obtained. High shear stress at the separation point ($x/S = 0$) leads to a peak value in the turbulence intensity level. This peak intensity grows initially as the shear layer develops, but decays farther downstream as the reattachment region is approached. An associated effect is the broadening of the peak, caused by convection and diffusion. The general behavior of turbulence is reproduced by the $k$–$\epsilon$ model, despite the underprediction of the turbulence level in the reattachment zone.

The same quantities, the $u$ component of the mean velocity and the turbulence level, are documented in Fig. 7 for the jet mixing flow. At $x/H = 0$, an interesting effect in the velocity distribution can be detected. The jet acts like an obstacle and, therefore, decelerates the main flow. This "stagnation" region is well predicted by the numerical results. Further, the calculations indicate a stronger jet penetration into the crossflow than observed experimentally, i.e., at $x/H = 0.19$. Again the reattachment length is underpredicted (see

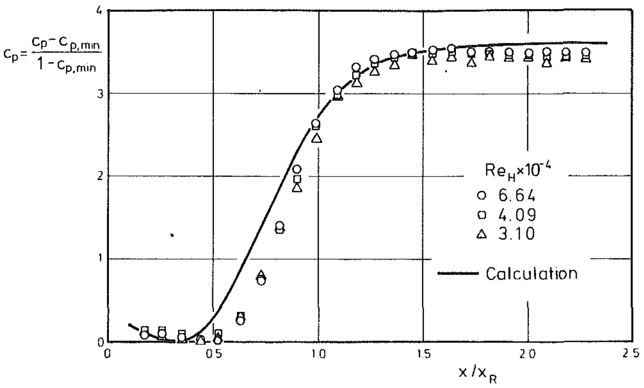

**Fig. 8 Similarity pattern of static pressure distribution (backward-facing step)**

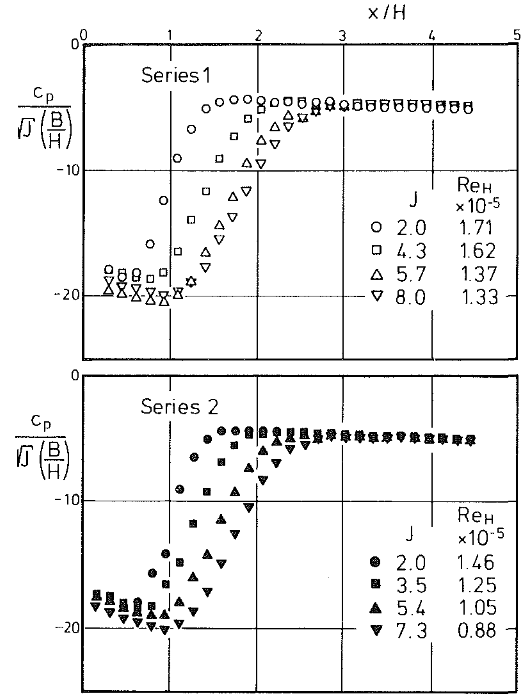

**Fig. 9 Similarity pattern of static pressure distribution (jet in a crossflow)**

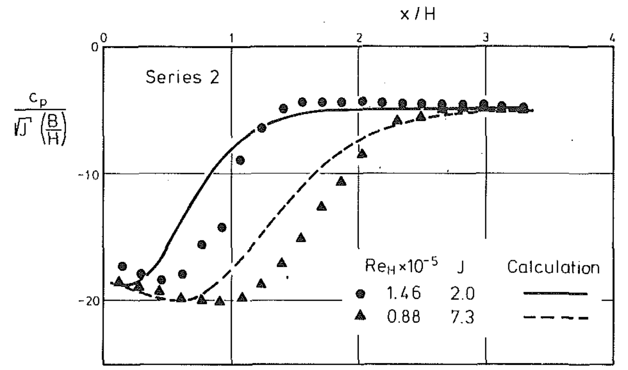

Fig. 10 Dependence of calculated and measured pressure distribution on momentum flux ratio

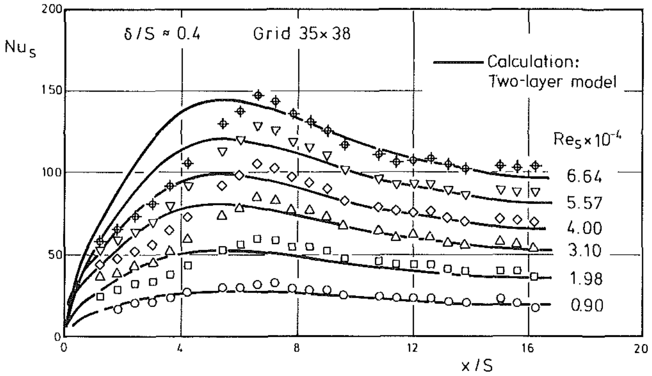

Fig. 11 Comparison of calculated and measured Nusselt numbers (backward-facing step)

$x/H = 2.08$). The turbulence level shows behavior similar to that for the backward-facing step flow. The peak value of turbulence level increases in the streamwise direction until the shear layer reaches the reattachment zone. Initially, the peak value is found at $y/H = 0.1$ at $x/H = 0$. Downstream of separation the peak value moves out toward $y/H = 0.19$ (at $x/H = 0.19$) and $y/H = 0.22$ (at $x/H = 1.08$). Near reattachment the peak value is again shifted closer to the wall as can be seen at $x/H = 2.08$. The broadening of the turbulence intensity distribution is overpredicted by the calculations, especially at the locations $x/H = 1.08$ and $x/H = 2.08$; however, the overall agreement is satisfactory.

The peak value of the turbulence intensity and the damping of the turbulence level near reattachment were qualitatively similar in both flow configurations. This similarity occurred despite the fact that the curvature of the streamlines is much higher in the jet mixing flow compared to the backward-facing step.

**Pressure Distribution.** The complete documentation of the flow characteristics downstream of the injection slot and the backward-facing step requires the measurement of the pressure distribution in this region. Usually, the pressure distribution for backward-facing step flows is presented using the coordinates of Roshko and Lau (1965). The results for three different Reynolds numbers are compared with the calculations in Fig. 8. It is obvious that the location of minimum pressure coefficient ($x/x_R = 0.3$) and the zone of pressure rise at the end of the recirculation region ($0.5 < x/x_R < 1.5$) predicted from the numerical simulation occur closer to the step than indicated by the experimental data. This phenomenon is confirmed by the $k$-$\epsilon$ calculations of Ilegbusi (1983) for flow past a backward-facing step.

The pressure distribution for the jet mixing flow is presented in a somewhat different manner. A simplified momentum balance indicates that for relatively low momentum flux ratios ($J < 10$) and low values of $B/H$ ($B/H = 0.06$), the ratio of $c_p$ to the square root of the momentum flux ratio multiplied by $B/H$ should be constant far downstream of reattachment. The excellent agreement of the measured values of Series 1 and 2 with this theoretical assumption can be seen in Fig. 9. In the recirculation zone, the pressure coefficient reaches a minimum (higher momentum flux ratios lead to an extended minimum) before rising to a maximum value. It is interesting to note that the shape of the pressure distributions is very similar to those of the backward-facing step. In addition, Fig. 9 illustrates the downstream shift of the minimum

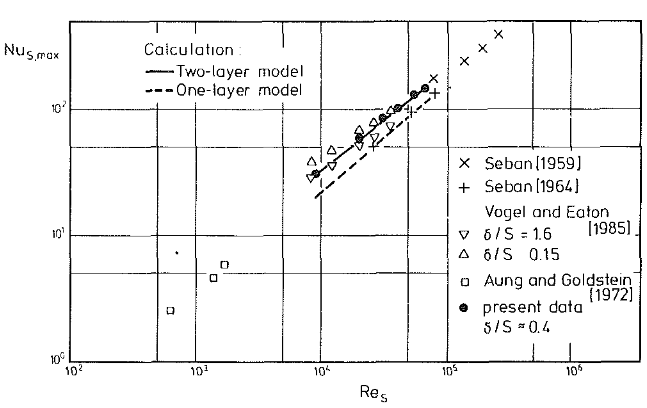

Fig. 12 Comparison of present heat transfer data with literature (backward-facing step)

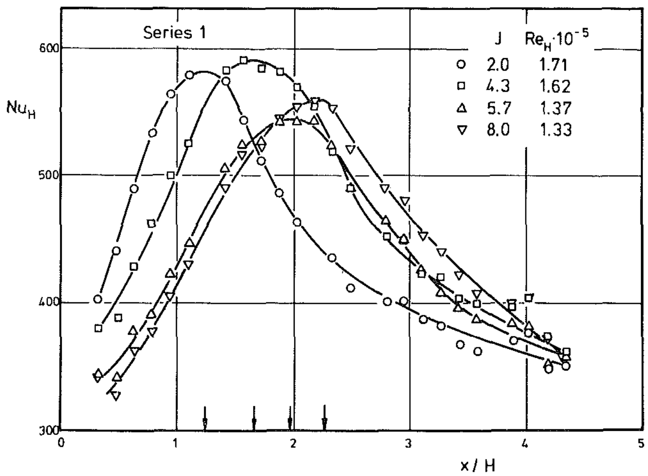

Fig. 13 Measured Nusselt numbers for a jet in a crossflow (Series 1)

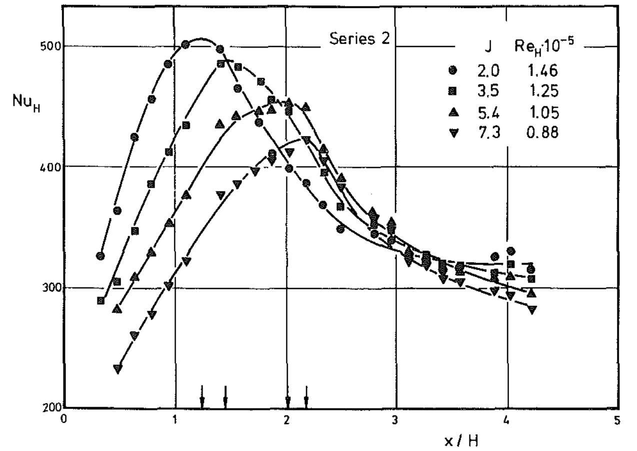

Fig. 14 Measured Nusselt numbers for a jet in a crossflow (Series 2)

pressure value and subsequent pressure rise with increasing momentum flux ratio. A comparison with the calculations is made in Fig. 10. The minimum and maximum level of the pressure coefficients are well predicted. The underprediction of the reattachment length by the $k$-$\epsilon$ model is one reason for the discrepancy between the location of calculated and measured pressure rise. Furthermore, the jet mixing experiments as well as the backward-facing step results show that the scaling of the $x$ axis by $x_R$ does not yield complete agreement between measurements and calculations.

**Heat Transfer.** It should be noted that the main emphasis of the present study was directed toward the heat transfer phenomena at the wall. Therefore, the backward-facing step as well as the jet mixing experiments were carried out under the boundary condition of constant wall temperature. For the mixing jet experiments the free-stream and jet temperatures were kept at similar levels. The momentum flux ratios were adjusted to cover those experienced in practical applications.

The experimental Nusselt number distribution downstream of the backward-facing step is compared with the calculations, using the two-layer model, in Fig. 11. Clearly, it can be seen that for increasing Reynolds numbers, the Nusselt numbers are increasing. Calculations and measurements confirm the heat transfer characteristics in a region of flow separation. These are: maximum heat transfer coefficients near flow reattachment, low values in the separation bubble itself, and a fast recovery downstream of reattachment. The maximum heat transfer and the recovery downstream of reattachment are well predicted by the two-layer near-wall model. In comparison to the measured values, the numerically predicted maximum Nusselt number is shifted toward the step. The underprediction of the reattachment length by the $k$-$\epsilon$ model is responsible for this effect. The measured Nusselt numbers show a slight tendency to increase near the step corner, which could not be reproduced numerically. This may be due to a small corner vortex at the step. This vortex was not predicted by the calculations, but is indicated in the oil film patterns as well as the LDA measurements. Additional numerical studies with varying grid size are underway.

To compare the data with literature, the peak Nusselt numbers are plotted versus the step Reynolds number in Fig. 12. The experiments of Vogel and Eaton (1985) cover a Reynolds number range similar to the present study and include additionally the variation of the boundary-layer thickness in front of the step (from $\delta/S=1.6$ to $\delta/S=0.15$). The boundary-layer thickness in the present data ($\delta/S=0.4$) lies between the values of Vogel and Eaton (1985). Taking into account the different boundary conditions (constant heat flux in Vogel and Eaton (1985), constant wall temperature in the present study), the agreement is relatively good. The results of the numerical calculations are shown in Fig. 12 as dashed (one-layer) and solid (two-layer) lines. The peak heat transfer is significantly underpredicted by the one-layer model. This seems to be a typical behavior of the one-layer model for backward-facing step flows and has been reported by other authors (Gooray et al., 1981). The backward-facing step results illustrate that, with the present experimental apparatus and the numerical code, experiments as well as calculations based on the two-layer model show close agreement with the literature and should give reliable data for heat transfer coefficients in separated flows.

The heat transfer pattern in the recirculation region, induced by a two-dimensional jet entering a crossflow, is very similar to that of a sudden geometry expansion. Local Nusselt numbers for a jet in a crossflow, as shown in our earlier paper (Wittig and Scherer, 1987), are plotted for Series 1 and 2 in Figs. 13 and 14, respectively. A distinct maximum in the Nusselt number is observed (indicated by arrows in Figs. 13 and 14), and is displaced downstream with increasing momentum flux ratio. A comparison of the Nusselt number distributions with flow field indicates that the maximum heat transfer rate occurs near the point of flow reattachment. The numerical and experimental Nusselt number distributions are compared in Fig. 15 and 16. In contrast to the backward-facing step, the two-layer model clearly overpredicts the heat transfer coefficients for mixing jet experiments; the one-layer model still underpredicts the Nusselt numbers. This is exactly the same result found by Amano and Sugiyama (1985) for the investigation of an axisymmetric jet impinging on a flat plate.

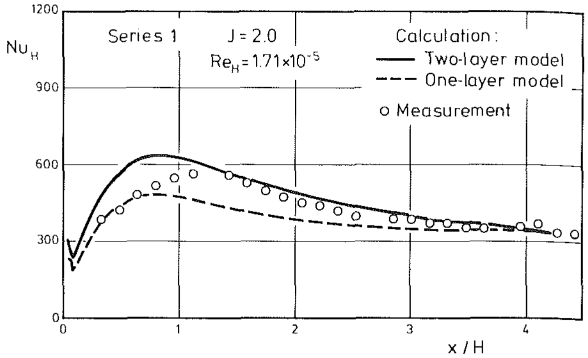

**Fig. 15** **Comparison of one- and two-layer model (jet in a crossflow, $J=2.0$)**

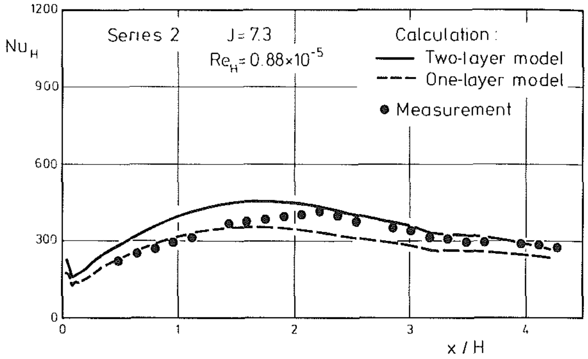

**Fig. 16** **Comparison of one- and two-layer model (jet in a crossflow flow, $J=7.3$)**

Additionally, the maximum calculated heat transfer was located approximately in the middle of the separation bubble, thus shifted upstream in comparison with the measurements. This is possibly due to the fact that the $k$ and $\epsilon$ equations, which strongly influence the heat transfer rates, have not been solved by the QUICK scheme, but by the Upwind[3] scheme. In general, it is assumed that the $k$ and $\epsilon$ equations are dominated by the source terms, i.e., production and dissipation. This is not valid for separated flows, where the production rate of $k$ vanishes at reattachment. Additional calculations using the Upwind scheme for the momentum equations confirm the assumption that a discretization effect may be the cause of the upstream shift in the peak of the Nusselt number distribution.

The maximum Nusselt number can be correlated with the crossflow Reynolds number and the momentum flux ratio. We have described this empirical relationship in our earlier work (Wittig and Scherer, 1987), as

$$\mathrm{Nu}_{H,\max}=0.108\ \mathrm{Re}_H^{0.704}\ J^{0.109} \tag{1}$$

This correlation, together with the numerical calculations obtained for Series 1 and 2, is presented in Fig. 17. Again the overprediction of the peak Nusselt number by the two-layer

---

[3] Upwind scheme: the value of a variable at a control volume interface is equal to the grid point value of the variable on the upwind side.

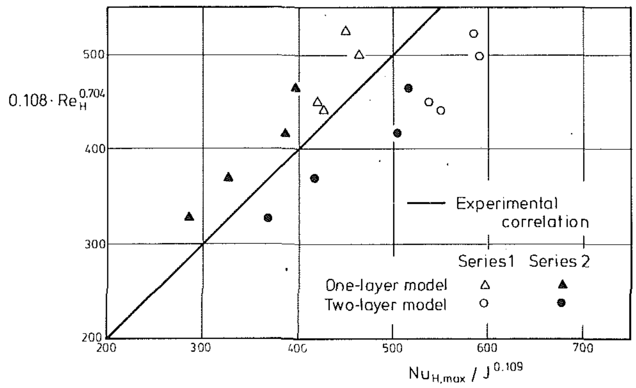

**Fig. 17 Comparison of experimental correlation and calculated heat transfer (jet in a crossflow)**

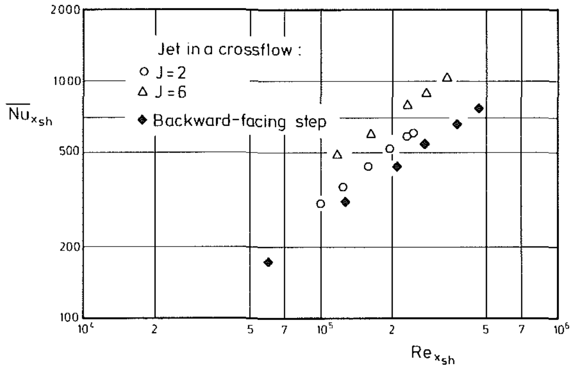

*Fig. 18 Shear layer model for heat transfer*

model and the underprediction by the one-layer model is obvious.

To compare the heat transfer rates of the two separated flows under consideration, a consistent coordinate system is introduced. Following a suggestion of Kottke (1983), the shear layer length $x_{sh}$ has been taken as the reference length scale to recalculate the Reynolds and Nusselt numbers of both flows. Kottke (1983) evaluated the shear layer length assuming that the shape of the shear layer behaves like an ellipse. Using an observation of Mikhail et al. (1975), namely, that the ratio of shear layer height to reattachment length is constant for a two-dimensional jet independent of $B/H$, the following relations can be obtained for the backward-facing step:

$$x_{sh} = 1.02\, x_R \tag{2}$$

and for the mixing jet

$$x_{sh} = 1.05\, x_R \tag{3}$$

The result of this modified presentation is documented in Fig. 18, where the averaged shear layer Nusselt number is plotted versus shear layer Reynolds number. It can be seen that for the same shear layer length the jet mixing flow yields higher Nusselt numbers than the backward-facing step. This might be due to the higher production rate of shear stress for a jet in a crossflow compared with a backward-facing step. Assuming the same crossflow velocity and shear layer length for both flows, the shear layer Reynolds number is identical. Because of the high momentum flux ratios ($J > 1$) the jet velocity is higher than the crossflow velocity and produces, therefore, additional shear stress, not experienced in flow past the backward-facing step. A second effect could be the strong streamline curvature in the jet mixing flow, which leads to enhanced turbulent kinetic energy production and, therefore, to higher heat transfer rates. It is also possible that larger flow structures develop in the jet mixing flow, which are somewhat inhibited in the step flow, due to a fixed separation point. The large structures would enhance turbulent mixing and contribute to higher heat transfer rates.

For a final clarification of these questions further detailed measurements of the turbulence structure of the flow are underway.

## Summary

In an attempt to show the similarities in heat transfer of separated flows, detailed flow field and heat transfer measurements downstream of a backward-facing step and a two-dimensional jet entering a crossflow were presented. For both types of flow the same characteristic heat transfer distribution was obtained: relatively low values of the heat transfer coefficient in the separation bubble, a maximum near the flow rattachment, and values typical for attached boundary layers downstream of reattachment. The experimental data have been compared with the results of a two-dimensional finite difference program for turbulent elliptic flows. The reattachment length of the separation bubble is underpredicted numerically by 10 to 20 percent. It has been documented that wall functions have a dominating influence on the calculated heat transfer. The two-layer near-wall model yields excellent agreement with measurements for the backward-facing step flow. The numerical prediction of heat transfer behavior in jet impingement flows is still unsatisfactory and should be the focus of future research.

## Acknowledgments

The authors are indebted to the Deutsche Forschungsgemeinschaft (German Science Foundation), which supports the work through the "Sonderforschungsbereich 167, High Intensity Combustors." Thanks are due to Dipl.-Ing. K. Dullenkopf for his generous assistance in carrying out the LDA measurements and to Dr. B. Noll for his help and discussions throughout the work.

## References

Amano, R. S., and Sugiyama, S., 1985, "An Investigation on Turbulent Heat Transfer of an Axisymmetric Jet Impinging on a Flat Plate," *Bull. of JSME*, Vol. 28, pp. 74–79.

Aung, W., and Goldstein, R. J., 1970, "Temperature Distribution and Heat Transfer in a Transitional Separated Shear Layer," in: *Heat Transfer*, U. Grigull and E. Hahne, eds., Elsevier Pub. Comp., Amsterdam, Vol. 2.

Aung, W., and Goldstein, R. J., 1972, "Heat Transfer in Turbulent Separated Flow Downstream of a Rearward-Facing Step," *Isr. J. of Technology*, Vol. 10, pp. 35–41.

Aung, W., 1983, "An Experimental Study of Laminar Heat Transfer Downstream of Backsteps," ASME *Journal of Heat Transfer*, Vol. 105, pp. 823–829.

Chieng, C. C., and Launder, B. E., 1980, "On the Calculation of Turbulent Heat Transport Downstream From an Abrupt Pipe Expansion," *Numerical Heat Transfer*, Vol. 3, pp. 189–207.

Fletcher, L. S., Briggs, D. G., and Page, R. H., 1974, "Heat Transfer in Separated and Reattached Flows: an Annotated Review," *Isr. J. of Technology*, Vol. 12, pp. 236–261.

Goldstein, R. J., and Taylor, J. R., 1982, "Mass Transfer in the Neighborhood of Jets Entering a Crossflow," ASME *Journal of Heat Transfer*, Vol. 104, pp. 715–721.

Gooray, A. M., Watkins, C. B., and Aung, W., 1981, "Numerical Calculations of Turbulent Heat Transfer Downstream of a Rearward-Facing Step," *Proc. of the 2nd Int. Conf. on Numerical Methods in Laminar and Turbulent Flows*, Venice, Italy, pp. 639–651.

Ilegbusi, J. O., 1983, "A Revised Two-Equation Model of Turbulence," PhD Thesis, University of London, United Kingdom.

Kamotani, Y., and Greber, I., 1974, "Experiments on Confined Turbulent Jets in Cross Flow," NASA CR-2392.

Kottke, V., 1983, "Strömung, Stoff-, Wärme- und Impulsübertragung in lokalen Ablösegebieten," *Fortschr. Ber. VDI*, Vol. 7, No. 77.

Leonard, B. P., 1979, "A Stable Accurate Convective Modelling Procedure Based on Quadratic Upstream Interpolation," *Computer Methods in Applied Mechanics and Engineering*, Vol. 19, pp. 59–98.

Maltby, R. L., and Keating, R. F. A., 1962, "The Surface Oil Flow Technique for Use in Low Speed Wind Tunnels," AGARDograph No. 70, pp. 29-38.

Mikhail, R., Chu, V. H., and Savage, S. B., 1975, "The Reattachment of a Two-Dimensional Jet in a Confined Cross Flow," *Proc. of the 16th IAHR Cong.*, Sao Paulo, Brazil, Vol. 3, pp. 414-419.

Noll, B., Wittig, S., and Steinebrunner, K., 1987, "Numerical Analysis of the Flame-Stabilizing Flow in the Primary Zone of a Combustor," *Proc. of the 1987 ASME-JSME Thermal Engineering Joint Conference*, Honolulu, HI, Vol. 1, pp. 151-159.

Patankar, S. V., and Spalding, D. B., 1972, "A Calculation Procedure for Heat, Mass and Momentum Transfer in the Three-Dimensional Parabolic Flows," *Int. J. Heat Mass Transfer*, Vol. 15, pp. 1787-1805.

Roshko, A., and Lau, J. C., 1965, "Some Observations on Transition and Reattachment of a Free Shear Layer in Incompressible Flow," *Proc. Heat Transfer and Mechanics Institute*, Stanford University Press, Stanford, CA, pp. 157-167.

Schmitt, F., 1987, "Untersuchungen der turbulenten Stufenströmung bei hohen Reynoldszahlen," *Fortschr. Ber. VDI*, Vol. 7, No. 117.

Seban, R. A., 1964, "Heat Transfer to the Turbulent Separated Flow of Air Downstream of a Step in the Surface of a Plate," ASME *Journal of Heat Transfer*, Vol. 86, pp. 259-264.

Sparrow, E. M., Kang, S. S., and Chuck, W., 1987, "Relation Between the Points of Flow Reattachment and Maximum Heat Transfer for Regions of Flow Separation," *Int. J. Heat Mass Transfer*, Vol. 30, pp. 1237-1246.

Vogel, J. C., and Eaton, J. K., 1985, "Combined Heat Transfer and Fluid Dynamic Measurements Downstream of a Backward-Facing Step," ASME *Journal of Heat Transfer*, Vol. 107, pp. 922-929.

Wittig, S. L. K., Elbahar, O. M. F., and Noll, B. E., 1984, "Temperature Profile Development in Turbulent Mixing of Coolant Jets With a Confined Hot Crossflow," ASME JOURNAL OF ENGINEERING FOR GAS TURBINES AND POWER, Vol. 106, pp. 193-197.

Wittig, S., Schelling, U., Kim, S., and Jacobsen, K., 1987, "Numerical Predictions and Measurements of Discharge Coefficients in Labyrinth Seals," ASME Paper 87-GT-188.

Wittig, S., and Scherer, V., 1987, "Heat Transfer Measurements Downstream of a Two-Dimensional Jet Entering a Crossflow," ASME *Journal of Turbomachinery*, Vol. 109, pp. 572-578.

# Thermal Barrier Characteristics of Partially Stabilized Zirconia Coatings on INCOLOY Alloy 909 (A Controlled Expansion Alloy)

**G. D. Smith**
Inco Alloys International, Inc.,
Huntington, WV 25720

*INCOLOY[1] alloy 909 is a low-expansion alloy used in critical seal and shaft applications within the gas turbine engine. However, because of its poor oxidation resistance at elevated temperatures, the maximum service temperature is limited. Since its coefficient of expansion is similar to that of partially stabilized zirconia for temperatures to 1200°F (649°C), it has been proposed to use this metal-ceramic combination for dimensionally critical, air-cooled jet engine components. This coating system should extend temperature limitations by reducing metal temperatures and providing oxidation resistance. The performance advantage offered by a thermal barrier coating has been investigated at temperatures up to 2000°F (1093°C) and the results are presented in this paper. Metal temperatures and heat flow rates of coated and bare specimens are compared for two air-cooling flow rates.*

## Introduction

An established practice for increasing power and reliability of gas turbine engines is to protect the metallic surfaces of the individual components with ceramic thermal barrier coatings (Richerson, 1982). This has not always been feasible because of the differences in the metal and ceramic coefficients of expansion. Due to this difference, cycling to and from high temperatures causes early rupture of the coating with subsequent exposure of the metal surface to the environment. Another important factor is the extra mass the coating adds to the engine as a whole, and also, the extra stress added to each individual component subjected to radial acceleration. Obviously, the minimum coating thickness that imparts satisfactory thermal protection must be used.

Published results demonstrate that the combination of air cooling and a thermal barrier coating permits either an increase in engine operational temperature for the coated components or the opportunity for reduction in air-coolant volumes, while keeping the ceramic–substrate boundary within compatible thermal expansion limits (Berndt and Miller, 1984; Carlson and Stoner, 1977; Liebert et al., 1976; Miller et al., 1980; Sheffler and Gupta, 1988; Strangman, 1985; Toriz et al., 1988). This paper measures the relative contribution to metal cooling afforded by the cooling air and by the thermal barrier. An estimate of the heat flow reduction resulting from the use of the thermal barrier is presented.

Yttria partially stabilized zirconia (PSZ) as a ceramic coating has been extensively investigated (Cawley, 1984; Johner et al., 1988; Miller, 1987; Secura, 1977; Tjong, and Wu, 1987). Apparently, yttria partially stabilized zirconia is presently the preferred ceramic coating material for most thermal barrier applications, mostly because of its toughness, low thermal conductivity, and relatively high coefficient of expansion for a ceramic material. In addition, as seen in Fig. 1, its coefficient of expansion is very similar to that shown by the controlled coefficient of expansion alloy INCOLOY alloy 909 at temperatures up to 1200°F (649°C). Matching the coefficient of expansion of the substrate and the thermal barrier coating should ameliorate coating system failures resulting from differential thermal expansion stresses. That these stresses are detrimental has been documented in both laboratory simulations and gas turbine engines (DeMasi, 1986; Miller and Lowell, 1983; Liebert and Miller, 1984). INCOLOY alloy 909 has poor high-temperature corrosion resistance due to the absence of chromium (Table 1). Therefore, a thin high-temperature corrosion-resistant layer has to be provided. A preferred protective coating is the NiCrAlY alloy (Table 1), which can be air or low-pressure plasma spray coated on the INCOLOY alloy 909 surface prior to ceramic coating. The goal of the present investigation was to assess the thermal advantage due to the thermal barrier coating deposited on air-cooled cylindrical specimens.

**Table 1 Nominal chemical compositions (w/o)**

| Alloy | Ni | Cr | Co | Nb | Si | Al | Ti | Y | $Y_2O_3$ | $ZrO_2$ |
|---|---|---|---|---|---|---|---|---|---|---|
| INCOLOY alloy 909 | 38 | - | 13 | 5 | .4 | - | 2 | - | - | - |
| NiCrAlY (Ni211) | 67 | 22 | - | - | - | 10 | - | 1 | - | - |
| 8%$Y_2O_3$-PSZ | - | - | - | - | - | - | - | - | 8 | 92 |

---

[1] INCOLOY is a trademark of the Inco family of companies.

Contributed by the International Gas Turbine Institute and presented at the 34th International Gas Turbine and Aeroengine Congress and Exhibition, Toronto, Ontario, Canada, June 4–8, 1989. Manuscript received at ASME Headquarters March 1990. Paper No. 89-GT-146.

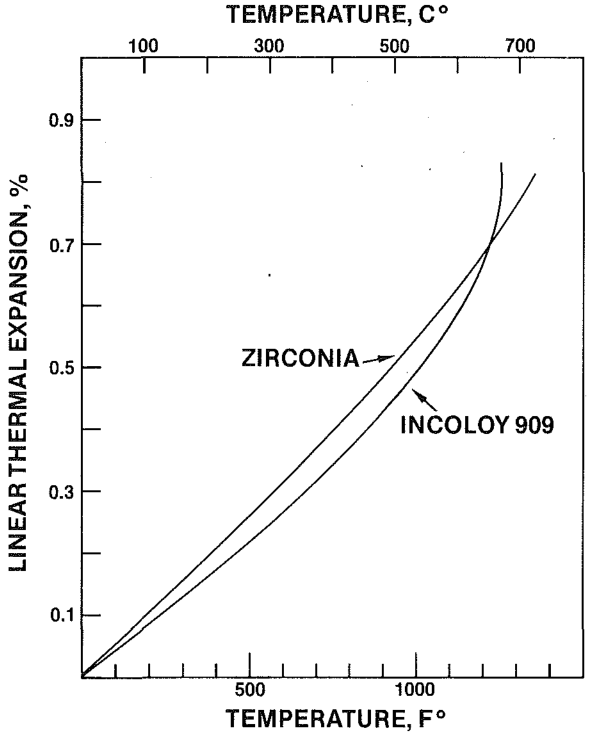

**Fig. 1 Linear thermal expansion of yttria partially stabilized zirconia and INCOLOY alloy 909 versus temperature**

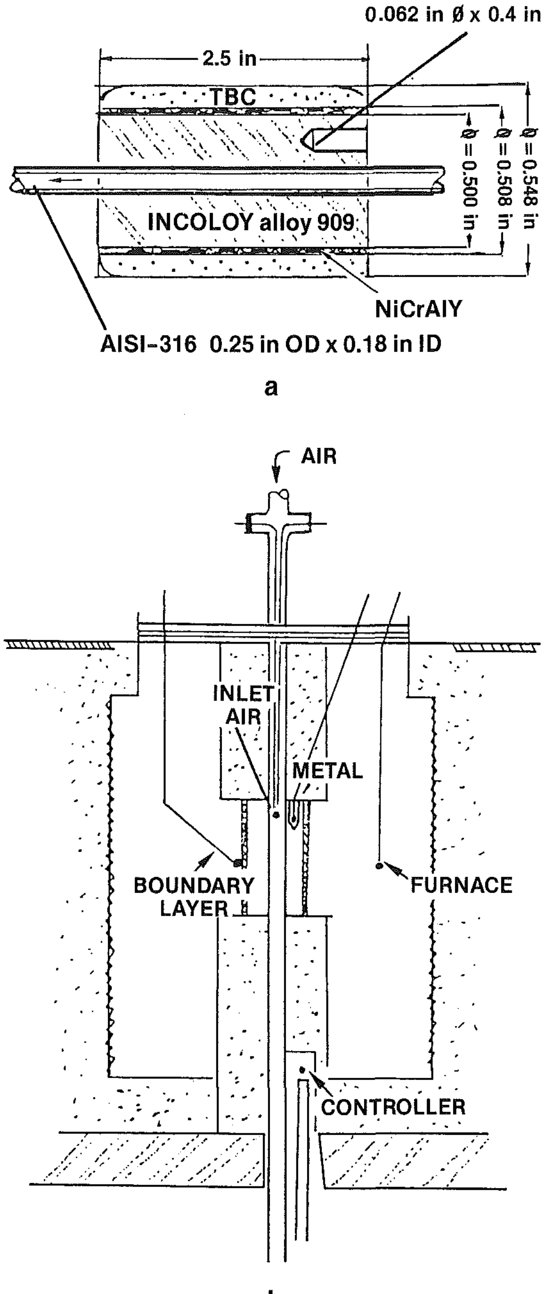

**Fig. 2 (*a*) Specimen configuration; (*b*) experimental setup showing the thermocouple positions in and around the specimen**

## Experimental Procedure

INCOLOY alloy 909 cylindrical specimens 0.500 in. (12.7 mm) diameter by 2.5 in. (63.5 mm) length with a 0.25 in. (6.35 mm) longitudinally centered bore were used (Fig. 2(*a*)). A 0.0625-in (1.59-mm) thermocouple well, 0.4 in. (10.1 mm) deep was drilled longitudinally in the specimen wall between the bore hole and metal/ceramic interface. The o.d. had been previously air plasma sprayed with NiCrAlY alloy 0.004 in. (100 $\mu$m) thick for oxidation protection. A 0.020-in. (0.50-mm) 8 percent yttria-zirconia thermal barrier coating was subsequently air plasma sprayed on a high austenitic NiCrAlY intermediate layer.

The following experimental setup was devised: a 0.250 in. (6.35 mm) o.d. $\times$ 0.18 in. (4.57 mm) i.d. AISI 316 stainless steel tube was used to carry the cooling medium and was driven into the specimen with a tight fit (Fig. 2(*a*)). This fit improves at high temperatures since the coefficient of expansion of AISI 316 is greater than that of INCOLOY alloy 909.

As seen in Fig. 2(*b*), the tube passes through diatomaceous bricks to assure that near ambient temperature air would flow into the specimen, by preventing exposure of the bare tube to the furnace environment. A slanted 1 in. (25.4 mm) deep $\times$ 0.125 in. (32 mm) wide channel had to be cut into the top diatomaceous brick to accommodate a chromel/alumel thermocouple. This thermocouple was used to measure the metal temperature. The bottom diatomaceous brick was used as a support and also to protect the AISI 316 stainless steel from exposure to high temperatures and allow easier removal of the specimen after testing.

The thermocouple assemblies are also shown in Fig.2(*b*). Except for the chromel/alumel thermocouple that was placed inside the well to measure metal temperatures, all were made of platinum/platinum-10 percent rhodium.

The cooling medium was compressed laboratory air, which passed through a filter and a pressure regulator with the lower pressure end at 80 psig (0.56 MNm$^{-2}$). The air flow rate was controlled by a mass flow controller, which had been calibrated throughout the range. The measurements were then corrected

### Nomenclature

$D$ = hydraulic diameter, ft (m)
$k$ = thermal conductivity, Btu/ft•sec•°F (W/m$^2$K)
$Q$ = time rate of heat transfer per unit area, Btu/ft$^2$•sec (W/m$^2$)
$R$ = outer radius, in. (m)
$r$ = inner radius, in. (m)
Re = Reynolds number
$T$ = temperature, °F (°C)
$V$ = velocity, ft/sec (m/s)
$\delta$ = difference between values
$\rho$ = air density at temperature $T$, lb/ft$^3$ (kg/m$^3$)
$\mu$ = absolute viscosity, lb/ft•sec (kg/m•s)

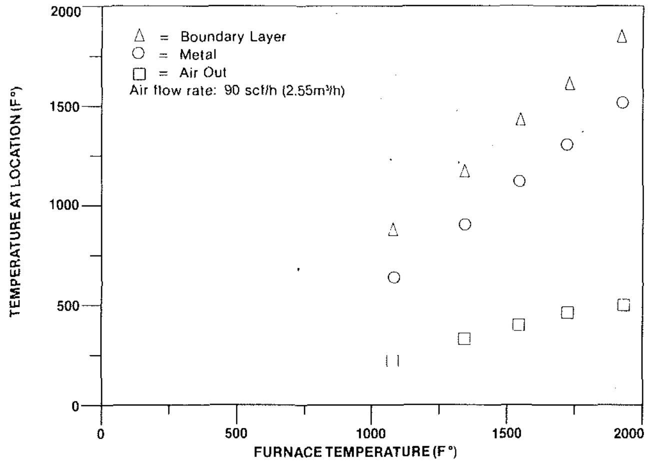

**Fig. 3 Temperatures at several locations for bare INCOLOY alloy 909**

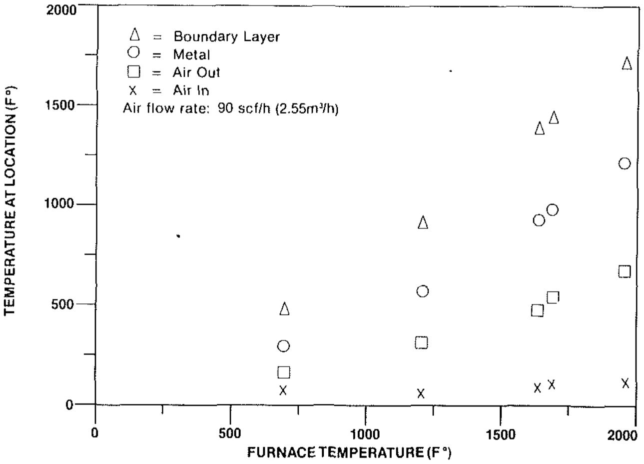

**Fig. 5 Temperatures at several locations for bare INCOLOY alloy 909**

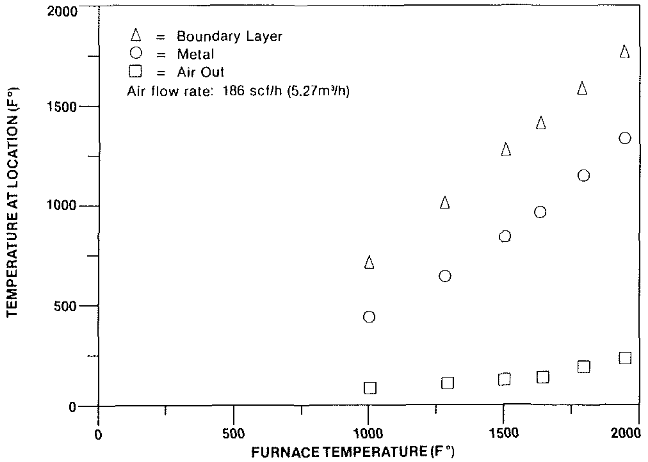

**Fig. 4 Temperatures at several locations for TBC INCOLOY alloy 909**

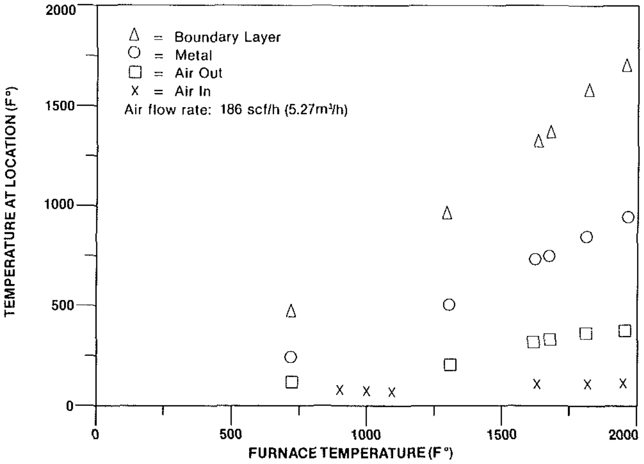

**Fig. 6 Temperatures at several locations for TBC INCOLOY alloy 909**

to STP conditions, and a least-squares fit analysis correlated the controller digital readout and the corrected air flow rates.

A pit-type furnace, with 6 in. (152 mm) i.d. electrically heated shells, insulated with glass wool on the outside, top and bottom, was used. As seen in Fig. 2(*b*), the AISI #316 stainless steel tubing outlet was positioned outside of the furnace shell to prevent the cooling air from disturbing the furnace temperature distribution. The furnace control thermocouple was also of the platinum/platinum-10 percent rhodium type and was inserted through the bottom insulation of the furnace. This thermocouple was only used to maintain the furnace temperature at the desired level through the use of a temperature controller.

The furnace temperature was measured at the same horizontal level as that of the specimen midlength and at about 2.5 in. (63.5 mm) from the specimen outside surface (Fig. 2(*b*)). One thermocouple was inside the air-coolant tube and could be positioned to measure either the inlet (near the top end of the specimen) or the outlet (near the bottom end of the specimen) air temperature. Because a mullite temperature protector was used, it was assured that the air temperature thermocouple bead was always in the center of the tube cross section.

In order to assess the temperature of the thermal barrier coating outside surface, a thermocouple bead was maintained touching the thermal barrier coating by means of a wire, which was wound around the specimen and tightened. Because half of the bead surface, approximately 0.030 in. (0.76 mm) in diameter, was exposed to direct radiation from the heating shells, and because the specimen was in the vertical position exposed to air in motion due to convective streams, it can be said that the assessed temperature was in reality that of the boundary layer, since only a small fraction of the bead surface was actually in contact with the thermal barrier. There is a degree of uncertainty in the correlation of this boundary layer temperature with the actual thermal barrier coating surface temperature.

The internal 0.010 in. (0.254 mm) diameter chromel-alumel thermocouple wires were protected by a double hole mullite thermocouple insulation. Only about 0.60 in. (15 mm) of the wire and bead were sticking out. The wires were spaced by plastically bending them away from each other to assure that only the bead would touch the bottom of the 0.0625 in. (1.588 mm) diameter × 0.40 (10 mm) deep well. The thermocouple assembly was tested for accuracy at room temperature and then inserted into the well. In addition, because this thermocouple oxidizes at higher temperatures, it was replaced after only eight hours of exposure.

The temperature measurements for this study were carried out after soaking at equilibrium temperature for one half hour. A continuous temperature measurement study showing the ramping difference in heat-up rate between bare and TBC INCOLOY alloy 909 is in progress.

## Results

The data gathered from thermocouples located at the boundary layer, in the well drilled in the specimen wall, and the estimated inlet and outlet air temperature were plotted as a function of furnace temperature. Figures 3 and 4 show the temperature distributions for the bare and TBC INCOLOY alloy 909 specimens for a cooling air flow rate of 90 scf/h

Table 2 Constants for linear equations TBC INCOLOY alloy 909

| Flow Rate scf/h | Level (**) | Boundary Layer A | Boundary Layer B | Metal A | Metal B | Air Out A | Air Out B |
|---|---|---|---|---|---|---|---|
| 90 | H | -472 | 1.15 | -553 | 0.91 | -300 | 0.50 |
| 90 | L | -124 | 0.87 | -111. | 0.59 | -34 | 0.30 |
| 186 | H | -725 | 1.26 | -413 | 0.71 | +91 | 0.15 |
| 186 | L | -147 | 0.86 | -71 | 0.45 | +43 | 0.13 |

(*) - correlation was not good
(**) - H - higher temperatures; L - lower temperature

Table 3 Constants for linear equations for bare INCOLOY alloy 909

| Flow Rate scf/h | Level (**) | Boundary Layer A | Boundary Layer B | Metal A | Metal B | Air Out A | Air Out B |
|---|---|---|---|---|---|---|---|
| 90 | H | -372 | 1.15 | -574 | 1.09 | -180 | 0.39 |
| 90 | L | (*) | (*) | -419 | 0.98 | -189 | 0.39 |
| 186 | H | -445 | 1.15 | -843 | 1.13 | -273 | 0.27 |
| 186 | L | (*) | (*) | -288 | 0.74 | -124 | 0.10 |

(*) - data fit high temperature equation
(**) - H - higher temperatures; L - lower temperature

(2.55 m$^3$/h), whereas Figs. 5 and 6 show the temperature distributions for a cooling air flow rate of 186 scf/h (5.27 m$^3$h). It appears that the data belong to two distinct data sets, one corresponding to higher temperatures where radiation may be more important, and the other corresponding to lower temperatures where convective heat transfer may predominate. The coefficient of correlation was calculated for each set and the 5 percent degree of confidence (Fisher and Yates, 1953) was used in deciding whether the linear hypothesis was valid. The equations were of the following type:

$$TL(X) = A + B(FT) \tag{1}$$

where $TL$ = local temperature (metal, boundary layer, etc), °F; $X$ = furnace temperature regime: $H$ = high, $L$ = low; $FT$ = furnace temperature (°F); $A$, $B$ = constants obtained from least-squares fit.

The values for $A$ and $B$ are shown in Table 2 for the TBC INCOLOY alloy 909, and Table 3 for the bare material. The letter $X$ is to be replaced by $H$ for high temperatures or $L$ for low temperatures. The furnace temperatures at which the low and high regime straight lines intercepted were calculated. These values are shown in Table 4. Furnace temperatures above 1400°F (760°C) essentially fit the high-temperature regime equations ($H$)

## Discussion

The Reynolds numbers for the different air speeds and air average temperatures within the sample length were obtained from the equation:

$$\mathrm{Re} = (V\,D)\mu \tag{2}$$

The calculated Reynolds number values are shown in Table 5. For the low air velocity, the calculated Reynolds numbers are in the laminar range (Kreith, 1973). The heat transfer coefficients in the laminar regime are relatively low. However, at air velocities equal to or greater than 142 ft/sec (43.3 m/s), the calculated Reynolds numbers are in transition to turbulent regimes and the metal temperatures undergo a substantial decrease.

Table 4 Low and high linear regime furnace temperature intercepts

| Type Specimen | Flow Rate scf/h | Flow Rate m$^3$/h | Boundary Layer °F | Boundary Layer °C | Metal °F | Metal °C | Air Out °F | Air Out °C |
|---|---|---|---|---|---|---|---|---|
| TBC | 90 | 2.55 | 1284 | 696 | 1348 | 731 | 1446 | 786 |
| TBC | 186 | 5.27 | 1340 | 727 | 1334 | 723 | - | - |
| Bare | 90 | 2.55 | - | - | 1375 | 746 | 1414 | 768 |
| Bare | 180 | 5.27 | - | - | 1418 | 770 | - | - |

Table 5 Reynolds numbers

| Air Temperature °F | Air Temperature °C | $\rho/\mu$ sec/ft$^2$ | $\rho/\mu$ sec/m$^2$ | Reynolds Numbers at 47 ft/sec (14.3 m/sec) | Reynolds Numbers at 142 ft/sec (43.3 m/sec) | Reynolds Numbers at 292 ft/sec (89 m/sec) |
|---|---|---|---|---|---|---|
| 100 | 38 | 5525 | 5947 | 3895 | 11768 | 22199 |
| 200 | 93 | 2937 | 4485 | 2937 | 8875 | 18251 |
| 300 | 149 | 2276 | 3476 | 2276 | 6877 | 14143 |
| 400 | 204 | 1536 | 2346 | 1536 | 4641 | 9544 |
| 600 | 316 | 1315 | 2008 | 1315 | 3972 | 8168 |

Table 6 Metal temperatures: low-temperature regime

| Furnace Temp. | | Flow Rate 90 scf/h (2.55 m$^3$/h) | | | | | | Flow Rate 186 scf/h (5.27 m$^3$/h) | | | | | |
|---|---|---|---|---|---|---|---|---|---|---|---|---|---|
| | | TBC | | Bare | | δT | | TBC | | Bare | | δT | |
| °F | °C | °F | °C | °F | °C | °F | °C | °F | °C | °F | °C | °F | °C |
| 1000 | 538 | 479 | 248 | 561 | 294 | 82 | 46 | 379 | 193 | 469 | 233 | 73 | 40 |
| 1200 | 649 | 597 | 316 | 757 | 402 | 160 | 89 | 469 | 234 | 600 | 315 | 131 | 73 |

Table 7 Metal temperatures: high-temperature regime

| Furnace Temperature | | Flow Rate 90 scf/h (2.55 m$^3$/h) | | | | | | Flow Rate 186 scf/h (5.27 m$^3$/h) | | | | | |
|---|---|---|---|---|---|---|---|---|---|---|---|---|---|
| | | TBC | | Bare | | δT | | TBC | | Bare | | δT | |
| °F | °C | °F | °C | °F | °C | °F | °C | °F | °C | °F | °C | °F | °C |
| 1600 | 871 | 903 | 484 | 1182 | 639 | 279 | 155 | 723 | 384 | 965 | 518 | 242 | 134 |
| 1800 | 982 | 1085 | 585 | 1402 | 761 | 317 | 176 | 865 | 463 | 1191 | 644 | 326 | 181 |
| 2000 | 1093 | 1267 | 686 | 1622 | 883 | 355 | 197 | 1007 | 542 | 1417 | 769 | 410 | 228 |

The metal temperature reductions due to the thermal barrier are observed in Figs. 3 and 4 at the 90 sch/h (2.55 m$^3$/h) air flow rate and in Figs. 5 and 6 at the 186 sch/h (5.27 m$^3$/h) air flow rate. The metal temperature intercepts between the low and high-temperature linear furnace regimes were determined and the results presented in Table 5. Typical results are shown in Table 6 for the low-temperature regime and in Table 7 for the high-temperature regime. Note that for the low furnace temperature regime ($L$), the $\delta Ts$, i.e., bare metal temperature - TBC metal temperature, are not very large, varying from 14 to 22 percent with respect to the bare metal (Table 6). However, in the high-temperature regime, where radiation is predominant, the $\delta Ts$ are larger, varying from 22 to 29 percent (Table 7). It is suggested that thermal barrier coatings become increasingly more effective at retarding heat flow with rising temperatures perhaps because thermal barrier coatings are more effective blockers of radiant heat flow than convectional heat flow. That increasing heat fluxes result in larger δTs across the thermal barrier is a well-known fact (Liebert and Gaugler, 1980; Miller and Berndt, 1984; Morrell and Taylor, 1985).

These experimental results are encouraging and thus prompted the determination of the differences in heat flow rates through the use of the following equation (Jakob and Hawkins, 1957):

$$Q = (2.0\pi\delta T)/((\Sigma \ln(R/r)/k) \tag{3}$$

For the zirconia thermal barrier coating, the $k$ value is 0.0013 Btu/ft•sec•°F (1.87E −4 W/m$^2$•K) (DeMasi, 1986), whereas for the INCOLOY alloy 909, the $k$ value is 0.0286 Btu in/ft•sec•°F (4.19E −3 W/m$^2$K) (Inco Alloys International, Inc. Publication No. IAI-18, 1987). Because the air coolant flowed through an AISI 316 stainless steel tube press fitted to the specimen i.d., its thermal conductivity, $k$ = 0.0413 Btu/

ft•sec•°F (5.95E −3 W/m$^2$•K) (Kreith, 1973) was also taken into consideration. The obtained heat transfer rates are:

$$Q_{\mathrm{TBC}}=6.28(\delta T)/(((\ln(0.548/0.508)/0.0013)$$
$$+((\ln(0.508/0.25))/0.0286)+((\ln(0.25/0.18))/0.0431))$$

$$Q_{\mathrm{TBC}}=0.0693(\delta T),\ \text{for TBC INCOLOY alloy 909, and} \qquad (4)$$

$$Q_{\mathrm{Bare}}=6.28(\delta T)/(((\ln(0.508/0.25)/0.0286)$$
$$+((\ln(0.25/0.18))/0.0431))$$

$$Q_{\mathrm{Bare}}=0.194(\delta T),\ \text{for bare INCOLOY alloy 909} \qquad (5)$$

Therefore, by defining the theoretical heat flow reduction advantage of the TBC alloy 909 over that of the bare alloy 909 specimen as

$$Q_{\mathrm{Bare}}-Q_{\mathrm{TBC}}/Q_{\mathrm{Bare}}\times 100 \qquad (6)$$

and using the information from equations (4) and (5) and assuming constant $T$, one obtains

$$0.194\ \delta T-0.0693\ \delta T/0.194\ \delta T\times 100=64.3\ \text{percent} \qquad (7)$$

This value (64.3 percent) contrasts with the experimental data of Figs. 5 and 6 at the same temperature, where using equation (6), one obtains

$$\frac{0.194\ (1800^{\circ}\mathrm{F}-200^{\circ}\mathrm{F})-0.0693\ (1750^{\circ}\mathrm{F}-350^{\circ}\mathrm{F})}{0.194(1800^{\circ}\mathrm{F}-200^{\circ}\mathrm{F})}\times 100=68.8\ \text{percent} \qquad (8)$$

A second evaluation of the comparative heat flow rate advantage of the TBC alloy 909 over that of the bare alloy 909 specimen can be obtained by calculating the values of $Q$ for the $\delta T$ of the environment temperature minus the metal temperature at the thermocouple position [$r=0.375$ in. (9.53 mm)].

$$Q_{\mathrm{TBC}}=2\pi(\delta T)/(((\ln\ 0.548/0.508)/0.0013)$$
$$+((\ln\ 0.0508/0.375)/0.0286))$$

$$Q_{\mathrm{TBC}}=0.091(\delta T) \qquad (9)$$

$$Q_{\mathrm{Bare}}=2\pi(\delta T)/(((\ln\ 0.508/0.325)/0.0286)$$

$$Q_{\mathrm{Bare}}=0.592(\delta T) \qquad (10)$$

Again using the experimental data from Fig. 5 and at 2000°F (1093°C) for the environmental temperature and the metal temperature at the thermocouple position and equations (9) and (10), one obtains:

$$\frac{0.592(1800^{\circ}\mathrm{F}-1300^{\circ}\mathrm{F})-0.091(1750^{\circ}\mathrm{F}-950^{\circ}\mathrm{F})}{0.92(1800^{\circ}\mathrm{F}-1300^{\circ}\mathrm{F})}\times 100=75.4\ \text{percent} \qquad (11)$$

The value (64.3 percent) of the theoretical heat flow rate advantage from equation (7) compares reasonably well with the experimental values of equation (8), i.e., 68.8 percent for the temperature gradient from the environment to the inside air temperature and equation (11), i.e., 75.4 percent for the temperature gradient from the environment to the metal temperature at the thermocouple position. Several factors can account for this discrepancy, including the uncertainty of the measurement of the surface temperatures and the possible lack of good contact between the cooling tube o.d. and the specimen i.d. In addition, the porosity of the TBC was assumed to be about 10 percent. Variations resulting from processing techniques during coating could affect the barrier thermal conductivity and the metal temperature as well.

## Summary

This investigation can be summarized as follows:

1 Bare and PSZ TBC INCOLOY 909 were thermally evaluated for their rates of heat flow at different furnace temperatures and different cooling air flow rates. The thermal expansion characteristics of the thermal barrier and the INCOLOY alloy 909 are very similar from room temperature to 1200°F (649°C), thus making the combination ideally suited for high-temperature applications especially where air cooling can be provided.

2 The advantage of having a 0.020-in. (500-$\mu$m) yttria stabilized zirconia thermal barrier has been demonstrated. Based on the heat conduction equation, the calculated theoretical reduction in heat flow should be 64.3 percent. Experimental results obtained for TBC and bare alloy 909 specimens at 2000°F (1093°C) yielded heat flow reductions of 68.8 and 75.4 percent, respectively, in two calculations.

3 Thermal barrier coatings appear to become increasingly more efficient with rising temperatures suggesting thermal barrier coatings may more effectively block radiant heat flow than convective heat flow.

4 With adequate air cooling, TBC INCOLOY alloy 909 can be operated in air environments at temperatures to 2000°F (1093°F) without the metal temperatures exceeding 1000°F (538°F).

## References

Berndt, C. C., and Miller, R. A., 1984, "Mechanical Property Measurements of Plasma-Sprayed Thermal-Barrier Coatings Subjected to Oxidation," *Ceram. Eng. Sci. Proc.*, Vol. 5, Nos. 7-8, pp. 479-490.

Carlson, N., and Stoner, B. L., 1977, "Thermal Barrier Coating on High Temperature Industrial Gas Turbine Engines," *Sci. Tech. Aerosp. Rep. 15(18)*, NASA Contract NASA-CR-135147, United Technologies Corporation, Power Systems Division.

Cawley, J. D., 1984, "Overview of Zirconia With Respect to Gas Turbine Applications," NASA Technical Paper No. 2286.

DeMasi, J. T., 1986, "Thermal Barrier Coating Life Prediction Modal Development," Technical Report No. CR-179508, NASA Contract NAS3-12944, United Technology Corporation, Pratt and Whitney Engineering Division.

Fisher, R. A., and Yates, F., 1953, *Statistical Tables for Biological, Agricultural and Medical Research*, Oliver and Boyd, Ltd., Edinburgh and London, Table VI.

Inco Alloys International Inc., 1987, Publication No. IAI-38, Huntington, WV, p. 26.

Jakob, M., and Hawkins, G. A., 1957, *Elements of Heat Transfer*, Wiley, New York, pp. 33-34.

Johner, G., Wilms, V., and Schweitzer, K. K., 1988, "How to Achieve Strain Tolerant Thermal Barrier Coatings (TBC's) by Means of Varying Spray Parameters," ASME Paper No. 88-GT-313.

Kreith, F., 1973, *Principles of Heat Transfer*, Harper and Row, New York, p. 634.

Liebert, C. H., Jacobs, R. E., and Stecura S., 1976, "Durability of Zirconia Thermal-Barrier Ceramic Coatings on Air-Cooled Turbine Blades in Cyclic Jet Engine Operation," NASA Tech. Memo. NASA-TM-X-3410.

Liebert, C. H., and Gaugler, R. E., 1980, "The Significance of a Thermal Contact Resistance in Two-Layer Thermal-Barrier-Coated Turbine Vanes," *Thin Solid Films*, Vol. 73, No. 2, pp. 471-475.

Liebert, C. H., and Miller, R. A., 1984, "Ceramic Thermal Barrier Coatings," *Ind. Eng. Chem. Prod. Res. and Dev.*, pp. 344-349.

Levine, S. R., Miller, R. A., and Stecura S., 1983, "Improved Performance Thermal Barrier Coatings," *High Temperature Corrosion NACE-6*, National Association of Corrosion Engineers, Houston, pp. 621-627.

Miller, R. A., Levine, S. R., and Hodge, P. E., 1980, "Thermal Barrier Coatings for Superalloys," *Am. Soc. Met.*, Metals Park, pp. 473-480.

Miller, R. A., and Lowell, C. E., 1983, "Failure Mechanisms of Thermal Barrier Coatings Exposed to Elevated Temperatures," *Thin Solid Films*, Vol. 95, pp. 265-273.

Miller, R. A., and Berndt, C. C., 1984, "Performance of Thermal Barrier Coatings in High Heat Flux Environments," *Thin Solid Films*, Vol. 119, pp. 195-202.

Miller, R. A., 1987, "Current Status of Thermal Barrier Coatings — An Overview," *Surf. Coat. Technol.*, Vol. 30, No. 1, pp. 1-11.

Morell, P., and Taylor, R., 1985, "Thermal Diffusivity of Thermal Barrier Coatings of Zirconia Stabilized With Yttria," *High Temperatures — High Pressures*, Vol. 17, No. 1, pp. 79-88.

Richerson, D. W., 1982, *Modern Ceramic Engineering*, Marcel Dekker Inc., New York, pp. 386-387.

Sheffler, K. D., and Gupta, D. H., 1988, "Current Status and Future Trends in Turbine Application of Thermal Barrier Coatings," ASME JOURNAL OF ENGINEERING FOR GAS TURBINES AND POWER, Vol. 110, pp. 605-609.

Secura, S., 1977, "Two-Layer Thermal Barrier Coating for High Temperature Components," *Amr. Cer. Soc. Bull.*, Vol. 56, No. 12, pp. 1082-1089.

Strangman, T. E., 1985, "Thermal Barrier Coatings for Turbine Airfoils," *Thin Solid Films*, Vol. 127, pp. 93-105.

Tjong, S. C., and Wu, C. S., 1987, "Some Aspects of the Plasma-Sprayed Thermal Barrier Coating on Hastelloy X," *Surf. Coat. Technol.*, Vol. 31, No. 3, pp. 289-295.

Toriz, F. C., Thakker, A. B., and Gupta, S. K., 1988, "Thermal Barrier Coatings for Jet Engines," ASME Paper No. 88-GT-279.

# Application of HOST Technology to the SSME HPFTP Blade

**R. L. McKnight**

**T. S. Cook**

**G. S. Bechtel**

**H. T. Huang**

General Electric Company,
Cincinnati, OH 45215

*The Hot Section Technology (HOST) program has focused on providing methods to solve difficult structural analysis problems. Few structures require as much effort to analyze as the modern aircraft gas turbine engine; heat transfer, constitutive relations, linear and nonlinear analysis, and multiple advanced materials are some of the key topics requiring attention in the structural analysis of engine components. Usually based on limited information and experience, these advanced methods must evolve from expert systems to widely verified user-friendly techniques available to the design community. This paper will discuss the development of turbine blade analysis tools as they moved from research contracts under the NASA HOST program to a PC-based system for preliminary design and their use in evaluating the SSME HPFTP blade, a similar but subtly different problem. Included in the discussion will be the heat transfer and structural analysis of the blade, development of a data base for constitutive modeling of the blade materials, including coatings, and the usage of advanced nonlinear finite element methods.*

## Introduction

At the 23rd International Gas Turbine Conference in Amsterdam in 1988 an entire day's session was devoted to reviewing the Aircraft Gas Turbine Engine (AGTE) hot section technology developed in the NASA HOST program. This technology was documented by Sokolowski (1988). In the same volume the paper by McKnight (1988), "Structural Analysis Applications," discussed the beginning of an effort to apply the HOST developed technology to the Space Shuttle Main Engine (SSME), and in particular to the High-Pressure Fuel Turbo Pump (HPFTP). This program has the acronym SADCALM, which stands for "Structural Analysis Demonstration of Constitutive and Life Methods."

The overall objective of this investigation is to demonstrate the applicability of NASA-developed advanced constitutive and life damage models for calculating cyclic structural response and crack initiation in selected components of reusable space propulsion systems. The computer model resulting from this program will be able to produce an accurate life prediction of hot gas path, life-limiting components of propulsion systems, such as the Space Shuttle Main Engines. Features of the program are to include:

- **Integration of Prior Developed Programs.** Previously developed computer models addressing constitutive modeling, nonlinear analysis, heat transfer, and life damage will be combined in an advanced finite element analysis to generate a sophisticated baseline life prediction program.
- **Test Verification of Synthesized Model.** A material data base is being established for the constitutive and life models involving (parametrically) temperature, strain range, strain rate, mean strain/stress, and dwell time. Structural problems are being run involving cyclic thermomechanical loading and multiaxial stress states. The structural assurance models are being verified for multiaxiality, cumulative damage, and damage mechanism interaction.
- **Model Utilization With SSME Components.** The verified computer program will be used to accomplish the functionality and life predictions of SSME critical components as evidence of the model capability.

It was originally envisioned that the program would examine a number of SSME components ranging from simple, relatively cool isotropic parts to geometrically complex anisotropic structures in the hot flow path. As the program evolved, however, it came to focus more and more on the High-Pressure Fuel Turbo Pump blade. This decision resulted from three factors:

1 The critical nature of these blades for mission success.

2 The combination of material properties, high temperature and load, and geometry provides a very severe test of the complete model.

3 There has already been a fairly extensive analysis of the blade, particularly in the area of heat transfer.

The overall program approach will produce a synthesis of the hot section work conducted by and for NASA. This integration has not been completed and so the current paper should be treated as a report on work in progress. Several topics are being actively studied and will be presented as modules for inclusion into the final program.

## FEM Analysis of the SSME HPFTP Blade

**Conversion of the SSME HPFTP Model.** As was noted, one reason for selecting the HPFTP blade for study was the work already carried out on this component. Abdul-Aziz, working with others at NASA Lewis, had performed three-

---

Contributed by the International Gas Turbine Institute and presented at the 34th International Gas Turbine and Aeroengine Congress and Exhibition, Toronto, Ontario, Canada, June 4–8, 1989. Manuscript received at ASME Headquarters January 23, 1989. Paper No. 89-GT-130.

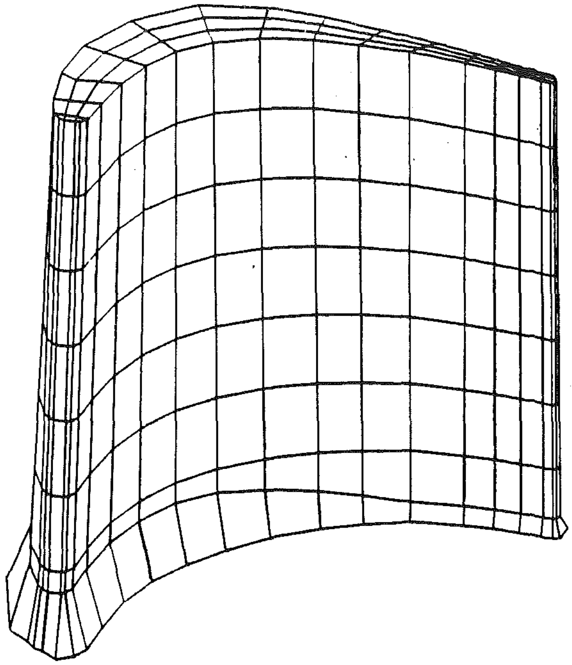

Fig. 1 Eight-noded brick model of the SSME high-pressure fuel turbopump blade

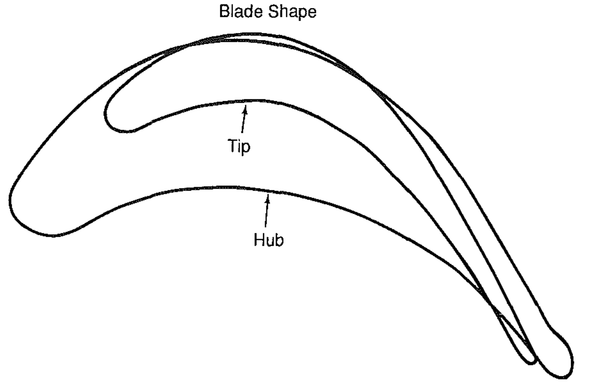

Fig. 2 Cross-sectional geometries of the airfoil tip and hub cross sections

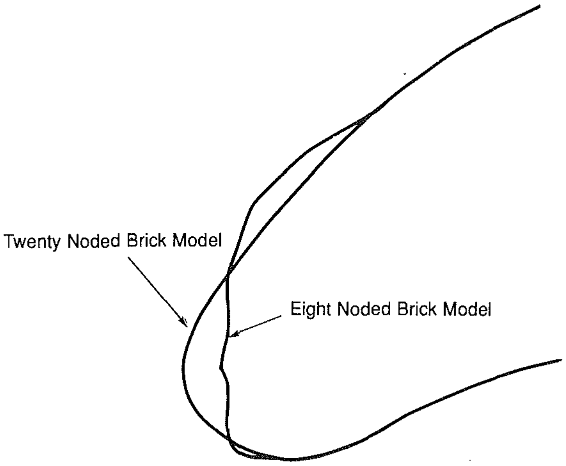

Fig. 3 Additional smoothing required at blade root

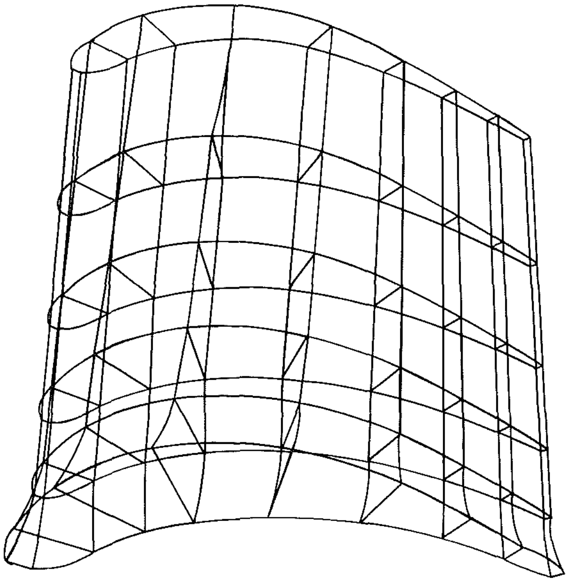

Fig. 4 Twenty-noded brick model of the SSME high-pressure fuel turbopump blade

dimensional nonlinear finite element heat transfer and structural analyses of the blade (Abdul-Aziz et al., 1987). This work was made available to the program and provided considerable insight into the geometry and heat transfer modeling of the blade.

The original model of the SSME HPFTP blade consisting of eight-noded isoparametric bricks was developed by personnel at Rocketdyne. As part of this program, the Rocketdyne model was converted from eight-noded to 20-noded isoparametric solid elements. The resulting 20-noded model uses considerably fewer elements than the eight-noded model. The curved edge 20-noded elements were well suited for modeling the curved surfaces of the airfoil, particularly the severe curvature of the leading edge. The higher order elements are also preferable for modeling the high temperature and strain gradients that result from the severe operating conditions. The 20-noded model has been used for steady-state and transient heat transfer analysis, as well as structural analysis.

All the steps required in conversion of the model were automated as much as possible. The original eight-noded model of the airfoil is shown in Fig. 1. Cross-sectional geometries of the airfoil tip and hub are shown in Fig. 2. These cross sections (and the cross sections in between) were calculated by curve-fitting surface nodes on the eight-noded model of the airfoil. As shown in Fig. 3, additional refinement of the model at the leading edge base of the blade was done to produce a smooth airfoil shape. This smoothing was necessary because the original mesh outline was too irregular to be used with an automatic airfoil mesh generation program. The mesh that was generated from the smoothed cross sections is shown in Fig. 4; note that the smoothed leading edge was achieved with a single 20-noded brick element. A leading edge and trailing edge correction was used with the mesh generation program. This was done to reduce aspect ratio problems on the leading and trailing edge elements.

**Heat Transfer Analysis of the SSME HPFTP Blade.** Boundary conditions for the heat transfer analysis were extracted from the original model supplied by NASA. For example, the turbine inlet gas temperature for the start-up is shown in Fig. 5. The convection coefficients for the transient analysis are scaled from the steady-state convection coefficients as shown in Fig. 6. Similar boundary condition plots for the cutoff are shown in Figs. 7 and 8. The start-up cooling boundary condition at the root of the blade was imposed by a linear variation in the root temperature from the initial temperature (21°C) to the steady-state temperature value (650°C). A similar approach was used to simulate the root boundary conditions during the cutoff.

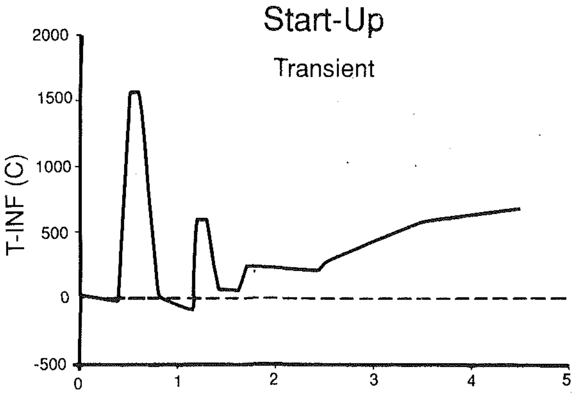

**Fig. 5** Start-up turbine inlet temperature (uncorrected)

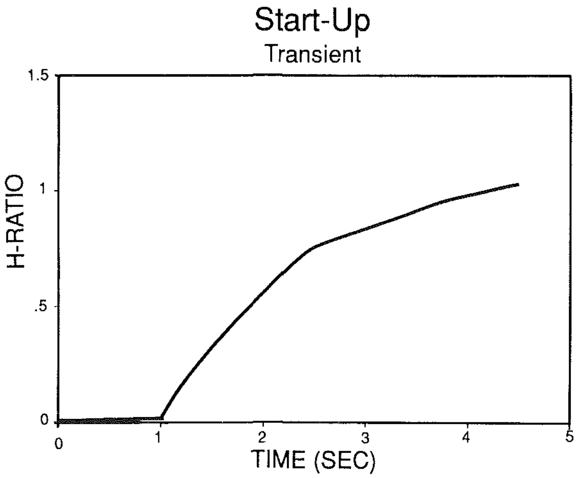

**Fig. 6** Start-up convection coefficient scale factor

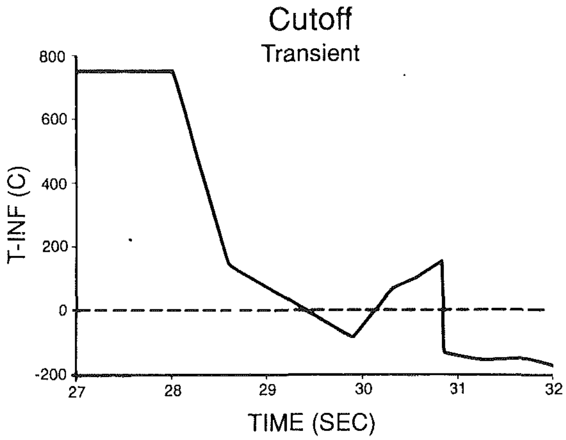

**Fig. 7** Cutoff turbine inlet temperature (uncorrected)

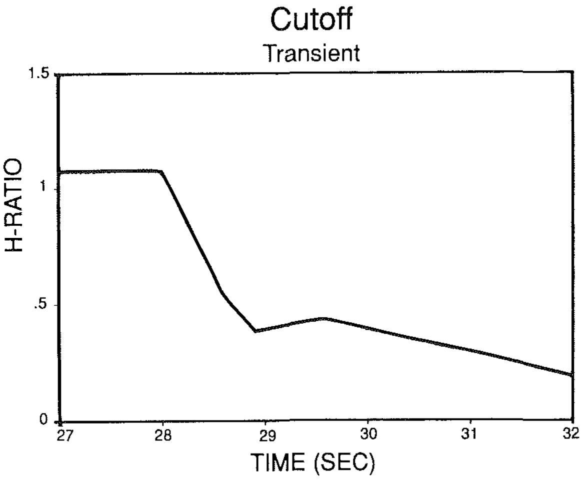

**Fig. 8** Cutoff convection coefficient scale factor

It was necessary to map the boundary conditions obtained for the original eight-noded brick model to the new geometry of the 20-noded brick model. This mapping from the eight-noded to 20-noded model was carried out in the following manner. First, the convection coefficients and ambient temperatures were mapped from the eight-noded element faces to the nodes using area-weighted averages. Next, constraint equations were generated relating surface nodes on the 20-noded brick model to surface nodes on the eight-noded brick model. The nodal values for the convection coefficients and ambient temperatures were then calculated for the surface nodes of the 20-noded brick model using these constraint equations. Finally, the nodal values for the convection coefficients and temperatures were mapped back to the element faces using average values.

The transient analysis boundary conditions for the 20-noded model were dealt with in exactly the same manner as for the eight-noded model. The convection coefficients for the transient analysis were scaled from the steady-state convection coefficients using the Reynolds number ratio.

The three-dimensional nonlinear heat transfer was carried out using a thermal analysis code developed under a companion NASA program (McKnight et al., 1987). This code was installed on a PC and was used to investigate the sensitivity of mesh density and dynamic time incrementing parameters for several heat transfer test cases. The results of these investigations provided insight into the mesh density requirements of models using the 20-noded solid heat transfer element. The results also helped to determine reasonable values for convergence tolerances and timestep calculation parameters. The accuracy (and economy) of a large nonlinear model can be significantly improved by keeping the mesh density and time-step sizes within certain limits.

These limits are a function of geometry, material, imposed loading, and loading rates. The necessity for investigating these effects was the major driver in deciding that PC versions of the structural and thermal codes would be both productivity and economy enhancers. The PCs are perfect for model generation, debugging, check-out, mesh density evaluation, time stepping evaluation, and convergence tolerance evaluation. Once these preliminary steps have been completed, the total transient analysis can be economically run on the CRAY-XMP.

An example of the results of a transient analysis carried out on the PC is shown in Fig. 9. These plots show the temperature contours on the blade immediately after the first ignition spike at 0.51 s (Fig. 5).

All subroutines of the thermal analyzer have been modified to run on an IBM PC-AT. This makes it compatible with the PC version of the monocrystal structural analysis program (see following section) and provides for fast, economical analysis of the SSME turbine blades.

**Material Properties and Modeling.** Several materials have been employed for the HPFTP blade, but the latest are made from nickel-base single crystals. In order to survive in the harsh turbine environment, these single crystals are usually coated. Coatings may be of the overlay type, e.g., NiCoCrAlY; aluminide, e.g., CODEP; or the thermal barrier coating. The latter, while not planned for the SSME application, provides an interesting example of the effects of coatings on high-temperature behavior. Some of these effects will be discussed in detail in a subsequent section.

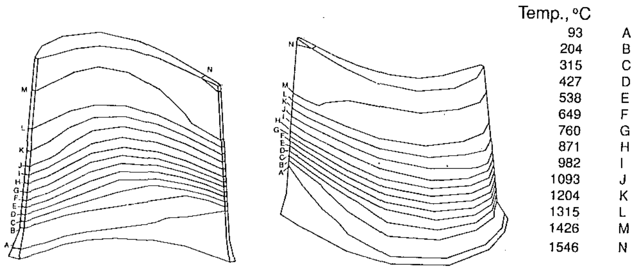

**Fig. 9 Transient heat transfer analysis temperature contours (time = 0.51 s)**

The monocrystal employed in this analysis is René N4. Like the other single crystals, N4 has cubic symmetry; that is, the material has three independent elastic constants. Of course, the elastic deformation for any material orientation can be obtained by a suitable transformation of these constants.

The inelastic deformation of single crystals is quite complex. The material's yield stress displays tension-compression asymmetry as well as being orientation dependent. The creep and strain rate properties depend on orientation as well.

The application of classical constitutive theory to single crystals has not been very successful; this has led to the development of unified theories based on crystallographic approaches. This technique determines the slip on each slip plane and then sums the contributions from the individual slip systems to yield the macroscopic inelastic strain rates. The initial application of a unified crystallographic theory to N4 was carried out by Dame and Stouffer (1986) and Dame (1985).

The Dame–Stouffer model uses the Lall–Chin–Pope modification to Schmid's law (Lall et al., 1979) to represent the tension/compression asymmetry and orientation dependence in octahedral slip. Schmid's law is used as a good approximation to the inelastic material response in cube slip. The flow rule for both octahedral and cube slip has the form

$$\dot{\gamma}^{\alpha\beta}=\left\{D_i\exp\left[-\left(\frac{Z_i^{\alpha\beta}}{|\tau^{\alpha\beta}|}\right)^{n_i}\right]+D_j\exp\left[-\left(\frac{Z_j^{\alpha\beta}}{|\tau^{\alpha\beta}|}\right)^{n_j}\right]\right\}\frac{\tau^{\alpha\beta}}{|\tau^{\alpha\beta}|} \qquad (1)$$

for the strain rate component in the $\beta$ direction on the $\alpha$ plane. For $i=1, j=2$ the equation describes octahedral slip while $i=3$, $j=4$ applies to cube slip. The subscripts 1 and 3 characterize high strain rate behavior while 2 and 4 apply to low strain rates. The state variables $Z_i^{\alpha\beta}$ and $Z_j^{\alpha\beta}$ describe the material's resistance to flow and are both related to a single state variable, $Z^{\alpha\beta}$, whose evolution is a function of the inelastic work rate.

Sheh (1988) sought to improve the cyclic predictions of the model of Dame and Stouffer by adding a second state variable, the back stress ($\Omega$). Thus the stress, $\tau^{\alpha\beta}$, in equation (1) is replaced by $\tau^{\alpha\beta}-\Omega^{\alpha\beta}$, the difference between the applied stress and the back stress. The state variable $Z^{\alpha\beta}$ then becomes the drag stress in the conventional unified theory nomenclature. The evolution of the back and drag stresses is computed for each slip direction on the active slip planes. The evolution expression for the drag stress is similar to that of Dame and Stouffer, while the back stress variable describes the strain rate sensitivity and the inelastic effects.

One of the problems associated with the application of these models is the evaluation of the sizable number of material constants. Thus, there is a question about their ability to predict behavior outside the range of the data base used to derive the constants. However, within the data base, at 982°C, the Sheh model was quite successful in analyzing the cyclic behavior of the monocrystal. This model is currently available in a version that simulates uniaxial test conditions, but it has not yet been implemented in a three-dimensional finite element code. The Dame–Stouffer model has been incorporated into a nonlinear finite element code.

**Implementation of the Crystallographic Constitutive Model.** The Dame–Stouffer crystallographic constitutive model has been implemented in a finite element code using the 20-noded solid element. The code was initially developed on a Honeywell mainframe computer and later was converted to run on a PC. The current PC version allows up to 400 nodes and 50 elements: The program allows for multiple load cases to be used to model complex load histories.

The initial strain method is employed in the finite element code as it is necessary to reform the stiffness matrix only for temperature changes. When the elemental equations are assembled, the global equilibrium equation

$$[K]\{d^T\}=\{F\}+\{F^I\} \qquad (2)$$

is obtained. The matrix $[K]$ is the global stiffness matrix, $\{d^T\}$ is the total displacement vector, $\{F\}$ is the vector of applied thermomechanical forces, and $\{F^I\}$ is the vector of inelastic pseudoforces.

The calculation of the inelastic strain rates and the state variable evolution rate is accomplished in the constitutive subroutines. Integration of the constitutive equations is done using a second-order Adams–Moulton predictor-corrector method.

Among the many features of the current code, dynamic time incrementing is one that can result in significant improvement in economy over constant time steps. The time increment is based on three separate time step control criteria. These are the maximum stress increment, maximum inelastic strain increment, and maximum rate of change of the inelastic strain rate. The minimum time step calculated from the three criteria is the value used. Since the calculations are based on values readily available from the previous time step, little computational effort is required. Another economic feature of the current code is the ability to restart the analysis from a previous load case. This capability is particularly useful for large models with a significant amount of time-dependent inelastic deformation.

One of the problems associated with these constitutive models is that they are computationally intensive. Up to the present, the models have been evaluated at the Gauss points of the elements; since this involves summing the contributions of 24 octahedral and 6 cube slip systems, an analysis can become very time consuming in a general structural model. Alternative approaches to speed up the computational procedure are being explored.

**Analysis of Thermal Barrier Coated Specimens.** As mentioned earlier, a thermal barrier coating (TBC) is one option for improving the life of a hot section component. It does this by increasing the temperature differential between the hot flowpath and the coated substrate material. The coatings, however, have a tendency to fail through a time-dependent process involving both creep and oxidation of the bond coat (Hillery et al., 1987). This failure process was recently modeled with a nonlinear finite element code and was used to investigate some TBC specimens thermally cycled in a furnace (Hartle et al., 1988). The actual process modeled was one in which the bond coat joining the TBC to the substrate develops an oxide layer. This oxide layer possesses distinct elastic and thermal properties and plays a key role in thermal fatigue of the ceramic top coat. For the particular materials tested, the oxide layer reaches a maximum thickness of 4 $\mu$m. By examining the TBC with no oxide layer and with a 4 $\mu$m layer, the influence of oxidation on the time-dependent deformation of the ceramic top coat was determined.

Figures 10 and 11 show the shear and creep strain as a function of time for the coating with and without an oxide layer. The third curve shows the detrimental effect of tripling the coating thickness. The figures depict the significant amount

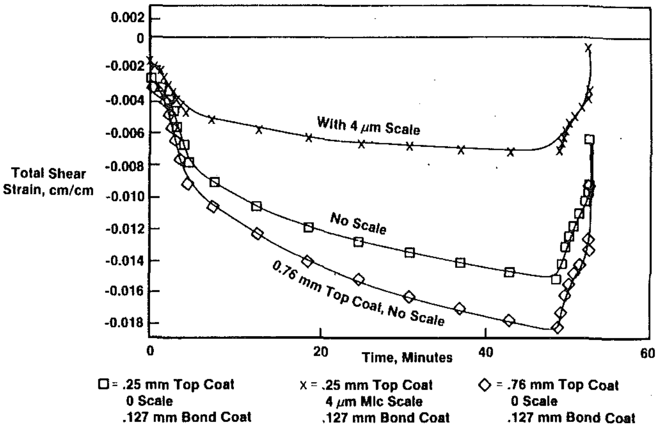

Fig. 10 Calculated shear strain at top coat/bond coat interface

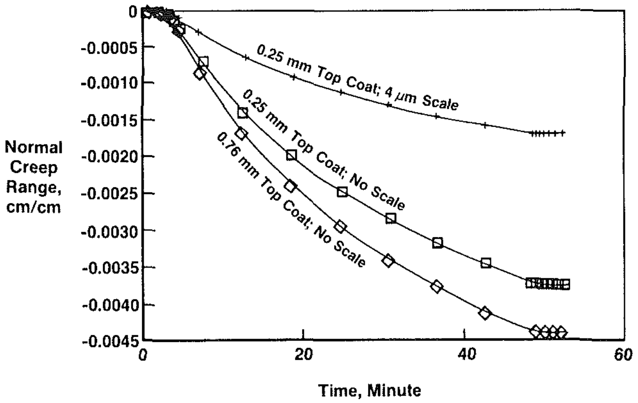

Fig. 11 Normal creep strain top coat/bond coat interface

of time-dependent strain that takes place during the 45 minute hold at 1093°C employed in the test program. Note also that the initial strain is nonzero at the start of the test cycle. This arises because the manufacturing cycle introduces a residual stress state in the coatings; this is an important factor and is fully accounted for in the model.

## Summary

This paper describes some structural analysis tools for AGTE that have been developed under the NASA HOST programs and are now becoming available to the design community. At present, the three-dimensional finite element heat transfer analysis has been implemented on both main frame and desk top machines and is available for hot section component analysis. The constitutive model of Dame has been incorporated in a three-dimensional nonlinear finite element analysis, but the Sheh model is not available yet in a finite element code. The next step is to adopt the Sheh model to the finite element method and make it part of the damage analysis.

As described, the current program is integrating the advances made under HOST and verifying the resulting model by applying it to the SSME HPTFP blade. As far as possible, the package is being developed for use on PC systems for productivity and economy. Even where it is not possible to run the complete structural model, it will still be possible to make parametric studies on the desktop machines. This will provide the opportunity for considerable savings throughout the entire design process.

## Acknowledgments

This investigation is being carried out under NASA contract No. NAS3-24861. The authors gratefully acknowledge this support.

## References

Abdul-Aziz, A., Tong, M., and Kaufman, A., 1987, "Thermal Finite-Element Analysis of an SSME Turbine Blade," presented at the ASME/AIChE National Heat Transfer Conference, Pittsburgh, PA.

Dame, L. T., 1985, "Anisotropic Constitutive Model for Nickel Base Single Crystal Alloys: Development and Finite Element Implementation," Ph.D. Dissertation, University of Cincinnati, Cincinnati, OH.

Dame, L. T., and Stouffer, D. C., 1986, "Anisotropic Constitutive Model for Nickel Base Single Crystal Alloys: Development and Finite Element Implementation," NASA CR-175015, Lewis Research Center.

Hartle, M. S., Cook, T. S., and McKnight, R. L., 1988, "Development of a Life Prediction Model for Thermal Barrier Coatings," *Constitutive Equations and Life Prediction Models for High Temperature Applications*, Berkeley, CA.

Hillery, R. V., Pilsner, B. H., McKnight, R. L., Cook, T. S., and Hartle, M. S., 1987, "Thermal Barrier Coating Life Prediction Model Development," NASA CR-180807.

Lall, C., Chin, S., and Pope, D., 1979, "The Orientation and Temperature Dependence of the Yield Stress of $Ni_3$ (Al, Nb) Single Crystals," *Metall. Trans.*, Vol. 10A, p. 1323.

McKnight, R. L., 1988, "Structural Analysis Applications," ASME IGTI-Vol. 2, pp. 83–95.

McKnight, R. L., Huang, H., and Hartle, M. S., 1987, "Coupled Structural/Thermal/Electromagnetic Analysis/Tailoring of Graded Composite Structures," Second Annual Report, NASA CR-.

Sheh, M. Y., 1988, "Anisotropic Constitutive Modeling for Nickel-Base Single Crystal Superalloys," Ph.D. Thesis, University of Cincinnati, Cincinnati, OH.

Sokolowski, D. E., 1988, "Toward Improved Durability in Advanced Aircraft Engine Hot Sections," ASME IGTI-Vol. 2.

**G. Bidini**

**S. S. Stecco**
Mem. ASME

Dipartimento di Energetica,
Universita di Firenze,
50139 Firenze, Italy

# A Computer Code Using Exergy for Optimizing Thermal Plants

*This paper presents an exergetic approach to reducing energy consumption in industrial plants. The minimum pinchpoint temperature difference is determined for several cases of heat exchange between hot and cold fluid streams with reduced thermal losses. The proposed method, designated TEXAS (Thermal and economic EXergetic Analysis of Systems), derives families of characteristic curves showing economic parameters versus exergetic efficiency in relation to factors such as heat transfer, surface, and scaling. As the method is highly affected by the economic parameter assumptions, the sensitivity of the variations in the parameters is also analyzed.*

## Introduction

Industrial energy processes can be analyzed through economic assessment of the losses associated with the production phases. In recent years, several authors have undertaken thermoeconomic analyses: Evans and Tribus (1965), Wepfer and Crutcher (1981), Valero et al. (1986), Gaggioli and El-Sayed (1987), Tsatsaronis (1987), and Moran (1989), among others.

The method used in the present thermoeconomic analysis, originally proposed by Stecco and Manfrida (1987), was compared with various approaches and found to produce comparable results in terms of accuracy and completeness of information. Our approach is heavily indebted to Linnhoff's pinchpoint method (PPM) (Linnhoff, 1986; Linnhoff and Ahmad, 1986), which allows the optimization of heat exchanger networks (and consequent minimization of costs). We have cast several of the PPM concepts in terms of exergy and added the thermoeconomic analysis.

The proposed method uses an exergetic (second law) approach to identify and reduce exergy losses in industrial processes. It can be applied both at the design stage to reduce the heat transfer area (and thus plant costs) and in an existing plant to verify component operation and recommend improvements through retrofit (Bidini and Guangsan, 1990). To do this, magnitudes relating to the components' physical reality (e.g., the finite temperature difference between the hot and cold fluids in heat exchangers) and those relating to nonoptimal operation of the component being analyzed must be discriminated for each type of loss.

Some of the optimization methods described in the literature (e.g., Umeda et al., 1978) make no distinctions among these magnitudes. In addition, they are usually based on improving a specific plant design to achieve optimization. However, owing to the large number of parameters involved, this kind of procedure rarely gives results that can be used on a practical level. Attempts also have been made to keep the number of parameters fixed, but optimization is guaranteed only for the fixed values, and not for overall plant optimization.

This paper presents a method for quantifying economically acceptable losses, in order to minimize the cost of the output energy.

## Calculation of Exergetic Losses

For heat exchanger networks or comparative processes, economically acceptable exergetic losses can be determined upstream of the heat exchangers at the same time as $\Delta T_{\mathrm{opt}}$ using techniques such as PPM. This paper proposes that the PPM be implemented to include thermoeconomic calculation of $\Delta T_{\mathrm{opt}}$ based on the exergetic approach.

The major losses upon which we can act in a heat exchanger

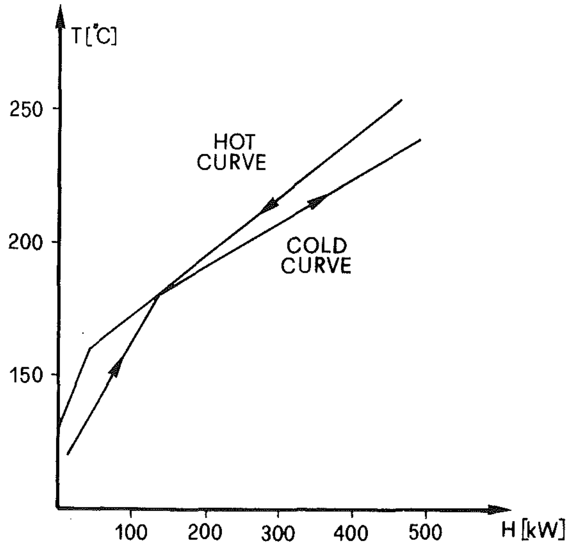

Fig. 1 Example of a composite curve

---

Contributed by the Advanced Energy Systems Division for publication in the JOURNAL OF ENGINEERING FOR GAS TURBINES AND POWER. Manuscript received by the Advanced Energy Systems Division October 25, 1989; revision received May 15, 1990.

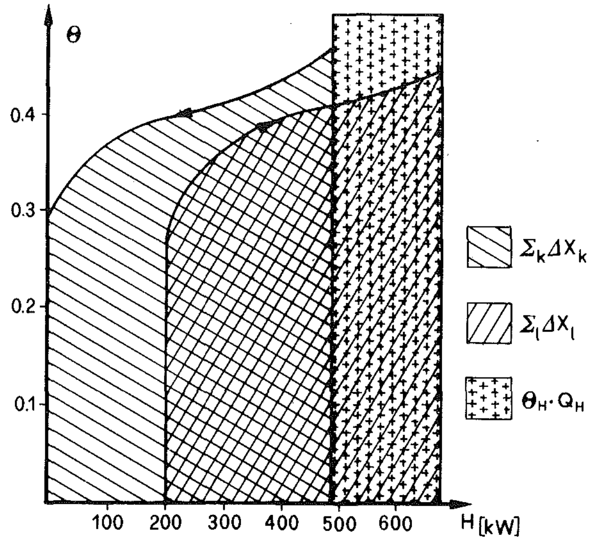

**Fig. 2 Geometric representation of exergy losses**

network are those deriving from heat transfer with a finite temperature drop. This problem can be best studied using the composite *T-H* curves proposed by Ghamarian et al. (1985). In the example in Fig. 1 (Grimaldi et al., 1988), the curves have been plotted for $\Delta T_{\min}=0$ deg, where $\Delta T_{\min}$ is the minimum temperature difference between the composite curves.

These curves can be analyzed by a newly developed code, designated TEXAS, which treats the curves in segmented form by the equation

$$T=A\,H+B \qquad (1)$$

in which $A$ [(K kg)/kJ] and $B$ [K] are constants. With $\theta=1-T_o/T$, a change in coordinates gives

$$\theta=1-T_o/(A\,H+B) \qquad (2)$$

Calling the exergy variation in the whole system represented by the composite curves and external sources $\Delta X$, and the exergetic losses $L_x$, we get

$$\Delta X+L_x=0 \qquad (3)$$

When all the data for the fluid and external sources are known, we can calculate the exergetic variation for a constant temperature so that

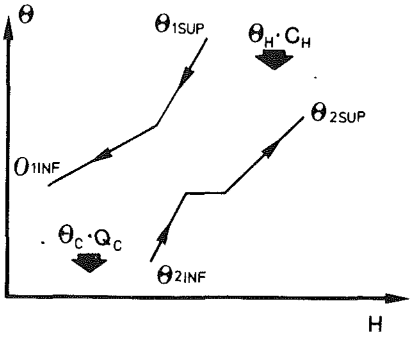

**Fig. 3 θ-H plane for a one-exchanger system**

$$\Delta X=\Delta H \cdot (1-T_o/T) \qquad (4)$$

and for a nonconstant temperature source

$$\Delta X=\Delta H \cdot (1-T_o/T_{ml}) \qquad (5)$$

where $T_o$ is the reference temperature and $T_{ml}$ is the logarithmic mean temperature. Both equations can be applied to the external sources and to the constant-slope sections of the composite curves.

We can now calculate the thermodynamic loss curves resulting from the composite curve shapes or process fluid properties. TEXAS calculates the exergetic losses in relation to $\Delta T_{\min}$. In the $k$th section of the composite curves, we find

$$\Delta X_k=\int_{H_i}^{H_{i+1}} \theta\, dH \quad (i \text{ and } i+1 \text{ extremes, } k\text{th interval}) \qquad (6)$$

which yields

$$\Delta X_k=H_{i+1}-H_i+T_o\ln(T_i/T_{i+1})/A_k \qquad (7)$$

By summing all the $k$ intervals along the hot fluid composite curve, we obtain the surface indicated in Fig. 2 ($\sum_k \Delta X_k$).

The exergetic losses are given by

$$L_x=\sum_k \Delta X_k-\sum_l \Delta X_l+\theta_H \cdot Q_H \qquad (8)$$

where $\sum_k \Delta X_k$ refers to the hot curve and $\sum_l \Delta X_l$ refers to the cold one (Fig. 2).

## Nomenclature

$A$ = heat exchange area
$AC$ = cost of heat exchanger unit area
$C$ = unit cost
$C^*$ = cost
CAF = annualization payment factor
$D$ = constant
$E$ = energy (specific), kJ/kg
$EA$ = equivalent exchange area
$H$ = enthalpy (specific), kJ/kg
$K$ = heat exchange coefficient
$L_x$ = exergy loss (specific), kJ/kg
NTU = number of heat exchange units
$p$ = generic parameter
$Q$ = heat recovered
$sf$ = scale factor
$T$ = temperature
$UC$ = cost of single heat exchange unit
$X$ = exergy (specific), kJ/kg
$\Delta$ = generic variation
$\Delta T_{\min}$ = minimum allowable approach temperature difference in heat exchanger network
$\Delta T_{\text{opt}}$ = optimum approach temperature difference in a heat exchanger network
$\eta$ = efficiency
$\theta$ = Carnot factor

**Subscripts**

1 = inlet
2 = outlet
$C$ = cold
$CA$ = refers to capital cost
$E$ = refers to energy cost
$H$ = hot
$i, k, l$ = indices defined in text
INF = refers to cold stream (Fig. 3)
max = maximum
$ml$ = logarithmic mean
$o$ = reference state
opt = optimum
$S$ = refers to service cost
SUP = refers to hot stream (Fig. 3)
$x$ = exergy

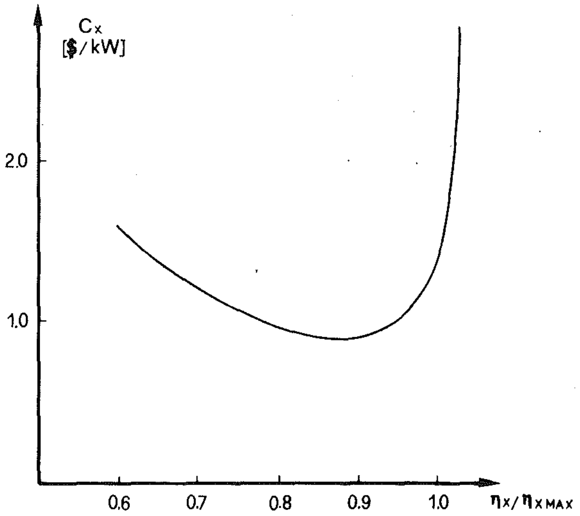

**Fig. 4 Cost per exergy unit referring to exergetic efficiency**

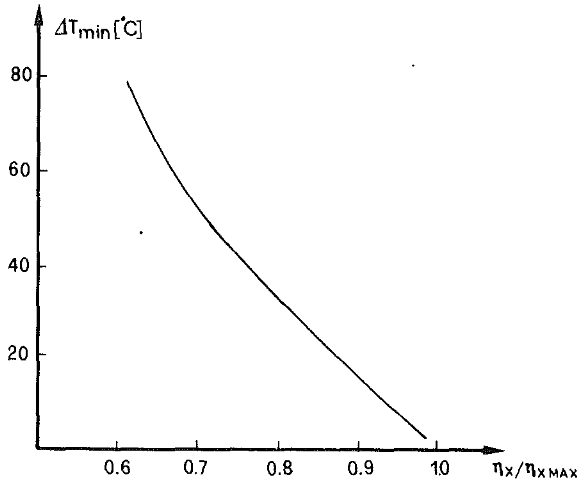

**Fig. 5 $\Delta T_{\min}$ versus exergetic efficiency**

The difference is computed only once, since the first two terms on the right-hand side are constants dependent upon the shape of the composite curves. Conversely, it is necessary to recompute the last term for each $\Delta T_{\min}$ to obtain the exergetic loss curve. Hence, the maximum exergetic efficiency obtained for each $\Delta T_{\min}$ is not unitary, but, as a logical consequence of the second-law analysis, dependent on the value of the existing losses.

## Structure of the Texas Program

The TEXAS program's first step is to read the enthalpies and temperatures of the hot and cold curves. Typical parameters for each flow, i.e., temperature interval, mass flow, and specific heat, must be set in order to be plotted as composite curves on the $\theta$-$H$ plane. The composite curves are then visualized on a computer screen where they are interactively shifted so that the minimum $\Delta T$ can be selected and calculated. On the basis of these values, the program indicates the heat transfer surfaces, the exergetic efficiency, the pinchpoint temperatures, the heat supplied at high temperatures, and the heat released at low temperatures. (These last two terms vanish at optimum conditions, as shown by Grimaldi et al. (1987).) The last step is the construction of the system's characteristic curves.

## Using TEXAS to Evaluate $T_{\text{opt}}$

Our purpose in performing a thermoeconomic analysis is to determine the minimum cost per exergy unit leaving the system. The total annual costs can be written, according to Stecco and Manfrida (1987), as

$$C^* = C_E^* + C_{CA}^* + C_S^* \tag{9}$$

Calling $E_2$ the outgoing energy, we get the following expression for the energy unit costs:

$$C = C_E^*/E_2 + C_{CA}^*/E_2 + C_S^*/E_2 \tag{10}$$

Assuming, for simplicity, that this particular system can be represented by a single heat exchanger (Fig. 3), we can write

(*a*) *For the cost per energy unit*

$$C_E = C_H\ Q_H + C_c\ Q_c \tag{11}$$

(*b*) *For the cost per exergy unit*

$$C_{Ex} = C_{x,H}\ \theta_H\ Q_H + C_{x,C}\theta_C Q_C \tag{12}$$

Introducing the equivalent exchange area ($EA$) to express the concept of the economy of scale achieved when the heat exchangers are individually increased in size

$$EA = \text{NTU}(A/\text{NTU})^{sf} \tag{13}$$

allows us to express capital expenditures as

$$C_{CA}^* = (EA\ AC + UC\ \text{NTU})\quad \text{CAF} \tag{14}$$

The number of units depends upon pinchpoint location, while the size of the heat exchange area depends on $\Delta T_{\min}$.

Ignoring operating costs in the first approximation, we get

$$C_x = \frac{[(C_{x,H}\theta_H Q_H + C_{x,C}\theta_C Q_C) + \text{CAF}\ (AC\ EA + UC\ \text{NTU})]}{X_2} \tag{15}$$

Indicating the incoming net exergy (hot fluids) as $\theta_1\ H_1$ and the outgoing net exergy (cold fluids) as $\theta_2 \Delta H_2$, we can define

(1) Incoming exergy: $X_1 = \theta_H Q_H + \theta_1 \Delta H_1$

(2) Outgoing exergy: $X_2 = \theta_2 \Delta H_2$

and therefore the rational efficiency is

$$\eta_x = \theta_2 \Delta H_2/(\theta_H Q_H + \theta_1 \Delta H_1) = 1 - \sum_i L_{xi}/(\theta_H Q_H + \theta_1 \Delta H_1) \tag{16}$$

where the only losses considered are those for heat transfer with a finite temperature drop:

$$\sum_i L_{xi} = L_x$$

The result is

$$C_x = \frac{(C_{x,H}\theta_H Q_H) + C_{x,C}\theta_C Q_C + (AC\ EA + UC\ \text{NTU})\text{CAF}}{\theta_2 \Delta H_2} \tag{17}$$

The expression for rational efficiency yields

$$\frac{\theta_H Q_H}{\theta_2 \Delta H_2} = \frac{1}{\eta_x} - \frac{\theta_1 \Delta H_1}{\theta_2 \Delta H_2} \tag{18}$$

Since the last term in the equation is a constant, we can use TEXAS, which supplies the values of $L_x$, $A$, NTU, and $Q_c$, to compute the others. Hence, we can plot the curve for cost per exergy unit in relation to exergetic efficiency and thus compute the economic rational efficiency ($\eta_{x\text{opt}}$) from Fig. 4. In addition, since the program also gives $\Delta T_{\min}$ as a function of the rational efficiency, we can determine $\Delta T_{\text{opt}}$ at $\eta_{x\text{opt}}$ (Fig. 5).

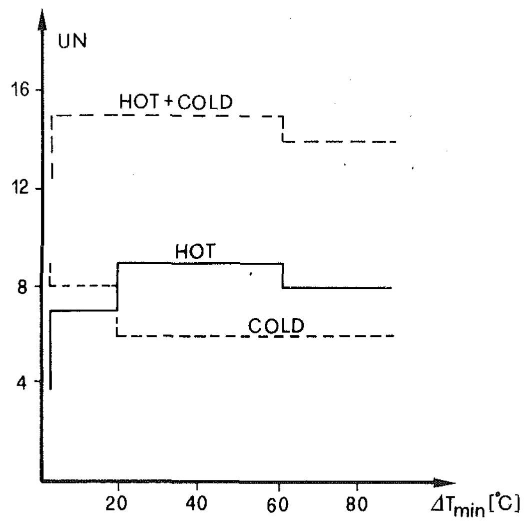

Fig. 6 Determination of heat exchange units as a function of $\Delta T_{\min}$

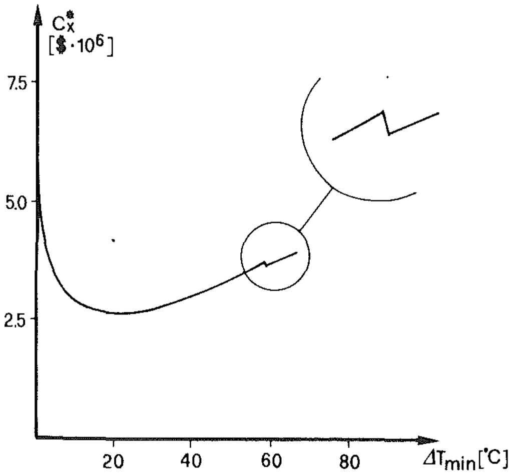

Fig. 7 Cost curve

The result is in accordance with that obtained using the PPM, meaning that the exergetic analysis furnishes $\Delta T_{\mathrm{opt}}$ necessary for the plant detail design under the same assumptions as the PPM.

## Characteristics Curve Method

Applying the foregoing considerations, we obtain a result *similar to that reported by Ghamarian et al. (1985) using the* incremental heat flux method. The result relates energy savings to capital expenditures. The relationship follows the principle of decreasing efficiencies, i.e., there is an increase in the heat recovered corresponding to each additional square meter of heat exchange area.

Once more commencing at the exergetic unit cost, we get

$$C_x = \frac{C_{x,H}}{\eta_x} + \frac{(AC\ EA + UC\ \mathrm{NTU})\mathrm{CAF} + C_{x,C}\theta_C Q_C - C_{xH}\theta_1 \Delta H_1}{(\theta_2 \Delta H_2)} \tag{19}$$

Differentiating with respect to $1/\eta_X$

$$\frac{\delta C_x}{\delta(1/\eta_x)} = C_{x,H} + \frac{\mathrm{CAF}}{\theta_2 \Delta H_2}\,\frac{\delta(AC\ EA + UC\ \mathrm{NTU})}{\delta(1/\eta_x)} + \frac{C_{x,C}\theta_C}{\theta_2 \Delta H_2}\,\frac{\delta Q_C}{\delta(1/\eta_x)} \tag{20}$$

Recalling that

$$(\theta_2 \Delta H_2)\bullet\delta(1/\eta_x) = \delta(\theta_1 \Delta H_1 + \theta_H Q_H) = \theta_H \delta Q_H \tag{21}$$

and

$$\delta Q_C = \delta Q_H = \delta Q \tag{22}$$

we find

$$C_{X,H}\theta_H \delta Q + \mathrm{CAF}\ \delta(AC\ EA + UC\ \mathrm{NTU}) + C_{x,C}\theta_C \delta Q = 0 \tag{23}$$

and finally

$$\frac{\delta(AC\ EA + UC\ \mathrm{NTU})}{\delta Q} = -\frac{\theta_H C_{xH} + \theta_C C_{x,C}}{\mathrm{CAF}} \tag{24}$$

Equation (24) resembles one given by Ghamarian et al. (1985), the main difference being the need to account for the variability of the heat exchange coefficient and the minimum number of heat exchange units in the *EA* calculation.

To derive a characteristic curve for the plant, it is first necessary to eliminate the economic parameters *AC* and *UC* in the first term. Since *UC* can always be expressed as $UC = D\bullet AC$, with $D$ being a suitable dimensional constant $[D] = m^2$, the result is

$$\frac{\delta(EA + D\ \mathrm{NTU})}{\delta Q} = -\frac{\theta_H C_{x,H} + \theta_C C_{x,C}}{AC\ \mathrm{CAF}} \tag{25}$$

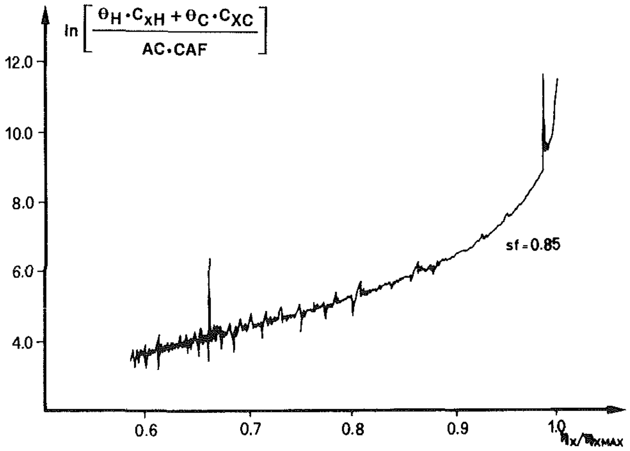

Fig. 8 Characteristic curve

We note that the number of heat exchange units varies irregularly (Fig. 6) and that the increase in the number of units from 14 to 15 affects the cost curve at a $\Delta T_{\min}$ of about 60°C (Fig. 7). This effect is a simple translation of the magnitude ($UC\bullet$CAF NTU) within the cost curves. Hence, we can conclude that the cost curve slope remains unchanged, except for the discontinuity where the number of heat exchange units changes. We can eliminate the last economic parameter (the scale factor in the equivalent area) by plotting the term $\ln[(\theta_H C_{C,H} + \theta_C C_{x,C})/(AC\ \mathrm{CAF})]$ in relation to $\eta_x/\eta_{x\max}$ for one specific value of the scale factor (Fig. 8). The curve's unusual shape derives from having determined the heat exchange area taking into account the local variations in the overall heat exchange coefficient. The result is that the slope of the curve representing the required heat exchange area does not vary continuously.

Not all process fluids fit into the two temperature intervals, which happen to be the only ones allowing heat exchange without conflicting with the assumption of countercurrent heat exchange. Hence, we can calculate a different heat exchange coefficient for each subinterval on the composite curve *H* axis that only considers the actual fluids present. Moreover, the effect of the interfluid heat exchange coefficient on the calculation of the heat exchange area will be proportional to

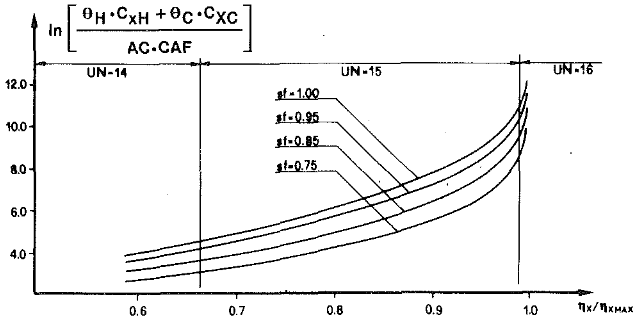

Fig. 9 Characteristic curves with averaged heat exchange coefficient and various scale factors

the amount of exchangeable heat. Obviously, the amount of heat transferred by the hot fluids will equal that transferred to the cold fluids.

In the method proposed by Ghamarian et al. (1985), the heat exchange areas must be imposed a priori. TEXAS is more accurate, since the computation of $K_{ik}$ and $K_{jk}$ ($k$ denoting the interval considered and $i$, $j$ the hot and cold fluids) only takes into account the fluids actually present and their maximum quantity of exchangeable heat (i.e., the minimum difference between the amount required by the cold fluid and the amount supplied by the hot fluid). In computing the average values, TEXAS accounts for the relative importance of the fluids in the heat transfer process and weighs their contributions to the heat exchange coefficient in terms of the heat actually exchanged.

Using mean values to plot the composite curves, we obtain the family of curves shown in Fig. 9, which refers to the scale factor as a parameter. The second term of equation (25) is then calculated for each economic situation and the corresponding value of economically optimal exergy efficiency determined. This yields a $\Delta T_{\text{opt}}$ value that can be used to set up the heat exchanger network.

With the proposed method, we are evidently not compelled to generate a cost curve for every economic situation as would be necessary with the method of Ghamarian et al. (1985). From the plant's characteristic curve, we can derive $\eta_{x\text{opt}}$, which in turn provides $\Delta T_{\text{opt}}$, which is required to define the heat exchanger network.

## Sensitivity of $C_X$ to Variations in the Thermoeconomic Parameters

It is surprising that no author makes reference to analyzing the sensitivity of $\Delta T_{\text{opt}}$ to variations in economic parameters. In terms of rate of return on investment (ROI), the $\Delta T_{\min}$ corresponding to minimal costs logically decreases as the ROI period increases. This is because the capital expenditures attributable to the heat exchange area have a lesser impact on the plant's total annual cost. Hence, greater energy recovery may be achieved by saving on external energy needs. The variability in interest rates is referred to indirectly using the annualization payment factor (CAF). Returning to the expression of cost per outgoing exergy unit (equation (19)), cost variability can be defined in relation to various parameters, among them

$$\delta C_x/\delta C_{x,H} = 1/\eta_x - \theta_1 \Delta H_1/(\theta_2 \Delta H_2) \tag{26}$$

$$\delta C_x/\delta C_{x,C} = \theta_C Q_C/(\theta_2 \Delta H_2) \tag{27}$$

$$\delta C_x/\delta UC = \text{NTU CAF}/(\theta_2 \Delta H_2) \tag{28}$$

$$\delta C_x/\delta AC = EA\ \text{CAF}/(\theta_2 \Delta H_2) \tag{29}$$

$$\delta C_x/\delta sf = EA \cdot \ln(A/\text{NTU}) AC\ \text{CAF}/(\theta_2 \Delta H_2) \tag{30}$$

$$\delta C_x/\delta \text{CAF} = [AC \cdot EA + UC \cdot \text{NTU}]/(\theta_2 \Delta H_2) \tag{31}$$

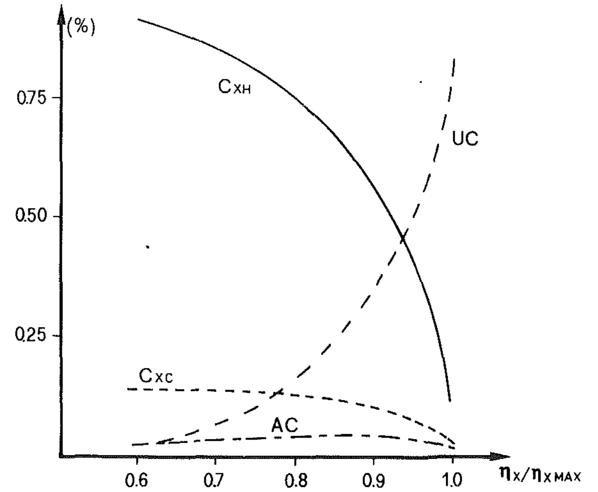

Fig. 10 Sensitivity of $C_x$ with respect to $C_{x,H}$, $C_{X,C}$, $AC$, and $UC$

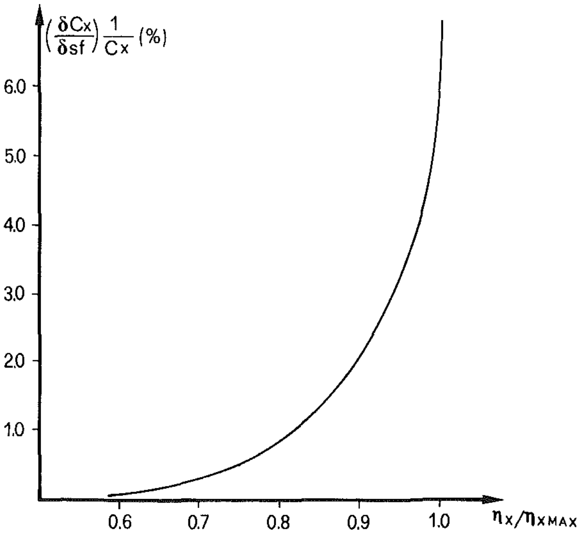

Fig. 11 Sensitivity of $C_x$ with respect to the scale factor

We can then calculate the percentage of cost variation in relation to variations of 1 percent in the single parameter $p$

$$[\delta C_x/\delta\, p]/(C_x) = f(\eta_x)$$

The effects on $C_x$ of variations in $C_{x,H}$, $C_{x,C}$, $AC$, and $UC$ are show in Fig. 10; the variability in relation to the scale factor is shown in Fig. 11. With maximum variability attributable to the scale factor and a sensitivity of notable magnitude, the rest of the analysis can be confined solely to the scale factor. In contrast to the method of Ghamarian et al. (1985), our method uses the equivalent heat exchange area to account for the actual size of each heat exchanger to reduce considerably the effects of the sensitivity to variations in the scale factor. According to Ghamarian et al., the cost equation can be written as

$$C_{x,A} = \text{CAF} \cdot AC \cdot A^{sf} (\theta_2 \Delta H_2) \tag{32}$$

which yields

$$\delta C_{x,A}/\delta sf = \text{CAF} \cdot AC \cdot A^{sf} \cdot \ln(A)/(\theta_2 \Delta H_2) \tag{33}$$

and thus

$$[\delta C_{x,A}/\delta sf]/C_{x,A} = \ln(A) \tag{34}$$

In the proposed method,

$$C_{x,A} = \text{CAF} \cdot AC\ EA/(\theta_2 \Delta H_2) \tag{35}$$

whereas

$$\delta C_{x,A}/\delta sf = EA \cdot \ln(A/\mathrm{NTU}) \cdot AC \cdot \mathrm{CAF}/(\theta_2 \Delta H_2) \quad (36)$$

which yields

$$[\delta C_{x,A}/\delta sf]/C_{x,A} = \ln(A/\mathrm{NTU}) = \ln(A) - \ln(\mathrm{NTU}) \quad (37)$$

Hence, since the number of units always exceeds unity, equation (37) will always give a smaller value than that of equation (34), which is less sensitive to variation in the scale factor. Of even greater significance, however, is the variation in the location of the minimum cost point with variations in the parameters, since this affects the final cost of the heat exchanger network.

The same sensitivity can also be found in the characteristic curves. The curves in Fig. 8 and 9 show that, once the ordinate has been set, the change from one scale factor to another implies that $\eta_x$ varies more for low, as opposed to high, exergetic efficiencies. This affects the variation in $\Delta T_{\min}$ in a virtually linear fashion (Fig. 5).

While $\Delta T_{\mathrm{opt}}$ is more sensitive to variations in the scale factor at lower exergetic efficiencies, the sensitivity of the cost curve increases at high exergetic efficiencies, as shown in Fig. 11. Examining the absolute error in determining the minimum point, and thus in calculating $\Delta T_{\mathrm{opt}}$, we find a lower error rate for low exergetic efficiencies. This means that the method used in the first attempt to determine $\Delta T_{\mathrm{opt}}$ is quite stable. The influence on cost is small in regions of low exergetic efficiency where high error rates (flat curves) could be expected. Where the exergetic efficiency is highest, the possible error in evaluating $\Delta T_{\mathrm{opt}}$ is minimum so that the cost error, which otherwise would be considerable, is reduced. Even though $\Delta T_{\mathrm{opt}}$ value is only a first try, no appreciable savings can be achieved through further definition of the heat exchanger network within $\Delta T_{\mathrm{opt}}$ and hence the first-try value can be considered valid. Conversely the network must be defined for several values of $\Delta T_{\mathrm{opt}}$, but the procedure is still simple, since no more than a few tries have to be made thanks to the low calculation error in $\Delta T_{\mathrm{opt}}$.

## Results and Conclusions

The pinchpoint method for defining the best heat exchanger network positioning is an excellent way of saving time once $\Delta T_{\min}$ has been determined. Using the second-law approach, we have demonstrated that the same results can be obtained for $\Delta T_{\mathrm{opt}}$ value with the proposed and classical methods. In addition, TEXAS provides information on plant exergetic losses (irreversibility) and relative costs. The end result is a plot representing the outgoing exergy costs.

TEXAS's main appeal lies in its ability to compare the plant exergetic efficiencies in the cost expression. This means that the method can be applied in a general way that also includes irreversibilities differing from those caused by heat transfer with a finite temperature drop. In this sense, the pinchpoint method supports the thermoeconomic analysis based on the second-law approach. A rigorous second-law approach must originate from a specific situation, with optimization achieved through successive transformations. However, it would be exceedingly difficult to reach optimum plant conditions in the case of a far-from-optimal initial situation because of the huge number of parameters whose variability must be considered.

Linnhoff and Ahmad (1986) claim that the PPM is an alternative to a thermoeconomic analysis, but we feel that exergetic analysis can be a better means of optimization in the case of more complex systems. Despite the difficulties in correctly calculating $\Delta T_{\mathrm{opt}}$, TEXAS is able to provide a set of plant characteristic curves. The curves and $\Delta T_{\min}$ can be used to derive the optimum exergetic efficiencies for each economic situation. This is of paramount importance, since a plant performance plot is created in which the variations relate solely to economic conditions. The plot also indicates how the plant should be built to minimize costs under the specified conditions.

TEXAS provides greater insight into the economic parameters and a better evaluation of the overall heat exchange coefficient than the method proposed by Ghamarian et al. (1985). Using TEXAS, possible errors were analyzed in relation to the uncertainty in determining the economic parameters. It emerged that the parameters that were not analyzed by Ghamarian et al. were those that most influenced the final result.

TEXAS is also stable, since the error generated in determining $\Delta T_{\mathrm{opt}}$ is only slight and does not heavily affect the final plant costs. Conversely, in the regions where uncertainty in evaluating $\Delta T_{\mathrm{opt}}$ is greatest, the impact on plant costs is quite low.

TEXAS is a rapid way of applying the exergetic (second-law) approach to the identification of exergy losses. Once the characteristics of the process fluids and the value of the economic parameters have been defined, only ten minutes of computational time on an IBM-AT PC is required to calculate $\Delta T_{\mathrm{opt}}$ and its related curves, expenditures, exergetic efficiencies, heat exchange area and energy requirements, pinchpoint temperatures, and plant characteristic curves. This allows the designer to review a vast assortment of solutions in an extremely brief time frame. In addition, it allows setting up a totally interactive program in which the designer can determine temperature and enthalpy values directly from the screen of a PC.

## References

Bidini, G., and Guangsan, S., 1990, "Improving a Distillation System," *25th IECEC Proceedings*, Reno, NV.

Evans, R. B., and Tribus, M., 1965, "Thermo-Economics of Saline Water Conversion," *Proceedings, I&EC Process Design and Development*, Vol. 4, No. 2, pp. 195–206.

Frangopoulos, G. A., and Evans, R. B., 1984, "Thermoeconomic Isolation and the Optimization of Thermal System Components," *Proceedings, Second Law Aspects of Thermal Design*, ASME HTD-Vol. 33, pp. 87–94.

Gaggioli, R. A., and El-Sayed, Y. M., 1987, "A Critical Review of Second Law Costing Methods," *Proceedings, 4th International Symposium on Second Law Analysis of Thermal Systems*, Rome, Italy.

Ghamarian, A., Thomas, W. R. L., Sideropoulos, T., and Robertson, J. L., 1985, "Incremental Heat Flux Method for Heat Exchanger Optimization," *Proceedings, ASME Winter Annual Meeting*, pp. 19–25.

Grimaldi, C. N., Bidini, G., and Stecco, S. S., 1988, "Il procedimento PPM ed i suoi riflessi nei processi di poligenerazione," *Proceedings, National ATI Conference*, Ancona, Italy.

Linnhoff, B., 1986,, "Pinch Technology for the Synthesis of Optimal Heat and Power Systems," *Proceedings, ASME Winter Annual Meeting*, Vol. 2-1, Anaheim, CA, pp. 23–36.

Linnhoff, B., and Ahmad, S., 1986, "Supertargeting: Optimum Synthesis of Energy Management Systems," *Proceedings, ASME Winter Annual Meeting*, Vol. 2-1, Anaheim, CA, pp.. 1–14.

Moran, M. J., 1989, "Availability Analysis: A Guide to Efficient Energy Use," ASME Press, New York.

Stecco, S. S., and Bidini, G., 1990, "A Possible Optimization of Combined Gas-Steam Cycles Using the TEXAS Procedure," *Proc. of 4th COGEN TURBO Conference*, New Orleans, LA.

Stecco, S. S., and Manfrida, G., 1987, "The Exergy and Capital Cost Factors: A New Approach to Exergy Conversion Economics," *Proceedings, 4th International Symposium on Second Law Analysis of Thermal Systems*, Rome, Italy.

Umeda, T., Itoh, J., and Shiroko, K., 1978, *Chemical Engineering Progress*, Vol. 74, No. 7, p. 70.

Valero, A., Lozano, M. A., and Munoz, M., 1986, "A General Theory of Exergy Saving: On the Exergetic Cost," *Computer-Aided Engineering of Energy Systems*, ASME AES-Vol. 2-3, pp. 1–8.

Wepfer, W. J., and Crutcher, B. G., 1981, "Comparison of Costing Methods for Cogenerated Process Steam and Electricity," *Proceedings, American Power Conference*, No. 43, pp. 1070–1082.

# A GCC Power Plant With Methanol Storage for Intermediate-Load Duty

**J. A. Paffenbarger**[1]
Department of Mechanical Engineering,
Stanford University,
Stanford, CA 94305-3032

*This paper describes the design and performance of a coal gasification combined-cycle power plant with an integrated facility for producing and storing methanol (GCC/methanol power plant). The methanol is produced at a steady rate and is burned in the combined cycle to generate additional power during periods of peak electrical demand. The GCC/methanol plant provides electricity generation and energy storage in one coal-based facility. It is of potential interest to electric utilities seeking to meet intermediate-load electrical demand on their systems. The plant configuration is determined by means of an innovative economic screening methodology considering capital and fuel costs over a range of cycling duties (capacity factors). Estimated levelized electricity production costs indicate that a GCC/methanol plant could be of economic interest as premium fuel prices increase relative to coal. The plant could potentially be of interest for meeting daily peak demands for periods of eight hours or less. The conceptual plant configuration employs a Texaco gasifier and a Lurgi methanol synthesis plant. Plant performance is estimated at peak and baseload output levels. No unusual design or operational problems were identified.*

## Introduction

The demand for electric power by utility customers varies continuously over daily cycles. There is a steady component of demand, called the baseload, which must be met at all times. During working hours, as commercial and industrial activities mount, demand rises to a peak. Most utilities meet the particular mix of peak and baseload demands on their systems in one of two ways:

- Large, capital-intensive coal or nuclear plants meet the baseload demand, and less expensive cycling units burning premium fuels (natural gas or distillate oil) meet the peak demand. Old (depreciated) coal plants may also be cycled.
- Baseload plants produce a constant electrical output, a portion of which is absorbed in an energy storage facility. During periods of peak demand, the stored energy is converted back to electricity. Pumped hydroelectric plants are the most common storage plant today.

It is normally undesirable to cycle new coal-burning power plants because of economic, mechanical, and environmental constraints, yet many utilities would like to do so because of the world's abundant supplies of low-cost coal and the uncertainty in premium fuel prices, which are tied to fluctuating world-wide petroleum prices. Pulverized coal power plants have relatively high capital costs, so are uneconomical unless used at design capacity for most of the time. They have massive boilers and other heat transfer systems, which can be damaged by repeated thermal cycling. Finally, their production of air pollutants may increase during periods of reduced output because combustion and environmental control systems tend to operate less efficiently at reduced load. Similar arguments apply to the more recent gasification combined-cycle (GCC) plant design.

Coal gasification combined-cycle power plants gasify coal to produce a combustible fuel gas, which, after removal of pollutant-forming compounds, is burned in a combined-cycle (CC) power plant. Like pulverized coal plants, they are relatively expensive to build and would not be economical to cycle at today's fuel prices. However, if a portion of the synthetic combustible fuel gas (syngas) were converted to a liquid, stored, and burned during periods of peak electrical demand, the economic and thermal factors weighing against cycling them might be reduced or eliminated. Therefore, they might offer a way of meeting cyclical electrical demand with a coal-based power plant.

This paper examines the design and performance of one particular combination of GCC plant and fuel storage to provide intermediate-load duty. The plant design is based on converting some of the syngas from the gasification plant into methanol, sending the rest of the syngas to the combined cycle to meet baseload power demand, and burning both syngas and methanol when maximum electrical output is needed. Such a plant combines electricity generation and energy storage in a single facility.

Following summaries of the basic GCC plant design and the storage idea, the economic screening study used to size the

---

[1] Present address: CERCHAR, BP 19, 62670 Mazingarbe, France.

Contributed by the Advanced Energy Systems Division for publication in the JOURNAL OF ENGINEERING FOR GAS TURBINES AND POWER. Manuscript received by the Advanced Energy Systems Division September 18, 1989; revision received July 12, 1990.

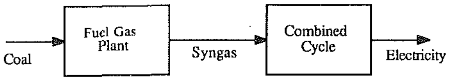

Fig. 1 GCC power plant functional blocks

gasification and methanol plant sections is described. Then the technical basis for the plant design, the process design itself, and performance estimates of the plant for one particular duty cycle are given. This work is described fully in a report by the Electric Power Research Institute (EPRI) (Eustis and Paffenbarger, 1990).

## GCC Power Plants

GCC plants are among the most likely candidates to fill the need for new baseload electrical generation facilities in the near future (Yeager, 1989; Mueller and Karg, 1987). Interest in GCC power plants has been steadily increasing in recent years as environmental concerns have grown. In the United States, operating experience with gasification technology at a near-commercial scale has been obtained at the Cool Water Demonstration Plant in Daggett, CA (Spencer et al., 1986), the Shell Coal Gasification Demonstration Plant in Deer Park, TX (Krewinghaus and Nager, 1988), and the Dow Syngas Project in Plaquemine, LA (Webb and Sundstrom, 1988). The major gasification processes have been reviewed by Simbeck et al. (1983) and Stanford researchers (Erbes, 1986; Phillips, 1986).

The two essential parts of a GCC plant are shown in Fig. 1. In the fuel gas plant, coal is gasified at high temperature to produce a combustible gas, from which sulfur compounds, particulates, and other gas impurities are removed before burning. The gas cleaning processes typically operate at 40°C (100°F) or less, so the hot syngas must be cooled, thereby providing heating duty for steam generation and other uses. Steam from syngas cooling is typically sent to the power plant to improve overall plant efficiency.

In the second major functional block, the combined cycle, the clean fuel gas is burned in a gas turbine, whose hot exhaust is used to raise steam for a steam turbine.

## A GCC/Methanol Power Plant

The GCC power plant described above may be modified to incorporate methanol storage, as shown in Fig. 2. This is referred to as a GCC/methanol plant in this paper. The syngas still flows directly to the combined-cycle plant, but a portion is diverted to the methanol production and storage area. The separation of the coal energy conversion from the power production means that the GCC/methanol plant would not face the same mechanical difficulties in cycling as a pulverized coal plant would because the fuel gas production train remains operating at a constant level. Only the gas-burning power plant operates cyclically, the same as do present-day combined cycles designed for cycling duty. The heat recovery steam generator (HRSG) heat transfer surfaces are exposed to lower temperatures, undergo smaller temperature changes, and are smaller in total surface area than the corresponding boiler surfaces in a pulverized coal plant of generation capacity equal to that of the GCC/methanol plant.

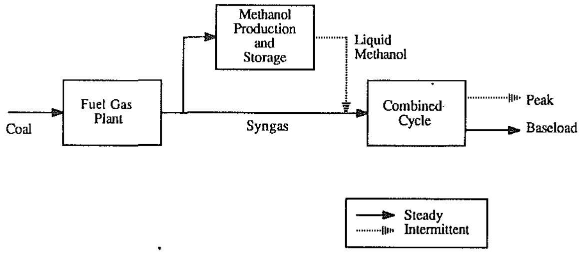

Fig. 2 GCC/methanol plant schematic

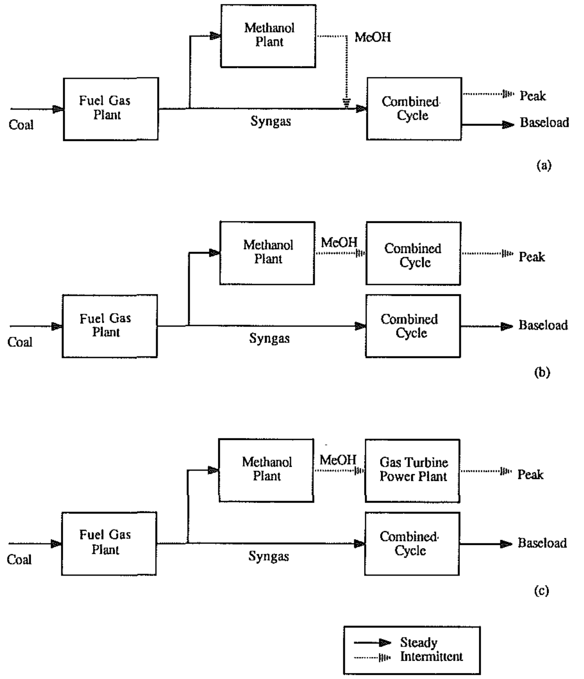

Fig. 3 GCC/methanol plant configurations considered in economic screening: (*a*) GCC/MeOH; (*b*) GCC/MeOH + CC; (*c*) GCC/MeOH + GT

The economic incentives that apply for incorporating energy storage facilities within electric utility systems also apply for combining GCC and methanol plants. Power from baseload plants may be stored during periods of low demand, and recovered during peak periods, although some of the original fuel energy is inevitably dissipated in the process. The cost of these losses and the cost of the storage facility itself are together less than the incremental cost of providing peak power in thermal plants for many utilities. Similarly, producing methanol from a low-cost feedstock, coal, and storing it for use during periods of heavy electrical demand, may be less expensive for some utilities than the conventional choice of burning premium fuels in gas turbines or combined-cycle plants.

The total electrical generation of the plant and its distribution between baseload and peak generation is called the plant duty cycle. The duty cycles for which a GCC/methanol plant might be economically feasible are not readily apparent. For example, if the plant includes a large methanol plant to handle long peaks, the cost of the methanol plant increases, and the losses in converting the syngas to methanol increase. Similarly, if the baseload output is low compared to the peak output, the fuel gas production plant will decrease in size (for a fixed maximum electric capacity), but the operation of the combined cycle may become less efficient. In general, both the capital cost and efficiency of the plant will depend strongly on the duty cycle for which it is designed. For this reason, an economic screening study was used to determine a range of duty cycles for which a GCC/methanol plant might be economically feasible. From this range, a particular duty cycle was chosen as the basis for a conceptual plant design and performance estimate.

## Economic Screening Study

The economic screening study considered two essential cost factors in the plant, capital and fuel, as follows: For a plant of fixed total electrical generation capacity, a simple model relating plant duty to the capacities and efficiencies of the major plant sections was developed. Separately, estimated plant costs as a function of capacity were taken from published cost

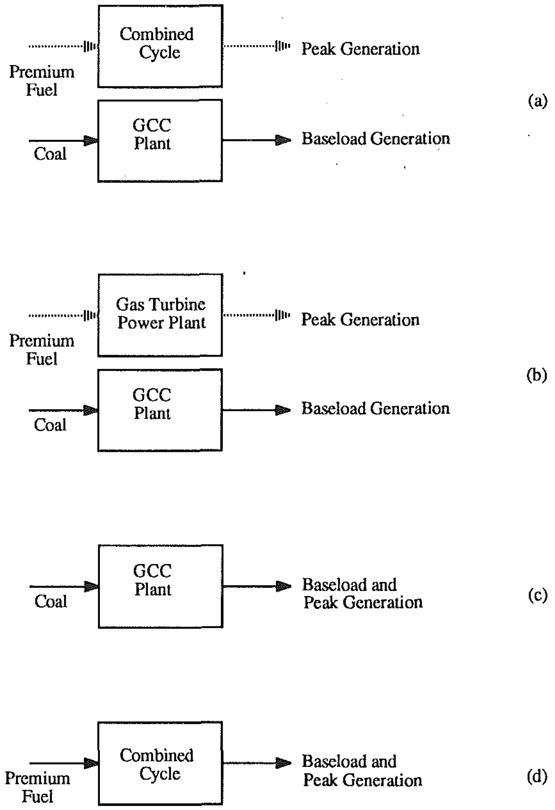

**Fig. 4 Utility generation alternatives considered in economic screening: (*a*) GCC + CC; (*b*) GCC + GT; (*c*) GCC; (*d*) CC**

studies of GCC and methanol plants. Then, using the capital cost data and representative fuel costs, the estimated levelized cost of producing electricity was calculated over a full range of duty cycles. The levelized cost estimates did not include all relevant costs. Notably, operation and maintenance costs were excluded.

**Plant Configurations.** There were three GCC/methanol plant types considered, as shown in Fig. 3. These are:

- A GCC/methanol plant with a single combined-cycle electrical generation plant (GCC/MeOH)
- A GCC/methanol plant with a separate combined-cycle peaking plant (GCC/MeOH + CC)
- A GCC/methanol plant with a separate gas turbine peaking plant (GCC/MeOH + GT).

In the first, a single generation plant cycles to meet the baseload and peak power demand. In the second two, a separate generation plant, either combined-cycle or gas turbine, meets the variable load, while the combined cycle burning syngas meets the baseload. The single generation facility will tend to cost less to build than two separate power plants, but will also tend to have a lower efficiency because the single combined cycle operates off-design during the period of baseload operation.

Four potential alternatives for generating a mix of baseload and peaking power were considered. As shown in Fig. 4, these are:

- A baseload coal plant plus a separate combined-cycle unit for peaking (GCC + CC)
- A baseload coal plant plus a separate gas turbine plant for peaking (GCC + GT)
- A GCC plant run at variable output to meet both baseload and peaking requirements (GCC)
- A combined-cycle plant run at variable output to meet both baseload and peaking requirements (CC).

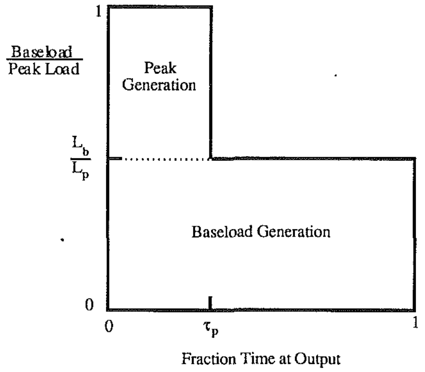

**Fig. 5 Nondimensional electrical load curve (duty cycle)**

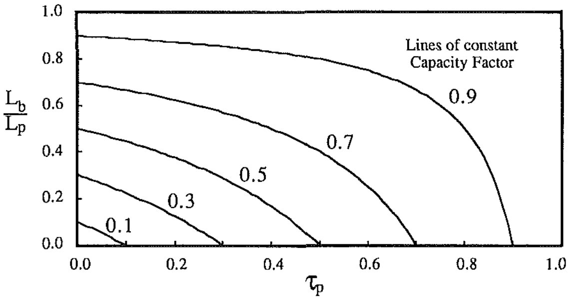

**Fig. 6 Lines of constant capacity factor on the duty cycle map**

**Duty Cycle.** The levelized electricity production cost of each of the alternatives above depends strongly on the duty cycle. A nondimensional duty cycle with two output levels is shown in Fig. 5. The duty cycle may be characterized by two nondimensional variables:

- Baseload power output as a fraction of plant capacity, $L_b/L_p$
- Fraction of time at which plant output is at peak level, $\tau_p$.

A purely baseload plant has $L_b/L_p = 1$ and $\tau_p = 1$; an on-off peaking plant might have $L_b/L_p = 0$ and $\tau_p = 0.2$. The more familiar measure of capacity factor, defined as the ratio of actual plant generation to total potential generation based on continuous operation at rated capacity, is implicitly defined by fixing $L_b/L_p$ and $\tau_p$. This relation is shown in Fig. 6, in which lines of constant capacity factor are shown on the duty cycle "map."

A priori, there is no duty cycle or range of duty cycles for which a GCC/methanol plant might be economically advantageous. Therefore, the electricity production costs of the seven plants noted above were calculated and compared to identify the duty cycles for which a GCC/methanol plant would *most likely* be the most economical choice.

The calculation of levelized costs, implemented on a computer spreadsheet, was carried out over the range of values of $0.2 < L_b/L_p < 0.9$ and $0 < \tau_p < 1$, for a fixed total capacity of 590 MW. Similar calculations were performed for the four alternative generation plants as well. Finally, the levelized costs of production of GCC/methanol plants were compared with those of the alternatives to identify the ranges of $L_b/L_p$ and $\tau_p$ over which the GCC/methanol plant appears attractive.

**Other Information.** The capital costs of all plants were estimated by scaling according to capacity using published EPRI cost studies (Matchak and Lawrence, 1982; Paul et al., 1983). Although the GCC cost trend data were developed some time ago, they have proven to be consistent with later estimates. The EPRI Technical Assessment Guide (TAG, 1986) provided the basic financial assumptions, fuel costs, capital costs, and performance estimates for stand-alone combined-cycle and gas

**Table 1 Financial parameters used in calculation of levelized cost**

| | |
|---|---|
| Nominal price level | December 1984 |
| Coal price (Illinois No. 6) | 14.7 ¢/MJ (1.55 \$/$10^6$ Btu) |
| Premium fuel base price | 23.7 ¢/MJ (2.50 \$/$10^6$ Btu) |
| Real annual inflation rate of capital and coal | 0% |
| Real annual inflation rate of premium fuel | 0, 5, and 10% |
| Capital equipment carrying charges[a] | 10.9 %/year |

Source: TAG, 1986

[a] Based upon 30 year book life, no real inflation, no tax preferences, weighted cost of capital = 6.1%

**Table 2 Capital cost estimating information**

| Plant or Plant Section | Base Capacity ($Cap_0$) | Capacity Measure | Cost Scaling Equation | Base Cost (\$1000s) | Price Level |
|---|---|---|---|---|---|
| Fuel gas section | 435,109 | lb/hr dry coal | $C/C_0 = 0.8632\ Cap/Cap_0 + 0.1348$ | 413,398 | mid-1981 |
| Combined cycle (within GCC plant) | 677 | MW gross output | $C/C_0 = 0.8595\ Cap/Cap_0 + 0.1289$ | 282,105 | mid-1981 |
| Methanol synthesis | 500,000 | lb/hr methanol | $C/C_0 = (Cap/Cap_0)^{0.6}$ | 183,000 | Dec 1984 |
| Stand-alone IGCC plant | 581 | MW net output | $C/C_0 = 0.8545\ Cap/Cap_0 + 0.1394$ | 695,502 | mid-1981 |
| Stand-alone combined cycle | 1 | MW net output | $C/C_0 = Cap/Cap_0$ | 600 | Dec 1984 |
| Stand-alone gas turbine | 1 | MW net output | $C/C_0 = Cap/Cap_0$ | 300 | Dec 1984 |

Principal data sources — GCC cost data from Matchak and Lawrence, 1982
— Methanol plant cost data from Paul et al. 1983.

turbine power plants. Important financial parameters are summarized in Table 1 and a summary of the capital costs is given in Table 2. Estimates of the efficiency of GCC plants at off-design operation were obtained from Phillips (1986).

**Results.** The essential results of the screening study are shown in Figs. 7(*a–c*). The figures show, for three premium fuel prices, the regions of $L_b/L_p$ and $\tau_p$ over which a given technology has the lowest levelized electricity production cost. The premium fuel prices are 23.7 ¢/MJ, 44.5 ¢/MJ, and 95.8 ¢/MJ (2.50 \$/$10^6$ Btu, 4.70 \$/$10^6$ Btu, and 10.11 \$/$10^6$ Btu) for Figs. 7(*a–c*), respectively. These are the levelized prices resulting from premium fuel real escalation rates of 0, 5, and 10 percent from an assumed starting value of 14.7 ¢/MJ (2.50 \$/$10^6$ Btu). The $X$ axis of each figure is $\tau_p$, and the $Y$ axis is $L_b/L_p$, so any given point within the rectangle represents a particular duty cycle.

For example, point A on Fig. 7(*a*) ($\tau_p = 0.7$, $L_b/L_p = 0.5$), represents a plant that produces electricity at its maximum capacity 70 percent of the time, and otherwise generates at half its capacity. At a fuel price of 23.7 ¢/MJ (2.50 \$/$10^6$ Btu), a stand-alone combined-cycle plant is the most economical alternative for this particular duty cycle.

Figure 7(*a*) shows that, if current-day fuel prices do not escalate, a GCC/methanol plant does not appear competitive at any duty cycle. Rather, gas turbine power plants combined with baseload plants (GCC+GT) are most economical for short peaking periods. For peaking periods beyond about 40 percent of the time, stand-alone combined cycles (CC) or combined cycles with baseload power plants (GCC + CC) are the least expensive options.

These results are consistent with the current utility technologies for peaking, intermediate load, and baseload power plants. They reflect the present economic balance of fuel and capital costs, which favor the different technologies at different capacity factors. To the upper right of the figure, a "baseload" GCC plant does not appear because of the relatively low price of premium fuel (natural gas). For duties having low capacity factors for the peaking component of generation (left end of Fig. 7(*a*), where values of $\tau_p$ are low), the low capital cost of gas turbine plants makes them attractive for meeting the short peaks.

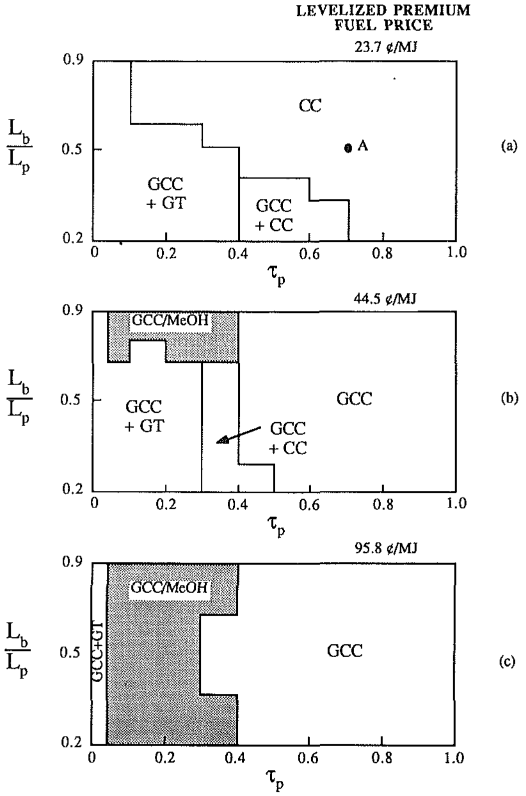

Fig. 7 Technology regions of lowest levelized cost on the duty cycle map: (*a*) premium fuel price = 23.7 ¢/MJ (2.50 \$/$10^6$ Btu); (*b*) premium fuel price = 44.5 ¢/MJ (4.70 \$/$10^6$ Btu); (*c*) premium fuel price = 95.8 ¢/MJ (10.11 \$/$10^6$ Btu)

As the price of premium fuels increases, a region does appear in which a GCC/methanol plant may be the least expensive option. This is shown as the shaded region in Figs. 7(*b*) and 7(*c*). The extent of the region varies with premium fuel price, but in all cases it is restricted to peaking periods of $\tau_p \leq 0.4$, or about ten hours of a daily cycle. At 44.5 ¢/MJ (4.70 \$/$10^6$ Btu), the GCC/MeOH option is least expensive in a limited range of $L_b/L_p$ and $\tau_p$, with combinations of gas turbine and baseload plants (GCC + GT) remaining the most economic option for the shortest peaking duties, and combined-cycle and GCC plants best at longer peaking periods. At 95.8 ¢/MJ (10.11 \$/$10^6$ Btu), the GCC/MeOH option "squeezes out" the GCC + GT option at short peaking periods, and reaches a maximum economic range of approximately $0.2 < L_b/L_p < 0.9$ and $0.05 < \tau_p < 0.33$. Above 95.8 ¢/MJ (10.11 \$/$10^6$ Btu), the technology regions shown in Fig. 7(*c*) do not change because the options do not depend on the premium fuel price. All the plants use coal, which is assumed to have a constant real price. The exception is the thin region of GCC + GT, which grows narrower as fuel prices increase.

The first important conclusion that can be drawn from Fig. 7 is that, of the GCC/methanol plant options, the one with a single generation plant (GCC/MeOH, Fig. 3(*a*)) is always the most economical. That is, the configurations having separate peaking units to burn the methanol (GCC/MeOH + CC, GCC/MeOH + GT) do not appear among the least expensive options at any fuel price. The GCC/MeOH plant is the least expensive of the GCC/methanol plant options for all values of $L_b/L_p$, although the difference among the options is never more than about two mills/kWh. The costs are close enough to one another that more complete estimates of all the relevant costs, particularly operation and maintenance costs, could potentially alter this conclusion. However, based on the screening assumptions, the added cost of a separate generation facility

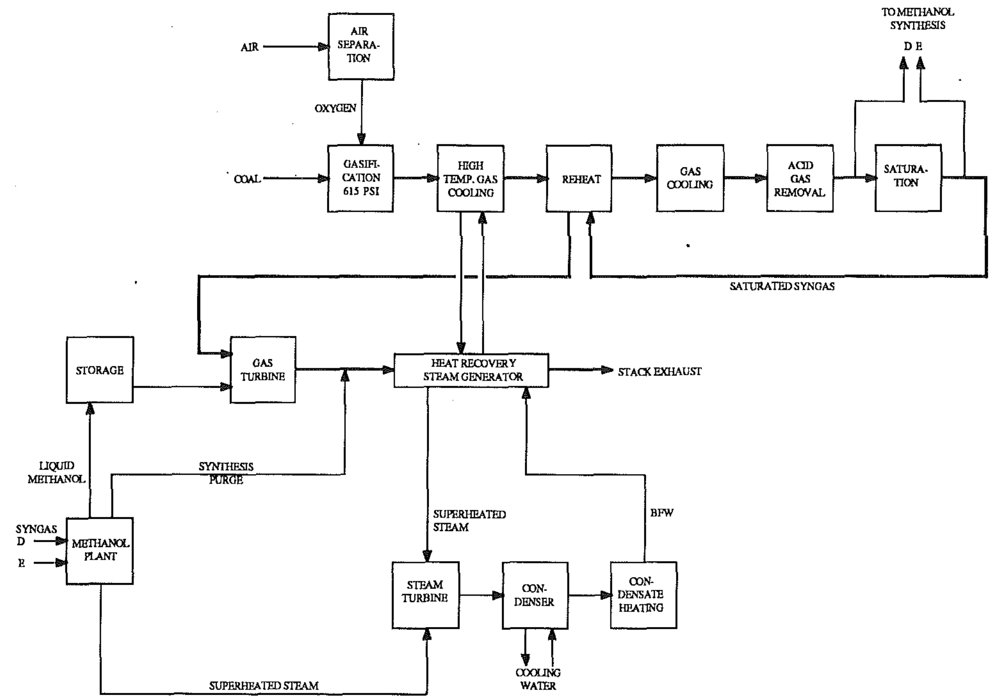

**Fig. 8 Overall GCC/methanol plant schematic**

**Table 3 Summary of fuel gas production design criteria**

| | |
|---|---|
| Gasification | Texaco entrained-flow |
| Oxidant | 95% oxygen |
| High-temperature syngas cooling | saturated steam production in radiant and convective boilers |
| Sulfur removal level | 95% |
| Acid gas removal | Selexol physical solvent |
| Sulfur recovery | Claus process |
| Tailgas treatment | SCOT process |
| Fuel gas saturation level | 30.5% (28.2 wt %) |
| Fuel gas reheat temperature | 299 C (570 F) |

**Table 4 Summary of steam cycle design criteria**

| | | |
|---|---|---|
| Stack temperature (minimum) | 124 C | (255 F) |
| Steam temperature (maximum) | 538 C | (1000 F) |
| Superheater approach (minimum at max. flow) | 22 C | (40 F) |
| Boiler approach (minimum) | 25 C | (45 F) |
| Economizer approach (minimum at max. flow) | 17 C | (30 F) |
| Pinch point (minimum at max. flow) | 22 C | (40 F) |
| Boiler feed water temperature (minimum) | 107 C | (225 F) |
| Deaerator approach (minimum) | 14 C | (25 F) |
| Deaerator pressure | 172 kPa | (25 psia) |
| Condenser pressure | 7 kPa | (2 in Hg) |

Note: Some parameters are labeled as minimum or maximum because steam cycle operating conditions change as the power plant output varies.

compared to a single, large facility narrowly outweighs the advantage of higher efficiency at the baseload power level.

Secondly, a GCC/methanol plant could potentially be the most economical choice for peaking times between 5 and 33 percent of a daily cycle as premium fuel prices increase. According to the analysis, the levelized fuel price at which the GCC/methanol plant becomes the least expensive option is about 56.9 ¢/MJ (6.00 \$/$10^6$ Btu). This corresponds to a real escalation rate of premium fuel of about 6.7 percent.

Based on these results, the following design criteria were established for the GCC/methanol plant:

| | |
|---|---|
| • Generation facility | single combined cycle (no separate peaking generation facility) |
| • Plant duty cycle | $\tau_p = 0.33$, $L_b/L_p = 0.5$ |

The chosen plant duty cycle falls within the region in which the GCC/MeOH option was estimated to be the most economical generation choice. In combination with the technical design criteria outlined below, these two criteria fix the basis for the conceptual plant design.

## Plant Design and Performance

**Technical Design Basis.** The GCC/methanol plant is intended to be representative of a commercially obtainable facility using known technology. In order to be consistent with previous studies sponsored by EPRI, many design criteria and the basic GCC process design are derived from the "Radiant Plus Convective" GCC plant design by Fluor Engineers (Matchak et al., 1984). This plant incorporated a Texaco gasifier, high-temperature radiant and convective coolers to cool the raw syngas and raise saturated steam, and a conventional combined cycle with an advanced gas turbine, as represented by the General Electric "MS 7001F" machine. To control emissions of nitrogen oxides from the gas turbine, and to increase the power output of the gas turbine, the water content of the syngas is increased in a saturator. The EPRI report by Matchak contains a complete discussion of the GCC design rationale, process design, equipment, and performance.

Ambient conditions are taken to be 15°C (59°F) and 99.3 kPa (14.4 psia). The design coal is Illinois No. 6 (TAG, 1986). The design criteria relating to fuel gas production and the steam cycle are summarized in Tables 3 and 4.

There are a number of commercial processes for converting syngas to methanol. Those by Imperial Chemical Industries and Lurgi are the most well established and proven in performance. The once-through or "liquid phase" methanol synthesis process, while potentially promising in GCC applications (Brown et al., 1989; Mednick et al., 1988), has not advanced beyond pilot plant testing and so was not a suitable option for this study. Because of the high-quality steam available from the process and its flexible operating characteristics, the Lurgi methanol synthesis process was chosen. The methanol plant is assumed to operate at steady output at all times to promote ease of operation and maintenance, constancy of steam flows, and investment protection of plant catalysts and equipment.

A sour shift plant before the actual methanol synthesis loop adjusts the ratio of hydrogen to carbon monoxide so that it is near the stoichiometric ratio.

**Plant Design.** The basic GCC/methanol process schematic developed in this study is shown in Fig. 8. Clean syngas is taken from the fuel gas processing train just before and just after the saturator. The saturated syngas is the main feedstock stream for the methanol plant, while the dry syngas is used for controlling the composition of the shifted syngas stream entering the actual methanol synthesis process.

Apart from liquid methanol, the methanol plant produces steam and a combustible purge gas. The steam is superheated using a portion of the purge gas and is sent to the steam turbine. The remaining purge gas is fired directly in the HRSG. The methanol storage area receives liquid methanol continuously and is drawn down during peaking periods only.

Considering as the starting poing a GCC plant based on the Texaco coal gasifier, as exemplified by the GCC plant of Matchak et al. (1984), this new design entails the following additions and modifications:

*Additions:*

- A methanol production facility, including syngas shift, acid gas removal, methanol synthesis, and methanol storage tanks.
- A fired heater to superheat steam from the methanol plant.

*Modifications:*

- The fuel gas production train is reduced in size, since it meets the average syngas demand rather than the peak implied by the maximum electrical output.
- Syngas is withdrawn from the fuel gas production train and is sent to methanol production.
- The gas turbine is modified to cofire liquid methanol.
- Methanol synthesis purge gas is burned in the HRSG to raise the temperature of the gas turbine exhaust gas.
- A nonreheat steam cycle is used. The HRSG and steam turbine are modified accordingly.
- Steam from the methanol synthesis plant is inducted into the steam turbine at an intermediate point.

As with the fuel gas production train, integrating heat recovery from the methanol plant with the steam power cycle improves the efficiency of the power plant as a whole. Thus, some adjustments to the methanol plant heat recovery design are warranted to obtain the best possible plant heat rate. Saturated steam at 250 °C (482 °F) is raised in the Lurgi reactor vessel and in the shift plant cooling train, which also heats boiler feedwater for both plant areas.

Approximately 1/4 of the purge gas from the methanol synthesis loop is devoted to superheating the saturated steam. The remaining 3/4 of the purge gas is sent to the HRSG to be burned in the gas turbine exhaust stream. The purge gas is sent to the HRSG rather than the gas turbine because of the operational simplicity of this arrangement.

**Plant Performance.** Energy and material balances for the plant were developed for both peak and baseload output levels to estimate performance and check operational behavior at steady-state conditions using the ASPEN process analysis software package, supplemented by user-written FORTRAN subroutines and stand-alone computer programs. Tables 5 and 6 summarize important plant performance information, including major material and power flows. Peak output is 580 MW and baseload ouput is 323 MW, resulting in an as-designed baseload/peak output ratio of 0.55. During the peak period methanol is consumed at a rate of 21.3 kg/s (169,000 lb/hr), allowing a peaking period of eight hours ($\tau_p = 0.33$).

**Table 5 Summary of constant-output plant areas**

| | | |
|---|---|---|
| Gasification | | |
| Coal feed rate | 3550 tn/d | (3920 tpd) |
| Gasification section pressure | 4240 kPa | (615 psia) |
| Oxygen flow | 37.6 kg/s | (299,000 lb/hr) |
| Crude gas flow | 97.6 kg/s | (775,000 lb/hr) |
| Crude gas temp. | 1330 C | (2430 F) |
| Crude gas HHV | 9780 kJ/kg | (4210 Btu/lb) |
| Clean, dry fuel gas flow | 75.6 kg/s | (600,000 lb/hr) |
| Methanol Synthesis | | |
| Total syngas feed, (dry) | 16.4 kg/s | (130,000 lb/hr) |
| Saturated steam prod. | 11.6 kg/s | (91,700 lb/hr) |
| Methanol production | 6.9 kg/s | (55,100 lb/hr) |
| Purge gas production | 1.1 kg/s | (8850 lb/hr) |
| Fuel-grade methanol HHV | 21,700 kJ/kg | (9300 Btu/lb) |

**Table 6 Summary of combined-cycle performance**

| | Peak Output | Baseload Output |
|---|---|---|
| Fuel gas temp.,C (F) | 299 (570) | 299 (570) |
| Moisture in fuel gas, wt % | 28.2 | 28.2 |
| Saturated fuel gas flow, kg/s (lb/hr) | 82.5 (655,000) | 82.5 (655,000) |
| Methanol flow, kg/s (lb/hr) | 21.3 (169,000) | 0 |
| Main steam flow, kg/s (lb/hr) | 223 (1,770,000) | 170 (1,350,000) |
| Steam conditions, MPa / C | 10.1 / 538 | 7.9 / 477 |
| (psia/ F) | (1470 / 1000) | (1140 / 891) |
| HRSG stack temp., C (F) | 126 (258) | 128 (262) |
| Gas turbine net power, MW | 392 | 210 |
| Steam turbine net power, MW | 257 | 179 |
| Internal plant power use, MW | 69 | 66 |
| Net plant output, MW | 580 | 323 |

**Table 7 Comparison of efficiencies of cyclically operated plants**

| | Peak | Baseload | Average |
|---|---|---|---|
| GCC/Methanol | 0.35 | 0.32 | 0.33 |
| GCC (Load-following) | 0.38 | 0.32 | 0.34 |
| Baseload GCC + Peaking GT | 0.35 | 0.38 | 0.37 |
| Baseload GCC + Peaking CC | 0.40 | 0.38 | 0.38 |
| Combined Cycle | 0.43 | 0.39 | 0.40 |

Note: Efficiencies are based upon a duty cycle with $\tau_p = 0.33$, $L_b/L_p = 0.55$ and are reported on the basis of higher heating value (HHV).

Overall electrical conversion efficiencies of the GCC/methanol plant and several other plants are given in Table 7. For the 24-hour duty cycle ($\tau_p = 0.33$, $L_b/L_p = 0.55$), the time-averaged efficiency is 33 percent, or 10,860 kJ/kWh (10,246 Btu/kWh) based on coal higher heating value. The GCC/methanol plant is one percentage point less efficient than the cycled GCC plant, showing the effective penalty in efficiency due to methanol storage. Baseload coal plants with gas turbines or combined cycles meeting the peak loads are more efficient since the baseload plants operate at full efficiency for the entire period. A stand-alone combined cycle has the highest overall efficiency.

The contribution of the steam and purge gas flows from the methanol plant to total plant output is relatively small in absolute terms. However, if these flows were not sent to the power block, steam turbine output would drop by 6 percent (16 MW) at peak load, in turn causing net plant output to drop by 2.7 percent. At baseload, the contribution of methanol plant byproduct streams would be about 5 percent. The time-averaged efficiency of the GCC/methanol plant would thus drop by over one percentage point (to 32 percent) if the methanol plant streams were not used.

Clearly, recovery of the energy flows from the methanol plant is needed to achieve the best possible plant efficiency. Because the material flows are not large compared to flows in the power block, they do not significantly perturb design conditions there. This conclusion holds for any GCC/methanol plant having $L_b/L_p \geq 0.5$ because its methanol plant will be smaller (relative to the fuel gas plant) than the methanol plant in this GCC/methanol plant design.

## Summary

This study has developed one potential intermediate-load, coal power plant design based on a gasification combined-cycle power plant that allows load cycling without thermal cycling of the coal handling and conversion equipment. The gasification train produces a steady output of syngas, a portion of which is stored via conversion to liquid methanol, and the combined-cycle portion of the plant cycles to meet variable electrical demand.

An analysis of levelized electricity production costs, not including operation and maintenance costs, indicates:

- A GCC/methanol plant with a single cycling generation facility is the preferred configuration. The additional cost of a separate generation facility outweighs its advantage in efficiency.
- At certain duty cycles, a GCC/methanol plant may have a lower levelized cost than typical utility alternatives as premium fuels increase relative to coal prices.
- The duty cycles for which a GCC/methanol plant appear economical have peaking periods of about one to eight hours of a daily cycle ($0.05 < \tau_p < 0.33$), and cover nearly the full range of baseload/peak load ratio.

At today's assumed prices the GCC/methanol plant does not have the lowest levelized electricity production cost at any duty cycle. Levelized premium fuel prices would have to rise to about four times the unit energy cost of coal before the GCC/methanol plant could be competitive.

The preceding conclusions need further definition, as the plant cost estimates are of a highly preliminary nature. However, the analytical methodology developed to investigate the influence of plant duty cycle is unique and could be of significant value in assessing other generation alternatives.

Based on the results of the screening study, a GCC/methanol plant was designed for a peaking period of eight hours and for a nominal baseload/peak load ratio of 0.5. A time-averaged thermal efficiency of about 1/3 was found for the design duty cycle.

## Acknowledgments

This research was supported by the Electric Power Research Institute under contract RP 8000-5. Prof. Robert H. Eustis, principal investigator, and Dr. Michael J. Gluckman, contract manager at EPRI, both provided a great deal of technical guidance and assistance in the completion of this work. This work also benefited from the guidance of an advisory committee whose members were: Dr. Berkely Davis of General Electric, Tom Matchak of Fluor, and Dale Simbeck of SFA Pacific. Their contributions were very helpful and were most appreciated.

## References

Brown, W. R., Moore, R. B., and Klosek, J., 1989, "Coproduction of Electricity and Methanol," *Proceedings: Eighth Annual EPRI Contractor's Conference on Coal Gasification* (Palo Alto, CA, Oct. 19-20, 1988), EPRI GS-6485, Electric Power Research Institute, Palo Alto, CA.

Erbes, M. R., 1986, "Phased Construction of Integrated Coal Gasification Combined Cycle Power Plants," Ph.D. Thesis, Stanford University, Stanford, CA.

Eustis, R. H., and Paffenbarger, J., 1990, *A Coal Gasification Combined-Cycle Power Plant With Methanol Storage*, EPRI GS/ER-6665, prepared by Stanford University, Electric Power Research Institute, Palo Alto, CA.

Krewinghaus, A. B., and Nager, M., 1988, "Start-up and Operating Experience With the Shell Coal Gasification Demonstration Plant," *Proceedings: Seventh Annual EPRI Contractor's Conference on Coal Gasification* (Palo Alto, CA, Oct. 28-29, 1987), EPRI AP-6007-SR, Electric Power Research Institute, Palo Alto, CA.

Matchak, T. A., and Lawrence, C. H., 1982, *Economic Assessment of the Impact of Plant Size on Coal Gasification Combined-Cycle Plants*, EPRI AP-3084, prepared by Fluor Engineers, Inc., Electric Power Research Institute, Palo Alto, CA.

Matchak, T. A., Rao, A. D., Ramanathan, V. R., and Sander, M. T., 1984, *Cost and Performance for Commercial Applications of Texaco-Based Gasification Combined-Cycle Plants*, 2 vols, EPRI AP-3486, prepared by Fluor Engineers, Inc., Electric Power Research Institute, Palo Alto, CA.

Mednick, R. L., Weatherington, R. W., and Wright, T. L., 1988, "Methanol Economics in Cycling IGCC Operation," *Proceedings of 13th Annual EPRI Conference on Fuel Science and Conversion* (Santa Clara, CA, May 19, 1988), Electric Power Research Institute, Palo Alto, CA.

Mueller, R., and Karg, J., 1987, "Assessment of Coal Gasification Systems for Combined-Cycle Power Plants," *Proceedings of the Joint ASME/IEEE Power Plant Generation Conference*, (Miami Beach, FL, Oct. 4-8, 1987).

Paul, E. V., Dharia, D. J., and Fay, S. J., 1983, *H-Coal and Coal to Methanol Liquefaction Processes—Process Engineering Evaluation*, EPRI AP-3290, prepared by Stone and Webster Engineering Corp., Electric Power Research Institute, Palo Alto, CA.

Phillips, J. N., 1986, "A Study of the Off-Design Performance of Integrated Coal Gasification Combined-Cycle Power Plants," Ph.D. Thesis, Stanford University, Stanford, CA.

Simbeck, D. R., Dickenson, R. L., and Oliver, E. D., 1983, *Coal Gasification Systems: A Guide to Status, Applications, and Economics*, EPRI AP-3109, prepared by Synthetic Fuels Associates, Electric Power Research Institute, Palo Alto, CA.

Spencer, D. F., Alpert, S. B., and Gilman, H. H., 1986, "Cool Water: Demonstration of a Clean and Efficient New Coal Technology," *Science*, Vol. 232, No. 609, pp. 609-612.

TAG, 1986, *Technical Assessment Guide, Vol. 1, Electricity Supply—1986*, EPRI P-4463-SR, Electric Power Research Institute, Palo Alto, CA.

Webb, R. M., and Sundstrom, D. G., 1988, "The Dow Syngas Project Start-up and Initial Operations," *Proceedings: Seventh Annual EPRI Contractor's Conference on Coal Gasification* (Palo Alto, CA, Oct. 28-29, 1987); EPRI AP-6007-SR, Electric Power Research Institute, Palo Alto, CA.

Yeager, K. E., 1989, "Power Generation to Meet the Competitive Challenge," *Proceedings: 1989 Conference on Technologies for Producing Electricity in the Twenty-First Century* (San Francisco, CA, Oct. 30-Nov. 2, 1989), Electric Power Research Institute, Palo Alto, CA.